*Gas Turbine Laboratory*
*Department of Aeronautics and Astronautics*
Massachusetts Institute of Technology
*Cambridge, MA 02139*

Final Report

NASA NRA Grant NAG3-2101

entitled

# Three-dimensional Aerodynamic Instability in Multi-stage Axial Compressors

Prepared for

Dr. Kenneth Suder
Technical Monitor

NASA Glenn Research Center
21000 Brookpark Road
Cleveland 44135 - 3191

Principal Investigator: Dr. Choon-Sooi Tan

May, 2003

## Table of Content

## ***ABSTRACT***

Four separate tasks are reported. The first task is on "A Computational Model for Short Wavelength Stall Inception and Development In Multi-Stage Compressors"; the second task is on "Three-dimensional Rotating Stall Inception and Effects of Rotating Tip Clearance Asymmetry in Axial Compressors"; the third task is on "Development of an Effective Computational Methodology for Body Force Representation of High-speed Rotor 37"; and the fourth task is on "Development of Circumferential Inlet Distortion through a Representative Eleven Stage High-speed axial compressor". The common theme that threaded throughout these four tasks is the conceptual framework that consists of quantifying flow processes at the fan/compressor blade passage level to define the compressor performance characteristics needed for addressing physical phenomena such compressor aerodynamic instability and compressor response to flow distoriton with length scales larger than compressor blade-to-blade spacing at the system level. The results from these two levels can be synthesized to: (1) simulate compressor aerodynamic instability inception local to a blade rotor tip and its development from a local flow event into the nonlinear limit cycle instability that involves the entire compressor as was demonstrated in the first task; (2) determine the conditions under which compressor stability assessment based on two-dimensional model may not be adequate and the effects of self-induced flow distortion on compressor stability limit as in the second task; (3) quantify multistage compressor response to inlet distortion in stagnation pressure as illustrated in the fourth task; and (4) elucidate its potential applicability for compressor map generation under uniform as well as non-uniform inlet flow given three-dimensional Navier-Stokes solution for each individual blade row as was demonstrated in the third task.

The physical principles involved are as follows. The action of a blade row in the flow field which gives rise to pressure changes, flow turning, and energy exchanges can be achieved by replacing the blade row with an "equivalent" body force. The body force representation itself can be arrived at by averaging the flow equations across a blade passage. The key to suitable representation is the ability to characterize the body force in terms of the blade row flow dynamics. The requirements are: (i) the physical laws (mass, momentum and energy conservation) must be satisfied on a blade average basis (i.e. the effects of the pertinent blade-passage flow features must be reflected in the representation on a blade-passage average basis); (ii) there must be correct dependencies on geometry for its application in design environment; (iii) for steady-state axisymmetric flow, the blade-row must reproduce the overall pressure rise and turning angle; (iv) the body forces must be able to respond to unsteady three-dimensional flow variations; and (v) the model must be able to capture the correct time and length scales of the relevant flow events.

The concept of body force representation of blade-row is not new. However modern CFD tools now provide the means to establish such body force representation of blade-row/compressor on a rigorous basis. An implication from the results of this research program is the potential of the use of row-by-row body force representation in a multistage compressor for characterizing the operability and performance on a first principle basis.

## ***INTRODUCTION***

This document constitutes a final report on NASA GRC Grant No. NAG3-2101. It consists of four tasks. These are as follows:

Task I: A Computational Model for Short Wavelength Stall Inception and Development In Multi-Stage Compressors

Task II: Three-dimensional Rotating Stall Inception and Effects of Rotating Tip Clearance Asymmetry in Axial Compressors

Task III: Development of an Effective Computational Methodology for Body Force Representation of High-speed Rotor 37

Task IV: Development of Circumferential Inlet Distortion through a Representative Eleven Stage High-speed Axial Compressor

The work and the results from each of the Tasks are described in the order delineated in the above; each task is described in a manner that it is self-contained. Task II constitutes the Doctoral Dissertation on "Three-dimensional Rotating Stall Inception and Effects of Rotating Tip Clearance Asymmetry in Axial Compressors" by K. Gordon. The report ends with an overall summary. Task III and IV are partially supported by *Pratt & Whitney Aircraft Engine, a Division of United Technologies Corporation, with Mr. M. Aubochon, Dr. R. Ni, and Dr. T. Shang serving as technical monitors.*

# TASK I: A COMPUTATIONAL MODEL FOR SHORT WAVELENGTH STALL INCEPTION AND DEVELOPMENT IN MULTI-STAGE COMPRESSORS


## SUMMARY

TASK I presents a computational model for simulating axial compressor stall inception and development via disturbances with length scales on the order of several (typically about three) blade pitches. The model was designed for multi-stage compressors in which stall is initiated by these "short wavelength" disturbances, also referred to as spikes. The inception process described is fundamentally nonlinear, in contrast to the essentially linear behavior seen in so-called "modal stall inception". The model was able to capture the following experimentally observed phenomena: (1) development of rotating stall via short wavelength disturbances, (2) formation and evolution of localized short wavelength stall cells in the first stage of a mismatched compressor, (3) the switch from long to short wavelength stall inception resulting from the re-staggering of the inlet guide vane, (4) the occurrence of rotating stall inception on the negatively sloped portion of the compressor characteristic. Parametric investigations indicated that (1) short wavelength disturbances were supported by the rotor blade row, (2) the disturbance strength was attenuated within the stators, and (3) the reduction of inter-blade row gaps can suppress the growth of short wavelength disturbances. It is argued that each local component group (rotor plus neighboring stators) has its own instability point (i.e. conditions at which disturbances are sustained) for short wavelength disturbances, with the instability point for the compressor set by the most unstable component group.


## NOMENCLATURE

$F$ : Body force per unit mass
$K_t$ : Throttle coefficient
$P$ : Static pressure
$U$ : Mid-span blade speed
$V$ : Velocity
$c$ : Pseudo-speed of sound
$x, \theta, r$ : Cylindrical coordinates
$\alpha$ : Blade metal angle
$\beta$ : Flow angle, $\tan(\beta) = V_\theta / V_x$
$\delta$ : Loss of stall margin, defined by Eq. (5)
$\rho$ : Density
$\phi$ : Flow coefficient, $V_x/U$
$\Psi_{ts}$ : Total-to-static pressure rise, $(P_{exit} - P_{t,inlet})/\rho U^2$
$\Psi_{tt}$ : Total-to-total pressure rise, $(P_{t,exit} - P_{t,inlet})/\rho U^2$
$\Omega$ : Rotating frequency of the blade rows

### Subscripts

$t$ : Stagnation property
$x, \theta, r$ : Axial, circumferential, radial component

## INTRODUCTION

Experiments performed on compressor rigs (Day, 1993, Longley et al., 1996, Silkowski, 1995, Tryfonidis et al., 1995, Weigl et al., 1997, Camp and Day, 1997) and engines (Day et al., 1997) have demonstrated that there are two routes to rotating stall in axial compressors. The first is characterized by the growth of small amplitude, essentially two-dimensional long wavelength disturbances (on the order of the circumference) which extend axially through the compressor. These disturbances, referred to as modal stall waves, can be detected from 10 to more than 100 rotor revolutions prior to stall, and they rotate at 0.2

to 0.5 times the rotor speed (McDougall, 1988, Haynes et al., 1996, Tryfonidis et al., 1995). Two-dimensional linearized stability analyses (Moore, 1984, Moore and Greitzer, 1986, Weigl et al., 1997) give a useful description of the modal wave shape, phase speed and growth rate for many compressors.

The second route to rotating stall is characterized by the development of three-dimensional "spike" disturbances (Day, 1993, Silkowski, 1995). These are localized to the tip region of a specific rotor in a multi-stage compressor and have a length scale on the order of the blade pitch. Spikes initially rotate at 0.7 to 0.8 times the rotor speed, but slow to 0.2 to 0.5 times the rotor speed as they develop into a full stall cell. The time between first detecting a spike and the final stall cell is less than five rotor revolutions, much shorter than for modal-type stall development.

Short wavelength stall inception behavior can not be captured by current linearized stability analyses. Isolated rotor calculations performed by Hoying et al. (1998) have shown a causal link between the rotor tip leakage flow and the *formation* of the incipient spike disturbances found in experiments, but the calculations do not provide a framework by which to examine the *development* of these localized flow events into rotating stall. Furthermore, there is currently no methodology for assessing the controlling design parameters and conditions that set the stalling behavior of a multi-stage compressor with short wavelength disturbances. It is the lack of such capabilities that motivated us to undertake the work presented in this paper.

The technical goal was to develop the simplest computational flow model with the capability of simulating both types of stall inception and development in a multi-stage axial compressor, and use the model to assess the effect of design parameters on the compressor stability to short wavelength disturbances.

The paper is organized as follows: We first describe the formulation of the computational model and the procedure for using the model to simulate stall inception. Model adequacy is assessed by comparison with two- and three-dimensional linearized stability analyses and experimental data of short wavelength stalling behavior in matched and mismatched compressors. The model is then applied to explore the design parameters and conditions that control the stalling behavior of a multi-stage axial compressor. The implications of these results on the two different routes to rotating stall are discussed by developing the "local component group" concept, and relating this concept to the recent short wavelength stall arguments set forth by Hoying, et al. (1998), and Camp and Day (1997).

## COMPUTATIONAL MODEL

To simulate short wavelength disturbances, a model must be capable of describing the three-dimensional and non-linear aspects of the flow in a multi-stage environment. Direct use of a three-dimensional unsteady Navier-Stokes solver to compute the flow within all blade passages of a compressor is not computationally feasible, nor is it suited to our requirements. The approach taken here is to use body force distributions to represent the effects of the discrete blades on the flow field.

The body force approach is not new (Marble, 1964, Billet et al., 1988) and has been recently used by Escuret and Garnier (1994) and Longley (1997) to simulate the onset of rotating stall from long wavelength disturbances. The work presented here constitutes the first effort, as far as the authors know, to exploit the potential for simulating three-dimensional nonlinear instability for short wavelength disturbances in multi-stage compressors.

The modeled compression system consisted of an inlet duct, blade rows, inter-blade row gaps, an exit duct, and a plenum followed by a throttle (Fig. 1). The computational domain extended to the end of the downstream duct where the exit pressure was determined by the plenum and throttle dynamics. The flow was assumed to be incompressible, consistent with the low speed compressor experiments against which the model was compared. Key elements for modeling each component are detailed in the following sub-sections.

## Upstream Duct, Downstream Duct and Gaps

Flow in the blade-free regions was described by the unsteady three-dimensional Euler equations:

$$\frac{\partial}{\partial t}\begin{bmatrix} 0 \\ rV_x \\ rV_\theta \\ rV_r \end{bmatrix} + \frac{\partial}{\partial x}\begin{bmatrix} rV_x \\ rV_x^2 + rP/\rho \\ rV_xV_\theta \\ rV_xV_r \end{bmatrix} + \frac{\partial}{\partial \theta}\begin{bmatrix} V_\theta \\ V_\theta V_x \\ V_\theta^2 + P/\rho \\ V_\theta V_r \end{bmatrix} + \frac{\partial}{\partial r}\begin{bmatrix} rV_r \\ rV_xV_r \\ rV_\theta V_r \\ rV_r^2 + rP/\rho \end{bmatrix} = \begin{bmatrix} 0 \\ 0 \\ -V_\theta V_r \\ V_\theta^2 + P/\rho \end{bmatrix} \tag{1}$$

## Blade Rows

The pressure rise and the turning produced by each blade row were modeled by a body force field, distributed continuously around the circumference (Fig. 1). The blade region is assumed to consist of an infinite number of blades which restrict circumferential flow variations from redistributing. Tangential flow gradients can exist, but they do not affect the local flow dynamics in the blade row reference frame. The relative flow was therefore described by "locally axisymmetric" Euler equations with source terms depicting the body forces. In the absolute frame, these equations are given by

$$(\frac{\partial}{\partial t} + \Omega\frac{\partial}{\partial \theta})\begin{bmatrix} 0 \\ rV_x \\ rV_\theta \\ rV_r \end{bmatrix} + \frac{\partial}{\partial x}\begin{bmatrix} rV_x \\ rV_x^2 + rP/\rho \\ rV_xV_\theta \\ rV_xV_r \end{bmatrix} + \frac{\partial}{\partial r}\begin{bmatrix} rV_r \\ rV_xV_r \\ rV_\theta V_r \\ rV_r^2 + rP/\rho \end{bmatrix} = \begin{bmatrix} 0 \\ rF_x \\ -V_\theta V_r + rF_\theta \\ V_\theta^2 + P/\rho + rF_r \end{bmatrix} \tag{2}$$

where

$$(F_x, F_\theta, F_r) = \mathbf{F}(\mathbf{V}(x, \theta, r), x, r). \tag{3}$$

The additional operator $\Omega\ \partial/\partial\theta$ in Eq. (2) arises from the transformation of the time derivative from the rotational frame to the absolute frame. The assumption of an infinite number of blades is well based for perturbations with wavelengths much longer than the blade pitch (such as modal waves). For short wavelength disturbances, tangential redistribution within individual blade passages would be expected. The applicability of the model to simulate these disturbances will be made apparent during the model assessment.

With short wavelength spikes there is a potential for substantial axial and radial flow redistribution within the blade row. The body force field accounts for this at every point in the blade region by responding to the local flow conditions. This contrasts with previous body force representations (Escuret and Garnier, 1994, Longley, 1997) in which the force responded only to the flow at the blade row inlet. Details of how local body force relations were generated from prescribed axisymmetric pressure rise and turning characteristics are given in the appendix.

## Plenum and Throttle

Standard plenum and throttle dynamics were used to determine the pressure at the exit of the downstream duct (Greitzer, 1976). Since the plenum has little effect on the development of short wavelength disturbances, its volume was set to zero for the calculations reported, so the exit pressure was determined by the throttle relation

$$P_{exit} - P_{ambient} = K_t\phi^2 \tag{4}$$

where $P_{exit}$ is the pressure at the exit of the downstream duct.

## Numerical Method

To allow for a standard time marching method, a pseudo-compressibility term, $(\partial/\partial t\ +\ \Omega\ \partial/\partial\theta)rP/c^2\rho$, was added to the mass conservation equation. It was found that the phase speeds and growth rates of disturbances were not sensitive to $c$ when $c$ is sufficiently large ( $c > 10\phi$ ). Spatial discretization of the governing equations was based on the finite volume

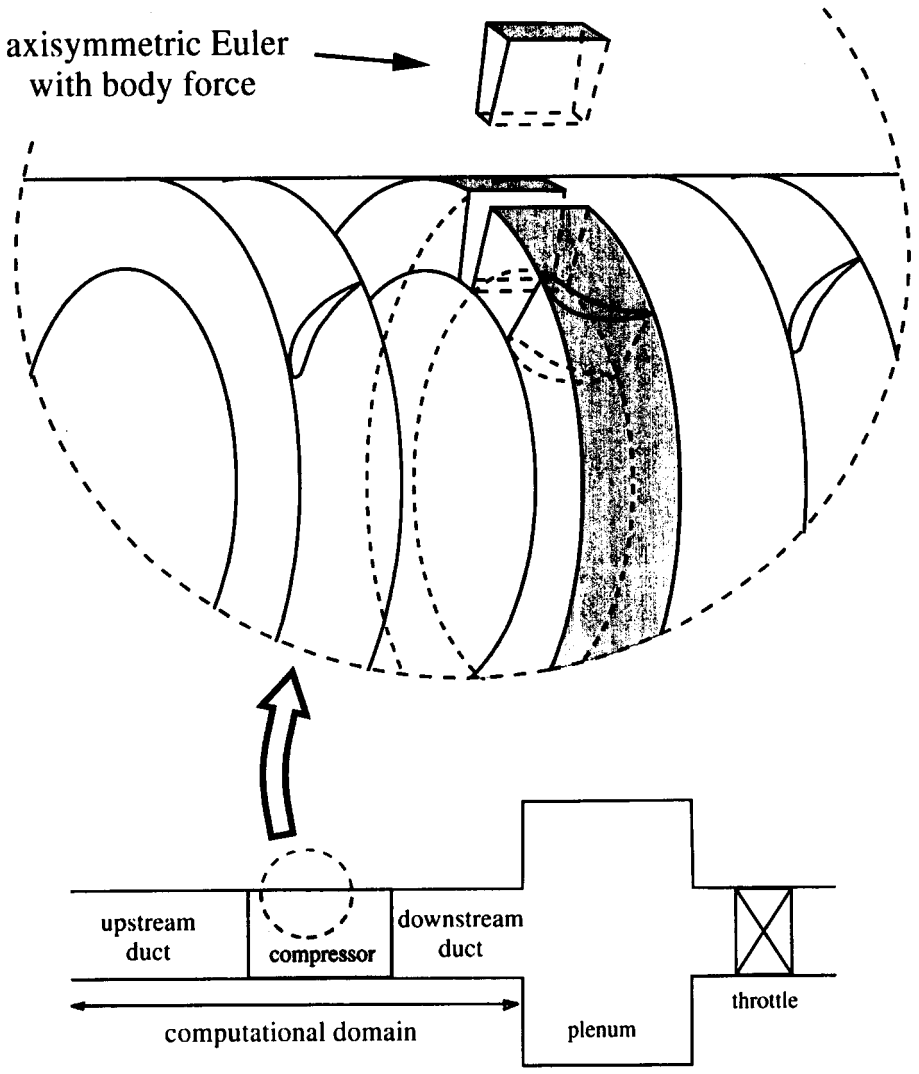


**Figure 1: Illustration of the blade row model in the compression system.**

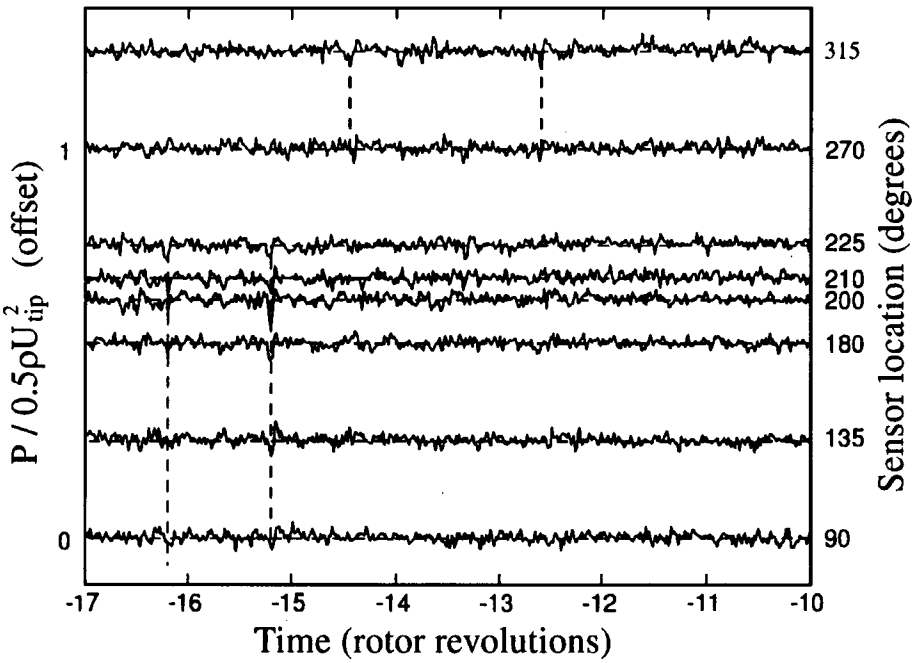


**Figure 2: Experimental evidence of tip-spikes prior to the development of stall at time=0. The pressure traces, from sensors at different circumferential positions, are shifted relative to first trace so that disturbances traveling at 71% of rotor speed line up vertically. Guide lines identify propagating spikes. (Park, 1994)**

method of Jameson et al. (1981). Since these were low speed calculations, only fourth order numerical smoothing was used. The temporal discretization used the four-stage Runge-Kutta scheme with a uniform time step to ensure a time-accurate solution.

## IMPLEMENTATION OF THE MODEL FOR COMPRESSOR INSTABILITY SIMULATIONS

This section addresses three issues concerning the use of the model to investigate compressor instability behavior: (1) appropriate initial flow disturbances used for initiating rotating stall, (2) the method for determining the stall point, (3) the procedure for differentiating between the two stall inception routes.

Two types of initial flow disturbances were used in the calculations. Long wavelength perturbations of small amplitude (less than 1% of the mean flow coefficient) were used to find the modal (linear) stability point. All other calculations used large amplitude spikes of small circumferential extent that were localized at the tip region of a rotor blade row. These spikes were based on the experimental observations by Park (1994) that such disturbances can appear in a rotor prior to the development of rotating stall (Fig. 2).

The spike disturbances were generated by prescribing an impulse to the rotor axial body force lasting for 0.1 rotor revolutions and traveling at the rotor speed. A disturbance was initiated at a random position about the circumference once every few rotor revolutions. The shape of the impulse (Fig. 3) was approximately 10 degrees wide, corresponding to about one blade passage in a 54 blade rotor. The magnitude of the force was equivalent to that effecting zero pressure rise in the outer 30% span of a blade passage, which was observed to precede stall in the simulations calculated by Hoying, et al. (1998).

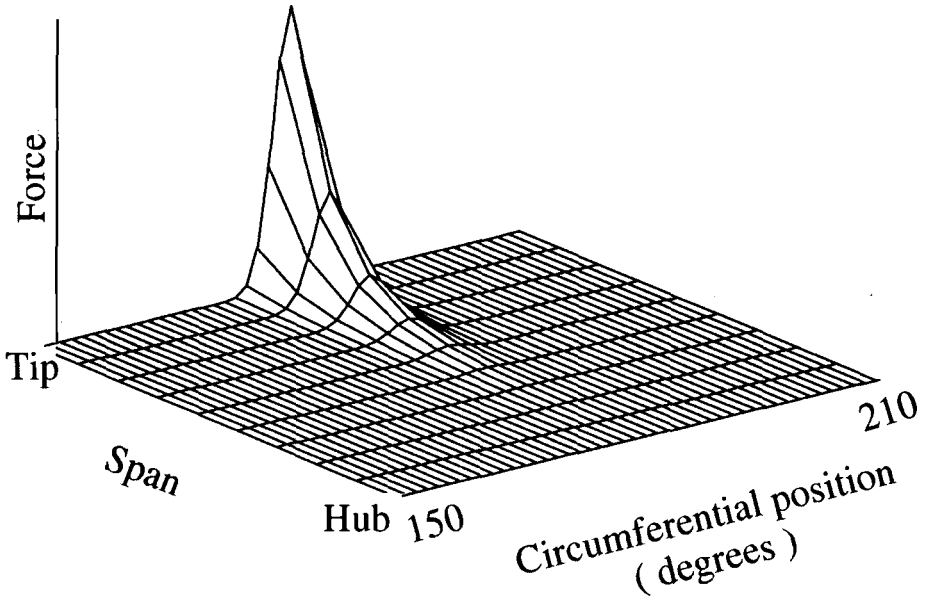


**Figure 3: Axial body force impulse used to generate spike-shaped disturbances.**

To determine the compressor stall point, the disturbances were first imposed on a steady flow at a fixed throttle coefficient known to produce a stable flow field. This procedure was repeated for lower throttle conditions until the disturbances no longer decayed, but rather grew into a full stall cell. A single simulation with a continuously closing throttle was avoided because any numerically acceptable closing rate would still be much faster than that used in experiments.

Once the stall point was determined, velocity traces were used to determine the route by which the stall cell formed. Long wavelength inception was characterized by decay of the spike disturbance followed by growth of a long wavelength stall cell. Figure 4 shows an example of flow coefficient traces leading to stall via this route. It is noted that this is not identical to modal stall behavior due to the large amplitude of the initial disturbance. For short wavelength stall inception (Fig. 5) the spike disturbance shape remained coherent and led directly to stall without decay.

## MODEL ASSESSMENT

The adequacy of the model and the above methodology were assessed by demonstrating that the model reproduced (1) modal stall behavior as predicted by linearized stability calculations, and (2) experimentally observed short wavelength instability phenomena. The short wavelength stall assessments address the question of whether a model based on the assumption of an infinite number of blades can be employed to describe flow events with a length scale of only two to three blade passages.

Three multi-stage experiments involving short wavelength disturbances were used for the latter assessment. The first showed a spike disturbance developing into full-scale rotating stall in a matched compressor. The second showed the localization of three-dimensional stall cells in the first stage of a mismatched compressor. The third showed a change from long wavelength to short wavelength stall inception routes as the incidence on the first rotor was increased; thereafter, short wavelength stall inception occurred at a constant rotor tip incidence.

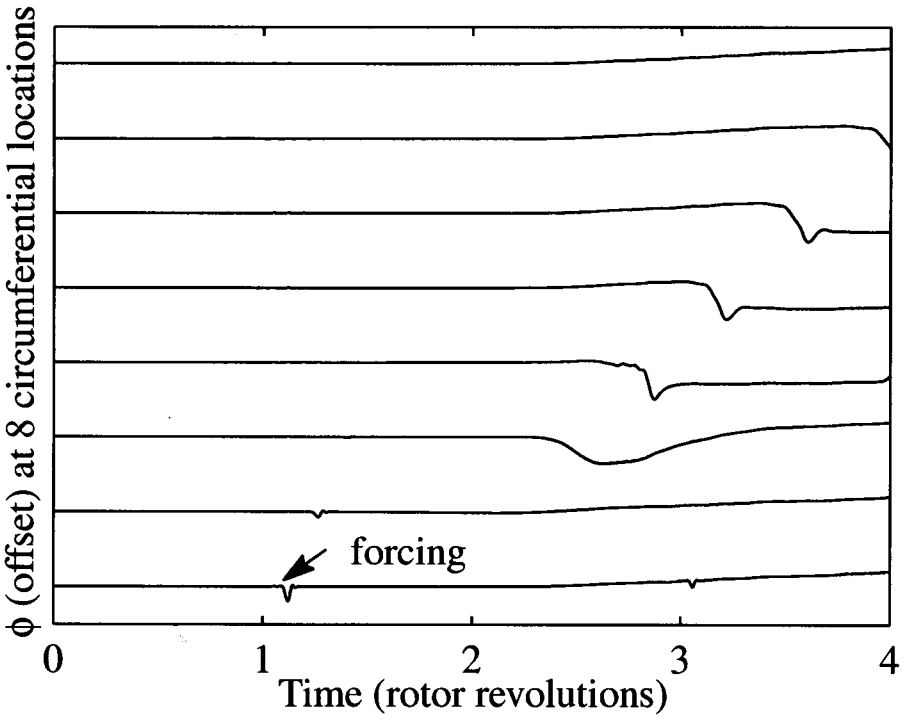


**Figure 4: Computed flow coefficient traces for a compressor stalling via long wavelength route.**

All calculations used 9 radial and 256 circumferential cells. Short wavelength events occupying 2 to 3 blade pitches in the experiments were adequately resolved over 10 to 14 cells in the tangential direction.

## Comparisons with Linear Theories

The computational model was first compared separately against two-dimensional and three-dimensional linearized theories for representative compressor geometries. The figures of merit were the growth rate and phase speed of an imposed sinusoidal perturbation with a wavelength equal to the circumference. The two-dimensional case used the parameters similar to a four-stage core compressor. The three-dimensional validation used the geometry of a single-stage fan with a hub-to-tip ratio of 0.43. Computed growth rates and phase speeds are compared in Table 1 with results of two-dimensional (Moore and Greitzer, 1986) and three-dimensional linearized models.

The excellent quantitative agreement between the computational model and the linearized analyses demonstrate that the present method can accurately capture modal instability inception and development. The more important aspect is the additional ability to reproduce short wavelength events, which we proceed to demonstrate next.

## Simulation of Short Wavelength Stall Inception

Measurements of short wavelength disturbances growing into fully developed rotating stall in a low speed compressor (Silkowski, 1995) were used as an experimental assessment of the computational model. The compressor (run at the General Electric Aerodynamics Research Laboratory) had a hub-to-tip ratio of 0.85, and consisted of an inlet guide vane (IGV) followed by four identical stages. A schematic which shows the scale of the blades and inter-blade axial gaps is given in Fig. 6. Details of the compressor geometry can be found in Wisler (1981).

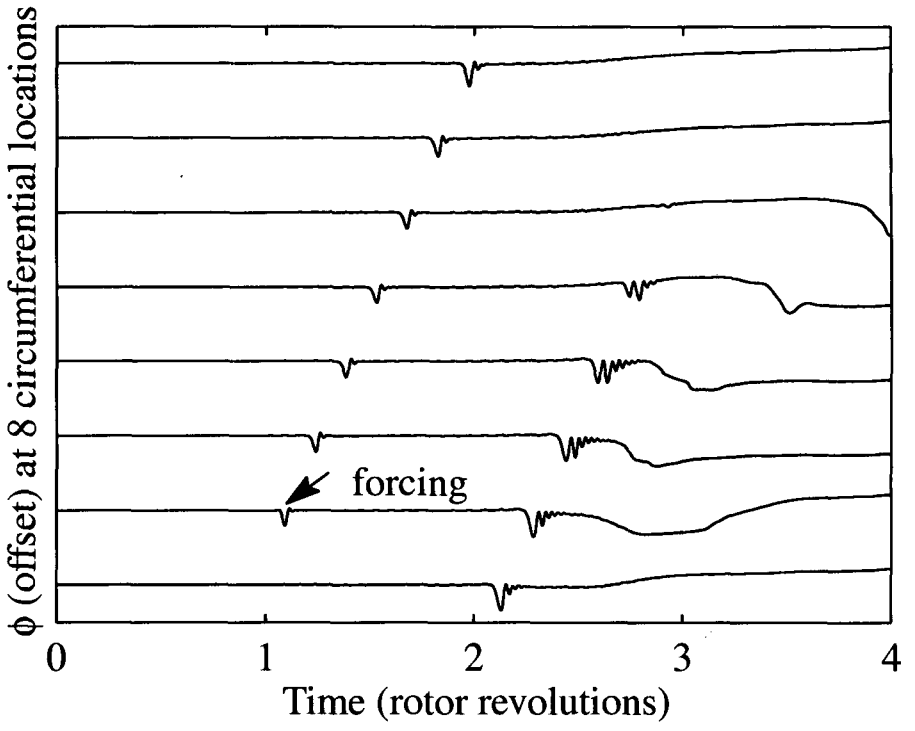


**Figure 5: Computed flow coefficient traces at the tip of the first rotor inlet for a compressor stalling via short wavelength route.**

The pressure rise characteristics used for every rotor and stage in the model are shown in Fig. 7. The rotor characteristic were higher at the tip than the hub to satisfy radial equilibrium at the rotor exit with a nearly uniform axial velocity profile, which was observed in the experiment. The unstalled portions (to the right of the peaks) were taken directly from the experiment. The criteria for selecting the characteristic shapes to the left of the peak, as well as information on their effect on short wavelength stall phenomena, are provided in Gong (1998). The point to be emphasized is that the qualitative stalling behavior is not strongly dependent on the precise curve shapes, other than the requirement that a trough exists in the rotor characteristic at a positive flow coefficient.

This compressor stalled via short wavelength disturbances, as shown by the axial velocity traces around the circumference (Fig. 8). The computational model qualitatively reproduced this behavior, as shown by the flow coefficient traces in Fig. 5 which are plotted to the same time scale. The same feature of a spike-shaped disturbance growing in amplitude prior to the formation of a fully developed stall cell is shown. Table 2 quantitatively summarizes the key figures of merit used for the assessment. Specifically, the rotating speed of the spike and the time taken for the spike to transition to the final stall cell were in good agreement.

The computed results show the time sequence for short wavelength stall inception events. The three-dimensional spike grows in amplitude until it triggers the formation of an incipient long wavelength disturbance, which then grows into the final essentially two-dimensional stall cell. During this process the short wavelength disturbances travel ahead of the stall cell, due to their faster rotational speed, and eventually decay in the region of higher local mass flow.

**Table 1: Comparison between modal growth rates and phase speeds for the present computational model and linearized analyses.**

| | growth rate | phase speed / rotor speed |
|---|---|---|
| Computational model | -0.26 | 0.27 |
| 2D linear model | -0.26 | 0.27 |
| Computational model | -0.11 | 0.10 |
| 3D linear model | -0.10 | 0.10 |

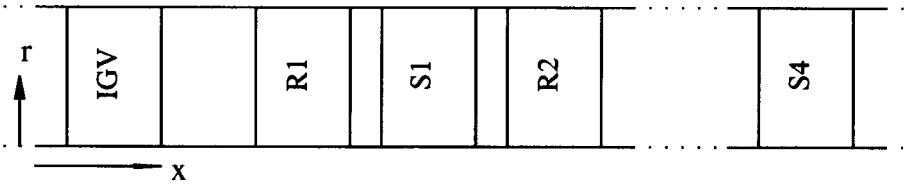


**Figure 6: A scale schematic of the GE compressor represented by nine blade rows and eight gaps.**

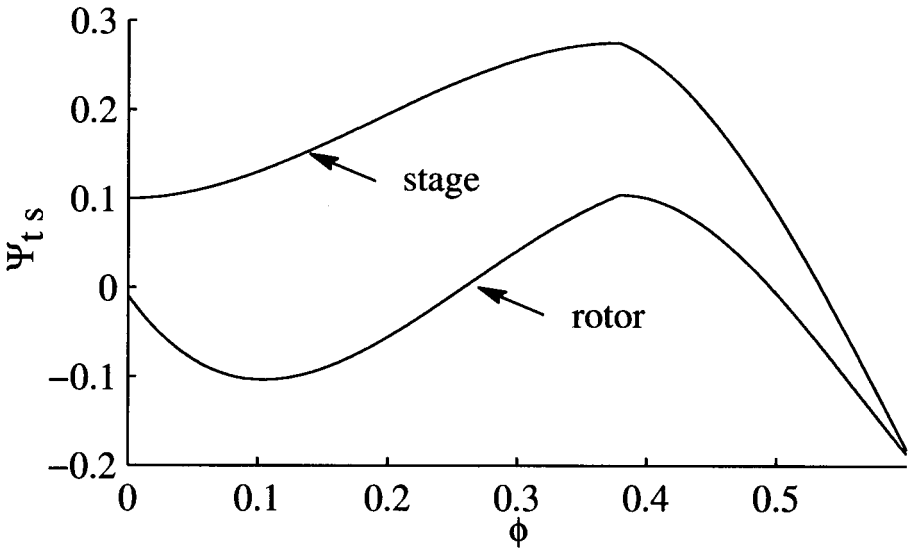


**Figure 7: The modeled axisymmetric pressure rise characteristic for each stage of the GE matched compressor.**

## Stall In A Mismatched Compressor

Another assessment of the model's ability to describe short wavelength stall behavior was performed for a mismatched compressor (Silkowski, 1995). By re-staggering the second through fourth rotors of the GE compressor rig so that their stage characteristics peaked at a lower flow coefficient (shown by the solid lines in Fig. 9), one or more fully developed short wavelength stall cells could be localized in the first stage. Note that stall (defined as when asymmetric flow disturbances were no longer suppressed) occurred at the same flow coefficient as for the matched configuration. The short length scale

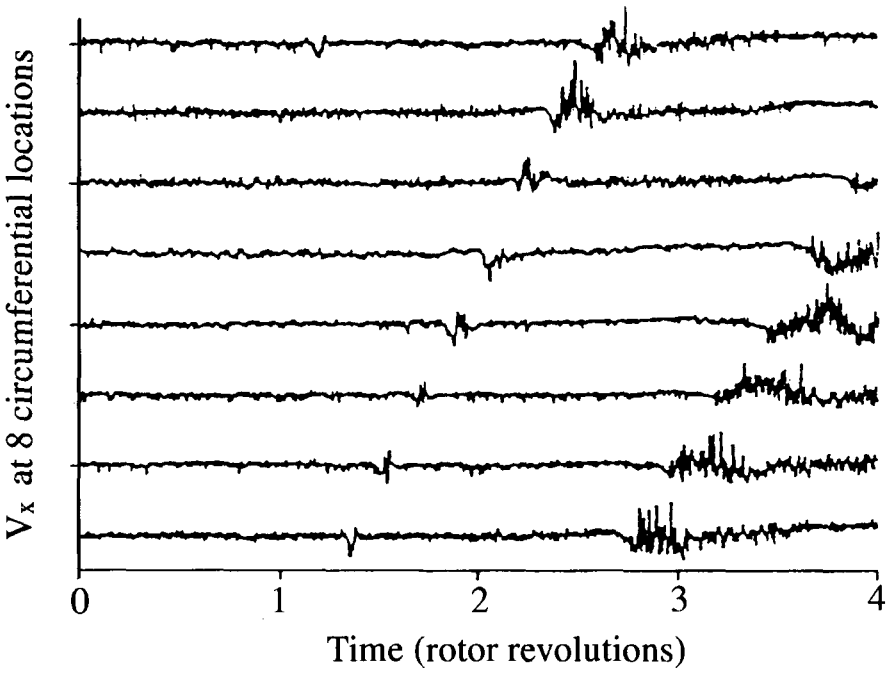


**Figure 8: Measured axial velocity traces at the tip of the first rotor inlet during stall inception (Silkowski, 1995).**

cells were prevented from growing into a long wavelength stall cell because of the stabilizing influence of the rear stages. The compressor characteristic behaved "progressively" in that the pressure rise increased and decreased smoothly without hysteresis as the overall mass flow was changed, as shown by the solid circles in Fig. 9. The number of localized cells increased from one to twelve as the flow rate decreased, until finally at a sufficiently low flow, a long wavelength full-scale rotating stall cell developed which extended through the entire compressor.

The computations carried out qualitatively demonstrated the progressive characteristic behavior as shown by the open circles in Fig. 9. Spike disturbances were periodically forced every rotor revolution, but only a limited number would grow into fully developed part-span stall cells, each of equal size. As the throttle was closed, the maximum number of disturbances that would develop into stall cells increased, as indicated on the figure. Disturbances imposed in excess of the maximum amount existed only as transients and decayed within one rotor revolution. The computed width of the localized stall cells compared well with the experiment, as indicated by the velocity traces in Figs. 10 and 11. The overall assessment criteria for the mismatched configuration are summarized in Table 3.

The roles of the rotor and stator in short wavelength stall can be understood better by examining the detailed structure of a localized cell. Figure 12 shows the computed axial velocity contours in a small segment of the first stage annulus where the cell is localized in the tip region. The flow deficit grows stronger through the rotor and diminishes in the stator, indicating that spikes are supported by the rotor and that the stator has a stabilizing influence.

## Switch Between Stall Routes and Unique Incidence For Spikes

Experiments performed by Camp and Day (1997) demonstrated that the route leading to stall could switch from long to short wavelength as the incidence on the first rotor was altered by changes in IGV stagger angle. They also showed that the incidence at the rotor tip is constant for all cases where stall occurred via spikes. Capturing this set of observations with the computational method gives another test of the model's ability to accurately predict short *and* long wavelength stall events.

**Table 2: Comparison of key features of the short wavelength stall inception for the GE matched configuration.**

| | Measurement | Computation |
|---|---|---|
| Stall Inception Route | Spike | Spike |
| Rotating Speed of Spike | 70-73% | 83% |
| Rotating Speed of Final Stall Cell | 45% | 20% |
| Transition Time (rotor revolutions) | about 3 | about 3 |

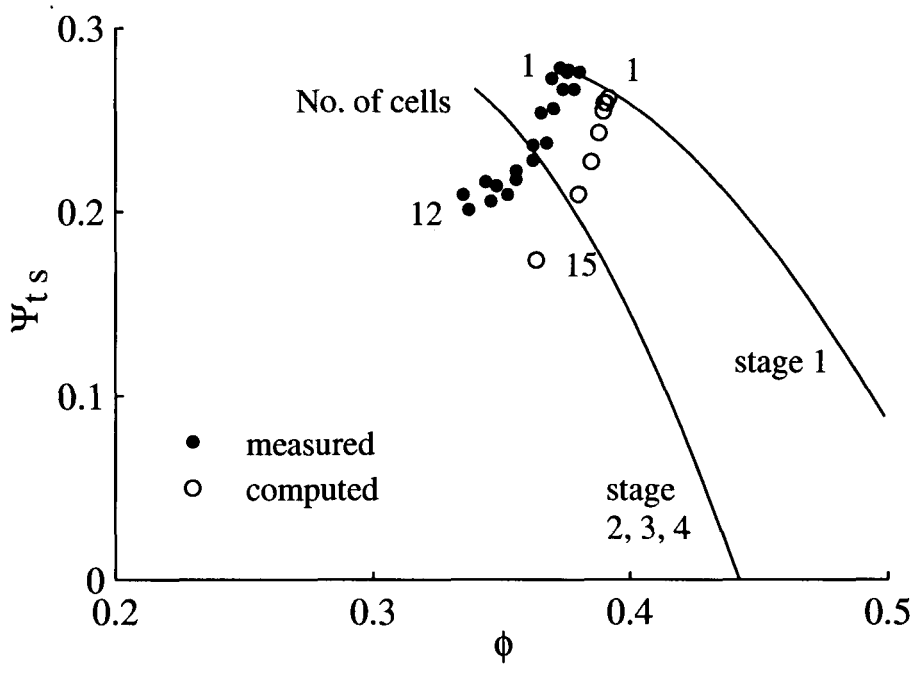


**Figure 9: Measured and computed stage characteristics for the GE mismatched compressor. Circles denote the progressive stall which deviates from the axisymmetric characteristic (solid line).**

The simulations were made using the matched GE compressor as the baseline configuration. The amplitude of force impulses was kept constant for all simulations. IGV stagger angle variations were chiefly reflected in the modified first stage pressure rise characteristics. Figure 13 shows these characteristics as well as the stall points, the corresponding incidences at the tip of the first rotor, and the types of stall inception routes. The trends are very similar to the observations made by Camp and Day (Fig. 14), in particular the condition of constant rotor incidence value for all cases of short wavelength stall inception.

In summary, the model reproduced both short wavelength and long wavelength stalling trends from previously accepted

**Table 3: Comparison of the short wavelength progressive stall behavior for the GE mismatched configuration.**

| | Measurement | Computation |
|---|---|---|
| location | first stage rotor tip | first stage rotor tip |
| width of spike | 2-3 pitches (out of 54) | 1/20 annulus (2.7 pitches) |
| rotating speed | 70-73% | 83% |
| progressive stall | yes | yes |
| no. of stall cells | 1 to 12 | 1 to 15 |

analytical results and experimental measurements, implying that the body force model gives a good description of both modal and spike initiated stalling events. The computational method will now be applied to determine the parameters that control multi-stage compressor instability behavior.

## PARAMETRIC STUDY

To identify the conditions that set the stall point of short wavelength disturbances in a multi-stage compressor, two aspects of the stall inception were examined: the types of initial flow disturbances, and the geometry of the compressor. The initial disturbances used were both small amplitude modal perturbations and large amplitude spike-shaped impulses localized to either the tip or hub of the first rotor. The amplitude of the tip-spikes and the rotor in which they appeared were also varied. Finally, the gap lengths between particular blade rows were varied to isolate the effects of different segments of the compressor.

The baseline configuration for all simulations was the GE four-stage compressor described above in the matched configuration. In this section changes to the stall point ($\delta$) are referenced to the computed modal stall point, which was at the peak of the pressure rise characteristic.

$$\delta = \frac{\phi_{stall} - \phi_{modal\ stall}}{\phi_{modal\ stall}} \tag{5}$$

A positive $\delta$ indicates that stall occurs at an operating point to the right of the peak, i.e. on the negatively sloped part of the overall characteristic.

### Type of initial disturbances

Stall point and type of stall inception were determined using three types of disturbances to the body force in the first rotor: (1) small amplitude, long wavelength; (2) large amplitude, spike-shaped at the tip; (3) large amplitude, spike-shaped at the hub. The shape and amplitude of these disturbances were the same as those described in the section on "Implementation of the Model".

The results are shown in Fig. 15 which shows the stall inception route and change in stall point for the three disturbance types. Only the tip-spike disturbances led to short wavelength stall inception and the largest loss in stall margin.

### Disturbance Amplitude

The effect of the disturbance size on the stalling behavior is shown in Fig. 16. The amplitude has been normalized by the baseline spike amplitude. The figure shows the following points:

1. Spike disturbances needed to be larger than a threshold amplitude to cause a short wavelength type inception. Below this amplitude, modal stall inception occurred.

2. The stall margin decreased as the disturbance amplitude increased. Spike inception always occurred on the negatively sloped part of the pressure rise characteristic.

3. There was an upper limit in the loss of stable flow range due to short wavelength disturbances for this configuration. Above a critical flow coefficient (given by $\delta = 7\%$) the compressor was stable to all spike disturbance sizes that were tried.

The computations show that compressor instability involving short length scale disturbances is inherently nonlinear, in contrast with long wavelength stall behavior which is essentially a linear phenomenon.

### Disturbance Location

In the matched compressor experiments, the short wavelength stall cells were always initiated in the first stage rotor. It was of interest to use the model to examine what happens when spikes are imposed in a rotor further downstream. The stalling behavior induced by tip-spikes in the third stage rotor is compared to the baseline in Fig. 17. Only disturbances in the first stage rotor were found to lead to short wavelength stall inception.

An explanation for this was offered by Camp (1995) who argued that rotors other than the first tended to be slightly less loaded when off-design because drops in the axial velocity increased the deviation of downstream stators more than that of the inlet guide vane. However, in the computed flow fields, the axial velocity profiles and incidence angles at all rotor inlets were essentially the same, so the loading differences between the first rotor and subsequent rotors were small. A different explanation for why spikes select the first rotor, at least in the present configuration, is suggested in the next section.

### Gap Lengths Between Blade Rows

In the GE compressor, the first rotor was unique in that the IGV-R1 gap was three times the length of all other gaps. The effect of rotor-stator gap length on the type and location of stall inception was numerically examined by independently varying the IGV-R1, R1-S1 and S1-R2 gaps. For all studies, the tip-spike impulses were imposed in the first rotor.

The results are shown in Fig. 18 which indicates that the stall point was set only by the spacing between the first rotor and its adjacent stators. Changing the S1-R2 gap had no effect on stall. Increasing the IGV-R1 or R1-S1 gaps destabilized the compressor to short length scale disturbances. Bringing the IGV or first stator sufficiently close to the first rotor suppressed the development of spikes entirely, so that stall occurred via long wavelength inception. This effect supports the notion that stators have a stabilizing influence on spikes.

Similar studies done for the mismatched GE configuration gave the same qualitative trends. It was also found that the size of the localized short wavelength stall cells increased with increasing R1-S1 gap, but were unaffected by the S1-R2 gap length.

All computations indicated that short length scale stalling behavior in a particular rotor was set by the adjacent blade row components, and not by the design of the rest of the compressor. The preference for spike stall in the first stage rotor is predominantly due to the relatively large IGV-R1 gap as compared to the gaps within the downstream stages.

## DISCUSSION

We have demonstrated that a computational model based on an infinite blade number representation of the blade-rows is capable of capturing the experimentally observed characteristics of short wavelength stall events. The significant features of this model are that it is three-dimensional, non-linear, represents each blade row individually, and uses finite amplitude spike-shaped disturbances to perturb the flow. During the model's development it was found that short length scale stall behavior would not be exhibited if any one of these aspects was missing. A model with these elements is therefore the simplest one that can be used to calculate the short wavelength stalling process.

Up to now we have not inquired as to the physical origin of the finite amplitude tip-spike disturbances observed by Park (1994). Insight is provided by the eight-blade passage isolated rotor calculations performed by Hoying et al. (1998). Simulations at stall demonstrated that the motion of the tip vortex in and out of a rotor passage produced spike-shaped disturbances. It would seem that discrete blade passage events, such as tip vortex dynamics, are likely the sources of the short length scale disturbances. These need to be computed with a discrete blade model, but the infinite blade number compressor model is adequate for determining the overall effect of these disturbances on compressor stability.

Spike disturbances may only be present in certain stages of a multi-stage machine since each rotor will generally have

different tip vortex dynamics. Recognizing where spikes exist, and only applying body force impulses to these stages, is an integral part of using the new model for compressor stall prediction. This aspect differs from linearized analyses which presume that infinitesimal disturbances of all wavelengths are always present throughout the compressor. Further research on the sources of spikes is needed to provide a rigorous basis for choosing initial disturbance locations.

Results from this paper indicate that the growth or decay of short length scale disturbances in a rotor is dependent on the the characteristics of that rotor and its neighboring stators. We refer to these three blade rows as a component group. Changing the spacing of the blade rows within a component group did affect stall point, the shape of the stall cell and stall route; however, changing the distance between the component group with spike forcing and the other blade rows had no effect. Further evidence comes from the GE assessment calculations which showed the first stage stalled via spikes at the same flow coefficient whether the downstream stages were mismatched or not. To find the stall point of a compressor with spike disturbances, it is thus only necessary to model each individual component group containing the spikes.

The model developed here may be used to determine specific short wavelength stall criteria which would be valuable for compressor design. The observation by Camp and Day (1997) that the rotor incidence at stall is constant for different blade loadings is augmented by our result that this incidence angle depends on the gaps within the component group. Further calculations may determine the link between blade spacing and the critical rotor incidence, and thus develop explicit rules for the prediction of short length scale stall in general component group designs.

## SUMMARY AND CONCLUSIONS

A three-dimensional computational model was developed for simulating the development of both long and short wavelength compressor instabilities. The adequacy of the model was quantitatively assessed against experimental measurements and known analytical results. In the model each individual blade row was represented by a body force formulated in terms of the blade's pressure rise and turning characteristics. The model has been used in a set of simulations to explore the parametric trend of the instability behavior of a four-stage low speed compressor.

The following conclusions were deduced from computed results based on applications of the model:

1. The necessary ingredients of the model are a three-dimensional, nonlinear, row by row representation of compressor response to finite amplitude disturbances. The short length scale stalling process can not be described if any one of these is missing.

2. Localized disturbances of sufficient amplitude (large enough to effect zero pressure rise in the tip) are required to initiate the short wavelength route to rotating stall.

3. The computations show instability occurring on the negatively sloped part of the overall compressor characteristic, in agreement with experimental measurements. This is in direct contrast to the predictions of the modal type of analyses in which the instability will occur at the peak of the characteristic.

4. The growth or decay of small length scale disturbances in a rotor is determined by the design characteristics of the isolated component group consisting of the rotor and its adjoining stators.

5. The point at which stall occurs (i.e. propagating asymmetrical disturbances do not decay) via the short wavelength route is set by the most unstable component group where large amplitude spike disturbances are present.

6. Closing the rotor-stator gaps within the most unstable component group suppresses the growth of short wavelength disturbances, thereby improving compressor stability.

## REFERENCES

Billet, G., Huard, J., Chevalier, P. and Laval, P., 1988, "Experimental and Numerical Study of the Response of an Axial Compressor to Distorted Inlet Flow," *ASME Journal of Fluids Engineering*, Vol. 110, pp. 355-360.

Camp, T. R. and Day, I. J., 1997, "A Study of Spike and Modal Stall Phenomena in a Low-Speed Axial Compressor," ASME paper, No. 97-GT-526.

Day, I. J., 1993, "Stall Inception in Axial Flow Compressors," *ASME Journal of Turbomachinery*, Vol. 115, pp. 1-9.

Day, I. J., Breuer, T., Escuret, J., Cherrett, M., and Wilson, A., 1997, "Stall Inception and The Prospects for Active Control in Four Speed Compressors," ASME paper, 97-GT-281.

Escuret, J. F. and Garnier, V., 1994, "Numerical Simulations of Surge and Rotating Stall in Multi-Stage Axial-Flow Compressors," AIAA paper, No. 94-3202.

Gong, Y., 1998, *A Computational Model For Rotating Stall and Inlet Distortions in Multi-stage Compressors*, Ph.D. Thesis, Massachusetts Institute of Technology.

Greitzer, E. M., 1976, "Surge and Rotating Stall in Axial Flow Compressors, Part I and II," *ASME Journal of Engineering for Power*, Vol. 98, pp. 190-217.

Haynes, J. M., Hendricks, G. J., and Epstein, A. H., 1994, "Active Stabilization of Rotating Stall in a Three-Stage Axial Compressor," *ASME Journal of Turbomachinery*, Vol. 116, pp. 226-239.

Hoying, D. A., Tan, C. S., Vo, H. D., and Greitzer, E. M., Role of Blade Passage Flow Structures in Axial Compressor Rotating Stall Inception, submitted for publication to the ASME TurboExpo98

Jameson, A., Schmidt, W., and Turkel, E., 1981, "Numerical Solutions of the Euler Equations by Finite Volume Methods with Runge-Kutta Time Stepping Schemes," AIAA paper, No. 81-1259.

Longley, J. P., Shin, H. W., Plumley, R. E., Silkowski, P. D., Day, I. J., Greitzer, E. M., Tan, C. S., and Wisler, D. C., 1996, "Effects of Rotating Inlet Distortion on MultiStage Compressor Stability," *ASME Journal of Turbomachinery*, Vol. 118, pp. 181-188.

Longley, J. P., 1997, "Calculating the Flowfield Behaviour of High-Speed Multi-Stage Compressors," ASME paper, No. 97-GT-468.

Marble, F. E., 1964, "Three-Dimensional Flow in Turbomachines," *Aerodynamics of Turbines and Compressors, Vol. X of High Speed Aerodynamics and Jet Propulsion*, Hawthorne, W. R., ed., Princeton University Press, Princeton, NJ., pp. 83-166.

McDougall, N. M., 1988, *Stall Inception in Axial Compressors*, Ph.D. Thesis, Cambridge University.

Moore, F. K., 1984, "A Theory of Rotating Stall of Multistage Axial Compressors: Part I-III," *ASME Journal of Engineering for Gas Turbines and Power*, Vol. 106, pp. 313-336.

Moore, F. K. and Greitzer, E. M., 1986, "A Theory of Post-Stall Transients in Axial Compression Systems: Part I,II," *ASME Journal of Engineering for Gas Turbines and Power*, Vol. 108, pp. 68-76, pp. 231-239.

Park, H. G., 1994, *Unsteady Disturbance Structures in Axial Flow Compressor Stall Inception*, Master's Thesis, Massachusetts Institute of Technology.

Silkowski, P. D., 1995, *Measurements of Rotor Stalling in a Matched and a Mismatched Multistage Compressor*, GTL Report No. 221, Gas Turbine Laboratory, Massachusetts Institute of Technology.

Tryfonidis, M., Etchevers, O., Paduano, J. D., Hendricks, G. F., and Epstein, A. H., 1995, "Prestall Behavior of Several High-Speed Compressors," *ASME Journal of Turbomachinery*, Vol. 117, pp. 62-80.

Weigl, H. J., Paduano, J. D., Frechette, L. G., Epstein, A. H. and Greitzer, E. M., 1997, "Active Stabilization of Rotating Stall and Surge in a Transonic Single Stage Axial Compressor," ASME paper, 97-GT-411.

Wisler, D. C., 1981, *Core Compressor Exit Stage Study, Volume IV - Data and Performance Report for the Best Stage Configuration*, NASA CR-165357, NASA Lewis Research Center.

## FORMULATION OF THE BODY FORCE FIELD

The derivation of the body force field used to represent the blade regions in the model is presented here. The forces, calculated separately for each blade row, must satisfy the following general requirements:

1. For steady state axisymmetric flow, the blade row model must reproduce the correct overall pressure rise and turning angle.

2. The body forces must be able to locally respond to unsteady three-dimensional flow variations.

The body force distribution depends on the following three characteristics of the blade row: the total pressure rise, $\Psi_{tt}(\phi, r)$, the exit flow angle, $\beta_{exit}(\phi, r)$, and the local angle along the blade camber line, $\alpha(x, r)$.

It is convenient to break the body force vector into two parts, one turning the flow without work being done, the other solely producing the total pressure rise:

$$\mathbf{F} = \mathbf{F_{turning}} + \mathbf{F_{\Psi_{tt}}} \tag{6}$$

The radial component of the body force, $F_r$, is assumed to be zero since the blades have little radial skewness. Only the axial component of $\mathbf{F_{\Psi_{tt}}}$ contributes to the pressure rise, so

$$F_{\Psi_{tt},\theta} = 0 \tag{7}$$

$$F_{\Psi_{tt},x}(x, r, \theta) = f(x)\ \Psi_{tt}(\phi(x, r, \theta), r) \tag{8}$$

where

$$\int_{leading\ edge}^{trailing\ edge} f(x)dl = 1. \tag{9}$$

$f(x)$ is a function used to distribute the force along the streamlines ($dl$) through the blade region. The distribution function is forced to be small near the leading and trailing edges to reduce numerical oscillations. Equation (9) is simplified by assuming the streamlines are parallel to the axis (i.e. $dl = dx$) since all compressors used in this paper have a high hub-to-tip ratio.

$\mathbf{F_{turning}}$ is constructed so the flow turns towards the camber line angle in the relative frame of the blade row. The tangential component of the force is given by

$$F_{\theta,turning} = CV_x(r\Omega + V_x tan(\alpha) - V_\theta). \tag{10}$$

The constant $C$ is calibrated to produce the correct deviation angle at the design flow coefficient. $\mathbf{F_{turning}}$ is chosen normal to the local velocity $\mathbf{V}$ so that it does not affect the total pressure. Therefore,

$$F_{turning,x} = \frac{V_x}{V_\theta} F_{turning,\theta}. \tag{11}$$

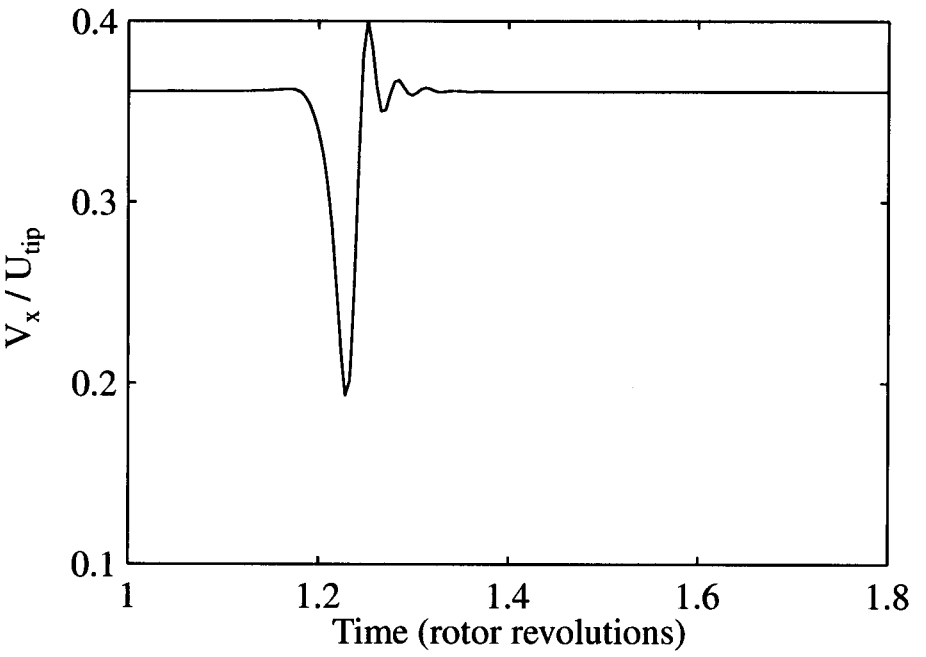


**Figure 10: Computed velocity trace showing a localized stall cell.**

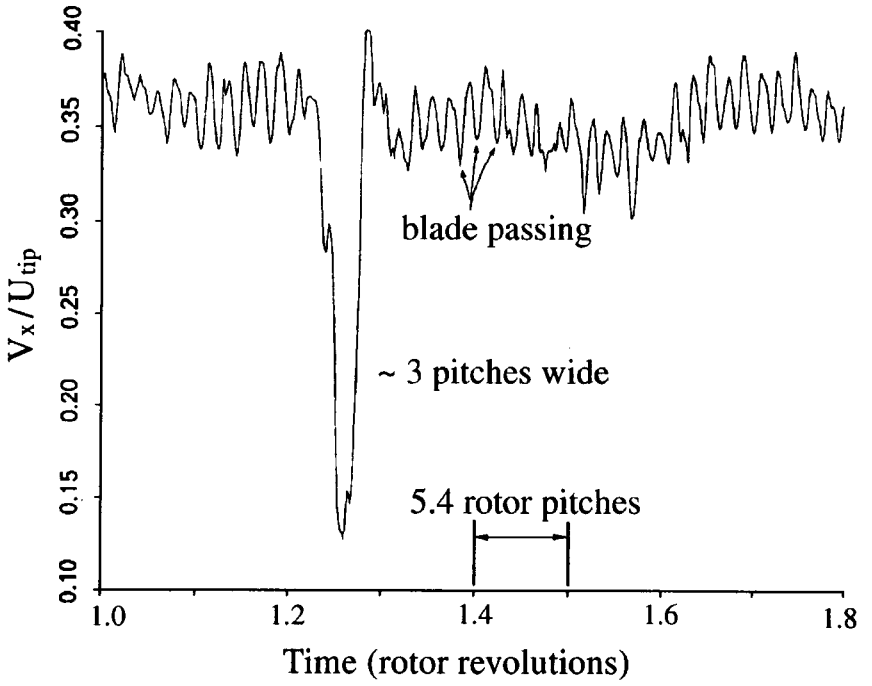


**Figure 11: Measured velocity trace showing a localized stall cell (Silkowski, 1995).**

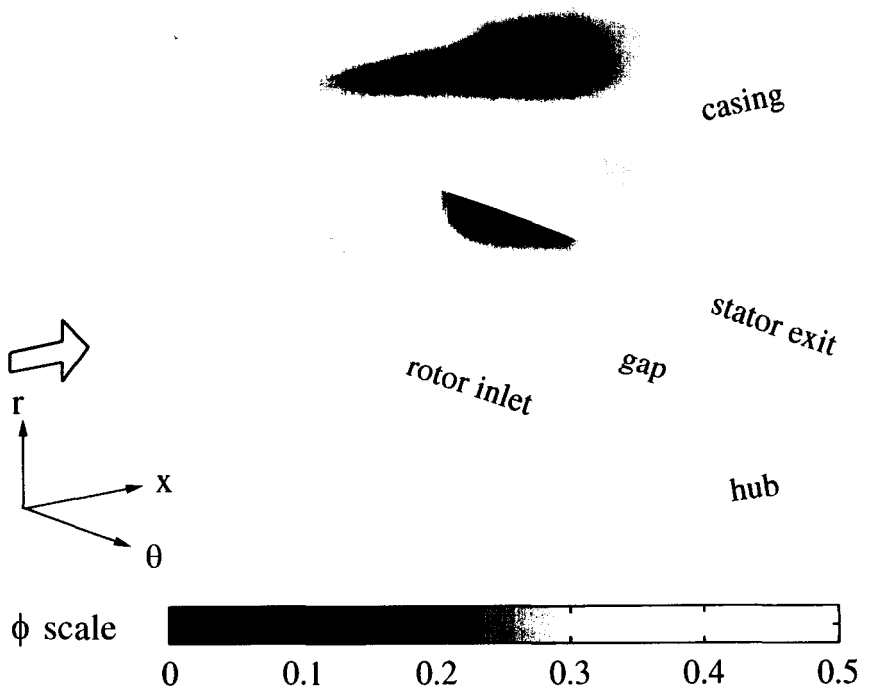


**Figure 12: Computed flow coefficient contours of a localized stall cell in the first stage of the GE mismatched configuration. A tangential extent equal to 6 blade pitches is shown.**

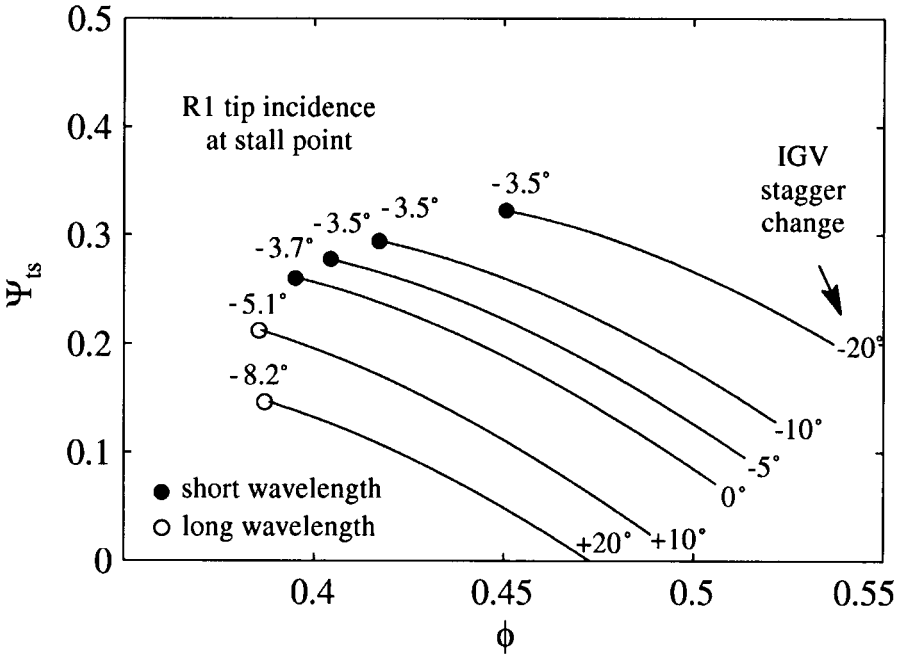


**Figure 13: First stage characteristics with the stall point and inception type computed for different IGV staggers.**

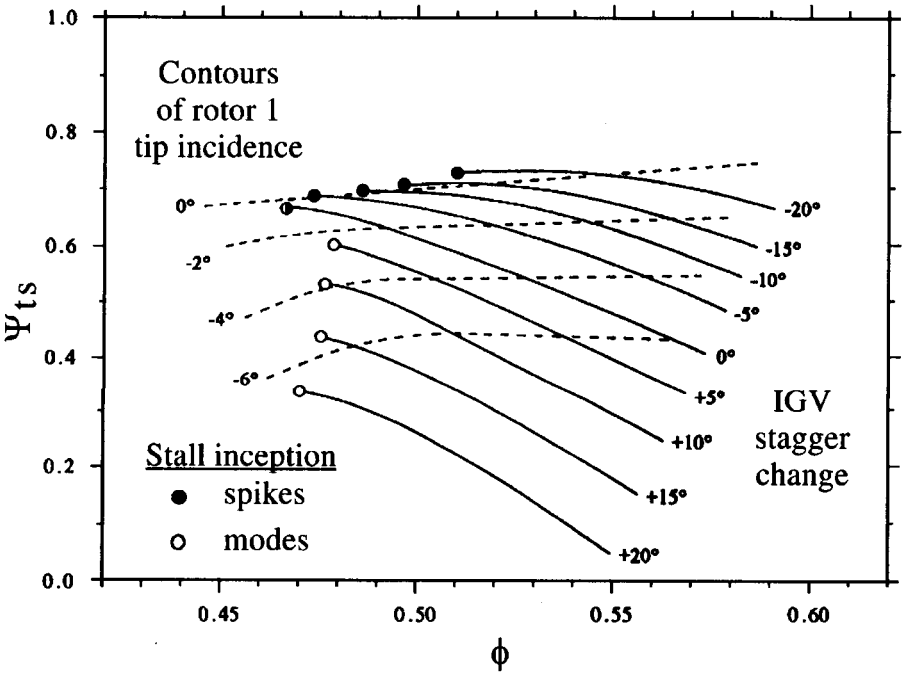


**Figure 14: First stage characteristics with the stall point and inception type indicated for different IGV staggers. Measured by Camp and Day (1997).**

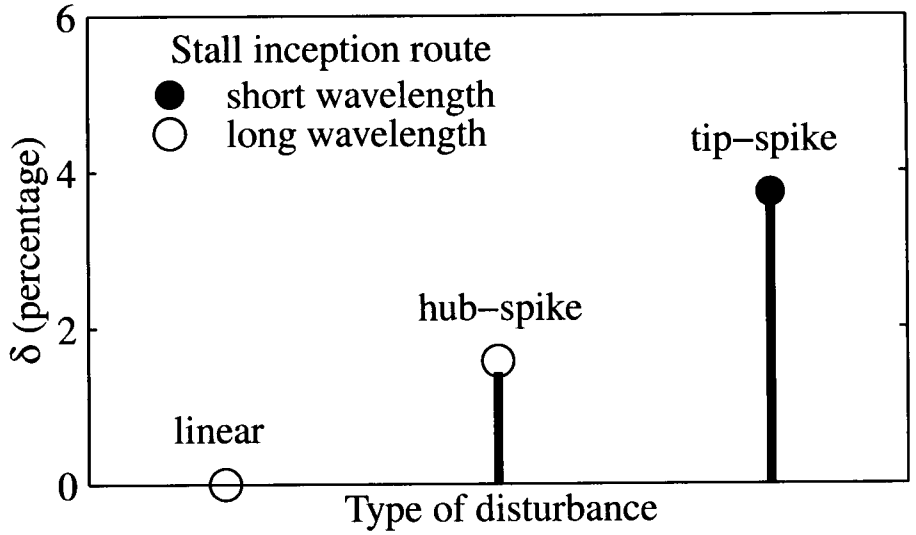


**Figure 15: Changes in stall point and inception type for different types of initial disturbances.**

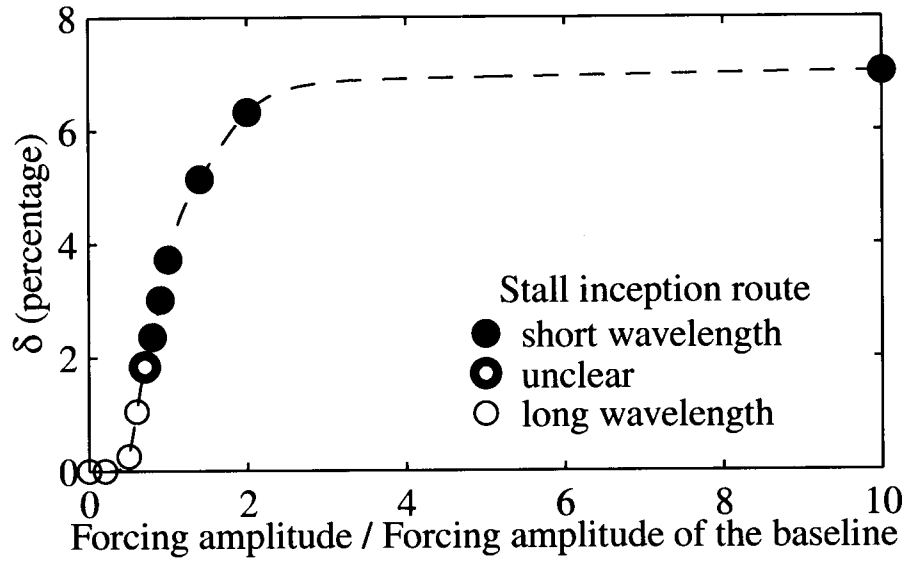


**Figure 16: Effects of initial spike forcing amplitude on stall point and inception type.**

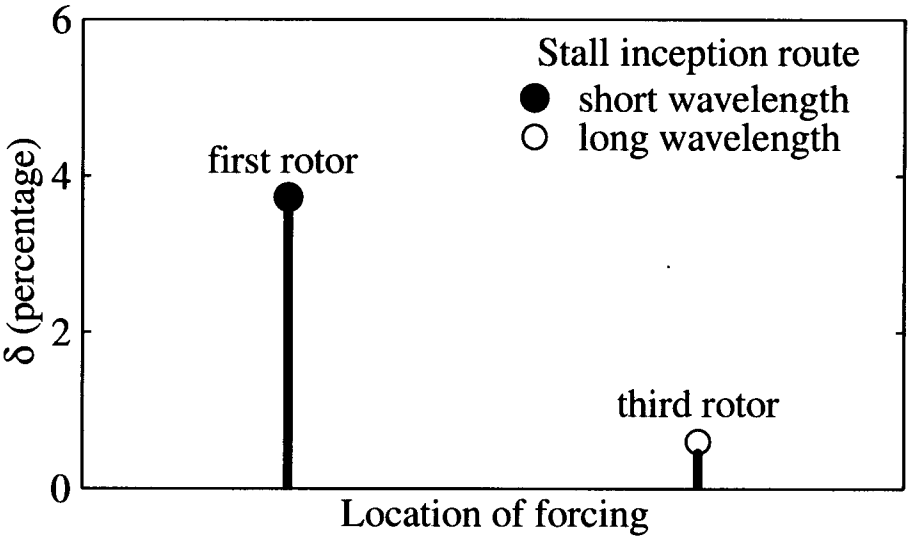


**Figure 17: Changes in stall point and inception type with location of initial spike.**

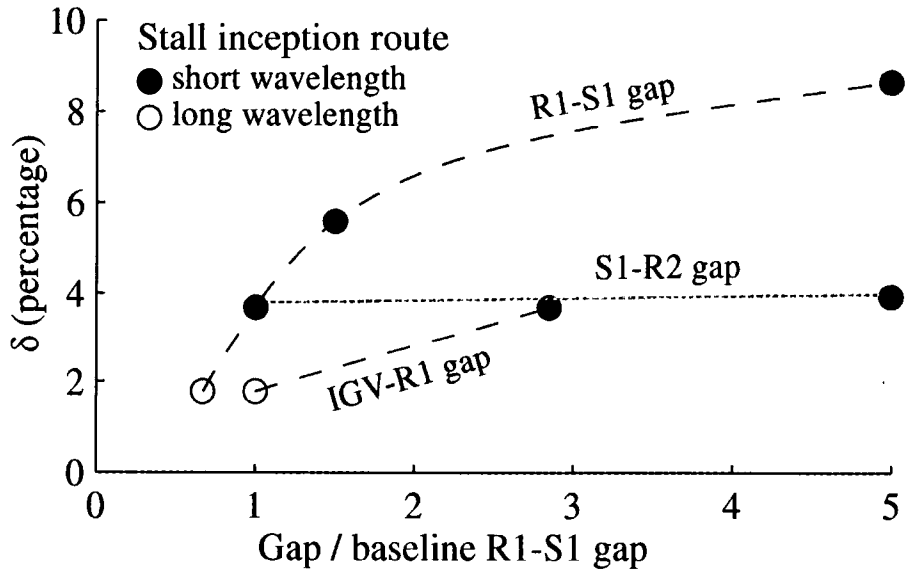


**Figure 18: Effects of IGV-R1, R1-S1, and S1-R2 gap lengths on stall point and inception type.**

## TASK II: Three-dimensional Rotating Stall Inception and Effects of Rotating Tip Clearance Asymmetry in Axial Compressors


### Summary:

The effects of two types of flow non-uniformity on stall inception behavior were assessed with linearized stability analyses of two compressor flow models. Response to rotating tip clearance asymmetries induced by a whirling rotor shaft or rotor height variations were investigated with a two-dimensional flow model. A 3-D compressor model was also developed to study the stability of both full-span and part-span rotating stall modes in annular geometries with radial flow variations. The studies focussed on (1) understanding what compressor designs were sensitive to these types of circumferential and spanwise flow non-uniformities, and (2) situations where 2-D stability theories were inadequate because of 3-D flow effects.

Rotating tip clearance non-uniformity caused the greatest performance loss for shafts whirling at the rotating stall frequency. A whirling shaft displacement of 1% chord caused the stalling mass flow to rise by as much as 10% and the peak pressure rise to decrease by 6%. These changes were an order of magnitude larger than for equivalent-sized stationary or rotor-locked clearance asymmetries.

Spanwise flow non-uniformity always destabilized the compressor, so that 2-D models over-predicted that stall margin compared to 3-D theory. The difference increased for compressors with larger spanwise variations of characteristic slope and reduced characteristic curvature near the peak. Differences between 2-D and 3-D stall point predictions were generally unacceptable (2 – 4 % of flow coefficient ) for single-stage configurations, but were less than 1 % for multistage compressors. 2-D analyses predicted the wrong stall mode for specific cases of radial inlet flow distortion, mismatching and annulus area contraction, where higher-order radial modes led to stall.

The stability behavior of flows with circumferential or radial non-uniformity was unified through a single stability criterion. The stall point for both cases was set by the integral around the annulus of the pressure rise characteristic slope, weighted by the amplitude of the mode shape. For the case of steady circumferential variations, this criterion reduced to the integrated mean slope (IMS) condition associated with steady inlet distortions.

The rotating tip clearance asymmetry model was also used to demonstrate the feasibility of actively controlling the shaft position to suppress rotating stall. In axisymmetric mean flow, this method only stabilized the first harmonic mode, increasing the operating range until surge or higher harmonic modes became unstable.

# NOMENCLATURE

| | |
|---|---|
| $\mathbf{A}, \mathbf{B}, \mathbf{C}, \mathbf{D}$ | State-space matrices |
| $A$ | Duct area |
| $AR$ | Aspect ratio |
| $B$ | $B$-parameter |
| $c, c_z$ | Blade chord, axial projection of chord |
| $F_r, F_\theta, F_z$ | Radial, tangential, axial body force |
| $F_L$ | Body force contributing to loss |
| $f$ | Body force shape factor |
| $j$ | Radial mode number |
| $\mathbf{K}$ | Feedback control compensator |
| $k$ | Compensator gain; Body force turning coefficient |
| $k_T$ | Throttle constant |
| $L$ | Duct length; Rotary total pressure loss |
| $n$ | Spatial Fourier harmonic number |
| $P, P_t, P_t^*$ | Static, total, rotary total pressure |
| $R$ | Mean annular radius |
| $r$ | Radial coordinate |
| $s$ | Temporal exponent; Streamline coordinate |
| $T, T_t$ | Static, total temperature |
| $t$ | Time |
| $U$ | Mean rotor speed |
| $U, V, W$ | Radial, tangential, axial velocity |
| $V_P$ | Plenum volume |
| $\vec{x}, \vec{y}, \vec{u}$ | State-space vectors |
| $z$ | Axial coordinate |

## Greek

| | |
|---|---|
| $\alpha$ | Compensator phase |
| $\beta, \beta_d$ | Relative flow, blade angle |
| $\gamma$ | Blade stagger angle |
| $\epsilon$ | Tip clearance |

| | |
|---|---|
| $\zeta$ | Horizontal computational coordinate |
| $\eta$ | Efficiency; Vertical computational coordinate |
| $\theta$ | Tangential coordinate |
| $\lambda, \mu$ | Rotor, compressor inertia parameter |
| $\nu$ | Tip clearance asymmetry rotation frequency |
| $\xi$ | Loss coefficient |
| $\rho$ | Density |
| $\sigma$ | Stage reaction |
| $\tau$ | Time lag parameter |
| $\Phi$ | Flow potential |
| $\Psi$ | Total-to-static pressure rise (with losses); Stream function |
| $\Psi_i$ | Isentropic total-to-static pressure rise |
| $\Psi_{SS}$ | Static-to-static pressure rise |
| $\omega$ | Temporal eigenvalue ($s = i\omega$) |
| $\Omega$ | Rotor rotation frequency |

## Superscripts, Subscripts and Operators

| | |
|---|---|
| $X$ | Entire flow quantity |
| $\bar{X}$ | Mean flow quantity |
| $x$ or $\delta x$ | Perturbational flow quantity |
| $\tilde{X}$ | Dimensional quantity |
| $X'$ | Relative quantity in rotating tip clearance asymmetry frame |
| $X^*$ | Complex conjugate (except $P_t^*$) |
| $\mathbf{X}$ | Matrix |
| $\vec{x}$ | Column vector |
| $\vec{x}^T$ | Transpose |
| $\|x\|$, $\angle x$ | Amplitude, phase angle of complex variable |
| $X_a$ | Quantity at ambient conditions |
| $X_C, X_T, X_P$ | Value in compressor, throttle, plenum |
| $X_h, X_t$ | Value at inner (hub), outer (tip) casing |
| $X_R, X_S$ | Value in rotor, stator |
| $X_{in}, X_{out}$ | Value at inlet, exit plane of blade row |
| $X_0, \ldots, X_8$ | Value at axial positions through compression system |
| $X_L, X_\delta$ | Corresponding to loss, deviation |
| $X_c, X_s$ | Cosine, sine components |
| $X_r, X_i$ | Real, imaginary components |
| $X_n$ | $n^{th}$ spatial Fourier harmonic |
| $\{X_n, Y_n\}_{a,b}$ | Fourier series representation of $\sum_{n=a}^{b}(X_n \cos n\theta' + Y_n \sin n\theta')$ |

# CHAPTER 1

# INTRODUCTION

## 1.1 General Description of Problem

The safe operating range of a gas turbine compressor is limited at low mass flow rates by the development of flow instabilities. The two classes of instabilities, *rotating stall* and *surge*, cause unsteady stresses in the compressor blades, and reduce the compressor performance. Sustained operation with rotating stall can also lead to excessively high turbine temperatures due to the decreased mass flow through the engine. The impact of flow instabilities on an engine can be so severe that rotating stall and surge must generally be avoided.

Instabilities are avoided by operating a safe distance away from the *stall line* on the compressor performance map (Figure 1-1). The *stall margin* is necessary to account for transient compressor operation, engine deterioration and flow nonuniformities that would otherwise render the compressor flow unstable. Unfortunately this margin impedes operation in desired regions of increased pressure rise and, sometimes, higher efficiency. Accurate stall line predictions are important for compressor design to optimize performance while still ensuring stability to typical flow variations.

The present research is concerned with the effect of two types of flow nonuniformities on stall inception. The first type is caused by variation of the tip clearance gap. Although the clearance is designed to be equal for each blade, circumferential nonuniformities arise that can be grouped into three categories (Figure 1-2). The first category includes steady, or stationary, nonuniformities caused by deformation of the casing. The second class of clear-

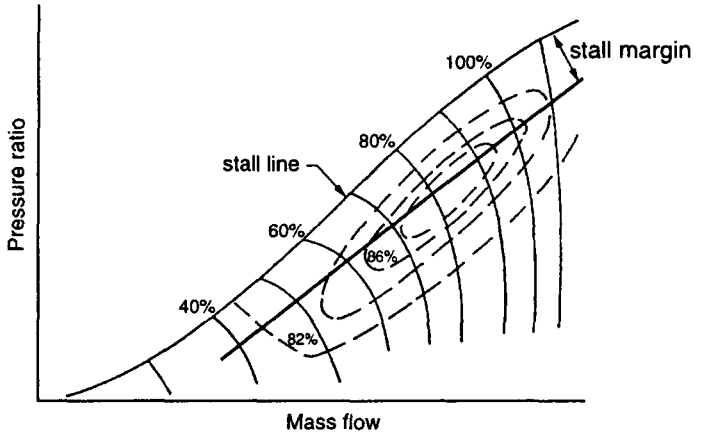


**Figure 1-1:** Typical compressor axisymmetric performance map depicting stall margin (adapted from [9]).

ance asymmetry includes rotor-locked asymmetries caused by variations in the rotor heights. These can arise from uneven machining, blade bending ("bowing"), or from abrasion of the tips against the outer casing wall. The third category originates from an off-centered rotor shaft. Here the tip clearance exhibits a sinusoidal variation, with the smallest clearance in the direction of the shaft displacement. This class of clearance nonuniformity is stationary if caused by a steady shaft deflection, or unsteady if caused by rotordynamic effects such as a flexing or whirling shaft.

The second type of flow nonuniformities considered in this thesis are radial flow variations. Important sources of radial nonuniformity are shown in Figure 1-3. Tip vortices can interact with the endwall flow to constitute a major source of blockage and loss, which extends to as far as 25% span [7, 81]. This blockage affects the spanwise incidence profiles on downstream blade rows, impacting their loss and loading distributions. Other sources of flow nonuniformity are caused by radial variations in the blade loading and exit swirl angles. Distorted flow can also enter the compressor ducts, caused by flow separation off the inlet lip, or by ingestion of inlet vortices, wakes or hot gases.

Spanwise flow variations are also observed in the rotating stall cells themselves. Full-span cells are relatively well-understood through an abundance of two-dimensional flow analyses that neglect radial flow variations. Part-span stall cells, localized to the hub or the tip, lead to instability in many compressor configurations but their origin is less clear.

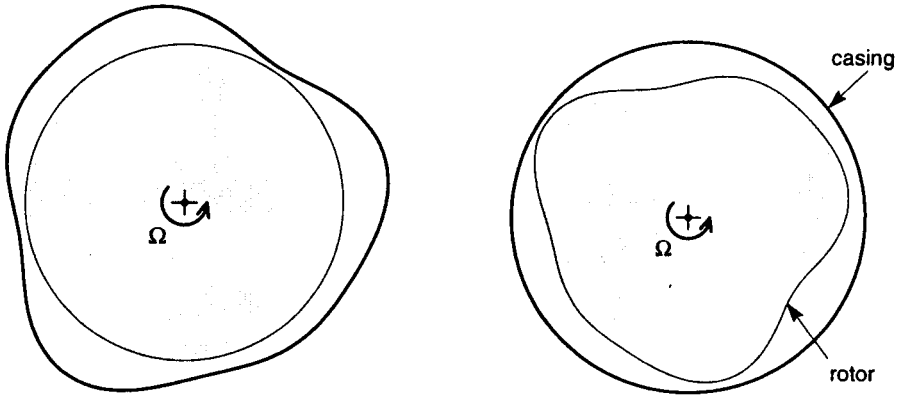


(a) Nonuniform casing, $\varepsilon = \varepsilon(\theta)$

(b) Nonuniform rotor heights, $\varepsilon = \varepsilon(\theta - \Omega t)$

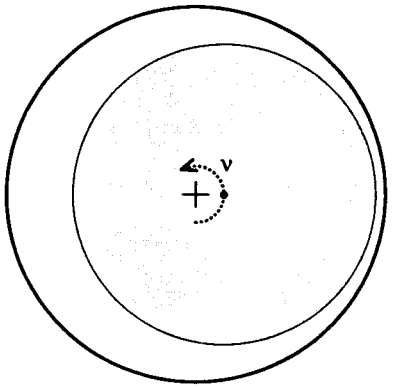


(c) Whirling (off-centered) rotor shaft, $\varepsilon = \varepsilon(\theta - \nu t)$

**Figure 1-2:** Categories of tip clearance asymmetry. The clearance variation, $\varepsilon(\theta)$, is shown to be (a) stationary; (b) locked to the rotor frequency, $\Omega$; and, (c) locked to the whirling shaft frequency, $\nu$.

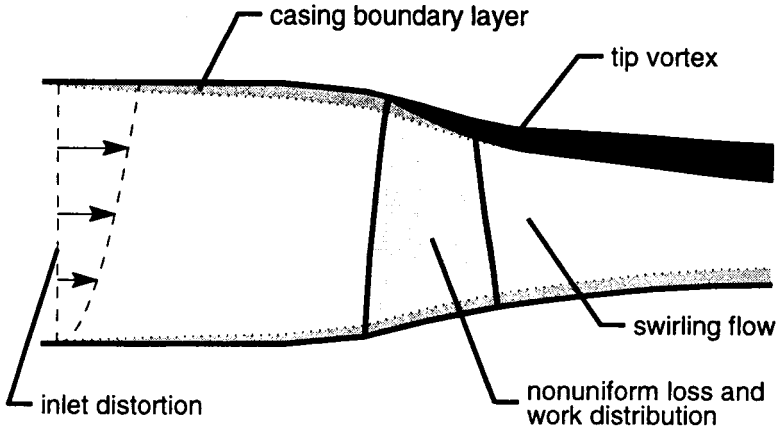


**Figure 1-3:** Meridional illustration of an axial compressor indicating sources of spanwise flow nonuniformities.

In summary, this research investigates the response of compressors to two types of flow nonuniformities: (1) unsteady tip clearance asymmetry arising from whirling shafts or rotor height variations, and (2) general spanwise flow nonuniformities. This analysis will also be used to understand the compressor situations the lead to part-span rather than full-span stall. Further motivation for choosing these particular aspects of flow nonuniformity is provided in the following section.

## 1.2 Background and Motivation

### 1.2.1 Three-Dimensional Rotating Stall Inception

Experiments performed on compressor rigs [11, 4] and engines [12, 13] demonstrate two routes for rotating stall inception. The first is characterized by the exponential growth of small-amplitude disturbances that rotate between 0.2 and 0.7 times the rotor speed. These disturbances, referred to as *modal* stall waves, have a wavelength on the order of the annular circumference. The second stall inception route is characterized by the sudden appearance of short length-scale disturbances that initially rotate at 0.7 to 0.8 times the rotor speed. These *spikes* are localized to the rotor tip region across only two to three blade pitches, and are three-dimensional [44, 63]. By contrast, modal disturbances can appear as radially uniform, larger at the tip or hub [52] or even largest at the midspan [33]. Compressor flow models have shown that these small amplitude, long wavelength perturbations are linear *modes* of the compression system, and that these modes become unstable at the peak (i.e. zero slope) of the total-to-static pressure rise characteristic [30, 47].

Two-dimensional models are limited in that they do not account for flow variations in the spanwise direction. Measurements in compressor rigs indicate that spanwise variations of axial velocity as large as 40% of the mean flow can arise before stall [59, 54, 73, 7]. Reid [58] and Spakovszky et al. [70] showed that radial total pressure distortions at the inlet of the compressor reduced the stalling pressure rise. Gorrell et al. [24] altered casing treatment designs and observed that rotors with the most uniform radial profile of pressure ratio led to the most stable compressors. These results reveal the importance of radial flow variations in affecting the stall point.

Two-dimensional models usually use either a radial average of the flow variation [28, 70], or else are applied at the mean-radius [53, 33, 78]. To account for spanwise flow nonuniformity, it has been proposed that the stability of a compressor can be determined by a two-dimensional model at the most unstable spanwise region [52]. The validity of such a proposition is not yet known, although experimental evidence indicates that the location of the stall cell is often linked to the location of highest loading and lowest velocity. McDougall et al. [52] observed that modal waves had the largest amplitude at either the hub or tip, determined by which region had excessive blockage before stall. Camp and Day [4] found that increased rotor tip loading led to spike stall inception at the outer radius; but increased hub blockage, which diverted the flow outward to unload the tip, led to a modal-type stall inception. On the other hand, Soundranayagam and Elder [67] measured stall inception occurring at the tip of a fan, despite forcibly degrading the root performance; and Jackson [44] first detected stall at the tip of a single stage compressor, although the diffusion factor was larger in the hub region of both blade rows. The three-dimensional instability behavior for general compressor configurations is clearly not well-understood.

Some three-dimensional models have attempted to capture the inception process of rotating stall. Yeh [83] was the first to examine 3-D modes, but the analysis was restricted to a radially uniform mean flow across a single blade row. Linearized flow models by Sekido et al. [62, 61], Mathioudakis [49] and Sun [74] were designed to represent nonuniform background flows. However, they were only applied to uniform rectilinear cascade geometries, and were not used to understand how spanwise flow nonuniformities affect the stability margin, or when part-span stall dominates over full-span stall modes.

Nonlinear CFD methods have been used to simulate rotating stall inception in general three-dimensional geometries [42, 17, 23]. These analyses were concerned with the development of short wavelength spikes, and were not used to understand the design parameters governing modal stall inception in nonuniform flows. Linearized stability models have an advantage over nonlinear simulations in that the rotating stall modes are directly calculated as the eigenmodes of the compression system. This permits the investigation of higher-order stable modes that are unobservable in time-accurate simulations, and can be used to develop theoretical, model-based active control methods [79]. Presently, however, there exist no linear rotating stall models that are applicable for arbitrary three-dimensional flow fields.

The present research was undertaken as the first effort to investigate the linear stability of three-dimensional modes for flows in general compressor geometries. The goal was to understand the parametric dependence of spanwise flow variations and compressor design on the modal stalling process, and to determine the limitations of two-dimensional stall prediction analyses in realistic flow situations.

### 1.2.2 Rotating Tip Clearance Asymmetry

Experiments have demonstrated that increasing the axisymmetric tip clearance in a compressor reduces the stable operating range, the pressure rise and the efficiency [64, 46, 82, 80]. This is illustrated in Figures 1-4a and 1-4b which depict the pressure rise and efficiency char-

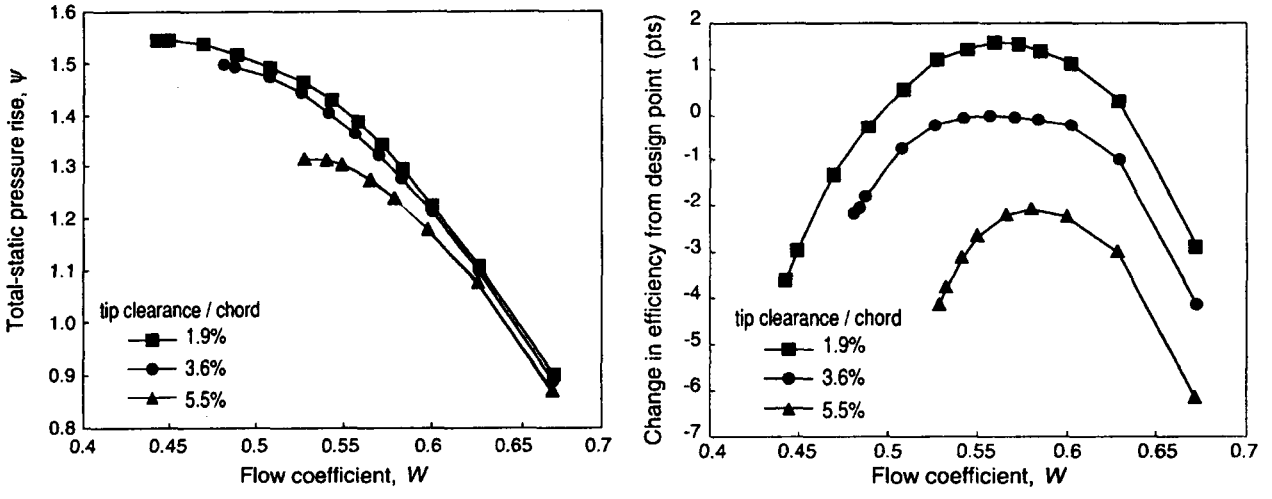


(a) Pressure rise

(b) Efficiency

**Figure 1-4:** Effect of tip clearance on pressure rise and efficiency for GE 4-stage engine (from Graf et al. [26]).

acteristics for a multistage compressor at three different clearances. The loss in efficiency and peak pressure rise has been correlated with tip clearance for a variety of compressors (Wisler [80] and Smith [64]). Typically, beyond a minimal clearance of 1% of the chord, the peak pressure rise decreases by 5% for a clearance increase of 1% of the chord (Figure 1-5).

Graf et al. [26] showed that *stationary* tip clearance asymmetries negatively affect the performance when compared to axisymmetric operation at the mean clearance level. Measurements were taken from a four-stage compressor rig with a uniform clearance, and with stationary sinusoidal clearance asymmetries of 1.5% to 4.3% of blade height. Losses in

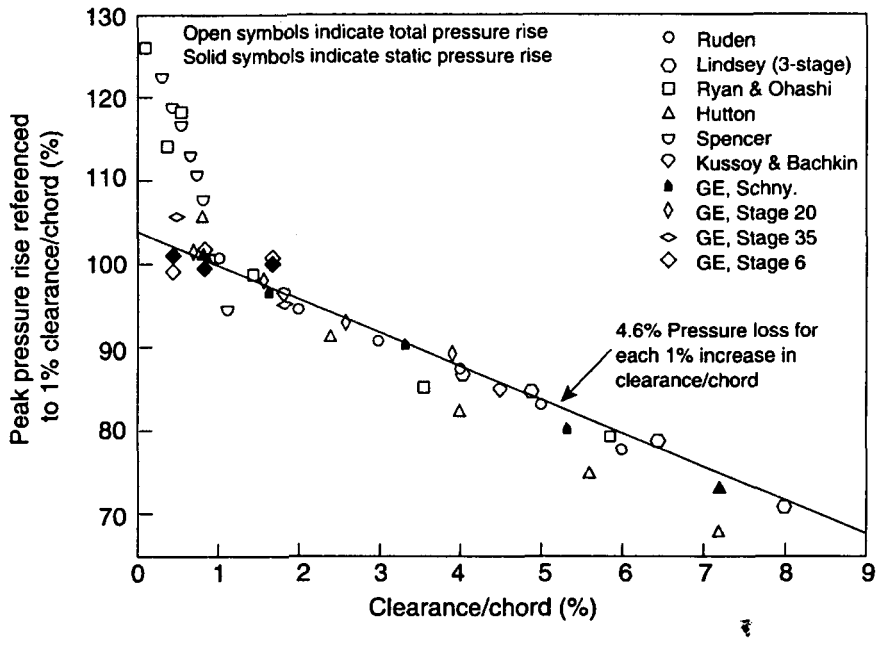


**Figure 1-5:** Effect of tip clearance on peak pressure rise. (Graf [25], adapted from Smith [64])

efficiency were small (less than 0.4%) for the nonuniform configuration near the design point. However, the stalling flow coefficient increased by up to 10%, and the peak pressure rise decreased by 8%, compared to the stall point in uniform flow. Therefore, nonaxisymmetric tip clearance cannot be neglected at off-design, low mass flow conditions.

The importance of *rotating* clearance asymmetries has not been experimentally measured, but can be estimated from linearized flow analyses. Rotating clearance asymmetries examined by Horlock and Greitzer [38] and Graf et al. [26] were only of the rotor-locked type. Their linearized analyses have been extended in Appendix A for clearance nonuniformities rotating at any general frequency. Appendix A calculates the ratio of the axial velocity nonuniformity induced by a small amplitude rotating asymmetry compared to that induced by a stationary tip clearance asymmetry of the same magnitude. This ratio is plotted in Figure 1-6 for a clearance variation caused by a whirling shaft rotating at frequencies between 0 and 1 times the rotor frequency, using parameters representative of a single-stage rig operating near design [59]. The bell-shaped curve is characteristic of all compressors, with the highest response corresponding to whirling at the rotating stall frequency (at 44% of the rotor frequency for this example).

The equations in Appendix A show that small amplitude rotating asymmetries induce a larger flow distortion than stationary ones in two situations: for high harmonic clearance

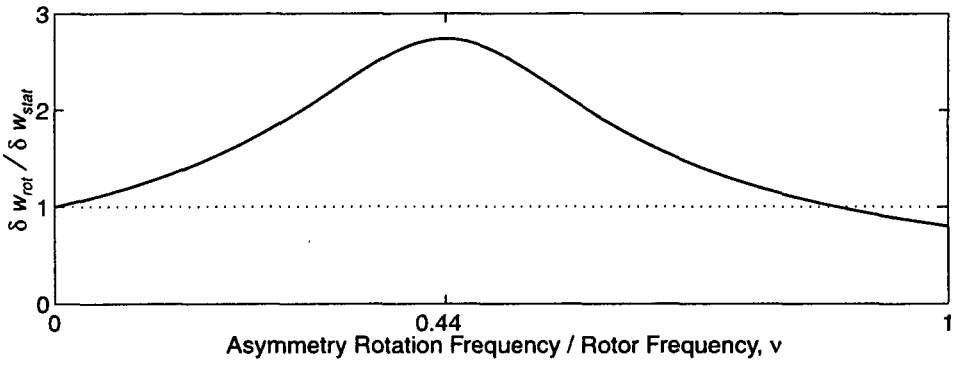


**Figure 1-6:** Comparison of magnitudes of velocity nonuniformity induced by equal-sized rotating ($\delta w_{rot}$) and stationary ($\delta w_{stat}$) clearance asymmetry; from equation (A.7).

variations, and for asymmetries rotating close to the rotating stall frequency. The effect on stability for these two rotating asymmetry cases will also likely be larger than for stationary variations. This deduction is based on Graf's results for stationary clearance asymmetries, which showed that the loss of stability scaled with the induced flow distortion [25]. Similar results have also been observed for rotating *inlet* flow distortions, modeled by Chue et al. [6] and experimentally investigated by Longley et al. [48]. Their work showed that a severe loss in stall margin was associated with flow distortions rotating near the resonant rotating stall frequency.

Further motivation for studying unsteady tip clearance variation is to develop a new method to actively control rotating stall. By inducing a nonuniform pressure rise around the circumference, a clearance variation acts similarly to an array of jet actuators or movable guide vanes, which have already been proven effective for controlling stall [34, 78]. The NASA Lewis Research Center is specifically interested in using magnetic bearings to actively position the rotor shaft to create unsteady clearance nonuniformity [72]. Such bearings are currently being designed for use with a transonic stage, Stage-37, in the Single Stage Axial Compressor Test Facility. The present studies can assess the utility of using this clearance control method to stabilize rotating stall.

In summary, it is important to be able to calculate the operational loss due to blade height variations or a whirling shaft in order to design robust compressors and to predict the performance and stall margin deterioration as an engine degrades. The linear approximation in Appendix A is only applicable to infinitesimal tip clearance variations, and cannot be used to predict changes to the stability point of a compressor. Developing a model for this purpose

would also be useful in assessing active control schemes, particularly the effectiveness of using unsteady tip clearance variation as an actuator for rotating stall control.

## 1.3 Research Objectives

The main objectives of this work related to rotating tip clearance asymmetries are:

1. Assess the effect of rotating tip clearance asymmetry on compressor performance at the design operating point.
2. Assess the effect of rotating tip clearance asymmetry on the stability margin and peak pressure rise.
3. Demonstrate the utility of tip clearance actuation to actively control rotating stall.

The main objectives of the present thesis related to three-dimensional stall inception are:

1. Develop a linearized model to predict the inception behavior of three-dimensional modes in flows within general compressor geometries.
2. Establish the effect of radial flow variations and compressor design on the stall inception process.
3. Identify compressor situations for which the two-dimensional stability model is sufficient (for stall prediction and active control applications), and situations for which the three-dimensional model is required.

To satisfy these objectives, the following specific research questions will be answered:

- How much blade height variation or whirling shaft offset is necessary to effect a significant (greater than 1%) change in design performance and stall margin?
- How effective is rotor shaft actuation at actively controlling compressor instability given the physical limitations of the Stage-37 compressor with magnetic bearings?
- What design parameters affect the three-dimensional structure of the rotating stall mode?
- Under what conditions does a three-dimensional mode lead to instability before a two-dimensional mode?

## 1.4 Approach and Scope

### 1.4.1 Rotating Tip Clearance Asymmetry

To accomplish the objectives concerning rotating tip clearance asymmetry, Graf's model [26] was modified to account for the solution of the flow in a rotating reference frame. The sensitivity of the compressor characteristic to inlet swirl was also included so the model would be appropriate for rigs, such as Stage-37, with a rotor as the first blade row.

The types of nonaxisymmetric tip clearances that could be examined with the model were limited to those that were steady with respect to some rotating frame. Thus, the origin of the clearance asymmetry was restricted to those dominated by *one* of the following sources: a nonuniform casing, a nonuniform rotor height distribution, or a (potentially whirling) shaft offset. Cases where two or more of these phenomena exist simultaneously are outside the scope of this work, since there is no frame in which the resulting flows appear steady. This restriction was made to permit the use of a straightforward method for hydrodynamic stability analyses. The limitation is not severe, in that the stated objectives were still met by investigating each source of rotating clearance nonuniformity independently.

The first research objective was accomplished by investigating steady performance changes due to both rotor blade height nonuniformity and a whirling shaft. Each case gave rise to tip clearance nonuniformities with different characteristics. A whirling shaft can only create a single-lobed sinusoidal clearance variation, but it may rotate at any frequency. Rotor height nonuniformities can consist of any general circumferential shape, but the asymmetry is locked to the rotor frame. Height distributions considered were: (1) high circumferential harmonic variations, pertaining to blade-to-blade machining variations; and (2) long wavelength variations, attributed to a localized tip rub against the casing. The effects of the clearance variations were assessed on two compressor configurations: the three-stage low-speed MIT compressor (described by Haynes et al. [34]), and the Stage-37 rig at NASA Lewis Research Center [54]. The MIT compressor geometry was the baseline for the stationary clearance calculations performed by Graf [25], against which a comparison for rotating clearance effects was desired. The NASA Stage-37 rig was chosen in anticipation of future experimental demonstrations at NASA Lewis.

The second objective was accomplished by analyzing the stability of the flow fields found from the above investigations. A *normal mode* method was used [14] since these background flow fields were circumferentially periodic and steady in the frame of the clearance asymmetry. The growth rates of all superimposed linear, unsteady modal perturbations were calculated, and the flow was unstable once any mode had a positive growth rate. Note that by using a linearized analysis, rotating stall inception from large-amplitude spike-shaped disturbances was not considered. This is only partially restrictive, since a wide class of compressors have been shown to stall through the growth of small-amplitude, rotating waves [10]. In particular, both the MIT 3-stage rig and NASA's Stage-37 exhibit modal stall inception.

To demonstrate stall control through active tip clearance variation, the linearized compressor model was formulated in state-space form. Standard control methodologies were then followed for these linear time-invariant matrices to develop feedback control laws. The parameters were chosen to match the Stage-37 rig fitted with magnetic shaft bearings as the actuator, and static pressure measurements at the rotor inlet face as the sensor output. Since the objective of this study was simply to provide a demonstration of stall margin extension, only basic constant-gain compensators were used.

### 1.4.2 Three-Dimensional Rotating Stall Inception

Theoretical studies of three-dimensional rotating stall inception were performed with two types of compressor models. The first model represented the compressor as an actuator plane embedded within rectilinear ducts, similar to those used by previous researchers. The second model incorporated the actual annular compressor geometry, and used distributed body forces to represent the effects of the blade rows. The body force formulation is new and therefore has been validated against experimental test cases in this thesis to demonstrate its applicability for 3-D stall investigations.

The actuator plane model was used for two purposes. First, it provided a simple configuration to understand both the stability of higher-order three-dimensional modes and the effects of flow nonuniformity on rotating stall. Studies were performed with uniform inlet flow in constant area, rectilinear ducts; only the pressure rise characteristic had spanwise variations. The simplicity of these configurations often led to analytic solutions and con-

clusions that were more easily understood than the results with the body force compressor model. The second purpose of the actuator plane model was to identify key elements that must be included in the subsequent compressor model in order to accurately predict three-dimensional rotating stall. Sensitivity studies were performed to reveal that the stability of radially varying modes were strongly dependent on both the chord-wise distribution of pressure rise and the redistribution of the disturbance flow within the blade rows. Such elements are unmodeled in current actuator disk studies, and were used to motivate the design of the generalized body force compressor model.

Quantifying the effects of flow nonuniformity on stall inception for actual compressor configurations was performed with the generalized body force model. Parameters examined included the spanwise nonuniformity of blade performance, inter-blade row gap length, hub-to-tip ratio, inlet flow distortion, annulus cross-sectional area variations and stage mismatching. Differences between 2-D and 3-D stall predictions were made by comparing these results to those calculated from a two-dimensional body force model. The 2-D model was designed to represent the radially-averaged flow conditions of the generalized three-dimensional model, which allowed back-to-back comparisons to establish how spanwise flow variations directly affected compressor stability.

## 1.5 Contributions

New theoretical models have been developed in this thesis for investigating the stability of compressors subject to either (1) rotating tip clearance asymmetry, or (2) spanwise flow nonuniformities in general annular geometries. The tip clearance asymmetry model has also been cast in state-space form, so that it can be applied to the anticipated NASA stall control experiments with magnetic shaft bearings. Active control of the rotor shaft position was demonstrated to be a feasible method to stabilize rotating stall, but only for compressors that stall from the first-harmonic mode. Higher-order modes were shown to be controllable only in nonuniform flow situations.

A universal stability criterion has been derived, appropriate for general compressor flows with circumferential or radial flow variations. This criterion relates compressor stability to the local compressor characteristic slope nonuniformity and the mode shape envelope.

Although not useful as a stall prediction tool since it requires prior knowledge of the disturbance flow structure, this stability criterion is useful for understanding the effects of flow nonuniformity on stall inception.

The specific processes that lead to performance and stability changes caused by whirling rotor shafts and rotor height variations were identified. The changes were shown to increase with (1) characteristic curvature, (2) size of clearance nonuniformity, and (3) proximity of rotating clearance frequency to rotating stall frequency (i.e. resonance). It has been shown that clearance asymmetry does not significantly affect the design performance, but it can strongly reduce the stall margin, especially for whirling shafts near the stall frequency. The change in stall point for this worst case scenario was found to be an order of magnitude larger than for an equally-sized stationary clearance asymmetry.

This work also proved that compressors with radial flow nonuniformities were more unstable than their corresponding 2-D flow representations. Two-dimensional stall predictions became more inaccurate for compressors with reduced characteristic curvature and larger spanwise nonuniformity of the characteristic slope. It was established that in nearly all linearly unstable compressors, rotating stall developed from full-span modes. Higher-order three-dimensional modes were likely to lead to stall only for operation with radially distorted inlet flow.

## 1.6 Thesis Organization

The analytic models describing the flow in compressors with a rotating tip clearance asymmetry are developed in Chapter 2. The solution process for determining the background flow field (steady with respect to the asymmetry) is presented, as well as the hydrodynamic stability method for determining the unsteady, linearized modes of the compression system.

Chapter 3 contains the results from numerical studies of compressor performance with rotating tip clearance nonuniformities. Descriptions of the two compressors used in the studies are first provided. Then the losses in pressure rise, efficiency and stall margin are linked to the amount of rotor height variation and whirling shaft offset. Mechanisms governing these losses are explained through examples of analytical compressor situations. Finally, implications of these results on other compressor configurations are discussed.

Chapter 4 describes the efforts to actively suppress the onset of rotating stall using control of the rotor shaft position. The control algorithms are developed and optimized, and the ability to extend the stable operating range of the compressor is presented.

The actuator plane model for calculating three-dimensional stall inception is shown in Chapter 5. Basic conclusions about modes in uniform and nonuniform flow are discussed. The inaccuracies and limitations of such actuator plane models for use in three-dimensional analyses are exposed, and used to motivate the generalized body force model.

Chapter 6 describes the generalized three-dimensional body force model in both steady-state, and unsteady forms. The model is assessed against two experiments, and limitations of applicability are discussed. The two-dimensional version of the model is also developed.

The results from parametric studies of three-dimensional stability behavior of many compressor configurations are contained in Chapter 7. The effect of three-dimensional flow structure on compressor stability is discussed. Implications are drawn as to the usefulness of two-dimensional models, the importance of three-dimensional modes, and their bearing on active control methods.

Finally, the overall conclusions of the present work and future recommendations are summarized in Chapter 8.

# Effects of Rotating Tip Clearance Asymmetry

# CHAPTER 2

# ASYMMETRIC TIP CLEARANCE MODEL DEVELOPMENT

This chapter develops the analytical model of the compression system used for calculating the time-averaged performance and unsteady dynamics of a compressor with a rotating tip clearance nonuniformity. Representations of each component in the compression system are described, and combined in forms useful for calculating the steady and unsteady flow fields. Finally, the methods used to calculate both the background flow and rotating stall modes are addressed.

## 2.1 Compression System Model

The model for studying rotating tip clearance asymmetries was based upon Graf's model for stationary asymmetries [25]. The compression system consisted of ducts separating a compressor, throttle and a plenum (Figure 2-1). Flow through the compressor and the adjoining ducts was assumed to be two-dimensional (axial–circumferential) and incompressible in order to simplify the solution process. These assumptions are physically realizable for low speed, high hub-to-tip ratio compressors, such as the MIT 3-stage rig.

The coordinate system was defined such that $\tilde{z}$ represents the axial direction, and $\theta$ represents the tangential direction. The axial and tangential velocities are given by $\tilde{W}$ and $\tilde{V}$. All variables (with one exception) were nondimensionalized with combinations of the following three parameters: the density $\tilde{\rho}$, the mean annular radius $\tilde{R}$, and the mean rotor

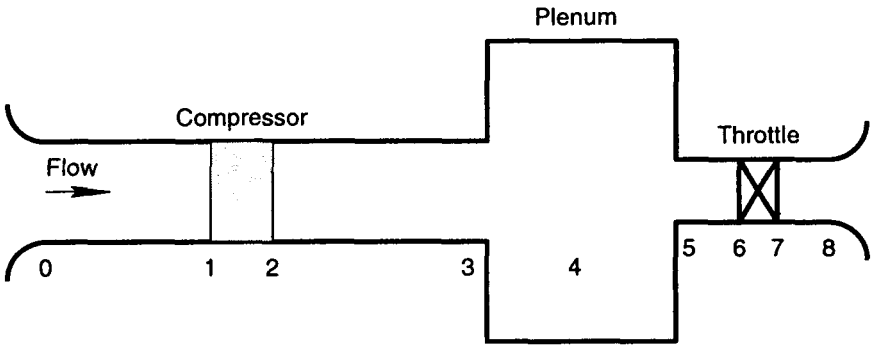


**Figure 2-1:** Schematic of the compression system model.

speed $\tilde{U}$. The rotor frequency derived from these values, $\tilde{\Omega} = \tilde{U}/\tilde{R}$, was also frequently used. Therefore, lengths were nondimensionalized as $z = \tilde{z}/\tilde{R}$, velocities as $V = \tilde{V}/\tilde{U}$, pressures as $P = \tilde{P}/\tilde{\rho}\tilde{U}^2$, and time as $t = \tilde{t}\,\tilde{\Omega}$. The exception was the tip clearance which was nondimensionalized by the rotor chord, $\varepsilon = \tilde{\varepsilon}/\tilde{c}$, for convenience in assessing against experimental measurements.

The modeling aspects for each compression system component are described below.

**Ducts:** The flow passing through the compressor ducts was assumed to be inviscid and two-dimensional. The flow entering at the inlet station 0 was uniform and steady. Therefore, throughout the upstream duct the flow was irrotational and could be expressed in terms of a potential, $\Phi$, such that

$$\frac{\partial^2\Phi}{\partial\theta^2} + \frac{\partial^2\Phi}{\partial z^2} = 0, \quad \text{where } V = \frac{\partial\Phi}{\partial\theta} \text{ and } W = \frac{\partial\Phi}{\partial z}. \tag{2.1}$$

Downstream of the compressor, the flow was not irrotational. The downstream flow field was described by the two-dimensional Euler equations:

$$\begin{aligned}
\frac{\partial V}{\partial t} + V\frac{\partial V}{\partial\theta} + W\frac{\partial V}{\partial z} + \frac{\partial P}{\partial\theta} &= 0 \quad \text{(tangential momentum)} \\
\frac{\partial W}{\partial t} + V\frac{\partial W}{\partial\theta} + W\frac{\partial W}{\partial z} + \frac{\partial P}{\partial z} &= 0 \quad \text{(axial momentum)} \\
\frac{\partial V}{\partial\theta} + \frac{\partial W}{\partial z} &= 0 \quad \text{(continuity)}
\end{aligned} \tag{2.2}$$

The compressor ducts were assumed to be long enough that there was no interaction between the nonaxisymmetric pressure field generated at the compressor and the far-field duct boundaries.

Downstream of the plenum, the flow in the ducts adjoining the throttle was assumed to be only one-dimensional. The pressure change along the throttle ducts was given by the unsteady Bernoulli equation,

$$P_8 - P_7 + P_6 - P_5 = -L_T \frac{dW_5}{dt}. \tag{2.3}$$

The compressor and throttle ducts were presumed to be constant area ($A_C$ and $A_T$) along their lengths ($L_C$ and $L_T$). The definition of the length of the compressor duct did *not* include the compressor itself — that is, $L_C = z_3 - z_2 + z_1 - z_0$.

**Plenum:** The flow in the plenum was assumed to be spatially uniform. The plenum pressure, $P_P$, was assumed to respond isentropically to fluctuations in stored mass, as described by

$$\frac{dP_P}{dt} = \frac{\gamma P_a}{V_P}(A_C W_3 - A_T W_5). \tag{2.4}$$

**Throttle:** The throttle was represented by a quasi-steady actuator disk. The pressure drop was specified by the throttle setting, $k_T$:

$$P_6 - P_7 = \frac{1}{2} k_T W_6^2. \tag{2.5}$$

**Compressor:** The compressor was represented by an actuator disk which specified the pressure rise and exit flow angles according to local inlet conditions. These specifications were based on the steady, axisymmetric performance, which was presumed to be known (either measured or otherwise computed). The most general compressor model in this thesis included the effects of blade passage inertias, unsteady losses, inlet swirl sensitivity and a non-zero exit flow angle. The implications of each of these effects on stall prediction are described in Longley's review of compressor stability models [47] and the work by Strang [71]. The equations representing the actuator disk model for compressor behavior in unsteady, nonaxisymmetric flow are developed below.

Velocity nonuniformities were assumed to redistribute only within the adjoining ducts and not within the compressor region itself. This assumption was a consequence of assuming the blade pitch and inter-blade row gaps to be small compared to the wave-

length of the flow asymmetry. Together with flow incompressibility, this assumption implies that the axial velocity at the compressor exit must be the same as at the inlet:

$$W_2(\theta, t) = W_1(\theta, t). \tag{2.6}$$

The flow field variation with $(\theta, t)$ is implied hereafter, so the explicit dependency on $(\theta, t)$ is dropped to simplify the notation.

The exit flow angle, $\beta_2$, was presumed to be known from compressor measurements. Its value was generally a function of the compressor inlet flow angle and local clearance level. The final blade row of the compressor was always taken to be a stator, so that the exit-plane velocity relationship was given in the absolute frame by

$$V_2 = W_2 \tan \beta_2(V_1, W_1, \varepsilon). \tag{2.7}$$

The local pressure change across the compressor was based on the known total-to-static pressure rise characteristic, $\Psi = P_2 - P_{t1}$, plus correction terms to account for unsteadiness. In steady-state, axisymmetric flow, the actual pressure rise, $\Psi$, was given by the *isentropic* characteristic, $\Psi_i$, minus the losses accrued in the rotor and stator, $L_R$ and $L_S$. The ratio of rotor to stator losses were assumed to scale with the blade reaction, $\sigma$, so that $L_R = \sigma(\Psi_i - \Psi)$ and $L_S = (1 - \sigma)(\Psi_i - \Psi)$.

Two sources of unsteadiness were included in the compressor model, added to the quasi-steady behavior described above. The first source accounted for the unsteady pressure rise associated with the acceleration of the fluid within each blade passage. This "inertial effect" modified the pressure rise by the term $(P_2 - P_1)_{unsteady} = -\lambda \frac{\partial W}{\partial \theta} - \mu \frac{\partial W}{\partial t}$, where the inertia terms were given by $\lambda = \sum_{rotors} c/\cos\gamma$ and $\mu = \sum_{blades} c/\cos\gamma$. The second source of unsteadiness accounted for the time delay for blade passage losses to accrue in a changing flow field [51]. The steady-state rotor and stator losses were modified by a first order time lag, with time constants $\tau_R$ and $\tau_S$ proportional to the convection time through the respective blade passages. Detailed derivations of these equations are found in Longley's review [47].

Combining the above contributions to the compressor pressure rise led to the following

pressure matching conditions at the actuator disk location:

$$\begin{aligned} P_2 - P_{t1} &= \Psi_i - L_R - L_S - \lambda\frac{\partial W_1}{\partial\theta} - \mu\frac{\partial W_1}{\partial t} \\ (1 + \tau_R\frac{\partial}{\partial t} + \tau_R\frac{\partial}{\partial\theta})L_R &= \sigma(\Psi_i - \Psi) \\ (1 + \tau_S\frac{\partial}{\partial t})L_S &= (1-\sigma)(\Psi_i - \Psi). \end{aligned} \tag{2.8}$$

To account for the experimentally observed change in performance with different clearance values, the pressure rise characteristics must also depend on the tip clearance geometry at that circumferential position. Thus, a *class* of characteristics must be specified to represent the modeled compressor (one for each clearance level), rather than a single curve representing the pressure rise behavior for the entire compressor. An example of the class of $\Psi$ speedlines for one compressor is shown in Figure 1-4. In general, the specified characteristics have the form $\Psi = \Psi(V_1, W_1, \varepsilon)$ and $\Psi_i = \Psi_i(V_1, W_1, \varepsilon)$.

**Boundary Conditions:** The upstream flow was assumed to arrive isentropically from the steady ambient conditions. At the end of the compression system, the flow was assumed to exit to ambient pressure. Therefore, the overall compression system boundary conditions were given by

$$P_{t0} = P_{s_\infty} = P_a\,. \tag{2.9}$$

Note that the above compression system model did not differ in concept from Graf's model for stationary clearance asymmetries. Differences arose only in the implementation of the model for cases where the clearance asymmetry was unsteady.

## 2.2 Transformation to the Rotating Frame

In this section, the equations for the modeled compression system are expressed in the reference frame rotating with the clearance asymmetry. The background flow field is then steady in this reference frame, simplifying both the solution process for the background flow and the ensuing stability analysis.

The tip clearance asymmetry was assumed to rotate at a constant frequency $\nu$, nondimensionalized by the rotor frequency:

$$\varepsilon = \varepsilon(\theta - \nu t). \tag{2.10}$$

Variables transformed into the reference frame rotating at frequency $\nu$ were defined with a prime superscript, $(\,)'$. The coordinate system was transformed as

$$\begin{aligned} \theta' &= \theta - \nu t \\ z' &= z \\ t' &= t, \end{aligned} \tag{2.11}$$

so that the derivatives in the transformed frame were

$$\begin{aligned} \frac{\partial}{\partial \theta'} &= \frac{\partial}{\partial \theta} \\ \frac{\partial}{\partial z'} &= \frac{\partial}{\partial z} \\ \frac{\partial}{\partial t'} &= \frac{\partial}{\partial t} + \nu \frac{\partial}{\partial \theta}. \end{aligned} \tag{2.12}$$

The transformed velocity and pressure fields were given by

$$\begin{aligned} V' &= V - \nu \\ W' &= W \\ P' &= P \\ P'_t &= P_t + \nu(\frac{\nu}{2} - V), \end{aligned} \tag{2.13}$$

where $P'_t$ is the relative total pressure in the transformed reference frame.

Upstream of the compressor, a potential, $\Phi'$, was defined such that

$$\frac{\partial^2 \Phi'}{\partial \theta'^2} + \frac{\partial^2 \Phi'}{\partial z'^2} = 0, \quad \text{where } V' = \frac{\partial \Phi'}{\partial \theta'} \text{ and } W' = \frac{\partial \Phi'}{\partial z'}. \tag{2.14}$$

The form of the two-dimensional Euler equations for the downstream duct remained un-

changed in the rotating frame. These transformed equations were given as

$$\begin{aligned}
\frac{\partial V'}{\partial t'} + V'\frac{\partial V'}{\partial \theta'} + W'\frac{\partial V'}{\partial z'} + \frac{\partial P'}{\partial \theta'} &= 0 \\
\frac{\partial W'}{\partial t'} + V'\frac{\partial W'}{\partial \theta'} + W'\frac{\partial W'}{\partial z'} + \frac{\partial P'}{\partial z'} &= 0 \\
\frac{\partial V'}{\partial \theta'} + \frac{\partial W'}{\partial z'} &= 0.
\end{aligned} \tag{2.15}$$

The transformed version of the compressor matching conditions (2.6)–(2.8) were

$$\begin{aligned}
P_2' - P_{t1}' &= \Psi_i - L_R - L_S - (\lambda - \nu\mu)\frac{\partial W_1'}{\partial \theta'} - \mu\frac{\partial W_1'}{\partial t'} + \nu(V_1' + \frac{\nu}{2}) \\
(1 + \tau_R\frac{\partial}{\partial t'} + (1-\nu)\tau_R\frac{\partial}{\partial \theta'})L_R &= \sigma(\Psi_i - \Psi) \\
(1 + \tau_S\frac{\partial}{\partial t'} - \nu\tau_S\frac{\partial}{\partial \theta'})L_S &= (1-\sigma)(\Psi_i - \Psi) \\
W_2' &= W_1' \\
V_2' &= -\nu + W_2'\tan\beta_2
\end{aligned} \tag{2.16}$$

where $\Psi_i = \Psi_i(V_1' + \nu, W_1, \varepsilon)$, $\Psi = \Psi(V_1' + \nu, W_1, \varepsilon)$ and $\beta_2 = \beta_2(V_1' + \nu, W_1, \varepsilon)$ for $\varepsilon = \varepsilon(\theta')$. Note that the local exit flow angle ($\beta$) and total-static pressure rise ($\Psi$ and $\Psi_i$) were still evaluated in the *stationary* frame. This notation was chosen because the axisymmetric characteristics and flow angle relation are specified in the stationary frame of reference.

Since the circumferential flow nonuniformities vanished beyond the plenum, the governing equations for the plenum, throttle and throttle ducts remained unchanged by the transformation:

$$\begin{aligned}
\frac{dP_P}{dt'} &= \frac{\gamma P_a}{V_P}(A_C W_3' - A_T W_5') \\
P_5' - P_8' &= \frac{1}{2}k_T W_6'^2 + L_T\frac{dW_5'}{dt'}.
\end{aligned} \tag{2.17}$$

The system of equations developed here could be used to solve for either the steady, background flow field (by dropping all $\frac{\partial}{\partial t'}$ terms) or for the unsteady, linearized rotating stall perturbations.

## 2.3 Calculation of the Steady Flow Field

A steady solution for the flow in the frame of the rotating asymmetry could be obtained by neglecting all temporal derivatives in the transformed equations (2.14)–(2.17). This steady solution provides the flow nonuniformity local to the compressor as well as the overall pressure rise and efficiency for the compression system operating with a tip clearance asymmetry. The steady flow field was also used as the background flow for the succeeding stability analysis. As is typical for stability analyses, by suppressing the time derivative terms, the background flow can often be obtained numerically even if the actual flow is dynamically unstable.

The system of nonlinear equations requires an iterative procedure to converge to a solution. The approach used for this study iteratively solved for the first $N$ Fourier harmonics of the nonuniform flow field around the compressor by writing the equations in matrix form with one equation for each harmonic. This procedure was preferable to a nonlinear CFD method because of its efficiency, and because it required only a relatively small number of states to accurately represent the entire flow. Keeping the number of states at a minimum was necessary to implement real-time active control laws.

Details for solving for the steady background flow are described in Appendix B.1. The compressor parameters that must have been specified in advance to determine the steady flow field are listed below. These parameters form the "inputs" to the model:

1. the type of tip clearance asymmetry, given by $\nu$ and $\varepsilon(\theta')$;
2. the duct areas $A_C$ and $A_T$;
3. the blade row geometry parameters $\lambda$, $\mu$, $c_R$, $c_S$, $\gamma_R$ and $\gamma_S$;
4. the stage reaction, $\sigma$, and unsteady loss first-order time lag parameter, $\bar{\tau}$;
5. the pressure rise and exit angle relations $\Psi_i(V_1, W_1, \varepsilon)$, $\Psi(V_1, W_1, \varepsilon)$ and $\beta_2(V_1, W_1, \varepsilon)$;
6. the throttle coefficient, $k_T$.

Once the nonuniform flow field was obtained for a given compressor geometry and tip clearance variation, the overall pressure rise and efficiency of the compressor could be determined. The overall total-to-static pressure rise, $\overline{\Psi}$, was defined as the difference

between the plenum pressure and the upstream total pressure. This value was set by the mean flow through the throttle:

$$\overline{\Psi} \equiv \bar{P}_P - P_a = \frac{k_T}{2}(\frac{A_C}{A_T}W_0)^2, \tag{2.18}$$

where $W_0$ was the mean axial velocity at the inlet to the compression system. The overall efficiency, $\overline{\eta}$ was defined as the ratio between the work required to isentropically raise the compressor exit pressure to $\bar{P}_{t2}(\theta')$ and the actual work done to achieve $\bar{P}_{t2}(\theta')$:

$$\overline{\eta} \equiv \frac{\int_0^{2\pi} \bar{W}_1(\bar{P}_{t2} - \bar{P}_{t1})\, d\theta}{\int_0^{2\pi} \bar{W}_1(\bar{\Psi}_i + \frac{1}{2}(\bar{V}_2^2 + \bar{W}_2^2))\, d\theta}. \tag{2.19}$$

For uniform flow, the isentropic efficiency reduces to the ratio

$$\overline{\eta} = \frac{\bar{\Psi} + \frac{1}{2}(\bar{V}_2^2 + \bar{W}_2^2)}{\bar{\Psi}_i + \frac{1}{2}(\bar{V}_2^2 + \bar{W}_2^2)}. \tag{2.20}$$

Equation (2.20) was useful for determining the isentropic pressure rise characteristics for a compressor, given measurements of the actual pressure rise and isentropic efficiency.

## 2.4 Unsteady, Small Amplitude Flow Disturbances

A linearized version of the model was developed to examine the behavior of unsteady, small amplitude perturbations to a known steady state flow field. The linearized equations representing each component in the compression system have been combined into a matrix state-space form for use in active stall control, and to predict the stability of the unforced natural stall modes of the compression system.

The linearized model was developed in the rotating frame of reference locked to the background tip clearance variation. The transformed flow field was decomposed into two parts: (1) the steady component locked to the clearance asymmetry (obtained in the previous section), and (2) the unsteady, small amplitude perturbation. The steady, background flow was denoted by capitals with an over-bar, and the linearized perturbations were denoted by lowercase letters, or preceded with a $\delta$. The decompositions used for the linearized

model were written as

$$\begin{aligned}
\varepsilon(\theta',t') &= \bar{\varepsilon}(\theta') + \delta\varepsilon(\theta',t') \\
V'(\theta',z',t') &= \bar{V}'(\theta',z') + v'(\theta',z',t') \\
W'(\theta',z',t') &= \bar{W}'(\theta',z') + w'(\theta',z',t') \\
P'(\theta',z',t') &= \bar{P}'(\theta',z') + p'(\theta',z',t') \\
\Phi'(\theta',z',t') &= \bar{\Phi}'(\theta',z') + \phi'(\theta',z',t') \\
L_R(\theta',t') &= \bar{L}_R(\theta') + l_R(\theta',t') \\
L_S(\theta',t') &= \bar{L}_S(\theta') + l_S(\theta',t').
\end{aligned} \tag{2.21}$$

The perturbations were then decomposed into their circumferential harmonics, as in

$$\begin{aligned}
\delta\varepsilon(\theta',t') &= \varepsilon_0(t') + \sum_{n=1}^{\infty}(\varepsilon_{c,n}(t')\cos n\theta' + \varepsilon_{s,n}(t')\sin n\theta') \\
w'(\theta',t') &= w_0(t') + \sum_{n=1}^{\infty}(w_{c,n}(t')\cos n\theta' + w_{s,n}(t')\sin n\theta') \\
l_R(\theta',t') &= l_{R0}(t') + \sum_{n=1}^{\infty}(l_{Rc,n}(t')\cos n\theta' + l_{Rs,n}(t')\sin n\theta') \\
l_S(\theta',t') &= l_{S0}(t') + \sum_{n=1}^{\infty}(l_{Sc,n}(t')\cos n\theta' + l_{Ss,n}(t')\sin n\theta').
\end{aligned} \tag{2.22}$$

Appendix B.2 develops the linearized equations governing the compression system dynamics as first-order time derivatives of only the above Fourier coefficients. Following this procedure, all the linearized equations for each compression system component were combined into a truncated matrix form, written as

$$\frac{d\vec{x}}{dt'} = \mathbf{A}\vec{x} + \mathbf{B}\vec{u}. \tag{2.23}$$

The vector $\vec{x}$ represents the relevant dynamic states of the model, and the vector $\vec{u}$ represents the harmonics of the tip clearance asymmetry. Both vectors contain only the first $N$

harmonics of flow nonuniformity:

$$\begin{aligned}\vec{x} &= [p_P \;\; w_T \;\; w_0 \;\; w_{c,1} \ldots w_{c,N} \;\; w_{s,1} \ldots w_{s,N} \;\; l_{R0} \;\; l_{Rc,1} \ldots l_{Rc,N} \;\; l_{Rs,1} \ldots l_{Rs,N} \\ &\qquad l_{S0} \;\; l_{Sc,1} \ldots l_{Sc,N} \;\; l_{Ss,1} \ldots l_{Ss,N}]^T \\ \vec{u} &= [\varepsilon_0 \;\; \varepsilon_{c,1} \ldots \varepsilon_{c,N} \;\; \varepsilon_{s,1} \ldots \varepsilon_{s,N}]^T . \end{aligned} \tag{2.24}$$

The stability of the steady background flow field was determined by examining the unforced linearized compression system dynamics:

$$\frac{d\vec{x}}{dt'} = \mathbf{A}\vec{x} \, . \tag{2.25}$$

Equation (2.25) describes the temporal development of small amplitude perturbations, $\vec{x}$, superimposed on the background flow field represented by the matrix $\mathbf{A}$. This typical matrix eigenvalue problem can be solved using numerical procedures found in linear algebra texts. The general solution for $\vec{x}$ can be written as the sum of independent modes, each with exponential temporal behavior:

$$\vec{x} = \sum_{m=1}^{6N+5} \vec{x}_m \, \mathrm{e}^{s_m t'} . \tag{2.26}$$

The set of $s_m$ are the *eigenvalues*, and $\vec{x}_m$ the *eigenvectors* of the matrix $\mathbf{A}$. There were $6N+5$ independent modes, corresponding to the size of $\mathbf{A}$.

The eigenvalues determined the stability and frequency of the modes. The stability of each mode depended on the sign of the real part of $s_m = s_{r,m} + i s_{i,m}$. The flow field was considered to be *linearly unstable* if any one of the $s_{r,m}$ was greater than zero, indicating exponential growth of that mode. Therefore, all $s_{r,m}$ must be less than zero for the background flow to be linearly stable. The imaginary part of the eigenvalues, $s_{i,m}$, set the oscillatory frequency of the modes.

The eigenvectors determined the structure of the flow perturbations. The eigenmodes were generally found in complex-conjugate pairs[1], $x_m$ and $x_m^*$. The physical behavior of each mode was given by the sum of the contributions from both eigenvectors. The axial

[1]Only for real-valued eigenvalues were the eigenvectors *not* found in pairs. This occurred when the mode frequency was equal to that of the reference frame locked to the rotating tip clearance asymmetry.

velocity at the compressor face for any one mode was then given by

$$w'_m(\theta', t') = (w_0 + \{w_{c,n}, w_{s,n}\}_{1,N})_m \, e^{s_m t'} + (w_0^* + \{w_{c,n}^*, w_{s,n}^*\}_{1,N})_m \, e^{s_m^* t'} \tag{2.27}$$

where the coefficients $(w_0, \{w_{c,n}, w_{s,n}\}_{1,N})_m$ were from the eigenvector $x_m$, and the coefficients $(w_0^*, \left\{w_{c,n}^*, w_{s,n}^*\right\}_{1,N})_m$ were from the eigenvector $x_m^*$. To better analyze the mode shapes, the axial velocity perturbation of the $m^{\text{th}}$ mode was rewritten as:

$$w'_m(\theta', t') = \mathcal{R}e\{ \sum_{n=-N}^{N} w_{n,m} e^{in\theta'} e^{(s_{r,m}+is_{i,m})t'} \} \tag{2.28}$$

where the complex coefficients $w_{n,m}$ were defined as

$$w_{n,m} = \begin{cases} (w_{c,n} - iw_{s,n})_m & \text{for } n > 0, \\ (w_0)_m & \text{for } n = 0, \\ (w_{c,n} + iw_{s,n})_m & \text{for } n < 0. \end{cases} \tag{2.29}$$

For the case of a nonuniform background flow, such as with tip clearance asymmetries or inlet distortions, all $w_{n,m}$ were generally non-zero, which implied the mode was made up of a spectrum of circumferential harmonics. Each harmonic in a mode rotated at its own phase speed $\frac{s_{i,m}}{n}$ (relative to the rotating asymmetry frame), but the harmonics all grew (or decayed) in time at the same rate set by $e^{s_{r,m}t'}$. Therefore the circumferential shape of the mode varied in time as the different harmonics passed each other. The studies in the following chapter often examined the *wave envelope*, which reflects the amount of mode amplitude modulation around the circumference. The wave envelope of the axial velocity disturbance was defined as

$$\|w'_m\| = \| \sum_{n=-N}^{N} w_{n,m} e^{in\theta'} \| \, . \tag{2.30}$$

The steady and unsteady versions of the compressor flow model developed here are used to investigate the effects of rotating tip clearance asymmetry on compressor performance and stability in the following chapter. The state-space form of the unsteady model is used to develop active control methods in Chapter 4.

# CHAPTER 3

# COMPRESSOR RESPONSE TO ROTATING TIP CLEARANCE ASYMMETRY

The effect of rotating tip clearance nonuniformities on compressor performance and stability was investigated using the models developed in Section 2. This chapter contains the results of studies of two compressor configurations with tip clearance asymmetries caused by either a whirling shaft or nonuniform rotor blade heights. It was found that the largest loss of pressure rise and efficiency occurred for near-stall operation with the rotor shaft whirling near the rotating stall frequency of each compressor. For this operating condition, a whirling shaft caused the pressure rise to drop as much as 10%, and caused the compressor to stall at a mass flow up to 18% higher than with a uniform tip clearance. The effect on performance was much less for all rotor-locked asymmetries, and for whirling shafts at design point operation. For these cases, the reduction in pressure rise and efficiency was at most one percent. Implications on how these results apply to high-speed compressors are given at the end of the chapter.

## 3.1 Description of Compressors

The two compression systems chosen for this study were the MIT three-stage compressor, and the single-stage NASA Stage-37 rig. The low-speed MIT compressor was used for Graf's analysis of stationary clearance variations [25]. It was chosen as the multi-stage compressor

for this study to permit comparisons against the results from Graf. Stage-37 is a transonic rig which is currently being prepared at the NASA Lewis Research Center for experimental analysis of rotating clearance nonuniformities induced by a whirling rotor shaft. It was used in the present study to predict the magnitude of the effects that will be seen experimentally.

For the purposes of this study, the primary difference between the two compressors was the sensitivity of their pressure rise characteristics to upstream swirling flow. The first blade row of the MIT compressor was an inlet guide vane, so that the compressor was *swirl-insensitive* meaning that the pressure rise characteristic, for a fixed clearance level, was not a function of the inlet tangential velocity. However, the leading blade row in Stage-37 was a rotor, and the characteristics were noticeably dependent on the upstream axial and tangential velocities. A detailed description of how both compressors were modeled is provided in the following subsections.

### 3.1.1 MIT 3-Stage

The MIT 3-stage compressor is a 0.9 hub-to-tip ratio, low-speed rig (axial Mach number of 0.2) with constant area ducts. Details of the compressor geometry are described in the thesis by Haynes [33]. Only the parameters required by the asymmetric tip clearance model are presented here.

The family of axisymmetric pressure rise characteristics for varying clearance levels are shown in Figure 3-1. The baseline isentropic and regular total-to-static pressure rise characteristics, taken at the nominal tip clearance value of 2.1% of the rotor chord, were taken from Graf [25]. The variations of the characteristics with tip clearance were estimated based on knowledge of similar multistage compressor measurements described in Section 1.2.2. It was assumed that an increase in the tip clearance of 1% of the chord would reduce the peak pressure rise by 5% and increase the corresponding flow coefficient at the peak by 4.5%. The isentropic characteristics were chosen so that a clearance increase of 1% of the chord caused a reduction in efficiency of 1.2 points at the design flow coefficient (Figure 3-2). Furthermore, both the pressure rise and efficiency curves were adjusted to be monotonic with tip clearance, as seen in compressor experiments [26]. This last treatment differed from Graf's MIT compressor characteristics, for which the efficiency increased with clearance over portions of the operating range. The explicit derivation of the characteristics used in

the present model, which justifies the quantities chosen above, is described in Appendix D.

The remaining nondimensional parameters representing the compression system are listed in Table 3.1. The nondimensionalizing parameters were the ambient density ($\tilde{\rho} = 1.125\,\mathrm{kg/m^3}$), the mean annular radius ($\tilde{R} = 18\,\mathrm{cm}$), and the rotor frequency ($\tilde{\Omega} = 100\,\mathrm{Hz}$) which resulted in a mean rotor speed of $\tilde{U} = 200\,\mathrm{m/s}$. Certain parameters in Table 3.1 differed from the experimental values, and require further explanation. Specifically, the throttle duct length, $L_T$, was set much smaller than $L_C$ in order to eliminate throttle dynamics, and the value of the plenum volume, $V_P$, was chosen to fix the $B$-Parameter at 0.05. The nondimensional $B$-parameter determines the preference for the compressor instability to be rotating stall or surge [27]. The low value of 0.05 ensured the compressor model first showed instability from rotating stall, similar to the MIT compressor experiments [33].

**Table 3.1:** Nondimensional parameters of the MIT 3-stage compressor.

| | | | | | |
|---|---|---|---|---|---|
| $A_C$ | Compressor duct area | 0.5 | $A_T$ | Throttle duct area | 0.5 |
| $L_C$ | Compressor duct length | 4.0 | $L_T$ | Throttle duct length | 0.01 |
| $V_P$ | Plenum volume | 0.702 | $B$ | $B$-parameter | 0.05 |
| $\mu$ | Compressor inertia | 1.012 | $\lambda$ | Rotor inertia | 0.679 |
| $c_R \cos\gamma_R$ | Rotor axial chord | 0.118 | $c_S \cos\gamma_S$ | Stator axial chord | 0.108 |
| $\sigma$ | Stage reaction | 0.75 | $\bar{\tau}$ | Unsteady loss time lag | 1.5 |
| $\bar{\varepsilon}$ | Nominal clearance / chord | 0.021 | $\beta_2$ | Exit flow angle | 0 |

Axisymmetric flow fields and modal behavior were calculated at three operating points, shown in Figures 3-1 and 3-2. The points represent the design point (maximum efficiency), the peak of the characteristic, and the neutral stability point which was at a flow coefficient just below the peak of the characteristic due to the effects of unsteady losses. The important flow parameters at these operating points have been summarized in Table 3.2 for later reference.

The linear stall dynamics of the nominal MIT compressor configuration at neutral stability are shown in Figure 3-3. The eight least damped modes are plotted, where the mode number, $n$, refers to the number of circumferential harmonics in the mode shape. The most unstable mode had a first harmonic sinusoidal shape around the annulus, and rotated at 30% of the rotor frequency. The circumferential shape distinguished this mode from the

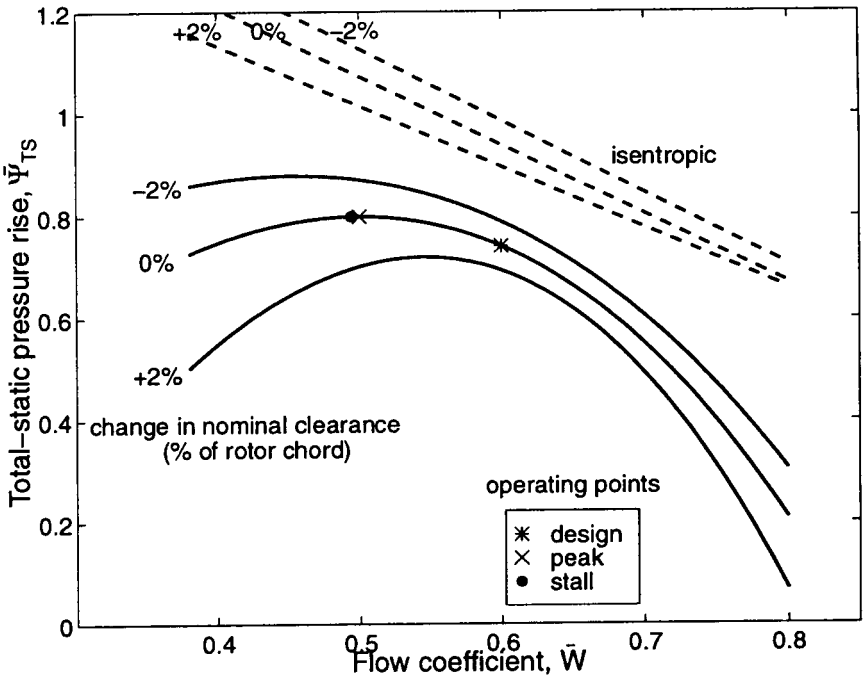


**Figure 3-1:** Family of total-to-static pressure rise characteristics for MIT three-stage compressor

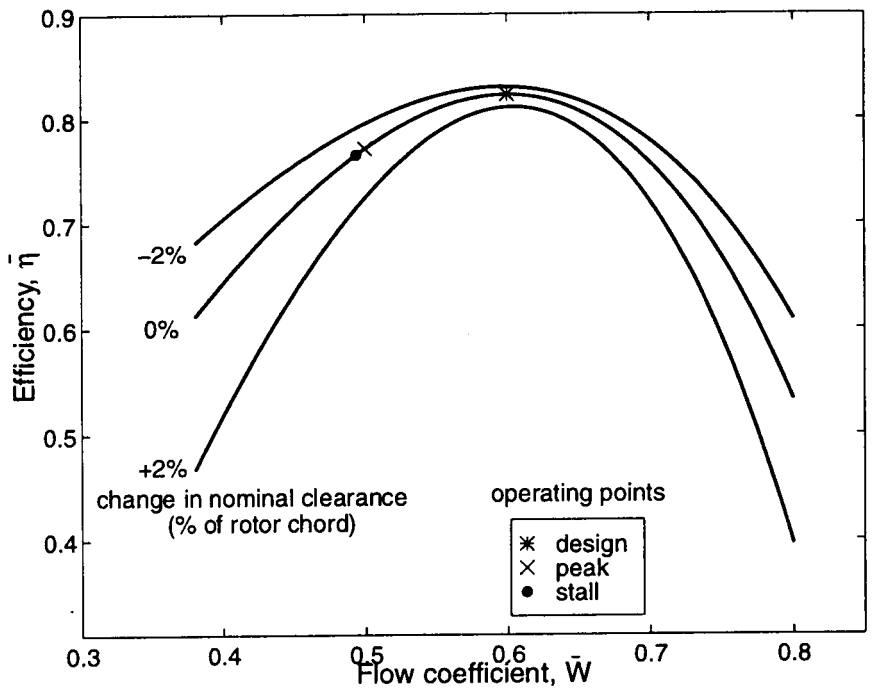


**Figure 3-2:** Family of efficiency curves for MIT three-stage compressor

**Table 3.2:** Comparison of axisymmetric flow properties at 3 operating points for the MIT compressor.

| | | Design | Peak | Stall |
|---|---|---|---|---|
| $k_t$ | Throttle coefficient | 4.12 | 6.40 | 6.56 |
| $\bar{W}$ | Flow coefficient | 0.600 | 0.500 | 0.494 |
| $\overline{\Psi}$ | Total-static pressure rise | 0.741 | 0.800 | 0.799 |
| $\overline{\eta}$ | Efficiency | 0.823 | 0.772 | 0.766 |
| $\partial\Psi/\partial W$ | Characteristic slope (with W) | -1.21 | 0.00 | 0.07 |
| $\partial\Psi/\partial V$ | Characteristic slope (with V) | 0.00 | 0.00 | 0.00 |
| $\partial\Psi/\partial\varepsilon$ | Characteristic slope (with $\varepsilon$) | -1.24 | -4.00 | -4.15 |
| $(s_r)_1$ | Growth rate of 1st harmonic mode | -0.397 | -0.018 | 0.000 |
| $(s_i)_1$ | Frequency of 1st harmonic mode | 0.233 | 0.294 | 0.297 |
| $(s_r)_0$ | Growth rate of surge mode | -0.777 | -0.634 | -0.625 |
| $(s_i)_0$ | Frequency of surge mode | 0.000 | 0.000 | 0.000 |

more stable rotating stall modes of higher harmonic shapes, and the axisymmetric surge mode.

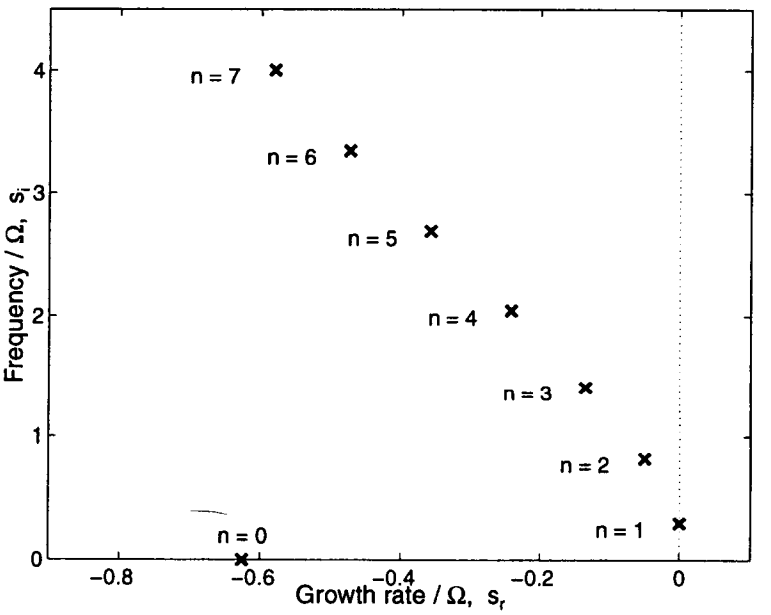


**Figure 3-3:** Location of the 8 least damped eigenvalues representing the modes of the axisymmetric flow field at the neutral stability operating point for the MIT compressor

### 3.1.2 NASA Stage-37

Many aspects of the Stage-37 geometry and flow [54] are not reproducible by the two-dimensional, low-speed, incompressible model developed in Section 2. The design flow is

high-speed (axial Mach number of 0.6), and the relative flow in the rotor is transonic. The compressor duct has a 2:1 area convergence from inlet to exit, and the mean axial velocity increases by 15% across the stage alone. There is no plenum at the end of the compressor duct, but rather a plug valve that acts as the throttle. Despite these differences, Stage-37 has been fit to a model that reflects the overall axisymmetric pressure rise characteristics (especially their sensitivity to tip clearance changes) as well as the velocities local to the compressor blades for near-stall operation. These parameters were considered to be the critical features that control the compressor's off-design response to tip clearance asymmetry. The methodology for fitting the actual compressor to the model is detailed in Appendix D, and summarized below.

The values for the parameters used to model the Stage-37 compression system are listed in Table 3.3. The nondimensionalizing parameters were the mean annular radius ($\tilde{R}$ = 21.6 cm), the rotor frequency ($\tilde{\Omega}$ = 286 Hz), and a density of $\tilde{\rho}$ = 1.808 kg/m$^3$. The compressor duct was modeled with constant area, $A_C$, equal to the stator inlet area. This value was approximately the average cross-sectional area through the stage. The duct length, $L_C$, was taken from experimental measurements. The blade chords and inertia parameters were calculated from the midspan geometry. Since the individual blade row losses were known, an average value of $\sigma$ could be read directly from data (Figure 3-4) rather than using the value of the stage reaction. To eliminate the throttle dynamics, the throttle duct was set to a length much smaller than the compressor duct. The plenum volume, $V_P$, was chosen to achieve a $B$-parameter that reflected the surge frequency of the compression system. This frequency was assumed to be similar to that of Stage-35, which was measured by Weigl [78] to be 8% of the rotor frequency at neutral stability. The plenum volume was then obtained from the definition of the $B$-parameter [27], $V_P = 4\gamma P_a A_C (L_C + \mu) B^2$.

The family of axisymmetric pressure rise characteristics and exit flow angles were based on CFD calculations of Stage-37 performance for different levels of tip clearance [32]. Adamczyk's APNASA blade passage code [1] was used to calculate the three-dimensional, viscous flow through the stage for axisymmetric clearances corresponding to the maximum, average and minimum local clearances obtained by displacement of the rotor shaft from the centerline. For the magnetic shaft bearing experiments, the nominal tip clearance will be increased to 0.02", and the shaft can be displaced by 0.01" [72]. Therefore, the three clearance values

**Table 3.3:** Nondimensional parameters of the NASA Stage-37 compressor.

| | | | | | |
|---|---|---|---|---|---|
| $A_C$ | Compressor duct area | 1.568 | $A_T$ | Throttle duct area | 1.568 |
| $L_C$ | Compressor duct length | 6.62 | $L_T$ | Throttle duct length | 0.015 |
| $V_P$ | Plenum volume | 23.394 | $B$ | $B$-parameter | 1.0 |
| $\mu$ | Compressor inertia | 0.620 | $\lambda$ | Rotor inertia | 0.421 |
| $c_R \cos\gamma_R$ | Rotor axial chord | 0.159 | $c_S \cos\gamma_S$ | Stator axial chord | 0.177 |
| $\sigma$ | Rotor loss / stage loss | 0.85 | $\bar{\tau}$ | Unsteady loss time lag | 2.0 |
| $\bar{\varepsilon}$ | Nominal clearance / chord | 0.910% | | | |

used in the CFD calculations were 0.01", 0.02" and 0.03", corresponding to 0.455%, 0.910% and 1.365% of the rotor chord. The procedure by which the three-dimensional, compressible flow CFD computations were fit to the present compression system model is detailed in Appendix D.

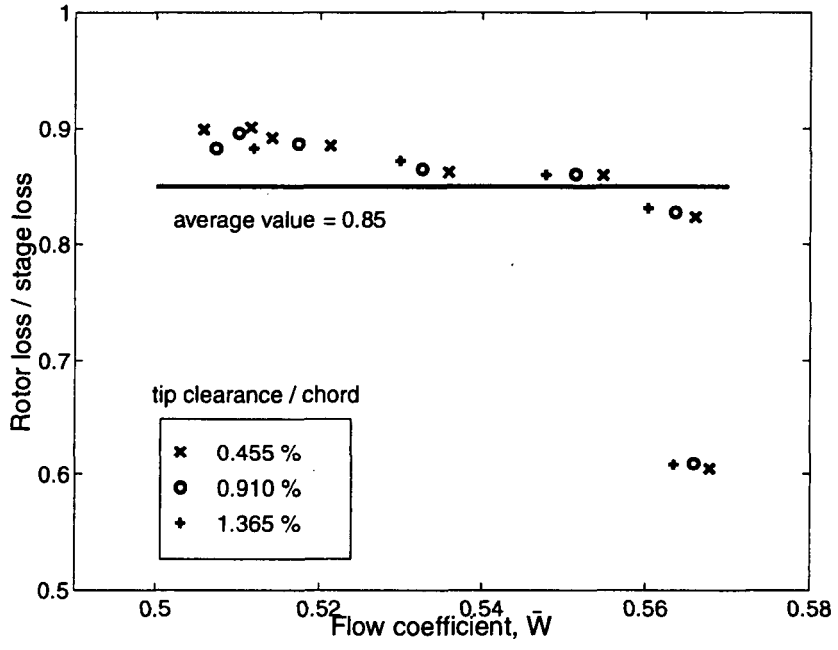


**Figure 3-4:** Ratio of rotor loss to stage loss in Stage-37 compressor, used to estimate an average value for $\sigma$ ($\approx 0.85$). Results for 3 axisymmetric clearance levels from computations performed at NASA [32].

Figure 3-5 shows the resultant total-to-static pressure rise characteristics for different tip clearances and inlet tangential velocities used in the Stage-37 model. An increase in clearance of 1% chord reduces the peak pressure rise by 14%, which is consistent with values

for other compressors at clearances below 1.5% chord in Figure 1-5. The compressor exit flow angle is plotted as a function of flow coefficient in Figure 3-6, which shows that $\beta_2$ is fairly constant for all operating conditions. The family of axisymmetric efficiency curves for the three tip-clearance values are shown in Figure 3-7, where the efficiency was defined from equation (2.20). A summary of the parameters characterizing the background flow field and the compressor dynamics for three operating conditions is provided in Table 3.4 for later reference.

**Table 3.4:** Comparison of axisymmetric flow parameters at 3 operating points for NASA Stage-37.

| | | Design | Stall | Peak |
|---|---|---|---|---|
| $k_t$ | Throttle coefficient | 1.140 | 1.923 | 1.929 |
| $\bar{W}$ | Flow coefficient | 0.550 | 0.494 | 0.493 |
| $\bar{\Psi}$ | Total-static pressure rise | 0.172 | 0.235 | 0.235 |
| $\bar{\eta}$ | Efficiency | 0.731 | 0.722 | 0.721 |
| $\partial\Psi/\partial W$ | Characteristic slope (with W) | -2.17 | -0.03 | 0.00 |
| $\partial\Psi/\partial V$ | Characteristic slope (with V) | -0.97 | -0.13 | -0.12 |
| $\partial\Psi/\partial\varepsilon$ | Characteristic slope (with $\varepsilon$) | -1.84 | -3.39 | -3.43 |
| $(s_r)_1$ | Growth rate of 1$^{st}$ harmonic mode | -0.813 | 0.000 | 0.008 |
| $(s_i)_1$ | Frequency of 1$^{st}$ harmonic mode | 0.428 | 0.341 | 0.340 |
| $(s_r)_0$ | Growth rate of surge mode | -0.077 | -0.020 | -0.018 |
| $(s_i)_0$ | Frequency of surge mode | 0.000 | 0.065 | 0.064 |

The linearized dynamics of the Stage-37 model compared well to experimental measurements. The nominal compressor configuration stalled just before the peak of the characteristic due to the growth of the first harmonic rotating stall mode, rotating at a frequency of 34% of the rotor shaft. This behavior is similar to open-loop stall experiments for Stage-35, where the stall mode rotated at 30% of the rotor frequency. Figure 3-8 plots the location of the 8 most unstable eigenmodes at the stall point for the nominal configuration. The surge mode was less damped (relative to the first mode) than for the MIT compressor. This suggests that the surge mode is more likely to limit the stability of the Stage-37 compressor under either nonaxisymmetric operation or with active control.

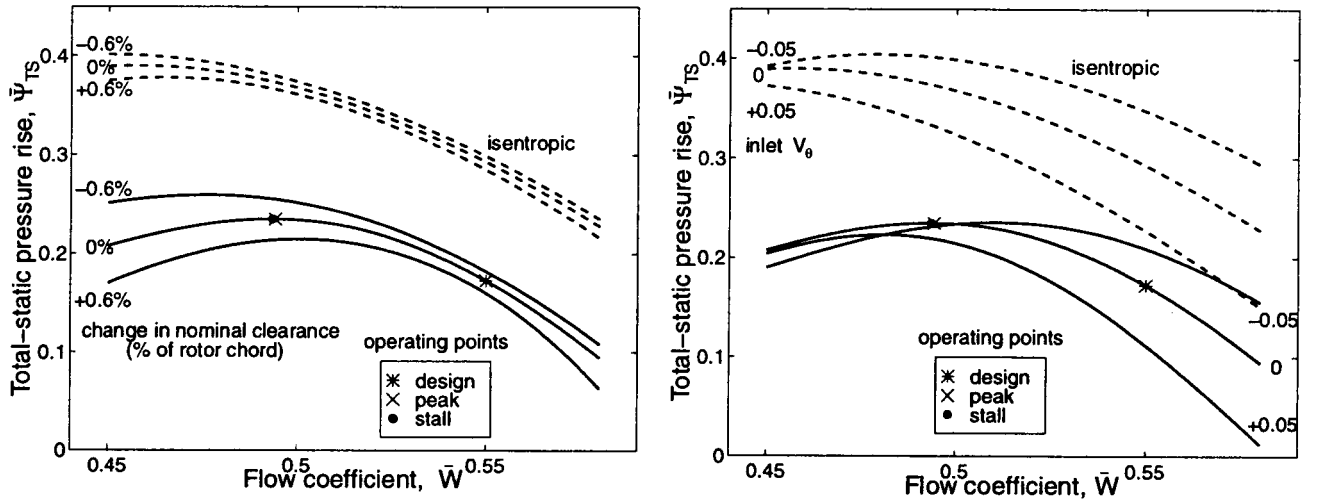


(a) Different tip clearance values ($\bar{V}_1 = 0$)

(b) Different inlet tangential velocity ($\bar{\varepsilon} = 0.0091$)

**Figure 3-5:** Family of axisymmetric total-to-static pressure rise characteristics for Stage-37, showing dependence on (a) tip clearance and (b) rotor inlet tangential velocity. Negative values of $V$ correspond to inlet velocities counter to rotor rotation.

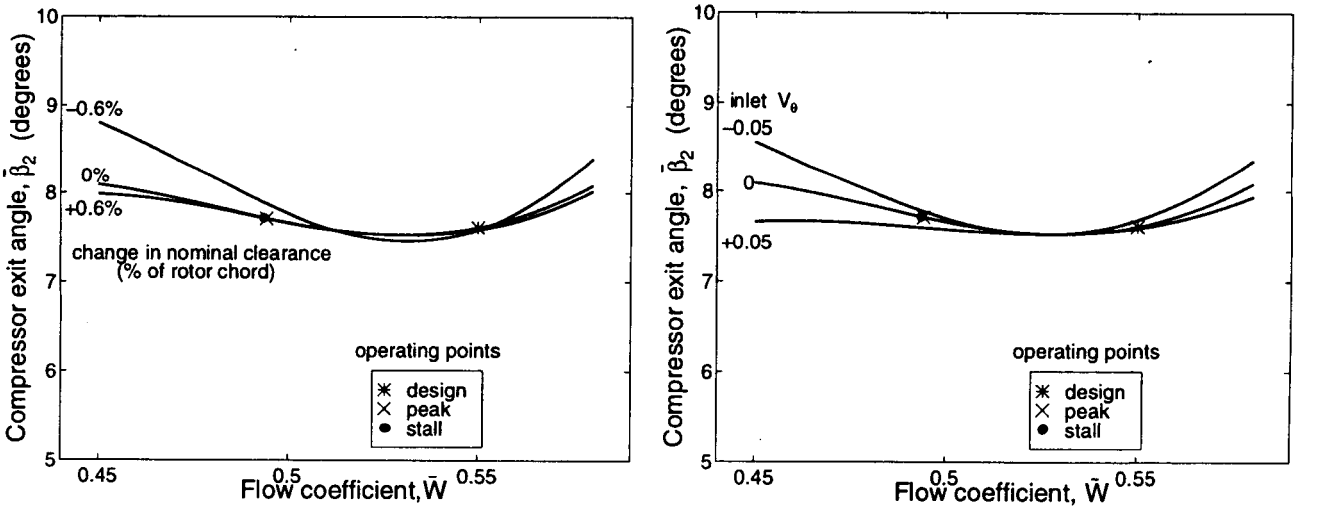


(a) Different tip clearance values ($\bar{V}_1 = 0$)

(b) Different inlet tangential velocity ($\bar{\varepsilon} = 0.0091$)

**Figure 3-6:** Family of compressor exit angle ($\beta_2$) curves for Stage-37, showing dependence on (a) tip clearance and (b) rotor inlet tangential velocity. Negative values of $V$ correspond to inlet velocities counter to rotor rotation.

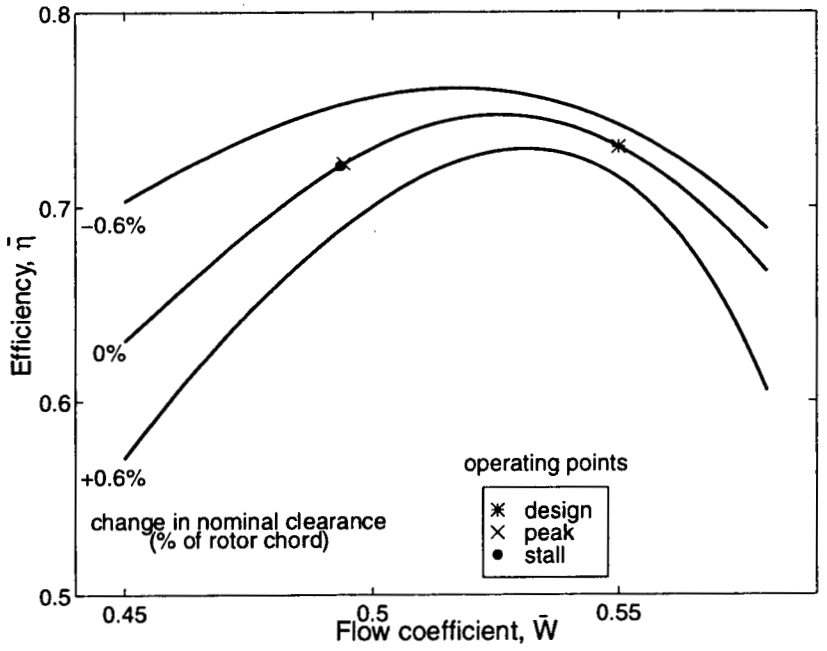


**Figure 3-7:** Family of efficiency curves for Stage-37 with varied axisymmetric tip clearance values.

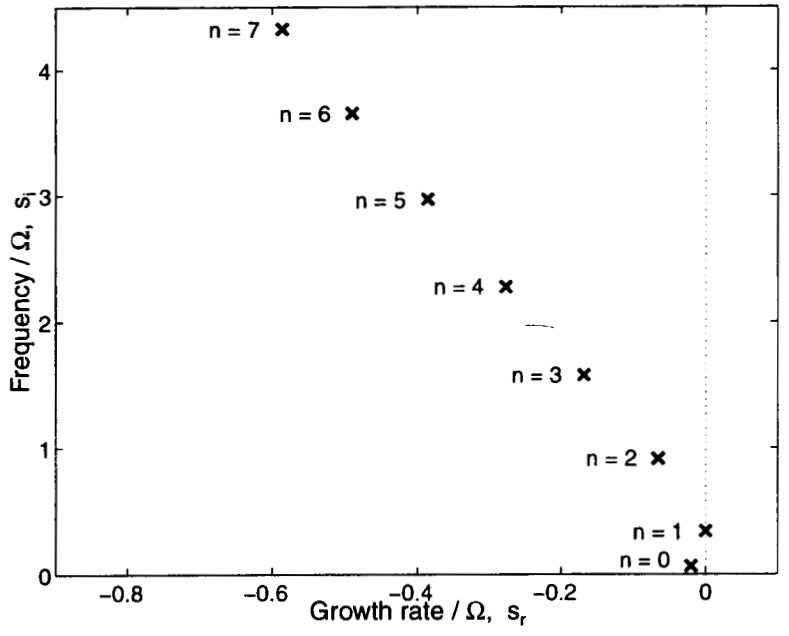


**Figure 3-8:** Location of the 8 least damped eigenvalues representing the modes of the nominal, axisymmetric flow field at the neutral stability operating point for Stage-37.

## 3.2 Scope of Study

The MIT 3-stage configuration was used to examine the effects of both whirling shaft and rotor height types of clearance asymmetry. Results from these studies were used to draw conclusions for general multistage compressors. The Stage-37 configuration was only used to examine the effect of a whirling shaft, to guide the future experimental work.

The tip clearance variation induced by a whirling shaft can be seen from Figure 1-2 to be $\bar{\varepsilon} = \varepsilon_0 + \varepsilon_1 \cos(\theta - \nu t)$, where $\varepsilon_0$ was the nominal, axisymmetric tip clearance and $\varepsilon_1$ was the shaft displacement from the compressor centerline. Flow fields for the whirling shaft studies were generated for various $\varepsilon_1$ and $\nu$. Whirling frequencies between -1 and 2 times the rotor frequency were examined (negative quantities indicate a shaft whirling counter to the rotor direction). These values bracket typical shaft whirling and flexing modes, which are described in Ehrich [15]. The values of shaft offsets used were different for the two compressors. For the MIT 3-stage, offsets of 0%, 1% and 2% of the chord were considered. These amounts were chosen to span the range of shaft offsets possible within the annulus, from 0% to 91% of the nominal clearance. For Stage-37, studies were performed for offsets of 0%, 0.15%, 0.3%, 0.455% and 0.6% of the chord, which equaled 0%, 17%, 33%, 50% and 67% of the nominal clearance. The values up to 0.3% of the chord spanned the variations of clearances used in the CFD calculations to produce the family of characteristics. Offsets beyond 0.6% chord required excessive extrapolation of the CFD calculations, which generated pressure rise characteristics that were not representative of physical compressors.

Flow fields for rotor-locked tip clearance asymmetries were generated for various patterns of blade height nonuniformity. The outer casing was presumed to be uniform, so that the only source of tip clearance asymmetry came from the rotor height variation. The tip clearance around the annulus was expressed as $\bar{\varepsilon} = \varepsilon_0 + \varepsilon_1(\theta - \Omega t)$, where $\varepsilon_0$ was the mean clearance level, and $\varepsilon_1$ the tip clearance variation rotating at the rotor frequency. Parametric studies examined the flow field in the MIT compressor configuration for three magnitudes and four shapes of $\varepsilon_1$. Sinusoidal shapes for the clearance variation of one, two, three and fifteen lobes were examined. The low harmonics were studied because they were found to be the most detrimental to compressor performance; the highest harmonic case

corresponded to the extreme case where the rotor height varied between every other blade around a 30 blade rotor disk. The magnitudes of these variations were chosen as 0%, 1% and 2% of the chord to compare with the whirling shaft results.

Background flow and linearized stability calculations were performed for every clearance nonuniformity at throttle positions corresponding to the design point and the peak of the pressure rise characteristic. A third point corresponding to neutral stability was also obtained by adjusting the throttle position until the most unstable mode had a zero growth rate. The inputs to each calculation are listed in Section 2.3. The output for each study consisted of the following parameters that characterized the flow: the overall pressure rise, $\overline{\Psi}$; the overall efficiency, $\overline{\eta}$; the amount of flow nonuniformity, $(\bar{W}_{max} - \bar{W}_{min})/W_0$; the growth rate of the most unstable mode, $s_r$; the frequency of the most unstable mode, $s_i$; and the structure of the mode, represented by the axial velocity perturbation, $w(\theta', t')$.

## 3.3 Effect of Whirling Shaft on Compressor Performance

This section describes and explains the changes to compressor performance (pressure rise and efficiency) for tip clearance asymmetries induced by a whirling rotor shaft. The effects on the stall margin, and the stall inception behavior are described in Section 3.4.

In general, the effect of an offset, whirling shaft was to reduce the performance of the compressor, relative to its performance under the same operating conditions with a centered shaft. The flow phenomena associated with the performance loss are summarized below:

1. Tip clearance variations induce flow nonuniformities.
2. Circumferential flow variations reduce the overall pressure rise and efficiency of the compressor.
3. The loss in performance increases as the compressor operates closer to the stall point.
4. The loss in performance increases as the whirling shaft frequency approaches the natural (*resonant*) rotating stall frequency of the compressor.

The first three phenomena have also been observed for stationary tip clearance asymmetries [25], but are included here for completeness. The fourth phenomenon was the most

important new effect examined by these studies. All the flow phenomena are individually established and explained below with illustrative calculations to first provide an understanding of how the compressors responded to rotating tip clearance asymmetries. The explanations are then followed by a quantification of the actual performance losses for the MIT and NASA compressors over the range of parametric studies performed.

### 3.3.1 Tip Clearance Variations Induce Flow Nonuniformity

A circumferential variation in the tip clearance caused the flow to redistribute to account for the high pressure rise characteristic in regions of tight clearance and the low pressure rise characteristic in regions of loose clearance. Figures 3-9a to 3-11a show the flow nonuniformity in the MIT compressor induced by an offset shaft, whirling at 0%, 30% and 100% of the rotor frequency. For the case of $\nu = 0$, the axial velocity variation lagged the clearance variation by 140°; whereas the axial velocity led the clearance variation by 120° for $\nu = 1$. The flow nonuniformity was largest for $\nu = 0.3$, for which the velocity and clearance variations were 180° out of phase. Figures 3-9b, 3-10b and 3-11b show this information in a more instructive way by plotting the locus of the local operating points around the annulus (i.e. the local total-to-static pressure rise characteristic vs. flow coefficient). These loci show how the flow nonuniformity compares with the family of axisymmetric pressure rise characteristics.

The different shapes of the flow nonuniformity can be understood by examining the response of a simplified compressor model. Consider a compressor that is swirl-insensitive, has axial exit flow and no unsteady losses. In the rotating reference frame of the whirling shaft, the expression for the local pressure rise, equation (B.6), reduces to

$$\bar{P}_2' - \bar{P}_{t1}' = \bar{\Psi} - (\lambda - \nu\mu)\frac{\partial \bar{W}_1'}{\partial \theta'} + \nu(\bar{V}_1' + \nu/2). \tag{3.1}$$

The case for a steady clearance asymmetry is the easiest to analyze. For this case, the pressure rise is given by

$$\bar{P}_2 - \bar{P}_{t1} = \bar{\Psi} - \lambda\frac{\partial \bar{W}_1}{\partial \theta}. \tag{3.2}$$

In steady flow, $\bar{P}_2$ and $\bar{P}_{t1}$ are uniform, so circumferential variations in $\bar{\Psi}$ must be directly

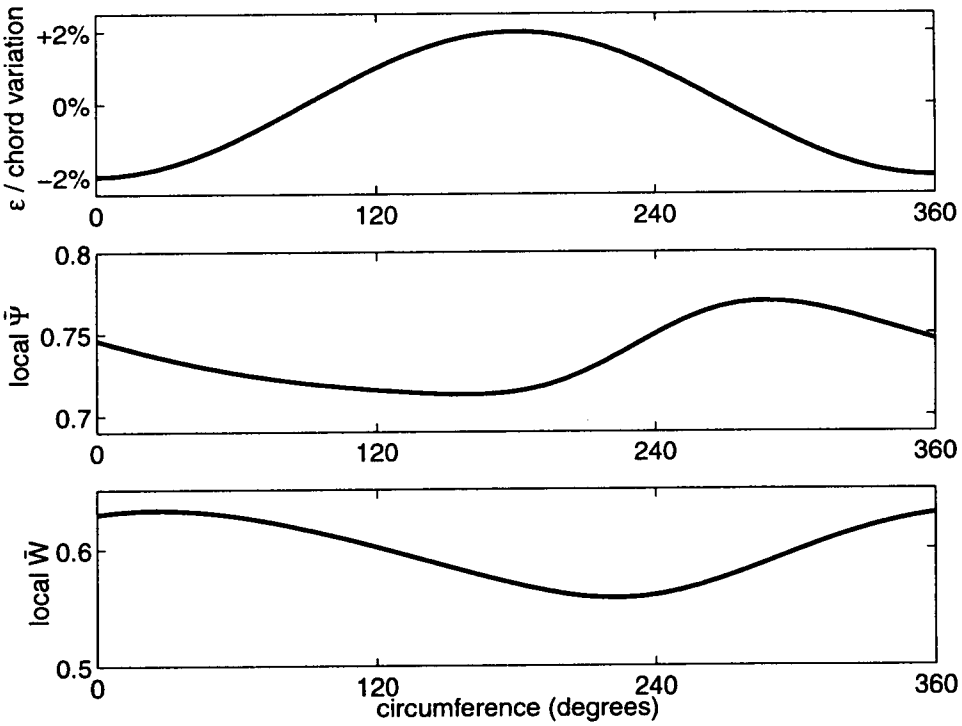


(a) Circumferential variation of clearance, axial velocity, and local pressure rise characteristic

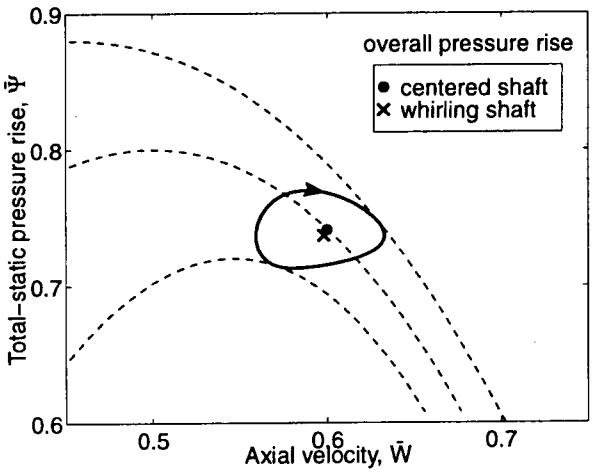


(b) Locus of local operating points around annulus

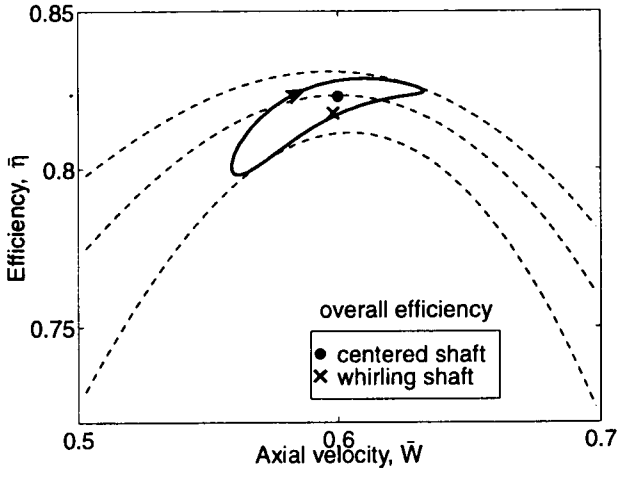


(c) Locus of local efficiency around annulus

**Figure 3-9:** Nonuniform flow in MIT compressor induced by steady rotor shaft offset of 2% chord from the centerline ($\nu = 0$, $\varepsilon_1 = 0.02$). Loci of operating points and efficiency are superimposed on the family of axisymmetric performance characteristics. The arrow denotes the loci path in the direction of rotor rotation.

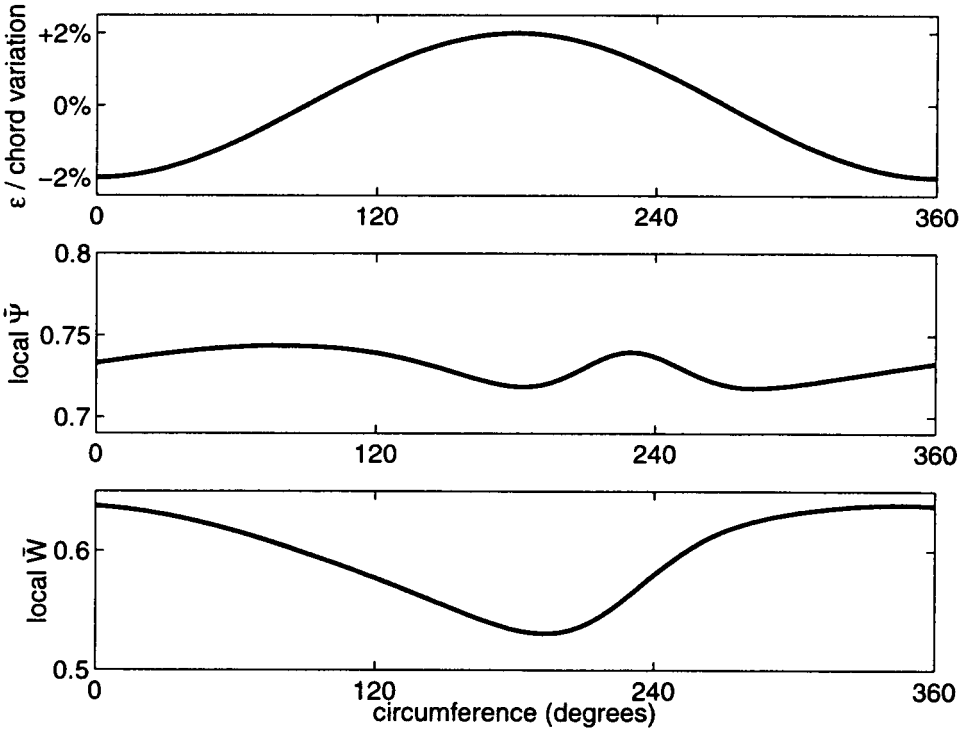


(a) Circumferential variation of clearance, axial velocity, and local pressure rise characteristic

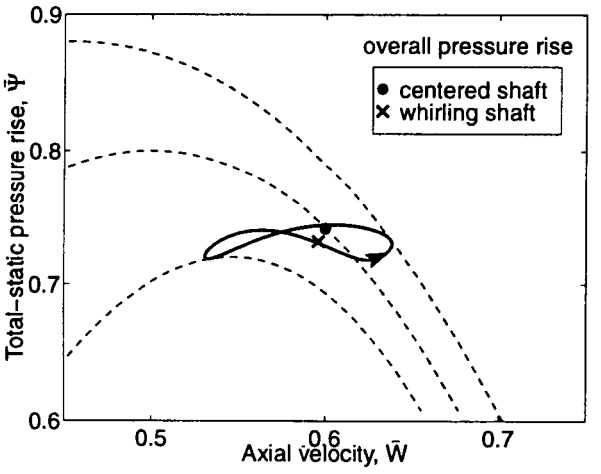


(b) Locus of local operating points around annulus

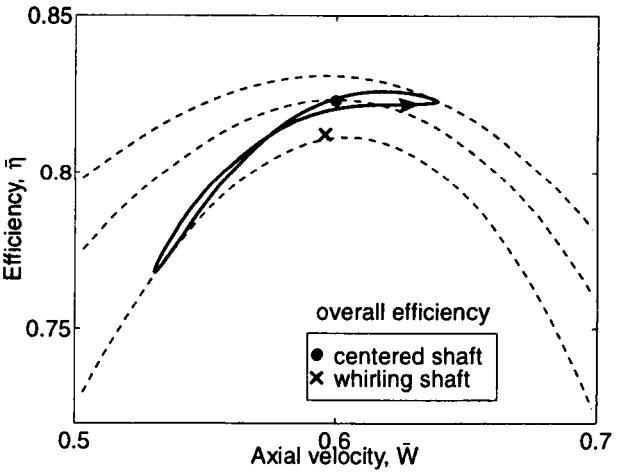


(c) Locus of local efficiency around annulus

**Figure 3-10:** Nonuniform flow in MIT compressor induced by whirling rotor shaft offset of 2% chord from the centerline at frequency of 30% of rotor frequency ($\nu = 0.3$, $\varepsilon_1 = 0.02$). Loci of operating points and efficiency are superimposed on the family of axisymmetric performance characteristics. The arrow denotes the loci path in the direction of rotor rotation.

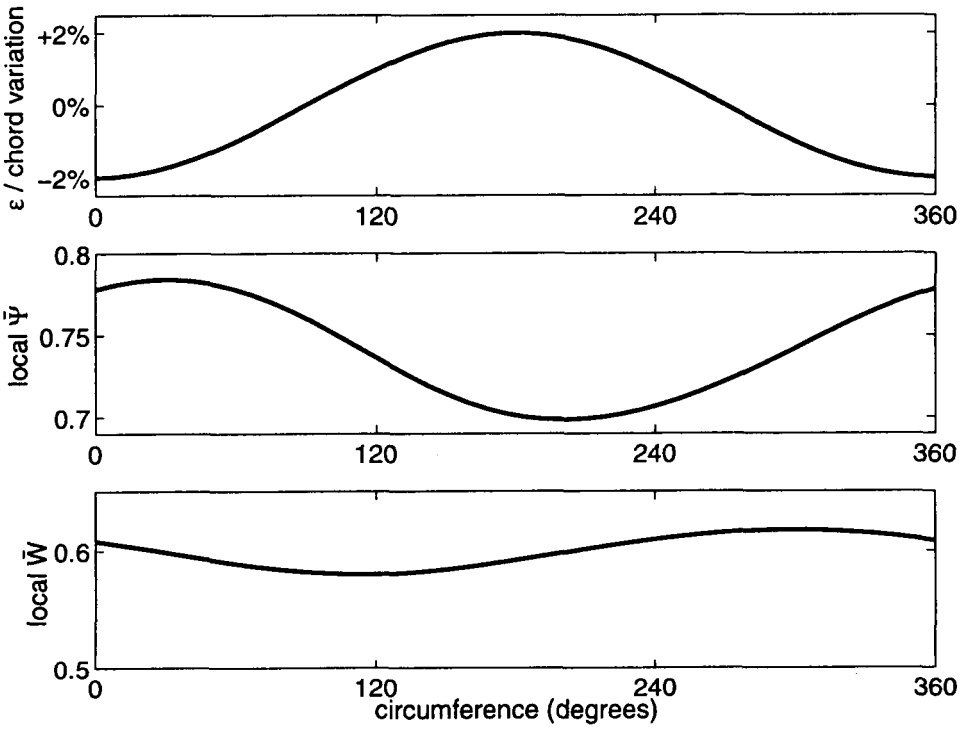


(a) Circumferential variation of clearance, axial velocity, and local pressure rise characteristic

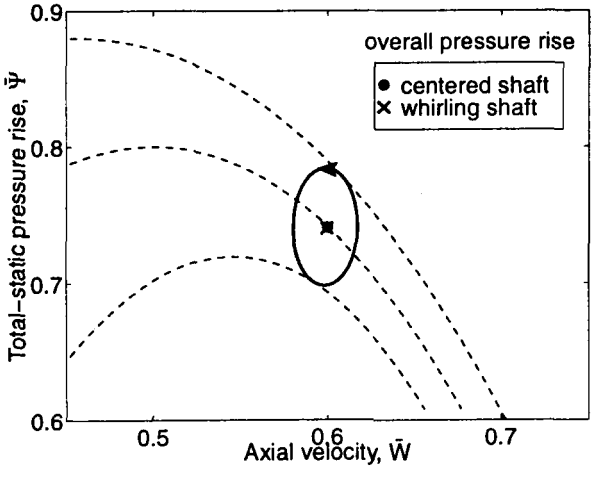


(b) Locus of local operating points around annulus

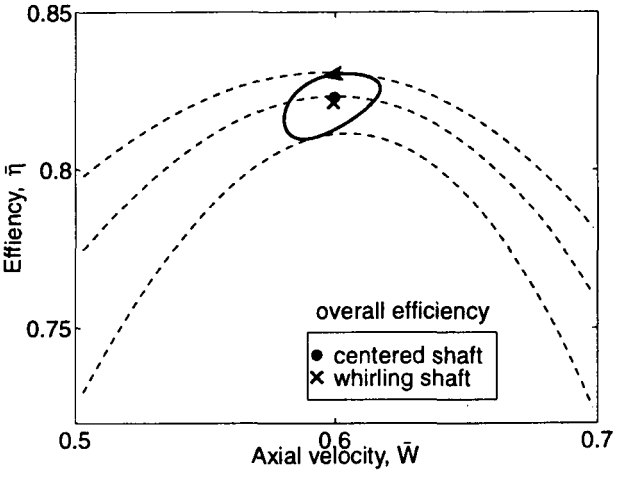


(c) Locus of local efficiency around annulus

**Figure 3-11:** Nonuniform flow in MIT compressor induced by whirling rotor shaft offset of 2% chord from the centerline at frequency of 100% of rotor frequency ($\nu = 1$, $\varepsilon_1 = 0.02$). Loci of operating points and efficiency are superimposed on the family of axisymmetric performance characteristics. The arrow denotes the loci path in the direction of rotor rotation.

balanced by variations in $\frac{\partial \bar{W}_1}{\partial \theta}$. Therefore, regions of tight clearance, which operate on a higher local pressure rise characteristic, have the highest gradient of axial velocity. This demonstrates why the axial velocity variation lags the clearance variation in Figure 3-9a.

For a whirling shaft, the exit static pressure, $\bar{P}_2'$ and inlet relative tangential velocity, $\bar{V}_1'$ are no longer uniform. To represent these parameters in terms of $\Psi$ and $W$ requires some assumptions. It is reasonable to assume the velocity and pressure nonuniformities are dominated by the shape of the clearance nonuniformity. Therefore, the pressure and velocity are assumed to have first-harmonic sinusoidal variations around the annulus. Since the downstream pressure field and upstream velocity field are elliptical, the axial change in these variables can be expressed in terms of their tangential variation. For pressure, $\left.\frac{\partial \bar{P}'}{\partial z'}\right|_2 = -\left.\frac{\partial \bar{P}'}{\partial \theta'}\right|_2 = P_P - \bar{P}_2'$, where $\left.\frac{\partial \bar{P}'}{\partial z'}\right|_2 = \nu \frac{\partial \bar{W}_1'}{\partial \theta'}$ from equation (B.18). For tangential velocity, $\left.\frac{\partial \bar{V}'}{\partial z'}\right|_1 = \left.\frac{\partial \bar{V}'}{\partial z'}\right|_1 = \bar{V}_1' + \nu$, where $\left.\frac{\partial \bar{V}'}{\partial z'}\right|_1 = \frac{\partial \bar{W}_1'}{\partial \theta'}$ in the irrotational upstream flow. Finally, equation (B.5) is used to replace $\bar{P}_{t1}'$. With these simplifications, equation (3.1) yields the relation

$$\bar{\Psi} \approx (P_P - P_a) + [\lambda - \nu(\mu + 1)] \frac{\partial \bar{W}_1'}{\partial \theta'}. \tag{3.3}$$

Any variation in $\bar{\Psi}$ must be again directly balanced by the variation in $\frac{\partial \bar{W}_1'}{\partial \theta'}$. The proportionality factor $[\lambda - \nu(\mu + 1)]$ introduces three frequency regimes to consider:

1. Negative frequencies (i.e. whirling counter to the direction of rotor rotation): The proportionality factor is positive and larger than $\lambda$. Thus, the induced flow nonuniformity is similar to that for the steady shaft offset, but of a smaller magnitude.

2. Large positive frequencies ($\nu \gg \lambda/(\mu + 1)$): The proportionality factor is negative. The velocity-clearance phase relationship is opposite to the above case, so in regions of tight clearance, where the pressure rise characteristic was higher, the axial velocity nonuniformity had the largest *negative* gradient.

3. Positive frequencies near the critical frequency $\nu \approx \lambda/(\mu + 1)$: The proportionality factor is small, so that $\frac{\partial \bar{W}_1'}{\partial \theta'}$ becomes large. This critical frequency was close to, but not identical to, the frequency of the first-harmonic rotating stall mode, $(\nu = \lambda/(\mu + 2))$. In practice, it was found that higher order harmonic flow variations became important in this case, and the approximations leading to equation (3.3) broke down. This

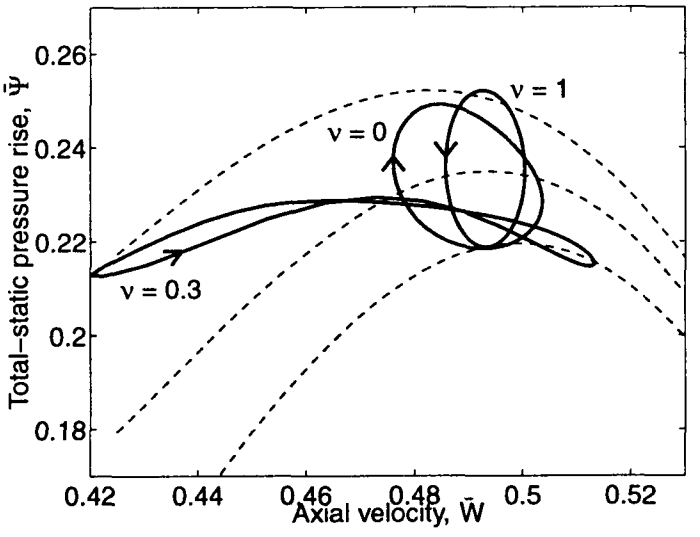


**Figure 3-12:** Loci of local operating points around annulus of Stage-37 caused by whirling rotor shaft offset of 0.455% chord from the centerline at frequencies of 0%, 30% and 100% of rotor frequency ($\nu = \{0, 0.3, 1\}$, $\varepsilon_1 = 0.00455$).

accounted for the flattened, figure-eight shaped locus in Figure 3-10b, which had the largest axial velocity nonuniformity of the three examples for the MIT compressor. The whirling shaft frequency for this case was 30% of the rotor frequency, which was close to the critical frequency of $\lambda/(\mu + 1) = 0.34$.

The flow nonuniformity induced by a whirling shaft in the NASA Stage-37 compressor showed similar results to the MIT compressor. The loci of local operating points for three whirl frequencies showed the highest flow nonuniformity at 30% of rotor frequency (Figure 3-12). This value is close to the Stage-37 critical frequency of 0.26. In general, the critical frequency, $\lambda/(\mu + 1)$, is between 0.2 and 0.5 for most compressors, so these results reflect the typical response to whirling shafts.

### 3.3.2 Flow Nonuniformity Reduces Compressor Performance

The overall pressure rise and efficiency of the compression system were reduced in the presence of nonuniform flow, relative to the case of uniform flow at the same throttle position. For example, the overall pressure rise, $\overline{\Psi}$, and efficiency, $\overline{\eta}$ of the MIT compressor are indicated on Figures 3-9b to 3-11b with both an offset and a centered rotor. The loss in performance was solely due to the downward concave curvature of the axisymmetric

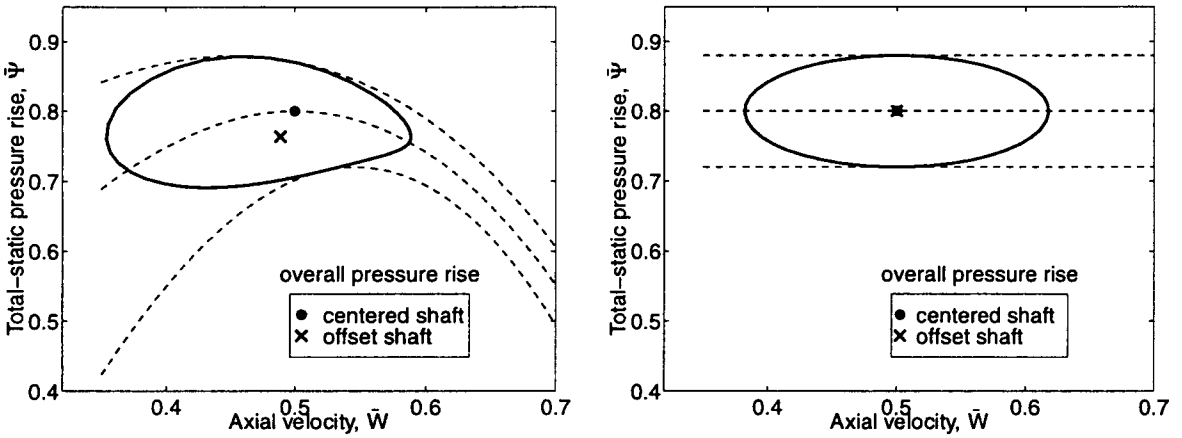


(a) Nominal characteristics

(b) Uniform characteristics

**Figure 3-13:** Overall pressure rise and locus of local operating points around annulus in MIT compressor for steady shaft offset of 2% chord using families of characteristics with (a) nominal curvature and (b) no curvature.

characteristics. This curvature caused the average of the local pressure rise and efficiency loci around the annulus to be lower than the nominal performance for the uniform flow case.

The effect of characteristic curvature was emphasized by directly comparing the loss in overall pressure rise using two different families of characteristics (Figure 3-13). Case (a) used the actual characteristics from the MIT compressor, and case (b) used hypothetical characteristics with no curvature. The absence of curvature resulted in no loss in overall pressure rise with a whirling shaft, despite the large flow nonuniformity.

### 3.3.3 Performance Loss Increases Near Stall

The magnitude of flow nonuniformity induced by tip clearance asymmetry increased as the compressor operated nearer to the stall point. Figure 3-14 shows the local operating points around the annulus for the Stage-37 compressor operating with a whirling shaft at both the design point and the stall point of the compressor. The axial velocity variation was 5 times larger when operating near the characteristic peak than at design. The sharper curvature to the characteristics near the peak then resulted in an increased loss to the overall pressure rise.

The compressor's increased sensitivity to tip clearance asymmetry near the characteristic peak was due to both the reduced natural damping associated with operating near

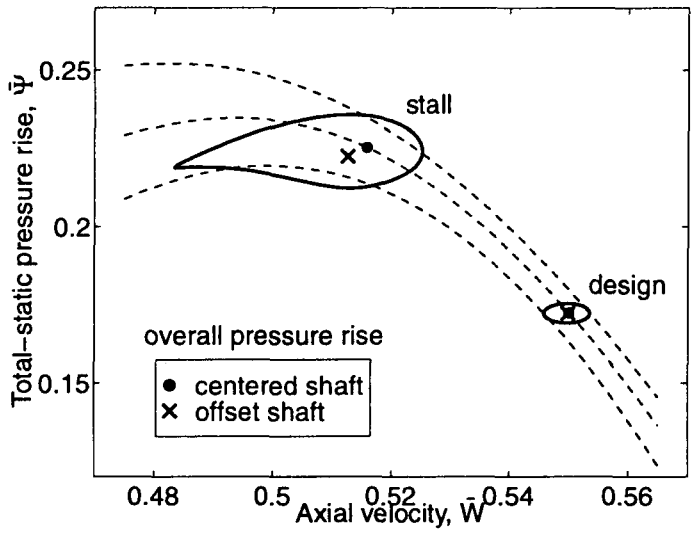


**Figure 3-14:** Loci of local operating points in Stage-37 operating at design and stall for whirling rotor shaft offset of 0.455% chord at a frequency of 50% rotor frequency.

stall, and the increased sensitivity of the axisymmetric pressure rise characteristics to tip clearance (shown by the values of $\partial\Psi/\partial\varepsilon$ in Tables 3.2 and 3.4). Compressors with higher sensitivity in their axisymmetric characteristics to uniform tip clearance changes would generally demonstrate larger flow nonuniformities induced by the tip clearance asymmetry.

### 3.3.4 Performance Loss Increases Near Resonance

The maximum flow nonuniformity induced by a whirling shaft occurred for whirling frequencies near the rotating stall frequency of the compressor. The nominal rotating stall mode for both compressors consisted of a single-lobed sinusoid which rotated at approximately 30–35% of the rotor frequency (Figures 3-3 and 3-8). The single-lobed clearance variation caused by the whirling shaft excited this mode for whirling frequencies between 20% and 50% of the rotor frequency. This resonant response resulted in an increased flow nonuniformity, and therefore, an increased loss of performance. For example, the velocity nonuniformity and loss in pressure rise when $\nu = 0.3$ (Figure 3-10b) was 47% larger than for $\nu = 0$ (Figure 3-9b), and 3 times larger than for $\nu = 1$ (Figure 3-11b).

### 3.3.5 Quantification of Performance Changes for MIT and NASA Compressors

The overall loss in pressure rise and efficiency caused by a whirling shaft for the two compressors is shown in Figures 3-15 to 3-18. The performance loss was defined as the difference between the performance with a whirling shaft and with a centered shaft at the same throttle setting. Results are plotted for the whole range of frequencies between -1 and 1.5 times the rotor frequency, and at both the design throttle and the stall inception point.

The most severe performance losses occurred for near-stall operation with resonant whirling frequencies. At this condition, the loss in overall pressure rise and efficiency were 3 to 6 times larger than for equivalent stationary clearance asymmetries. An important value of shaft offset used to compare results is the maximum tolerable whirling shaft displacement for sustained compressor operation. Based on rotordynamic considerations, this value is on the order of one-half the nominal clearance [15] (i.e. $\varepsilon_1 = 0.01$ for the MIT compressor and $\varepsilon_1 = 0.005$ for Stage-37). At these offsets, the maximum performance losses were approximately 3–4 percent in pressure rise and 2–3 points in efficiency. Losses of this magnitude indicate that sustained performance with a whirling shaft at off-design conditions is not acceptable.

At the design operating point, the effect of a whirling shaft on compressor performance was acceptable. For the maximum tolerable shaft offset values, the loss in pressure rise was less than 0.2% and the efficiency loss was within 0.16 points. The values were over an order of magnitude smaller than for near-stall operation because of both the increased damping of flow nonuniformities away from stall, and the reduced curvature of the characteristics away from the peak.

The same information at the design point can be viewed in the context of the question posed in Section 1.3: how much shaft deflection is required to cause a significant loss in performance? The results for fixed values of shaft displacement were extrapolated using polynomial fits to estimate the whirling shaft offsets needed to incur losses of one percent in pressure rise and 1 point in efficiency (Figure 3-19). The minimum required displacement, at resonance, is about 2% of the chord. This offset can not even be achieved in Stage-37, and would imply that the rotor tips for the MIT compressor are rubbing against the casing.

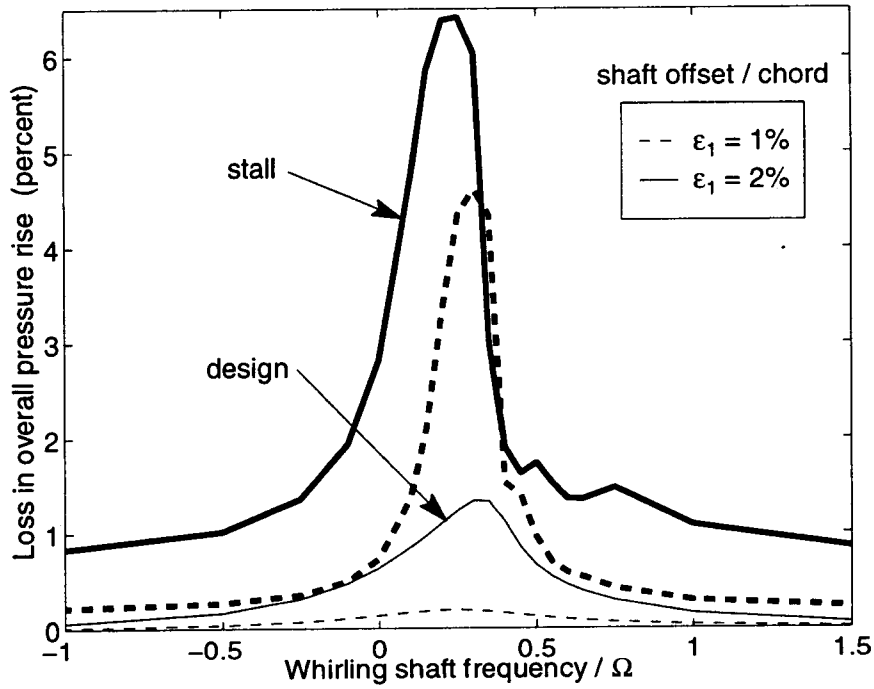


**Figure 3-15:** Loss in overall pressure rise caused by whirling shaft in MIT compressor at design (light lines) and stall (heavy lines) for offsets of 1% and 2% of the chord.

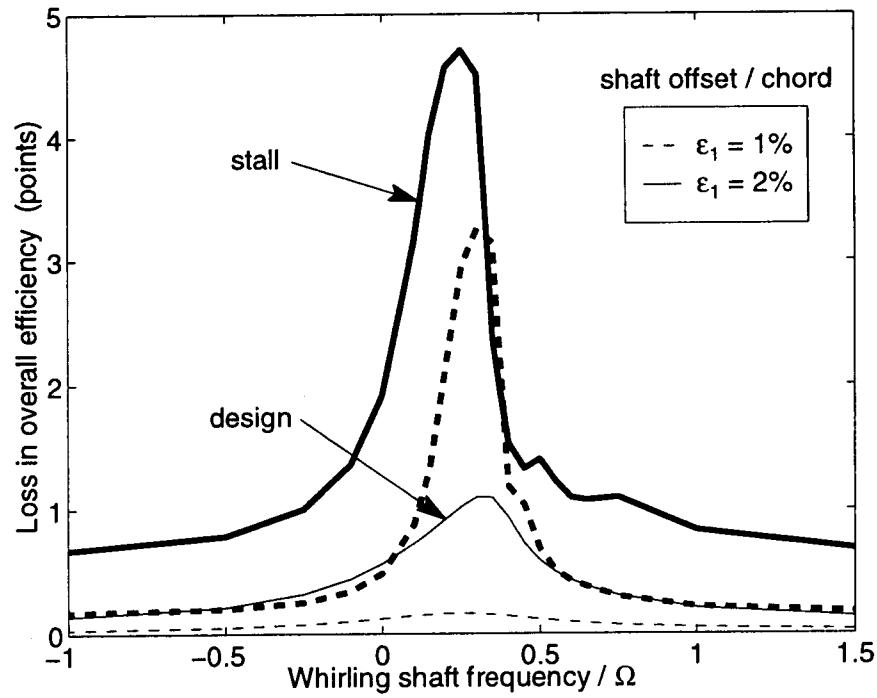


**Figure 3-16:** Loss in overall efficiency caused by whirling shaft in MIT compressor at design (light lines) and stall (heavy lines) for offsets of 1% and 2% of the chord.

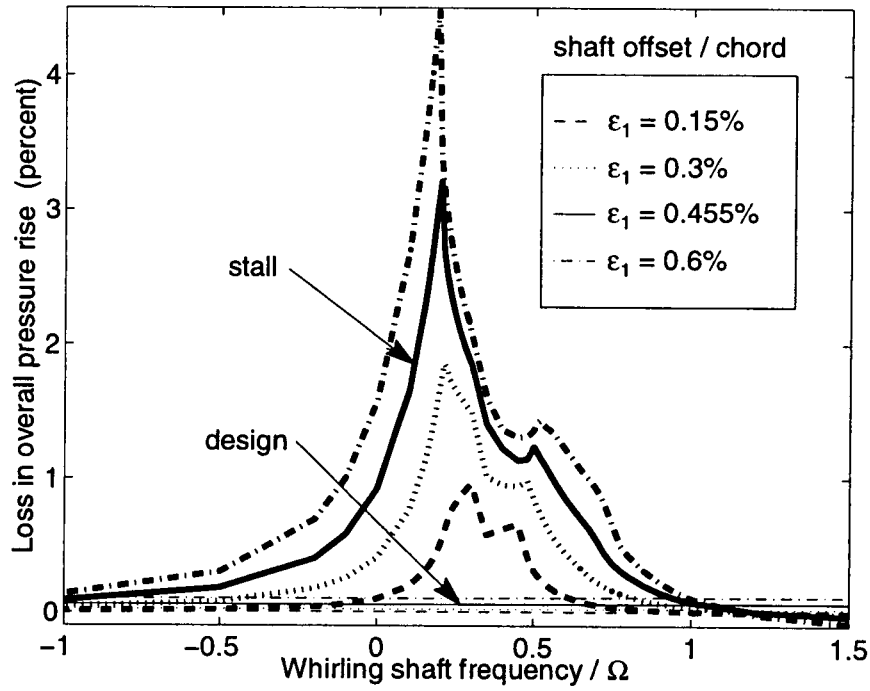


**Figure 3-17:** Loss in pressure rise caused by whirling shaft in NASA compressor at design (light lines) and stall (heavy lines) for offsets of 0.15%, 0.3%, 0.455% and 0.6% chord.

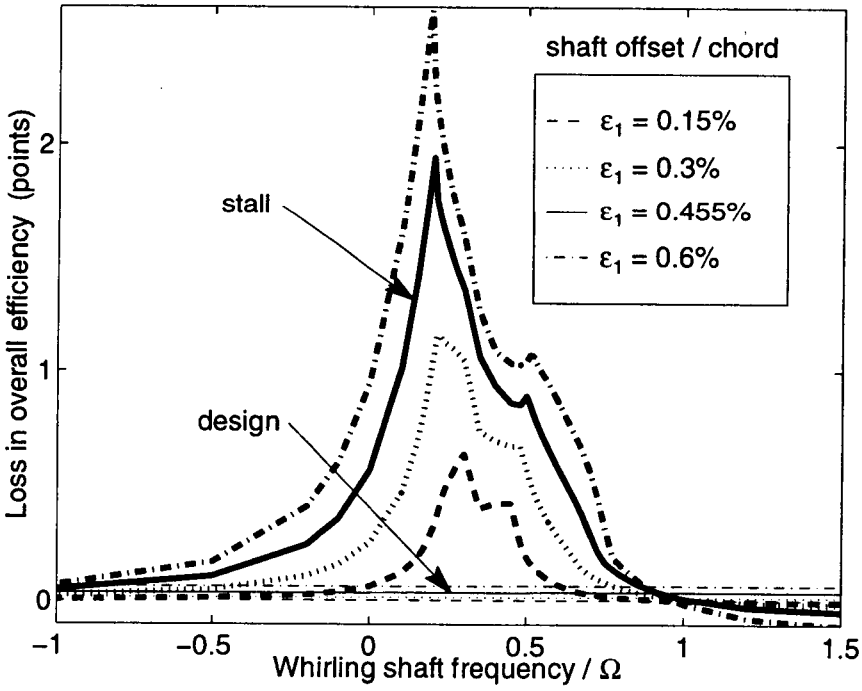


**Figure 3-18:** Loss in efficiency caused by whirling shaft in NASA compressor at design (light lines) and stall (heavy lines) for offsets of 0.15%, 0.3%, 0.455% and 0.6% chord.

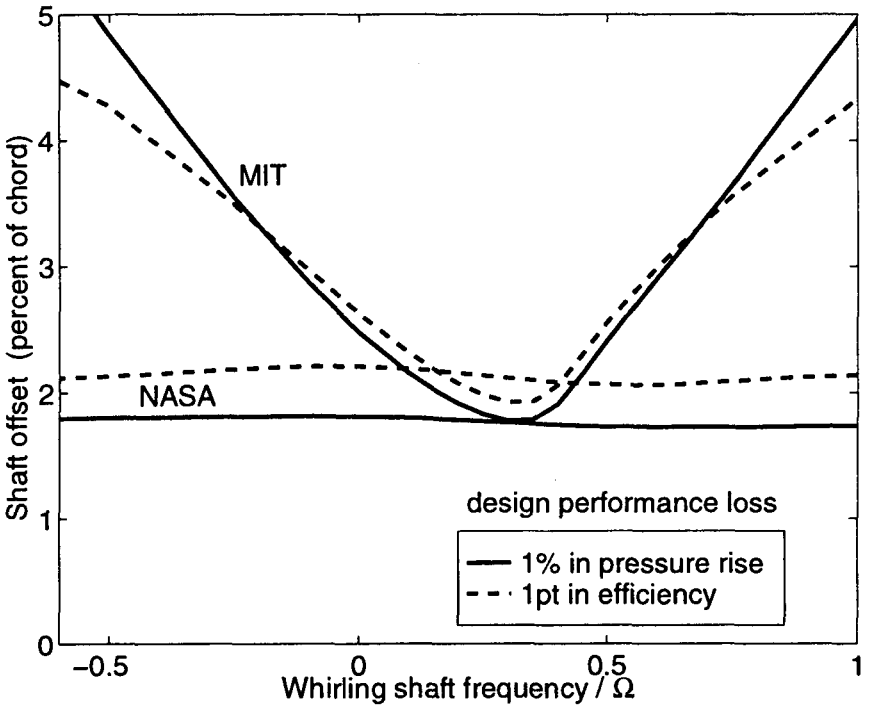


**Figure 3-19:** Amount of whirling shaft offset to effect 1% drop in pressure rise and 1 point loss in efficiency. Results extrapolated from design performance of MIT and NASA compressors in Figures 3-15 to 3-18.

Therefore, at the design throttle condition, mechanical problems due to whirling shafts would limit the performance before concerns of aerodynamic losses.

## 3.4 Effect of Whirling Shaft on Stall Inception

Rotating tip clearance asymmetries generally caused rotating stall at higher flow coefficients than for uniform flow. For resonant whirling frequencies, the stall points were even higher than those predicted using the integrated mean slope (IMS) criterion, examined by Chue et al. [6] for rotating inlet distortions. Near resonance, the phase speed of the stall modes was *locked* to the whirling shaft speed. As will be shown, this caused the mode amplitude to be largest in regions of positive slope. Weighting the IMS criterion with the modal amplitude distribution resulted in an improved stall condition that captured the observed trends for the change in stall margin. The following sections quantify the losses in stall margin, describe the changes to the rotating stall mode, and develop the *weighted integrated mean slope* (WIMS) stall prediction criterion for compressors with rotating tip clearance

nonuniformities.

### 3.4.1 Effect of Whirling Shaft on Stall Margin

The effect of an off-centered, whirling shaft was to reduce the stall margin of the compressors. The loci of neutrally stable operating points for the MIT and NASA compressors are shown in Figures 3-20a and 3-21a for shafts whirling between frequencies of -2 and 2 times the rotor frequency. The stall points for the three specific values of $\nu = 0$, 0.35 and 1 are noted on the graphs to demonstrate the direction of the loci for increasing whirling frequency. Similarly to the pressure rise and efficiency results, the loss in stall margin peaked for whirling frequencies near the resonant rotating stall frequency (Figures 3-20 and 3-21). For a whirling shaft offset of 50% of the nominal clearance at the resonant frequency, the stalling flow coefficient for the MIT and NASA compressors rose by 11% and 4% respectively, and the stalling pressure rise dropped by 6% for both configurations. These values are an order of magnitude larger than the changes in the stall points for steady offset shafts, and represent a significant detriment to the stall margin.

The change in the stall margin due to a whirling shaft was a consequence of two effects: (1) the pressure rise characteristic for nonuniform flow had lower pressure rise and generally peaked at a higher flow coefficient than for uniform flow; (2) near resonant frequencies, the stall point did not necessarily occur near the peak of the nonuniform flow characteristic.

The change in the characteristic was simply a consequence of the results of the previous section. Figures 3-22 and 3-23 show the nonuniform flow characteristics for the MIT and NASA compressors with whirling shafts at fixed frequency and displacement from the centerline. At any throttle condition, the overall pressure rise was reduced by the nonuniformity of the flow field and the downward concave curvature of the pressure rise characteristic. The change in the location of the characteristic peak was caused by increased losses induced by the larger flow nonuniformities near resonant frequencies.

The conditions that set the stalling flow coefficient were less clear. For both compressors, the stall points for a whirling shaft frequency of $\nu = 0.3$ were on the positively-sloped part of the characteristics, while a whirling frequency of $\nu = 0.6$ exhibited stall on the negatively-sloped part. To understand the locations of the stall points, it is first required to

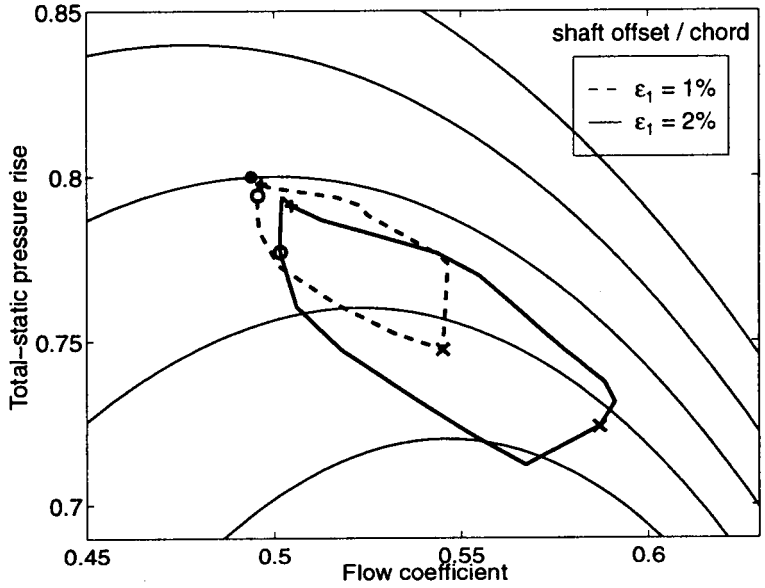


(a) Locus of stall points on family of axisymmetric characteristics for $\varepsilon_1 = 0\%, \pm 1\%, \pm 2\%$ chord ($\bullet$, stall point for uniform flow; $\circ$, $\nu = 0$; $\times$, $\nu = 0.35$; $+$, $\nu = 1$).

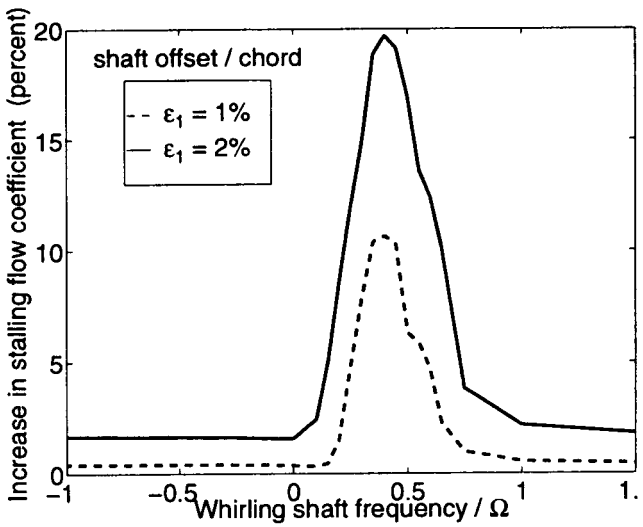


(b) Loss in stalling flow coefficient

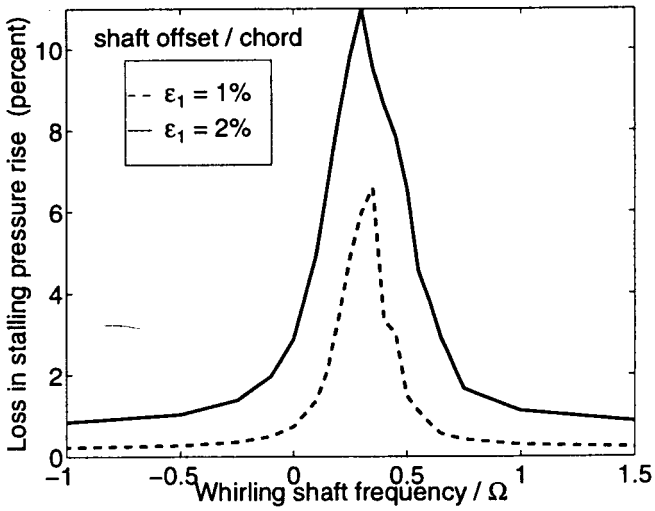


(c) Loss in stalling pressure rise

**Figure 3-20:** Change in stalling flow coefficient and pressure rise for MIT compressor with whirling shaft.

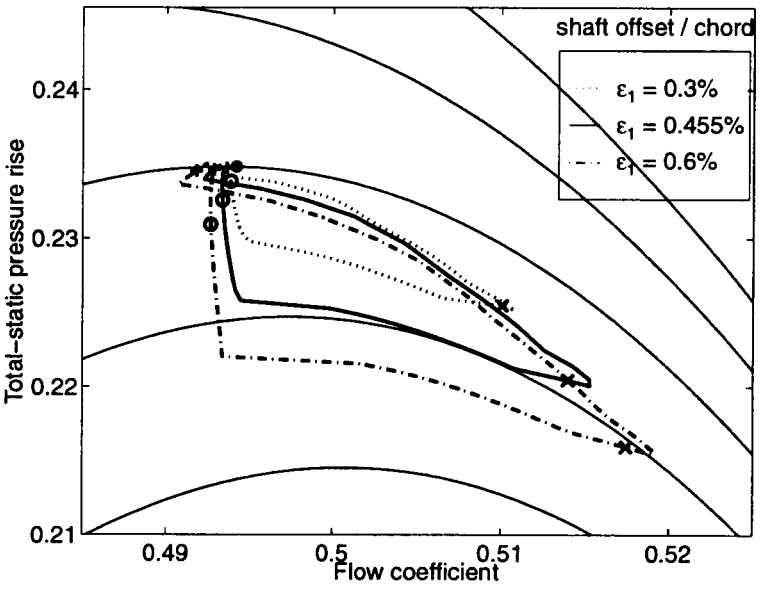


(a) Locus of stall points on family of axisymmetric characteristics for $\varepsilon_1 = 0\%, \pm 0.3\%, \pm 0.6\%$ chord (•, stall point for uniform flow; ∘, $\nu = 0$; ×, $\nu = 0.35$; +, $\nu = 1$).

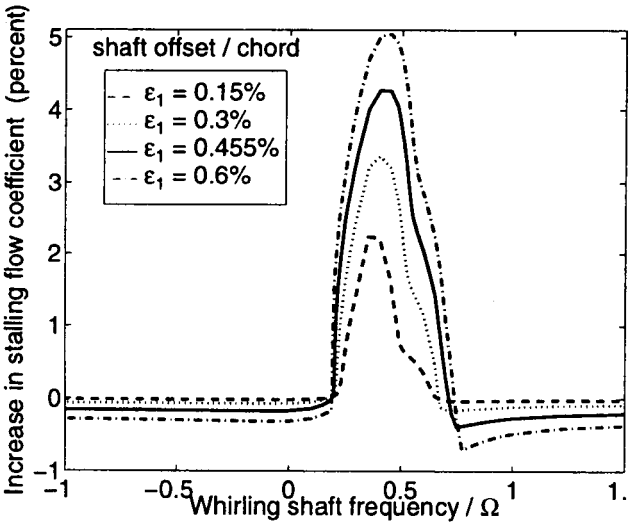


(b) Loss in stalling flow coefficient

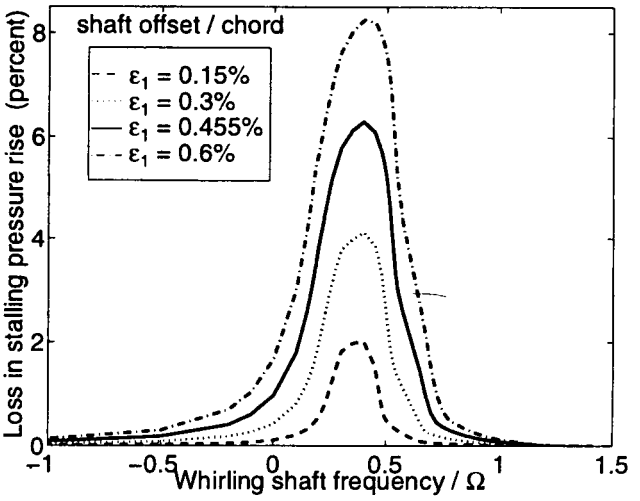


(c) Loss in stalling pressure rise

**Figure 3-21:** Change in stalling flow coefficient and pressure rise for NASA compressor with whirling shaft.

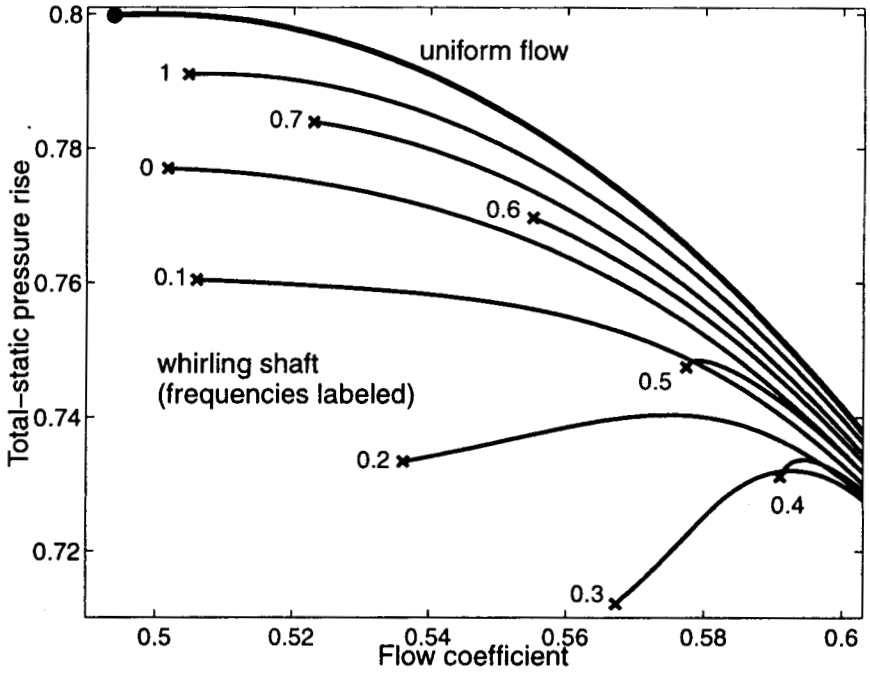


**Figure 3-22:** MIT compressor total-static pressure rise characteristics and stall points for uniform flow and nonuniform flow caused by a whirling shaft (offset of 2% chord).

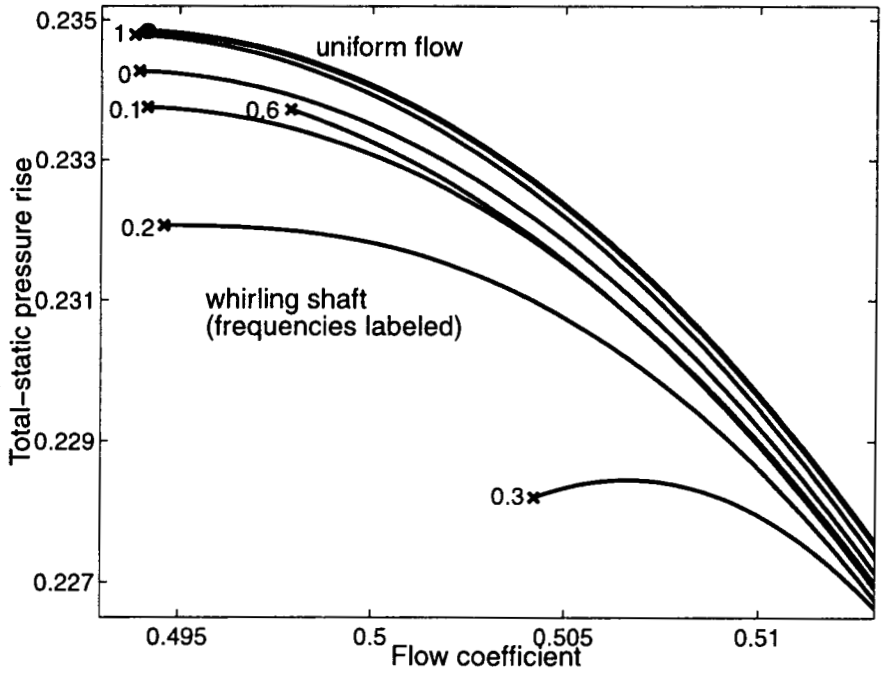


**Figure 3-23:** Stage-37 total-static pressure rise characteristics and stall points for uniform flow and nonuniform flow caused by a whirling shaft (offset of 0.228% chord).

understand how the shape of the rotating stall mode was affected by the nonuniform flow caused by a whirling shaft. This topic is addressed in the following section.

### 3.4.2 Effect of Whirling Shaft on Rotating Stall Mode Structure

The circumferential structure of the rotating stall modes was distorted by flow nonuniformity. In uniform background flow, the most unstable mode consisted of a single-lobed (first-harmonic) sinusoidal perturbation that travelled at a constant speed and amplitude. Circumferential flow nonuniformity caused the amplitude of the mode to be modulated as it travelled around the annulus, which was reflected in the harmonic distribution of the mode shapes. The shapes of the axial velocity perturbations are plotted in Figure 3-24 for the MIT compressor with whirling shaft frequencies between -1 and 1 times the rotor frequency. The mode shapes are plotted in the *transformed* frame of reference, locked to the rotating clearance asymmetry, at six time intervals as the mode completes one period around the circumference. Superimposed on these plots is the envelope of maximum wave amplitude, which reflects the amount of amplitude modulation around the circumference. Below each mode shape is a representation of its Fourier decomposition into circumferential harmonics, which are the amplitudes of the coefficients $w_n$ defined in equation (2.29). Positive harmonics indicate waves travelling in the rotor direction *relative* to the frame of reference of the rotating tip clearance asymmetry. For example, the mode travelling at 30% of rotor speed, as viewed in the reference frame locked to the rotor (Figure 3-24h), appears to travel counter to the rotor direction, and so is dominated by negative harmonics.

For frequencies away from resonance ($\nu < 0$ or $\nu > 1$), the background flow nonuniformity was small and the mode shape was approximately a first-harmonic sinusoid (Figure 3-24a). As the whirl frequency approached the resonant frequency, the background flow nonuniformity increased, inducing higher harmonics and larger amplitude modulation. For whirl frequencies of 0.25 and 0.6 times rotor frequency, the maximum amplitude of the mode varied by a factor greater than 10 around the circumference, indicating a strong localization of the mode over a specific region of the clearance asymmetry. The localization of the mode was most acute at resonance (Figures 3-24d and 3-24e) where the disturbance attained a standing wave pattern in the whirling shaft frame of reference.

For cases of a standing wave, the rotating speed of the mode must have been identical

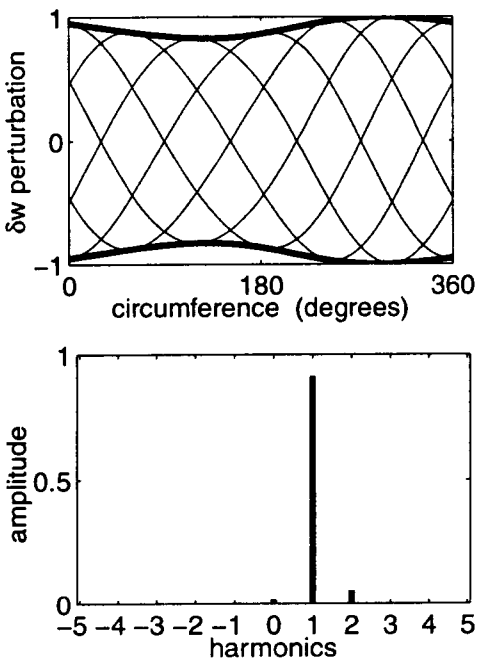


(a) $\nu = -1$

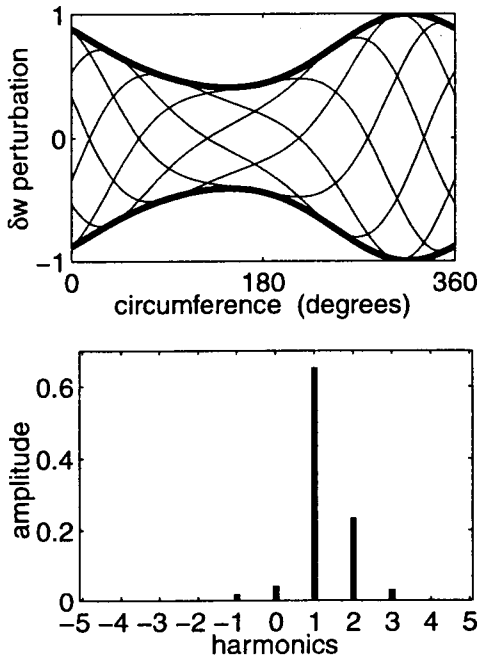


(b) $\nu = 0$

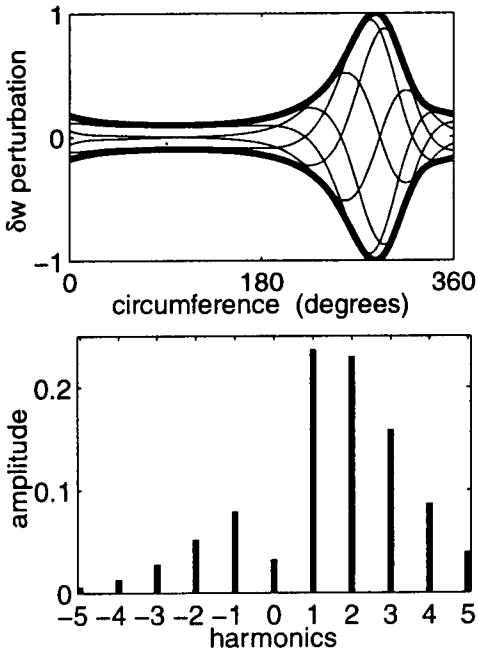


(c) $\nu = 0.25$

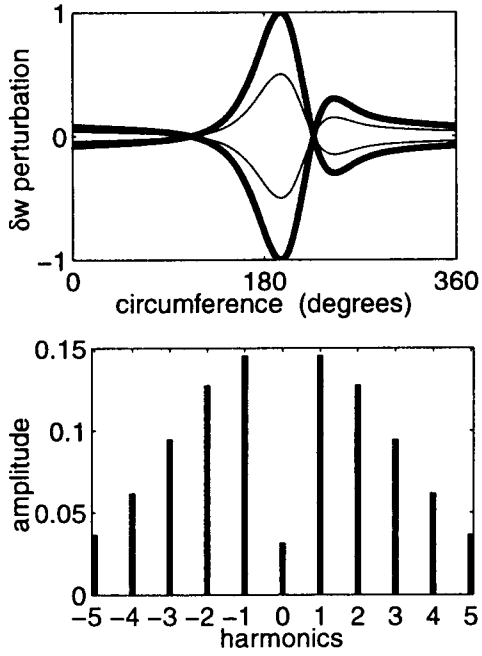


(d) $\nu = 0.4$

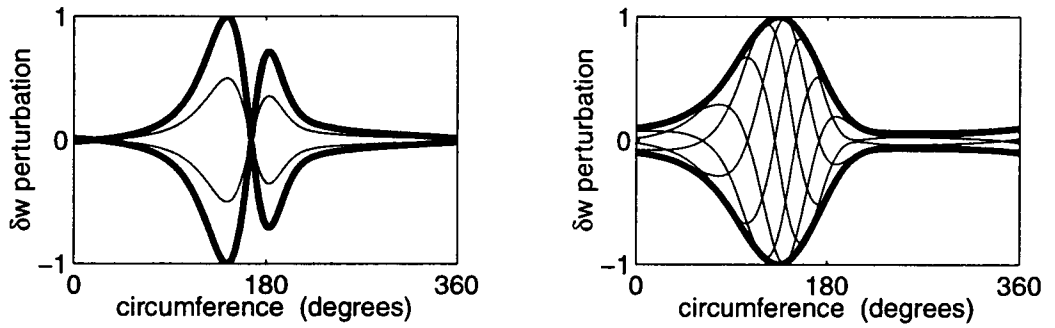


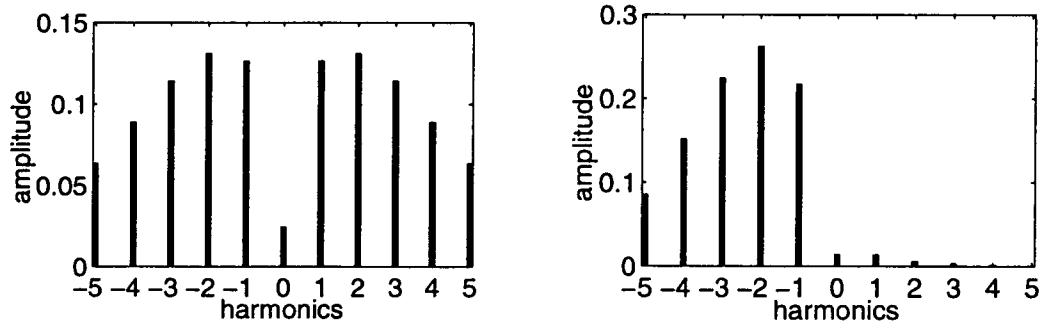


(e) $\nu = 0.5$ (f) $\nu = 0.6$

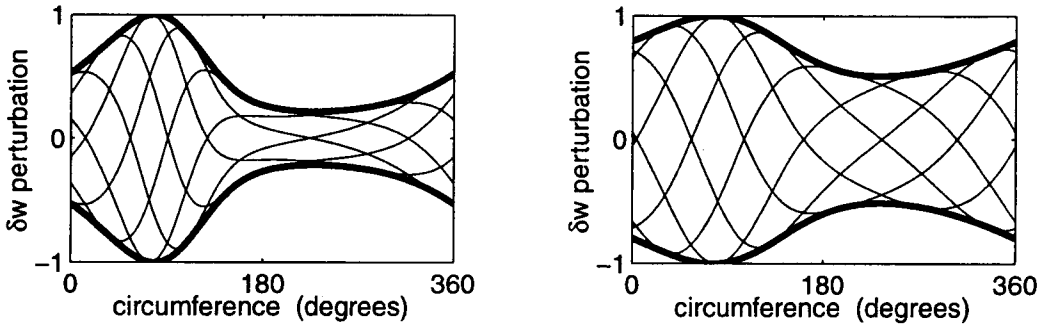


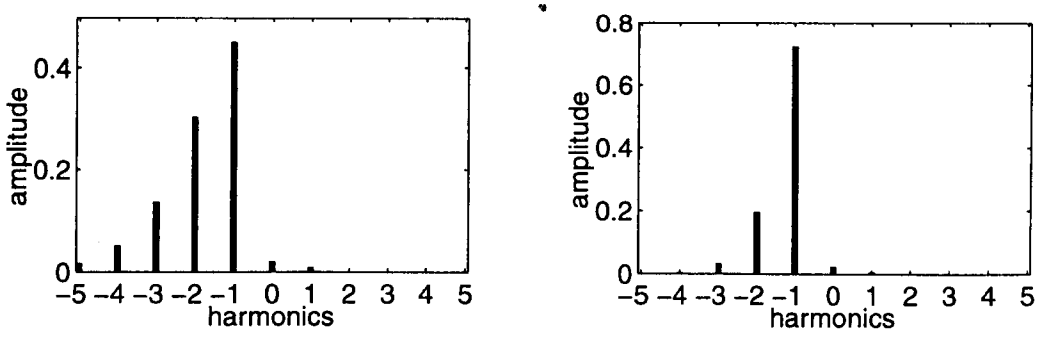


(g) $\nu = 0.75$ (h) $\nu = 1$

**Figure 3-24:** Rotating stall mode shapes at neutral stability for MIT compressor with whirling shaft (offset of 2% chord in the direction of 0°). Upper figures show axial velocity perturbation in whirling reference frame at compressor inlet for six equally-spaced time intervals. Overall wave envelope is drawn in bold. Lower figures show harmonic decomposition of mode shape, where positive harmonics travel in direction of the rotor, relative to the whirling shaft.

to the rotating speed of the tip clearance asymmetry. Therefore, the rotating speed of the mode must have increased from the nominal value of 30% rotor speed to as much as 50% rotor speed to account for this frequency coincidence. This explains why in Section 3.3.5 the performance loss was largest for whirling shaft frequencies in this range (the *true* resonant frequencies) rather than at the rotating stall frequency ($\nu = 0.3$) in uniform flow. Figure 3-25 plots the phase speed of the first harmonic component of the rotating stall mode for the MIT compressor. The phase speed of the rotating clearance asymmetry is also plotted to clearly indicate the region of frequency coincidence between the mode and the whirling shaft. In this region, the frequency ($s_i$) of the mode in the clearance asymmetry frame was identically zero, so the phase speeds of *all* harmonics were equal to the whirling speed of the shaft. This *phase-locking* was a nonlinear phenonmenon, and the frequency range over which it occured was larger for flows with increased nonuniformity. For the MIT compressor, phase-locking was evident for $0.4 \leq \nu \leq 0.45$ for a shaft displacement of 1% chord, and $0.35 \leq \nu \leq 0.5$ for a displacement of 2% chord.

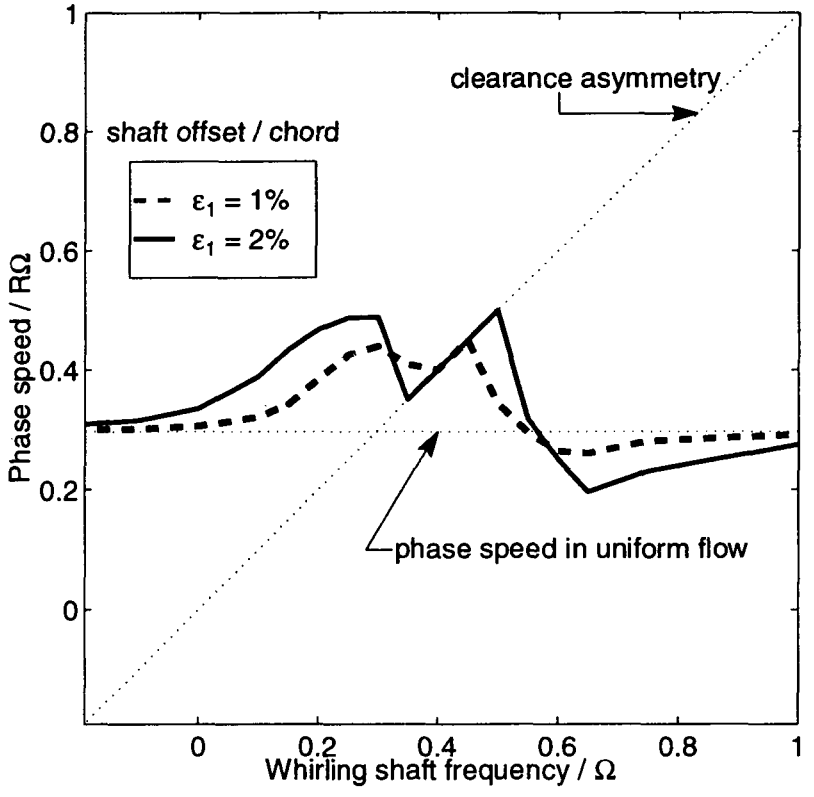


**Figure 3-25:** Rotating speed of first harmonic component of rotating stall mode at neutral stability in MIT compressor with whirling shaft. *Phase-locking* is evident for phase speeds equal to the whirling speed of the rotor shaft.

Existing experimental evidence may confirm the presence of phase-locking between the rotating stall mode and a large-amplitude rotating flow nonuniformity. One of Weigl's Stage-37 experiments [78] encountered defective journal bearings that caused the shaft to whirl at a frequency 5–7% below the rotating stall speed in axisymmetric flow. Forced response tests indicated that the modal rotating stall speed in the nonuniform flow then coincided exactly with the whirl frequency. Other evidence comes from compressor tests with rotating inlet distortions (Longley et al. [48]). These tests showed that the maximum loss in stall margin occured at rotation rates higher than the modal stall speed in uniform flow, up to 12% of the rotor speed for one configuration. Such observations are in agreement with the present results that show the peak resonant region corresponded to modes phase-locked to flow nonuniformities at frequencies higher than the nominal rotating stall speed.

The two factors that determine the shape of the mode amplitude envelope were the frequency of the mode relative to the whirling shaft and the circumferential variation of the pressure rise characteristic slope. For stationary inlet flow distortions, Hynes and Greitzer [43] and Van Schalkwyk [76] observed that the mode envelope grew as the crest passed into regions of positive slope, and decayed as the crest passed into regions of negative slope. Therefore, the amplitude envelope had a maximum where the slope changed from positive to negative, causing it to lag the slope variation by 90 degrees. The same argument applies for the present studies of rotating flow distortions, except that the phase difference between the slope and mode envelope variation is dependent on the speed of the rotating stall mode *relative* to the slope variation. Figure 3-26 compares the variation in slope to the axial velocity perturbation envelope ($||\delta w||$) for different whirl frequencies. The slope and mode envelope variations were all normalized to range between 0 and 1 in order to best illustrate their relative shapes. For whirling speeds lower than the modal phase speed (such as for $\nu \leq 0.3$ in Figure 3-26), the mode travelled from left to right relative to the slope variation. The wave envelope peak then lagged the maximum slope, similar to the stationary inlet distortion studies. For whirling speeds greater than the modal phase speed ($\nu \geq 0.6$), the mode travelled from right to left relative to the slope variation, and so the wave envelope peak appeared to *lead* the maximum slope. At resonance, when the mode was locked in phase to the whirling shaft ($\nu = 0.45$), the mode did not rotate relative to the slope variation, and so the mode amplitude envelope peak was *in phase* with the maximum local slope.

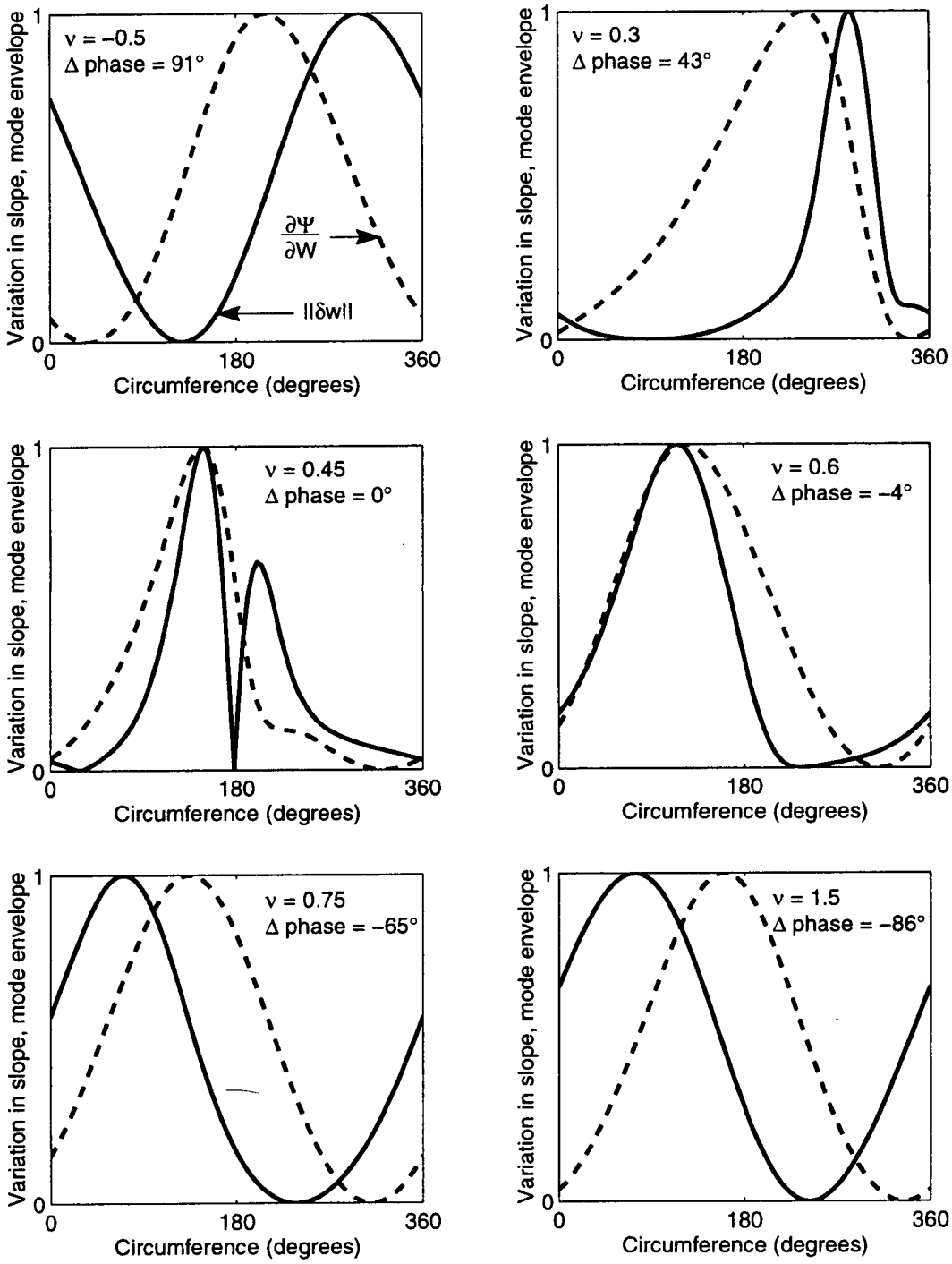


**Figure 3-26:** Comparison of variation in velocity perturbation envelope ($||\delta w||$) to variation in slope ($\partial\Psi/\partial W$) shown in rotating reference frame locked to tip clearance asymmetry. "Δ phase" is defined as the difference between upper peaks (in degrees). Results for MIT compressor at neutral stability with whirling shaft (offset of 1% chord). All variations are normalized to range between 0 and 1.

In summary, there existed a finite range of resonant frequencies (higher than the rotating stall frequency in uniform flow by 5% to 20% of the rotor speed) for which the rotating stall mode was locked in phase to the whirling shaft. For these whirling frequencies, the mode shape principally consisted of harmonics beyond the 1st harmonic, and was localized to the region of highest local slope. For whirling frequencies away from resonance, the mode was dominated by the 1st harmonic, which rotated close to the rotating stall frequency in axisymmetric flow.

### 3.4.3 Weighted Integrated Mean Slope (WIMS) Criteria

The most critical element in determining the stability of rotating stall modes is the slope of the pressure rise characteristic with respect to the axial velocity. Actuator disk models of axisymmetric compressor flow [30, 47] indicate that modes are stable during operation on the negatively sloped portion of the characteristics, and become unstable only on the positively sloped region. For steady nonuniform background flow, Hynes and Greitzer [43] showed that compressors become unstable once the area of the circumference locally operating on the positively sloped part of the characteristic dominates the area operating on the negatively sloped portion. This led to the *integrated mean slope* (IMS) criterion, applicable for neutral stability in a distorted flow:

$$\int_0^{2\pi} \frac{d\Psi}{dW}\, d\theta = 0. \tag{3.4}$$

Chue et al. [6] found that the IMS criterion broke down when an imposed rotating inlet distortion was near the frequency of the rotating stall mode. No other stall prediction criterion was developed for this situation, although it was recognized that the effectiveness of the IMS condition was influenced by the relative phase between the mode shape harmonics and the slope variation.

A more general stability criterion has been developed here (based on the conservation of energy in the compressor), applicable for steady or rotating flow nonuniformity produced by tip clearance asymmetry. An expression of the disturbance flow "energy" production in the compressor was first used by Epstein et al. [16] as the product of the axial velocity perturbation and the pressure rise perturbation, integrated around the annulus area. The

pressure rise perturbation can be expressed for a simple compressor model, which ignores unsteady losses and swirl sensitivity, as the characteristic slope times the axial velocity perturbation. Thus, as shown by Gysling [31], the disturbance flow "energy" production is given by

$$\delta E = \frac{1}{2\pi} \int_0^{2\pi} \frac{d\Psi}{dW} w^2 \, d\theta \,. \tag{3.5}$$

The term "energy" is used cautiously because an actual expression for the perturbation to the total fluid energy would also include second-order terms that were neglected in the present linearized flow model. However, $\delta E$ is a useful energy-like, second-order quantity that is shown in Appendix K to vanish at neutral stability.

For the case of rotating tip clearance nonuniformities, it was useful to calculate this integral in the rotating frame of reference locked to the clearance asymmetry. The slope variation was then constant in time, but the mode shape oscillated within the maximum amplitude envelope (Figure 3-24). Over one period of revolution around the annulus, the time-averaged disturbance "energy" production of the mode was given by

$$\overline{\delta E} = \frac{1}{4\pi} \int_0^{2\pi} \frac{d\Psi}{dW}(\theta') \, ||w(\theta')||^2 \, d\theta' \,. \tag{3.6}$$

It was seen that equation (3.6) governed the stability of the compression system to rotating stall modes. Disturbance flow "energy" was locally produced in annular regions with a positive characteristic slope, but the production was weighted towards regions where the mode amplitude was the largest. At neutral stability, local "energy" production was balanced by dissipation in regions of negative slope, so that the total disturbance "energy" production was zero. Thus, the stall point of the compressor was given by the operating point that satisfied the following *weighted integrated mean slope* (WIMS) stall criterion:

$$\int_0^{2\pi} \frac{d\Psi}{dW} \, ||w||^2 \, d\theta = 0. \tag{3.7}$$

The WIMS criterion was not exact for compressors with unsteady losses, swirl sensitive characteristics, or unsteady exit angle deviations; nor did WIMS account for the "energy" production from the interaction of the disturbance flow velocity with the mean vorticity in

the downstream flow. Rigorous energy flux requirements for the stability of two-dimensional compressible flow have been derived by Fréchette [18] that account for *all* sources of energy production. Similar requirements for incompressible flow are derived in Appendix K. The advantage of WIMS was that it was simple enough, yet sufficiently accurate, to demonstrate the dominant physical process that governs the stability of the compressor, which could not have been so easily understood with Fréchette's analysis.

The applicability of the WIMS criterion is seen with the following example of the MIT compressor subjected to a whirling shaft near the resonant frequency. The variation in compressor slope at neutral stability is plotted in Figure 3-27a. The integrated mean value of the slope was -0.62, indicating that the IMS stall prediction criterion in equation (3.4) did not apply. Even though the region of positive slope was only one-fifth of the circumference, it encompassed the region of largest mode amplitude (Figure 3-27b). The disturbance "energy" production around the circumference confirmed that the time-averaged energy input was balanced by energy subtraction (Figure 3-27c). The value of the weighted IMS was 0.05, much closer to zero than the IMS value, and nearly equal to the slope at stall in uniform flow (0.07).[1]

The value of the WIMS at stall was approximately zero for whirling shafts of all frequencies and offsets (Figures 3-28 and 3-29). In calculating the WIMS, the mode amplitude has been normalized to have a maximum value of one, so that the WIMS reverts to the IMS for the case of uniform flow. The figures show that the WIMS was much closer to zero than the IMS, especially near resonance. Also, the WIMS stability criterion in equation (3.7) was seen to be more applicable to the MIT compressor than Stage-37 which was swirl sensitive and had exit flow angle deviations.

The best assessment of the WIMS criterion was to compare the actual stall points for the MIT compressor with those determined by equation (3.7) (shown in Figure 3-30a). These stall points were also compared to those determined by the IMS criterion (Figure 3-30b), and by the IMS and WIMS criteria with the right-hand-side set to the slope at stall in uniform flow. These last two comparisons attempted to account for the unsteady losses and other real compressor effects not included in the WIMS and IMS conditions. Figure 3-30a

[1]The slightly positive value for the WIMS at stall resulted from the modeling of unsteady losses, which caused the compressor to stall on the positively sloped side of the characteristic.

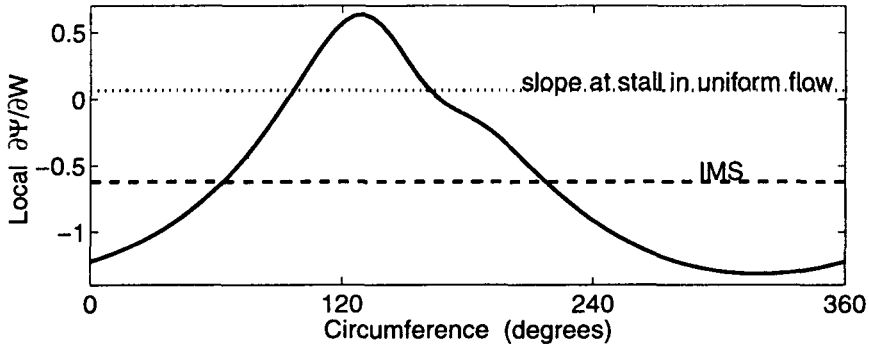


(a) Local value and integrated average of slope of total-static pressure rise characteristic around circumference.

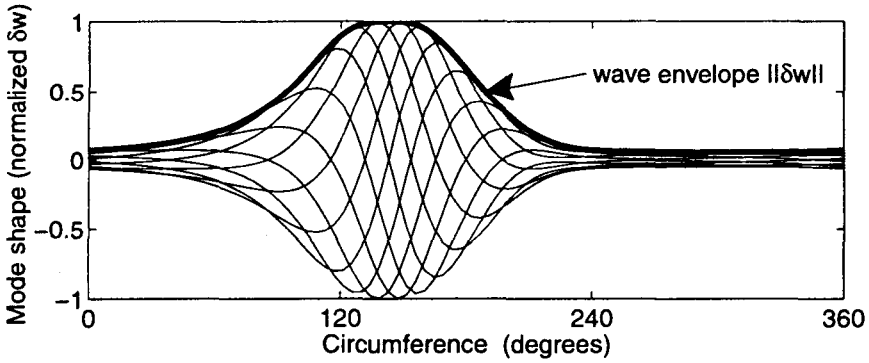


(b) Overall wave envelope of rotating stall axial velocity perturbation, and actual mode shape at 10 equally spaced intervals of time.

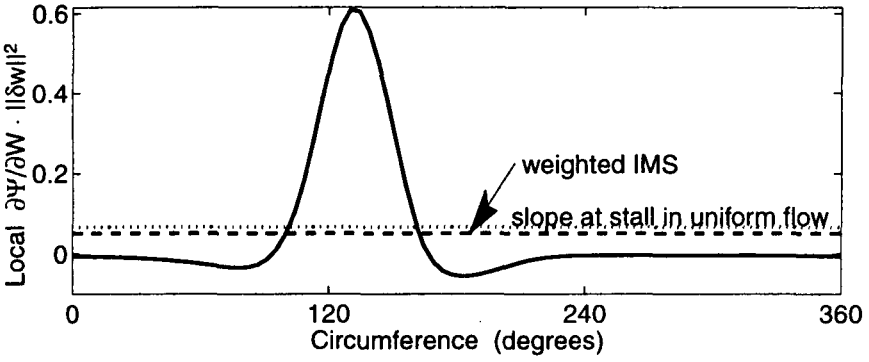


(c) Local value and integrated average of *weighted* slope of pressure rise characteristic around circumference.

**Figure 3-27:** Circumferential nonuniformity in slope of characteristic, with and without weighting by mode shape. Case for MIT compressor at stall point for whirling shaft offset of 2% chord and frequency $\nu = 0.55$.

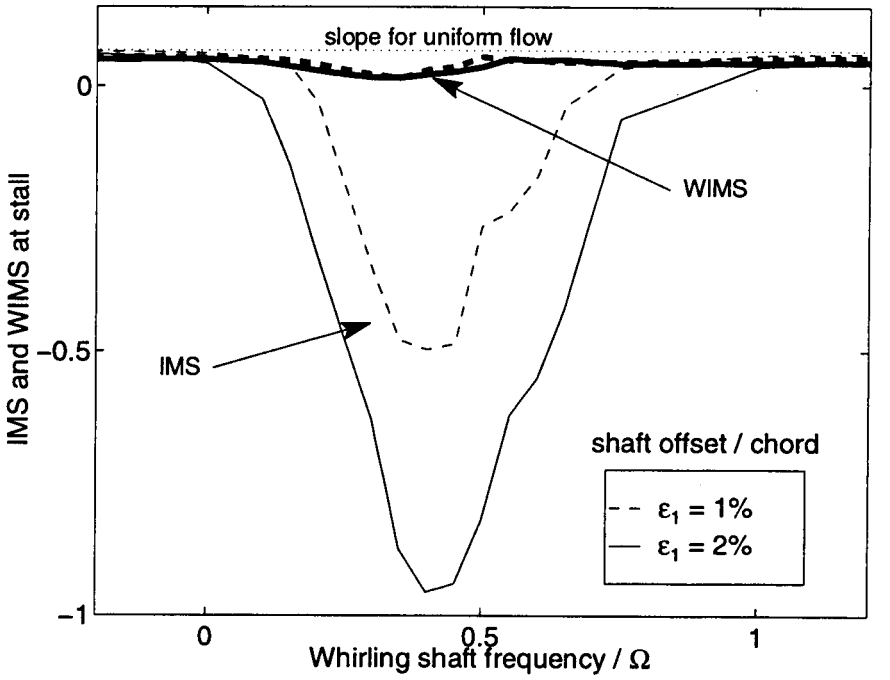


**Figure 3-28:** Value of integrated mean slope (with and without weighting by mode shape) at stall for MIT compressor with whirling shaft.

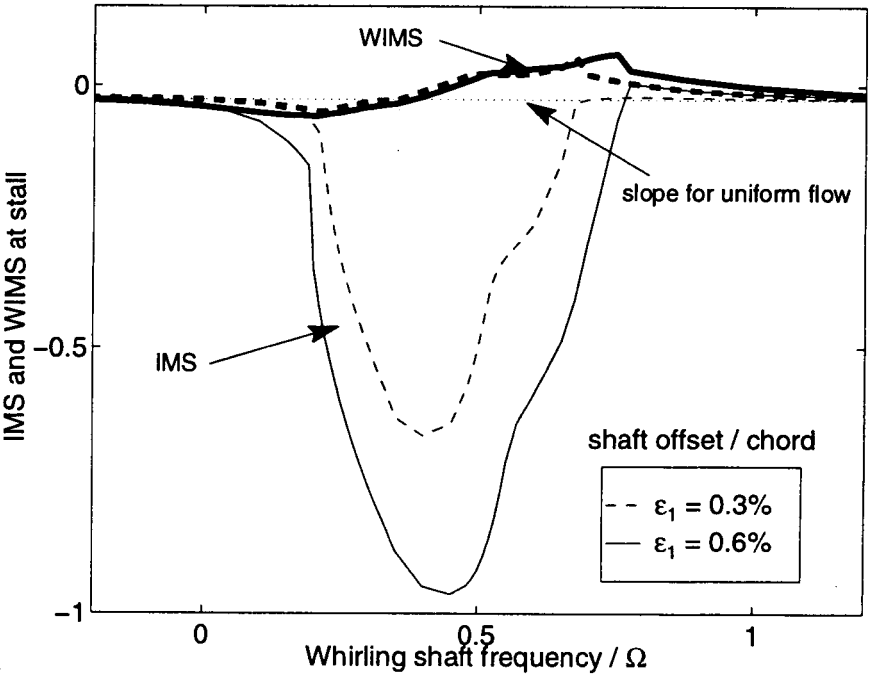


**Figure 3-29:** Value of integrated mean slope (with and without weighting by mode shape) at stall for NASA compressor with whirling shaft.

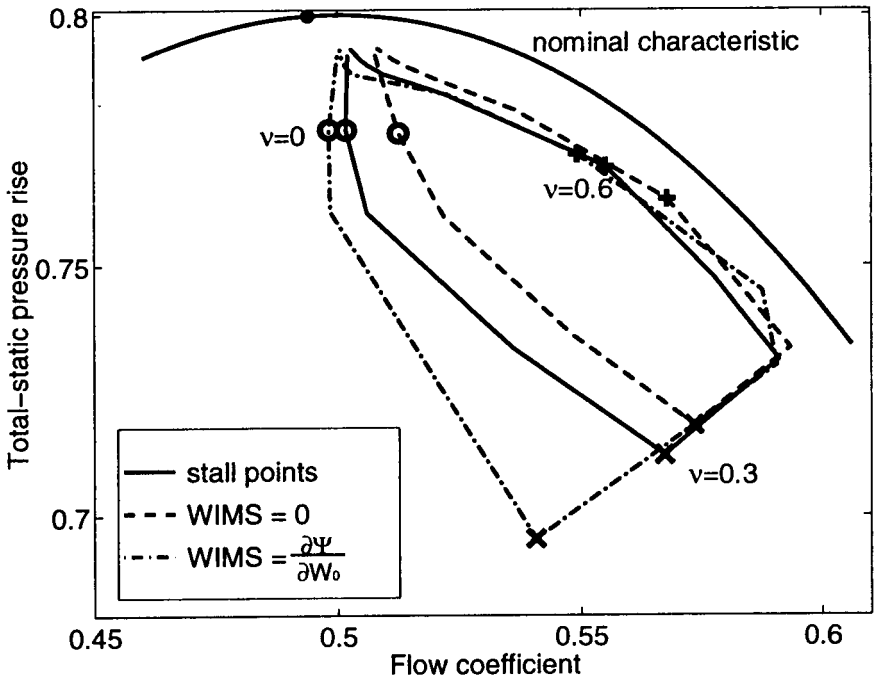


(a) Prediction using weighted IMS values

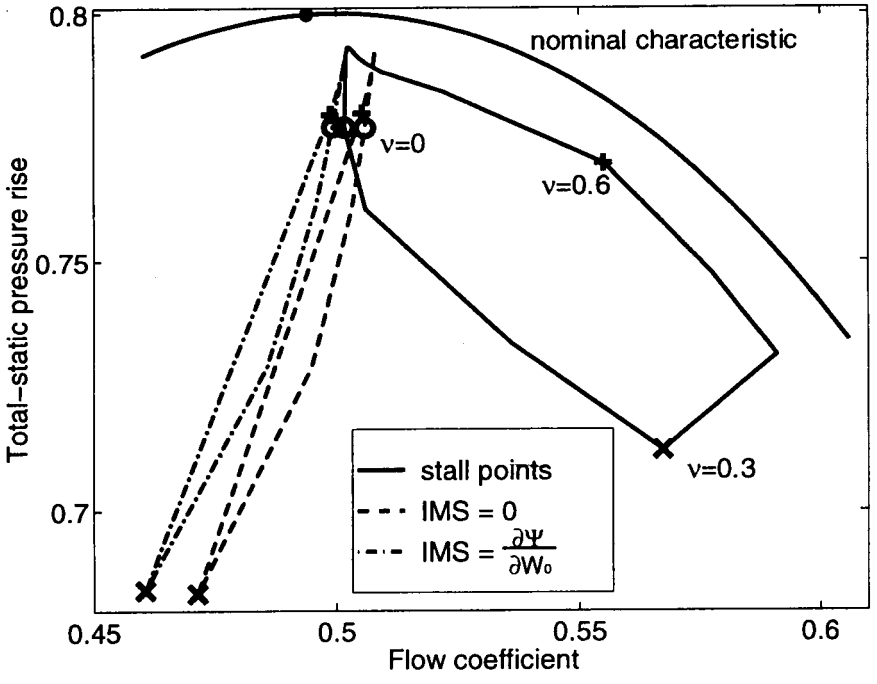


(b) Prediction using IMS values

**Figure 3-30:** Locus of predicted and actual stall points for MIT compressor with whirling shaft at offset of 2% chord. Predictions used (a) *weighted* IMS or (b) IMS values equal to 0 or the nominal slope at stall for uniform flow ($\frac{d\Psi}{dW}_0$). Symbols for $\nu = \{0, 0.3, 0.6\}$ are shown to clarify comparisons.

shows that the WIMS stall criteria was reasonably accurate in finding the stall point, and, unlike the IMS criteria, captured the trend of the loss in stall margin for changing whirl frequency. The WIMS criteria was accurate to within 3% of the stalling flow coefficient, whereas the IMS condition would predict the stall point up to 20% lower in flow coefficient for whirl frequencies near resonance.

### Applications of the WIMS stability condition

Since the WIMS stability criterion requires knowledge of the stall mode shape, it is not generally useful for stall prediction. However, it does explain why tip clearance asymmetries rotating near the stall frequency cause instability at higher flow coefficients than for uniform flow. For this condition, the mode amplitude is largest in regions of higher local slope. Therefore at neutral stability, the disturbance energy production is zero, even though the majority of the compressor annulus is operating on a negatively sloped characteristic.

It is proposed here that the WIMS condition is also applicable for compressors with inlet distortions. Although not formally verified, this statement is based on two facts. First, the rigorous derivation of the WIMS condition from conservation of energy laws in Appendix K is applicable for general flow nonuniformities, not just those caused by tip clearance asymmetry. Second, the analyses for rotating inlet distortions by Chue et al. [6] show similar stability trends as those demonstrated with the WIMS condition in the present studies.

The accuracy of the IMS stability criterion for steady inlet distortions can now be understood based on the new WIMS condition. The value of the WIMS approaches the IMS when the background flow nonuniformity is small because the mode amplitude envelope is essentially uniform around the circumference. But Appendix K.5 shows that even for *large* flow nonuniformities, the WIMS also equals the IMS for the case when the mode amplitude envelope is 90° out of phase with the slope variation. Recall from Section 3.4.2 that this phase relationship was satisfied for steady flow nonuniformities. Therefore the IMS=0 stability condition for steady background flow nonuniformities is merely a consequence of the WIMS=0 criterion for the case when the slope variation is in quadrature with the mode amplitude variation.

## 3.5 Asymmetry Caused by Nonuniform Rotor Blade Heights

The second type of rotating tip clearance asymmetries investigated for the MIT compressor were those caused by rotor height variations. An illustration of the tip clearance asymmetry caused by an $n^{th}$ harmonic variation of rotor heights around the annulus is shown in Figure 3-31. The overall tip clearance was then expressed as $\bar{\varepsilon} = \varepsilon_0 + \varepsilon_1 \cos[n(\theta - \Omega t)]$. In this

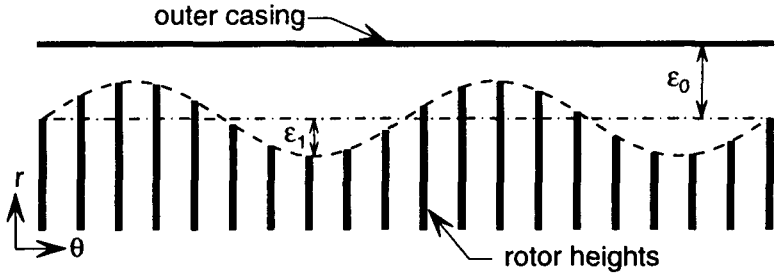


**Figure 3-31:** Illustration of tip clearance asymmetry caused by rotor height nonuniformity.

section, most comparisons are made between a compressor operating with a rotor height variation given by $\bar{\varepsilon}(\theta, t)$ and the same compressor with an axisymmetric tip clearance equal to the mean, $\varepsilon_0$. The performance losses associated with asymmetric rotor heights are also compared to those from stationary asymmetries of the same shape, $\bar{\varepsilon}(\theta)$. By understanding the relation between the two, the effect of rotor height asymmetry for any compressor can be estimated from flow field measurements with stationary clearance asymmetries, which are easier to generate experimentally.

The next two sections describe the effects of rotor height asymmetry on both the design performance and the stall inception behavior. Note that the response to a single-lobed sinusoidal blade height variation are equivalent to the previous results for an offset shaft whirling at the rotor frequency. Therefore, only cases for higher harmonic rotor height nonuniformities need be examined here.

### 3.5.1 Effect of Rotor Height Asymmetry on Compressor Performance

The calculated pressure rise and efficiency of the MIT compressor were reduced when the rotor heights were nonuniform, relative to the case of an axisymmetric tip clearance at the mean value of the nonuniformity. The performance losses were small (Figure 3-32), less than 0.2% when operating at the design point, and could generally be neglected when

accounting for sources of loss. The flow phenomena contributing to the performance loss will still be discussed here so that the losses can be understood for compressors other than the MIT configuration, where the effect of rotor height asymmetry may be more prominent. Examples of such compressors are discussed in Section 3.6.

Two trends characterizing the performance changes caused by rotor height variations were identified:

1. *Long* wavelength asymmetries were more detrimental to compressor performance than *short* wavelength asymmetries.

2. Long wavelength *rotor height* variations were less detrimental than *stationary* asymmetries of the same shape; but rotor-locked variations became more important than comparable stationary variations as the wavenumber of the asymmetry increased.

Similarly to the whirling shaft analyses, these trends could be explained in terms of the ability of the clearance asymmetry to excite the resonant modes of the compression system. In contrast to the whirling shaft studies, high harmonic rotor height asymmetries could induce a resonance with one of the higher harmonic rotating stall modes. Each rotating stall mode of harmonic $n$ had a distinct frequency and decay rate, both of which determined the flow field response to similarly shaped clearance asymmetries. The largest flow nonuniformities were induced for rotating clearance asymmetries of the same shape as the least damped mode, especially when the rotating frequencies were similar.

The first observed trend was that long wavelength asymmetries were more detrimental to compressor performance than short wavelength asymmetries (Figure 3-32). The higher harmonic asymmetries generated the least loss because the corresponding modes being excited were more damped, as seen in Figure 3-3. However, all the performance changes were small for the MIT compressor. The amounts of tip clearance variation required to effect a 1% drop in pressure rise or a 1 point drop in efficiency are shown in Figure 3-33 for both rotor-locked and stationary asymmetries at the design throttle condition. Rotor height variations were required to be greater than 4% of the chord to cause such a loss in performance. The extreme variation in clearance required for high harmonic asymmetries precludes random blade-to-blade height variations in this compressor from ever inducing a significant performance loss.

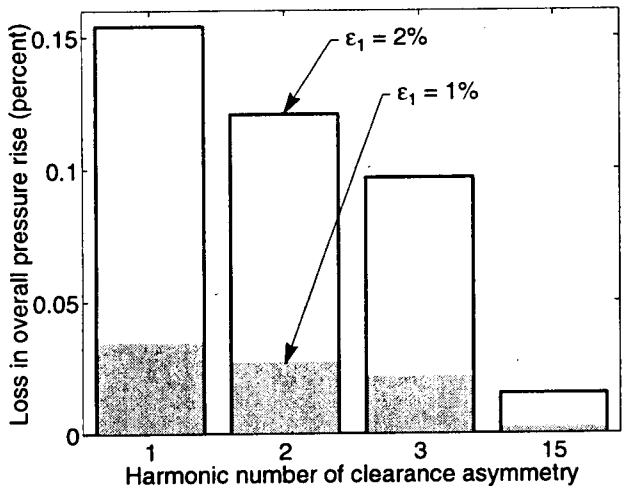


(a) Loss in overall pressure rise

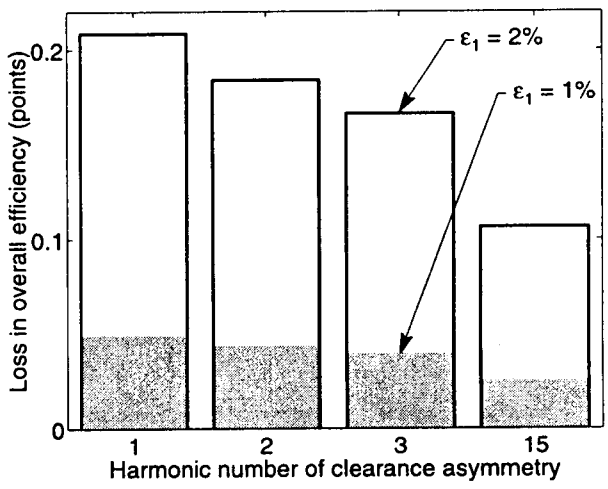


(b) Loss in overall efficiency

**Figure 3-32:** Loss in overall (a) pressure rise and (b) efficiency for MIT compressor at design caused by rotor height nonuniformities of various harmonics with amplitudes of 1% chord (shaded) and 2% chord (open).

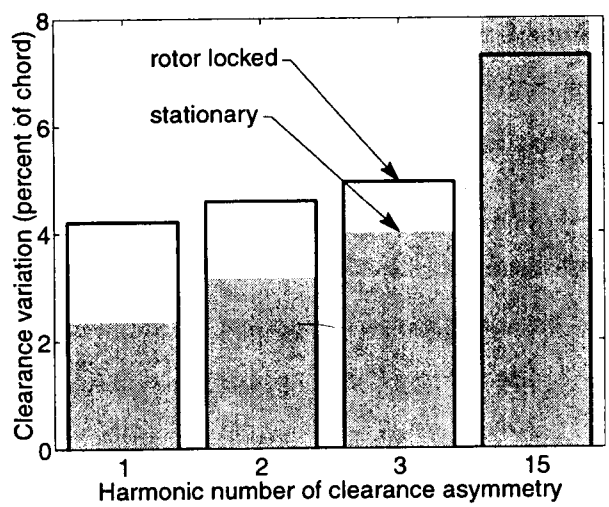


(a) 1% loss in pressure rise

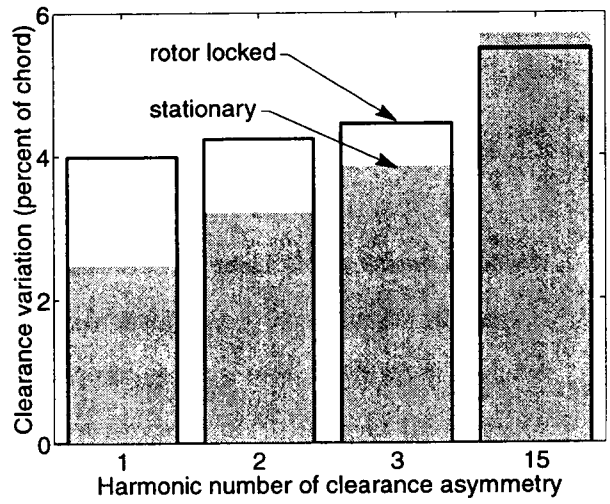


(b) 1 pt loss in efficiency

**Figure 3-33:** Amount of tip clearance nonuniformity required to effect a 1% drop in (a) pressure rise or (b) efficiency for the MIT compressor at the design throttle coefficient. Results for both rotor height (outlined) and stationary (shaded) clearance nonuniformities.

The second observed trend was that long wavelength clearance asymmetries were more detrimental to the performance if they were stationary, but short wavelength asymmetries were more detrimental if they were rotor-locked. Figure 3-33 shows that the amplitude of a single-lobed clearance variation required to effect a 1% drop in pressure rise was 78% larger for a rotor height nonuniformity than for a stationary nonuniformity. However, a 15-lobed stationary clearance nonuniformity needed to be 9% larger than a 15-lobed rotor height variation to cause the same drop in pressure rise. The relative importance of stationary versus rotor-locked asymmetries depended on the phase speed of the similarly shaped rotating stall mode. For the case of uniform background flow and no unsteady losses, the phase speed of the $n^{\text{th}}$ harmonic mode could be expressed analytically [47] as

$$\frac{s_i}{n} = \frac{n\lambda}{\mu + \frac{2}{n}} \,. \tag{3.8}$$

The phase speeds for the first 15 harmonic modes for the MIT compressor are shown in Figure 3-34. The lowest harmonic modes had phase speeds closer to that of the stationary asymmetry ($\nu = 0$) than to the rotor speed ($\nu = 1$). However, modes consisting of wavenumbers of six or more had a phase speed closer to the rotor speed. Therefore the low wavenumber modes would be preferentially excited by stationary clearance asymmetries, and higher wavenumber modes would be preferentially excited by rotor-locked asymmetries. The amount that the modes were excited was then reflected in the induced background flow nonuniformity and the overall performance losses.

### 3.5.2 Effect of Rotor Height Asymmetry on Stall Inception

Rotor height asymmetries reduced the stall margin of the compressor compared to operation with a uniform tip clearance equal to the mean value of the asymmetry. The loss in stall margin was comprised of both an increase in the stalling flow coefficient and a reduction in the stalling pressure rise (Figure 3-35). For rotor height variations as large as the nominal clearance, (i.e. $\varepsilon_1 = 2\%$ chord), the increase in flow coefficient and decrease in pressure rise at stall were between 1–2%. However, a rotor height variation this large would only arise from a serious tip rub over one portion of the rotor disk. More typical rotor height variations (less than 1% of the chord) had little effect on the stall point, changing it by one-half percent or less.

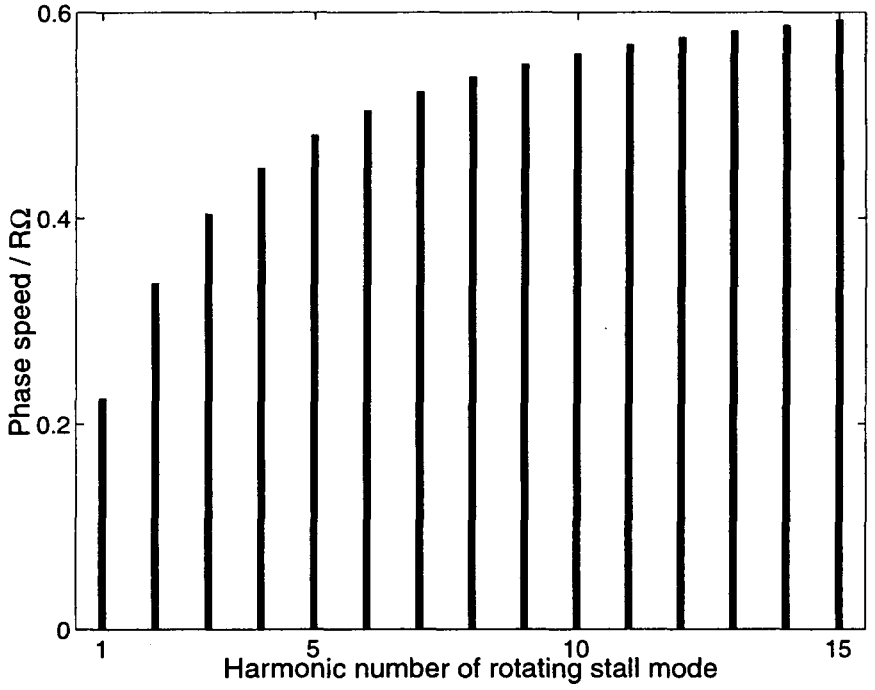


**Figure 3-34:** Phase speed of the first 15 rotating stall modes for the MIT compressor with axisymmetric background flow.

Stationary long wavelength clearance asymmetries were more detrimental to the peak pressure rise than similarly shaped rotor height asymmetries, but this trend was reversed for short wavelength asymmetries (Figure 3-36). This phenomenon was identical to the trend seen for design performance changes in Section 3.5.1, and can be explained with the same reasoning.

The mode leading to stall was dominated by a first harmonic sinusoid for all shapes of rotor height nonuniformities. Despite excitation by short wavelength rotor height variations, the higher order modes were more stable than the first mode because of the effects of unsteady losses. The shapes of the axial velocity disturbance for the critical modes at neutral stability are shown in Figure 3-37. The mode amplitude envelope was modulated by the variation in the characteristic slope in the same manner as described for a whirling shaft. Higher harmonic rotor height asymmetries induced less background flow nonuniformity, hence less slope variation, and less mode amplitude modulation. For example, the second-harmonic rotor height asymmetry created a two-lobed nonuniformity in the background flow field, which modulated the wave envelope of the rotating stall mode with a two-lobed variation (Figure 3-37b); yet the mode essentially had a first harmonic shape.

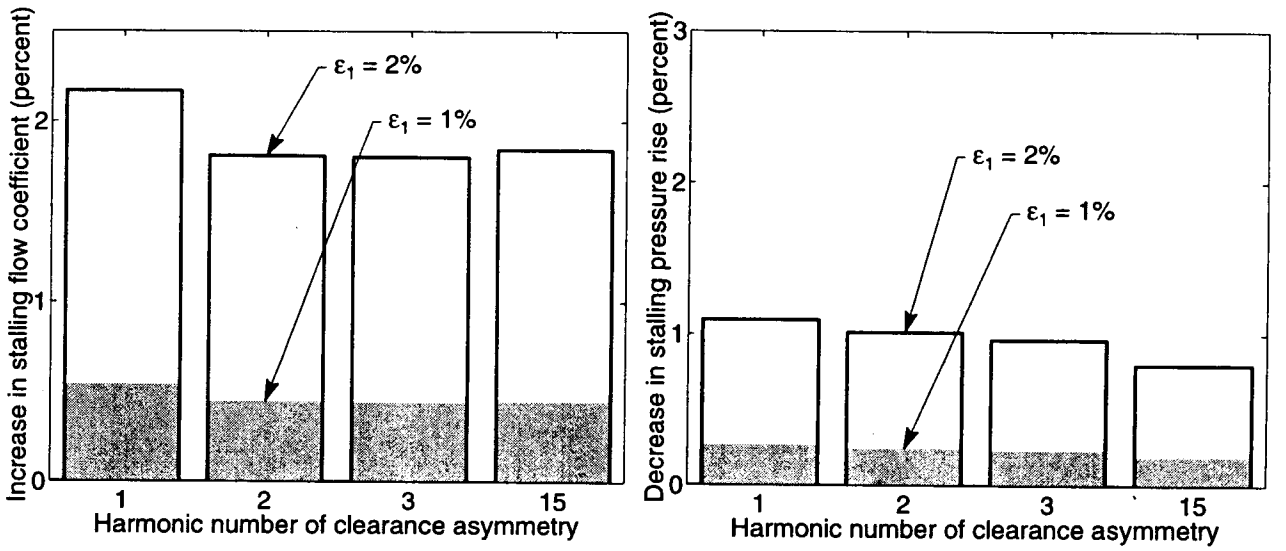


(a) Increase in stalling flow coefficient

(b) Loss in peak pressure rise

**Figure 3-35:** Change in stalling flow coefficient and peak pressure rise for MIT compressor with rotor height asymmetry of amplitude 1% chord (shaded) and 2% chord (outlined).

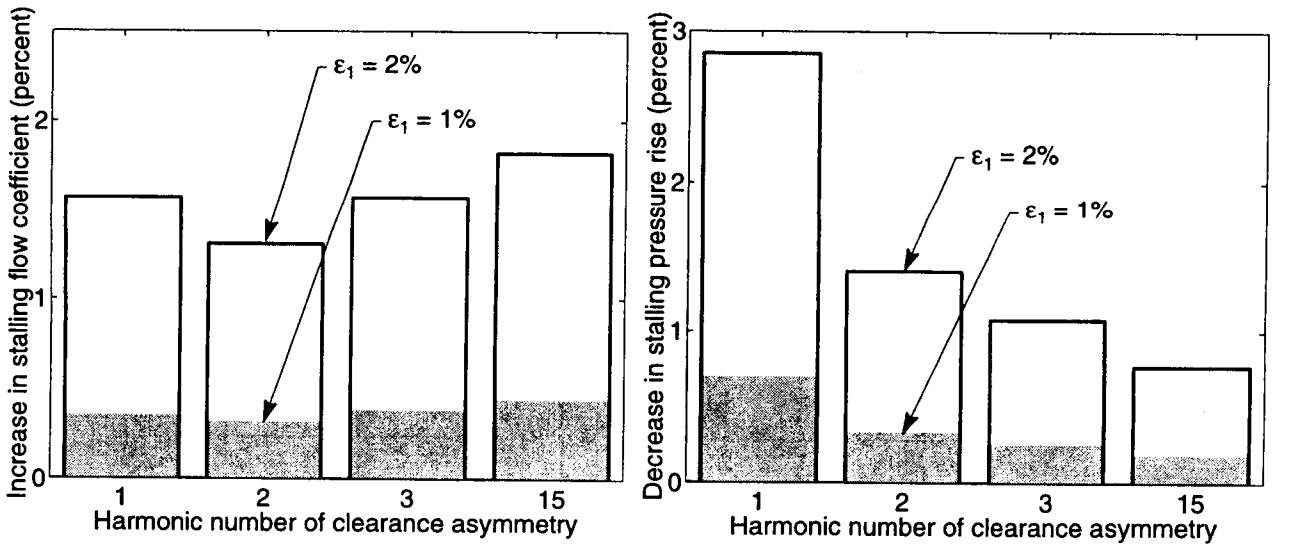


(a) Increase in stalling flow coefficient

(b) Loss in peak pressure rise

**Figure 3-36:** Change in stalling flow coefficient and peak pressure rise for MIT compressor with stationary tip clearance asymmetry of amplitude 1% chord (shaded) and 2% chord (outlined).

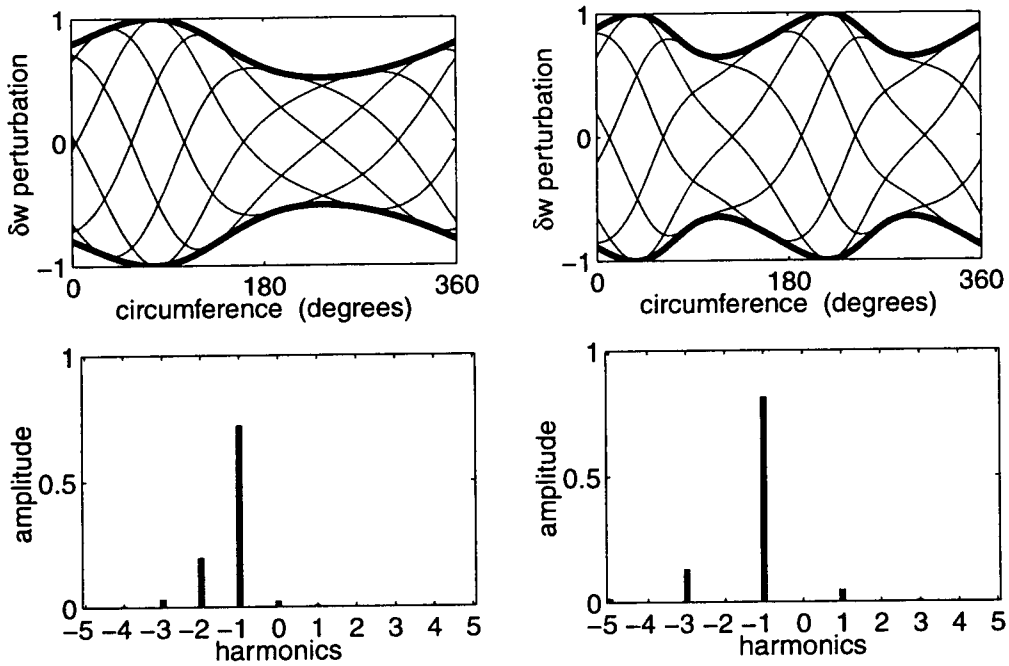


(a) $n = 1$

(b) $n = 2$

(c) $n = 3$

(d) $n = 15$

**Figure 3-37:** Rotating stall mode shapes at neutral stability in MIT compressor with rotor height asymmetry (asymmetry magnitude $\varepsilon_1$ of 2% chord). Upper figures show axial velocity perturbation in rotor-locked reference frame for six equally-spaced time intervals. Overall wave envelope is drawn in bold. Lower figures show harmonic decomposition of mode shape, where positive harmonics travel in the direction of the rotor, relative to the rotor-locked frame.

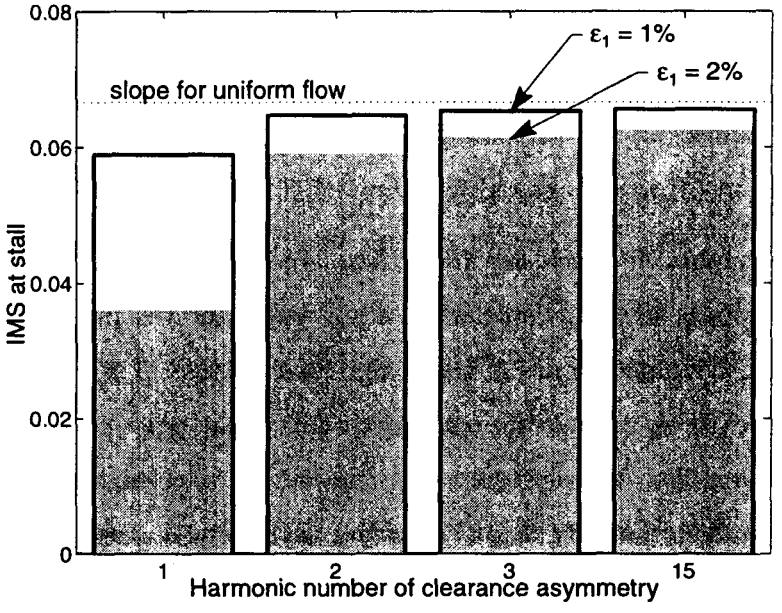


**Figure 3-38:** Value of integrated mean slope at stall for MIT compressor with rotor height nonuniformity of amplitude 1% chord (outlined) and 2% chord (shaded).

The stability point of the compressor with rotor height asymmetry was set by the point where the integrated mean slope was approximately zero (Figure 3-38) which corresponded closely to the peak of the nonuniform flow characteristic. Since the rotating frequency of the clearance asymmetry was not near the compressor resonant frequencies, weighting the slope variation by the mode amplitude envelope gave no improvement in finding the stall point.

## 3.6 Implications for General Compressor Configurations

General implications of the effects of whirling shafts and rotor height asymmetries on other compressors can be drawn from the results for the MIT 3-stage and NASA Stage-37 compressors. The primary factors leading to overall performance loss due to tip clearance asymmetries were the induced circumferential flow nonuniformity and the curvature of the pressure rise characteristic. The factors affecting the shape of the characteristic have been examined in other studies (i.e. [45]) and will not be discussed here. In general, multistage compressors with steep off-design loss buckets have characteristics with strong curvature, and so would exhibit the greatest overall performance loss for a given flow nonuniformity.

Of more importance here are the factors that affect the size of induced flow nonuniformity caused by a rotating tip clearance asymmetry. The key compressor properties are (1) the sensitivity to axisymmetric tip clearance changes, (2) the frequency and damping of the rotating stall modes, (3) the proximity of the design operating point to the peak of the characteristic, and (4) the shape and frequency of the rotating tip clearance asymmetry.

The most important conclusion from these studies is that the magnitude of induced flow nonuniformity is strongly dependent on how much the rotating clearance asymmetry excites the lightly damped modes of the compression system. Therefore, knowledge of the types of modes existing in the compressor determine what types of clearance asymmetries are most detrimental to the performance. The longest wavelength mode is typically the most unstable, and so similarly shaped clearance asymmetries cause the largest compressor response. Short wavelength modes tend to be most heavily damped in multistage compressors; therefore, short wavelength rotor height variations may cause increased flow distortion in single-stage fans compared to multistage machines. Nonuniformity of the flow field increases as the damping of the excited modes decreases. This implies that compressors with narrow operating ranges, where the design point is close to the stall point, will be more sensitive at design to tip clearance asymmetry than the MIT or NASA compressors.

Although predicting the magnitude of induced flow nonuniformity requires the use of the nonlinear solution process in Section 2.3, a linearized analysis can provide information about the factors that influence the response to rotating clearance asymmetries. Appendix A derives the axial velocity variation ($\delta w$) caused by an $n^{\text{th}}$ harmonic small-amplitude tip clearance nonuniformities ($\delta\varepsilon$), rotating at frequency $\nu$. The ratio of the magnitudes of $\delta w$ to $\delta\varepsilon$ in equation (A.5) can be re-written as

$$\left\| \frac{\delta w}{\delta \varepsilon} \right\| = \frac{\left\| \frac{\partial \Psi}{\partial \varepsilon} \right\|}{\left( \frac{\partial \Psi}{\partial W} \right)^2 + (\nu - \nu^*)^2 (2 + n\mu)^2} \tag{3.9}$$

where $\nu^*$ is the frequency of the $n^{\text{th}}$ harmonic rotating stall mode, given by equation (A.8). This ratio is a bell-shaped function of frequency, centered around the frequency of the rotating stall mode, as (Figure 3-39).

Equation (3.9) can be used to relate the magnitude of velocity nonuniformity to certain compressor parameters for a fixed clearance asymmetry shape and rotating frequency. If

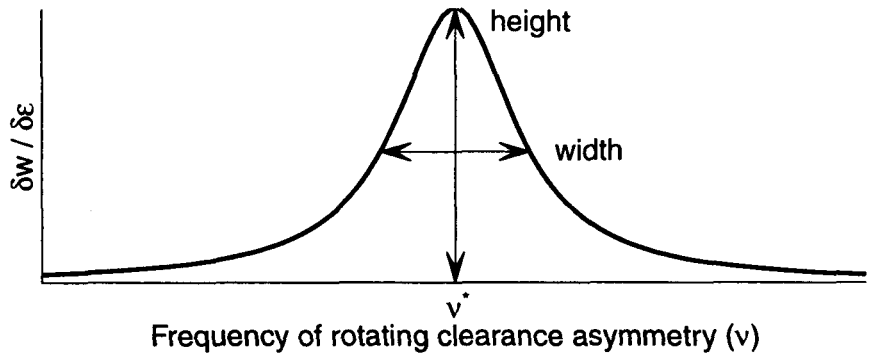


**Figure 3-39:** Illustration of axial velocity nonuniformity induced by small-amplitude rotating clearance asymmetry (from equation 3.9) depicting height and width of curve centered about rotating stall frequency ($\nu^*$)

the frequency of the clearance asymmetry is near the rotating stall frequency, then the height of the response curve in Figure 3-39 has the greatest effect on the size of the velocity nonuniformity. The height is linearly proportional to the magnitudes of both $\frac{\partial \Psi}{\partial \varepsilon}$ and $\frac{\partial \Psi}{\partial W}$. Therefore, compressors with high sensitivity to axisymmetric changes in clearance, and compressors operating close to a zero slope on the characteristic, would be most sensitive to rotating clearance asymmetries. The sensitivity of the compressor to rotating clearance asymmetries at frequencies away from $\nu^*$ is also determined by the width of the response curve. From equation (3.9), the width is inversely proportional to $2+n\mu$. This implies that compressors with long wavelength clearance asymmetries and short axial extent (i.e. low inertia, $\mu$) would show the largest response to tip clearance nonuniformity over the widest range of frequencies.

### 3.6.1 Implications for High-Speed Compressors

The incompressible flow model used for the present calculations can only capture a limited number of the modes often seen in high-speed compressors. These "incompressible" modes usually have phase speeds between 20% and 70% of the rotor speed, so resonant response to rotating tip clearance asymmetries does not occur at the rotor frequency. This explains why rotor height nonuniformities did not produce a significant performance change in the MIT and NASA configurations.

High-speed compressors may be more sensitive to rotor height variations than the calculations in this chapter have demonstrated. Here, high-speed compressors are defined

as having through-flow Mach numbers of 0.4 or greater. Certain high-speed compressors have demonstrated additional "compressible" modes that rotate at frequencies between 0.8 and 1.2 times the rotor frequency (Tryfonidis et al. [75], Weigl et al. [78]). These modes would likely be excited by rotor-locked clearance asymmetries, and could cause performance losses as large as at the peak resonance of the "incompressible" modes. The present model calculated performance losses from rotor-locked asymmetries to be up to 10 times smaller than at peak resonance. Thus, the calculations using incompressible flow could have underestimated the effects of rotor height nonuniformities by an order of magnitude for these types of high-speed compressors. This change can be confirmed by experiment, or by future modeling efforts incorporating compressible flow in the asymmetric tip clearance model.

Rotor height variations that excite "compressible" modes near the rotor frequency may also give rise to phase-locking of the mean flow nonuniformity to the rotor frequency. Such excitation will always be present due to the slight blade asymmetries inherent in the rotor blade row. This phase locking may explain experimental observations of the compressible mode frequency coinciding exactly with the rotor frequency [75]. Phase-locking also makes it more difficult to measure these small-amplitude modal perturbations traveling at rotor speed, which could be lost in the signal of the rotating mean flow nonuniformity.

# CHAPTER 4

# CONTROL OF ROTATING STALL USING TIP CLEARANCE ACTUATION

## 4.1 Overview of Compressor Configurations for Control

This chapter describes how tip clearance control through shaft deflection was used to increase the stall margin of a compressor. These analytic results were intended to assess the feasibility of using magnetic bearings to control the rotor shaft position in order to stabilize the growth of the rotating stall modes. Therefore, the feedback control models were based on specifications for the magnetic bearings experiments designed for the Stage-37 compressor. These experiments, proposed to begin at the NASA Lewis Research Center in 1999 [68], will be the first effort to actively control rotating stall through unsteady tip clearance nonuniformity.

The controllability of the MIT and Stage-37 compressors were each examined with the rotor shaft nominally centered, and with the shaft offset from the casing centerline. In both cases, the rotor heights and casing radii were assumed to be uniform so that the only variation in tip clearance arose from shaft deflections. In the first case, the rotor shaft was nominally centered within the casing and the control consisted of small-amplitude shaft deflections about the centerline. This configuration resulted in the best performance without control because the background flow field was circumferentially uniform. Constant gain stall control was able to increase the stall margin without affecting the axisymmetric performance of the compressor. It will be shown that this control configuration was limited because linear

perturbations to the shaft position only controlled the 1st harmonic mode. Although this method would provide a useful operating range extension for many compressors, the stalling mass flow can only be decreased until uncontrollable, higher order modes become unstable. Furthermore, the stall margin cannot be increased at all for compressors that stall through inception of a different mode (such as the axisymmetric surge mode). The 1st harmonic mode was the most unstable mode for both the Stage-37 and MIT compressors. Therefore, this control scheme was able to increase their stable operating ranges by reducing the stalling flow coefficient at stall by up to 0.9% and 2.7% percent, respectively, for these compressors.

In the second case, the rotor was nominally offset from the casing centerline before applying shaft deflection control. Although the overall performance was reduced by inducing a nonuniform background flow field, it will be shown that this approach enabled controllability of all rotating stall modes to some degree. The flow coefficients at stall for the MIT and Stage-37 compressors with control were reduced by as much as 7.2% and 1.2% respectively, compared to the stall points in uniform flow without control. These values reflected a substantial increase in the range extension over the control method that used a nominally centered shaft; however, the range increase was accompanied by a minor penalty in overall pressure rise and efficiency.

The tip clearance control schemes assumed that the magnetic bearings could arbitrarily set the rotor shaft position within the annulus at any point in time. The dynamics of the magnetic bearings themselves were not considered, nor was the effect of fluid dynamic forces on the rotor disk. Enhancements to the present control scheme are currently being examined to include these effects [2, 68]. The steady, finite offset of the rotor shaft from the centerline was defined as $\varepsilon_1$, which created a background tip clearance nonuniformity of $\bar{\varepsilon} = \varepsilon_0 - \varepsilon_1 \overline{\cos}\,\theta$ (Figure 4-1). The rotor shaft was controlled through small-amplitude deflections $u_x(t)$ and $u_y(t)$, defined to be parallel and perpendicular, respectively, to the shaft offset direction. These deflections caused temporal variations to the tip clearance, which could be represented as

$$\varepsilon(\theta, t) = \bar{\varepsilon}(\theta) - u_x(t)\cos\theta - u_y(t)\sin\theta. \tag{4.1}$$

Since the linearized model in Chapter 2 was developed in terms of perturbations in the tip clearance variation, the above equation was rewritten using the harmonic notation intro-

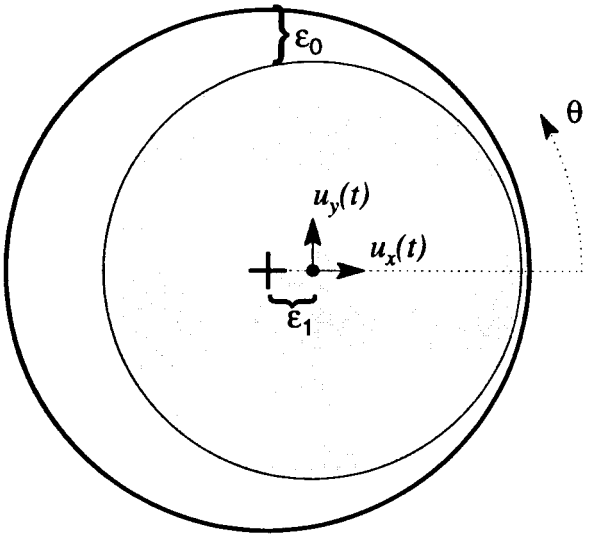


**Figure 4-1:** Illustration of the cross-section of the compressor annulus, depicting control of the rotor shaft.

duced in equation (2.22):

$$\varepsilon(\theta, t) = \bar{\varepsilon}(\theta) + \varepsilon_{c,1} \cos\theta + \varepsilon_{s,1} \sin\theta. \tag{4.2}$$

Constant gain feedback control was implemented by using the static pressure perturbations upstream of the compressor face (station 1 in Figure 2-1) as the controller input. This arrangement is in accordance with previous Stage-35 active control experiments described by Weigl [78], as well as the proposed Stage-37 magnetic bearing experiments [68, 72].

## 4.2 State-Space Model Development

A state-space model representing the dynamics of the compression system was developed so that linear feedback control laws could be designed to stabilize the rotating stall modes. The forced response of the flow field to linear variations in tip clearance was already developed as equation (2.23). The full control model also included the output vector $\vec{y}$ to represent the static pressure variation upstream of the compressor face:

$$\begin{aligned} \frac{d\vec{x}}{dt} &= \mathbf{A}\vec{x} + \mathbf{B}\vec{u} \\ \vec{y} &= \mathbf{C}\vec{x} + \mathbf{D}\vec{u} \end{aligned} \tag{4.3}$$

$$
\begin{aligned}
\vec{x} &= [p_P \;\; w_T \;\; w_0 \;\; w_{c,1} \ldots w_{c,N} \;\; w_{s,1} \ldots w_{s,N} \;\; l_{R0} \;\; l_{Rc,1} \ldots l_{Rc,N} \;\; l_{Rs,1} \ldots l_{Rs,N} \\
&\qquad l_{S0} \;\; l_{Sc,1} \ldots l_{Sc,N} \;\; l_{Ss,1} \ldots l_{Ss,N}]^T \\
\vec{u} &= [\varepsilon_{c,1} \;\; \varepsilon_{s,1}]^T \\
\vec{y} &= [p_{c,1} \;\; p_{s,1}]^T \, .
\end{aligned} \tag{4.4}
$$

The matrices $\mathbf{A}, \mathbf{B}, \mathbf{C}$ and $\mathbf{D}$ described the pre-stall compressor dynamics. The construction of these matrices in terms of the steady background flow and compression system geometry is described in Appendix C.

The variables in equation (4.4) were chosen specifically for the rotor shaft control illustrated in Figure 4-1. Since shaft deflection can only cause a first-harmonic variation in tip clearance, the input vector, $\vec{u}$, only needed to include the first harmonic terms for tip clearance variation, $\varepsilon_{c,1}$ and $\varepsilon_{s,1}$. Truncating $\vec{u}$ to only two terms simplified subsequent derivations of the control law. Other control methods, such as active casing deformation, would require the inclusion of all tip clearance harmonics, as described in equation (2.24). The output vector, $\vec{y}$, similarly contained only terms for the first-harmonic pressure perturbations. This simplification allowed for the design of an easily optimized constant gain feedback controller (Section 4.3). For the case of a uniform background flow, higher harmonic pressure variations were not important since only the first harmonic mode could be controlled. However, for the case of nonuniform background flow, a more effective control scheme than that presented in Section 4.3 may be able to use higher harmonic pressure variations to improve the active stabilization of rotating stall. Examples of such control methods are described by Weigl [78] and Van Schalkwyk [76].

## 4.3 Constant Gain Feedback Control Law Design

To analytically demonstrate active control of rotating stall using tip clearance asymmetry, a constant gain feedback controller was developed for the state-space model in equation (4.3). The purpose of the controller was to feed back the first-harmonic pressure perturbation ($\vec{y}$) to the tip clearance variation ($\vec{u}$) through the $2 \times 2$ compensator matrix $\mathbf{K}$:

$$
\vec{u} = \mathbf{K}\,\vec{y} \, . \tag{4.5}
$$

The controller was based on the constant gain, harmonic feedback control law used by Van Schalkwyk et al. [77] and Spakovszky et al. [69] to effectively suppress rotating stall in circumferentially distorted flow. The form of the constant gain controller is given by equation (4.6), where $k$ is the gain, and $\alpha$ is an arbitrary phase angle between 0 and $2\pi$.

$$\mathbf{K} = k \begin{bmatrix} \cos\alpha & -sin\alpha \\ \sin\alpha & \cos\alpha \end{bmatrix} \tag{4.6}$$

The effect of the controller was to rotate the $1^{st}$ harmonic pressure variation by the angle $\alpha$, and multiply it by the gain $k$ to produce the desired $1^{st}$ harmonic tip clearance perturbation through shaft deflection.

To realistically limit the effectiveness of the controller, the gain was bounded by the specifications of the Stage-37 compressor experiment. The magnetic bearings are designed to produce a maximum shaft displacement of 0.01 inches at a frequency of 150 Hz (0.52% of rotor frequency), which is approximately the frequency required to control the most unstable mode. The maximum gain was chosen so the shaft displacement peaks at this value for the largest expected pressure perturbations:

$$k_{\max} = \frac{\delta\varepsilon_{\max}}{\delta p_{\max}}. \tag{4.7}$$

The value of $k_{\max}$ was determined for each compressor based on their unique nondimensional parameters. The maximum shaft displacement of 0.01 inches corresponded to 0.56% and 0.455% chord for the MIT and NASA compressors, respectively. Observations by Weigl [78] showed that pressure perturbations remained below 0.1 times the dynamic head during active control experiments. The dynamic head of the duct flow was based on the flow coefficient at stall, which was about 0.5 for either compressor. Therefore, the maximum values of gain used to stabilize each compressor were 0.45 for the MIT compressor and 0.36 for Stage-37.

For a fixed gain, the controller effectiveness can be optimized by suitably choosing the phase, $\alpha$, to achieve the largest stable operating range extension. The optimal phase was found by comparing the flow coefficients at stall for all $\alpha$ between 0 and $2\pi$. This method was identical to the trial-and-error experimental procedures followed by Haynes [33] and

Van Schalkwyk [76] to optimize the phase of their harmonic feedback laws.

## 4.4 Scope of Active Control Studies

Control of rotating stall was simulated for both the MIT and NASA compressors using different initial configurations to determine the best control strategy. Each compressor was controlled with the rotor shaft nominally centered within the casing, and at two off-centered positions. The values of the nominal shaft displacement for the cases examined are listed in Table 4.1.

The actuator was presumed to have as much bandwidth for a centered rotor as for an offset rotor. Therefore, the control gain used for every configuration was fixed at the maximum gain values determined in Section 4.3. The *maximum* shaft displacement encountered with active control was the sum of the initial displacement and the maximum control actuation. For compressor experiments, this value must be less than the nominal tip clearance to prevent the rotor tips from rubbing the outer casing. The maximum shaft displacement, normalized by the nominal tip clearance, is listed in Table 4.1 for each configuration. The values indicate that all configurations are experimentally realizable, except for the MIT compressor case with the largest initial shaft offset.

**Table 4.1:** Scope of compressor configurations for active control simulations.

| Nominal shaft offset / chord ($\varepsilon_1$) | | Maximum shaft displacement with control / nominal clearance ($\max\|\varepsilon(\theta)\| / \varepsilon_0$) |
|---|---|---|
| NASA | 0% (centered) | 50% |
| | 0.228% | 75% |
| | 0.455% | 100% |
| MIT | 0% (centered) | 27% |
| | 1% | 75% |
| | 2% | 122% |

The numerical implementation of the control model was similar to the open-loop stability model in Chapter 3. The steady background flow was first obtained with the rotor shaft in the nominal position. This flow was used to determine the $\mathbf{A}, \mathbf{B}, \mathbf{C}$ and $\mathbf{D}$ matrices. The behavior of the closed-loop modes was obtained from the eigenvalues of the controlled

system, given by

$$\frac{d\vec{x}}{dt} = \left[\mathbf{A} + \mathbf{BK}[\mathbf{I} - \mathbf{DK}]^{-1}\mathbf{C}\right] \vec{x}. \tag{4.8}$$

Twenty-one circumferential harmonics were found to be sufficient to accurately capture the background flow and the relevant mode shapes.

The stall point of the controlled compressor, for a fixed controller phase, was found by repeating the above steps for a decreasing throttle coefficient until any one mode had a positive growth rate. This entire procedure was then repeated for different values of $\alpha$ to calculate the optimal extension of the stable operating range.

## 4.5 Assessment of Active Stall Control

### 4.5.1 Controllability of Rotating Stall Modes

A rotor shaft is limited as an actuator for rotating stall control because it can only effect first harmonic variations in tip clearance. Therefore, controlling the shaft position can only stabilize modes that have a first harmonic component in their circumferential shape. The control effectiveness of rotor shaft actuation on the rotating stall modes is investigated in this section for the cases of both a uniform and a nonuniform background flow field.

#### Uniform background flow

Rotor shaft actuation can only stabilize *one* of the many rotating stall modes when the background flow is uniform. This condition arises when the rotor shaft is nominally centered, which is the desired operating condition for the compressor without control. Since each rotating stall mode is composed of a unique circumferential wavenumber when the background flow is axisymmetric, only the mode with the first harmonic variation can be controlled. This effect is demonstrated in Figure 4-2, which shows the effect of control on the least damped eigenvalues. The loci of the closed-loop eigenvalues at maximum gain for all values of $\alpha$ are superimposed on the open-loop eigenvalues, where the number of each mode refers to the circumferential wavenumber of the mode shape. The figure shows that

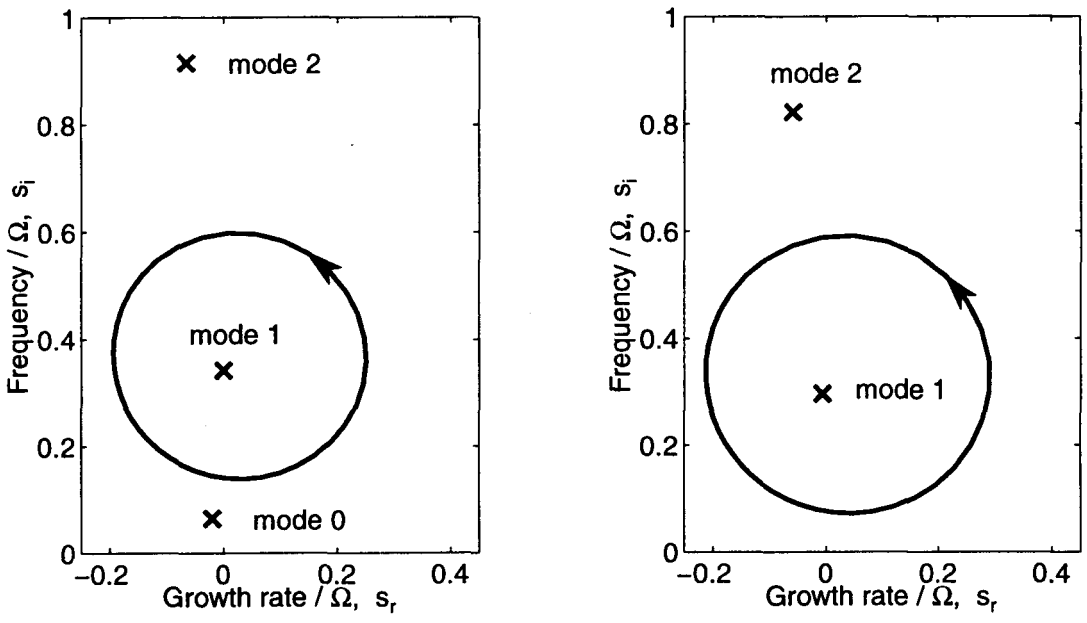


(a) NASA (b) MIT

**Figure 4-2:** *Locus of closed loop eigenvalues at maximum gain for $\alpha$ increasing between 0 and $2\pi$. Open-loop eigenvalues are indicated by ×'s. Results for nominally centered shaft for (a) NASA compressor at $k_T$=1.923, and (b) MIT compressor at $k_T$=6.56.*

the control had no effect on the zero or second modes, for which the closed-loop and open-loop eigenvalues were identical. Only the first mode was further stabilized or destabilized with active control, depending on the choice of $\alpha$.

The effectiveness of the controller was evident as the compressors were throttled into stall. The root loci, with and without control, are shown in Figures 4-3 and 4-4 as the flow coefficient was reduced towards stall. Although rotor shaft actuation was limited in terms of what modes could be controlled, it had more control authority than needed to stabilize the first mode. The first mode was stabilized well below the growth rate of the second mode. With the control acting, the stability points of the two compressors were set by the growth rate of their respective second modes. The controller gain could be reduced by a factor of five and still maintain the growth rate of the first mode below that of the second mode. Therefore, in the case of using magnetic bearings, only one-fifth of the designed actuator power (two thousandths of an inch at 150 Hz) would be needed to provide the same measurable operating range extension.

The effectiveness of rotor shaft actuation on controlling the first mode indicated that general tip clearance asymmetries were likely to be similarly effective at stabilizing higher

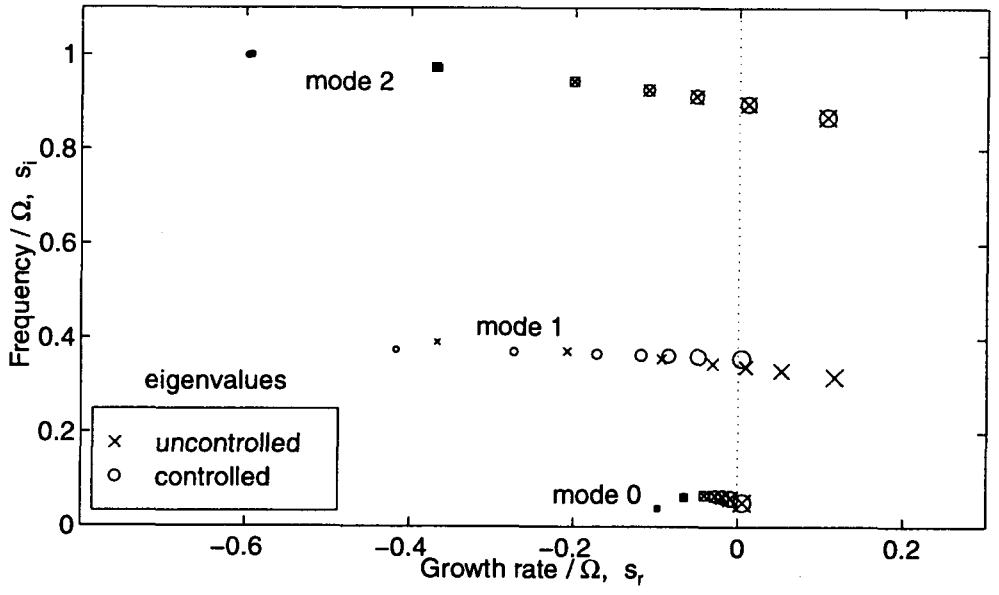


**Figure 4-3:** Root loci of first three stall modes for NASA compressor entering stall with and without control. Controller optimized with $\alpha = 115°$ for nominally centered shaft. The marker size increases approaching stall, from a flow coefficient of 0.522 to 0.480.

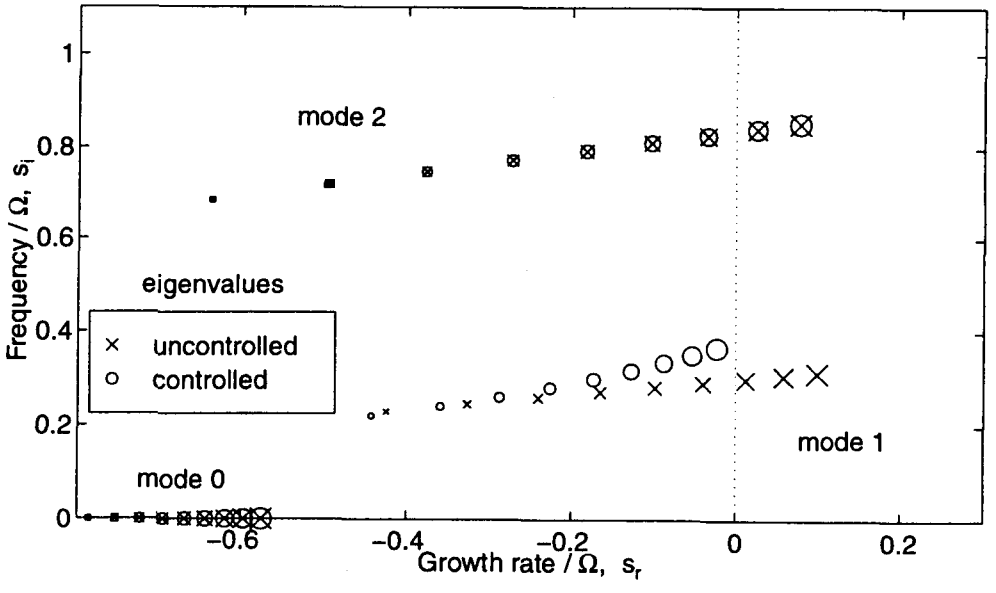


**Figure 4-4:** Root loci of first three stall modes for MIT compressor entering stall with and without control. Controller optimized with $\alpha = 120°$ for a nominally centered shaft. The marker size increases approaching stall, from a flow coefficient of 0.604 to 0.451.

harmonic rotating stall modes. Such control could be generated by actuators outside the outer casing wall that deflect the casing, providing small-amplitude tip clearance nonuniformities of arbitrary wavenumber. Casing deflections of 0.01 inches would stabilize the first mode as effectively as the shaft actuation described above, but they could also stabilize higher harmonic modes. The state-space model in equation (4.3) could be used to quantify the effectiveness of this control method by including the higher order harmonic terms in the input and output vectors, as described in Appendix C.

### Nonuniform background flow

First harmonic tip clearance variations could linearly control more than just the first mode when the background flow was nonuniform. Figure 3-24b shows that each mode shape consisted of more than one harmonic when the rotor shaft was nominally offset from the centerline. Small-amplitude rotor shaft actuation could then control the first harmonic component of each mode shape, thereby stabilizing the mode as a whole.

The controllability of all the modes in nonuniform background flow is indicated in Figure 4-5 and Figure 4-6. The closed-loop eigenvalues for the zero and second modes were not identical to the corresponding open-loop eigenvalues when the rotor shaft was off-centered. The amount that each mode was stabilized depended on the fraction of the mode shape that was comprised of the first harmonic. The higher the nonuniformity in the background flow, the more these modes could be controlled. Stage-37 demonstrated very little controllability of the zero and second modes compared to the MIT compressor. The MIT compressor had a larger nominal tip clearance, and so the rotor shaft could be initially displaced further from the centerline, thereby increasing the flow nonuniformity.

Although all modes in a nonuniform flow could be controlled to some degree, they could not be *independently* controlled using the compensator described in equation (4.6). The only optimization variable was the phase, $\alpha$, which set the value of every closed-loop eigenvalue. The optimal choice of $\alpha$ did not necessarily stabilize the first mode the most. More control power existed than needed to stabilize the first mode below the growth rate of the second mode. Therefore, a more appropriate choice of $\alpha$ sufficiently stabilized the first mode, and simultaneously controlled the growth of the second mode. An example of the optimal choice of phase is shown in Figure 4-7 for the MIT compressor with a shaft offset

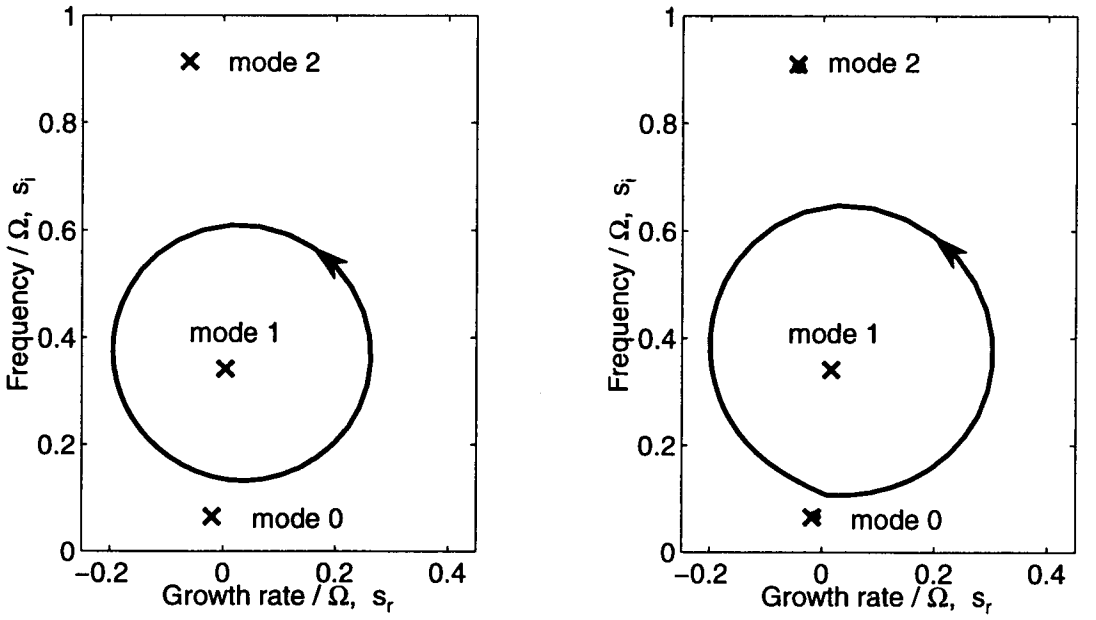


(a) $\varepsilon_1 = 0.228$ (b) $\varepsilon_1 = 0.455\%$

**Figure 4-5:** Locus of closed loop eigenvalues at maximum gain for $\alpha$ increasing between 0 and $2\pi$. Open-loop eigenvalues are indicated by ×s. Results for Stage-37 at $k_T$=1.923, with nominal shaft offset of (a) 0.228%, and (b) 0.455% chord.

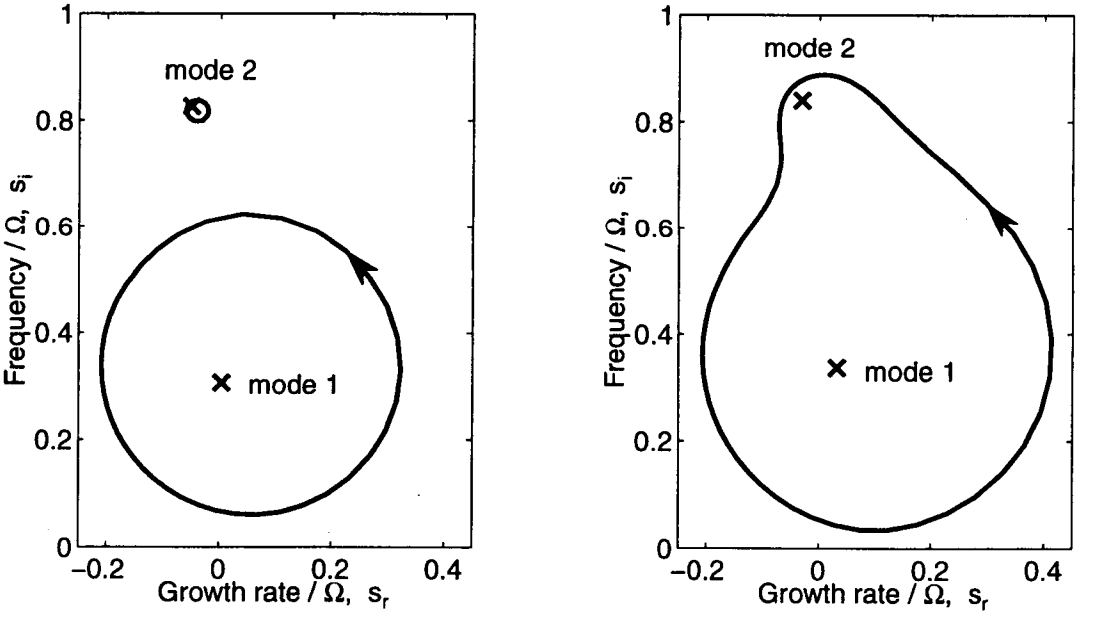


(a) $\varepsilon_1 = 1\%$ (b) $\varepsilon_1 = 2\%$

**Figure 4-6:** Locus of closed loop eigenvalues at maximum for $\alpha$ increasing between 0 and $2\pi$. Open-loop eigenvalues are indicated by ×s. Results for MIT compressor at $k_T$=6.56, with nominal shaft offset of (a) 1%, and (b) 2% chord.

of 1% chord. A value of $\alpha$ near 120° would have further stabilized the first mode, but at the cost of destabilizing the second mode.

For every configuration, an optimal value of $\alpha$ could be found that controlled the first, second *and* zero modes sufficiently to reduce the stall point beyond what was possible with a centered rotor. The root loci for the NASA and MIT compressors throttled into stall are shown in Figures 4-8 and 4-9. The controller phase was optimized in these figures to achieve the greatest overall stable flow range extension. Compared to Figures 4-3 and 4-4 for uniform background flow, the growth rate of the controlled first mode has increased, but the growth rate of the second mode has decreased. The net effect in terms of the stall margin is quantified in the following section.

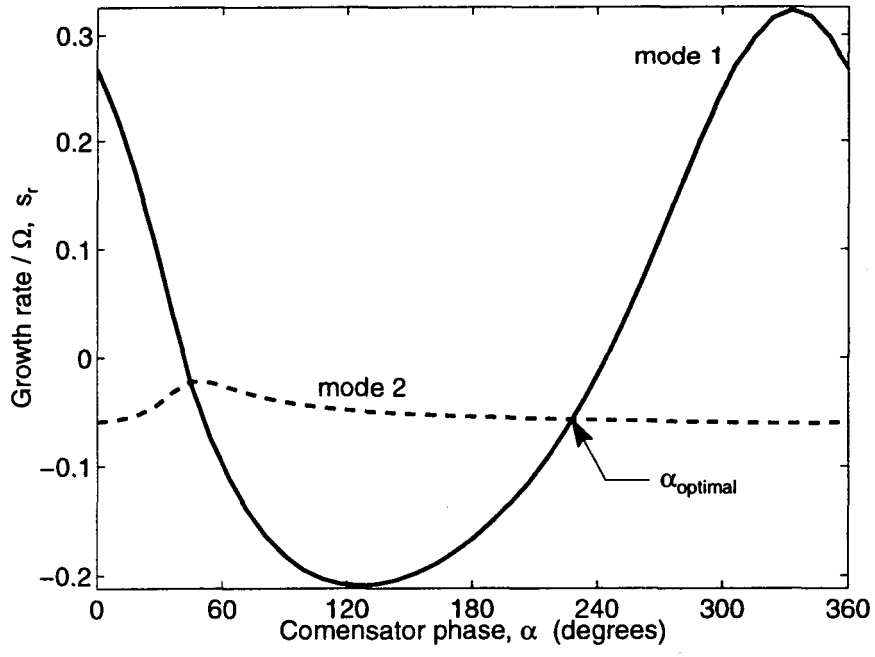


**Figure 4-7:** Growth rate of first and second modes in controlled MIT compressor as function of controller phase. Results at $k_T$=6.56 with shaft offset of 1% chord.

### 4.5.2 Extension of Stall Margin

The ultimate figure of merit for active stall control is the increase of stable operating flow range. This allows the compressor to either operate steadily in the region that is inaccessible without control, or else provides a greater safety margin between the design operating point

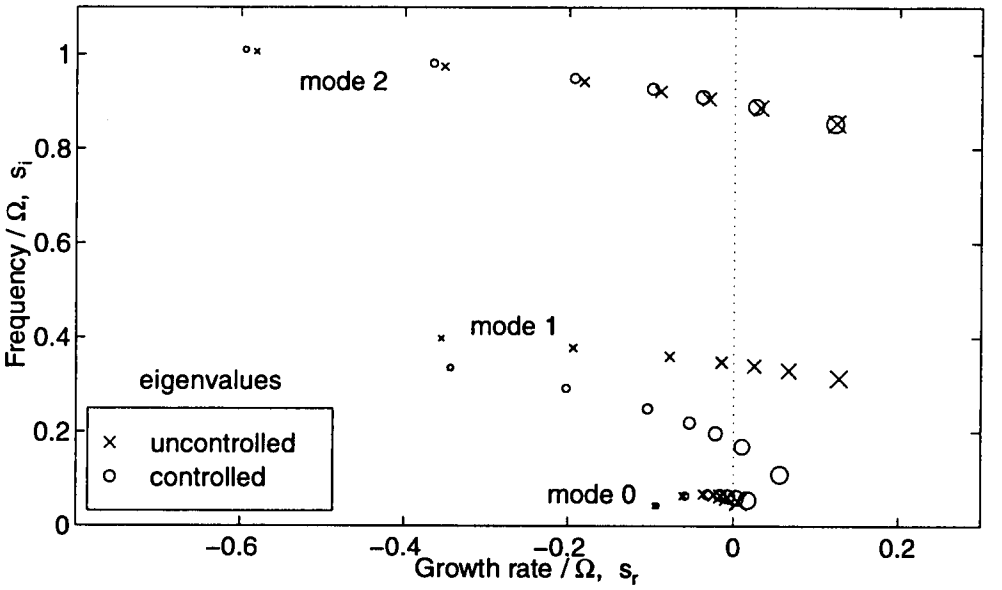


**Figure 4-8:** Root loci of first three stall modes for NASA compressor entering stall with and without control. Controller optimized with $\alpha = 210°$ for a nominal shaft offset of 0.455% chord. The marker size increases approaching stall, from a flow coefficient of 0.522 to 0.480.

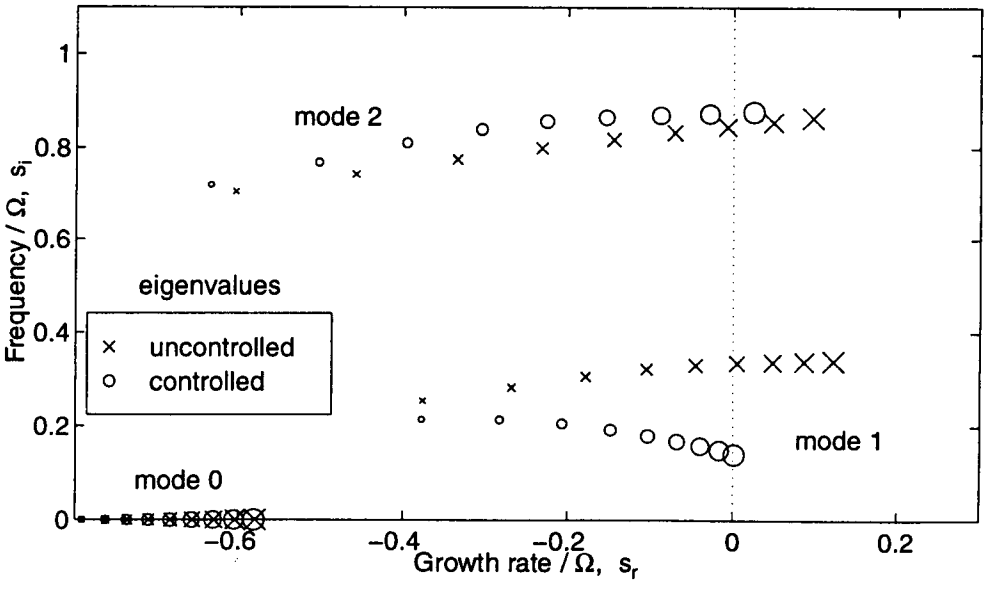


**Figure 4-9:** Root loci of first three stall modes for MIT compressor entering stall with and without control. Controller optimized with $\alpha = 204°$ for a nominal shaft offset of 2% chord. The marker size increases approaching stall, from a flow coefficient of 0.604 to 0.451.

and the stall point. The effectiveness of the constant gain controller is described in this section in terms of the increased range of stable operation.

The constant gain control method described in Section 4.3 consistently stabilized the most unstable modes, which decreased the stalling flow coefficient. The optimized stall point for each baseline compressor configuration, with and without control, is shown in Figures 4-10 and 4-11. The dashed lines indicate the extensions of the overall pressure rise characteristics that can be stably accessed.

The effectiveness of the control for the six compressor configurations is quantified in Table 4.2. For the cases using nominally offset rotor shafts, comparisons were not made between the stall points with and without control in nonuniform flow. Instead, differences were measured between the stall point with control in the nonuniform flow, and the uncontrolled stall point *with a centered rotor shaft.* This comparison was a better indication of the abilities of rotor shaft actuation with an off-centered rotor. The uncontrolled compressor would not purposely operate with an off-centered rotor shaft; the shaft would be offset only when rotating stall waves are detected.

**Table 4.2:** Effect of optimized controller on stability margin of NASA and MIT compressors.

| Configuration | | Decrease in $W_{\text{stall}}$ | Increase in $W_{\text{design}} - W_{\text{stall}}$ | Decrease in $\Psi_{\text{peak}} - \Psi_{\text{stall}}$ |
|---|---|---|---|---|
| NASA | 0% (centered) | 0.86% | 7.6% | 0.1% |
| | 0.228% | 0.94% | 8.3% | 0.3% |
| | 0.455% | 1.2% | 11% | 1% |
| MIT | 0% (centered) | 2.7% | 13% | 0.2% |
| | 1% | 4.7% | 22% | 1% |
| | 2% | 7.2% | 34% | 4% |

Three figures of merit are used in Table 4.2 to assess control effectiveness. The absolute change to the stall point is listed in the first column. Changes of over one percent have been considered significant in previous active control experiments for both compressors [33, 78]. The minimal decrease in the stalling flow coefficient for the NASA compressor of nearly 0.9% is favorable for the proposed magnetic bearing control experiments. A better indication of control effectiveness is the increase in stall margin, listed in the second column. Here, the stall margin is defined as the difference between the flow coefficients at design and stall.

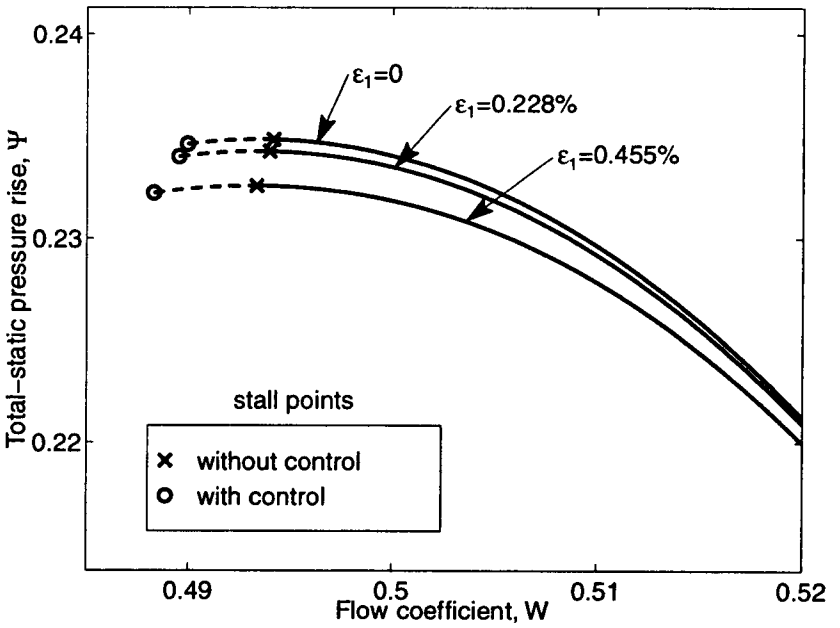


**Figure 4-10:** Extension of stable pressure rise characteristics (dashed lines) for the NASA compressor at three nominal rotor shaft positions.

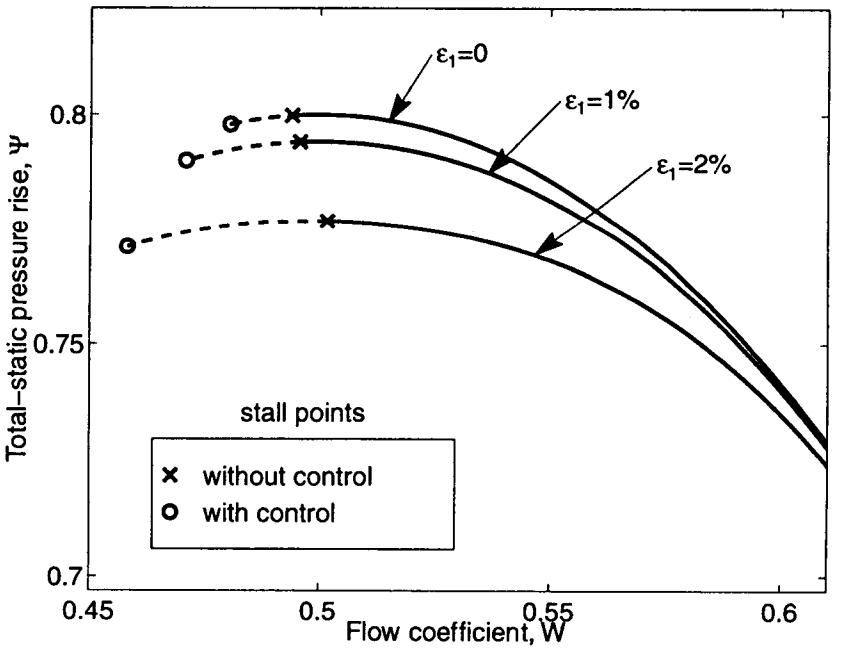


**Figure 4-11:** Extension of stable pressure rise characteristics (dashed lines) for the MIT compressor at three nominal rotor shaft positions.

The increase in the stall margin is at least 7% for the NASA compressor model, and twice that value for the MIT compressor.

The values in Table 4.2 confirm that a significant flow range extension was obtained for control with an initially offset rotor. The penalty for operating with a nonuniform background flow was evident in the loss of overall pressure rise. The difference between the stalling pressure rise with control for an offset shaft and the peak pressure rise in uniform flow is listed in the third column of the table. These values are large enough that sustained operation with nonuniform flow would not be desired. However, pressure drops of 1–4% are much smaller than that typically encountered in full scale rotating stall. The increased stable operating range for control with an off-centered shaft can be used to suppress stall during low mass flow transients that would otherwise have led to rotating stall. Therefore, the accompanying temporary loss in pressure is minor compared to the benefits of the substantially increased stall margin.

Note that the amount of range extension in Table 4.2 may underestimate the effectiveness of the control method in the Stage-37 experiment. The present studies show that the range extension is not limited by the controllability of the first-harmonic mode, but rather the flow coefficient where the next mode becomes unstable. This point is set by the shape of the positively-sloped region of the pressure-rise characteristic and the value of the unsteady loss parameter, $\tau$, both of which can only be accurately determined *after* actively controlling the compressor. For the present Stage-37 model, the positively-sloped part of the characteristic was only based on extrapolations of the stable region, and the parameter $\tau$ was chosen to match typical compressor values. Weigl's active control experiments on a similar compressor, Stage-35 [79], showed that the stall points of the first and second modes differed by 3% in flow coefficient — a value three times larger than shown in Table 4.2. This amount may provide a better estimate of the range extension actually possible with the magnetic bearing experiments.

In summary, rotor shaft actuation was an effective control method to actively stabilize compressors that stalled from the first harmonic mode. Surge, and higher order modes could be controlled to a lesser degree only when the background flow was nonuniform. Inducing a nonuniform flow with an off-centered shaft provided sufficient control authority over the

higher order modes to temporarily increase the stall margin, accompanied by a minor loss in performance. The simulated stable range extensions indicated that the proposed magnetic bearing control experiments for Stage-37 will demonstrate measurable range improvements from active stall control.

# Three-Dimensional Rotating Stall Inception

# Chapter 5

# 3-D Stall Predictions Using an Actuator Plane Model

The simplest compressor model that predicts three-dimensional rotating stall is an actuator disk. In this chapter, an actuator plane model of an unwrapped, rectilinear compressor cascade was developed, similar to those in [83, 5]. This model was applied first to uniform flow to characterize the fundamental differences between two-dimensional and higher-order 3-D modes. Studies were then performed with spanwise variation in the pressure rise characteristic slope and the background velocity field. Results from these studies, while somewhat simplistic, are presented here because this basic model allows insight which is helpful for interpreting the behavior seen with the complex, body force compressor model in Chapter 7.

The most important result was that spanwise nonuniformity of the background flow and the pressure rise characteristic slope changed the mode shapes and destabilized the compression system compared to compressors with uniform properties. The most unstable mode in these studies always corresponded to the mode from two-dimensional stability analyses; higher-order three-dimensional modes were more stable. Therefore 2-D stall predictions would correctly choose the critical stall modes, but would over-predict the stability of compressors with spanwise variations in performance.

In the second half of this chapter, the ability of the actuator plane model to predict the stability of 3-D modes was shown to be limited by two unmodeled effects. Actuator *duct* blade row models were used to demonstrate that redistribution of the disturbance flow

within blade passages stabilized three-dimensional modes. Also proven important were the chord-wise distribution of work and loss through the blade row, factors which have been ignored by past actuator disk and two-dimensional stall theories. The sensitivity of three-dimensional stall inception on such blade row details was used to motivate the development of the *generalized body force* compressor model in Chapter 6.

## 5.1 Three-dimensional Actuator Plane Model

The three-dimensional actuator plane model was essentially developed by extending the two-dimensional model in Section 2.1 into the spanwise direction. The fundamental concepts remained the same, meaning the compressor was approximated by a surface of discontinuity separating two ducts of inviscid, incompressible flow. Only the differences specific to the three-dimensional model will be described here.

The scope of the analysis was to examine 3-D rotating stall, not surge, so the compression system model included only the actuator plane and the adjoining constant area, rectilinear ducts (Figure 5-1). Although a Cartesian co-ordinate system was used, the spanwise, pitchwise and axial directions were represented by $\tilde{r}$, $\tilde{\theta}$ and $\tilde{z}$, where $(\tilde{})$ represents a dimensional quantity. Corresponding velocities were denoted by $\tilde{U}$, $\tilde{V}$ and $\tilde{W}$, respectively. Periodicity was enforced in the tangential direction after every $\tilde{\theta} = 2\pi\tilde{r}_t$ units, where $r_t$ was the outer casing spanwise co-ordinate. Variables were nondimensionalized by combinations of $\tilde{r}_t$, the rotor frequency $\tilde{\Omega}$, and the density $\tilde{\rho}$. Therefore the non-dimensional spanwise coordinate measured within $r \in [r_h, 1]$ and the tangential coordinate spanned $\theta \in [0, 2\pi]$. The actuator plane was assumed to be located at $z = 0$.

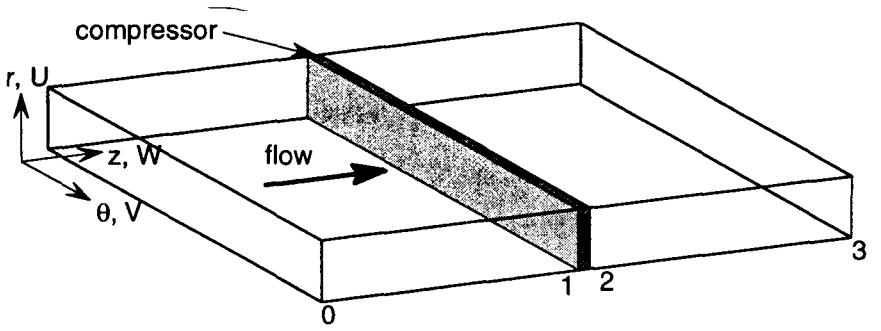


**Figure 5-1:** Illustration of three-dimensional actuator plane compressor model.

The effects of circumferential and radial flow nonuniformities on compressor stall were intended to be analyzed separately in this thesis. Therefore, for all analyses of three-dimensional modes, the steady background flow fields were assumed to be axisymmetric; nonuniformities existed only in the spanwise and axial directions, caused either by an imposed inlet flow distortion or compressor performance nonuniformities. Methods used for calculating the steady background and unsteady disturbance flow through the compression system are developed in Appendix E.

Far-field boundary conditions for the compression system were prescribed at stations (0) and (3) (as labeled on Figure 5-1). Unsteady flow perturbations were assumed to be generated only by the compressor, so the disturbance amplitudes at (0) were identically zero. The downstream duct was assumed to end at a plenum, implying that the pressure fluctuations vanished at station (3).

The actuator plane specified conditions across the compressor to relate the upstream and downstream flow perturbations. Four matching conditions were applied at every spanwise position:

1. continuous spanwise velocity: $u_1 = u_2$;
2. continuous axial velocity: $w_1 = w_2$;
3. specified exit flow angle: $v_2 = w_2 \tan\beta_2$;
4. pressure jump prescribed by the quasi-steady pressure rise characteristic plus correction terms to account for axial flow acceleration and unsteady losses:

$$\begin{aligned} p_2 - p_{t1} &= \frac{d\Psi_i}{dW} w - l_R - l_S - \lambda \frac{\partial w}{\partial \theta} - \mu \frac{\partial w}{\partial t} \\ (1 + \tau_R \frac{\partial}{\partial t} + \tau_R \frac{\partial}{\partial \theta})\, l_R &= \sigma (\frac{d\Psi_i}{dW} - \frac{d\Psi}{dW}) w \\ (1 + \tau_S \frac{\partial}{\partial t})\, l_S &= (1 - \sigma)(\frac{d\Psi_i}{dW} - \frac{d\Psi}{dW}) w \ . \end{aligned} \tag{5.1}$$

Except for the addition of item 1, these conditions are identical to those for the two-dimensional actuator disk model with no tip clearance asymmetry (equation B.35). Nonuniform compressor properties were accounted for with spanwise variations of $\Psi$, $\beta_2$, $\mu, \lambda$, $\tau_R$, $\tau_S$ and $\sigma$.

## 5.2 Instability of Compressors with Uniform Parameters

Identifying three-dimensional rotating stall modes was easiest for compressors with uniform properties in a uniform background flow. The background flow was assumed to be only axial, so $\bar{U} = \bar{V} = \beta_2 = 0$, and $\bar{W}$ was uniform throughout the ducts. For this case, the modes were described by distinct spanwise and circumferential harmonics.

Following the detailed solution process in Appendix E.1.1, general rotating stall disturbances at the compressor face could be written as

$$\begin{pmatrix} u \\ v \\ w \\ p \end{pmatrix} = \mathcal{R}e\{ \sum_{n=-\infty}^{\infty} \sum_{j=0}^{\infty} \begin{pmatrix} \hat{u}_{n,j} \sin(\pi j \frac{r-r_h}{1-r_h}) \\ \hat{v}_{n,j} \cos(\pi j \frac{r-r_h}{1-r_h}) \\ \hat{w}_{n,j} \cos(\pi j \frac{r-r_h}{1-r_h}) \\ \hat{p}_{n,j} \cos(\pi j \frac{r-r_h}{1-r_h}) \end{pmatrix} e^{in\theta} e^{i\omega_{n,j} t} \} \tag{5.2}$$

for complex constants $\hat{u}_{n,j}$, $\hat{v}_{n,j}$, $\hat{w}_{n,j}$, $\hat{p}_{n,j}$. Every term in the summation represented an individual mode of the compression system, each with unique temporal behavior given by the eigenvalues, $\omega_{n,j}$. The mode shape was sinusoidal in both the circumferential and spanwise directions, with $n$ and $j/2$ wavelengths respectively. For each harmonic $n$, the mode for $j = 0$ was uniform across the span, and therefore two-dimensional. However, there also existed an infinite number of three-dimensional modes corresponding to $j \geq 1$.

Example mode shapes at the compressor face for $n = 1, 2$ and $j = 0, 1, 2$ are shown in Figure 5-2. The vertical axes plot the normalized pressure or axial velocity disturbance frozen at one time instant. The three-dimensional modes were denoted by the $(n, j)$ notation in Table 5.1, where $n$ is the circumferential harmonic, and $j$ is the spanwise mode number. The class of $(n, 0)$ modes were the two-dimensional modes, with the specific case of $(0, 0)$ representing surge. The class of $(n, j \geq 1)$ modes represented three-dimensional modes, with $(0, j)$ referring to axisymmetric "ring" stall.

Three-dimensional modes were found to be more stable than the corresponding two-dimensional modes for the same harmonic $n$. Figure 5-3 shows the growth rate and phase speed of some two- and three-dimensional rotating stall modes in a 0.5 hub-to-tip ratio compressor. For $n = 1$, the most unstable mode was (1,0), followed by (1,1), (1,2), and so on for increasing $j$. The group of modes for each $n$ followed this trend, but each

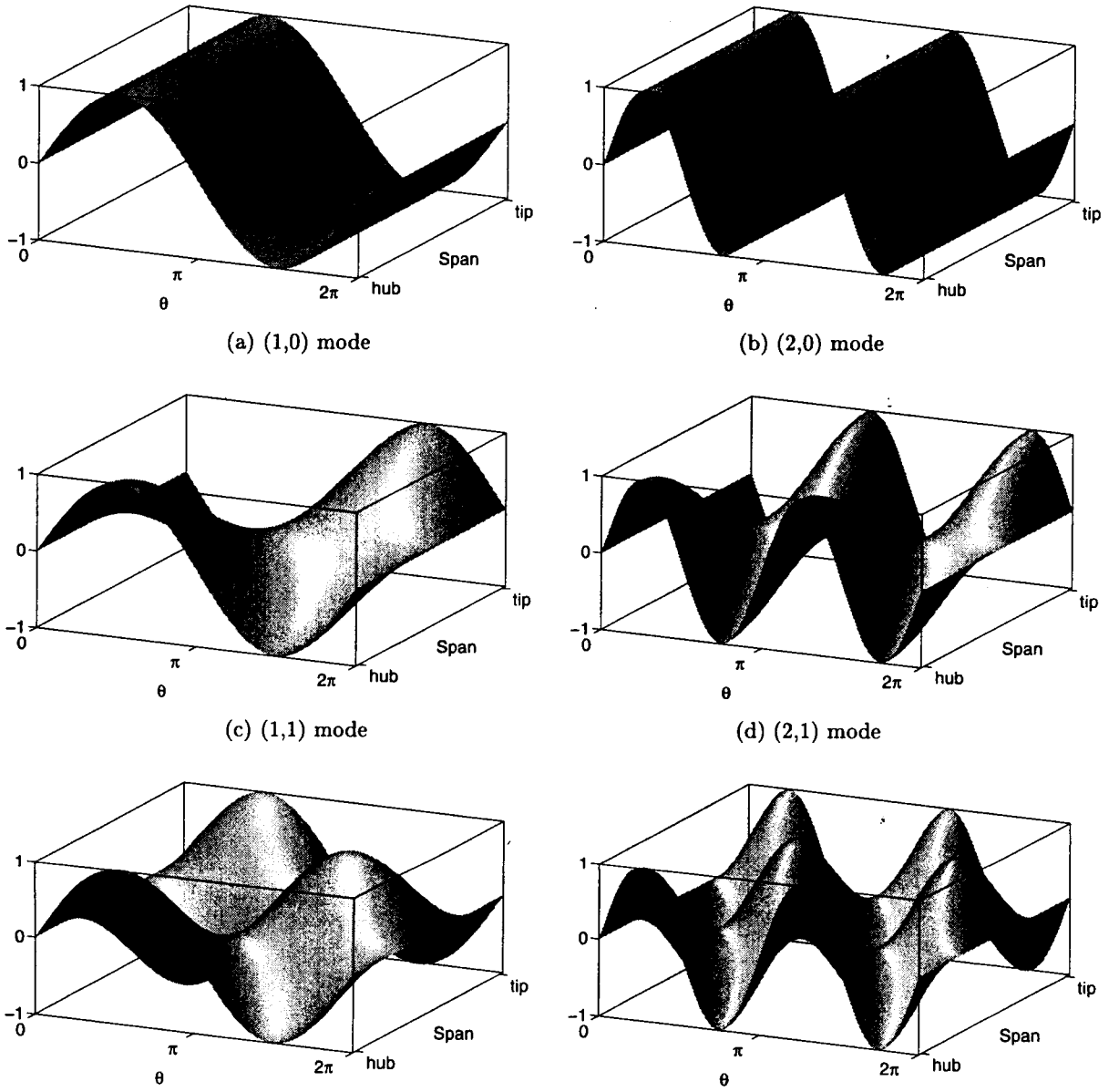


(a) (1,0) mode

(b) (2,0) mode

(c) (1,1) mode

(d) (2,1) mode

(e) (1,2) mode

(f) (2,2) mode

**Figure 5-2:** $(n, j)$ mode shapes for $w(r, \theta)$ or $p(r, \theta)$ perturbations in uniform background flow in a rectilinear duct. Amplitudes have been normalized by the maximum amplitude.

**Table 5.1:** Table of $(n, j)$ stalling modes.

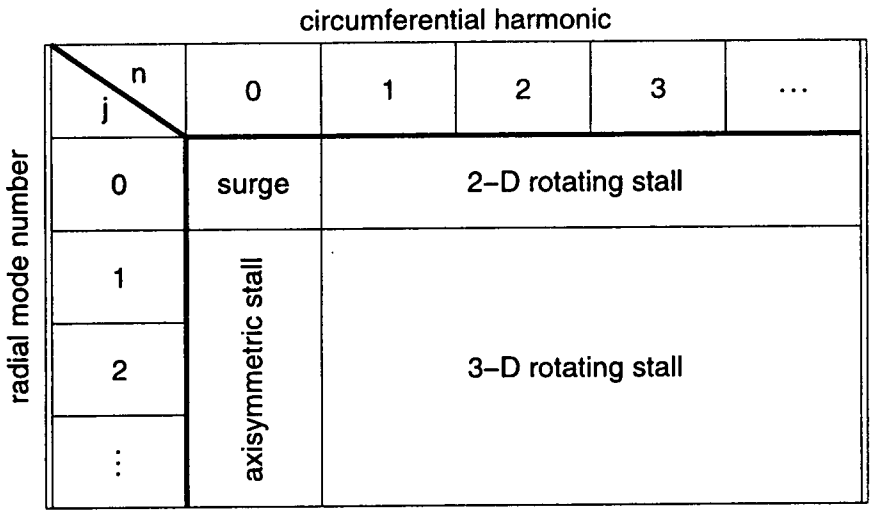


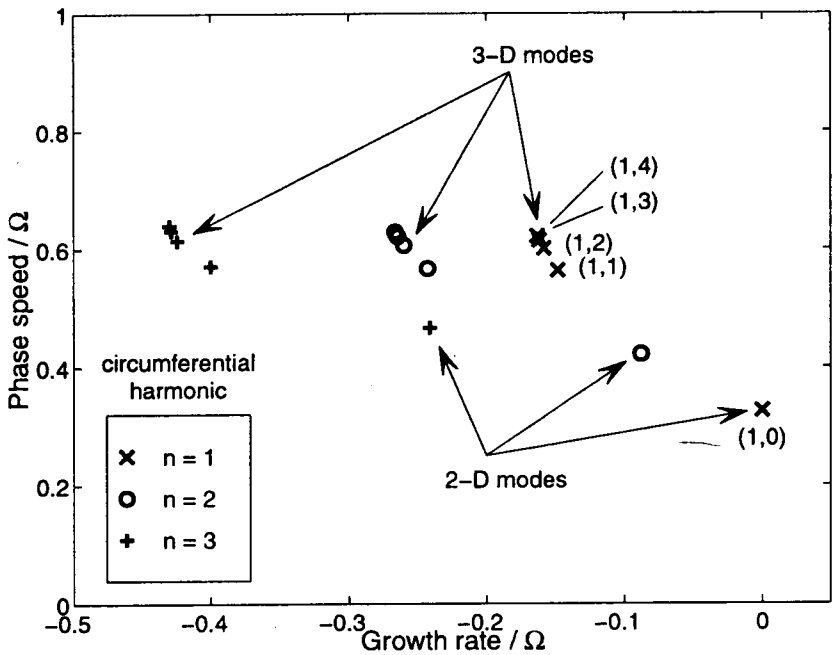


**Figure 5-3:** Eigenvalues for lowest order two- and three-dimensional modes in uniform background flow. Results from rectilinear actuator plane analysis using $r_h = 0.5$, $\bar{W} = 0.43$, $\mu = 1.22$, $\lambda = 0.64$, $\beta_2 = 0$, $\bar{\tau} = 1.5$, $\sigma = 0.75$, $c_z = 0.1$, $\frac{d\Psi}{dW} = 0.2$, $\frac{d\Psi_i}{dW} = -2.54$.

group for increasing $n$ was further stabilized due to the effects of unsteady losses. Three-dimensional modes also propagated faster than two-dimensional ones because they had less inertia. The potential decay rate away from the compressor for the $(n,j)$ mode scaled as $exp\left\{-z\sqrt{n^2+j^2\pi^2/(1-r_h)^2}\right\}$; therefore the modes extended less into the upstream and downstream ducts as $j$ increased.

The relative importance of the $(n,j)$ modes could be seen from the neutral stability points for a three-stage compressor characteristic (Haynes [33]) in Figure 5-4. The three-dimensional modes were strongly damped; the stalling flow coefficient of the (1,1) mode was 5% lower than for the (1,0) mode.

Trends concerning the stability of three-dimensional modes could be obtained analytically by assuming the losses were quasi-steady. Setting $\bar{\tau} = 0$ in equation (E.22), the eigenvalues could then be expressed as:

$$\omega_{n,j} = -\frac{n\lambda + i\left(\frac{d\Psi}{d\bar{W}} - \bar{W}\frac{k^2}{n^2+k^2}\right)}{\mu + \frac{2}{\sqrt{n^2+k^2}}}, \tag{5.3}$$

where $k = j\pi/(1-r_h)$. Therefore, the stability point of the $(n,j)$ mode corresponded to the operating point with the following slope:

$$\frac{d\Psi}{d\bar{W}} = \bar{W}\frac{k^2}{n^2+k^2}. \tag{5.4}$$

This relation indicates that three-dimensional modes ($k > 0$) become unstable on the positively-sloped part of the characteristic, compared to two-dimensional modes ($k = 0$) which stall at the characteristic peak. The difference between the instability points for two- and three-dimensional modes would be reduced for two cases. Figure 5-5 plots the (1,0) and (1,1) eigenvalues for compressor configurations with different hub-to-tip ratios and mean axial velocity operating at the characteristic peak. The 2-D mode was always neutrally stable, but the 3-D mode was most unstable for compressors with lower hub-to-tip ratios (hence larger $k$), or those operating at lower flow coefficients, $\bar{W}$.

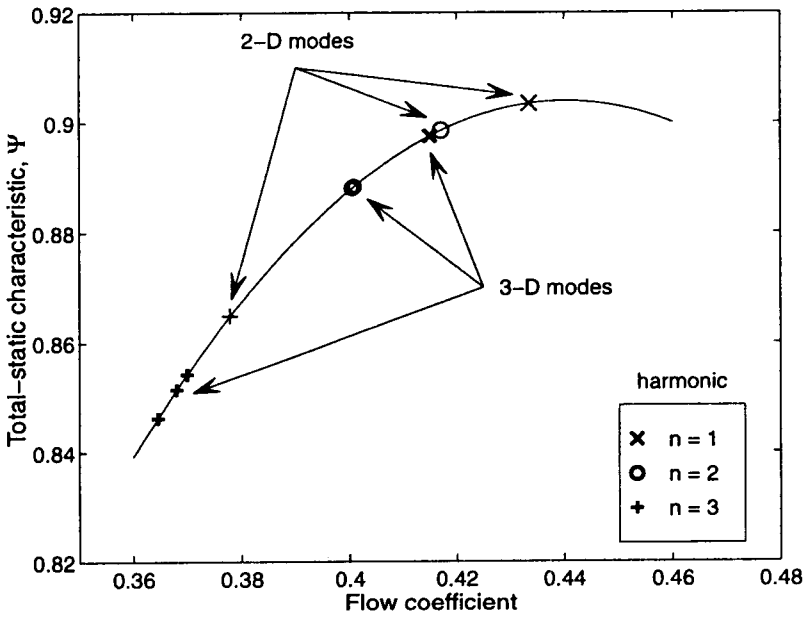


(a) Stall points indicated on the total-static pressure rise characteristic

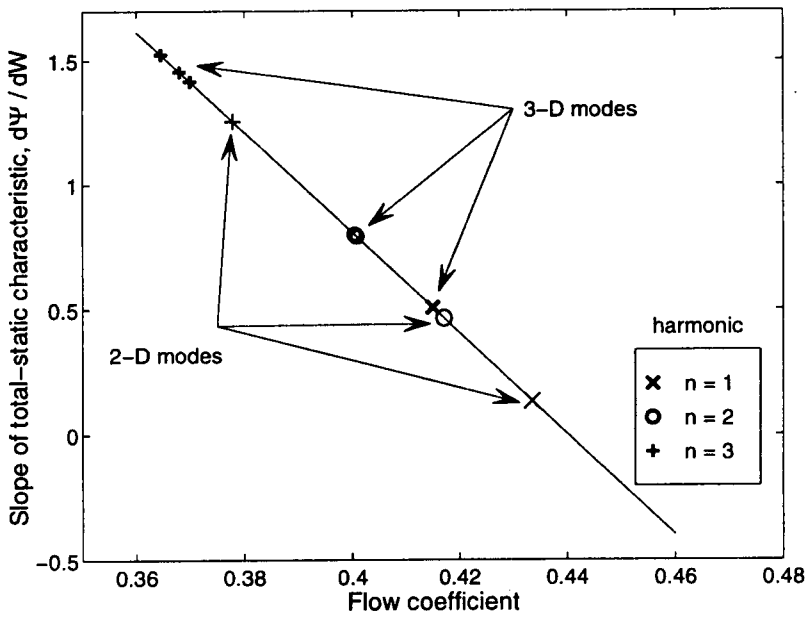


(b) Stall points indicated on the slope of total-static pressure rise characteristic

**Figure 5-4:** Stall points of $(n, j)$ modes indicated on the multistage pressure rise characteristic from Haynes [33]. Results for $n \in \{1 \ldots 3\}$ and $j \in \{0 \ldots 3\}$, using compressor parameters listed in Figure 5-3.

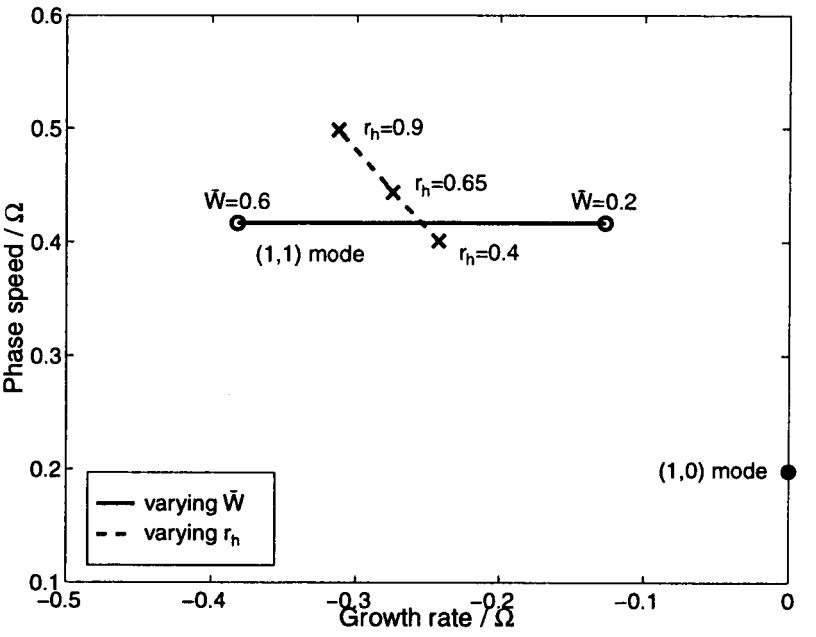


**Figure 5-5:** Locus of (1,0) and (1,1) eigenvalues for varying $\bar{W}$ and $r_h$ in uniform background flow at the characteristic peak (from equation (5.3) using $\frac{d\Psi}{dW} = 0, \mu = 1.22, \lambda = 0.64$). Results for varying $\bar{W}$ use $r_h = 0.5$; results for varying $r_h$ use $\bar{W} = 0.4$.

## 5.3 Instability of Compressors with Nonuniform Characteristic Slope

Two aspects of nonuniformity were independently examined using the actuator plane theory: variations in compressor characteristic slope and background flow field. This section examines spanwise variations of the characteristic slope, since the slope was found in Chapter 3 and previous references [43, 61] to be the most critical parameter determining the stall point of a compressor. Background flow nonuniformities generated by spanwise variation in compressor performance are examined in Section 5.4.

Blade row performance generally varies along the span causing spanwise nonuniformity of the local characteristic, and hence the local characteristic *slope*. To appreciate the magnitude of nonuniformity in a single stage compressor, the total-to-static characteristic slopes were calculated at five spanwise positions for an IGV-rotor combination. These values, shown in Figure 5-6, were determined in Appendix F based on a lossless inlet guide vane followed by a rotor with total pressure loss characteristics obtained from cascade data in [61]. The important feature of Figure 5-6 is that at low flow coefficients, the difference

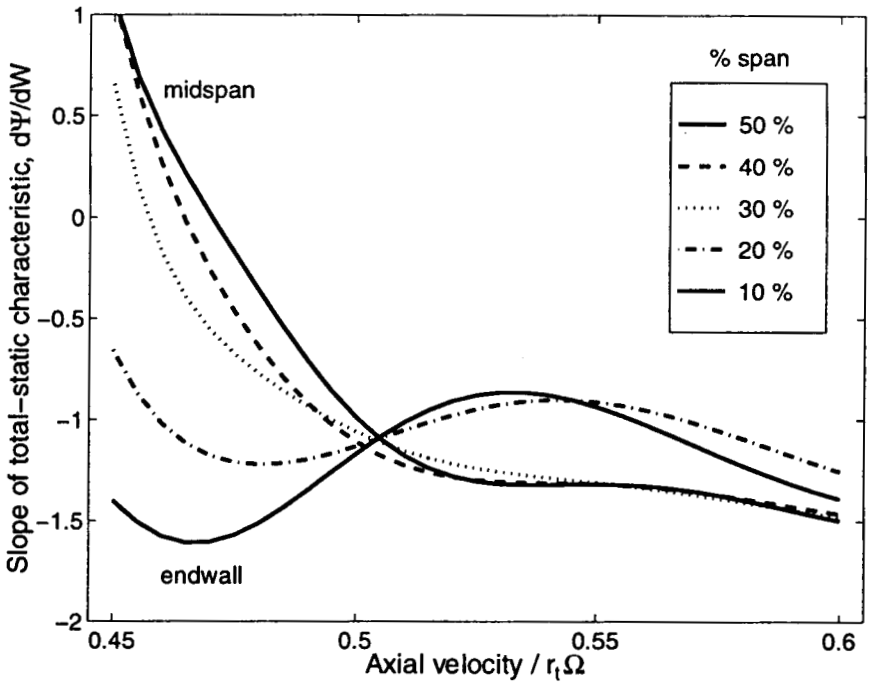


**Figure 5-6:** Spanwise variation of total-static characteristic *slope* for single blade row cascade. Results calculated from cascade data measured by Sasaki and Takata [61].

in slope across the span was between 1 and 2.

The actuator plane model was used to calculate the modes in a uniform background flow for a spanwise nonuniformity in slope. The solution process was similar to that for Section 5.2, except that the value of $d\Psi/dW$ in the pressure matching condition was a function of $r$. An analytical expression for the eigenvalues and mode shapes was not possible because the slope nonuniformity coupled the spanwise harmonics in each mode. The modes were numerically determined by truncating their shape to the first 20 spanwise harmonics, and calculating the solution to the remaining set of matching conditions across the actuator plane (Appendix E.3).

To examine the effect of spanwise slope nonuniformities on instability, three slope distributions were examined: a linear variation, and sinusoidal variations with one full wavelength and one-half wavelength from hub to tip (Figure 5-7). The sinusoidal variations were chosen because they duplicate spanwise mode shapes in uniform flow, and so may have a strong effect in exciting these modes. The two parameters that determine each spanwise slope variation are the mean (spanwise-averaged) slope, $\overline{d\Psi/dW}$, and the maximum difference in slope, $\Delta\, d\Psi/dW$ (defined as positive if the slope is highest at the tip).

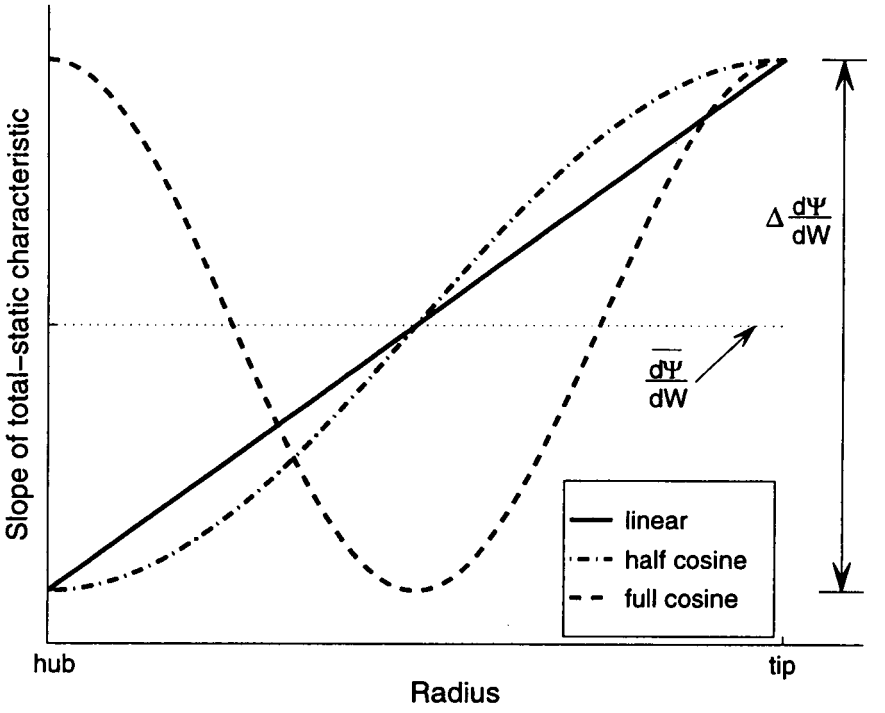


**Figure 5-7:** Illustration of three types of spanwise profiles of characteristic slope used in the actuator plane studies. Depicted are the mean ($\overline{\frac{d\Psi}{dW}}$) and the maximum variation ($\Delta\frac{d\Psi}{dW}$).

### Effect on mode shape

Spanwise slope variations caused the mode shapes to have higher amplitudes in regions of higher characteristic slope. Figure 5-8 shows the (1,0) and (1,1) mode envelopes for a half-wavelength sinusoidal slope variation with $\Delta\, d\Psi/dW = 0.4$. The (1,0) mode had a maximum amplitude at the hub 60% as large as at the tip. Similarly, the (1,1) mode amplitude at the hub was only 24% of the magnitude at the tip. The distortion was significant enough that the amplitude of the (1,1) mode no longer had a distinct minimum at the mid-span position, as compared to the mode shape in uniform flow (also indicated on the figure).

The $r$–$\theta$ mode shapes for the (1,0) and (1,1) pressure perturbations at the compressor face are shown in Figure 5-9. Comparing these shapes to those in a compressor with uniform slope distribution (in Figure 5-2) it can be seen that the slope variation not only affected the local amplitude of the mode, but also the relative phase of the perturbation at each spanwise location. Amplitude and phase are important in stall management for detecting stall precursors and for actively controlling the mode shape at one location based on mea-

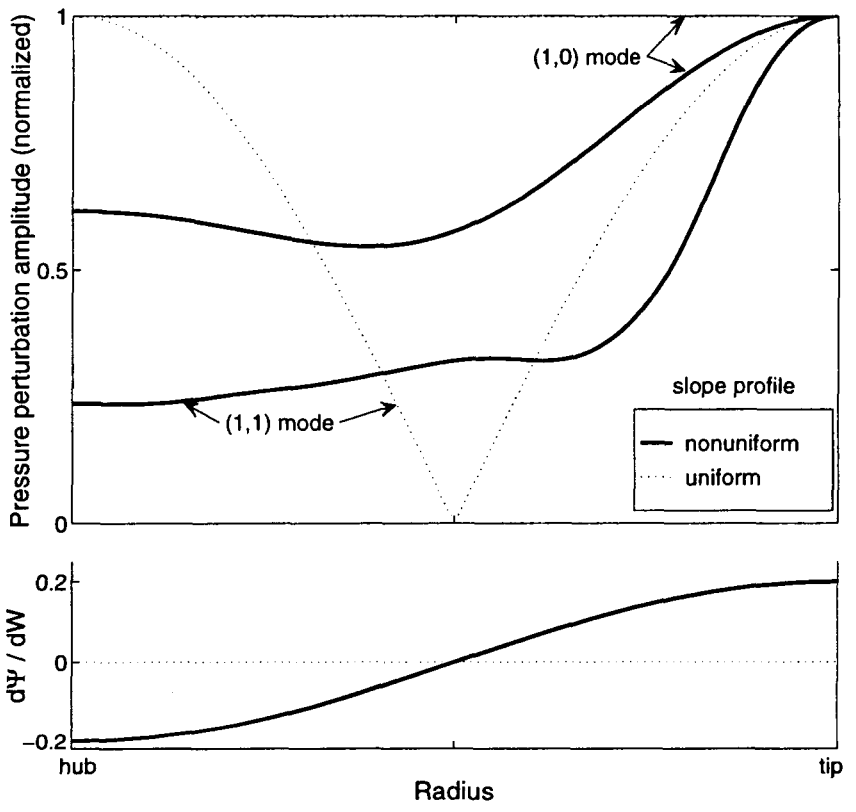


**Figure 5-8:** Amplitude of compressor exit pressure perturbations, $||\delta p||$, for a compressor with the indicated spanwise variation of characteristic slope. Results for (1,0) and (1,1) modes using rectilinear actuator plane analysis with $r_h = 0.5$, $\bar{W} = 0.5$, $\mu = 1.6$, $\lambda = 0.8$, $\beta_2 = 0$, $\bar{\tau} = 0$, $\overline{\frac{d\Psi}{dW}} = 0$, $\Delta\frac{d\Psi}{dW} = 0.4$.

surements at another. For example, stall detection would be best achieved at the tip for the compressor in Figure 5-8. Also, from Figure 5-9a, the (1,0) pressure perturbation at the tip lagged the hub by 80 degrees. One could speculate that two-dimensional control schemes that actuate near the hub based on measurements at the tip may be flawed. Assessing this statement must be postponed to future three-dimensional flow analyses that include active control terms.

### Effect on stability

Two-dimensional stability analyses based on the mean slope would under-predict the growth rate of the modes that occur with slope nonuniformity. Figure 5-10 shows the (1,0), (1,1) and (1,2) eigenvalues calculated with increasing variation in slope, holding the mean slope equal to zero. Slope nonuniformity increased the modal propagation rate, and shifted the eigenvalues towards the right-half plane, indicating a loss in stability. The cause of the higher

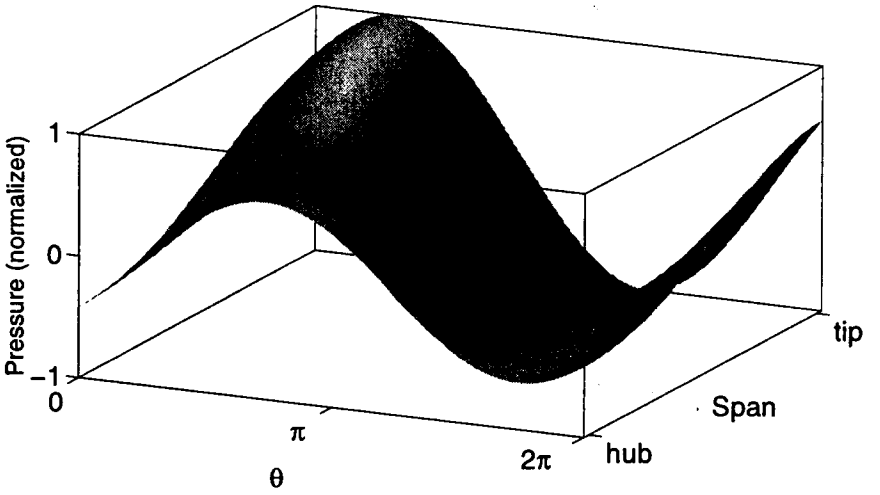


(a) (1,0) mode

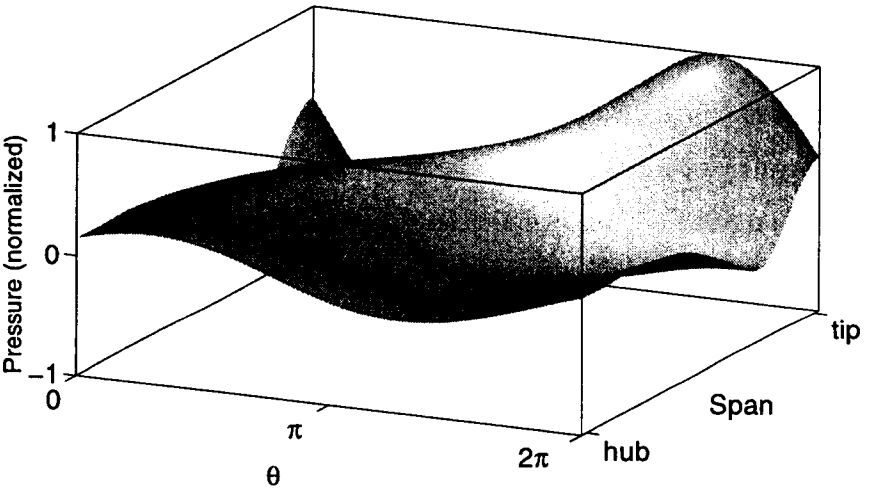


(b) (1,1) mode

**Figure 5-9:** Compressor exit pressure perturbations, $p(r, \theta)$, for (1,0) and (1,1) modes with spanwise variation of $d\Psi/dW$. Values of compressor parameters listed in Figure 5-8. Mode shapes were normalized to have maximum amplitude of 1.

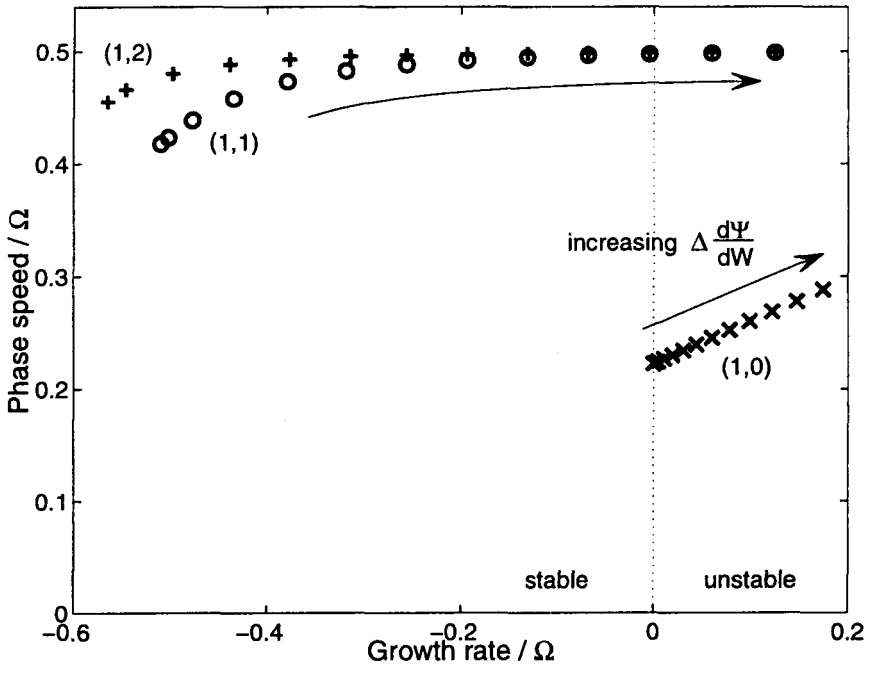


**Figure 5-10:** Loci of eigenvalues for (1,0), (1,1) and (1,2) modes with increasing spanwise variation in characteristic slope. Linear slope profiles were used with $\Delta\frac{d\Psi}{dW}$ increasing from 0 to 1.2 and $\overline{\frac{d\Psi}{dW}} = 0$. Results for rectilinear actuator plane analysis with $r_h = 0.5$, $\bar{W} = 0.5$, $\mu = 1.6$, $\lambda = 0.8$, $\beta_2 = 0$, $\bar{\tau} = 0$.

phase speed was not clear, but the loss in stability was due to the same principle found for tip clearance asymmetry in Section 3.4.3: the stall point was set by the average of the slope variation *weighted* by the mode amplitude. With spanwise compressor nonuniformity, the mode shape was largest in regions where the slope was highest. The weighted slope average was thus higher than the mean, $\overline{d\Psi/dW}$, leading to higher growth rates. The weighted slope criteria for spanwise flow nonuniformities is addressed in detail in Section 7.2.3.

Figure 5-11 shows the mean value of slope at neutral stability for different spanwise slope variations. The growth rates of all modes were increased by slope nonuniformity, but the (1,0) mode was always the most critical mode leading to stall. At neutral stability, the mean slope at stall was between -0.1 and -0.5 for $\Delta\frac{d\Psi}{dW}$ between 1 and 2. These values represented an increase in stalling flow coefficient of 1% to 5.5% for the multi-stage compressor characteristic in Figure 5-4. As expected, the highest loss in stability was induced by slope variations that resembled the shape of the natural modes. In particular, the mean slope at stall for a half-wavelength sinusoidal slope variation was 1.5 times that for a linear slope profile.

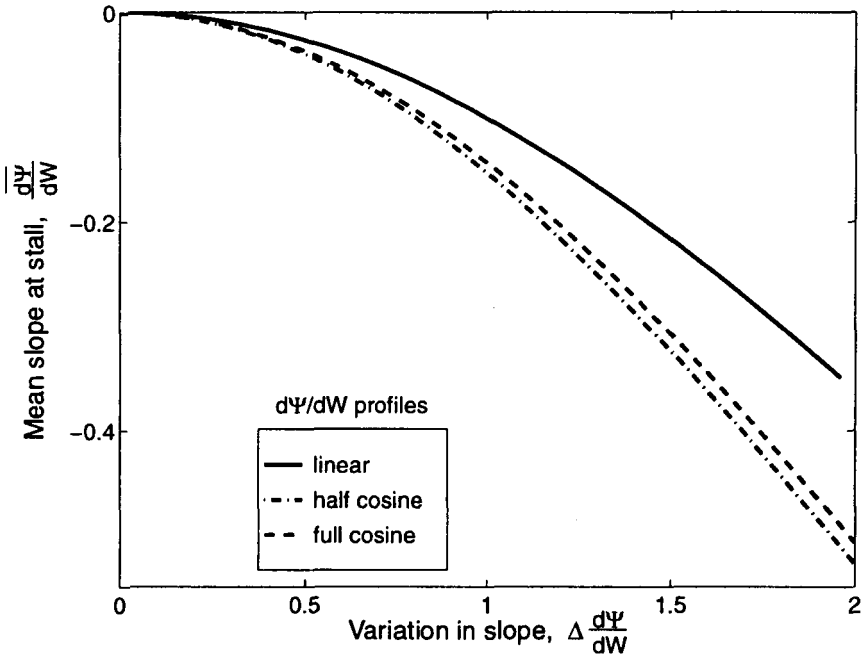


**Figure 5-11:** Mean slope at neutral stability for compressors with three types of spanwise slope variations. Results for rectilinear actuator plane analyses with $r_h = 0.5$, $\bar{W} = 0.5$, $\mu = 1.6$, $\lambda = 0.8$, $\beta_2 = 0$, $\bar{\tau} = 0$.

## Notation

The $(n, j)$ notation was still used to identify a mode in nonuniform flow, even though the mode shape no longer consisted of a unique sinusoid with $j/2$ wavelengths along the span. There was never a problem with identifying the $(n, 0)$ modes for all studies in this thesis. For each value of $n$, one mode always stood alone with a relatively low propagation rate (near 20 to 40% of rotor speed), and which contained the least mode shape nonuniformity along $r$. These were referred to as the $(n, 0)$, or *quasi-2D modes* since they represented the class of modes that are most closely predicted by two-dimensional analyses. For the remaining *higher-order 3-D modes*, the notation was adopted to rank these modes in $j$ according to their order of becoming unstable. With this system, the $(n, j)$ notation in nonuniform flow is consistent with the notation developed originally for uniform flow.

## 5.4 Instability of Compressors with Nonuniform Background Flow

The steady velocity field in a compressor is often characterized by spanwise nonuniformities, especially at off-design conditions. Flow field perturbations behave differently in background flows with mean vorticity compared to uniform flow [14]. In uniform flow, the perturbations can be decomposed into a purely convected disturbance that is decoupled from pressure fluctuations, and potential disturbances that are directly related to pressure fluctuations. However, in background flows with velocity gradients, the pressure disturbances are governed by an inhomogeneous wave equation with a source term that convects with the mean flow (Goldstein [20]). Thus, pressure disturbances in nonuniform flow will generally not decay downstream and the location of the downstream plenum boundary condition may affect stability.

The actuator plane compressor model was used to examine the effects of nonuniform background flow and the location of the downstream boundary condition on stability. Appendix E.4 describes the numerical method used to calculate the modes in nonuniform flow. The background flow was assumed uniform far upstream, but redistributed through the compressor ducts to a linear spanwise profile, simulating the effect of a steady pressure rise characteristic nonuniformity. The magnitude of flow nonuniformity was measured as the difference between the maximum and minimum axial velocity as a percentage of the average velocity. Figure 5-12 shows $W(r,z)$ and $U(r,z)$ for a 50% linear variation in downstream axial velocity, which represents a large variation in a practical situation.[1] For all the following computations, the slope of the characteristic was held constant along the span in order to isolate the effects of steady flow nonuniformity from variations in slope.

Background velocity nonuniformity coupled the spanwise harmonics in each mode, but the impact on mode shape was smaller than for typical variations in slope. Figure 5-13 shows the normalized mode shapes corresponding to the 50% variation in downstream axial velocity. The amplitudes of the (1,0) and (1,1) modes at the hub were reduced by 23% and 50% of the tip amplitude, which was one-half of the effect seen for the slope variation in

[1] Based on a survey of experimental data with uniform inlet flow [65, 37, 59, 54, 7], the average spanwise variation of axial velocity within the core 80% span of compressors was approximately 25% to 50% of the mean velocity.

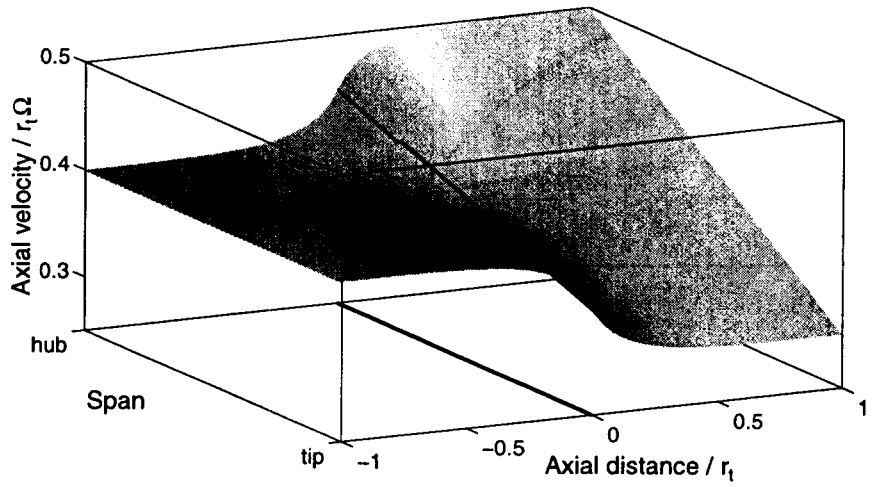


(a) Axial velocity

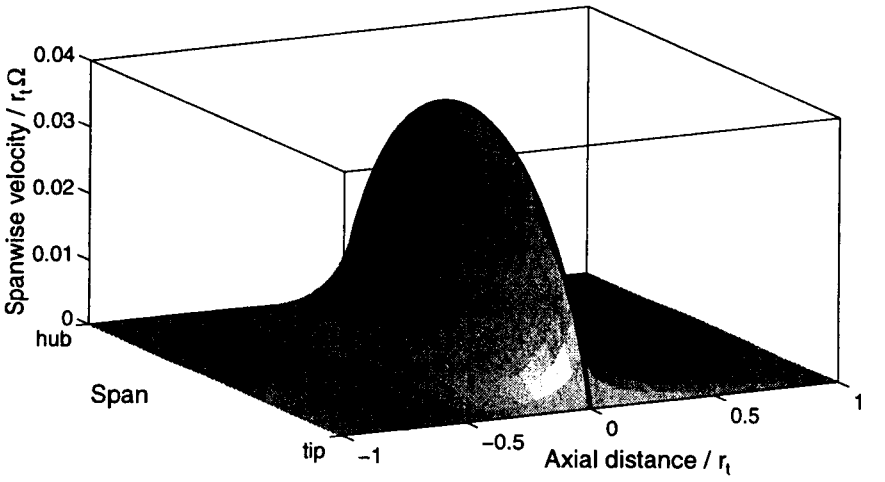


(b) Spanwise velocity

**Figure 5-12:** Variation of background velocity field through compressor duct corresponding to 50% linear variation in far-downstream axial velocity. Compressor actuator plane is indicated at the zero axial position. Results for rectilinear duct with $r_h = 0.5$.

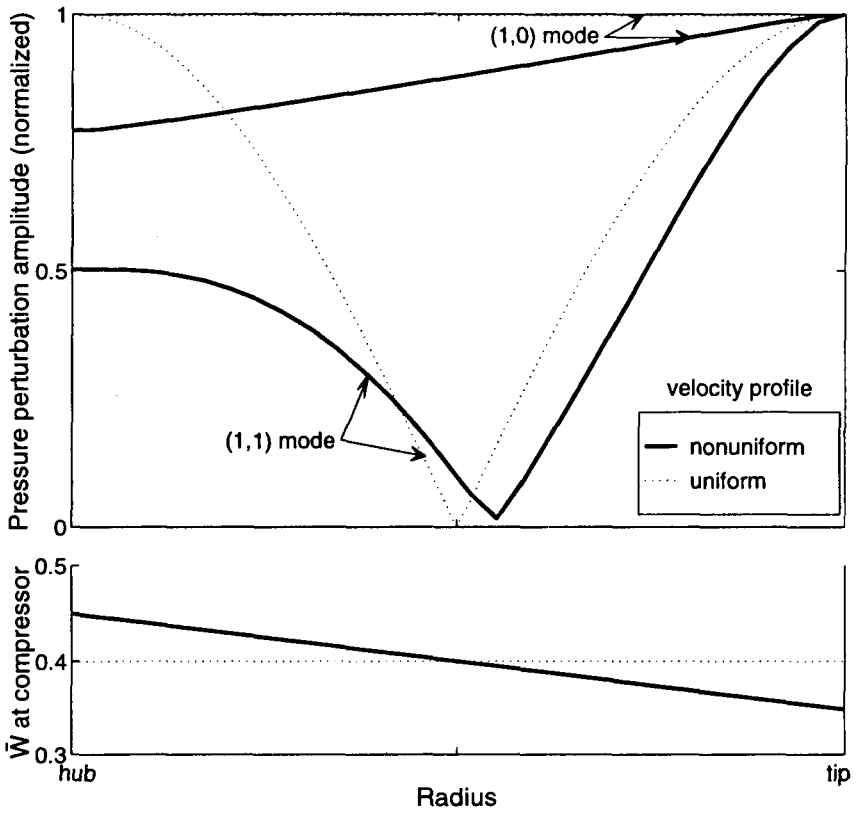


**Figure 5-13:** Amplitude of compressor exit pressure perturbations, $||\delta p||$, for the above background axial velocity variation at compressor plane (corresponding to 50% linear variation in far-downstream axial velocity). Results for (1,0) and (1,1) modes using $r_h = 0.5$, $\mu = 1.22$, $\lambda = 0.64$, $\beta_2 = 0$, $\bar{\tau} = 0$, $\frac{d\Psi}{dW} = 0$.

Figure 5-9. Also, the (1,1) mode qualitatively resembled the shape in uniform flow, in that there was one distinct node of zero amplitude near the midspan. This behavior was not seen in the equivalent mode with the slope variation.

Spanwise nonuniformity in the background flow destabilized the modes compared to modes in uniform flow (Figure 5-14), but again this effect was much smaller than the effect for slope variations. Axial velocity nonuniformities of 100% of the mean velocity affected the growth rates of the (1,0) and (1,2) modes one-twentieth as much as for a spanwise slope variation of 1; the effect of velocity nonuniformity on the (1,1) mode compared to the slope variation was nine times less.

Figure 5-15 shows the effect of velocity nonuniformity on the stall point of the compressor, measured in terms of the total-to-static characteristic slope at stall. A variation of background axial velocity equal to 100% of the mean caused the compressor to stall at a negative slope value six times smaller than that caused by a spanwise slope nonuniformity

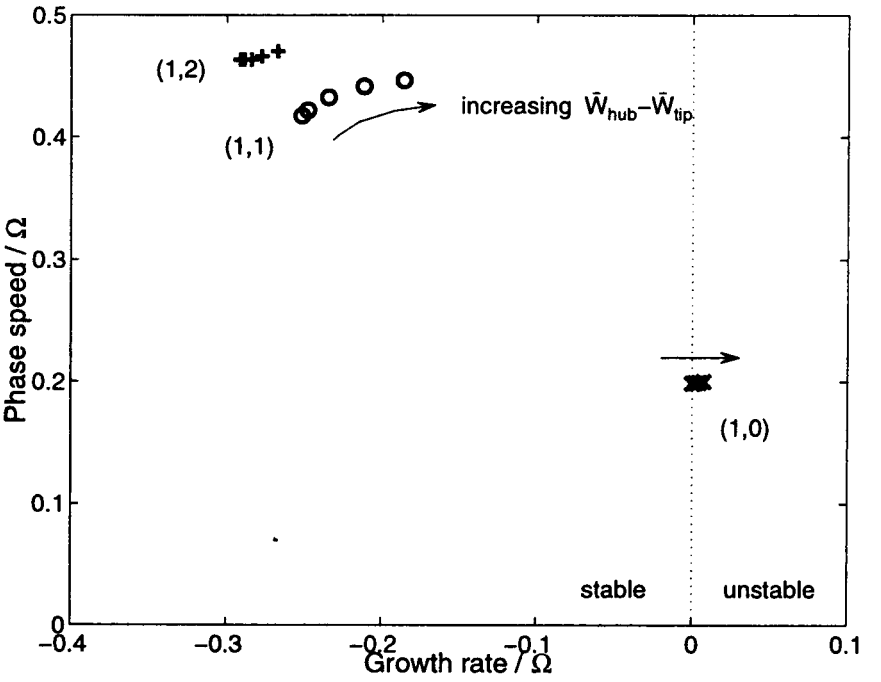


**Figure 5-14:** Loci of eigenvalues for (1,0), (1,1) and (1,2) modes with increasing spanwise nonuniformity of background axial velocity. Far downstream $\bar{W}_{hub} - \bar{W}_{tip}$ varied between 0 and 100% of the mid-span $\bar{W}_{mean}$. Results for $\bar{W}_{mean} = 0.4$, $r_h = 0.5$, $\mu = 1.22$, $\lambda = 0.64$, $\beta_2 = 0$, $\bar{\tau} = 0$, $\frac{d\Psi}{d\bar{W}} = 0$.

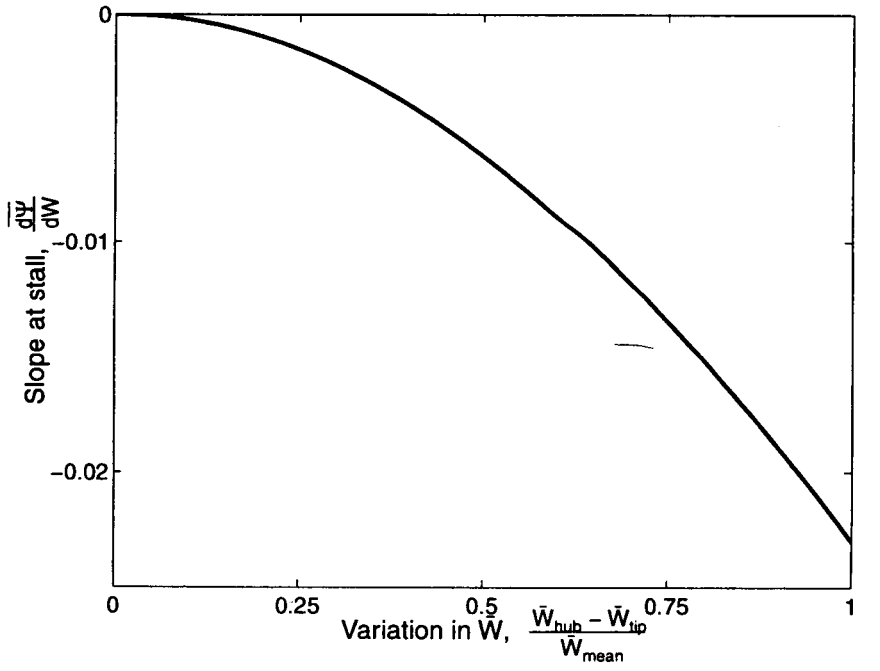


**Figure 5-15:** Calculated slope at neutral instability for increasing spanwise nonuniformity of background axial velocity. Results for $\bar{W}_{mean} = 0.4, r_h = 0.5, \mu = 1.22, \lambda = 0.64, \beta_2 = 0, \bar{\tau} = 0$.

of 1. For a more realistic velocity variation of 50% of the mean, the ratio of slopes at stall dropped to 1 : 20. It can be concluded that for compressors with typical variations in background velocity and slope, the effect of the slope nonuniformity on the stall point would be dominant.

### 5.4.1 Effect of Downstream Boundary Location

The other main effect of background flow nonuniformity was to create a source for the pressure disturbances that convects with the mean flow. This implies that the magnitude of the far-downstream pressure perturbation corresponds to an earlier flow disturbance at the compressor plane. Therefore, the mode shape for a stable pressure perturbation appears to grow in the axial direction, which opposes the downstream boundary condition of zero pressure disturbances at the duct exit. The effect of the downstream boundary condition was assessed by comparing the modes in nonuniform flow for downstream compressor duct lengths of 3 $r_t$ and 6 $r_t$. (A minimal duct length of 3 $r_t$ was chosen so that the interaction of potential disturbances between the compressor and the exit plane would be small.) The background flow for these calculations had a downstream axial velocity nonuniformity of 50% of the mean.

The location of the exit plane did not have an important effect on compressor stability. Figure 5-16 compares the (1,1) pressure disturbances for each case, normalized by the maximum disturbance magnitude at the compressor face. Although the mode in the longer duct grew to be over 7 times larger than for the shorter duct, this had a negligible effect on the eigenvalues (Figure 5-17). Therefore, provided the downstream duct length is at least 3 $r_t$, stability predictions for compressors in nonuniform flow are not sensitive to the location of the exit plane boundary condition.

Overall, the four most important pieces of information about stall behavior found with the actuator plane model are: (1) higher-order 3-D modes were more stable than the quasi-2D modes; (2) the difference between growth rates for 2-D and 3-D modes decreased for compressors with low hub-to-tip ratio, low mean axial velocity, and spanwise variations in slope or mean velocity; (3) mode amplitudes were larger in regions of high slope and low mean velocity; (4) all the modes were destabilized by spanwise variations in slope or

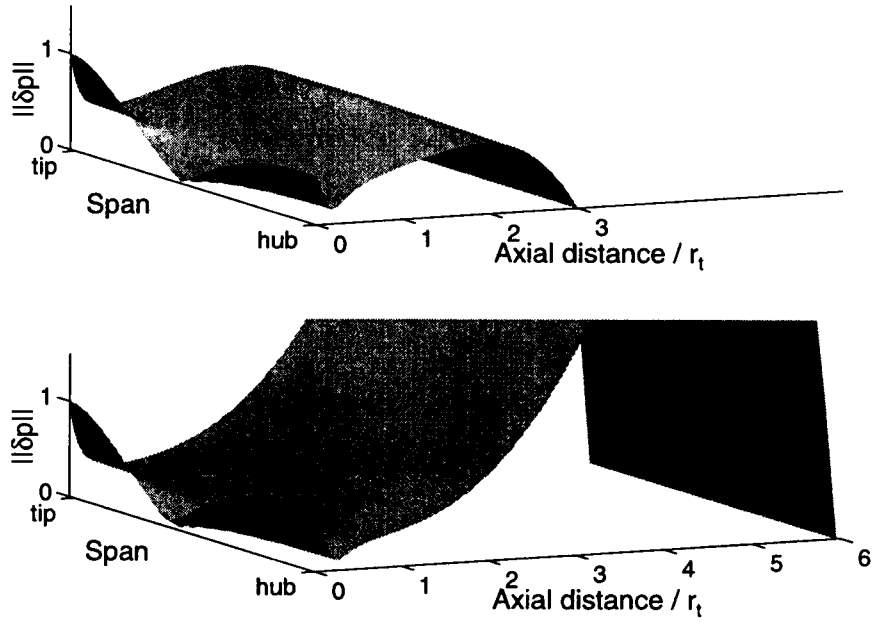


**Figure 5-16:** Amplitude of pressure perturbation for (1,1) mode in a nonuniform background flow for downstream duct lengths of 3 and 6 $r_t$. Results obtained using far downstream $\bar{W}_{hub} - \bar{W}_{tip} = 0.2$, $\bar{W}_{mean} = 0.4$, $r_h = 0.5$, $\mu = 1.22$, $\lambda = 0.64$, $\beta_2 = 0$, $\bar{\tau} = 0$, $\frac{d\Psi}{dW} = 0$.

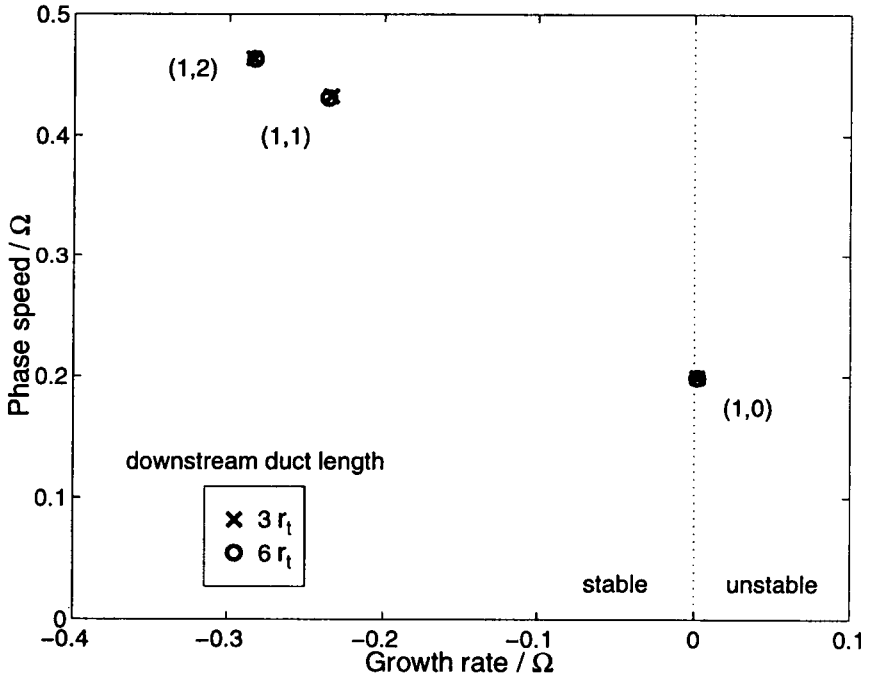


**Figure 5-17:** Eigenvalues of (1,0), (1,1) and (1,2) modes in nonuniform background flow with downstream duct lengths of 3 and 6 $r_t$. Results obtained using compressor parameters listed in Figure 5-16.

mean flow. These results are key to understanding the investigations in Chapter 7 with the *general body force* compressor model.

## 5.5 Actuator Duct Blade Row Representation

The actuator plane model was useful to understand the basic behavior of three-dimensional modes, but the accuracy of the model was limited by preventing flow redistribution within the blade rows. Neglecting *circumferential* redistribution was justified because compressor blades restrict flow from traveling between adjacent blade passages, but the flow can still redistribute in the $r$–$z$ plane for a three-dimensional stall process.

The importance of this flow redistribution on stall inception was investigated using an *actuator duct* model of a rotor cascade in uniform flow. The difference between the actuator plane and actuator duct blade row models is shown in Figure 5-18. With the duct model, the flow can be discontinuous at the leading and trailing edges, but can continuously redistribute within the blade row.

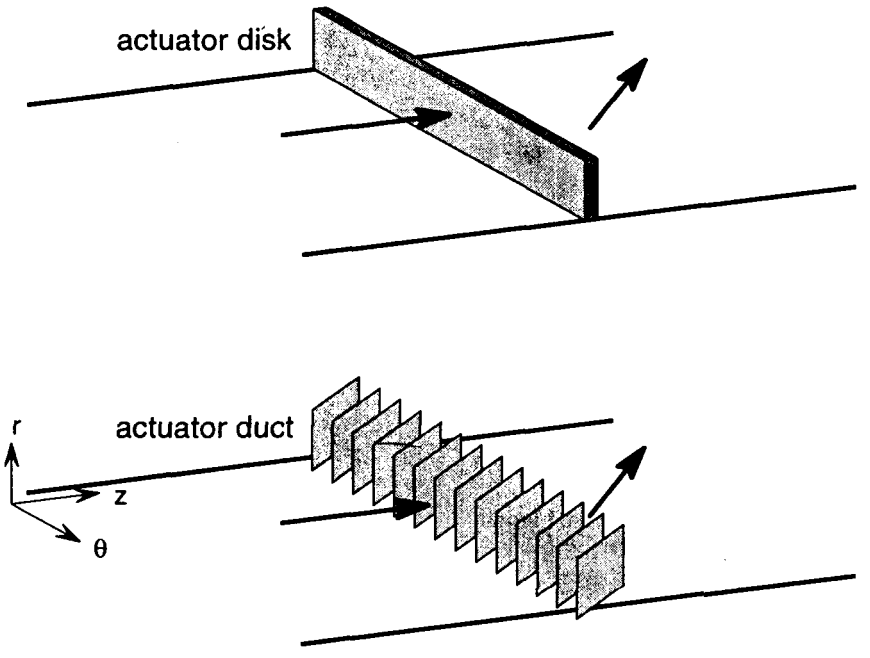


**Figure 5-18:** Illustration of actuator plane and actuator duct models for a single blade row cascade.

The rectilinear actuator duct model used here represented the rotor blades as flat-plates, aligned at stagger angle $\gamma$. The tangential flow velocity was turned instantaneously

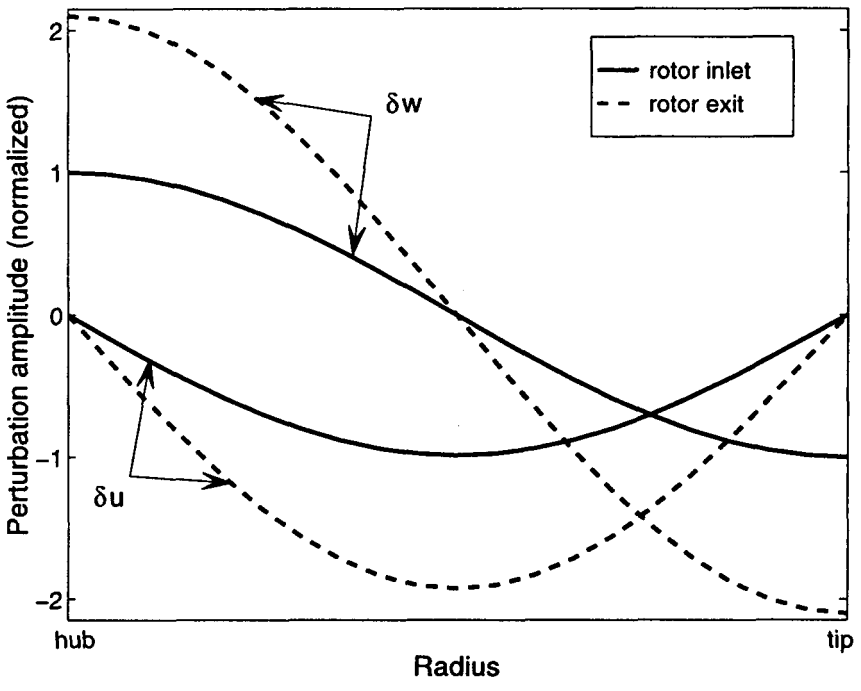


**Figure 5-19:** Comparison of axial and spanwise velocity perturbations across actuator duct model of a single rotor cascade. Results obtained for (1,1) mode at neutral stability, using $r_h = 0.5, \bar{W} = 0.5, c = 0.2, \gamma = 60°, \bar{\tau} = 0, \frac{d\Psi}{dW} = 0.5825$.

at the leading edge to align the relative flow with the stagger angle. All other velocities were continuous across the leading and trailing edge planes. The pressure rise due to flow turning and blade losses was assumed to occur at the leading edge plane. The uniform background flow field was axial upstream of the blade row and was aligned in the rotor-relative frame with the blade stagger angle downstream of the blade row. Details of the flow disturbances within the actuator duct and methods to solve for the modes of the compression system are in Appendix G.

Spanwise velocity perturbations associated with three-dimensional rotating stall induced axial velocity variations through the blade row according to mass conservation:

$$\frac{\partial u}{\partial r} + \frac{\partial (w/\cos\gamma)}{\partial (z/\cos\gamma)} = 0 \,, \tag{5.5}$$

where $w/\cos\gamma$ and $z/\cos\gamma$ represent the velocity and distance in the direction of the chord. Figure 5-19 shows the changes in the axial and spanwise velocity disturbances associated with the (1,1) mode across the blade row. The disturbance amplitude more than doubled between the leading and trailing edges even though this blade had a high aspect ratio of 2.5.

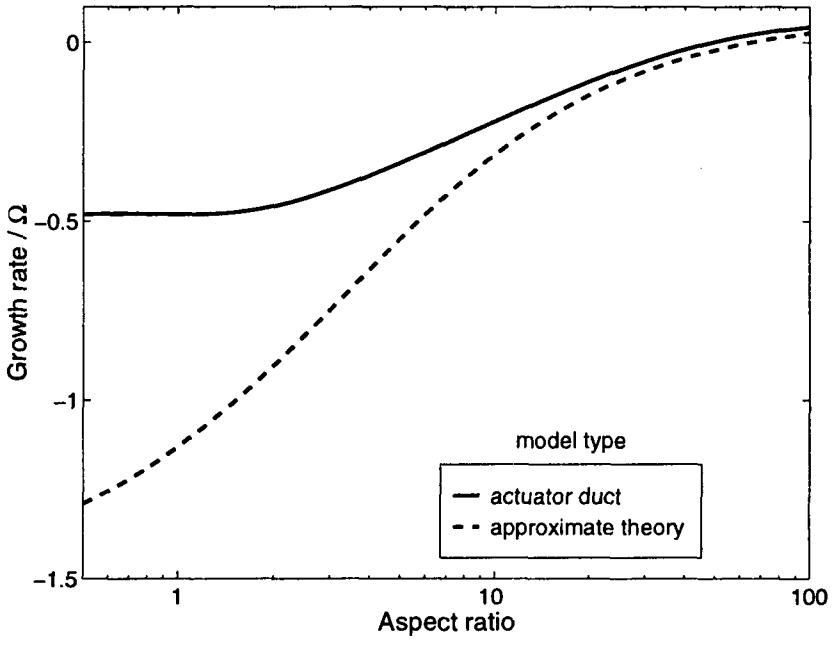


**Figure 5-20:** Growth rate of (1,1) mode for increasing blade aspect ratio. Results for both exact actuator duct theory (solid) and approximate theory (equation 5.10) using $r_h = 0.5$, $\bar{W} = 0.5$, $\gamma = 60°$, $\bar{\tau} = 0$, $\frac{d\Psi}{d\bar{W}} = 0.5$.

An order-of-magnitude analysis of equation (5.5) shows that the change in axial velocity across the blade row was approximately $\|\Delta w\| \approx \bar{u} \cos\gamma / AR$, where $\bar{u}$ is the maximum spanwise velocity at the blade inlet and $AR$ was the blade aspect ratio. Therefore the axial velocity changes are larger for lower aspect ratio blades.

Flow redistribution in the blade stabilized the three-dimensional modes, compared to predictions using an actuator plane. This is demonstrated in Figure 5-20 by comparing the growth rate of the (1,1) mode for compressors with increasing chord lengths, but otherwise identical steady performance. Blade rows with lower aspect ratios, hence higher chord-wise velocity nonuniformity, exhibited the most stable 3-D modes.

The important cause of this change in stability was not the velocity redistribution itself, but rather how it affected the unsteady pressure rise across the blade row, which can be shown with the following order-of-magnitude approximation. The rotor-relative momentum equation along the chord (from equation G.3) was

$$\cos^2\gamma \frac{\partial p}{\partial z} + \bar{W} \frac{\partial w}{\partial z} + \frac{\partial w}{\partial t'} = 0 \,. \tag{5.6}$$

By considering a flow disturbance from only the $(n,j)$ mode (given by perturbation magnitudes $\hat{u},\hat{v},\hat{w}$ and $\hat{p}$ from equation 5.2), the approximate pressure rise could be expressed as

$$\Delta\hat{p} \approx \frac{\bar{W}}{\cos^2\gamma}\Delta\hat{w} + \frac{c_z}{\cos^2\gamma} i(\omega+n)\hat{w} \; . \tag{5.7}$$

The change in axial velocity, from equation (5.5), was approximated as $\Delta\hat{w} \approx -kc_z\hat{u}$, where $k = j\pi/(1-r_h)$. Finally, the axial and spanwise velocities could be related just upstream of the blade where the flow was potential by $\partial u/\partial z = \partial w/\partial r$, which implied that $\hat{u} \approx -(k/\sqrt{n^2+k^2})\,\hat{w}$. The overall pressure rise across the blade row was comprised of the change along the duct from equation (5.6) plus the quasi-steady term from the pressure rise characteristic. Combining all these approximations yielded the total-static pressure rise across the blade for the $(n,j)$ mode:

$$\hat{p}_2 - \hat{p}_{t1} \;\approx\; \left[\frac{d\Psi}{dW} - \mu\bar{W}\frac{k^2}{\sqrt{n^2+k^2}} - i(\omega+n)\mu\right]\hat{w}\,, \tag{5.8}$$

where $\mu = c_z/cos^2\gamma$ was the blade row inertia term. This equation was similar to the pressure rise equation for an actuator plane representation of the rotor row, except for the added real term $-\mu\bar{W}k^2/\sqrt{n^2+k^2}$. Therefore the previous actuator plane eigenvalues could be used to estimate stall points for the actuator duct model by using an *effective* characteristic slope:

$$\frac{d\Psi}{dW}_{\text{plane}} = \frac{d\Psi}{dW}_{\text{duct}} - \mu\bar{W}\frac{k^2}{\sqrt{n^2+k^2}} \; . \tag{5.9}$$

Applying the effective slope to equation (5.3), the approximate $(n,j)$ eigenvalues for an actuator duct were given by

$$\omega_{n,j} = -\frac{n\lambda + i\left(\frac{d\Psi}{dW} - \bar{W}\frac{k^2}{n^2+k^2}(1+\mu\sqrt{n^2+k^2})\right)}{\mu + \frac{2}{\sqrt{n^2+k^2}}} \; . \tag{5.10}$$

Thus, the stall point was predicted to occur at the following slope:

$$\frac{d\Psi}{dW} \approx \frac{\bar{W}k^2}{n^2+k^2}\left(1+\underline{\underline{\mu\sqrt{n^2+k^2}}}\right) \; . \tag{5.11}$$

The underscored term in the above equation is the new term (compared to the actuator disk) caused by pressure changes across the blade row due to velocity redistribution. This term is positive, demonstrating that lower aspect ratio blades (higher $\mu$ for the same $k$) are more stable to three-dimensional modes than higher aspect ratio blades.

To verify that it was this change to the effective pressure rise equation that caused the increased stability for three-dimensional modes in actuator ducts, the approximate and exact growth rates of the (1,1) mode are compared in Figure 5-20 over the same range of aspect ratios. For very high aspect ratio blades ($AR > 10$) the change in stability was almost entirely set by the effective slope. However, for more realistic aspect ratios of 1–2, the axial velocity change across the blade became too large for the linearized approximations in equations (5.7) and (5.8) to hold, and the approximated theory overestimated the stability of the mode.

In summary, the two most important conclusions of this section were: (1) low aspect ratio blades exhibited higher stability to three-dimensional modes than high aspect ratio blades, and (2) this effect was primarily driven by three-dimensional flow redistribution within the blade row which affects the real part of the transfer function between $p_2 - p_{t1}$ and $w$. As demonstrated by Gysling [31], the real part of this transfer function sets the unsteady energy production produced by the rotating stall mode, and is directly associated with the modal growth rate.

### 5.5.1 Sensitivity of Results to Axial Distribution of Pressure Rise

In the actuator duct model of the previous section, the pressure change due to flow turning and losses was confined to occur at the leading edge of the blade. In actual blade rows, flow turning and losses develop throughout the blade passage. Figure 5-21 shows results from CFD calculations demonstrating that, near stall, 85% of the total pressure loss occurs in the last half of the chord, and the change in tangential velocity can be distributed nearly evenly along the passage.

The location and distribution of the pressure rise was varied in the actuator duct model to demonstrate the sensitivity of three-dimensional stall prediction on modeling choices. Four modifications to the actuator duct model were examined. Each model employed the

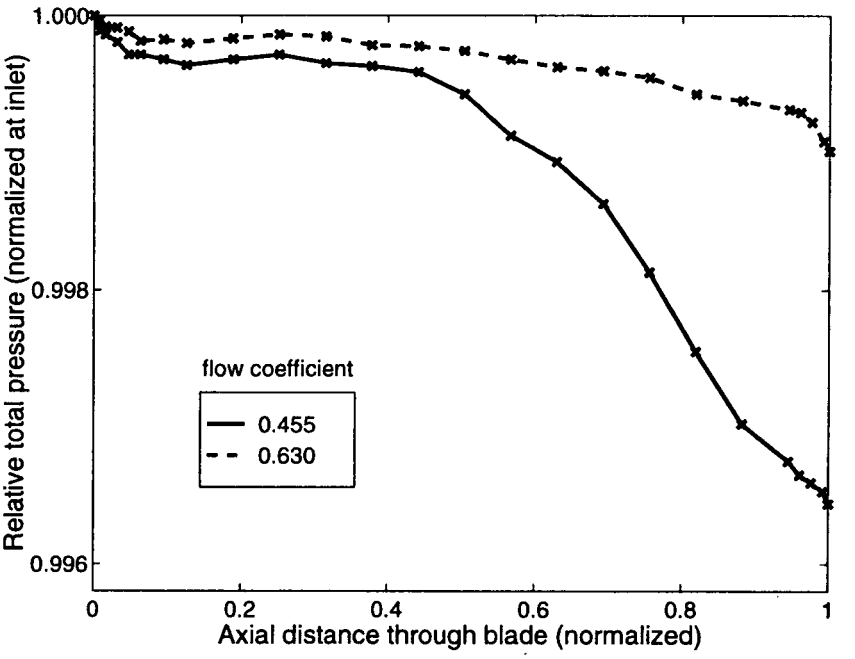


(a) Change in relative total pressure

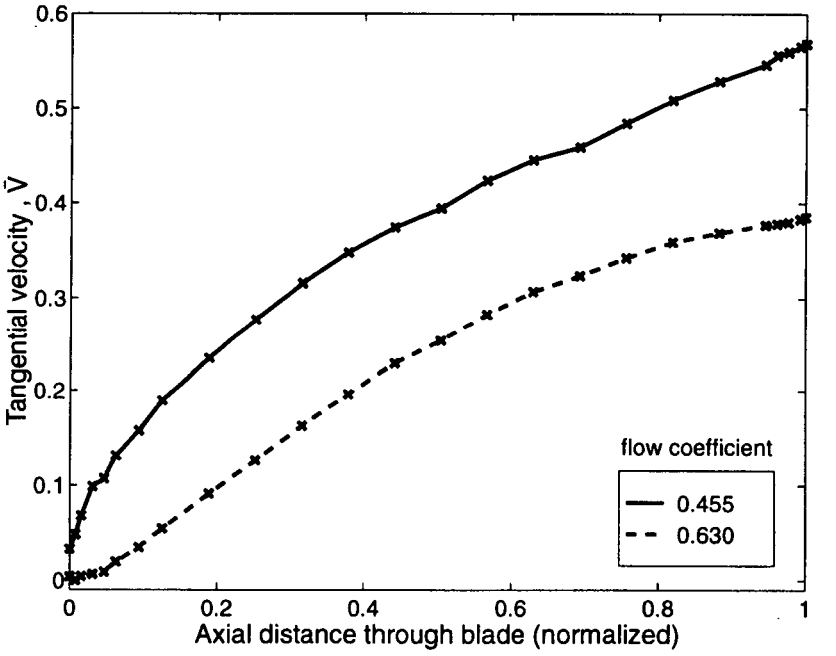


(b) Change in absolute tangential velocity

**Figure 5-21:** Axial variation of relative total pressure and absolute tangential velocity through a rotor passage at operating points near and away from stall. Results based on pitch-wise averages of CFD flow fields by Hoying [40] using the two-dimensional code from [41]. Relative total pressure is normalized by value at inlet. Axial distance through blade is normalized by the axial projection of the chord.

same compressor geometry, pressure rise characteristic, steady background flow, and velocity matching conditions across the blade. The only difference was how the pressure rise was distributed through the blade row to match the specified total-to-static characteristic (Table 5.2). Detailed relations for the pressure rise in each model are developed in Appendix G.2.

**Table 5.2:** Comparison of pressure rise sources within blade row for five actuator duct models.

| | leading edge | body force in blade | trailing edge |
|---|---|---|---|
| (a) | all $\Delta P$ | none | $\Delta P = 0$ |
| (b) | turning $\Delta P$ | none | loss $\Delta P$ |
| (c) | $\Delta P = 0$ | none | all $\Delta P$ |
| (d) | turning $\Delta P$ | loss $\Delta P$ | $\Delta P = 0$ |
| (e) | $\Delta P = 0$ | all $\Delta P$ | $\Delta P = 0$ |

Model (a) was the original actuator duct model in Section 5.5, for which the pressure rise characteristic was enforced at the leading edge. Model (b) separated the contributions of pressure rise due to flow turning and losses to occur at the leading and trailing edge planes, respectively. Model (c) enforced the pressure rise characteristic entirely at the trailing edge. Model (d) separated the pressure rise contributions for turning and losses, and applied the turning at the leading edge. The losses were distributed uniformly along the chord from a chord-wise body force in the axial momentum equation. Model (e) had continuous pressure across both the leading and trailing edges, and enforced the entire pressure rise characteristic through the chord-wise body force. These models were chosen partly because some more accurately represented the physical sources of turning and loss (models b,d,e), and partly because they were easy to implement (models a,c) and provided a chance to compare the sensitivity of results to modeling changes.

The five models predicted identical behavior for the two-dimensional modes, but the difference in growth rates for the three-dimensional modes was large. For typical blade aspect ratios of 1–2, the predicted growth rates for the (1,1) mode varied between actuator duct models by a factor of 3 (Figure 5-22). The highest degree of stability was predicted by models with distributed losses from body forces. The difference in predicted growth rates was again caused by flow redistribution within the blade passage. The quasi-steady pressure rise depended on the axial velocity through terms like $\delta p = d\Psi/dW\ \delta w$ (or $\delta p = dF/dW\ \delta w$

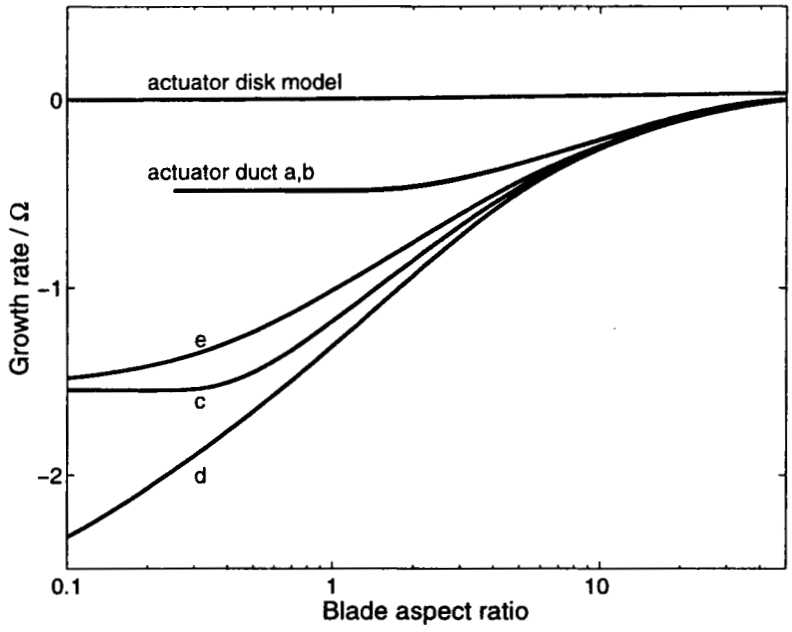


**Figure 5-22:** Comparison of growth rates of (1,1) mode between actuator plane and five actuator duct representations of a single rotor cascade. Results obtained using compressor parameters listed in Figure 5-20.

if a body force was used), so chord-wise variations in axial velocity would alter the overall pressure rise. Predictions of two-dimensional modes were identical for all models because, with a constant axial velocity through the blade passage, it did not matter whether these terms were concentrated at the leading edge, trailing edge, or distributed within.

The neutral stability points of the (1,0), (1,1) and (1,2) modes predicted by the different actuator duct models are compared on an example rotor characteristic in Figure 5-23. All two-dimensional modes, independent of the choice of model, stalled at the peak of the characteristic since unsteady losses were ignored. The (1,1) mode stalled at slopes between +1.0 and +2.7, depending on the model, which corresponded to a 2.2% variation in stalling flow coefficient. Increased inner-blade flow redistribution for the (1,2) mode effected an even larger variation in the stall point. The stalling slope for this mode varied between +1.0 and +4.8, corresponding to a flow coefficient variation of 4.3%.

In conclusion, the stability of three-dimensional modes was sensitive to the manner by which the blade row model prescribed the specified pressure rise. Abrupt discontinuities in pressure rise across the leading edge should be avoided because they over-predict the growth

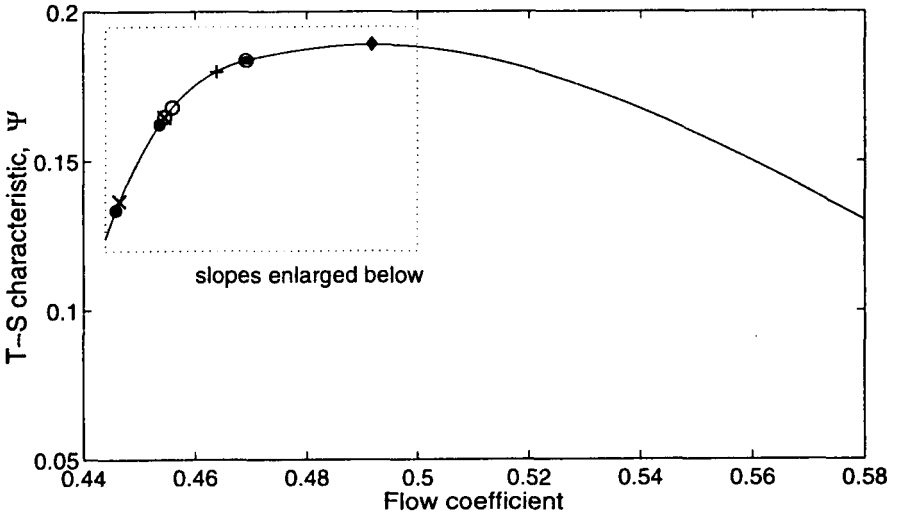


(a) Stall points indicated on total-static pressure rise characteristic

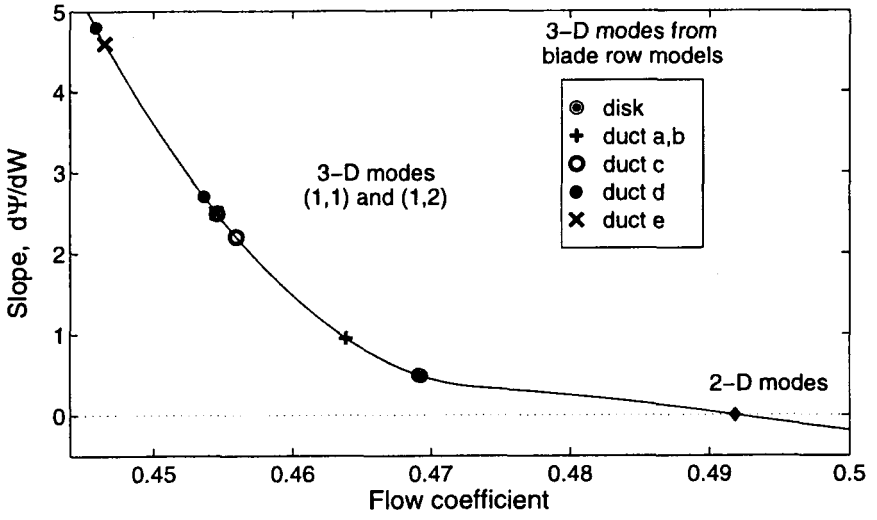


(b) Stall points indicated on the slope of total-static pressure rise characteristic

**Figure 5-23:** Comparison of stall points of $(n, 0)$, (1,1) and (1,2) modes between 6 actuator plane/duct models. Neutral stability points were drawn on an example rotor characteristic from Hoying [40]. Results obtained for single blade row cascade of aspect ratio equal to 1, using $r_h = 0.5$, $\bar{W} = 0.5$, $c = 0.5$, $\gamma = 60°$, $\bar{\tau} = 0$. Two symbols are indicated for the 3-D modes of each model; the symbol at a higher flow coefficient corresponds to the (1,1) mode.

rate of 3-D modes. The pressure rise needs to be enforced continuously, based on blade row measurements or other CFD data such as in Figure 5-21. This conclusion implies that previous actuator disk and duct models with discontinuous pressure rise [83, 62, 49, 5, 74] have over-estimated the importance of three-dimensional modes.

## 5.6 Summary and Implications of Results from Actuator Plane and Actuator Duct Models

The existence of an infinite number of $(n, j)$ rotating stall modes were predicted using an actuator plane model. A subset of these have been considered "two-dimensional" in previous stability analyses; however, only in a compressor with spanwise uniform properties were the class of $(n, 0)$ modes exactly two-dimensional. In compressors with nonuniform slope or velocity profiles, these "quasi-two-dimensional" modes exhibited spanwise variations.

Higher-order three dimensional modes (for $j \geq 1$) had more spanwise nonuniformity, higher rotating speeds, and were always more stable than the quasi-2D modes for the same harmonic $n$. As of yet, they appear to only be important once the two-dimensional modes have been controlled, or perhaps if forcibly excited as lightly damped modes near stall.

Enhancements to the actuator plane model examining spanwise compressor nonuniformities and flow redistributions within the blade row point to two competing trends. Three-dimensional flow variations were found to both stabilize or destabilize the modes in the following manner:

1. Spanwise nonuniformity in compressor performance distorted and destabilized the modes so that instability occurred at a negative average characteristic slope. The mode amplitude was amplified in regions of relatively higher slope. Background flow variations induced similar trends, but the effects for practical situations were an order of magnitude smaller when compared to the effects of typical slope nonuniformities.

2. The capability for flow redistribution within the blade passage that is inherent in three-dimensional modes altered the unsteady pressure rise–velocity relationship to further stabilize three-dimensional modes. These modes were most stable in low aspect ratio blades.

Each of these trends was correct in the limited scope under which they were uncovered. However, the trends, alone by themselves, are not sufficient to state with any certainty the fate of three-dimensional stall inception in realistic compressors with *both* typical low aspect ratio blades, *and* nonuniformities in background flow, compressor geometry or performance.

To unequivocally establish the usefulness of two-dimensional stall analyses compared to three-dimensional predictions, a model that includes the above sources of nonuniformities must be developed and used to examine realistic compressor situations. The sensitivity of the three-dimensional stall predictions to the five actuator duct models in this chapter indicates that the new model should distribute continuous losses and turning that resemble the conditions in actual blade passages. Such a model is developed in the following chapter.

# CHAPTER 6

# DEVELOPMENT OF 3-D BODY FORCE COMPRESSOR STABILITY MODEL

A body force compressor model is developed in this chapter to calculate three-dimensional modes in steady, axisymmetric flows. This model is applicable for compressors with varying annulus geometry and general background flow nonuniformities such as inlet distortions. Solution processes for both the steady background flow field and the linearized modes of the compression system are described. Assessments are made against both analytic solutions and experimental stall data to verify the model's accuracy.

## 6.1 Key Modeling Features

The three-dimensional body force model in this chapter was designed to address the limitations of the actuator plane and duct models found in Chapter 5. The actual meridional geometry of the compressor was represented, as in Figure 6-1, to capture the flow field redistribution within the blade-free and blade row regions. The background flow fields were restricted to being steady and axisymmetric to allow for linearized hydrodynamic stability analyses similar to those in Chapters 2 and 5; however, general flow nonuniformities in the meridional plane were permissible, including radial inlet distortions.

Body forces were used to represent the action of the blades on the flow. These forces were distributed continuously along the chord to duplicate the physical sources of loss observed in discrete blade simulations. Endwall phenomena, such as increased loss and

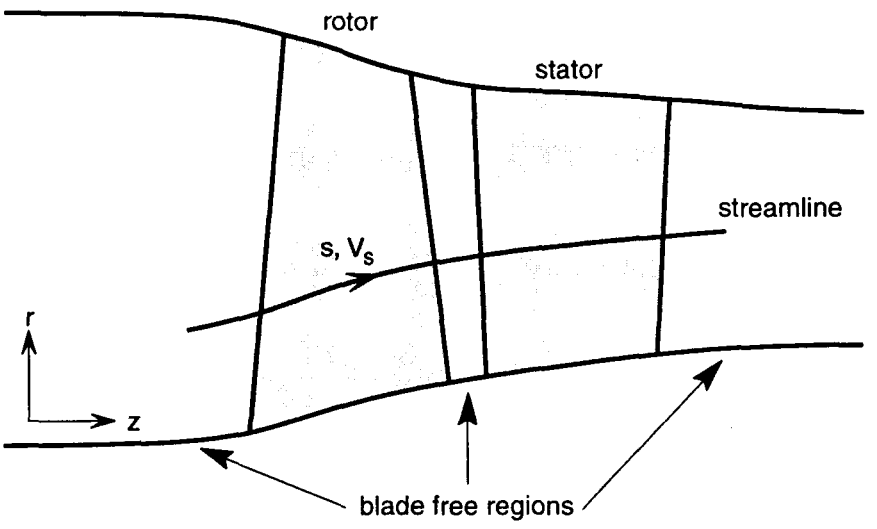


**Figure 6-1:** Illustration of three-dimensional body force compressor model for a single stage compressor.

blockage due to tip clearance effects, and nonuniform loss and deviation along the blade span were reflected through the radial variation of these forces.

Implementing this model to predict rotating stall involved two steps. First, steady body forces were found that best reproduced the distribution of loss and turning through the compressor at specified operating points. These points corresponded to instances where the steady flow field was known from measurements. Second, linearized stability analyses were performed using correlations of these body forces. Since linearized analyses examine changes to the steady flow field, the local body forces were required to be functions of the local flow conditions at that radial and chordwise position. The compressor characteristic "slope" was thus not an input to this model; in its place was an array of body force derivatives with local flow conditions.

Figure 6-1 shows the compression system model. The flow in the blade-free regions was modeled by the Euler equations written in the cylindrical coordinate system:

$$\begin{aligned}
\frac{\partial U}{\partial t} + U\frac{\partial U}{\partial r} + \frac{V}{r}\frac{\partial U}{\partial \theta} + W\frac{\partial U}{\partial z} - \frac{V^2}{r} + \frac{\partial P}{\partial r} &= 0 \\
\frac{\partial V}{\partial t} + U\frac{\partial V}{\partial r} + \frac{V}{r}\frac{\partial V}{\partial \theta} + W\frac{\partial V}{\partial z} + \frac{UV}{r} + \frac{1}{r}\frac{\partial P}{\partial \theta} &= 0 \\
\frac{\partial W}{\partial t} + U\frac{\partial W}{\partial r} + \frac{V}{r}\frac{\partial W}{\partial \theta} + W\frac{\partial W}{\partial z} + \frac{\partial P}{\partial z} &= 0 \\
\frac{1}{r}\frac{\partial rU}{\partial r} + \frac{1}{r}\frac{\partial V}{\partial \theta} + \frac{\partial W}{\partial z} &= 0 \,. \qquad (6.1)
\end{aligned}$$

The equations were nondimensionalized with the parameters $\tilde{r}_t$, $\tilde{\Omega}$ and $\tilde{\rho}$; for compressors with nonuniform outer casing radius, $\tilde{r}_t$ was taken as the tip radius at the leading edge of the first rotor blade row.

Within the blade regions, tangential variation of the disturbance flow was permissible, but the circumferential *redistribution* of flow between blade passages was prevented. This was achieved by removing the $d/d\theta$ terms in the Euler equations (6.1) when written in the relative frame of each blade row. The resultant equations would therefore treat the flow at each tangential position as if it was "locally axisymmetric". Written in the absolute frame of reference, the locally-axisymmetric Euler equations applicable in the blade regions were given by

$$\begin{aligned}
\frac{\partial U}{\partial t} + U\frac{\partial U}{\partial r} + \Omega\frac{\partial U}{\partial \theta} + W\frac{\partial U}{\partial z} - \frac{V^2}{r} + \frac{\partial P}{\partial r} &= F_r \\
\frac{\partial V}{\partial t} + U\frac{\partial V}{\partial r} + \Omega\frac{\partial V}{\partial \theta} + W\frac{\partial V}{\partial z} + \frac{UV}{r} &= F_\theta \\
\frac{\partial W}{\partial t} + U\frac{\partial W}{\partial r} + \Omega\frac{\partial W}{\partial \theta} + W\frac{\partial W}{\partial z} + \frac{\partial P}{\partial z} &= F_z \\
\frac{1}{r}\frac{\partial rU}{\partial r} + \frac{\partial W}{\partial z} &= 0,
\end{aligned} \tag{6.2}$$

where $\Omega = 1$ or 0 depending on whether the blade row was a rotor or stator. This treatment is equivalent to the pitchwise-averaged model developed by Horlock and Marsh [39], which provides a rigorous derivation of the body forces in terms of the differences in flow properties across the blade surfaces.

Within the blade rows, the axial body force was decomposed into an inviscid term and a term that contributed to the loss. The body force component contributing to loss, $F_L$, was defined as

$$V_s F_L = -U F_r - (V - r\Omega) F_\theta - W F_z, \tag{6.3}$$

where $V_s = \sqrt{U^2 + W^2}$ is the meridional velocity along the streamline $s$. (It can be verified that by setting $F_L = 0$, the remaining inviscid body force vector resulting from $F_z = -U/W F_r - (V - r\Omega)/W F_\theta$ is perpendicular to the relative velocity, and so would not contribute to the losses.) This formulation was used so that the body forces could be expressed directly in terms of relative total pressure loss and deviation, for which data are

readily available.

The body forces in equation (6.2) were functions of $r, z$ and the local flow velocities $U$, $V$ and $W$. The process to determine these dependencies is explained in Section 6.3. Once functional relations for $F_\theta$ and $F_z$ have been determined, the flow through the compression system can be calculated by specifying inlet flow conditions, an exit boundary condition, and enforcing continuity of flow properties across the blade row and blade-free interfaces.

## 6.2 Steady Flow Model

The steady, axisymmetric background flow for both the blade rows and blade-free regions was described by

$$\begin{aligned}
\bar{U}\frac{\partial \bar{U}}{\partial r} + \bar{W}\frac{\partial \bar{U}}{\partial z} - \frac{\bar{V}^2}{r} + \frac{\partial \bar{P}}{\partial r} &= \bar{F}_r \\
\bar{U}\frac{\partial \bar{V}}{\partial r} + \bar{W}\frac{\partial \bar{V}}{\partial z} + \frac{\bar{U}\bar{V}}{r} &= \bar{F}_\theta \\
\bar{U}\frac{\partial \bar{W}}{\partial r} + \bar{W}\frac{\partial \bar{W}}{\partial z} + \frac{\partial \bar{P}}{\partial z} &= \bar{F}_z \\
\frac{1}{r}\frac{\partial r\bar{U}}{\partial r} + \frac{\partial \bar{W}}{\partial z} &= 0,
\end{aligned} \tag{6.4}$$

where, in the blade-free regions, the body forces were set to zero.

The axisymmetric flow field was calculated for prescribed body forces and boundary conditions using a stream function ($\Psi$) technique. Relations for $\Psi$, $\bar{P}_t$ and $r\bar{V}$ have been derived in Appendix H.1.1, applicable for both ducts and blade row regions with body forces. At the inlet to the compression system the radial profiles of total pressure, tangential velocity, and axial velocity (through the stream function) were specified, along with the assumption that the radial velocity was zero. Far downstream, where the casing boundaries were at constant radius, the radial velocity was again assumed to be zero by enforcing the streamlines to be parallel to the axial direction. A description of the numerical procedure used to converge upon steady flow solutions is provided in Appendix H.

## 6.3 Calculation of Body Forces

It was assumed that radial profiles of pressure and velocity at the inlet and exit of each blade row were known, and could be used to establish initial values for the body forces. $F_\theta$ was based on the change in $r\bar{V}$ across the chord, and $F_L$ was based on the total pressure loss. $F_r$, which could arise for blades inclined off the radial direction, was assumed to be negligible in this thesis.

The tangential body force was designed to turn the relative flow towards the blade angle. In steady two-dimensional flow, $\bar{F}_\theta = \bar{W}\,\partial\bar{V}/\partial z$. The magnitude of $F_\theta$ thus scales with the axial velocity and the change in tangential velocity, so the local tangential body force was defined as

$$F_\theta = k\,W[W\tan\beta_d - (V - r\Omega)]\,, \tag{6.5}$$

where $\beta_d(r,z)$ was the *desired* flow angle along the chord (i.e. the metal angle) and $k(r,z)$ was an undetermined, positive valued field. Therefore, the difference between the relative flow angle and the blade angle induces a tangential force to reduce the deviation. Radial nonuniformity of deviation could be scaled through $k(r,z)$ to match an experiment. Larger values of $k$, corresponding to machines with higher solidity, reduced the local deviation. The derivatives of $F_\theta$ with respect to $V$ and $W$, used in the linearized stability analysis, were found from equation (6.5):

$$\begin{aligned} \frac{\partial F_\theta}{\partial V} &= -k\,W \\ \frac{\partial F_\theta}{\partial W} &= k(2W\tan\beta_d - V + r\Omega)\,. \end{aligned} \tag{6.6}$$

The body force contributing to the loss, $F_L$, was determined by matching the radial distribution of losses across the blade row. In rotating flow, total pressure loss is measured by changes in *rotary total pressure*, nondimensionally expressed as $P_t^* = P_{t,rel} - (\Omega r)^2 = P_t - \Omega r V$. By manipulating the steady, locally-axisymmetric Euler equations (6.4), the change in $P_t^*$ can be expressed solely in terms of $F_L$:

$$\frac{\partial \bar{P}_t^*}{\partial s} = \frac{\partial \bar{P}_t - \Omega r \bar{V}}{\partial s} = -\bar{F}_L\,. \tag{6.7}$$

The overall $P_t^*$ loss along a streamline is then given by $\bar{L} = \int_0^{\Delta s} \bar{F}_L \, ds$.

Two methods for calculating the body force contributing to loss were used. The first method matched a given value of loss over any streamline by distributing $\bar{F}_L(s)$ along the streamline according to some desired shape factor, $f(s)$:

$$\bar{F}_L(s) = \frac{f(s)}{\Delta s}\bar{L} \ , \ \text{where} \int_0^{\Delta s} f(s)\, ds = \Delta s \ . \tag{6.8}$$

The shape factor could be chosen to weight the losses near the second half of the chord, or according to other information known about the blade row. Equation (6.8) was used to approximate the steady distribution of $\bar{F}_L(r,z)$ through the blade row at one operating point given the spanwise distribution of loss, $\bar{L}(r)$, and some idea of the streamline pattern. However, equation (6.8) does not provide a dependency between the body force and the local velocity conditions. Therefore, a different relation was required for calculating flows at operating points without known loss distributions, and for the linearized stability analyses.

The second method correlated $F_L$ in terms of the local velocity based on two-dimensional compressor performance theory. For low-speed cascade flow, the loss across a blade can be written [36] in terms of the inlet relative velocity magnitude and an overall loss-coefficient, $\hat{\xi}$, that depends only on the incidence, as in $L = \frac{1}{2} \parallel \vec{V}_{in,rel} \parallel^2 \hat{\xi}(\beta_{in})$. Since $F_L \propto L/\Delta s$, the body force at every $(r,z)$ position in the blade row was assumed to locally behave according to equation (6.9) for some loss coefficient relation $\xi(\beta)$ valid at that location:

$$F_L = \frac{1}{2\Delta s}\left[W^2 + (V - r\Omega)^2\right]\xi(\beta) \ . \tag{6.9}$$

The derivatives of $F_L$ with velocity were then given by

$$\begin{aligned} \frac{\partial F_L}{\partial V} &= \frac{1}{\Delta s}\left[2(V - r\Omega)\xi + W\frac{d\xi}{d\beta}\right] \\ \frac{\partial F_L}{\partial W} &= \frac{1}{\Delta s}\left[2W\xi - (V - r\Omega)\frac{d\xi}{d\beta}\right] \ . \end{aligned} \tag{6.10}$$

To determine the local loss coefficient, $\xi(\beta)$, at all locations in the blade row, the following two-step procedure was used:

- The steady flow fields were calculated corresponding to the specific operating points

for which performance data were known. $\bar{F}_L(r,z)$ was specified at each operating point according to equation (6.8) for some desired shape factor $f(s)$. Without any prior knowledge, the initial streamlines through the blade rows were assumed to lie at a constant percent span. The radial distribution of $k$ in equation (6.5) was chosen to effect the desired deviation at the blade row exits. Some iteration was usually required to choose a reasonable profile for $k$.

- The above flow fields for each operating point were used to correlate the local loss coefficients with the local relative flow angle. Relations for $\xi(\beta)$ were determined at each computational grid node within the blade passages, and stored for future calculations.

An operating speedline for any range of inlet conditions could then be calculated by solving the steady flow fields a second time using extrapolated or interpolated polynomial fits of each local loss coefficient, $\xi(\beta)$. The polynomial fits were also used to calculate $d\xi/d\beta$ in equation (6.10) to produce the body force derivatives for the linearized stability model.

An assessment of the accuracy of these procedures to determine the body forces and calculate the background flow is provided in Section 6.5.1.

## 6.4 Unsteady, Linearized Model

A linearized version of the body force model was developed to determine the stability of a given steady, axisymmetric background flow field. The values of $\bar{U}$, $\bar{V}$, $\bar{W}$, $\bar{P}$, $\bar{F}_\theta$ and $\bar{F}_L$ (hence $\bar{F}_z$) were assumed to be known throughout the compression system from previous steady flow calculations. Also prescribed were the derivatives of the body forces in the blade rows with respect to local flow velocities, $dF_\theta/dV$, $dF_\theta/dW$, $dF_L/dV$ and $dF_L/dW$. Expressions for the evolution of disturbance flow variables in terms of these known quantities are developed in this section.

Small amplitude flow disturbances were expressed in the general exponential form:

$$v(r,\theta,z,t) = \mathcal{R}e\left\{\sum_{n=-\infty}^{\infty} v_n(r,z)\mathrm{e}^{in\theta}\mathrm{e}^{i\omega_n t}\right\} . \tag{6.11}$$

Similar harmonic decompositions were assumed for the perturbations $u$, $w$, $p$, $f_\theta$, $f_L$ and

$f_z$. Since the background flow was steady and axisymmetric, the perturbations for each harmonic $n$ were decoupled, and so could be studied independently.

The linearized form of the equations for each harmonic $n$ differed between the blade row and blade-free regions. In the blade-free regions, equation (6.1) could be linearized as

$$\begin{bmatrix} \bar{W} & 0 & 0 & 0 \\ 0 & \bar{W} & 0 & 0 \\ 0 & 0 & \bar{W} & 1 \\ 0 & 0 & 1 & 0 \end{bmatrix} \frac{\partial}{\partial z} \begin{pmatrix} u_n \\ v_n \\ w_n \\ p_n \end{pmatrix} + \begin{bmatrix} \bar{U} & 0 & 0 & 1 \\ 0 & \bar{U} & 0 & 0 \\ 0 & 0 & \bar{U} & 0 \\ 1 & 0 & 0 & 0 \end{bmatrix} \frac{\partial}{\partial r} \begin{pmatrix} u_n \\ v_n \\ w_n \\ p_n \end{pmatrix} + \cdots$$

$$\cdots + \begin{bmatrix} i\omega_n + \frac{\partial \bar{U}}{\partial r} + \frac{in\bar{V}}{r} & -2\frac{\bar{V}}{r} & \frac{\partial \bar{U}}{\partial z} & 0 \\ \frac{\partial \bar{V}}{\partial r} + \frac{\bar{V}}{r} & i\omega_n + \frac{\bar{U}}{r} + \frac{in\bar{V}}{r} & \frac{\partial \bar{V}}{\partial z} & \frac{in}{r} \\ \frac{\bar{W}}{r} & 0 & i\omega_n + \frac{\partial \bar{W}}{\partial z} + \frac{in\bar{V}}{r} & 0 \\ \frac{1}{r} & \frac{in}{r} & 0 & 0 \end{bmatrix} \begin{pmatrix} u_n \\ v_n \\ w_n \\ p_n \end{pmatrix} = 0 \ . \quad (6.12)$$

This linearized system of 4 equations in 4 variables, with appropriate boundary conditions, was sufficient to determine the flow in any blade-free region.

The linearized equations within the blade rows were

$$\begin{bmatrix} \bar{W} & 0 & 0 & 0 & 0 & 0 \\ 0 & \bar{W} & 0 & 0 & 0 & 0 \\ 0 & 0 & \bar{W} & 1 & 0 & 0 \\ 0 & 0 & 1 & 0 & 0 & 0 \end{bmatrix} \frac{\partial}{\partial z} \begin{pmatrix} u_n \\ v_n \\ w_n \\ p_n \\ f_{\theta,n} \\ f_{z,n} \end{pmatrix} + \begin{bmatrix} \bar{U} & 0 & 0 & 1 & 0 & 0 \\ 0 & \bar{U} & 0 & 0 & 0 & 0 \\ 0 & 0 & \bar{U} & 0 & 0 & 0 \\ 1 & 0 & 0 & 0 & 0 & 0 \end{bmatrix} \frac{\partial}{\partial r} \begin{pmatrix} u_n \\ v_n \\ w_n \\ p_n \\ f_{\theta,n} \\ f_{z,n} \end{pmatrix} + \cdots \quad (6.13)$$

$$\cdots + \begin{bmatrix} i\omega_n + in\Omega + \frac{\partial \bar{U}}{\partial r} & -2\frac{\bar{V}}{r} & \frac{\partial \bar{U}}{\partial z} & 0 & 0 & 0 \\ \frac{\partial \bar{V}}{\partial r} + \frac{\bar{V}}{r} & i\omega_n + in\Omega + \frac{\bar{U}}{r} & \frac{\partial \bar{V}}{\partial z} & 0 & -1 & 0 \\ \frac{\bar{W}}{r} & 0 & i\omega_n + in\Omega + \frac{\partial \bar{W}}{\partial z} & 0 & 0 & -1 \\ \frac{1}{r} & 0 & 0 & 0 & 0 & 0 \end{bmatrix} \begin{pmatrix} u_n \\ v_n \\ w_n \\ p_n \\ f_{\theta,n} \\ f_{z,n} \end{pmatrix} = 0 \ .$$

Two more relations were required to complete the flow representation within the blade rows. The unsteady force disturbances, $f_{\theta,n}$ and $f_{L,n}$, were assumed to be modeled by a first-order

lag equation, with time constants $\tau_\delta$ and $\tau_L$:

$$(1 + i\omega_n\tau_\delta + in\Omega\tau_\delta)f_{\theta,n} = \frac{\partial F_\theta}{\partial W}w_n + \frac{\partial F_\theta}{\partial V}v_n \tag{6.14}$$

$$(1 + i\omega_n\tau_L + in\Omega\tau_L)f_{L,n} = \frac{\partial F_L}{\partial W}w_n + \frac{\partial F_L}{\partial V}v_n \ . \tag{6.15}$$

$f_{L,n}$ was then related to $f_{z,n}$ through a linearized version of equation (6.3):

$$-\bar{W}f_{z,n} = \bar{V}_s f_{L,n} + (\bar{V} - r\Omega)f_{\theta,n} + \frac{\bar{U}\bar{F}_L}{\bar{V}_m}u_n + \bar{F}_\theta v_n + (\bar{F}_z + \frac{\bar{W}\bar{F}_L}{\bar{V}_m})w_n \ . \tag{6.16}$$

Combining equations (6.15) and (6.16) resulted in

$$\begin{aligned}
&[(i\omega_n + in\Omega)\tau_L + 1]\left[\frac{\bar{U}\bar{F}_L}{\bar{V}_m}\right]u_n + \left\{[(i\omega_n + in\Omega)\tau_L + 1]\bar{F}_\theta + \bar{V}_m\frac{\partial F_L}{\partial V}\right\}v_n + \cdots \\
&\cdots + \left\{[(i\omega_n + in\Omega)\tau_L + 1]\left[\bar{F}_z + \frac{\bar{W}\bar{F}_L}{\bar{V}_m}\right] + \bar{V}_m\frac{\partial F_L}{\partial W}\right\}w_n + \bar{W}[(i\omega_n + in\Omega)\tau_L + 1]f_{z,n}\cdots \\
&\cdots + (\bar{V} - r\Omega)[(i\omega_n + in\Omega)\tau_L + 1]f_{\theta,n} = 0 \ .
\end{aligned} \tag{6.17}$$

Equations (6.14) and (6.17) represent the last two conditions, along with the four equations in (6.13), needed to resolve the 6 flow variables within the blade regions.

In the interior of the compressor grid, the continuity equations in equations (6.12) and (6.13) were replaced by a second-order elliptical equation for pressure. This is a common procedure in incompressible analyses because it reduces numerical inaccuracy by providing a dominant equation for pressure (Ghia et al. [19]). In the blade-free regions, the linearized form of this equation was given by

$$\begin{aligned}
&\frac{\partial^2 p_n}{\partial r^2} + \frac{\partial^2 p_n}{\partial z^2} + \left\{\begin{bmatrix} 2\frac{\partial \bar{W}}{\partial r} & 0 & 2\frac{\partial \bar{W}}{\partial z} & 0 \end{bmatrix}\frac{\partial}{\partial z} + \begin{bmatrix} 2\frac{\partial \bar{U}}{\partial r} & -2\frac{\bar{V}}{r} & 2\frac{\partial \bar{U}}{\partial z} & \frac{1}{r} \end{bmatrix}\frac{\partial}{\partial r} + \cdots\right. \\
&\left.\cdots + \begin{bmatrix} \frac{2}{r}\left(\frac{\bar{U}}{r} + in\frac{\partial \bar{V}}{\partial r}\right) & \frac{2}{r}\left(in\frac{\bar{U}}{r} - \frac{\partial \bar{V}}{\partial r}\right) & 2\frac{in}{r}\frac{\partial \bar{V}}{\partial x} & -\frac{n^2}{r^2} \end{bmatrix}\right\}\begin{pmatrix} u_n \\ v_n \\ w_n \\ p_n \end{pmatrix} = 0 \ ,
\end{aligned} \tag{6.18}$$

and in the blade rows,

$$\frac{\partial^2 p_n}{\partial r^2} + \frac{\partial^2 p_n}{\partial z^2} + \left\{ \left[ \begin{array}{cccccc} 2\frac{\partial \bar{W}}{\partial r} & 0 & 2\frac{\partial \bar{W}}{\partial z} & 0 & 0 & -1 \end{array} \right] \frac{\partial}{\partial z} + \cdots \right.$$

$$\left. \left[ \begin{array}{cccccc} 2\frac{\partial \bar{U}}{\partial r} & -2\frac{\bar{V}}{r} & 2\frac{\partial \bar{U}}{\partial z} & \frac{1}{r} & 0 & 0 \end{array} \right] \frac{\partial}{\partial r} + \left[ \begin{array}{cccccc} 2\frac{\bar{U}}{r^2} & -\frac{2}{r}\frac{\partial \bar{V}}{\partial r} & 0 & 0 & 0 & 0 \end{array} \right] \right\} \left( \begin{array}{c} u_n \\ v_n \\ w_n \\ p_n \\ f_{\theta,n} \\ f_{z,n} \end{array} \right) = 0 \,. \tag{6.19}$$

**Boundary conditions**

The flow at the inner and outer tip radii was enforced to be tangent to the casing wall:

$$u_n = \frac{dr_h}{dz} w_n \text{ along } r = r_h, \quad \text{and } u_n = \frac{dr_t}{dz} \text{ along } r = r_t \,. \tag{6.20}$$

At the downstream exit plane, the pressure perturbation was identically set to zero. Downstream duct lengths were chosen to be greater than 3 tip radii so that this boundary condition would not significantly affect the stability analysis, even for nonuniform background flow fields (as shown in Section 5.4.1). At the upstream inlet plane, the slowest decaying pressure disturbance originating from the blade rows would be the radially uniform component, behaving as $p_n \propto \exp(nz)$. The upstream vortical disturbances were assumed to derive only from the interaction of the compressor disturbances on the mean flow, and not to convect into the annulus from outside. These boundary conditions were expressed as

$$\begin{aligned} \text{far upstream:} \quad & \frac{\partial p_n}{\partial z} = n\,\overline{p_n} \\ & \frac{\partial u_n}{\partial z} - \frac{\partial w_n}{\partial r} = 0 \\ & \frac{\partial v_n}{\partial z} - \frac{in}{r} w_n = 0 \\ \text{far downstream:} \quad & p_n = 0 \,. \end{aligned} \tag{6.21}$$

The fourth equation used at the inlet boundary was continuity. Orszag et al. [57] showed it is important to enforce continuity at the inlet plane to suppress spurious mass flow sources

within the domain of computations using the elliptical pressure equation.

### 6.4.1 Calculation of Rotating Stall Modes

To compute the rotating stall modes for each $n$, the linearized governing equations and boundary conditions were arranged as a generalized eigenvalue problem for $\omega_n$. Each equation was discretized over the computational grid, following the procedures in Appendix I. Since the governing equations in (6.12) and (6.13) were linear in $\omega_n$, the entire eigenvalue problem could be expressed in the matrix form:

$$\mathbf{A}\vec{x}_n + i\omega_n \mathbf{B}\vec{x}_n = 0 \; . \tag{6.22}$$

The eigenvector $\vec{x}_n$ contained the flow disturbance variables $u_n$, $v_n$, $w_n$, $p_n$, $f_{\theta,n}$ and $f_{z,n}$ at every $r$-$z$ node in the computational domain. This vector had $K = M(4N_f + 6N_b)$ entries, where $M$ was the number of radial nodes, and $N_f$ and $N_b$ were the total number of axial nodes in the blade-free and blade row regions, respectively.

The $K \times K$ matrices $\mathbf{A}$ and $\mathbf{B}$ grew very large for a modest number of grid points. A typical single stage compressor computation used 17 radial nodes and 120 axial nodes, spaced 40 upstream, 40 downstream, 5 in the gap, 15 in the rotor and 20 in the stator. For this example, $K = 9350$, and $\mathbf{A}$ and $\mathbf{B}$ contained 87 million complex-valued entries each. Numerical procedures described in Appendix H.2 saved computational resources by using the banded properties of $\mathbf{A}$ and $\mathbf{B}$, and iteratively converging on one radial mode at a time. Given an initial value of $\omega_n$, this procedure would converge to the nearest eigenvalue and calculate the related eigenvector. The full set of three-dimensional modes for each $n$ were found by repeating the procedure over a fine grid of initial guesses for $\omega_n$ in the complex plane. Each calculation still required approximately 100 megabytes of memory, but a converged solution for each mode took only 5 minutes on an IBM RS6000 workstation.

## 6.5 Model Validation

Three assessments were made to ensure the accuracy of the body force compressor representation and the numerical schemes. The first assessment compared the steady axisymmetric

flow field predicted by the model with experimental measurements from a single stage compressor. The second assessment demonstrated the numerical accuracy of the linearized model by comparing calculated eigenmodes for a simple compressor situation with known analytical results. The third assessment demonstrated that the linearized body force model could predict non-trivial features of three-dimensional stall observed in a low-speed fan experiment.

### 6.5.1 Steady Background Flow Assessment

The steady body force model was assessed by reproducing the axisymmetric flow field in the NASA Stage-35 compressor rig. Measurements near stall showed spanwise nonuniformities in axial velocity of 30–40% of the mean velocity, and losses 7 times higher at the tip than near the hub [59]. The magnitude of these spanwise flow variations enabled an assessment that would challenge the model's capability to represent radial flow nonuniformities through body force distributions. Since the model assumed incompressible flow, the assessment was made against the results for five flow coefficients at the lowest rotor speed (70% design speed).

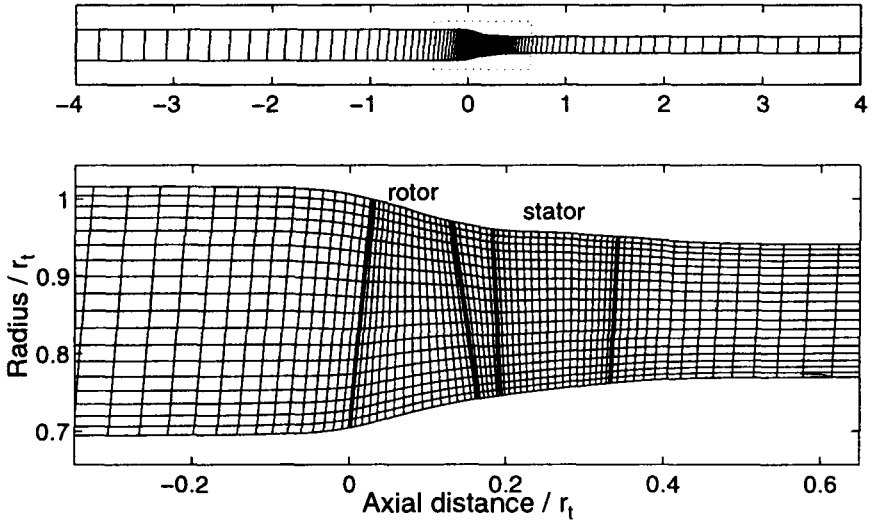


**Figure 6-2:** Computational mesh for Stage-35 compressor, with enlarged region indicated.

Stage-35 is a transonic compressor with a converging annulus (Figure 6-2), so an accurate representation of the flow throughout the entire compression system could not be expected with the incompressible flow model. The figures of merit for the assessment were

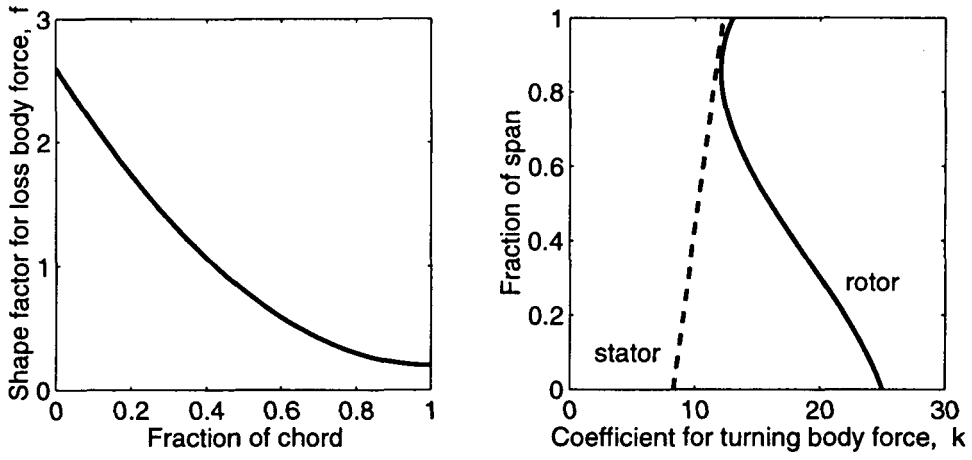


**Figure 6-3:** loss shape factor $f(s)$, and turning coefficient $k(r)$ used in Stage-35 calculations.

chosen as the velocity and pressure profiles local to the blade rows. Therefore, the density value used in the model was measured at the mid-gap, and the mass flow at each operating point was chosen to reflect the correct average axial velocity at the mid-gap plane.

The two-step procedure in Section 6.3 was followed to calculate the background flows. First, the measured losses at each of the five operating points were distributed along the chord according to the shape factor in Figure 6-3. The steady flow fields were calculated, adjusting the turning coefficients, $k(r)$, in the rotor and stator to provide the correct deviations (the final choice for $k$ is also in Figure 6-3). Second, correlations for the local loss coefficients were obtained from these five flow fields at each point in the blade rows. New steady flows were calculated again using these loss coefficient correlations.

The final loss and exit flow angles are compared against the experimental values in Figure 6-4. The comparison is very good because these were based on the "inputs" to the model. Spanwise profiles of the "output" variables (velocities and pressure) are compared in Figure 6-5. These values also compared well, especially at the rotor exit plane (near the mid-gap location). Upstream of the rotor, the average axial velocity was slightly low because of the annulus area change, but the spanwise variations have been reproduced.

Based on this comparison, it was judged that the steady computational model, using local loss coefficient correlations calculated from the two-step procedure in Section 6.3, could adequately reproduce the steady radial flow nonuniformities in a compressor.

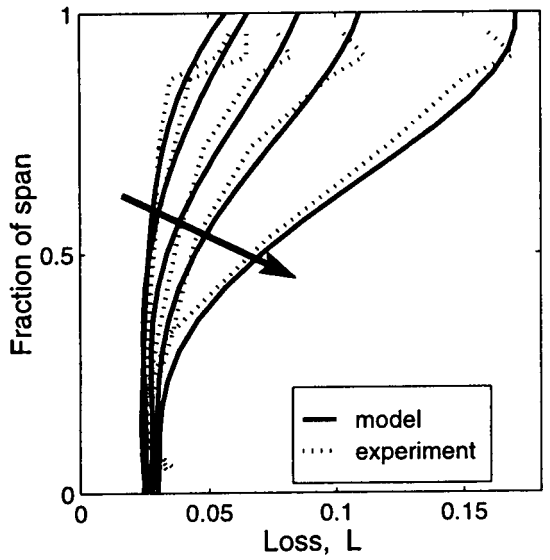


(a) Rotor loss

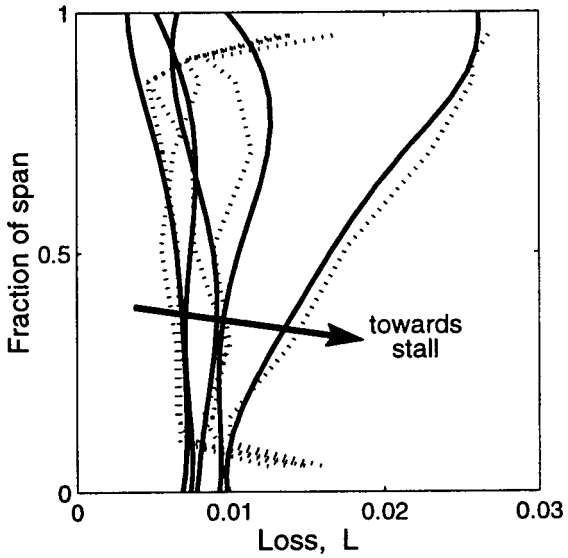


(b) Stator loss

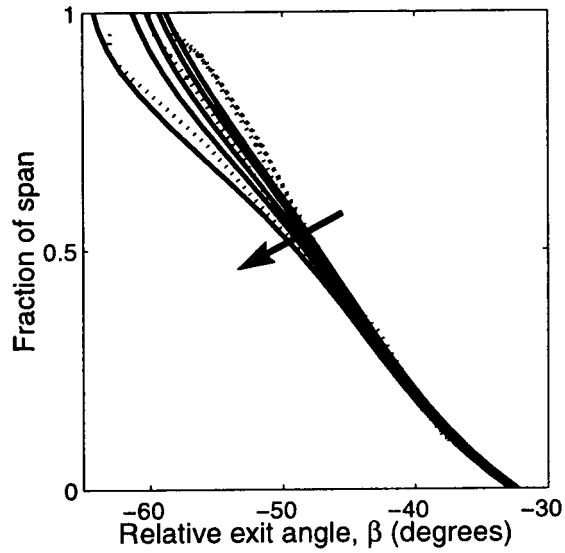


(c) Rotor relative exit flow angle

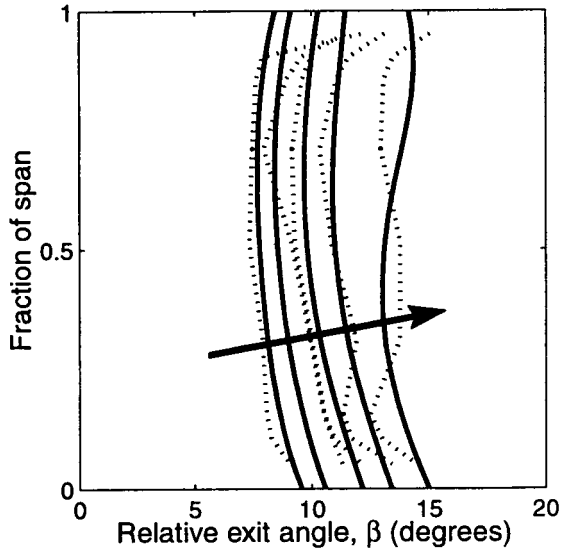


(d) Stator exit flow angle

**Figure 6-4:** Comparison of loss and relative exit flow angles between body force calculation and Stage-35 experiment. Comparisons made for 5 operating points approaching stall (indicated by arrow).

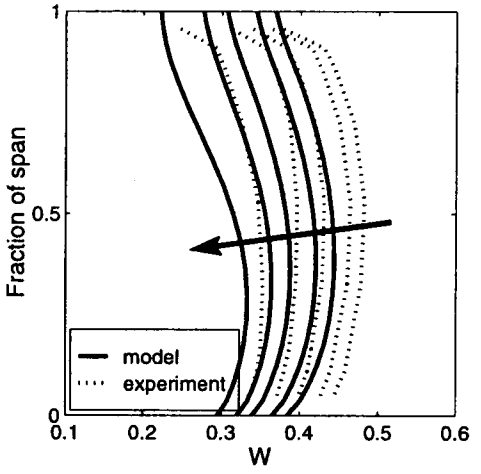


(a) Rotor inlet axial velocity

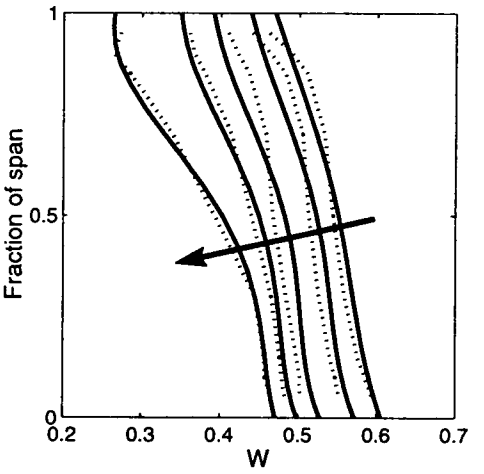


(b) Rotor exit axial velocity

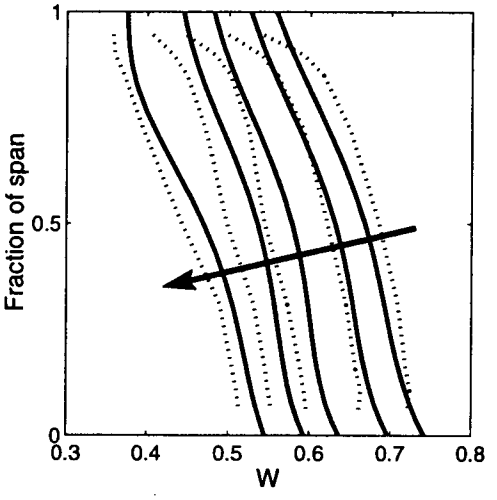


(c) Stator exit axial velocity

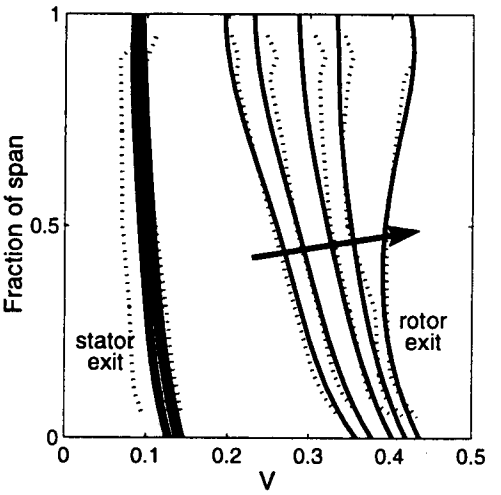


(d) Tangential velocity

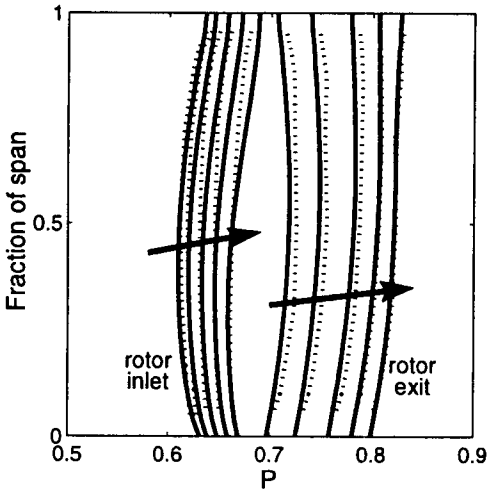


(e) Rotor static pressure

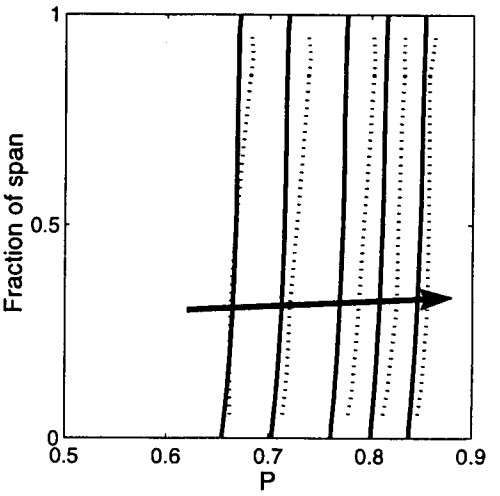


(d) Stator exit static pressure

**Figure 6-5:** Comparison of $\bar{V}$, $\bar{W}$ and $\bar{P}$ between body force calculation and Stage-35 experiment. Comparison made at 5 operating points approaching stall (indicated by arrow).

### 6.5.2 Assessment of Numerical Accuracy of Linearized Model

Analytical solutions for the modes in a uniform compressor geometry were used to assess the numerical accuracy of the linearized body force model. The computational mesh, shown in Figure 6-6, used 15 radial and 93 axial nodes, similar to the resolution used for the compressor studies in Chapter 7. To permit analytical solutions of the rotating stall modes (following the procedure in Section G.3), the compression system geometry was taken as rectilinear. Therefore, solely for the purpose of this assessment, the $1/r$-type terms for flow in a cylindrical geometry were neglected in the linearized body force model.

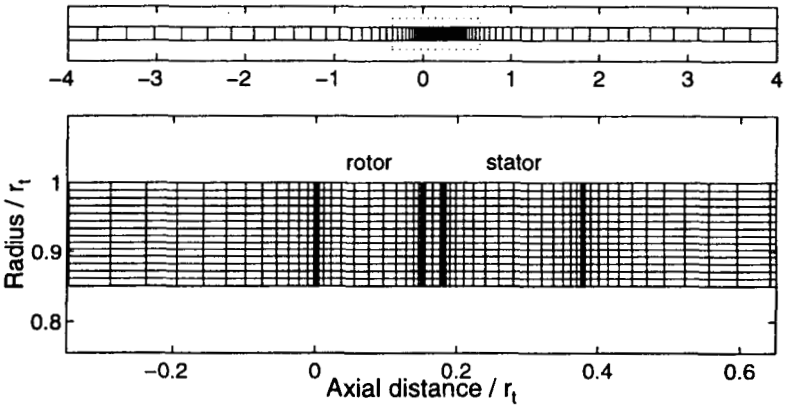


**Figure 6-6:** Computational mesh for analytic stall assessment, with enlarged region indicated..

The rotors and stators were modeled as flat-plates, inclined at $-60°$ and $10°$ respectively. The background flow was given by $\bar{W} = 0.5$ and $\bar{U} = 0$. Upstream of the rotor, $\bar{V} = 0$, but in subsequent regions, $\bar{V}$ changed to match the blade angles. Values for the body force derivatives and unsteady time constants used in the linearized model are shown in Table 6.1. These values are loosely based on average properties for the Stage-35 compressor.

**Table 6.1:** Compressor parameters used for the numerical accuracy assessment.

| Rotor | | Stator | |
|---|---|---|---|
| $\partial F_L/\partial W = -8.67$ | $\partial F_L/\partial V = -4.33$ | $\partial F_L/\partial W = -6.50$ | $\partial F_L/\partial V = 2.50$ |
| $\partial F_\theta/\partial W = -11.55$ | $\partial F_\theta/\partial V = -6.67$ | $\partial F_\theta/\partial W = 0.88$ | $\partial F_\theta/\partial V = -5.00$ |
| $\tau_L = 0.15$ | $\tau_\delta = 0.03$ | $\tau_L = 0.20$ | $\tau_\delta = 0.04$ |

The computed eigenvalues for the (1,0) and (1,1) modes compared well to the analytic

values (Figure 6-7a). The phase speeds differed by less than 0.25% of the rotor speed, and the growth rates differed by less than 3% of the rotor frequency. The magnitudes of the $p$, $w$ and $v$ perturbations for both modes also compared very well through the blade rows, as shown in Figures 6-7 and 6-8. Therefore, the numerical accuracy of the linearized body force model was sufficiently accurate to resolve both two- and three-dimensional stall modes.

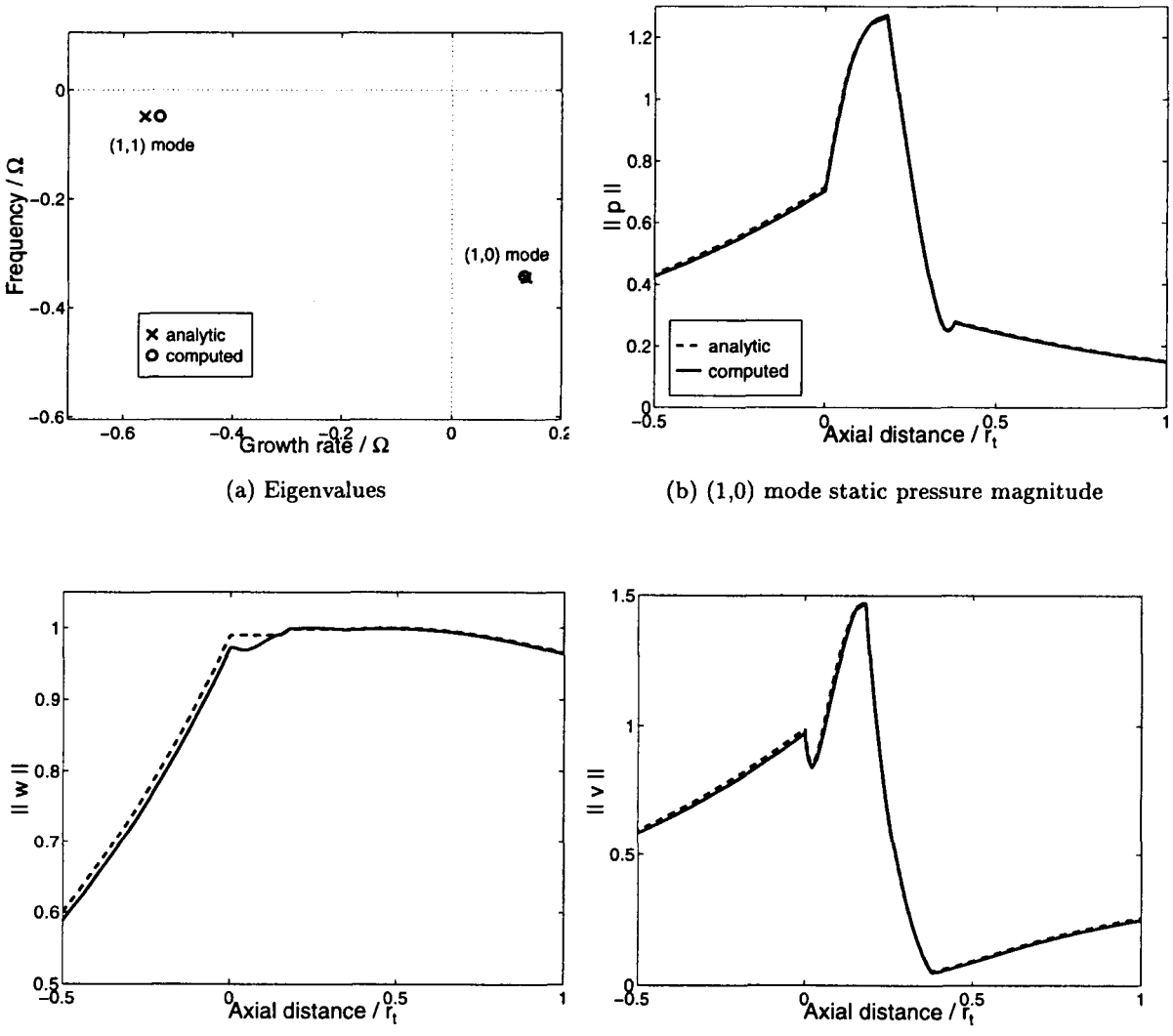


(a) Eigenvalues

(b) (1,0) mode static pressure magnitude

(c) (1,0) mode axial velocity magnitude

(d) (1,0) mode tangential velocity magnitude

**Figure 6-7:** Comparison of modes between body force calculation and analytic solution. (a) eigenvalues for (1,0) and (1,1) modes; (b), (c), and (d) magnitude of mode shapes (uniform across span) through compressor for (1,0) mode. Analytic and computational mode shapes are normalized so that maximum value of $\| w \|(z)$ is one.

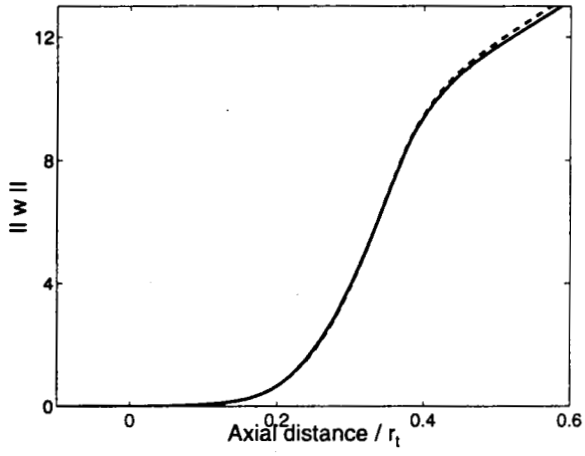


(a) (1,1) mode axial velocity magnitude

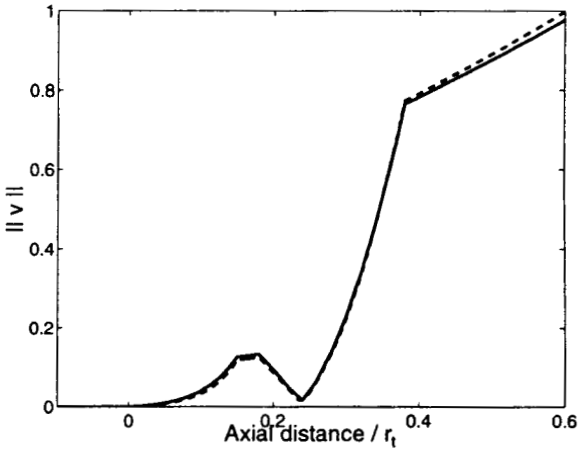


(b) (1,1) mode tangential velocity magnitude

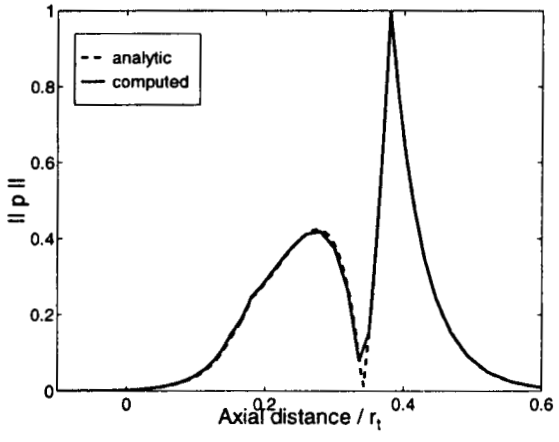


(c) (1,1) mode static pressure (plotted axially)

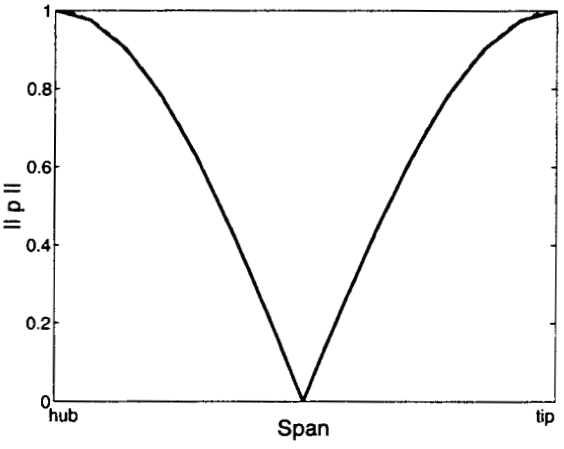


(d) (1,1) static pressure (across span)

**Figure 6-8:** Comparison of (1,1) mode between body force calculation and analytic solution. (a), (b), and (c) magnitude of mode shape along hub and tip casing through compressor; (d) magnitude of $p$ at stator exit plane. Analytic and computational mode shapes are normalized so that maximum value of $\| p \|(z)$ is one.

### 6.5.3 Assessment of Stall Inception in Low-speed Fan

The third evaluation of the body force model was its ability to reproduce three-dimensional rotating stall behavior observed in a low-speed fan experiment [67]. This particular experiment was chosen because the stalling behavior appeared to be modal, the flow was essentially incompressible (axial Mach numbers less than 0.07), and because there existed radial profile measurements of both the background flow and the rotating stall modes during stall inception for different compressor configurations. A comparison of two configurations demonstrated that increased radial nonuniformity of the background flow caused the compressor to stall at a more negative total-to-static characteristic slope. The more uniform velocity profiles corresponded to the *Reduced Tip Clearance* configuration, whereas increased nonuniformity in the *Thick Hub Boundary Layer* configuration was induced by a slotted fence attached to the hub at 0.83 mean-radii upstream of the fan. For the *Reduced Tip Clearance* case, the rotating stall mode was visibly larger in the tip region.

The figures of merit for the body force model assessment were (1) to observe stall at a more negative characteristic slope for the *Thick Hub Boundary Layer* simulation, compared to the *Reduced Tip Clearance* case, and (2) to reproduce the radial variation of the mode shape. These are phenomena that can not be captured using a two-dimensional analysis.

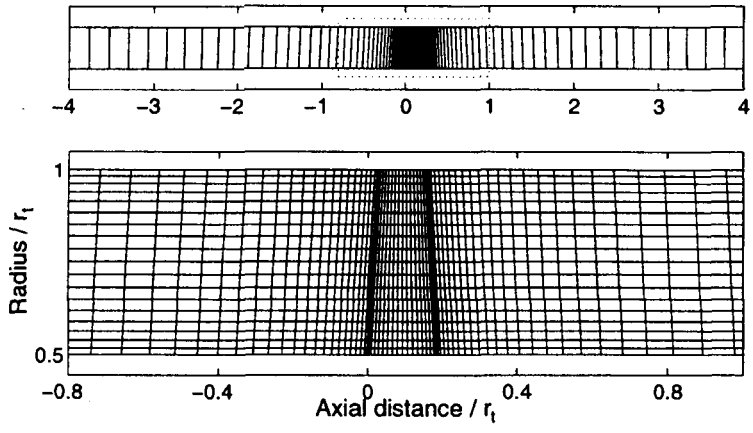


**Figure 6-9:** Computational mesh for low-speed fan, with enlarged region indicated..

The fan was modeled by the computational domain in Figure 6-9. For each configuration, measurements of $\bar{W}$, $\bar{V}$, and the characteristic $\Psi$ were provided at many radial positions [66]. The loss profiles required for the model were calculated as the difference between an isentropic pressure rise characteristic and the measured characteristic. The

isentropic pressure rise characteristic was calculated from the velocity measurements as

$$\Psi_i = r_{out}\bar{V}_{out} - r_{in}\bar{V}_{in} - \frac{1}{2}(\bar{U}_{out}^2 + \bar{V}_{out}^2 + \bar{W}_{out}^2)\,,$$

where $\bar{V}_{in} = 0$ upstream of the fan, and $\bar{U}_{out}$ was assumed to be negligible. The computed losses were distributed across the chord using the same shape factor $f(s)$ as for the Stage-35 model in Figure 6-3.

The inlet boundary condition for the model used uniform axial velocity for the *Reduced Tip Clearance* case, but radially distorted flow in the *Thick Hub Boundary Layer* configuration to account for the blockage caused by the slotted fence. The distorted flow profiles were based on linear fits of the fan inlet velocity near the hub and in the free stream, joined smoothly near the junction of the linear segments (Figure 6-10). The steady velocity profiles calculated by the model compared well with the experimental measurements in Figures 6-11 and 6-12.

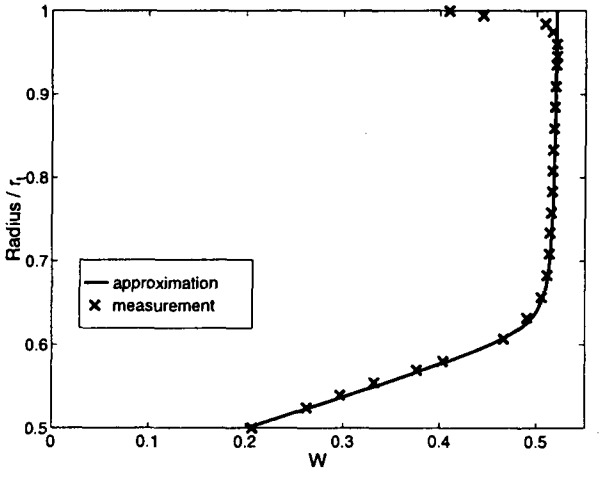


**Figure 6-10:** Example of distorted inlet $\bar{W}(r)$ profile for "thick hub boundary layer" configuration calculated from rotor inlet velocity profile.

For each configuration, the linearized body force model predicted stall on the negatively sloped part of the overall compressor characteristic (Figure 6-14), which was consistent with the experiment (Figure 6-15). Furthermore, for both the model and experiment, the *Thick Hub Boundary Layer* case stalled at a slope approximately twice as negative as for the *Reduced Tip Clearance*. This demonstrated that the model could capture the destabilizing effect of background flow nonuniformities.

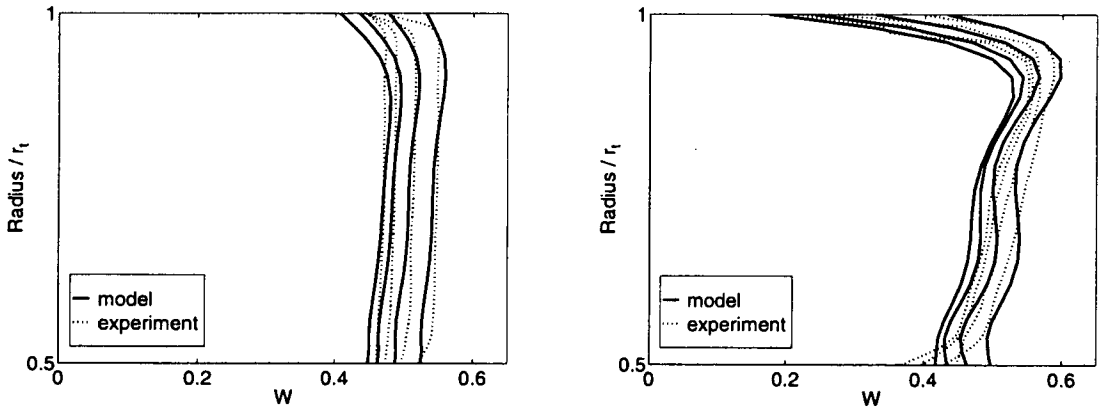


(a) Rotor inlet (b) Rotor exit

**Figure 6-11:** Comparison of axial velocity between body force model and low-speed fan experiment (reduced tip clearance configuration).

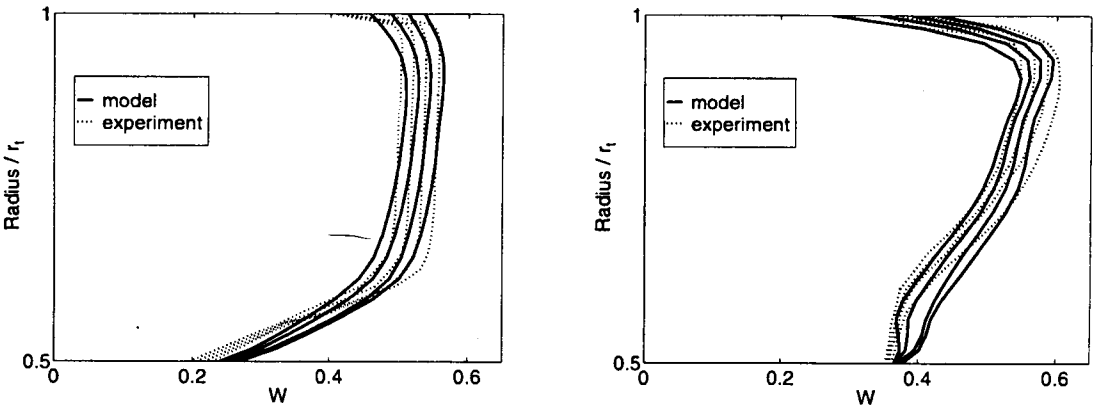


(a) Rotor inlet (b) Rotor exit

**Figure 6-12:** Comparison of axial velocity between body force model and low-speed fan experiment (thick hub boundary layer configuration).

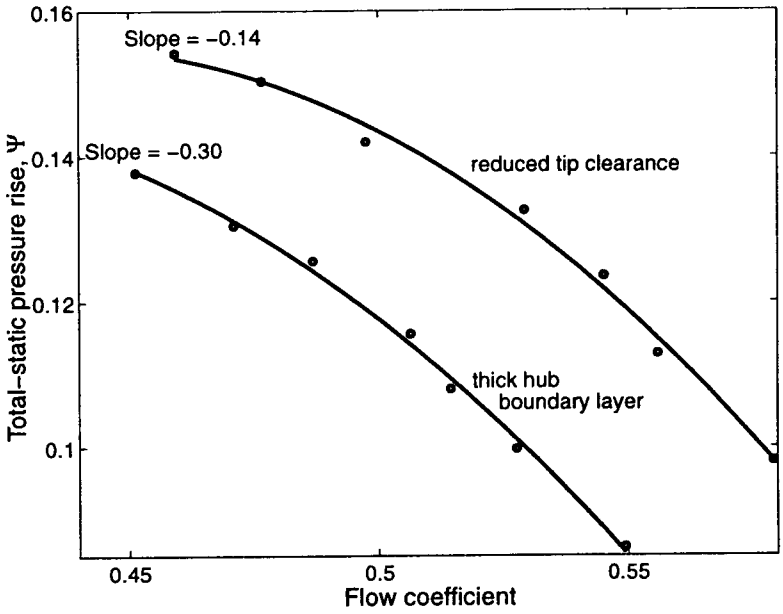


**Figure 6-13:** Measured characteristics and cubic polynomial fits for low-speed fan experiments (from [67]). The compressor stalled at the indicated slope of the best-fit curves.

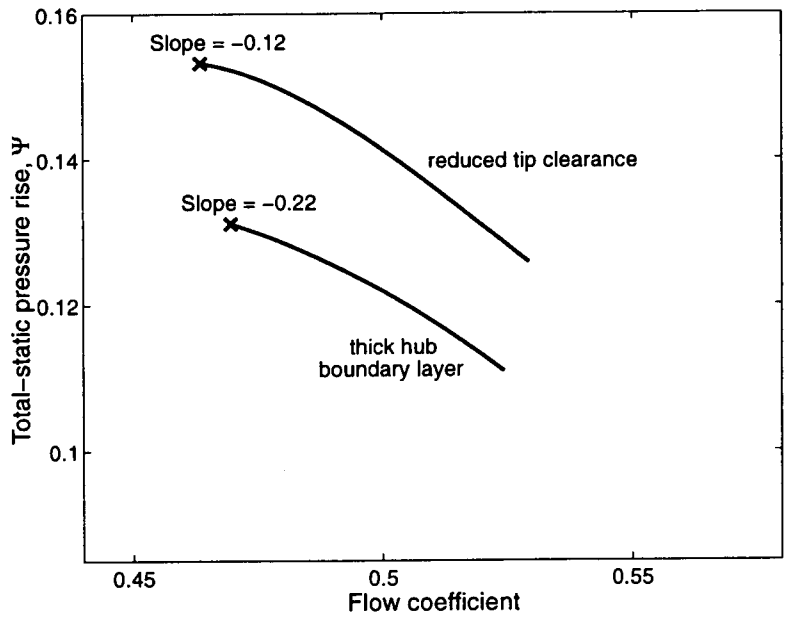


**Figure 6-14:** Computed characteristics and stall points using the body force model. The slopes at stall are indicated at the peaks of the characteristics.

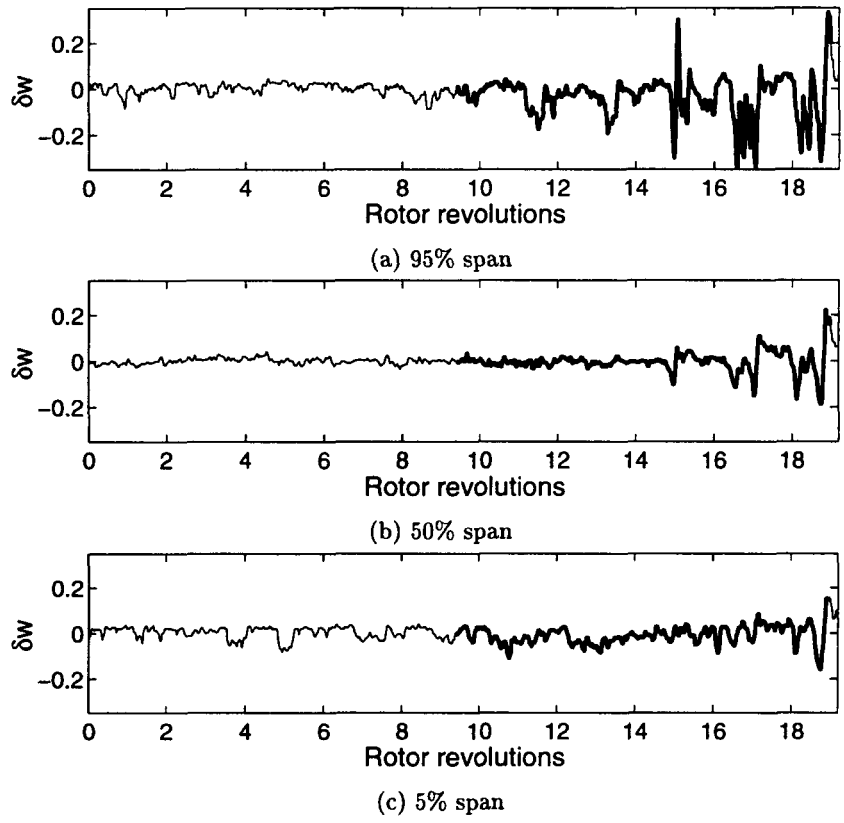


**Figure 6-15:** Axial velocity measurements during stall inception for reduced tip clearance configuration. Traces from hot wire measurements at three radial locations, 40% chord upstream of rotor (from Soundranayagam [66]).

The radial shape of the stall mode in the experiment was determined from the raw axial velocity traces. Stall inception measurements were taken upstream of the fan at 5%, 50% and 95% span (Figure 6-15). The strength of the signals associated with each frequency was computed for the darkened portions of the three traces during the growth of the stall cell. MATLAB's Power Spectral Density (PSD) routine [50] demonstrated that the strongest signal was at the tip, with a frequency near 65% of the rotor (Figure 6-16). This frequency was close to the predicted value of 70% rotor frequency for the most unstable mode computed by the linearized model. The square root of the shaded areas under the PSD curves provides a measure of the perturbation amplitude traveling at this frequency. These values are compared to the predicted mode shapes in Figure 6-17. For both cases, the disturbance magnitude near the hub is about one-third as large as at the tip.

In summary, the three-dimensional generalized body force model developed in this chapter has demonstrated the ability to accurately reproduce steady background flow fields, as well as unsteady three-dimensional stall behavior. It has been shown to be adequate to

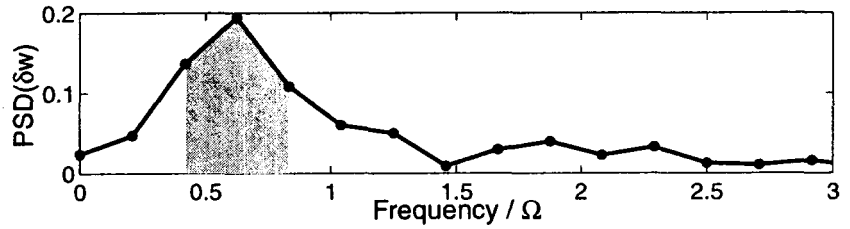


(a) 95% span

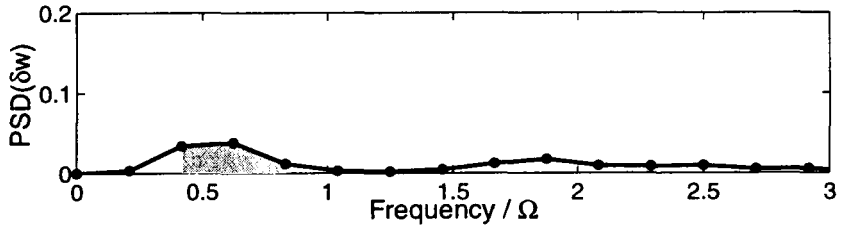


(b) 50% span

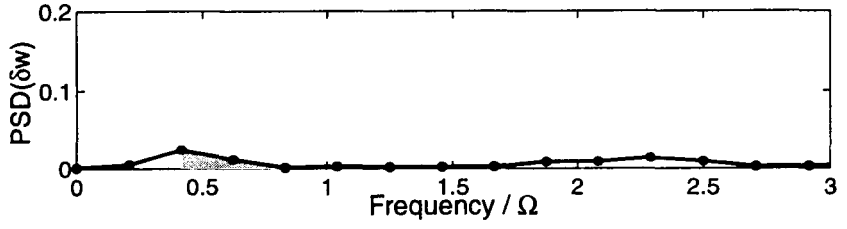


(c) 5% span

**Figure 6-16:** Power spectral density of velocity traces in Figure 6-15 denoting shaded region used to calculate magnitude of rotating stall mode.

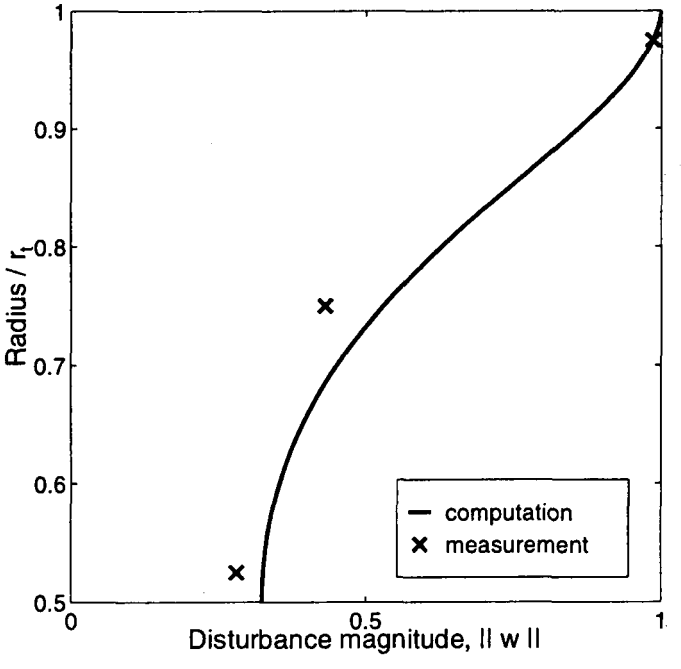


**Figure 6-17:** Comparison of calculated and measured rotating stall mode shape. Axial velocity disturbances normalized to have equal amplitude at 95% span.

be used for the parametric studies of spanwise compressor nonuniformities on stall inception in the following chapter.

## 6.6 Two-dimensional Version of Body Force Model

A two dimensional version of the body force compressor stability model was also developed to allow comparisons with the three-dimensional model. Such comparisons were required to answer the question posed in the objectives: "when are two-dimensional stability methods sufficient, and when are three-dimensional analyses necessary?" It would have been misleading to compare the 3-D body force model to existing 2-D actuator disk models, since the blade row representations would be different. Even two-dimensional stall predictions are sensitive to variations in the actuator disk model such as including unsteady losses and deviations, swirl-sensitivity, replacing lumped blades with individual blade rows, etc. [71, 47].

The new two-dimensional body force model was based on spanwise averages of radially-varying compressor properties (both annulus geometry and blade performance). Axial variations of flow properties were therefore maintained. This allowed back-to-back comparisons with the 3-D model to establish how radial flow variations directly affected compressor stability. Details of the 2-D model are described in Appendix J.

# CHAPTER 7

# STUDIES OF ROTATING STALL WITH 3-D BODY FORCE COMPRESSOR MODEL

Parametric studies of rotating stall in various compressor geometries were performed using the three-dimensional generalized body force model to determine whether the two-dimensional analysis was sufficient, or whether there existed practical compressor situations for which the three-dimensional analysis was required. The studies were also used to unequivocally resolve the effect of radial flow variations on compressor stability. Recall from Chapter 5 that flow field variations destabilized the modes in the actuator plane model, and also induced spanwise nonuniformities in the mode shape. For uniform background flow, however, mode shapes with spanwise nonuniformity were stabilized through redistributions within the blade passage. The present body force compressor model was designed to account for both radial flow nonuniformities *and* flow redistribution in the blade rows.

The studies in this chapter constitute the first numerical investigations of three-dimensional modes in annular compressor geometries with radial flow variations. Eighteen compressors were studied, divided between single and multistage configurations. Basic properties of the compressor geometries and steady performance characteristics are described first in this chapter, as well as the reasons each were considered.

The effect of radial flow variations on stall inception is best understood by separately examining the effects on "quasi-2D" and "higher-order 3-D" modes. Characteristics of the quasi-2D modes are examined first, since they were usually found to be the mode leading to

instability. The radial profile of the pressure rise characteristic *slope* was isolated as the key factor affecting these modes. Spanwise variation in the rotor characteristic slope was found to directly influence the mode shape nonuniformity. The stall point was determined by the integrated average of the blade row characteristic slopes weighted by this mode shape. These links between the slope variation, mode shape and stall point show how radial flow nonuniformities destabilize a compressor.

Higher-order three-dimensional modes were generally more stable than quasi-2D modes. The radial variation of the compressor slope, the blade aspect ratio and the gap length all affected the relative importance between the two classes of modes. Three compressor configurations are described for which the higher-order modes actually led to rotating stall first. For each of these cases, one with an annulus area contraction, one with radial inlet flow distortion, and one with mismatched blade rows, the controlling principles that caused the higher-order modes to have a higher growth rate than the quasi-2D modes are explained.

Finally, trends from these studies are synthesized to quantify the differences between two-dimensional and three-dimensional stability analyses. The 2-D analysis predicted stall at a higher flow coefficient than the 3-D analysis. The difference was largest for compressors with a flat characteristic shape near the peak and large radial variations in characteristic slope. Two-dimensional analyses did not even predict the correct stall mode for the three configurations with higher-order 3-D mode inception. The relevance of these cases to practical compressor operation is discussed, as well as a potential connection between higher-order 3-D modes and spike stall inception.

## 7.1 Scope

Descriptions of the eighteen compressor configurations used for the studies are provided here, highlighting variations in their geometry and steady background flows that led to differences in stall behavior. The methodology used to analyze the stability of each configuration is outlined at the end of the section. Details required to reproduce these flows are deferred to Appendix M. Also in the appendix are plots of the overall pressure rise characteristic and radial profiles of blade row performance and background flow for each study.

The scope of the parametric studies were limited to low-speed, steady axisymmetric

background flows. The modeled flow was incompressible and linear, eliminating so-called *compressible modes* [35] from consideration and precluding investigation of nonlinear spike stall inception. These restrictions were reasonable in context of the goal of this research, which was to investigate differences between two-dimensional and three-dimensional analyses.

### 7.1.1 Compressor Configurations

The effect of radial flow nonuniformities on stall was mostly investigated using single-stage compressors. This was chosen to keep computational resources tolerable but still provide the level of numerical accuracy seen in the model assessment (Section 6.5). Key features of each compressor configuration (indicated by a letter from A to X) are summarized in Table 7.1. The modes leading to instability are listed at the right for later reference.

**Table 7.1:** Parametric studies performed using the 3-D body force model.

Single-Stage

| | Compressor geometry/flow | Critical mode |
|---|---|---|
| A | Baseline | (1,0) |
| B | Maximum rotor loss nonuniformity (tip/hub=8) | (1,0) |
| C | Uniform rotor loss profile | (1,0) |
| D | Uniform rotor and stator loss profile | (1,0) |
| G | Maximum rotor exit angle variation (tip−hub=50°) | (1,0) |
| H | Uniform rotor exit angle | (1,0) |
| J | Maximum stator exit angle variation (tip−hub=20°) | (1,0) |
| K | High hub-to-tip ratio (0.9) | (1,0) |
| L | Low hub-to-tip ratio (0.35) | (1,0) |
| P | Small gap (9% chord) | (1,0) |
| Q | Large gap (60% chord) | (1,0) |
| R | Slowly converging duct | (1,0) |
| S | Rapidly converging duct | (1,1) |
| T | Inlet $\bar{W}(r)$ distortion (high velocity at tip) | (1,0) |
| U | Inlet $\bar{W}(r)$ distortion (low velocity at tip) | (1,1) |

Multistage

| | Compressor geometry | Critical mode |
|---|---|---|
| V | Baseline | (1,0) |
| W | Inlet guide vane turned −15° | (1,0) |
| X | Inlet guide vane turned −25° | (1,1) |

Compressor parameters varied between studies include the overall meridional geometry (annulus shape, hub-to-tip ratio, gap lengths), nonuniformities in blade performance (losses and turning), stage mismatching, and inflow distortion. Generally, one parameter was varied at a time from the baseline configurations to isolate its effect on stall. Values of these parameters were chosen to reflect the range of compressor designs in current engines and experimental rigs.

### Single-stage baseline (A)

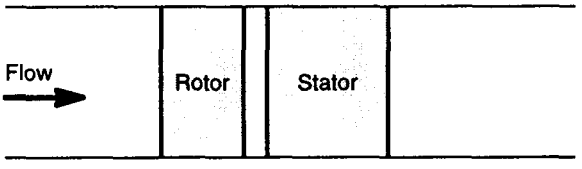


**Figure 7-1:** Scale meridional view of baseline single-stage compressor.

The baseline single-stage configuration (case A) was a 0.7 hub-to-tip ratio compressor, depicted in Figure 7-1. The blade design and performance were loosely based on the Stage-35 compressor rig, which was in turn characteristic of the inlet stages of an advanced-core compressor [59]. Blade design parameters are listed in Table 7.2 for comparison with subsequent configurations. Radial profiles of the losses, deviation, axial velocity and pressure are provided in Appendix M.

**Table 7.2:** Blade row design for single-stage baseline compressor.

| | Rotor | Stator |
|---|---|---|
| Height / mid-span chord | 1.2 | 1.2 |
| Mid-span stagger angle | $-50°$ | $20°$ |
| Loss profile ratio (tip:hub) | 4 : 1 | 2 : 1 |
| Blade exit angle (tip,mid,hub) | $-53°, -43°, -25°$ | $2.5°, 3°, 3.5°$ |
| Gap / mid-span rotor chord | 0.18 | |

### Radial nonuniformity of blade performance (B,C,D,G,H)

The blade loss profile was varied from the baseline in three studies. Studies B and C used extreme variations of the rotor loss nonuniformity. For B, the ratio of rotor loss from tip to hub was twice that of the baseline at each operating point, so that the tip loss was 8 times

higher than at the hub. For C, the loss in the rotor was held uniform across the span. Case D was the same as C, except the loss profiles in the stator were also radially uniform.

The extent of blade twist was varied in studies G and H to change the radial distribution of work done on the fluid. For G, the blade twist was increased so that the relative exit angles at the tip, mid-span and hub were -73, -43 and -23 degrees. The difference of 50° across the span was extreme for the blade size, and was as large as the variation in a 0.5 hub-to-tip ratio fan [67]. The opposite extreme was taken for H, for which the rotor exit angle was uniform across the span.

The rotor loss and turning distributions indirectly affected the axial velocity profiles. The velocity was lowest in regions of high loss and low turning (high relative exit angle), which can be seen from radial equilibrium arguments. At the mid-gap plane, axial velocity variations of 60–80% of the mean value were generated by cases B and G (Table 7.3). Cases with uniform losses and rotor geometry induced velocity variations of less than 20%. These values bound typical compressor values of 25–50%, demonstrating that studies A through H constitute a wide range of flow variations.

**Table 7.3:** Axial velocity nonuniformity at mid-gap for studies A through H.

| | A | B | C | D | G | H |
|---|---|---|---|---|---|---|
| $(\bar{W}_{max}-\bar{W}_{min})/\bar{W}_{mean}$ | 47% | 62% | 16% | 15% | 83% | 18% |

### Swirling downstream flow (J)

The effect of nonuniform, swirling downstream flow was examined with the twisted stator blade in case J. The stator exit angle varied between -5° at the hub to 15° at the tip, a difference larger than 5 to 10 degrees for typical stators [60].

### Hub-to-tip ratio (K,L)

Studies K and L were designed to investigate compressors with much higher (0.9) and lower (0.35) hub-to-tip ratios (Figure 7-2). The rotor blade geometries were interpolated or extrapolated from the baseline rotor so that the incidence profile remained approximately

constant at the design flow conditions. Therefore, the difference in exit angle from the tip to hub for case L (42°) was larger than for the baseline (28°) or for case K (10°). However, the difference in loss across the span was kept the same for each configuration. This assumed that the dominant source of losses near the tip were tip clearance and endwall effects, and profile losses dominated the core region, which would not necessarily change for blades of different hub-to-tip ratio.

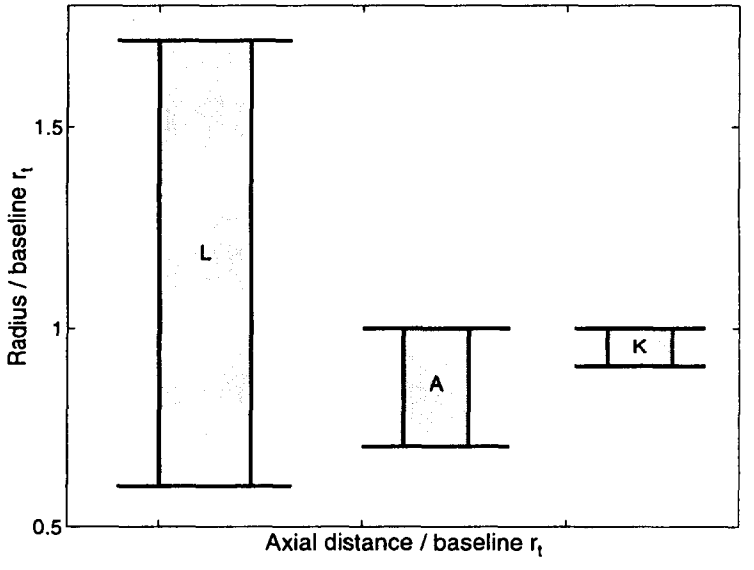


**Figure 7-2:** Scale meridional view of rotor blades with low (L), baseline (A) and high (K) hub-to-tip ratio.

### Inter-blade row gaps (P,Q)

The interaction between the rotor and stator was varied by changing the gap length. A minimal value of 9% rotor chord was used for case P. A large gap of 60% chord, representative of compressor rigs outfitted with inter-blade row instrumentation, was used for Q.

### Convergent annuli (R,S)

It was anticipated that acceleration of the mean flow in the axial direction would affect stability by reducing the total-to-static pressure rise across the compression system. Studies R and S both used an annulus with an overall 2:1 area ratio, keeping the same mid-gap area as the baseline case (Figure 7-3). This ratio was large compared to typical area changes

across a single blade row in engines, but was similar to the 1.9:1 area ratio in the Stage-35 rig. Local blade performance for each case was held as similar as possible to the baseline performance, meaning that the overall blade losses and turning were the same for each configuration at the same mid-gap flow coefficient. These studies investigated whether annulus area convergence could stabilize long wavelength 2-D modes while driving 3-D modes unstable through the local blade row characteristics.

For case R, the area changed proportionally to $\exp(\pm z)$ from the mid-gap location. This was specifically chosen as the potential decay rate of the most unstable two-dimensional rotating stall mode. The area change for study S was proportional to $\exp(\pm 8z)$. This was a more rapid convergence, similar to the Stage-35 annulus, that induced larger radial velocities.

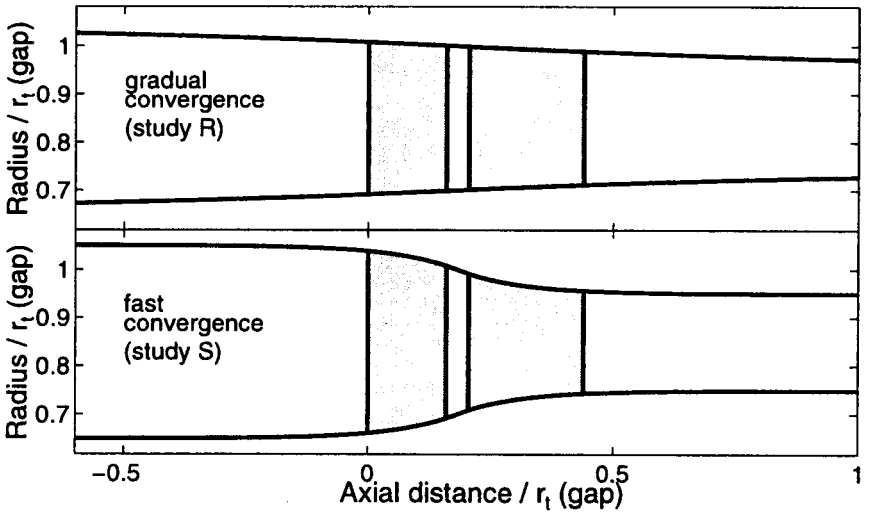


**Figure 7-3:** Illustration of converging annuli local to compressor blades (actual domain extends to $\pm 4r_t$)

### Radial distortion of inlet flow (T,U)

The largest compressor flow nonuniformities were caused by radial distortions of axial velocity imposed at the annulus inlet. Studies T and U imposed inlet distortions with low velocity at the hub and tip respectively. The velocity profiles were sinusoidal in $r$, with a ratio of 1.5 across the span (Figure 7-4). For an example low-speed compressor at a flow coefficient of 0.45, with mean wheel-speed of 200m/s, these distortions corresponded to a total pressure ratio of 0.96, and a total pressure difference of 0.8 times the mean dynamic head.

Therefore the strength of the inlet distortion was meaningful, similar to the largest radial distortions in stall experiments by Reid (total pressure ratio of 0.952) [58], and Spakovszky et al. (total pressure difference of 1.0 dynamic head) [70].

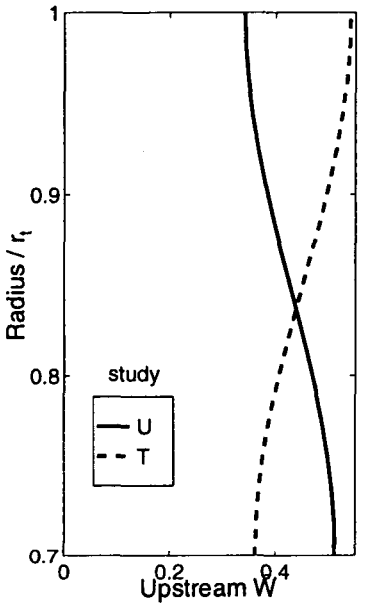


**Figure 7-4:** Radial profiles of inlet axial velocity

### Multistage baseline (V)

The baseline multistage configuration (Figure 7-5) was loosely based on the 0.75 hub-to-tip ratio, low-speed compressor rig at the University of Cambridge [4]. Only the first 2 1/2 stages were modeled to reduce the computational requirements. For this configuration, the blade exit angles for the stators and inlet guide vane were identical, so that the incidence on each rotor was similar.

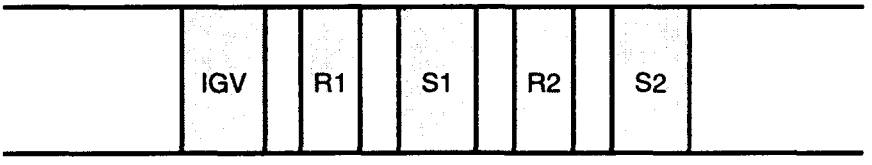


**Figure 7-5:** Scale meridional view of baseline multistage compressor.

### Mismatched compressor stages (W,X)

The goal of the mismatched compressor studies was to investigate whether three-dimensional modes local to the most unstable stage could be destabilized before the entire compressor became unstable to longer wavelength, quasi-2D modes. Mismatched configurations were obtained by re-staggering the inlet guide vane to increase the loading on the first rotor. For cases W and X, the IGV was rotated by -15° and -25° respectively. Figure 7-6 shows that this had the desired effect of causing the first-stage characteristics to peak before the overall characteristics.

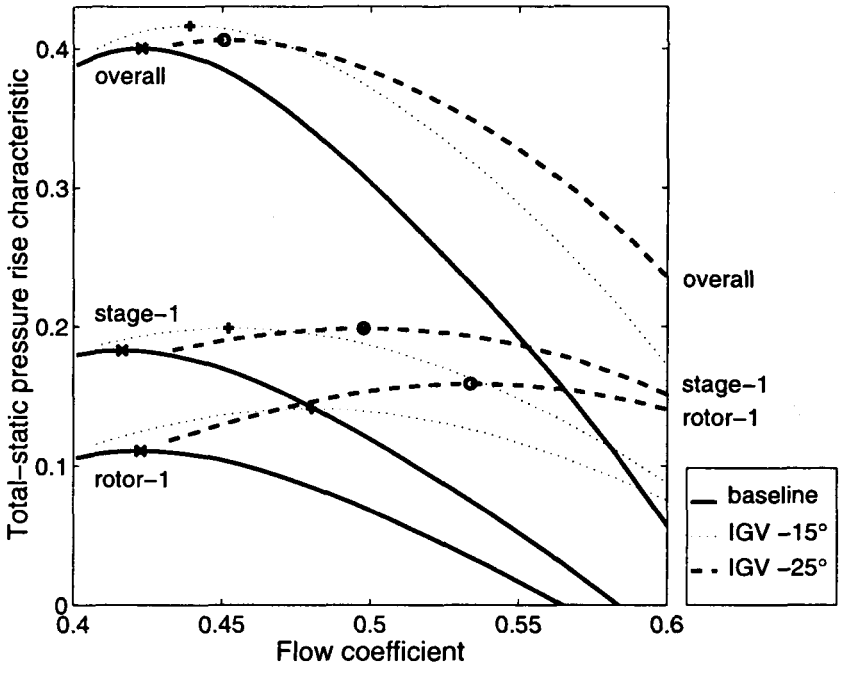


**Figure 7-6:** Total-to-static characteristics for the multistage compressors with varying degrees of mismatch. Three characteristics are drawn for each case corresponding to the first rotor, the first stage, and the overall compressor; peaks are marked with a symbol.

## 7.1.2 Approach

The stability analyses for each configuration used the following methodology:

- Steady, axisymmetric flow fields were calculated using the steady version of the three-dimensional body force compressor model (Section 6.2). The background flows were calculated at a minimum of 25 operating points to establish the overall compressor

characteristic up to, and past, the peak. The "two-step" procedure described in Section 6.3 was followed: the body force contributing to loss was initially fixed to produce the desired blade performance, then loss coefficient correlations based on those flows were used to recalculate the flow fields.

- Stability analyses were performed using the linearized version of the three-dimensional body force compressor model (Section 6.4). The modes of the compression system were calculated at a minimum of 5 operating points corresponding to the steady flows calculated above. For each operating point, modes with circumferential harmonics of $n = 1, 2, 3$ and 15 were calculated. The first harmonic was chosen based on the most unstable modes in previous actuator plane analyses. To confirm this would be the most unstable mode, the higher harmonics were investigated, including $n = 15$ which has a wavelength that approximates the circumferential length-scale of spikes.

- Steady, axisymmetric *two-dimensional* flows were computed corresponding to all background flows calculated with the 3-D model. The methodology for completing this step is outlined in Appendix J.

- Stability analyses of these background flows were performed using the linearized two-dimensional body force model in Appendix J. Purely two-dimensional modes corresponding to $n = 1, 2, 3$ and 15 were found at the same operating points chosen for the 3-D stability analyses.

Individual results of the three-dimensional background flows, eigenvalues and mode shapes for each study appear in Appendix M. Rather than presenting the stability results for each study here, the remainder of this chapter synthesizes these results to provide trends useful for understanding stall behavior. Three-dimensional results were compared between different studies to establish the effects of compressor design on stall. The merits of 3-D versus 2-D analysis were determined by comparing their respective predictions for each individual study.

An important parameter used to compare the stall points of the different studies was the slope of the total-to-static characteristic. Unless otherwise indicated, the slope corresponds to the *overall* characteristic, measured between the inlet and exit planes of the entire compression system, plotted against the average inlet flow coefficient. The character-

istics were constructed from the results of the background flow calculations, and the slopes numerically determined.

Local characteristics for the *compressor* or *rotor* were also used between planes bounding only the compressor or the individual blade row, respectively. Two forms of characteristics were used. The *mean* characteristics were defined as the difference between the area-averaged static pressure at an exit plane and the mass-averaged total pressure at an inlet plane. The slope was then taken as the derivative with the area-averaged axial velocity at the inlet plane. *Radially varying* characteristics were defined by the difference between the radial profiles of pressure at the exit and inlet planes, matched according to percent immersion from the hub. The slope was found at all radii using the local inlet velocity at the corresponding spanwise location.

## 7.2 "Quasi- Two-dimensional" Modes

The behavior of quasi-2D modes is discussed first because they were generally the most unstable modes in the studies. Understanding the effect of radial flow nonuniformities on these modes establishes the effect on typical compressor stability. The definition of a "quasi-two-dimensional" mode (as compared to "higher-order three-dimensional" modes) was discussed in Chapter 5. Put simply, quasi-2D modes correspond to the purely 2-D modes in two-dimensional analyses. Differences in how these modes behaved in three-dimensional flow are described in terms of rotating frequency, mode shape, and stability.

### 7.2.1 Rotating Frequency of Quasi-2D Modes

The rotating frequencies of the quasi-2D modes were not significantly different from the frequencies calculated by two-dimensional analyses (Figure 7-7). For the (1,0) mode in the baseline configurations (A and V), this difference was less than 0.5% of the rotor frequency. Even for the most extreme cases with inlet distortion, the difference was less than 10% of the rotor frequency. Therefore radial flow variations do not have a significant effect on the frequency of the rotating stall modes.

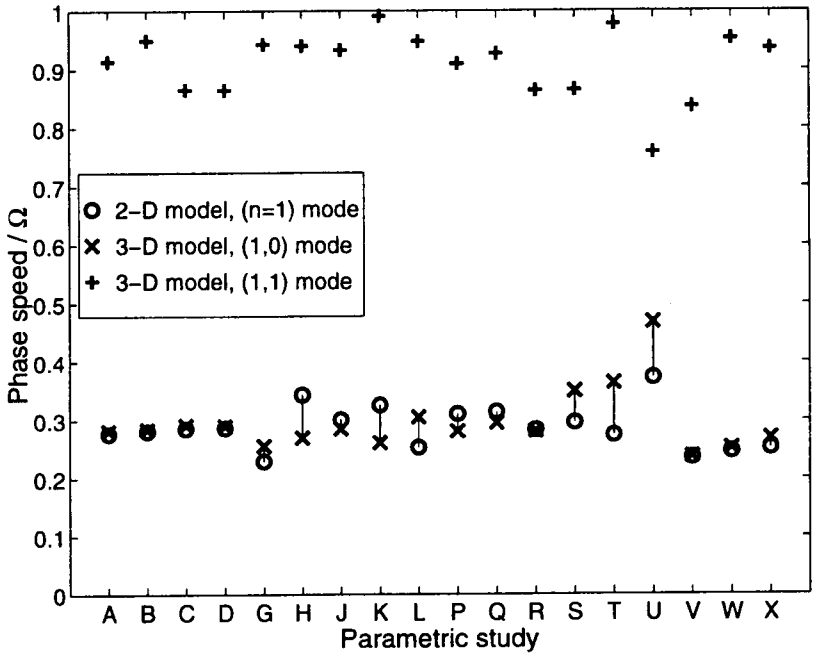


**Figure 7-7:** Phase speed for (1,0) and (1,1) modes calculated using 3-D analysis, and phase speed for 1st harmonic mode calculated using 2-D analysis.

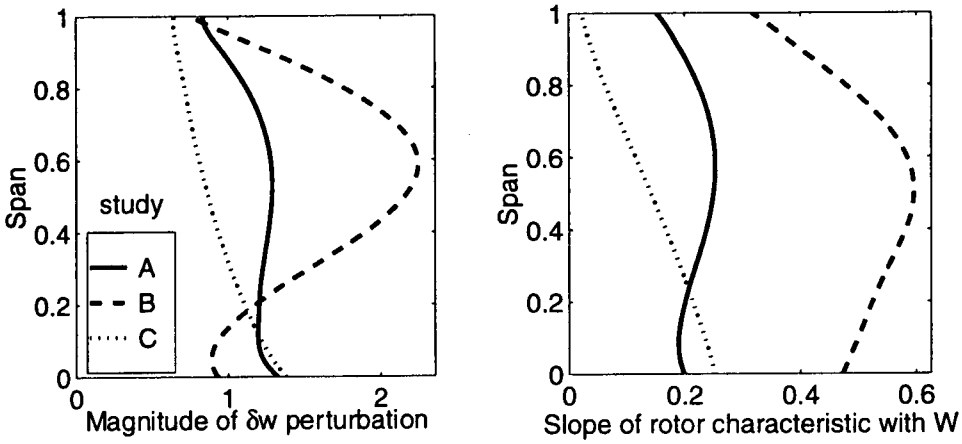


**Figure 7-8:** Comparison of (1,0) mode shape with nonuniformity of rotor characteristic slope for single-stage studies A, B and C. Axial velocity perturbations, plotted at mid-gap plane, have been normalized by perturbation magnitude at hub of rotor-inlet location.

### 7.2.2 Shape of Quasi-2D Modes

The radial structure of the quasi-2D modes was primarily determined by the spanwise variation of $d\Psi/dW$ across the individual blade rows. The mode amplitude was larger in regions of higher slope, similar to the trends observed with the actuator-plane model. In particular, it was the slope of the rotor characteristic that dominated the mode shape variation because the rotor was the more "unstable" component, operating on a positively sloped characteristic, whereas the stator operated on a negatively sloped characteristic (see Appendix M for plots of the characteristic slopes of each blade row). For example, Figure 7-8 demonstrates how closely the shape of the disturbance velocity amplitude after the rotor compared with the slope of the rotor characteristic for studies A, B and C.

Away from the rotor that originated the disturbance nonuniformity, pressure perturbations tended to become uniform, whereas velocity disturbance nonuniformities increased downstream of the rotor. A measure of the nonuniformity of both flow variables at the compressor inlet and exit is shown in Figure 7-9. This behavior is understood by examining the potential and vortical components of the disturbance generated by the rotor.

- Radially varying *potential* components of the disturbance flow quickly decayed away from the rotors. To illustrate this, the analytic solution for potential disturbances in uniform flow (Appendix E.1.1) showed that the decay rate of the $j^{\text{th}}$ radial mode was approximately $\exp(-j\pi z/[r_t - r_h])$. For $j = 1$ in a 0.7 hub-to-tip ratio compressor, this rate was over 10 times faster than the decay rate of the radially uniform mode ($\exp(-z)$). Therefore by the end of the compressor, the pressure perturbation was essentially uniform. Similarly, for the multistage configurations, the distance between the IGV and rotor was sufficient for the pressure nonuniformity to decay to less than 4% spanwise variation at the compressor inlet.

- Vortical disturbances generated by the rotor convected downstream with the mean flow. These disturbances grew in amplitude in spanwise regions of low mean velocity, just like the modes for the actuator plane model in sheared background flow. By the exit of the compressor, the amplitude of velocity perturbations could vary along the span by a factor of over an order of magnitude for the worst case examples. Even for the baseline configurations, the factor was between 2–4.

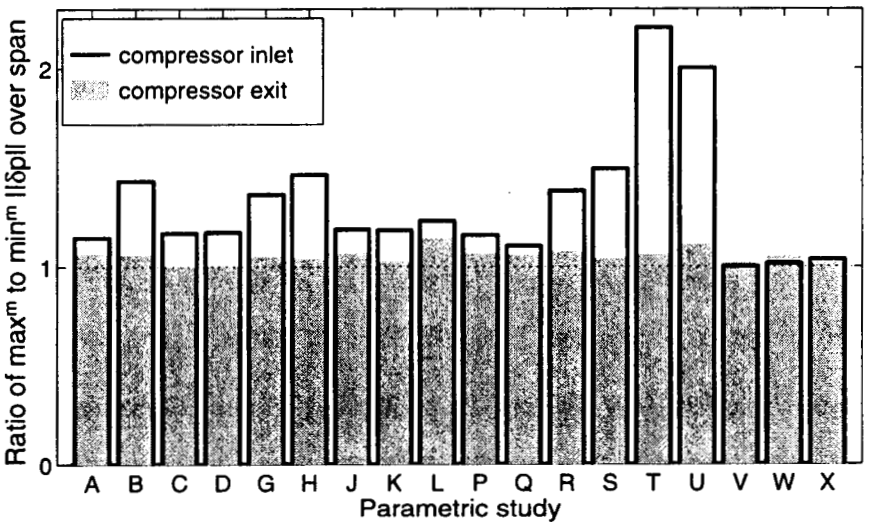


(a) Spanwise nonuniformity of static pressure disturbance

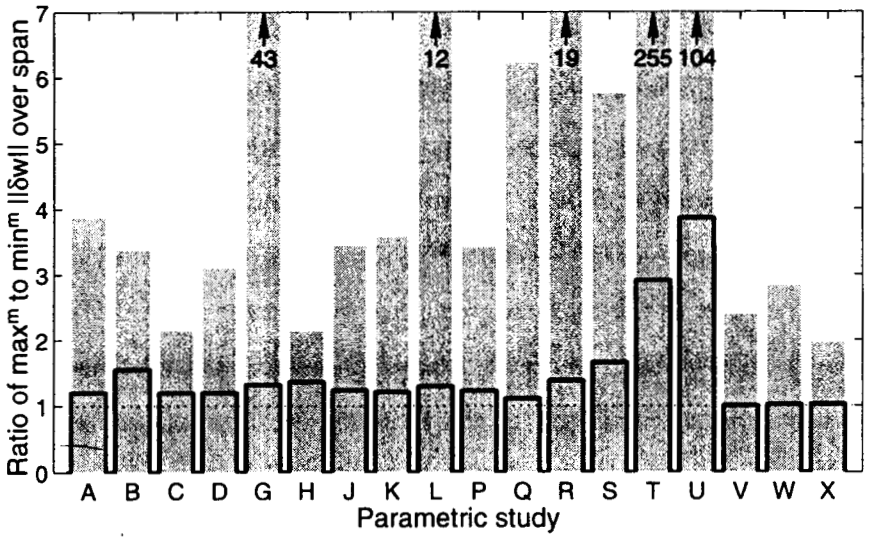


(b) Spanwise variation of axial velocity disturbance

**Figure 7-9:** Ratio of maximum to minimum amplitude of (1,0) mode shape across span. Results plotted for both inlet and exit planes of compressor.

The radial structure of the quasi-2D modes has implications for sensor placement and active control schemes, as discussed in Section 7.4. More importantly, radial mode shape variations are shown in the next section to be a key feature in understanding the mode's stability.

### 7.2.3 Stability of Quasi-2D Modes

The most unstable mode for each study was generally the lowest-order ($n = 1$) quasi-2D mode (Table 7.1). The relative values of all eigenvalues at stall are plotted for each study in Appendix M. Due to unsteady loss behavior, quasi-2D modes of higher circumferential harmonics were always more stable than their $n = 1$ counterpart, so only the (1,0) mode is discussed here.

The instability point for these quasi-2D modes was not at the peak of the total-to-static characteristic, but rather at various slopes ranging from -0.33 to 2.0 (Figure 7-10). However, the figure shows the important trend that the (1,0) mode stalled at a more negative slope than that calculated from the purely two-dimensional analysis.[1] Therefore radial flow nonuniformities had the effect of destabilizing quasi-2D modes.

The effect of flow field nonuniformities on stall inception can be better understood through disturbance energy conservation arguments. Fréchette [18] used such arguments to develop stability criteria for two-dimensional high-speed compressor flows. An extension of Fréchette's work, applicable for low-speed three-dimensional flow, is provided in Appendix K. The law of conservation of total fluid energy can be applied to quasi-2D modes, yielding the following stability criterion (from equation K.9):

$$\int_{\mathcal{A}_2} pw \, d\mathcal{A}_2 - \int_{\mathcal{A}_1} p_t w \, d\mathcal{A}_1 = 0 \,, \tag{7.1}$$

where $\mathcal{A}_1$ and $\mathcal{A}_2$ refer to the cross-sectional areas at axial planes at the inlet and exit of the compressor, respectively.

[1] The only exceptions were cases T and U, where the inlet distortion caused the overall characteristic to peak very sharply. As will be shown in Section 7.4, the differences in stalling flow coefficient between 2-D and 3-D analyses were minor for these cases (less than 1%), but were exaggerated in terms of slope in Figure 7-10 since the curvature of the characteristics near the peak were over 50 times higher than for the baseline configuration A.

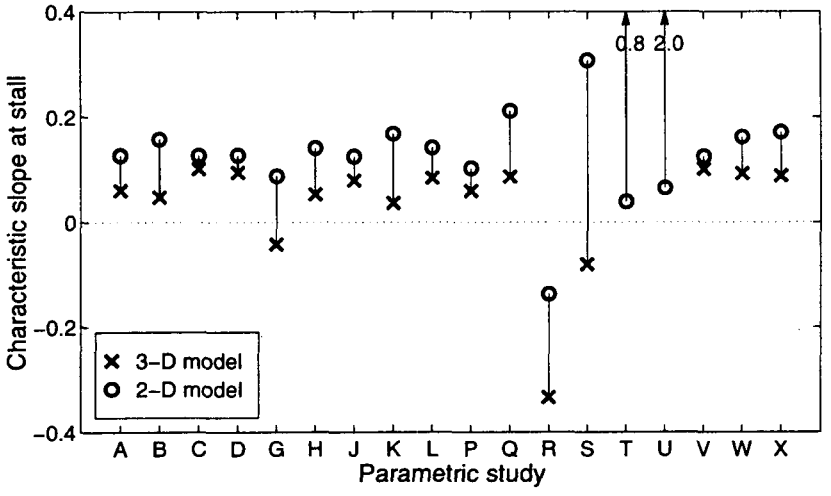


**Figure 7-10:** Overall characteristic slope ($d\Psi/dW$) at neutral stability for the (1,0) mode. Results calculated using 3-D and 2-D analyses. Note that the stall points for compressor studies S, U and X occurred sooner than shown here due to instability of higher-order 3-D modes.

Equation (7.1) implies that at neutral stability, there is a balance between the total *disturbance intensity*, $pw$, at the compressor exit and the energy-like quantity, $p_t w$, at the inlet. The physical meaning of this balance is more apparent for purely two-dimensional flow in an actuator disk compressor model. Then the cross-sectional areas and axial velocity perturbation are constant across the compressor, and the perturbational total-to-static pressure rise is related to the characteristic slope. Under these conditions equation (7.1) reduces to the *weighted integrated mean slope* criterion developed in Section 3.4.3 for circumferential flow nonuniformities:

$$\int_0^{2\pi} \frac{d\Psi}{dW}\, w^2\, d\theta = 0\ . \tag{7.2}$$

This demonstrates that the three-dimensional stability criterion (7.1) for quasi-2D modes is a more general expression of the WIMS criterion.

An analogy for the stability criterion (7.2) in three-dimensional flow has been derived in Appendix K and is reprinted below (from equation K.14):

$$\int_{\mathcal{A}} \left\{ \left[ \left( \frac{\partial \Psi_{TS}}{\partial W} w_{in} + \frac{\partial \Psi_{TS}}{\partial V} v_{in} \right) w_{in} \right]_{\text{blade}_1} + \sum_{i=2}^{N} \left[ \left( \frac{\partial \Psi_{SS}}{\partial W} w_{in} + \frac{\partial \Psi_{SS}}{\partial V} v_{in} \right) w_{in} \right]_{\text{blade}_i} \right\} d\mathcal{A} = 0. \tag{7.3}$$

This equation represents the integral of the blade row slopes weighted by the velocity disturbance, taken over the cross-sectional area at the inlet of each blade row. The slopes of the total-static characteristic are used for the first blade row and the static-static characteristic for subsequent rows.

Equation (7.3) approximates the perturbation to the total-to-static pressure rise across the compressor as the sum of the changes across each individual blade row. This is required since the axial velocity disturbance for quasi-2D modes varies through the compressor. Although equation (7.3) can be made more accurate by including unsteady losses, etc., the important message is that the stability of a quasi-2D mode is mainly determined by the integrated average of the slopes of the local blade rows, weighted by the mode shape.

This relation shows *why* radial flow nonuniformities destabilize compressors. The mode was distorted to larger amplitudes in regions of locally higher blade row characteristic slope. These regions of positive slope were then weighed more heavily in the balance between positive and negative slopes at stall in equation (7.3), so that the compressor was more unstable than for a configuration using the radially-averaged blade performance.

The stability criterion also demonstrates why it would not be correct to predict stall according to the "most unstable" spanwise region of the compressor based on two-dimensional strip-theory. This approach would only be correct if the mode shape was entirely localized at just one region of the compressor, which was not the case for the quasi-2D modes. A weighted balance of compressor performance must be made across the entire span.

It should be noted that the above stability criteria can not be directly used for stall *prediction* since they require prior knowledge of the mode shape. However, given the mode shape, equation (7.1) is useful for determining the compressor regions contributing to an increase in disturbance intensity. Redesigning the blade in regions of positive "energy" production could most effectively delay the onset of stall. For example, the profile of $p_2 w_2 - p_{t1} w_1$ for configuration P at stall (Figure 7-11) indicates that the tip region was responsible for the creation of disturbance "energy" that needed to be balanced by "energy" reduction near the hub. By reducing the rotor losses at the tip, such as for compressor design C, the corresponding profile of $p_2 w_2 - p_{t1} w_1$ was more uniform at stall. The result was that compressor C was more stable, stalling at a more positive slope and at a flow coefficient 1.1% lower than compressor P (Table 7.4).

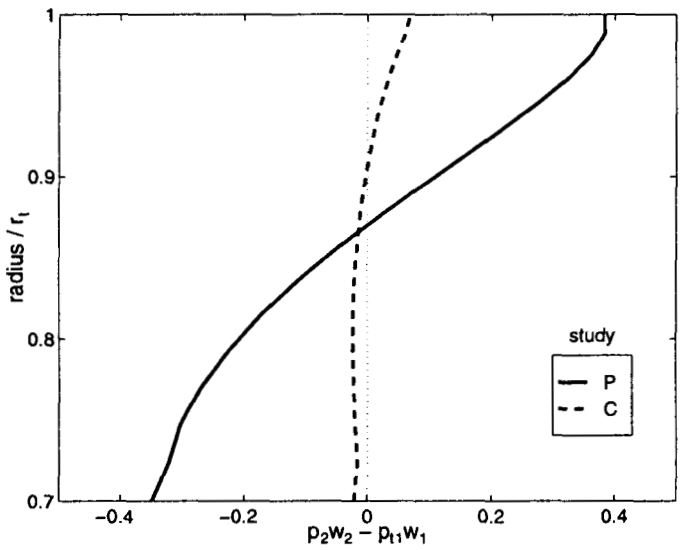


**Figure 7-11:** Radial profile of $p_2 w_2 - p_{t1} w_1$ at neutral stability for compressors P and C. Results for (1,0) mode, normalized by maximum amplitude of axial velocity disturbance at rotor inlet.

**Table 7.4:** Comparison of stall points between compressor P (nonuniform rotor losses) and compressor C (uniform rotor losses).

| | Compressor P | Compressor C |
|---|---|---|
| Slope at stall | 0.06 | 0.1 |
| Flow coefficient at stall | 0.366 | 0.362 |

### 7.2.4 Summary of Quasi-2D Mode Stall Inception

A summary of the behavior of quasi-2D modes is provided before continuing to the higher-order three-dimensional modes. Of the quasi-2D modes, the (1,0) mode was always the most unstable, and generally led to the instability of the compression system. The frequency of quasi-2D modes was essentially unchanged from that determined by two-dimensional analysis, but the mode shape was induced to larger amplitudes in spanwise regions of higher rotor characteristic slope. The stability point of these modes was related to an average through the compressor of the blade row characteristic slopes weighted by the mode amplitude. Regions of higher slope dominated this balance because of correspondingly large disturbance amplitudes, proving that radial blade performance nonuniformities tend to destabilize compressors.

## 7.3 Higher-order Three-dimensional Modes

Although the higher-order three-dimensional modes were generally more stable than the (1,0) mode, their importance to compressor stability can not be dismissed. Higher-order modes were often found at stall as lightly damped modes, which may become important with suitable forcing, or after actively controlling quasi-2D modes. To appreciate their importance, general characteristics of higher-order modes are discussed in this section in terms of their rotating frequency, shape and stability. Furthermore, three specific conditions are examined for which these modes were induced to go unstable *before* the quasi-2D modes. These results are used at the end of the section as the basis for a proposed connection between 3-D modes and spike stall inception.

### 7.3.1 Rotating Frequency of Higher-order Modes

The rotating frequency of the (1,1) mode was between 75% and 100% of rotor frequency, generally at least twice as high as for the (1,0) modes (Figure 7-7). Stall cell speed was shown by Cumpsty and Greitzer [8] to depend on the balance of inertia-induced pressure perturbations between stationary and rotating components. The higher frequency for the (1,1) modes was a consequence of being more localized, both radially and axially, so that they comprised less fluidic inertia in the inlet and exit flow fields. The eigenvalue plots in Appendix M show that the phase speeds for all other higher-order 3-D modes were bounded within 60–120% of rotor speed. Such observations were similar to the actuator disk results in Chapter 5 for which the phase speed approached the rotor speed for disturbances with increasing radial wavenumber.

### 7.3.2 Shape of Higher-order Modes

Higher-order 3-D modes were more radially localized and had larger axial variations than the quasi-2D modes. Figure 7-12 shows the radial profiles of the amplitude and phase of the (1,1) mode compared to the (1,0) mode for the baseline single-stage compressor. The amplitude of the higher-order disturbance was greatest near the hub and tip, with a minimum near the mid-span region. Generally, the sign of the velocity perturbation was opposite between these regions, evidenced by the rapid phase change. The disturbance

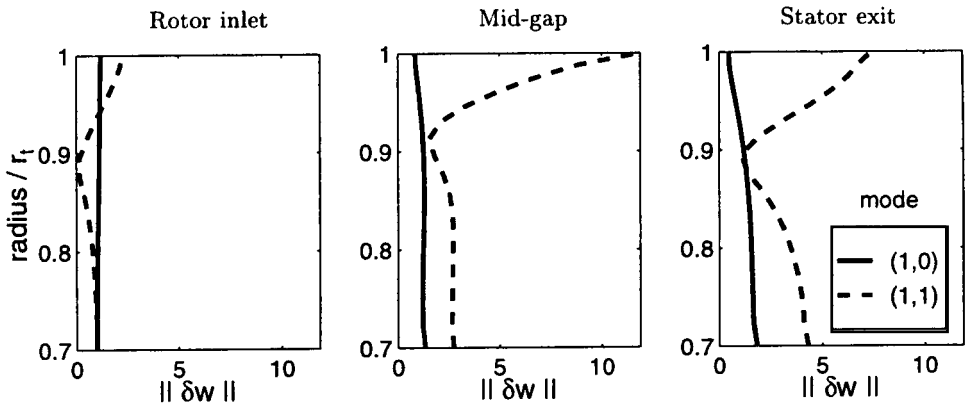


(a) Magnitude of axial velocity disturbance (normalized)

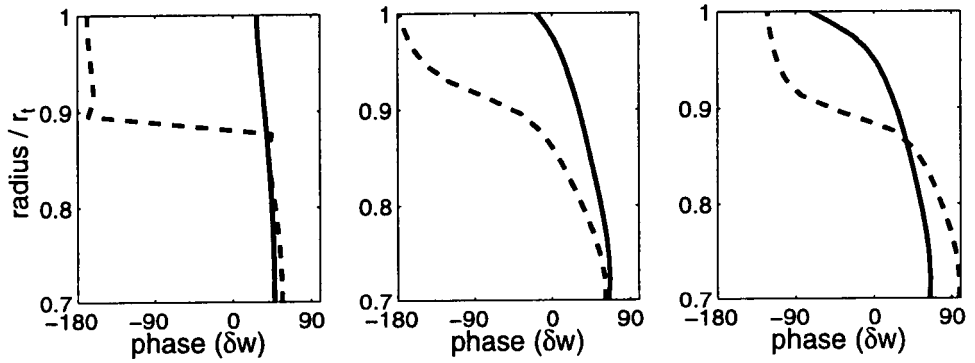


(b) Phase of axial velocity disturbance (in degrees)

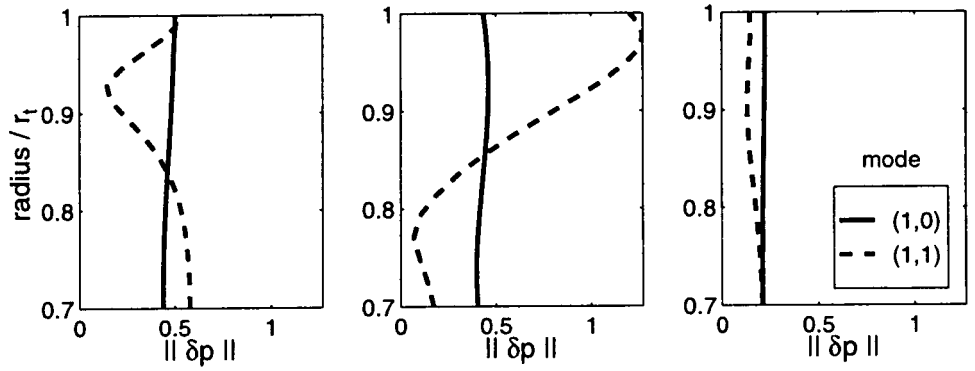


(c) Magnitude of static pressure disturbance (normalized)

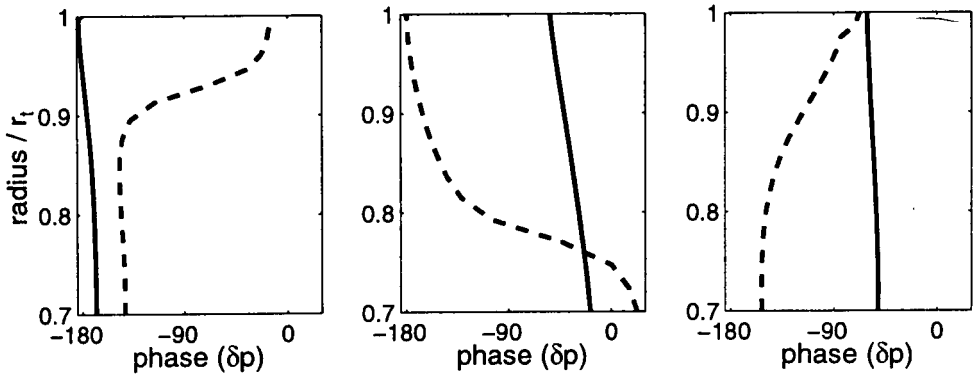


(d) Phase of static pressure disturbance (in degrees)

**Figure 7-12:** Radial profiles of the amplitude and phase of the (1,1) mode compared to the (1,0) mode. Mode shapes for compressor A at neutral stability, each normalized by the amplitude of the axial velocity disturbance at the hub of the rotor inlet.

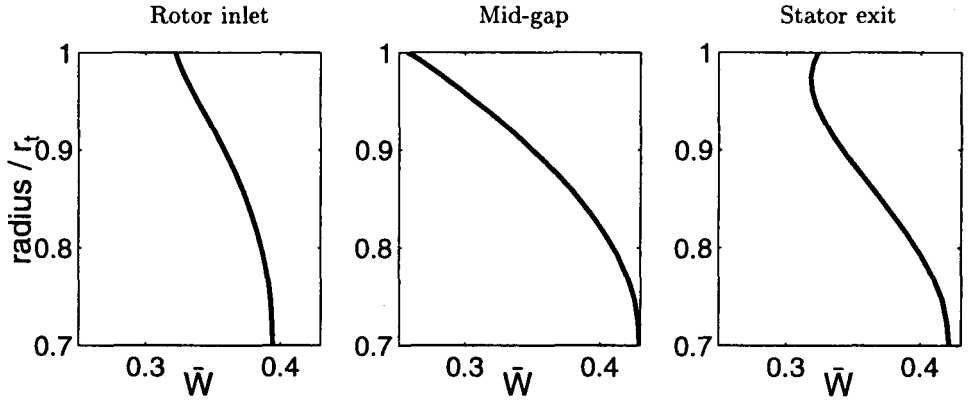


**Figure 7-13:** Radial profiles of background axial velocity for compressor A at stall.

flow field redistributed within the blade passages, causing large axial variations in the flow variables (the amplitude of tip $\delta w$ increased by a factor of four across the rotor alone).

Unlike the quasi-2D modes, the shape of higher-order 3-D modes did not necessarily reflect the rotor slope variation. For one reason, even in uniform flow, 3-D modes by definition include one or more amplitude minima across the span. For another, the concept of radial strip-theory across the blades is questionable for higher-order modes because of the large disturbance flow redistribution, so the local characteristic slope becomes less relevant to the disturbance pressure rise across each spanwise location. This was the case for compressor A, where the rotor characteristic slope (Figure 7-8) was smaller at the tip than the hub, but the amplitude of the (1,1) $\delta w$ disturbance was 4 times larger at the tip.

In many compressor cases, the background velocity profile was more important than the slope profile in determining the relative mode amplitude between the hub and tip. Recall from the actuator plane results with sheared background flow that the mode shape was larger in regions of low background velocity. Similar behavior explains the shape of the (1,1) mode for compressor A, which can be seen by comparing the steady axial velocity profiles in Figure 7-13 with the disturbance magnitude in Figure 7-12a. The mean axial velocity along the outer casing decreased through the rotor, then increased through the stator. Correspondingly, the mode amplitude at the tip radius increased through the rotor then decreased through the stator. Such trends were especially evident for the compressors with inlet distortion. For case U, the (1,1) mode shape was highly localized to the region of low background velocity at the tip, despite the maximum slope value occurring at the mid-span location (see Figures M-43 and M-45 in Appendix M).

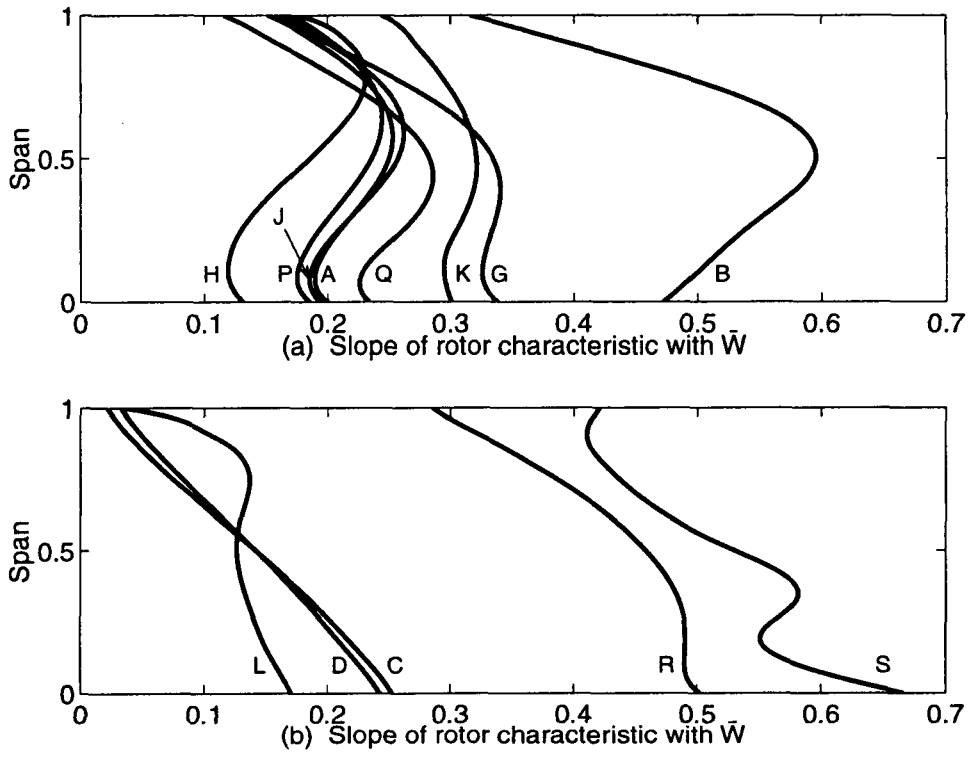


**Figure 7-14:** Radial profiles of rotor characteristic slope at stall. Results for all single-stage compressors are divided into two groups: those for which the (1,1) mode shape is dependent on (a) mean velocity profile, or (b) slope profile.

Overall, whether the disturbance velocity would be largest at the tip or hub was determined by the location of the maximum rotor characteristic slope. Figure 7-14 divides the radial profiles of rotor characteristic slope at stall into two groups. Characteristic slope profiles that had a global maximum in the mid-span region (Figure 7-14a), where the (1,1) mode amplitude was inherently small, had little effect on the mode shape. For these cases, the largest disturbance amplitude occurred in the region of lowest mean velocity. However, the five slope variations that were clearly highest at the hub and lowest at the tip (Figure 7-14b) were able to dominate the effects of the mean velocity profile. The largest mode amplitude then corresponded to the region of highest slope, similar to quasi-2D mode behavior.

### 7.3.3 Stability of Higher-order Modes

Higher-order 3-D modes were typically more stable than the (1,0) mode (the three compressor exceptions are dealt with separately in the next section). However, the studies revealed

four parameters that affected the relative growth rates between higher-order 3-D modes and the quasi-2D modes. These are the spanwise nonuniformity of slope, the blade aspect ratio, inter-blade row gaps, and the axial distribution of mean pressure rise through the compression system.

### Compressor characteristic slope nonuniformity

To isolate the effect of radial slope nonuniformity, seven configurations (A,B,C,D,G,H,J) were examined which differed only in their blade row performance. To compare between configurations, a measure of "slope nonuniformity" was defined as the integral of the variation in slope along the radius:

$$\textit{slope nonuniformity} \;=\; \frac{1}{r_t - r_h} \int_{r_h}^{r_t} \left\| \frac{d\ \text{slope}}{dr} \right\| dr \;. \tag{7.4}$$

For the case of a linear slope profile, this measure of nonuniformity would reduce to [max(slope)-min(slope)]/($r_t - r_h$).

For each configuration at stall, the difference between the growth rates of the (1,1) and (1,0) modes is plotted in Figure 7-15 as a function of the measure of nonuniformity of the overall characteristic slope. As the slope nonuniformity increased, the difference between the growth rates of these modes decreased. This is because higher-order radial modes were more localized to specific regions of the compressor, and so were more sensitive to spanwise variations in performance than the quasi-2D modes. Therefore, slope nonuniformity destabilizes all modes, but affects 3-D modes the most.

### Blade aspect ratio

The growth rates of 3-D modes were closer to the quasi-2D modes in compressors with higher aspect-ratio blades (Figure 7-16). In particular, for the 0.35 hub-to-tip ratio compressor (case L) the (1,1) mode was just barely stable when the compressor stalled. The stabilizing effect on 3-D modes in low aspect-ratio blades was caused by the increased redistribution of the disturbance flow within the blade passage, as demonstrated with the actuator duct models in Section 5.5.

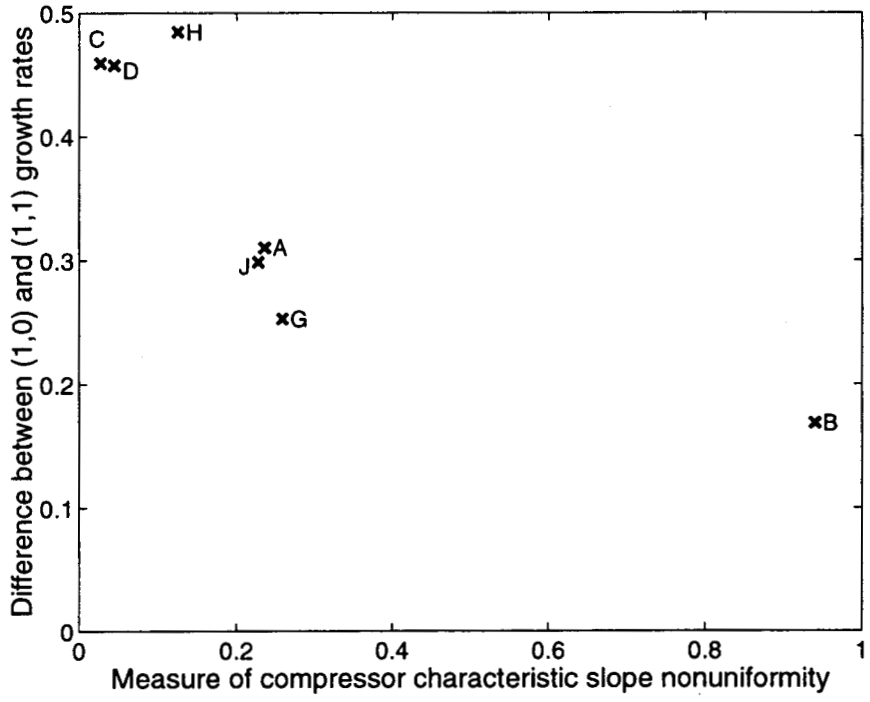


**Figure 7-15:** Difference between growth rates of (1,0) and (1,1) modes as a function of spanwise nonuniformity of overall compressor characteristic slope (equation 7.4). Results obtained at stall for each compressor configuration.

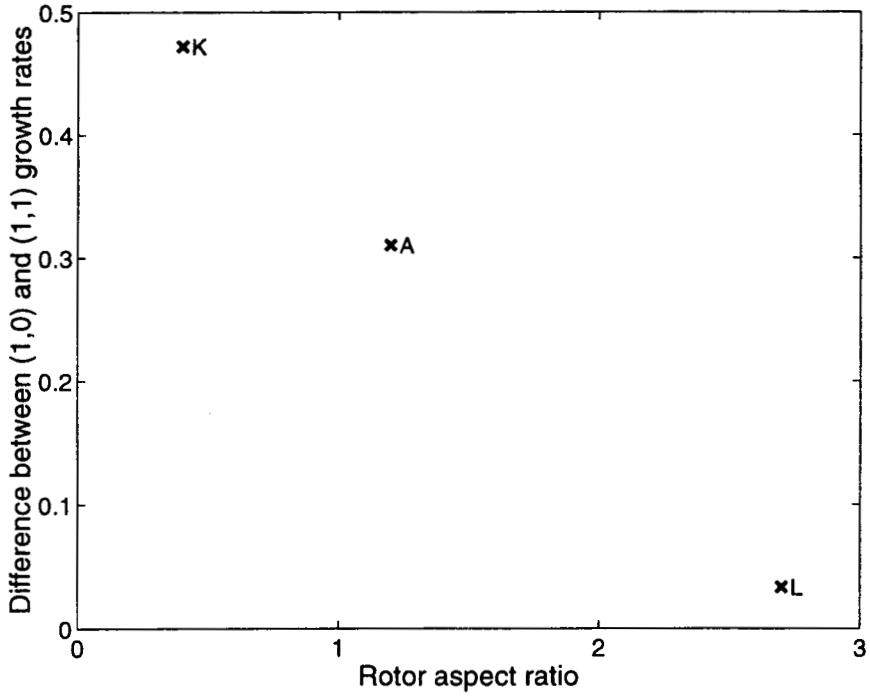


**Figure 7-16:** Difference between growth rates of (1,0) and (1,1) modes at stall as a function of rotor aspect ratio for configurations A, K and L.

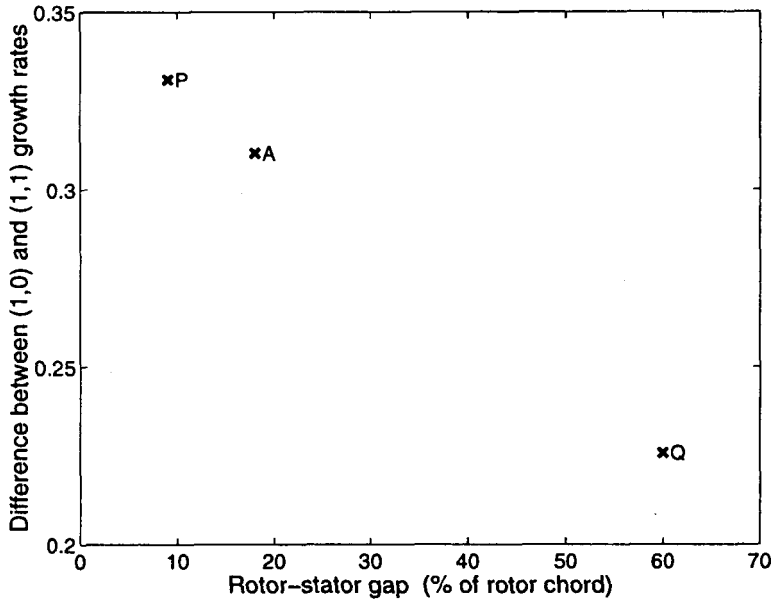


**Figure 7-17:** Difference between growth rates of (1,0) and (1,1) modes at stall as a function of rotor-stator gap length.

### Rotor-stator gap lengths

Figure 7-17 shows that increasing the gap length between the blades reduced the stability of the higher-order 3-D modes. Since the stator generally operated on a negatively-sloped characteristic, it acted as a stabilizing influence to the rotor. Increasing the distance between the blades allowed radially varying potential disturbances generated by the rotor to decay before reaching the stator, reducing the stator's effectiveness to stabilize the mode. Similar trends were found by Gong [23] for three-dimensional spike disturbances. Spacing had less effect on the quasi-2D modes because, as shown in Section 7.2.2, their axial decay rate was approximately an order of magnitude smaller than for three-dimensional potential disturbances.

### Axial distribution of mean pressure rise

The relative importance of higher-order modes could be increased by selectively stabilizing the quasi-2D modes. Since higher-order radial modes were more localized than the 2-D modes, compressor designs that caused the overall compressor characteristic slope to become more negative, while maintaining the same local blade performance, would tend to stabilize the modes with the lowest axial decay rate. Two such designs were examined: an

annulus with an area contraction, and mismatched compressor stages. In fact, both these methods led to designs for which the higher-order modes went unstable first, and so are discussed in the next section.

### 7.3.4 Cases of Compressor Instability Through Higher-order Modes

Three exceptions were found to the general rule that higher-order 3-D modes were more stable than quasi-2D modes. These cases represent serious limitations for two-dimensional stability analyses in that the stalling process was not even correctly predicted. The three cases corresponded to an inlet distortion with low velocity at the tip (study U), the most rapidly convergent annulus geometry (S), and the most strongly mismatched compressor (X). Explanations for the behavior of each configuration are discussed below.

#### Radial inlet distortion

Radial inlet distortions caused larger background flow and compressor slope nonuniformities than could be induced in uniform inlet flow by blade design variations alone. Using the measure of slope nonuniformity defined in equation 7.4, the nonuniformity for cases T and U with inlet distortion are 5–6 times larger than the worst case example in clean flow (Figure 7-18). Recall from Section 7.3.3 that higher-order 3-D modes were more susceptible to slope and mean flow nonuniformities than the quasi-2D modes.

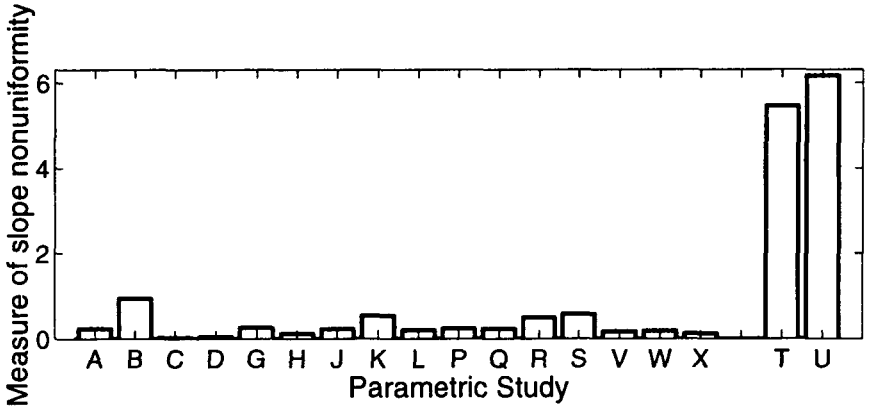


**Figure 7-18:** Comparison of spanwise nonuniformity of overall compressor characteristic slope (equation 7.4) for all configurations.

Only the inlet distortion with low tip velocity (U) caused stall inception through a

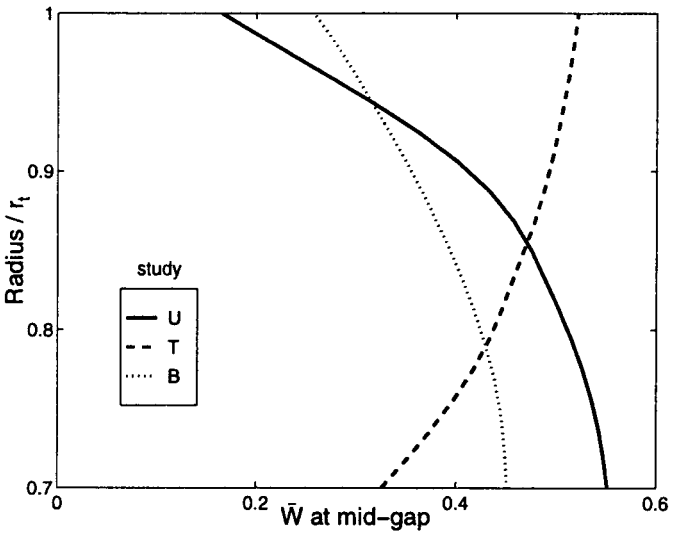


**Figure 7-19:** Axial velocity nonuniformity at rotor inlet for cases of inlet distortion compared to configuration B.

higher-order mode; the same strength distortion with high tip velocity (T) stalled through the typical quasi-2D mode. An examination of the velocity variation *local* to the compressor showed that reduced flow at the tip accentuated the natural tendency of the off-design blade performance to divert flow away from the outer casing. Figure 7-19 compares the axial velocity profile at the mid-gap plane for the inlet distortion cases, and also with compressor B, which had the largest flow nonuniformity in clean inlet flow. The ratio of maximum to minimum velocity was twice as high for case U (3.3) as for case B (1.7) and case T (1.6). Driven by slope and background flow nonuniformities of this magnitude, the radial inlet distortion in case U was able to excite higher-order 3-D modes to go unstable before the quasi-2D mode.

### Converging annulus

A consequence of a convergent annulus in low-speed flow is to accelerate the flow in the axial direction, thereby decreasing the downstream pressure so the slope of the overall characteristic becomes more negative. This is a 1-D flow effect since the pressure difference between the far downstream plane to the compressor exit is given by $\Delta P = -W_2^2(AR^2-1)/2$, where $W_2$ is the velocity at the exit of the compressor, and $AR$ is the area ratio across the downstream annulus. Therefore, $d\Delta P/dW_2$ is negative for area ratios greater than one implying that the slope of the overall characteristic decreases.

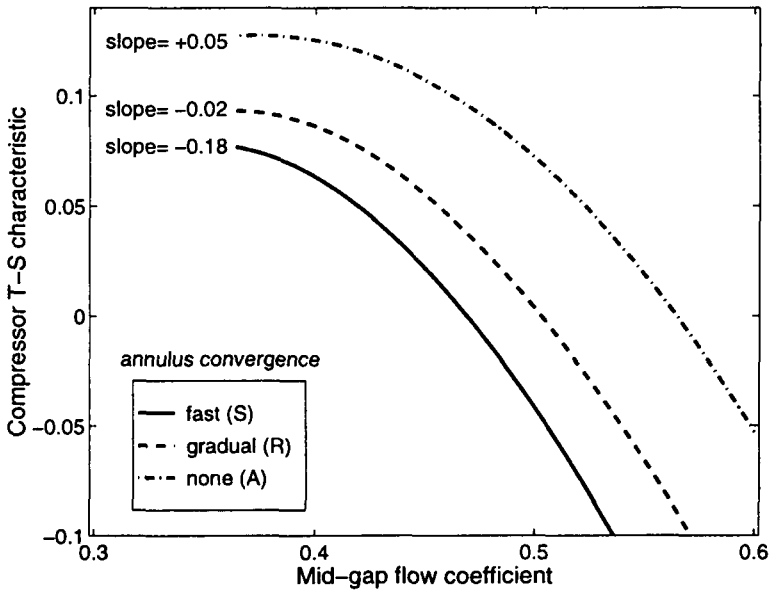


**Figure 7-20:** Comparison of total-to-static pressure rise characteristics with increasing annulus convergence. Characteristics measured across planes $0.75\,r_t$ upstream and downstream of compressor, and plotted against average axial velocity at mid-gap plane.

This effect is observed in Figure 7-20 for the characteristics of configurations R and S, representing annuli with an overall 2:1 area ratio occurring over a length scale of the circumference (*gradual*) and the blade height (*fast*), respectively. The total-to-static characteristics in this figure were calculated from planes $0.75\,r_t$ upstream and downstream of the blade rows, rather than over the entire compression system (which extends to $\pm 4\,r_t$), for reasons that will soon be discussed. Between these planes, the annulus area ratio for cases S, R and A were 2, 1.65 and 1, which is reflected in the figure by the increasing values of slope at the same mid-gap flow coefficient. The characteristics were plotted against the average axial velocity at the mid-gap plane for which each configuration was designed to have the same blade row performance. This way, differences between the characteristics in Figure 7-20 are solely due to the one-dimensional effect of annulus area contraction.

Figure 7-21a shows that the growth rate of the (1,0) mode for each configuration correlated with the slope of the characteristics in Figure 7-20. Extending the definition of the characteristic to the far field planes would only have affected the characteristic for R, because the area changes for compressors S and A beyond $\pm 0.75\,r_t$ were less than 0.1%. Based on the close correlation in Figure 7-21a, area contractions beyond $0.75\,r_t$ downstream of the stator had little effect on the stability of the (1,0) mode. The important conclusion

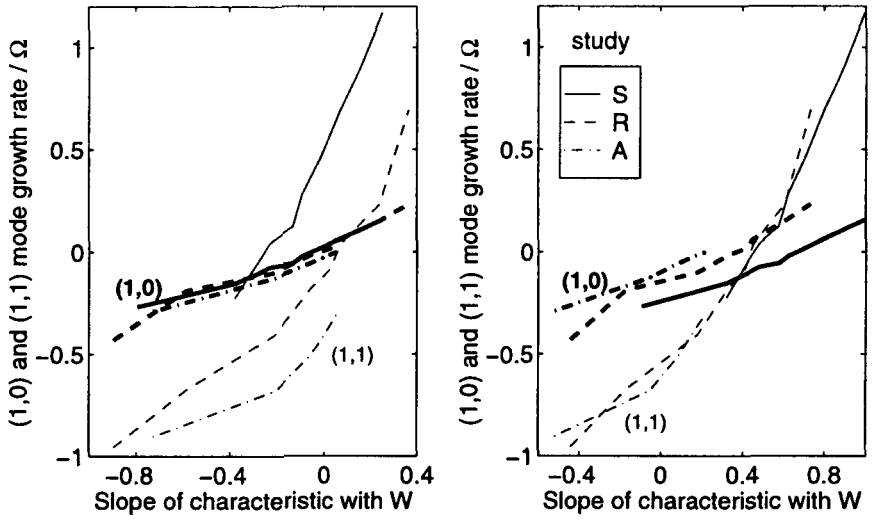


(a) "Overall" characteristic (b) Rotor characteristic

**Figure 7-21:** Growth rates of (1,0) and (1,1) modes correlated to (a) slope of "overall" and (b) slope of rotor characteristics. "Overall" characteristics are defined from Figure 7-20. (1,0) modes are denoted by the heavier lines, (1,1) modes by the lighter lines.

is that the growth rate of the (1,0) mode was essentially set by the slope of the "overall" characteristic (within $\pm 0.75\, r_t$), whereas the (1,1) mode was not. However, the growth rate of the (1,1) modes for each configuration did correlate to the slope of the *rotor* characteristic (Figure 7-21b) because of the localized nature of the higher-order 3-D modes.

Comparisons between Figures 7-21a and 7-21b explain why the higher-order mode led to stall before the quasi-2D modes for compressor S. Since the compressors were designed with the same local blade performance at the same mid-gap flow coefficient, this implied that the rotor characteristics were similar. Therefore, for the same local rotor operation, configuration S operated with a more negatively sloped "overall" characteristic than case R or A, thereby suppressing the growth rate of the (1,0) mode the most. In the case of configuration S, the 2:1 area ratio sufficiently stabilized the (1,0) to allow the (1,1) mode to lead to rotating stall.

It is important to note that this scenario is not likely to arise in typical engine operation. The rate of annulus convergence shown in S is designed for high-speed flow, where increasing density through the compressor reduces the mean pressure drop compared to incompressible flow. The disparity between the slopes of the overall and local characteristics would not be as apparent, except, perhaps, at low operating speeds, such as at take-off conditions.

### Mismatched blade rows

Recall for the multistage configurations that re-staggering the inlet guide vane had the effect of shifting the peak of the first rotor characteristic to higher flow coefficients than for the overall characteristic (Figure 7-6). For the matched compressor (V), the difference between the characteristic peaks of the first rotor and overall compressor was 0.05% in flow coefficient. For cases W and X, this difference rose to 9% and 18% of the overall peak flow coefficient, caused by an increase in the first rotor incidence of 15 and 25 degrees, respectively.

The qualitative behavior of the (1,0) and (1,1) modes was the same as for the convergent annuli configurations. The growth rate of the (1,0) mode was essentially determined by the slope of the overall characteristic (Figure 7-22). However, for operation at the same overall slope, the growth rate of the (1,1) mode was highest for case X, which had the most positively sloped characteristic across the first rotor.

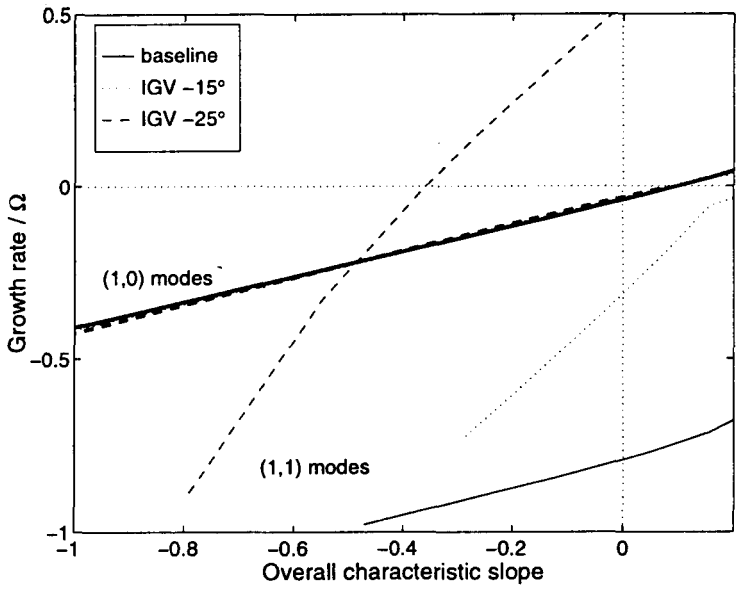


**Figure 7-22:** Growth rates of (1,0) and (1,1) modes correlated against slope of overall characteristic for three multistage configurations. (1,0) modes are denoted by the heavier lines, (1,1) modes by the lighter lines.

As the loading on the first rotor increased by re-staggering the IGV, the (1,1) mode became more localized to the first stage. The difference in mode shape between the baseline configuration and case X is shown in Figure 7-23 (the region within the IGV was not plotted because the mode amplitude was very small). Therefore, for maximum mismatched

operation, the higher-order 3-D modes were localized to the rotor, which had a sufficiently positively-sloped characteristic to drive them unstable before the (1,0) mode.

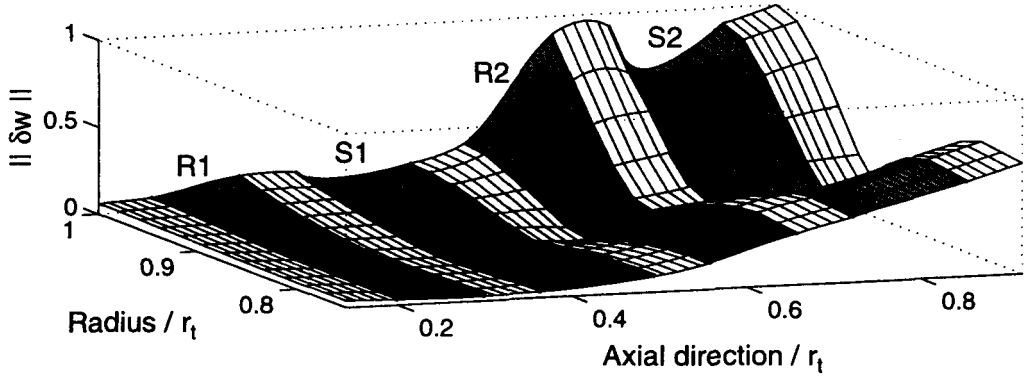


(a) Matched compressor (study V)

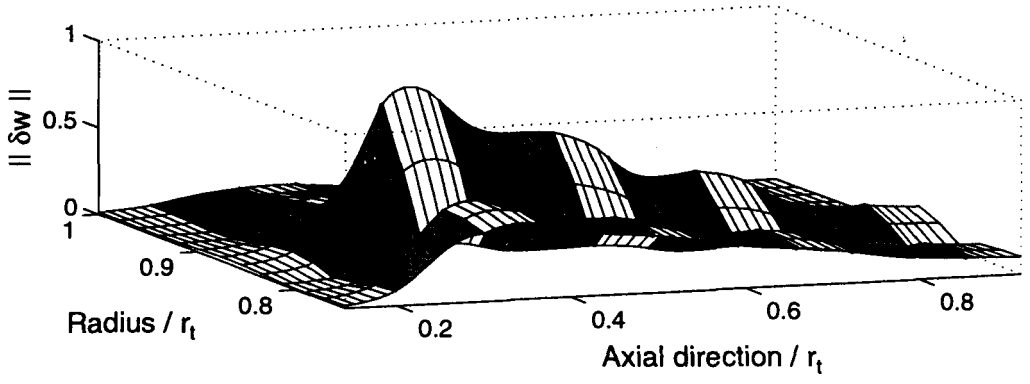


(b) Mismatched compressor (study X)

**Figure 7-23:** Magnitude of axial velocity disturbance from (1,1) mode within the compressor for (a) baseline configuration V, and (b) mismatched configuration X. Shaded regions correspond to regions within the blade rows.

### 7.3.5 Summary of Higher-order 3-D Mode Behavior

In summary, higher-order 3-D modes were generally more stable than the quasi-2D modes, although they became less damped with increasing characteristic slope nonuniformity, higher aspect ratio blades and longer inter-blade row gaps. An inlet flow distortion that accentuated the flow nonuniformities induced by the blade rows was shown to sufficiently raise the growth rate of the (1,1) mode so that it caused stall. It was also demonstrated that quasi-2D modes could be sufficiently stabilized by compressor mismatching or area contraction to enable stall inception via higher-order radial disturbances.

### 7.3.6 Relation Between Higher-order Modes and Spikes

It has been generally considered that spikes and modes are independent phenomena, each with a unique process leading to stall. Spikes are known to begin as large-amplitude, short-wavelength cells that are strongly localized to the tip region of a blade row [4]. Perhaps originating from a local blade passage event [42], these disturbances initially rotate near 70-80% of the rotor speed, often growing into stall within 3 rotor revolutions. This behavior contrasts the evolution of slower propagating, long-wavelength modal disturbances, that were thought to be fairly uniform across the span.

The current research shows the existence of higher-order three-dimensional modes that propagate at a frequency near that of spikes, which can be localized to the rotor tip in nonuniform, off-design flow fields. Although the baseline compressor configurations indicate these modes to be stable when the compressor stalls, conditions were found where the higher-order modes can approach the instability line, or even cross it first.

Furthermore, under such conditions, a whole spectrum of higher-order 3-D modes with increasing circumferential harmonics tend to cluster closely together near the instability line. Examples of this behavior can be found on the eigenvalue plots for many of the cases in Appendix M, but it is specifically noticeable in Figure M-50 for the multistage compressor with moderate mismatching (case W). This configuration produces a whole spectrum of lightly damped, higher-order modes with phase-speeds between 85%–95% rotor speed.

It is *not* being proposed here that spikes and short-wavelength, higher-order modes are the same phenomena. However, the initial growth of spikes would likely be encouraged by the presence of resonant, lightly damped modes. Therefore it is proposed that compressor configurations like W would be more susceptible to short-wavelength, localized disturbances generated by blade passage events than a configuration such as the matched compressor (case V), where the higher-order modes are well-damped. Circumstantially supporting this argument are experiments (Camp and Day [4]) and calculations (Gong et al. [23]) that indicate mismatching plays a strong role in triggering the development of spikes before traditional 2-D modes.

## 7.4 Applicability of 2-D Stability Model

The characteristics of quasi-2D and higher-order 3-D modes are used here to explicitly answer the question posed in the objectives: for what compressor conditions are 2-D models sufficient, and when is the use of the three-dimensional flow model required? This question is answered in terms of the functions of 2-D theory for stall detection, active control schemes, and stall line prediction. For the first two functions, knowledge of the frequency of the mode determines the required bandwidth of the schemes, and the stall cell shape is related to sensor and actuator placement. The last function calls for an assessment of the accuracy of 2-D stall point predictions in compressor annuli with intrinsic flow field variations.

### Compressors stalling from quasi-2D mode

The most crucial figure of merit for the 2-D analysis was that it generally predicted the correct stalling mode. Temporarily excepting the three cases where the (1,1) mode was critical, for all other compressor geometries and flow conditions the most unstable mode was quasi-2D. This encompassed high and low hub-to-tip ratio configurations, and blade designs with extreme spanwise loss and turning variations. The frequency of the mode was predicted by the 2-D model to within 10% of rotor frequency for the worst case examples, and within 1% for the baseline configurations. This order of accuracy is sufficient to establish necessary requirements for sensors or actuators for use in active stall management. Despite inaccuracies in stall point prediction, by capturing the correct stalling mode, 2-D analyses have already demonstrated their usefulness in uncovering compressor stability trends in previous research efforts. Such exercises have included understanding the effects on stability from circumferential inlet distortion [77, 69], tip clearance nonuniformity [26], 2-D active control methods [34, 79] and interaction with downstream components [29].

The 2-D model does not capture the radial nonuniformity of the velocity disturbances downstream of the compressor, which can impact sensor placement to measure stall inception. This is not a concern upstream of the compressor, or for pressure sensors downstream of the compressor, which can be located at any span since potential disturbances were essentially uniform outside the compressor blades. Only downstream of the compressor did vortical disturbances lead to significant radial nonuniformities of axial velocity. The ratio of

maximum to minimum disturbance amplitude across the span was at least 2, and up to an order of magnitude. Hot wires or total pressure probes can benefit from a stronger signal at certain radial locations; or, more critically, incorrectly placed hot wires will not observe the stall precursor above the background noise until the mode has already grown much larger in other regions. The use of 3-D stability analyses to prescribe stall sensor locations within a compressor is only useful for this one case.

Where the 2-D theory often failed was in predicting the stall point. This is especially problematic because the two-dimensional stall predictions were *unconservative*, predicting stall at a slope value between 0.02 to 0.4 too high on the overall characteristic. The loss in stall margin was shown in Section 7.2.3 to be caused by the spanwise nonuniformity in characteristic slope. Figure 7-24 quantifies how this disparity in stalling slope prediction increased for larger measures of slope nonuniformity. Note that for studies S and X, the 2-D analysis was compared to the stall point of the (1,0) mode, rather than the (1,1) mode that actually led to stall. This way Figure 7-24 directly represents the error associated with predicting neutral stability of the quasi-2D mode with the 2-D model.

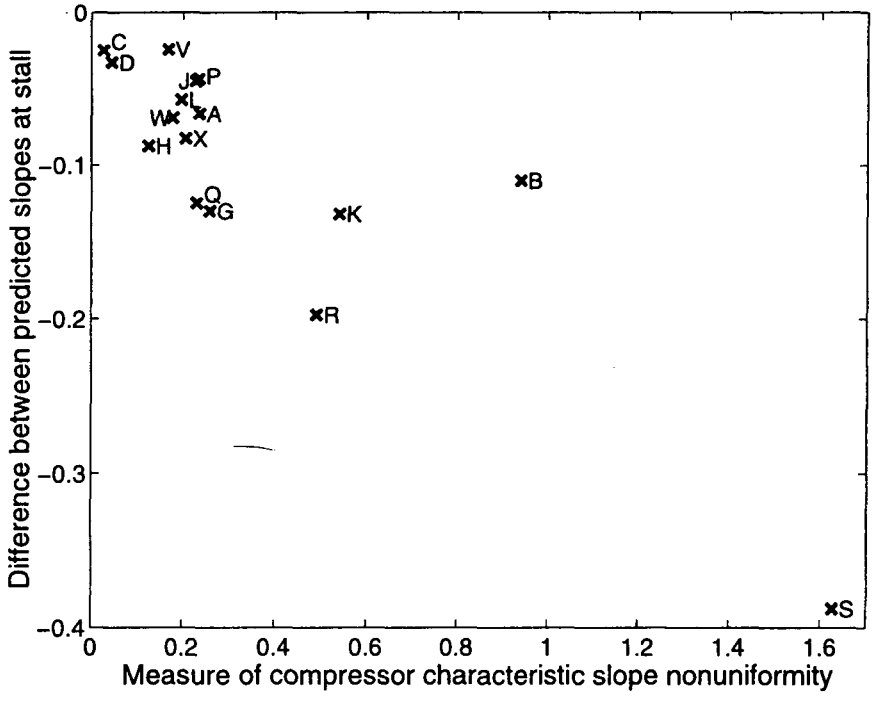


**Figure 7-24:** Difference between overall characteristic slopes at stall predicted by 3-D and 2-D analyses, correlated against the spanwise nonuniformity of overall compressor characteristic slope (equation 7.4). Note that *stall* is defined here as neutral stability point of (1,0) mode; actual stall points for compressor studies S and X occurred sooner than indicated due to instability of higher-order 3-D modes

The most useful measure of accuracy of the 2-D stall predictions, however, is not the difference in compressor slope, but rather the difference in flow coefficient. Stability models see the compressor in terms of the derivatives of performance variables with local flow conditions, but the actual stall margin is based on the overall flow coefficient or pressure rise at stall. Figure 7-25 plots the difference between flow coefficients at neutral stability for the (1,0) mode predicted by 2-D and 3-D analyses. These differences did not necessarily scale with the slope nonuniformity; flatter characteristics were more sensitive than sharply peaked characteristics to prediction errors of stalling slope.

Single-stage characteristics (without inlet distortion) were relatively flat, so the differences in slope led to differences in the stall point of 1–6% flow coefficient. This is a significant error, which can be seen by examining the stall margin of an example low-speed single-stage compressor [52] with a design flow coefficient of 0.55, and a stall point at 0.4 (Table 7.5). The calculation assumes a 2-D analysis error of 3% flow coefficient, equal to the error for the baseline configuration A. If the compressor was designed with a 20% stall margin based on the 2-D stability prediction, then nearly 40% of this anticipated stall margin is lost due to the unconservative prediction error. For the worst case example of 6% under-prediction of the stall point, 70% of the stall margin would vanish. For such compressors, the errors associated with 2-D prediction are unacceptable.

**Table 7.5:** Loss of stall margin for example compressor with 2-D stability prediction error of 3% flow coefficient.

| | design | stall (3-D) | stall (2-D) |
|---|---|---|---|
| Flow coefficient | 0.550 | 0.400 | 0.388 |
| Difference in stall point (0.400-0.388) | | 0.012 | |
| Designed stall margin (0.550-0.388)×20% | | 0.032 | |
| Loss in stall margin (0.012/0.032) | | 37% | |

Characteristics with sharper peak curvature, such as for multistage compressors, or operation with inlet distortion, were less sensitive to stall prediction errors. The large disparity between 2-D and 3-D predictions in terms of stalling slope for cases of inlet distortion (0.8 for T and 2.0 for U) caused less than 1% error in terms of flow coefficient. Similarly, in the multistage configurations, 2-D stall predictions compared within 1% flow coefficient to the actual stall point of the (1,0) mode.

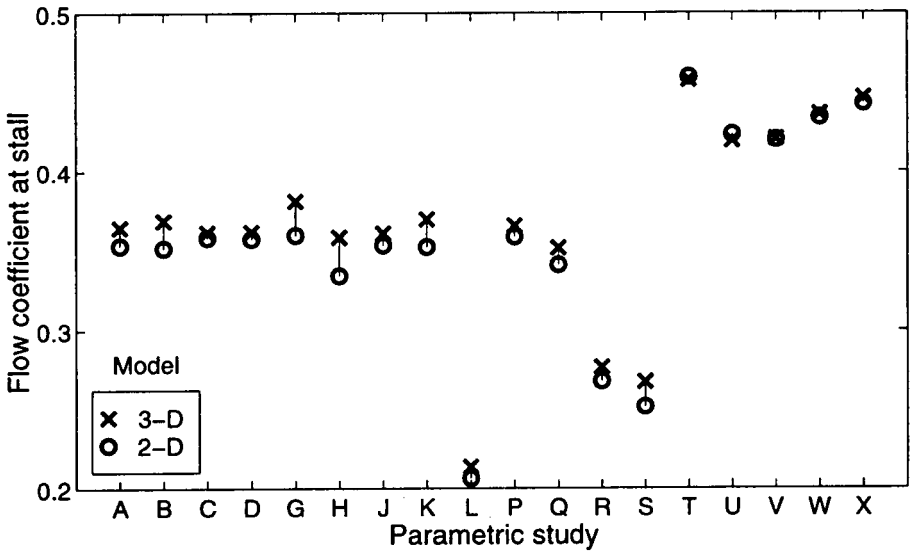


(a) Flow coefficient at stall

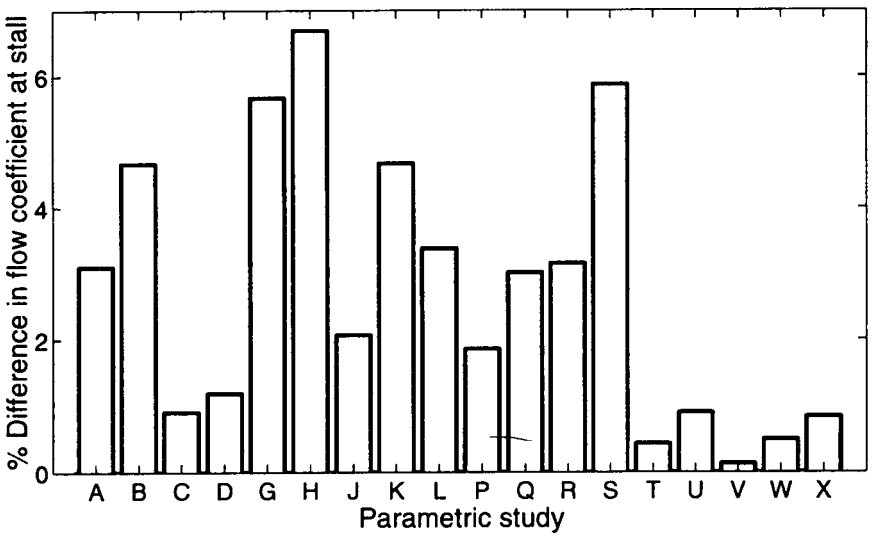


(b) Difference between predicted stall points

**Figure 7-25:** Comparison of 2-D and 3-D model predictions of neutral stability point of (1,0) mode in terms of (a) flow coefficient, and (b) percent difference in flow coefficients. Note that *stall* is defined here as neutral stability point of (1,0) mode; actual stall points for compressor studies S, U and X occurred sooner than indicated due to instability of higher-order 3-D modes

Therefore, whether the two-dimensional stability model is acceptable for a specific compressor depends on both the radial performance nonuniformity and the shape of the overall characteristic. The error in predicting the characteristic slope at stall must first be estimated based on the characteristic slope variation from Figure 7-24. The error in slope can then be related to an error in flow coefficient or pressure rise according to the known characteristic for that compressor. Based on the configurations used in the parametric studies, 2-D predictions of the quasi-2D mode would be unacceptable for most single-stages, but acceptable for the multistage compressors.

### Compressors stalling from higher-order 3-D mode

Up to now, assessments of the 2-D model ignored its most conspicuous liability in the three cases where the quasi-2D mode did not lead to stall. The three cases corresponded to higher-order 3-D perturbations stalling before the (1,0) mode because of radial inlet flow distortion, component mismatching, or duct convergence. For these cases, the 2-D stall predictions were even more unconservative than when based on the (1,0) mode in Figure 7-25. A comparison of the stall points predicted by 2-D and 3-D analyses for these cases is shown in Figure 7-26. The mismatched multistage configuration (X) stalled at a flow coefficient 6% higher than predicted by the 2-D model, so the 2-D stability prediction of a multistage compressor is no longer adequate once a higher-order radial mode becomes critical.

These three cases represent extreme design and operating conditions which mitigate their relevance to practical compressor operation. As discussed in Section 7.3.4, the rate of annulus convergence for configuration S is not designed for low-speed operation, and the higher-order 3-D mode may only be relevant at take-off conditions. The degree of mismatching for case X represents a 25° change in incidence on the first rotor. The maximum incidence changes described in [7] for a typical six-stage compressor operating as low as 60% design speed are closer to 15°, similar to compressor W which stalled via the quasi-2D mode. Considering that many modern engines use bleed valves or variable stators during off-design operation to reduce the mismatching, it is likely that the degree of mismatching for case X may not be encountered. Finally, although radial inlet distortions as large as case U are not unusual, the resulting steep curvature about the peak of the distorted

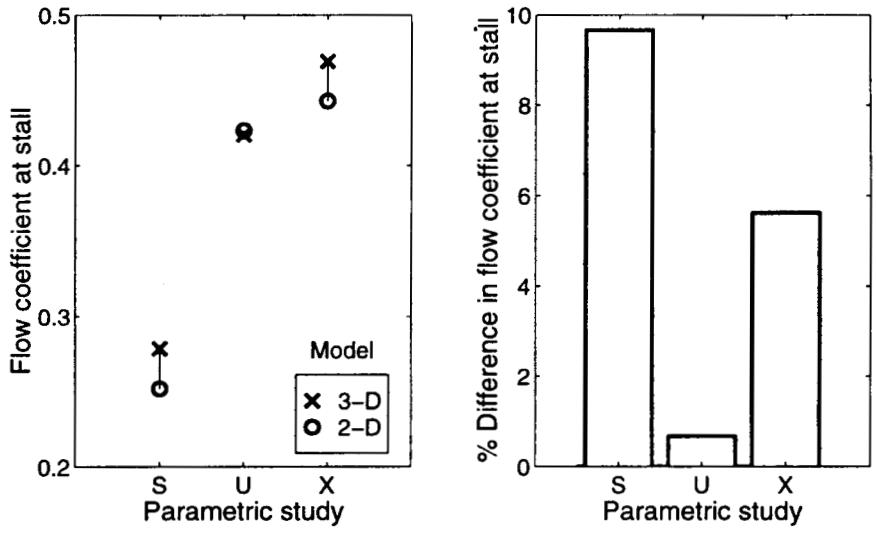


(a) Flow coefficient at stall (b) Difference between predicted stall points

**Figure 7-26:** Comparison of 2-D and 3-D model predictions of actual stall point for studies S, U and X in terms of (a) flow coefficient, and (b) percent difference in flow coefficient.

flow characteristic led to tolerable errors for 2-D stall point prediction, even when higher-order modes became critical. Therefore, the presence of higher-order modes in these cases would not have a significant impact on two-dimensional stall point predictions for typical compressor operation.

## 7.5 Summary of Three-dimensional Rotating Stall Predictions

Stability analyses of a range of compressor designs were performed with the general three-dimensional body force model. Results of these studies provided information on general characteristics of low and high-order radial modes in uniform and radially nonuniform flow. The studies were also used to determine the conditions for which 2-D stall prediction analyses are inadequate.

The 2-D analysis generally predicted the correct stalling mode as the first circumferential harmonic, low-order radial mode. These quasi-2D modes were more unstable than predicted by the 2-D theory, because of the destabilizing effect of radial flow variations. Stall point discrepancies between 1–6% of flow coefficient made two-dimensional stability

predictions unsuitable for the single-stage compressor configurations. However, 2-D theory was adequate for the multistage configurations, predicting the stall point within 1% flow coefficient for all but the most extreme mismatching case.

Radial flow nonuniformities affected stall by distorting the modes and reducing their stability. Larger disturbance amplitudes corresponded to regions with higher rotor characteristic slope. The loss in compressor stability was caused by regions of larger mode amplitude emphasizing the more "unstable" parts of the blade rows with higher slope. This reasoning was verified by the new three-dimensional stability criterion developed for quasi-2D modes. The criterion is a more general form of the two-dimensional WIMS condition developed for circumferential flow nonuniformity.

Higher order modes were generally more stable than the (1,0) mode, although the relative difference between growth rates could be decreased in certain situations. Spanwise slope nonuniformity affected the stability of higher-order radial disturbances even more than quasi-2D modes. Stall inception from the (1,1) mode was possible with an inlet flow distortion that caused larger radial variations in mean flow and compressor slope than could be generated by intrinsic flow redistribution in uniform inlet flow.

Because higher-order modes were more localized to the rotors than quasi-2D modes, they could also be selectively destabilized by compressor design variations in the axial direction. Increased rotor-stator gaps, annulus area contraction and stage mismatching all acted to raise the growth rates of the higher-order disturbances closer to the (1,0) mode. Sufficient area contraction and stage mismatching could cause the 3-D modes to become critical, although such extreme cases were shown to be unlikely for practical compressor situations.

# CHAPTER 8

# SUMMARY, CONCLUSIONS AND RECOMMENDATIONS

## 8.1 Overview of Research Program

Analytic compressor models have been developed to investigate the compressor response to two classes of nonuniformity: rotating tip clearance asymmetry and spanwise flow variations.

The effects of circumferential flow variations induced by unsteady tip clearance asymmetry were assessed with a two-dimensional actuator disk model. The model was applied to clearance asymmetries from both a whirling shaft and nonuniform blade heights on two compressor configurations. A basic linear control scheme was also added and used to demonstrate the controllability of rotating stall through unsteady shaft position actuation.

Three-dimensional stall inception was examined with both actuator plane and generalized body force compressor representations. The actuator plane model was used to understand the basic behavior of three-dimensional disturbances within the ducts, and to motivate important features that must be included in the second model. The generalized body force model was designed for actual compressor geometries with general spanwise flow nonuniformities caused by both compressor performance variations and inlet distortion. This model was used for parametric studies of radial performance and flow variations affecting stall inception behavior, and to examine the potential of higher-order radial modes leading to stall.

A universal stability criterion was developed, applicable for compressors stalling from

2-D (or quasi-2D) modes in either circumferential or radial flow nonuniformities:

$$\int_{A_{exit}} pw\, dA_{exit} - \int_{A_{inlet}} p_t w\, dA_{inlet} = 0\,.$$

This condition was useful for demonstrating how nonuniformity in compressor performance (specifically the blade row characteristic slopes) affected the stall point.

## 8.2 Results and Conclusions

### 8.2.1 Effects of Rotating Tip Clearance Asymmetry

Compressor performance was most adversely affected by rotating clearance asymmetries that excited lightly damped rotating stall modes. Therefore the worst case was from a whirling shaft within 25%–40% of rotor frequency. For operation near the design point, the maximum performance changes were small. Whirling shafts with a displacement of 50% nominal clearance (approximately the rotordynamic limit of tolerable displacement) caused less than 0.2% change in pressure rise and efficiency. The effect of rotor height variations on design performance was negligible, with at most 0.05% loss in pressure rise and efficiency.

Changes to the stall margin were driven by two factors:

- The overall pressure rise characteristic for nonuniform flow was lower than for uniform flow because of the associated performance losses.
- The stall point on the nonuniform flow characteristic was generally at a higher flow coefficient than for undistorted flow.

The stall point corresponded to the condition when the *Weighted Integrated Mean Slope* (WIMS) was zero, given by

$$\int_0^{2\pi} \frac{d\Psi}{dW}\, w^2\, d\theta = 0\,.$$

The usefulness of this condition was seen for rotating clearance frequencies in two regimes:

- For frequencies away from resonance (such as stationary or rotor-locked nonuniformities), the circumferential slope nonuniformity was out-of-phase with the mode envelope

for $w$. The WIMS condition then reduced to the IMS condition ($\int_0^{2\pi} \frac{d\Psi}{dW}\, d\theta = 0$), indicating that the stall point was approximately at the peak of the nonuniform flow characteristic.

- For frequencies near resonance (between 30%–60% rotor frequency) the mode envelope for $w$ was nearly in phase with the slope variation, for which larger disturbance amplitudes were associated with regions of more positive slope. Therefore, positive slope values were weighted more than negative values, and the compressor stalled sooner than in uniform flow.

The stall point was affected most by clearance asymmetries that excited lightly damped rotating stall modes. The worst case was for a first-harmonic asymmetry at a frequency near 50% of the rotor frequency. Such a tip clearance variation induced both high performance losses and a large slope variation in-phase with the mode amplitude envelope. For a whirling shaft offset of 1% chord, the stalling flow coefficient increased by 10% and the stalling pressure rise dropped by over 6%. Rotor height variations had a frequency too far from resonance to significantly affect stability. For rotor-locked clearance asymmetries of 1% chord, the stall point changed by 0.5% in flow coefficient and 0.3% in pressure rise.

The rotating stall mode was found to lock-on to the rotating asymmetry over a finite range of frequencies near the original mode frequency in uniform flow. This new (nonlinear) phenomenon has never before been reported.

Using shaft deflection to actively stabilize rotating stall was demonstrated to be a feasible technique in some situations, but was limited by the controllability of modes other than the first.

- In axisymmetric flow, only the first-harmonic mode can be controlled. The flow range can only be increased as far as other disturbances (surge or higher harmonic modes) go unstable. For the Stage-37 model, the stalling flow coefficient was reduced by 0.9%, thereby increasing the flow range from the design point by 8%. The results indicate further range extension is possible for multistage compressors not prone to surge.

- Controllability of other modes is possible when the flow is nonuniform, due to the coupling of harmonics within modes. This could be achieved by nominally offsetting

the rotor shaft. Such a demonstration with the Stage-37 compressor model reduced the stalling flow coefficient by 1.2%, giving an 11% range extension.

### 8.2.2 Three-dimensional Rotating Stall Inception

Spanwise flow variations destabilized compressors, as compared to the situation with uniform flow at the radially-averaged conditions. The stall point for compressors stalling from quasi-2D modes was set by the universal stability criterion, which was approximated in terms of the individual blade row characteristics as

$$\int_{\mathcal{A}} \left\{ \left[ \left( \frac{\partial \Psi_{TS}}{\partial W} w_{in} + \frac{\partial \Psi_{TS}}{\partial V} v_{in} \right) w_{in} \right]_{\text{blade}_1} + \sum_{i=2}^{N} \left[ \left( \frac{\partial \Psi_{SS}}{\partial W} w_{in} + \frac{\partial \Psi_{SS}}{\partial V} v_{in} \right) w_{in} \right]_{\text{blade}_i} \right\} d\mathcal{A} = 0,$$

where the integrals are taken over the cross-sectional area at the inlet of each blade row. Nonuniform rotor characteristic slope caused the mode shape to have larger amplitudes in regions of higher local slope. This mode shape weighed higher values of slope more heavily, causing instability at a more negative overall slope than for radially uniform flow conditions.

Radial variations of flow and characteristic slopes raised the growth rates of higher-order 3-D modes closer to that of quasi-2D modes. However, the effect was generally not enough to cause the higher-order modes to become critical. Only a radial inlet flow distortion of 0.8 dynamic head was able to induce sufficiently large radial flow gradients to destabilize the higher-order 3-D mode first.

Higher-order radial modes were also sensitive to the design of the compressor in the axial direction. Because 3-D modes were more localized than quasi-2D disturbances, components further from the most loaded rotor tended to affect the slower-decaying quasi-2D modes the most. Therefore, increased rotor-stator spacing, annulus area contraction and stage mismatching all raised the growth rates of the higher-order 3-D modes closer to the quasi-2D growth rate.

Three-dimensional modes could be induced to go unstable first for sufficiently large area contractions and mismatching. The first case required the incompressible flow to accelerate through a 2:1 area ratio over a distance of 0.75 tip radii on either side of the compressor. The mismatching case required one rotor to have an incidence change of 25 degrees more than the other blade rows. These amounts of contraction and mismatch are unlikely to be

observed in typical compressor operation, limiting the possibility of observing higher-order 3-D instability from these effects.

For certain compressor designs and operating conditions, two-dimensional stability predictions were found to be inadequate compared to the three-dimensional theory according to one or more of the following figures of merit: (1) predicting the correct stall mode, (2) predicting the stall margin, (3) indicating poor sensor location for stall detection.

1. The two-dimensional model generally predicted the correct stalling mode. Higher-order 3-D modes were only found to induce stall for the three specific cases noted above, of which only the radial inlet distortion case is likely to be observed in practice.

2. The two-dimensional model always over-predicted the stall margin for compressors with radial flow variations. The error in stall point prediction for quasi-2D modes depended on both the spanwise nonuniformity of slope and the curvature of the characteristic in the following manner:
   - The spanwise nonuniformity in slope induced stall at a lower average slope on the overall compressor characteristic (observed differences in slope were between 0.02 to 0.4 depending on the radial nonuniformity of blade performance).
   - The curvature of the overall characteristic near the peak set the stalling flow coefficient based on the above value of slope at stall.

   Two-dimensional analyses would thus tend to provide worse stall predictions for fans or single-stage compressors, where the rotor slope nonuniformity dominates the entire compressor nonuniformity, and the characteristic is generally flatter near the peak. 2-D stability analyses of single-stage compressors had prediction errors of at least 1% and more typically between 2-4% of flow coefficient. Two-dimensional theory fared better for multistage compressors with sharply peaked characteristics, where stall predictions were within 1% flow coefficient of the 3-D model predictions.

3. Basing sensor placement for stall detection on purely 2-D mode shapes was adequate upstream of the compressor, and adequate for pressure measurements downstream of the compressor. However, the structure of the axial velocity disturbance downstream of the compressor could include large (>10×) variations across the span. The signal quality of downstream hot wire or total pressure probes would benefit from careful placement in regions of larger mode amplitude.

Actuator plane analyses demonstrated similar effects of radial flow nonuniformity on stability as the generalized body force model and are useful for understanding basic trends of how spanwise loading distribution affects stability. However, the sensitivity of their results to disturbance flow redistribution within the blade passages (characteristic of radially-varying modes) make this type of model unsuitable for accurate stall point prediction.

## 8.3 Recommendations for Future Work

The compressor model for rotating tip clearance asymmetry should be extended to include compressible flow effects. All results in this thesis indicate that the compressor response to clearance asymmetry depends on the excitation of the modes of similar shape and frequency. By ignoring compressible modes with phase speeds near that of the rotor, the present incompressible model may be underestimating the effect of rotor-locked nonuniformities in many high-speed compressors.

Future experiments are currently planned to verify stall suppression by using magnetic shaft bearings to control the rotor shaft position. An important step before attempting these experiments is to couple the aerodynamic model developed here with a model of the shaft dynamics. The present research assumed that the shaft position had a fixed displacement and frequency that was unaffected by the induced aerodynamic forces, which is likely not true, especially near resonant conditions.

The following preliminary experiments should also be performed with the magnetic bearing rig to confirm the new compressor phenomena predicted by the model. Performance characteristics with whirling shafts of various frequencies need to be measured to establish the resonant response peak for clearance asymmetries near the stall frequency. Unsteady stall inception measurements at the end of each characteristic should be taken to demonstrate the effect of rotating circumferential nonuniformity on the stall frequency, in particular the phase-locking phenomenon. Such measurements are useful on their own as experimental verification of the predicted trends, but they also provide necessary information about the sensitivity of the compressor performance and rotating stall dynamics on tip clearance, which are important for the active control demonstration.

With respect to three-dimensional stall inception, the effectiveness of active control

on radially nonuniform modes should be examined. The present results indicate that even quasi-2D axial velocity disturbances can vary in amplitude by a factor of 10:1 and have up to 120° variation in phase across the span. Current control techniques may prove inadequate for these situations, or else could be better optimized, especially for recent actuator designs that act over a limited span such as tip clearance control or jet injection at the casing wall. Unfortunately there are too many dynamic states in the present CFD-like compressor representation to directly add control terms. Such studies must incorporate mode shapes from this full model into a simplified reduced-order model.

Finally, with the amount of circumstantial evidence comparing higher-order three-dimensional modes to spikes, relations between the two should be investigated. The ability for the growth of spike disturbances to be promoted by excited, lightly damped 3-D modes can be tested with the combination of nonlinear compressor simulations and the present linear model. The linear model could be used to demonstrate the existence and structure of such modes, whereas the nonlinear simulation would then follow the interaction between the modes and the finite-amplitude disturbance as it develops.

# APPENDIX A

# ANALYSIS OF SMALL AMPLITUDE ROTATING CLEARANCE ASYMMETRIES

In this appendix, the velocity disturbance induced by small amplitude rotating clearance asymmetries is calculated. The relation developed by Graf [25] is augmented by allowing for general rotating frequencies (*i.e.* not rotor locked) and using a more general compressor representation.

Assume the clearance asymmetry is prescribed by a rotating sinusoidal perturbation,

$$\delta\varepsilon = \delta\varepsilon_n e^{in(\theta-\nu t)}, \tag{A.1}$$

then the linearized induced velocity perturbation at the compressor will have the same form,

$$\delta w = \delta w_n e^{in(\theta-\nu t)} \tag{A.2}$$

for complex $\delta\varepsilon_n$ and $\delta w_n$. The compressor is assumed to be represented by a quasi-steady actuator disk with inlet swirl sensitivity, axial exit flow, and quasi-steady losses. The linearized compressor matching condition (B.35) is then reduced to

$$\delta p_2 - \delta p_{t1} = \frac{\partial\Psi}{\partial W}\delta w + \frac{\partial\Psi}{\partial V}\delta v_1 + \frac{\partial\Psi}{\partial\varepsilon}\delta\varepsilon - \lambda\frac{\partial\delta w}{\partial\theta} - \mu\frac{\partial\delta w}{\partial t}. \tag{A.3}$$

The upstream tangential velocity, total pressure, and downstream static pressure perturbations are found by simplifying the equations in Appendix B.2 for the case of a steady,

uniform background flow. These perturbations are of the form

$$\begin{aligned} \delta v_1 &= i\delta w \\ \delta p_{t1} &= -\frac{1}{n}\frac{\partial \delta w}{\partial t} \\ \delta p_2 &= \frac{1}{n}\frac{\partial \delta w}{\partial t}. \end{aligned} \tag{A.4}$$

Substituting this into the compressor pressure rise condition, and collecting terms yields

$$\delta w_n = \frac{\frac{\partial \Psi}{\partial \varepsilon}}{i[n(\lambda - \nu\mu) - 2\nu - \frac{\partial \Psi}{\partial V}] - \frac{\partial \Psi}{\partial W}} \delta \varepsilon_n. \tag{A.5}$$

This can be compared with the situation for a stationary clearance asymmetry ($\nu = 0$),

$$\delta w_n = \frac{\frac{\partial \Psi}{\partial \varepsilon}}{i[n\lambda - \frac{\partial \Psi}{\partial V}] - \frac{\partial \Psi}{\partial W}} \delta \varepsilon_n \tag{A.6}$$

so that the ratio of velocity asymmetry induced by a rotating clearance nonuniformity to that of a stationary nonuniformity of the same amplitude is

$$\frac{\delta w_{rot}}{\delta w_{stat}} = \frac{i[n\lambda - \frac{\partial \Psi}{\partial V}] - \frac{\partial \Psi}{\partial W}}{i[n(\lambda - \nu\mu) - 2\nu - \frac{\partial \Psi}{\partial V}] - \frac{\partial \Psi}{\partial W}}. \tag{A.7}$$

We are interested in conditions for which the induced perturbations for the rotating case are of the same order (or larger) than the stationary situation. The most important case is when the bracketed portion of the denominator in (A.7) approaches zero. The resonant frequency at which this occurs is given by

$$\nu = \frac{n\lambda - \frac{\partial \Psi}{\partial V}}{2 + n\mu} \tag{A.8}$$

which is equal to the frequency of rotation of the rotating stall modes. This value is within 20%–70% of the rotor frequency for most compressors. Since this is less than the rotor frequency, this resonance effect would not arise from rotor-locked nonuniformities, but rather would come from a whirling rotor shaft.

Conditions when clearance variations rotating at rotor speed become important (relative to the stationary case) can be found by examining equation (A.7) for $\nu = 1$ and the

case of $\frac{\partial \Psi}{\partial V} = \frac{\partial \Psi}{\partial W} = 0$,

$$\left| \frac{\delta w_{rot}}{\delta w_{stat}} \right| = \frac{\lambda}{\mu - \lambda + 2/n}. \tag{A.9}$$

Long, multistage machines generally have $\mu \approx 2\lambda$, so this ratio approaches unity only for large n. Single stage machines, especially fan stages, can have $\mu - \lambda < \lambda$, for which $\delta w_{rot}$ can be larger than $\delta w_{stat}$ for all harmonics $n$.

In summary, this linearized analysis shows velocity nonuniformities induced by small amplitude rotor-locked clearance asymmetries are as important as their stationary counterparts in machines with few blade rows, and/or for high harmonic variations. Clearance nonuniformities rotating close to the rotating stall frequency excite a resonant effect, thereby inducing an even larger response.

# APPENDIX B

# DETAILS OF COMPRESSOR MODEL WITH ROTATING TIP CLEARANCE ASYMMETRY

This appendix contains the details for solving the steady background flow and the unsteady linearized modes of the compression system with a rotating tip clearance asymmetry. The general nonlinear compressor flow model is derived in Chapter 2.

## B.1 Background Flow Field

A solution for the steady flow in the frame of the rotating clearance asymmetry can be obtained by neglecting all temporal derivatives in the equations derived in Section 2.2. In this section, the steady form of these equations are rewritten in terms of the Fourier harmonics of the flow field within each compression system component. Steady flow variables are denoted with an over-bar ($\bar{}$) to differentiate them from the general terms in the unsteady analyses.

**Upstream Duct:** The form of the steady velocity field upstream of the compressor is found by solving equation (2.14) with the boundary conditions

$$\frac{\partial \bar{\Phi}'}{\partial z'} \to W_0, \ \frac{\partial \bar{\Phi}'}{\partial \theta'} \to -\nu \text{ as } z' \to z'_0, \text{ and } \bar{\Phi}'(\theta', z') = \bar{\Phi}'(\theta' + 2\pi, z'),$$

where $W_0$ is the far upstream (uniform) axial velocity. The solution for $\bar{\Phi}'$ (to within an arbitrary constant) is given as

$$\bar{\Phi}' = W_0 z' - \nu\theta' + \sum_{n=1}^{\infty} \frac{1}{n}(W_{c,n}\cos n\theta' + W_{s,n}\sin n\theta')\mathrm{e}^{n(z'-z_1')}.$$

The upstream velocity field described by this potential is

$$\bar{W}' = W_0 + \sum_{n=1}^{\infty}(W_{c,n}\cos n\theta' + W_{s,n}\sin n\theta')\mathrm{e}^{n(z'-z_1')} \tag{B.1}$$

$$\bar{V}' = -\nu + \sum_{n=1}^{\infty}(W_{s,n}\cos n\theta' - W_{c,n}\sin n\theta')\mathrm{e}^{n(z'-z_1')}. \tag{B.2}$$

The (as of yet) unknown constants $W_0$, $W_{c,n}$ and $W_{s,n}$ for $n \geq 1$ represent the Fourier coefficients of the axial velocity nonuniformity at the compressor face ($z' = z_1'$). As Fourier series are used often in the thesis, a notation was adopted to simplify this summation:

$$\{X_n, Y_n\}_{a,b} \equiv \sum_{n=a}^{b}(X_n\cos n\theta' + Y_n\sin n\theta'). \tag{B.3}$$

Thus, the velocities at the compressor face ($z' = z_1'$) are given as

$$\begin{aligned}\bar{W}_1'(\theta') &= W_0 + \{W_{c,n}, W_{s,n}\}_{1,\infty} \\ \bar{V}_1'(\theta') &= -\nu + \{W_{s,n}, -W_{c,n}\}_{1,\infty}.\end{aligned} \tag{B.4}$$

The upstream relative total pressure is uniform throughout the duct region. This fact can be demonstrated by combining the transformed Euler equations (2.15) to show $\bar{V}'\frac{\partial P_t'}{\partial\theta'} + \bar{W}'\frac{\partial \bar{P}_t'}{\partial z'} = 0$. Therefore, $P_t'$ is convected, unchanged, along relative streamlines from the inlet:

$$\bar{P}_{t1}'(\theta') = \bar{P}_{t0}' = P_a + \frac{\nu^2}{2}. \tag{B.5}$$

**Compressor:** Setting all time derivatives to zero in the transformed compressor pressure rise equations (2.16) yields

$$\bar{P}_2' - \bar{P}_{t1}' = \bar{\Psi}_i - \bar{L}_R - \bar{L}_S - (\lambda - \nu\mu)\frac{\partial \bar{W}_1'}{\partial \theta'} + \nu(\bar{V}_1' + \frac{\nu}{2}) \quad \text{(B.6)}$$

$$(1 + (1-\nu)\tau_R \frac{\partial}{\partial \theta'})\bar{L}_R = \sigma(\bar{\Psi}_i - \bar{\Psi}) \quad \text{(B.7)}$$

$$(1 - \nu\tau_S \frac{\partial}{\partial \theta'})\bar{L}_S = (1-\sigma)(\bar{\Psi}_i - \bar{\Psi}). \quad \text{(B.8)}$$

The unsteady loss time constants, $\tau_R$ and $\tau_S$, are assumed to be proportional to the mean convection time through a rotor or stator blade row respectively. The time constants are written as

$$\begin{aligned} \tau_R &= \bar{\tau}\,\frac{c_R \cos\gamma_R}{W_0} \\ \tau_S &= \bar{\tau}\,\frac{c_S \cos\gamma_S}{W_0}, \end{aligned} \quad \text{(B.9)}$$

where $c$ is the blade chord, $\gamma$ the stagger angle, and $\bar{\tau}$ the proportionality factor. Experimental studies [56, 51, 33] have shown that $\bar{\tau}$ can vary from 1 to 1.5 for different compressors.

The three pressure rise matching relations (B.6–B.8) can be combined into one equation. To do so, the isentropic and actual pressure rise relations, and the rotor and stator losses are first written as series of their Fourier coefficients:

$$\begin{aligned} \Psi_i(\theta') &\equiv \{\Psi_{icn}, \Psi_{isn}\}_{0,\infty} \\ \bar{\Psi}(\theta') &\equiv \{\Psi_{c,n}, \Psi_{s,n}\}_{0,\infty} \\ \bar{L}_R(\theta') &\equiv \{L_{Rc,n}, L_{Rs,n}\}_{0,\infty} \\ \bar{L}_S(\theta') &\equiv \{L_{Sc,n}, L_{Ss,n}\}_{0,\infty}. \end{aligned} \quad \text{(B.10)}$$

The Fourier series form of equations (B.7) and (B.8) are then expressed as

$$\begin{aligned} \{L_{Rc,n}, L_{Rs,n}\}_{0,\infty} + (1-\nu)\tau_R \{nL_{Rs,n}, -nL_{Rc,n}\}_{0,\infty} &= \sigma\{\Psi_{ic,n} - \Psi_{c,n}, \Psi_{is,n} - \Psi_{s,n}\}_{0,\infty} \\ \{L_{Sc,n}, L_{Ss,n}\}_{0,\infty} - \nu\tau_S \{nL_{Ss,n}, -nL_{Sc,n}\}_{0,\infty} &= (1-\sigma)\{\Psi_{ic,n} - \Psi_{c,n}, \Psi_{is,n} - \Psi_{s,n}\}_{0,\infty} \end{aligned} \quad \text{(B.11)}$$

The explicit solution for the rotor and stator loss Fourier coefficients are obtained by equating the sine or cosine terms of the same harmonic:

$$\begin{aligned}
L_{Rc,n} &= \frac{\sigma[\Psi_{ic,n} - \Psi_{c,n} - n\tau_R(1-\nu)(\Psi_{is,n} - \Psi_{s,n})]}{1 + [n\tau_R(1-\nu)]^2}, \quad n \geq 0 \\
L_{Rs,n} &= \frac{\sigma[\Psi_{is,n} - \Psi_{s,n} + n\tau_R(1-\nu)(\Psi_{ic,n} - \Psi_{c,n})]}{1 + [n\tau_R(1-\nu)]^2}, \quad n \geq 1 \\
L_{Sc,n} &= \frac{(1-\sigma)[\Psi_{ic,n} - \Psi_{c,n} + n\tau_S\nu(\Psi_{is,n} - \Psi_{s,n})]}{1 + [n\tau_S\nu]^2}, \quad n \geq 0 \\
L_{Ss,n} &= \frac{(1-\sigma)[\Psi_{is,n} - \Psi_{s,n} - n\tau_S\nu(\Psi_{ic,n} - \Psi_{c,n})]}{1 + [n\tau_S\nu]^2}, \quad n \geq 1. \qquad \text{(B.12).}
\end{aligned}$$

These coefficients are substituted into the Fourier series form of equation (B.6) to give the following single pressure rise condition in series form:

$$\begin{aligned}
\bar{P}'_2 - \bar{P}'_{t1} &= \{\Psi_{ic,n} - L_{Rc,n} - L_{Sc,n} + [\nu - n(\lambda - \nu\mu)]W_{s,n}, \\
&\quad \Psi_{is,n} - L_{Rs,n} - L_{Ss,n} - [\nu - n(\lambda - \nu\mu)]W_{c,n}\}_{0,\infty} - \frac{\nu^2}{2}. \qquad \text{(B.13)}
\end{aligned}$$

**Downstream Duct:** At the compressor exit face, the steady velocity nonuniformity is

$$\begin{aligned}
\bar{W}'_2 &= \bar{W}'_1 = W_0 + \{W_{c,n}, W_{s,n}\}_{1,\infty} \\
\bar{V}'_2 &= -\nu + \bar{W}'_2 \tan\bar{\beta}_2 \,. \qquad \text{(B.14)}
\end{aligned}$$

An expression for the exit static pressure, $\bar{P}'_2$, is needed to complete the compressor pressure rise equation (B.13); however it is generally not a simple function of the local velocity components. The unsteadiness of the flow in the absolute frame precludes the assumption that the exit pressure is uniform. Previous actuator disk analyses in nonuniform flow by Graf [25], Hynes and Greitzer [43], and van Schalkwyk [76] were restricted to compressors with stationary velocity nonuniformities ($\nu = 0$) and uniform exit angles ($\bar{\beta}_2 = 0$). The downstream velocity fields were always parallel shear flows in these cases, implying that the pressure at the compressor exit was uniform.

For the case of rotating tip clearance asymmetries, where $\nu \neq 0$ and $\bar{\beta}_2$ may be nonuniform about the compressor, some approximation is needed to represent $\bar{P}'_2$ as a function of $\bar{W}'_2$, $\bar{V}'_2$ and the plenum pressure $\bar{P}_P$. Without such an approximation, the solution to the Euler equations representing the flow throughout the entire down-

stream duct must be found numerically, which greatly increases the complexity of the approach.

The approximation adopted here is to assume that steady downstream flow variations are small compared to the mean. The mean flow has a uniform axial velocity equal to $W_0$, so the mean relative tangential velocity at the compressor exit is $-\nu + W_0 \tan\hat{\beta}_2$, where $\hat{\beta}_2$ is the average exit angle. The mean downstream pressure is equal to the plenum pressure, $\bar{P}_P$. Steady variations to the mean flow are defined by $\delta W'$, $\delta V'$ and $\delta P'$, where

$$\begin{aligned} \bar{W}'(\theta', z') &= W_0 + \delta W'(\theta', z') \\ \bar{V}'(\theta', z') &= -\nu + W_0 \tan\hat{\beta}_2 + \delta V'(\theta', z') \\ \bar{P}'(\theta', z') &= \bar{P}_P + \delta P'(\theta', z'). \end{aligned} \tag{B.15}$$

For small perturbations compared to the mean, the Euler equations (2.15) reduce to an elliptic equation for the pressure nonuniformity, $\nabla^2 \delta P' = 0$, which has the solution:

$$\delta P'(\theta', z') = \sum_{n=1}^{\infty} (\delta P'_{c,n} \cos n\theta' + \delta P'_{s,n} \sin n\theta') e^{-n(z'-z'_2)}. \tag{B.16}$$

Note that this solution includes only the pressure variations that exponentially decay away from the compressor. The part of the solution for exponentially growing pressure nonuniformities are unphysical, and are omitted.

The pressure at the compressor face ($z' = z'_2$) is written as

$$\bar{P}'_2(\theta') = \bar{P}_P + \left\{ \delta P'_{c,n}, \delta P'_{s,n} \right\}_{1,\infty}. \tag{B.17}$$

To solve for the unknown pressure coefficients in terms of the compressor exit velocity field, the first-order linearized approximation to the Euler axial momentum equation (2.15) is used:

$$\frac{\partial \delta P'}{\partial z'} = W_0 \frac{\partial \delta V'}{\partial \theta'} + (\nu - W_0 \tan\hat{\beta}_2) \frac{\partial \delta W'}{\partial \theta'}. \tag{B.18}$$

This equation is applied at the compressor exit using the solution for $\delta P_2'$ from equation (B.16):

$$\left\{n\delta P'_{c,n}, n\delta P'_{s,n}\right\}_{1,\infty} = -W_0 \frac{\partial \bar{V}_2'}{\partial \theta'} + (-\nu + W_0 \tan \hat{\beta}_2) \frac{\partial \bar{W}_2'}{\partial \theta'}. \tag{B.19}$$

The coefficients $\delta P'_{c,n}$ and $\delta P'_{s,n}$ are found by expanding the right-hand-side of equation (B.19) as a Fourier series in $n\theta'$, and equating the terms of identical harmonic number.

This linearized approximation needs justification because significant velocity nonuniformities (up to 20% of the mean velocity) have been found for cases of stationary clearance asymmetries [26]. A comparison is made in Figure B-1 between the actual and approximated pressure at the compressor exit for the case of a large velocity nonuniformity. The axial velocity profile represents a variation about the circumference of 20% of the mean (Figure B-1a). The flow is steady with respect to a clearance asymmetry rotating at 70% rotor speed, and exits the compressor axially in the absolute frame. The *actual* pressure profile was calculated using a two-dimensional, inviscid, nonlinear code for the downstream duct flow with a uniform far-field backpressure [22]. Figure B-1b shows that the approximated pressure profile is very close to the actual solution (within 3% of the peak-to-peak variation), which substantiates the adequacy of using the linearized pressure approximation.

**Plenum and Throttle:** At steady state, the plenum has a constant, uniform pressure, implying $\bar{P}_5' = \bar{P}_3' = \bar{P}_P$. The mass flow in the throttle ducts is also constant and uniform, and equal to the mass flow through the compressor. Thus, $\bar{W}_5' = \bar{W}_6' = \bar{W}_7' = \bar{W}_8' = \frac{A_C}{A_T} W_0$. Substituting these relationships into the throttle equation gives

$$\bar{P}_P - P_a = \frac{k_T}{2} \left(\frac{A_C}{A_T} W_0\right)^2. \tag{B.20}$$

The steady nonuniform flow in the compression system is obtained by combining the compressor pressure rise equation (B.13) with the throttle condition (B.20), using the equations for the upstream total pressure (B.5) and downstream static pressure (B.17). Upon making these substitutions, and equating sines and cosines of the same circumferential

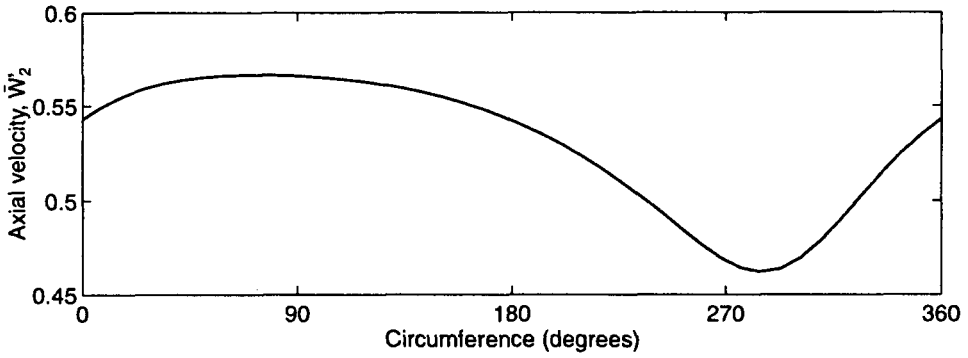


(a) Axial velocity profile at compressor exit

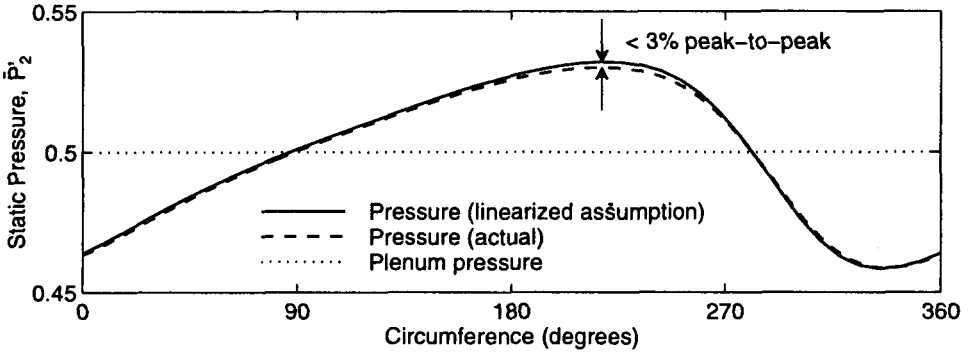


(b) Static pressure profiles at compressor exit

**Figure B-1:** Comparison of approximated and actual compressor exit static pressure profiles used to validate equation (B.19). Results for velocity nonuniformity locked to reference frame rotating at 70% of rotor speed.

harmonics, the following system of nonlinear equations is obtained:

$$\begin{aligned}
\Psi_{ic,0} - L_{Rc,0} - L_{Sc,0} - \frac{1}{2}k_T(\frac{A_C}{A_T})^2 W_0^2 &= 0 \\
\Psi_{ic,n} - L_{Rc,n} - L_{Sc,n} + [\nu - n(\lambda - \nu\mu)]W_{s,n} - \delta P'_{c,n} &= 0 \quad (n \geq 1) \\
\Psi_{is,n} - L_{Rs,n} - L_{Ss,n} - [\nu - n(\lambda - \nu\mu)]W_{c,n} - \delta P'_{s,n} &= 0 \quad (n \geq 1). \qquad \text{(B.21)}
\end{aligned}$$

The Fourier coefficients of loss and downstream pressure can be expressed explicitly in terms of the axial velocity from equations (B.12) and (B.19), respectively.

A packaged nonlinear, multi-variable equation solver from MATLAB [50] was used to solve (B.21) for the unknown velocity coefficients, $W_0$, $W_{c,n}$ and $W_{s,n}$. The solver used an iterative Gauss-Newton least-squares procedure based on an arbitrary initial guess of the axial velocity profile. The number of Fourier coefficients was restricted to $n \leq N$, which required $2N+1$ equations from the above system to determine the flow field. $N$ was chosen to be large enough so that higher harmonics had negligible contribution to the flow

variation. Restricting the analyses to the first 21 harmonics was sufficient to capture the flow field variations and provide a rapid numerical solution. The time to obtain each steady flow field was on the order of one minute.

## B.2 Linearized Flow Disturbances

A linearized version of the compressor model is developed here, appropriate for small amplitude, unsteady perturbations superimposed on a known background flow field. The notation for the unsteady flow perturbations is described in equations (2.21) and (2.22). Equations for each component in the compression system are written in the rotating frame of reference locked to the background tip clearance variation.

**Upstream Duct:** The linearized form of the Laplacian equation (2.14) for the upstream potential is given by

$$\frac{\partial^2 \phi'}{\partial \theta'^2} + \frac{\partial^2 \phi'}{\partial z'^2} = 0, \quad \text{where } v' = \frac{\partial \phi'}{\partial \theta'} \text{ and } w' = \frac{\partial \phi'}{\partial z'}, \tag{B.22}$$

with the boundary conditions

$$\phi' \to 0 \text{ as } z' \to z'_0, \quad \text{and} \quad \phi'(\theta', z') = \phi'(\theta' + 2\pi, z').$$

The solution for $\phi$ (to within an arbitrary constant) is

$$\phi' = w_0(t')z + \sum_{n=1}^{\infty} \frac{1}{n}(w_{c,n}(t') \cos n\theta' + w_{s,n}(t') \sin n\theta') e^{n(z'-z'_1)}, \tag{B.23}$$

where the perturbational Fourier coefficients $w_0$, $w_{c,n}$ and $w_{s,n}$ for $n \geq 1$ need to be determined.

From equation (B.23), the perturbation velocity at the compressor inlet face is expressed using the series notation introduced in equation (B.3):

$$\begin{aligned} w'_1 &= w_0 + \{w_{c,n}, w_{s,n}\}_{1,\infty} \\ v'_1 &= \{w_{s,n}, -w_{c,n}\}_{1,\infty}. \end{aligned} \tag{B.24}$$

The total pressure in the upstream irrotational flow field is related to the axial velocity through the linearized axial momentum equation

$$\frac{\partial w'}{\partial t'} + \frac{\partial p'_t}{\partial z'} = 0. \tag{B.25}$$

Assuming the total pressure perturbation is zero at $z' = z'_0$, equations (B.24) and (B.25) are used to describe the total pressure at the compressor inlet face as

$$p'_{t1} = -(z'_1 - z'_0)\frac{dw_0}{dt'} - \left\{\frac{1}{n}\frac{dw_{c,n}}{dt'}, \frac{1}{n}\frac{dw_{s,n}}{dt'}\right\}_{1,\infty}. \tag{B.26}$$

**Downstream Duct:** Since the axial velocity does not change across the compressor, the perturbational quantity is also conserved. Therefore, the axial velocity perturbation at the compressor exit is given as

$$w'_2 = w'_0 + \{w_{c,n}, w_{s,n}\}_{1,\infty}. \tag{B.27}$$

The tangential velocity is governed by the exit angle of the compressor, $\beta_2$, through equation (2.16). The linearized form of this relation is

$$\begin{aligned} v_2 &= \bar{W}_2 \delta \tan\beta_2 + w_2 \tan\bar{\beta}_2 \\ &= \bar{W}_2 (v_1 \frac{\partial \overline{\tan\beta_2}}{\partial V_1} + w_2 \frac{\partial \overline{\tan\beta_2}}{\partial W_1}) + w_2 \tan\bar{\beta}_2. \end{aligned} \tag{B.28}$$

Therefore, the linearized compressor exit velocities are expressed solely in terms of $w_0$, $w_{cn}$, $w_{sn}$, and the known background flow field.

A similar representation of the pressure perturbation is not as simple, so an approximation similar to the steady downstream pressure field approximation in Section B.1 is used. The pressure perturbations are assumed to behave in the downstream duct as they would in uniform flow:

$$\nabla^2 p' = 0. \tag{B.29}$$

To understand this approximation, the exact relation for $\nabla^2 p'$ can be found from the linearized form of the Euler equations (2.15),

$$\begin{aligned}
\frac{\partial v'}{\partial t'} + \bar{V}'\frac{\partial v'}{\partial \theta'} + v'\frac{\partial \bar{V}'}{\partial \theta'} + \bar{W}'\frac{\partial v'}{\partial z'} + w'\frac{\partial \bar{V}'}{\partial z'} + \frac{\partial p'}{\partial \theta'} &= 0 \\
\frac{\partial w'}{\partial t'} + \bar{V}'\frac{\partial w'}{\partial \theta'} + v'\frac{\partial \bar{W}'}{\partial \theta'} + \bar{W}'\frac{\partial w'}{\partial z'} + w'\frac{\partial \bar{W}'}{\partial z'} + \frac{\partial p'}{\partial z'} &= 0 \\
\frac{\partial v'}{\partial \theta'} + \frac{\partial w'}{\partial z'} &= 0. \qquad \text{(B.30)}
\end{aligned}$$

These equations combine to form

$$\nabla^2 p' = -2\left(\frac{\partial \bar{W}'}{\partial \theta'}\frac{\partial v'}{\partial z'} + \frac{\partial \bar{V}'}{\partial z'}\frac{\partial w'}{\partial \theta'} + \frac{\partial \bar{V}'}{\partial \theta'}\frac{\partial v'}{\partial \theta'} + \frac{\partial \bar{W}'}{\partial z'}\frac{\partial w'}{\partial z'}\right). \qquad \text{(B.31)}$$

For a nonuniform background flow, the interaction of the perturbation with the mean velocity gradients induce source terms on the right-hand-side of equation (B.31). Inclusion of these terms requires a more complex solution process for the unsteady flow field in the entire downstream duct. This process would drastically increase the numerical complexity of the approach. Prior stability analyses of nonuniform flows by Chue et al. [6], van Schalkwyk [76] and Graf [25] have also assumed these source terms to be negligible. The validity of their approximation has been demonstrated by the excellent comparisons between the predicted and experimentally observed stability trends for these cases. Furthermore, the results in Figure B-1 reinforce the adequacy of neglecting the interaction between the pressure field and the velocity shear.

The solution to equation (B.29) for the downstream pressure perturbations is given by

$$p' = p_P + (z_3' - z')p_{c0}' + \sum_{n=1}^{\infty}(p_{c,n}'\cos n\theta' + p_{s,n}'\cos n\theta')\mathrm{e}^{-n(z'-z_2')}. \qquad \text{(B.32)}$$

The constants in the above solution for $p'$ are chosen to enforce the boundary condition at $z' = z_3'$, where the duct pressure perturbation equals the plenum pressure perturbation ($p_P$).

To match the unknown pressure coefficients with the axial velocity coefficients, the linearized axial momentum equation (B.30) is applied at the compressor face:

$$\frac{\partial p_2'}{\partial z'} + \bar{V_2}' \frac{\partial w_2'}{\partial \theta'} + v_2' \frac{\partial \bar{W}_2'}{\partial \theta'} - \bar{W}_2' \frac{\partial v_2'}{\partial \theta'} - w_2' \frac{\partial \bar{V}_2'}{\partial \theta'} + \frac{\partial w_2'}{\partial t'} = 0, \tag{B.33}$$

where from equation (B.32), the pressure gradient is given by

$$\frac{\partial p_2'}{\partial z'} = -p_{c0}' - \left\{ n p_{c,n}', n p_{s,n}' \right\}_{1,\infty}. \tag{B.34}$$

The pressure coefficients are found by expanding equation (B.33) in terms of $w_0$, $w_{c,n}$, $w_{s,n}$, and equating terms of identical harmonics.

**Compressor:** The linearized form of the compressor pressure rise matching conditions (2.16) are given by

$$\begin{aligned} p_2' - p_{t1}' &= \delta\Psi_i - l_R - l_S - (\lambda - \nu\mu)\frac{\partial w_1'}{\partial \theta'} - \mu \frac{\partial w_1'}{\partial t'} + \nu v_1' \\ (1 + \tau_R \frac{\partial}{\partial t'} + (1-\nu)\tau_R \frac{\partial}{\partial \theta'})\, l_R &= \sigma(\delta\Psi_i - \delta\Psi) \\ (1 + \tau_S \frac{\partial}{\partial t'} - \nu\tau_S \frac{\partial}{\partial \theta'})\, l_S &= (1-\sigma)(\delta\Psi_i - \delta\Psi), \end{aligned} \tag{B.35}$$

where $\delta\Psi$ is defined from $\Psi(V_1, W_1, \varepsilon) = \bar{\Psi}(\bar{V}_1, \bar{W}_1, \bar{\varepsilon}) + \delta\Psi$. $\Psi$ and $\Psi_i$ are assumed to be quasi-steady functions of the local inlet velocities and tip clearance value, so their perturbed quantities are expressed as

$$\begin{aligned} \delta\Psi &= \overline{\frac{\partial \Psi}{\partial W}} w_1' + \overline{\frac{\partial \Psi}{\partial V}} v_1' + \overline{\frac{\partial \Psi}{\partial \varepsilon}} \delta\varepsilon \\ \delta\Psi_i &= \overline{\frac{\partial \Psi_i}{\partial W}} w_1' + \overline{\frac{\partial \Psi_i}{\partial V}} v_1' + \overline{\frac{\partial \Psi_i}{\partial \varepsilon}} \delta\varepsilon. \end{aligned} \tag{B.36}$$

**Plenum and Throttle:** The perturbation to the one-dimensional axial velocity through the throttle ($w_T$) is uniform throughout the throttle ducts because of mass conservation. Similarly, the $0^{\text{th}}$ harmonic of the axial velocity perturbation ($w_0$) is uniform throughout the compressor ducts. Therefore, changes to the plenum pressure perturbation ($p_P$) are governed by

$$\frac{dp_P}{dt'} = \frac{\gamma P_a}{V_P}(A_C w_0 - A_T w_T). \tag{B.37}$$

Linearizing equation (2.17) for the pressure drop across the throttle gives

$$p_P = k_T \frac{A_C}{A_T} \bar{W}_0 w_T + L_T \frac{dw_T}{dt'}. \tag{B.38}$$

All the linearized equations within the compression system component can be combined into a truncated matrix form:

$$\frac{d\vec{x}}{dt'} = \mathbf{A}\vec{x} + \mathbf{B}\vec{u}, \tag{B.39}$$

where vectors $\vec{x}$ and $\vec{u}$ are

$$\begin{aligned} \vec{x} &= [p_P \;\; w_T \;\; w_0 \;\; w_{c,1} \ldots w_{c,N} \;\; w_{s,1} \ldots w_{s,N} \;\; l_{R0} \;\; l_{Rc,1} \ldots l_{Rc,N} \;\; l_{Rs,1} \ldots l_{Rs,N} \\ &\qquad l_{S0} \;\; l_{Sc,1} \ldots l_{Sc,N} \;\; l_{Ss,1} \ldots l_{Ss,N}]^T \\ \vec{u} &= [\varepsilon_0 \;\; \varepsilon_{c,1} \ldots \varepsilon_{c,N} \;\; \varepsilon_{s,1} \ldots \varepsilon_{s,N}]^T. \end{aligned} \tag{B.40}$$

Elements of the $\{6N+5 \times 6N+5\}$ matrix $\mathbf{A}$ and the $\{6N+5 \times 2N+1\}$ matrix $\mathbf{B}$ come from the terms before the entries of $\vec{x}$ in the equations (B.35), (B.37) and (B.38). The detailed procedure for constructing these matrices in terms of the compression system parameters and the steady background flow field is described in Appendix C.

# APPENDIX C

# CONSTRUCTION OF STATE-SPACE MATRICES FOR LINEARIZED ROTATING TIP CLEARANCE MODEL

In this appendix, the **A** and **B** state-space matrices are developed for equation (2.23) which determines the linearized dynamic behavior for a compressor with a rotating tip clearance asymmetry. The **C** and **D** matrices used for active control in equation (4.3) are also developed, using upstream static pressure perturbations as the output.

Contained within the equations representing the linearized components of the compression system are products such as $\bar{V}w$, where both the steady term ($\bar{V}$) and the unsteady term ($w$) vary around the circumference. A method is presented here to represent the Fourier coefficients of this product in terms of the unknown coefficients of $w$ and the known representation of $\bar{V}$.

Define the harmonic expansions of $\bar{V}$ and $w$ with the following series (truncated at the $N^{\text{th}}$ harmonic):

$$\begin{aligned} \bar{V}(\theta') &= V_0 + \sum_{n=1}^{N} (V_{c,n} \cos n\theta' + V_{s,n} \sin n\theta') \\ w(\theta', t') &= w_0(t') + \sum_{n=1}^{N} (w_{c,n}(t') \cos n\theta' + w_{s,n}(t') \sin n\theta'). \end{aligned} \tag{C.1}$$

Multiplying these two series together gives the product

$$\begin{aligned}\bar{V}w &= V_0 w_0 + V_0 \sum_{n=1}^{N}(w_{c,n}\cos n\theta' + w_{s,n}\sin n\theta') + w_0 \sum_{n=1}^{N}(V_{c,n}\cos n\theta' + V_{s,n}\sin n\theta') \\ &\quad + \sum_{n=1}^{N}\sum_{m=1}^{N}(V_{c,n}w_{c,m}\cos n\theta'\cos m\theta' + V_{c,n}w_{s,m}\cos n\theta'\sin m\theta' \\ &\qquad + V_{s,n}w_{c,m}\sin n\theta'\cos m\theta' + V_{s,n}w_{s,m}\sin n\theta'\sin m\theta'). \qquad \text{(C.2)}\end{aligned}$$

Substitute into equation (C.2) the following trigonometric identities

$$\begin{aligned}\cos n\theta'\cos m\theta' &= \frac{1}{2}[\cos(n+m)\theta' + \cos(n-m)\theta'] \\ \cos n\theta'\sin m\theta' &= \frac{1}{2}[\sin(n+m)\theta' - \sin(n-m)\theta'] \\ \sin n\theta'\cos m\theta' &= \frac{1}{2}[\sin(n+m)\theta' + \sin(n-m)\theta'] \\ \sin n\theta'\sin m\theta' &= -\frac{1}{2}[\cos(n+m)\theta' - \cos(n-m)\theta'], \qquad \text{(C.3)}\end{aligned}$$

and collect terms of $\cos(n\theta')$ and $\sin(n\theta')$ up to the $N^{\text{th}}$ harmonic for

$$\begin{aligned}\bar{V}w &= V_0 w_0 + \frac{1}{2}\sum_{n=1}^{N}(V_{c,n}w_{c,n} + V_{s,n}w_{s,n}) + \cdots \\ &\quad + \frac{1}{2}\sum_{n=1}^{N}\cos n\theta'\left[\sum_{m=1}^{N-n}(V_{c,m}w_{c,m+n} + w_{c,m}V_{c,m+n} + V_{s,m}w_{s,m+n} + w_{s,m}V_{s,m+n}) + \cdots\right. \\ &\qquad \left. + \sum_{m=0}^{n}(V_{c,m}w_{c,n-m} - V_{s,m}w_{s,n-m}) + V_0 w_{c,n} + w_0 V_{c,n}\right] + \cdots \\ &\quad + \frac{1}{2}\sum_{n=1}^{N}\sin n\theta'\left[\sum_{m=1}^{N-n}(w_{c,m}V_{s,m+n} - V_{s,m}W_{c,m+n} - w_{s,m}V_{c,m+n} + V_{c,m}w_{s,m+n}) + \cdots\right. \\ &\qquad \left. + \sum_{m=0}^{n}(V_{c,m}w_{s,n-m} + V_{s,m}w_{c,n-m}) + V_0 w_{s,n} + w_0 V_{s,n}\right] \qquad \text{(C.4)}\end{aligned}$$

where $V_{c,0}$ and $w_{c,0}$ are defined as $V_0$ and $w_0$ respectively, and we define $V_{s,0} = w_{s,0} = 0$. This can also be written as

$$\bar{V}w \equiv \sum_{n=0}^{N}(f_{c,n}\cos n\theta + f_{s,n}\sin n\theta) \qquad \text{(C.5)}$$

where

$$
\begin{aligned}
f_{c,0} &= w_0 V_0 + \frac{1}{2}\sum_{n=1}^{N}(w_{c,n}V_{c,n} + w_{s,n}V_{s,n}) \\
f_{s,0} &= 0 \\
f_{c,n} &= \frac{1}{2}\Bigg[w_0 V_{c,n} + w_{c,n}V_0 + \sum_{m=0}^{n}(w_{c,m}V_{c,n-m} - w_{s,m}V_{s,n-m}) + \cdots \\
&\quad + \sum_{m=1}^{N-n}(w_{c,m}V_{c,n+m} + w_{s,m}V_{s,n+m}) + \sum_{m=n+1}^{N}(w_{c,m}V_{c,m-n} + w_{s,m}V_{s,m-n})\Bigg] \\
f_{s,n} &= \frac{1}{2}\Bigg[w_0 V_{s,n} + w_{s,n}V_0 + \sum_{m=0}^{n}(w_{s,m}V_{c,n-m} + w_{c,m}V_{s,n-m}) + \cdots \\
&\quad + \sum_{m=1}^{N-n}(w_{c,m}V_{s,n+m} - w_{s,m}V_{c,n+m}) + \sum_{m=n+1}^{N}(w_{s,m}V_{c,m-n} - w_{c,m}V_{s,m-n})\Bigg]
\end{aligned}
\tag{C.6}
$$

Thus, matrices $\mathbf{P}, \mathbf{Q}, \mathbf{R}, \mathbf{S}$ can be created such that

$$
\begin{aligned}
f_{c,n} &= \sum_{m=0}^{N}(\mathbf{P}_{n,m}w_{c,m} + \mathbf{Q}_{n,m}w_{s,m}) \\
f_{s,n} &= \sum_{m=0}^{N}(\mathbf{R}_{n,m}w_{c,m} + \mathbf{S}_{n,m}w_{s,m}),
\end{aligned}
\tag{C.7}
$$

where the matrix elements $(n, m)$ are indexed from 0 to $N$. Equation (C.5) can be written using the series notation from equation (B.3),

$$
\bar{V}w = \left\{\sum_{m=0}^{N}(\mathbf{P}_{n,m}w_{c,m} + \mathbf{Q}_{n,m}w_{s,m}), \sum_{m=0}^{N}(\mathbf{R}_{n,m}w_{c,m} + \mathbf{S}_{n,m}w_{s,m})\right\}_{0,N}. \tag{C.8}
$$

The $\{N+1 \times N+1\}$ elements of each matrix $\mathbf{P}, \mathbf{Q}, \mathbf{R}, \mathbf{S}$ contain only combinations of the coefficients of the background flow, $V_{c,n}$ and $V_{s,n}$, as dictated by equation (C.6).

Define six such $\mathbf{P}, \mathbf{Q}, \mathbf{R}, \mathbf{S}$ matrices for the products found in the linearized matching

equations in Appendix B.2:

$$\begin{aligned}
\overline{\frac{\partial\Psi}{\partial W}}w_1' &\equiv \left\{\sum_{m=0}^{N}(\mathbf{P}^1_{n,m}w_{c,m}+\mathbf{Q}^1_{n,m}w_{s,m}),\sum_{m=0}^{N}(\mathbf{R}^1_{n,m}w_{c,m}+\mathbf{S}^1_{n,m}w_{s,m})\right\}_{0,N}\\
\overline{\frac{\partial\Psi_i}{\partial W}}w_1' &\equiv \left\{\sum_{m=0}^{N}(\mathbf{P}^2_{n,m}w_{c,m}+\mathbf{Q}^2_{n,m}w_{s,m}),\sum_{m=0}^{N}(\mathbf{R}^2_{n,m}w_{c,m}+\mathbf{S}^2_{n,m}w_{s,m})\right\}_{0,N}\\
\overline{\frac{\partial\Psi}{\partial V}}v_1' &\equiv \left\{\sum_{m=0}^{N}(\mathbf{P}^3_{n,m}w_{c,m}+\mathbf{Q}^3_{n,m}w_{s,m}),\sum_{m=0}^{N}(\mathbf{R}^3_{n,m}w_{c,m}+\mathbf{S}^3_{n,m}w_{s,m})\right\}_{0,N}\\
\overline{\frac{\partial\Psi_i}{\partial V}}v_1' &\equiv \left\{\sum_{m=0}^{N}(\mathbf{P}^4_{n,m}w_{c,m}+\mathbf{Q}^4_{n,m}w_{s,m}),\sum_{m=0}^{N}(\mathbf{R}^4_{n,m}w_{c,m}+\mathbf{S}^4_{n,m}w_{s,m})\right\}_{0,N}\\
\overline{\frac{\partial\Psi}{\partial\varepsilon}}\delta\varepsilon &\equiv \left\{\sum_{m=0}^{N}(\mathbf{P}^5_{n,m}\varepsilon_{c,m}+\mathbf{Q}^5_{n,m}\varepsilon_{s,m}),\sum_{m=0}^{N}(\mathbf{R}^5_{n,m}\varepsilon_{c,m}+\mathbf{S}^5_{n,m}\varepsilon_{s,m})\right\}_{0,N}\\
\overline{\frac{\partial\Psi_i}{\partial\varepsilon}}\delta\varepsilon &\equiv \left\{\sum_{m=0}^{N}(\mathbf{P}^6_{n,m}\varepsilon_{c,m}+\mathbf{Q}^6_{n,m}\varepsilon_{s,m}),\sum_{m=0}^{N}(\mathbf{R}^6_{n,m}\varepsilon_{c,m}+\mathbf{S}^6_{n,m}\varepsilon_{s,m})\right\}_{0,N}. \qquad \text{(C.9)}
\end{aligned}$$

Note that for the above representations of $\overline{\frac{\partial\Psi}{\partial V}}v_1'$ and $\overline{\frac{\partial\Psi_i}{\partial V}}v_1'$, equation (B.24) has been implicitly used to express $v_1'$ in terms of the coefficients of $w_1'$.

$\mathbf{P},\mathbf{Q},\mathbf{R}$ and $\mathbf{S}$ matrices can also be made for the products on the right-hand-side of equation (B.28) to express the exit tangential velocity, $v_2'$ in terms of $w_1'$. This representation of $v_2'$ is substituted into equation (B.33) so that the downstream static pressure coefficients in equation (B.34) can be written as

$$\begin{aligned}
p'_{c,0} &= \frac{dw_0}{dt'}+\sum_{m=0}^{N}(\mathbf{P}^7_{0,m}w_{c,m}+\mathbf{Q}^7_{0,m}w_{s,m})\\
p'_{c,n} &= \frac{dw_{c,n}}{dt'}+\frac{1}{n}\sum_{m=0}^{N}(\mathbf{P}^7_{n,m}w_{c,m}+\mathbf{Q}^7_{n,m}w_{s,m})\\
p'_{s,n} &= \frac{dw_{s,n}}{dt'}+\frac{1}{n}\sum_{m=0}^{N}(\mathbf{R}^7_{n,m}w_{c,m}+\mathbf{S}^7_{n,m}w_{s,m}). \qquad \text{(C.10)}
\end{aligned}$$

All the terms in the compressor matching equations (B.35) are now in a form which uses only the linear states found in $\vec{x}$, defined in equation (2.24). Substitute the above

equations (C.9) and (C.10) into equation (B.35) to give the following three relations:

$$p_P + (z_3' - z_2')\left[\frac{dw_0}{dt'} + \sum_{n=0}^{N}(\mathbf{P}^7_{0,n}w_{c,n} + \mathbf{Q}^7_{0,n}w_{s,n})\right] + \left\{\frac{1}{n}\sum_{m=0}^{N}(\mathbf{P}^7_{n,m}w_{c,m} + \mathbf{Q}^7_{n,m}w_{s,m}),\right.$$
$$\left.\frac{1}{n}\sum_{m=0}^{N}(\mathbf{R}^7_{n,m}w_{c,m} + \mathbf{S}^7_{n,m}w_{s,m})\right\}_{1,N} + (z_1' - z_0')\frac{dw_0}{dt'} + 2\frac{d}{dt'}\left\{\frac{w_{c,n}}{n}, \frac{w_{s,n}}{n}\right\}_{1,N} = \cdots$$
$$\left\{\sum_{m=0}^{N}([\mathbf{P}^2_{n,m} + \mathbf{P}^4_{n,m}]w_{c,m} + [\mathbf{Q}^2_{n,m} + \mathbf{Q}^4_{n,m}]w_{s,m}), \sum_{m=0}^{N}([\mathbf{R}^2_{n,m} + \mathbf{R}^4_{n,m}]w_{c,m} + [\mathbf{S}^2_{n,m} + \mathbf{S}^4_{n,m}]w_{s,m})\right\}_{0,N}$$
$$-l_{R0} - \{l_{Rc,n}, l_{Rs,n}\}_{1,N} - l_{S0} - \{l_{Sc,n}, l_{Ss,n}\}_{1,N} - (\lambda - \nu\mu)\{nw_{s,n}, -nw_{c,n}\}_{1,N} + \nu\{w_{c,n}, -w_{s,n}\}_{1,N}$$
$$-\mu\frac{d}{dt'}\left\{\frac{w_{c,n}}{n}, \frac{w_{s,n}}{n}\right\}_{1,N} + \left\{\sum_{m=0}^{N}(\mathbf{P}^6_{n,m}\varepsilon_{c,m} + \mathbf{Q}^6_{n,m}\varepsilon_{s,m}), \sum_{m=0}^{N}(\mathbf{R}^6_{n,m}\varepsilon_{c,m} + \mathbf{S}^6_{n,m}\varepsilon_{s,m})\right\}_{0,N} \quad \text{(C.11)}$$

$$l_{R0} + \tau_R\frac{dl_{R0}}{dt'} + \{l_{Rc,n}, l_{Rs,n}\}_{1,N} + \tau_R\frac{d}{dt'}\{l_{Rc,n}, l_{Rs,n}\}_{1,N} + (1-\nu)\tau_R\{l_{Rs,n}, -l_{Rc,n}\}_{1,N} = \cdots$$
$$\left\{\sum_{m=0}^{N}([\mathbf{P}^6_{n,m} - \mathbf{P}^5_{n,m}]\varepsilon_{c,m} + [\mathbf{Q}^6_{n,m} - \mathbf{Q}^5_{n,m}]\varepsilon_{s,m}), \sum_{m=0}^{N}[(\mathbf{R}^6_{n,m} - \mathbf{R}^5_{n,m}]\varepsilon_{c,m} + [\mathbf{S}^6_{n,m} - \mathbf{S}^5_{n,m}]\varepsilon_{s,m})\right\}_{0,N}$$
$$+\sigma\left\{\sum_{m=0}^{N}([\mathbf{P}^2_{n,m} + \mathbf{P}^4_{n,m} - \mathbf{P}^1_{n,m} - \mathbf{P}^3_{n,m}]w_{c,m} + [\mathbf{Q}^2_{n,m} + \mathbf{Q}^4_{n,m} - \mathbf{Q}^1_{n,m} - \mathbf{Q}^3_{n,m}]w_{s,m}),\right.$$
$$\left.\sum_{m=0}^{N}([\mathbf{R}^2_{n,m} + \mathbf{R}^4_{n,m} - \mathbf{R}^1_{n,m} - \mathbf{R}^3_{n,m}]w_{c,m} + [\mathbf{S}^2_{n,m} + \mathbf{S}^4_{n,m} - \mathbf{S}^1_{n,m} - \mathbf{S}^3_{n,m}]w_{s,m})\right\}_{0,N} \quad \text{(C.12)}$$

$$l_{S0} + \tau_S\frac{dl_{S0}}{dt'} + \{l_{Sc,n}, l_{Ss,n}\}_{1,N} + \tau_S\frac{d}{dt'}\{l_{Sc,n}, l_{Ss,n}\}_{1,N} - \nu\tau_S\{l_{Ss,n}, -l_{Sc,n}\}_{1,N} = \cdots$$
$$\left\{\sum_{m=0}^{N}([\mathbf{P}^6_{n,m} - \mathbf{P}^5_{n,m}]\varepsilon_{c,m} + [\mathbf{Q}^6_{n,m} - \mathbf{Q}^5_{n,m}]\varepsilon_{s,m}), \sum_{m=0}^{N}[(\mathbf{R}^6_{n,m} - \mathbf{R}^5_{n,m}]\varepsilon_{c,m} + [\mathbf{S}^6_{n,m} - \mathbf{S}^5_{n,m}]\varepsilon_{s,m})\right\}_{0,N}$$
$$+(1-\sigma)\left\{\sum_{m=0}^{N}([\mathbf{P}^2_{n,m} + \mathbf{P}^4_{n,m} - \mathbf{P}^1_{n,m} - \mathbf{P}^3_{n,m}]w_{c,m} + [\mathbf{Q}^2_{n,m} + \mathbf{Q}^4_{n,m} - \mathbf{Q}^1_{n,m} - \mathbf{Q}^3_{n,m}]w_{s,m}),\ \cdots\right.$$
$$\left.\sum_{m=0}^{N}([\mathbf{R}^2_{n,m} + \mathbf{R}^4_{n,m} - \mathbf{R}^1_{n,m} - \mathbf{R}^3_{n,m}]w_{c,m} + [\mathbf{S}^2_{n,m} + \mathbf{S}^4_{n,m} - \mathbf{S}^1_{n,m} - \mathbf{S}^3_{n,m}]w_{s,m})\right\}_{0,N}. \quad \text{(C.13)}$$

These can be arranged into the following $6N + 3$ independent equations by collecting the

sine and cosine terms for each harmonic in $\theta'$:

$$
\begin{aligned}
(L_C+\mu)\frac{dw_0}{dt'} &= \sum_{m=1}^{N}\Big\{[\mathbf{P}^2_{0,m}+\mathbf{P}^4_{0,m}-(z_3'-z_2')\mathbf{P}^7_{0,m}]w_{c,m}+[\mathbf{Q}^2_{0,m}+\mathbf{Q}^4_{0,m}-(z_3'-z_2')\mathbf{Q}^7_{0,m}]w_{s,m}\Big\} \\
&\quad -p_P+[\mathbf{P}^2_{0,0}+\mathbf{P}^4_{0,0}-(z_3'-z_2')\mathbf{P}^7_{0,0}]w_0-l_{R0}-l_{S0} \\
&\quad +\mathbf{P}^6_{0,0}\varepsilon_0+\sum_{m=1}^{N}\{\mathbf{P}^6_{0,m}\varepsilon_{c,m}+\mathbf{Q}^6_{0,m}\varepsilon_{s,m}\} \qquad \text{(C.14)} \\
(\mu+\frac{2}{n})\frac{dw_{c,n}}{dt'} &= \sum_{m=1}^{N}\Big\{[\mathbf{P}^2_{n,m}+\mathbf{P}^4_{n,m}-\mathbf{P}^7_{n,m}]w_{c,m}+[\mathbf{Q}^2_{n,m}+\mathbf{Q}^4_{n,m}-\mathbf{Q}^7_{n,m}]w_{s,m}\Big\} \\
&\quad +[\mathbf{P}^2_{n,0}+\mathbf{P}^4_{n,0}-\mathbf{P}^7_{n,0}]w_0+[\nu-n(\lambda-\nu\mu)]w_{s,n}-l_{Rc,n}-l_{Sc,n} \\
&\quad +\mathbf{P}^6_{n,0}\varepsilon_0+\sum_{m=1}^{N}\{\mathbf{P}^6_{n,m}\varepsilon_{c,m}+\mathbf{Q}^6_{n,m}\varepsilon_{s,m}\} \qquad \text{(C.15)} \\
(\mu+\frac{2}{n})\frac{dw_{s,n}}{dt'} &= \sum_{m=1}^{N}\Big\{[\mathbf{R}^2_{n,m}+\mathbf{R}^4_{n,m}-\mathbf{R}^7_{n,m}]w_{c,m}+[\mathbf{S}^2_{n,m}+\mathbf{S}^4_{n,m}-\mathbf{S}^7_{n,m}]w_{s,m}\Big\} \\
&\quad -[\nu-n(\lambda-\nu\mu)]w_{c,n}-l_{Rs,n}-l_{Ss,n}+\sum_{m=1}^{N}\{\mathbf{R}^6_{n,m}\varepsilon_{c,m}+\mathbf{S}^6_{n,m}\varepsilon_{s,m}\} \qquad \text{(C.16)}
\end{aligned}
$$

$$
\begin{aligned}
\tau_R\frac{dl_{R0}}{dt'} &= \sigma\sum_{m=1}^{N}\Big\{[\mathbf{P}^2_{0,m}+\mathbf{P}^4_{0,m}-\mathbf{P}^1_{0,m}-\mathbf{P}^3_{0,m}]w_{c,m}+[\mathbf{Q}^2_{0,m}+\mathbf{Q}^4_{0,m}-\mathbf{Q}^1_{0,m}-\mathbf{Q}^3_{0,m}]w_{s,m}\Big\} \\
&\quad +\sigma[\mathbf{P}^2_{0,0}+\mathbf{P}^4_{0,0}-\mathbf{P}^1_{0,0}-\mathbf{P}^3_{0,0}]w_0-l_{R0}+\sigma(\mathbf{P}^6_{0,0}-\mathbf{P}^5_{0,0})\varepsilon_0 \\
&\quad +\sigma\sum_{m=1}^{N}\{(\mathbf{P}^6_{0,m}-\mathbf{P}^5_{0,m})\varepsilon_{c,m}+(\mathbf{Q}^6_{0,m}-\mathbf{P}^5_{0,m})\varepsilon_{s,m}\} \qquad \text{(C.17)} \\
\tau_R\frac{dl_{Rc,n}}{dt'} &= \sigma\sum_{m=1}^{N}\Big\{[\mathbf{P}^2_{n,m}+\mathbf{P}^4_{n,m}-\mathbf{P}^1_{n,m}-\mathbf{P}^3_{n,m}]w_{c,m}+[\mathbf{Q}^2_{n,m}+\mathbf{Q}^4_{n,m}-\mathbf{Q}^1_{n,m}-\mathbf{Q}^3_{n,m}]w_{s,m}\Big\} \\
&\quad +\sigma[\mathbf{P}^2_{n,0}+\mathbf{P}^4_{n,0}-\mathbf{P}^1_{n,0}-\mathbf{P}^3_{n,0}]w_0-l_{Rc,n}-n\tau_R(1-\nu)l_{Rs,n} \\
&\quad +\sigma(\mathbf{P}^6_{n,0}-\mathbf{P}^5_{n,0})\varepsilon_0+\sigma\sum_{m=1}^{N}\{(\mathbf{P}^6_{n,m}-\mathbf{P}^5_{n,m})\varepsilon_{c,m}+(\mathbf{Q}^6_{n,m}-\mathbf{P}^5_{n,m})\varepsilon_{s,m}\} \qquad \text{(C.18)} \\
\tau_R\frac{dl_{Rs,n}}{dt'} &= \sigma\sum_{m=1}^{N}\Big\{[\mathbf{R}^2_{n,m}+\mathbf{R}^4_{n,m}-\mathbf{R}^1_{n,m}-\mathbf{R}^3_{n,m}]w_{c,m}+[\mathbf{S}^2_{n,m}+\mathbf{S}^4_{n,m}-\mathbf{S}^1_{n,m}-\mathbf{S}^3_{n,m}]w_{s,m}\Big\} \\
&\quad -l_{Rs,n}+n\tau_R(1-\nu)l_{Rc,n}+\sigma\sum_{m=1}^{N}\{(\mathbf{R}^6_{n,m}-\mathbf{R}^5_{n,m})\varepsilon_{c,m}+(\mathbf{S}^6_{n,m}-\mathbf{S}^5_{n,m})\varepsilon_{s,m}\} \qquad \text{(C.19)}
\end{aligned}
$$

$$\tau_S \frac{dl_{S0}}{dt'} = (1-\sigma)\sum_{m=1}^{N}\left\{[\mathbf{P}^2_{0,m}+\mathbf{P}^4_{0,m}-\mathbf{P}^1_{0,m}-\mathbf{P}^3_{0,m}]w_{c,m}+[\mathbf{Q}^2_{0,m}+\mathbf{Q}^4_{0,m}-\mathbf{Q}^1_{0,m}-\mathbf{Q}^3_{0,m}]w_{s,m}\right\}$$
$$+(1-\sigma)[\mathbf{P}^2_{0,0}+\mathbf{P}^4_{0,0}-\mathbf{P}^1_{0,0}-\mathbf{P}^3_{0,0}]w_0 - l_{S0}+(1-\sigma)(\mathbf{P}^6_{0,0}-\mathbf{P}^5_{0,0})\varepsilon_0$$
$$+(1-\sigma)\sum_{m=1}^{N}\{(\mathbf{P}^6_{0,m}-\mathbf{P}^5_{0,m})\varepsilon_{c,m}+(\mathbf{Q}^6_{0,m}-\mathbf{P}^5_{0,m})\varepsilon_{s,m}\} \quad \text{(C.20)}$$

$$\tau_S \frac{dl_{Sc,n}}{dt'} = (1-\sigma)\sum_{m=1}^{N}\left\{[\mathbf{P}^2_{n,m}+\mathbf{P}^4_{n,m}-\mathbf{P}^1_{n,m}-\mathbf{P}^3_{n,m}]w_{c,m}+[\mathbf{Q}^2_{n,m}+\mathbf{Q}^4_{n,m}-\mathbf{Q}^1_{n,m}-\mathbf{Q}^3_{n,m}]w_{s,m}\right\}$$
$$+(1-\sigma)[\mathbf{P}^2_{n,0}+\mathbf{P}^4_{n,0}-\mathbf{P}^1_{n,0}-\mathbf{P}^3_{n,0}]w_0 - l_{Sc,n}+n\tau_S\nu l_{Ss,n}+(1-\sigma)(\mathbf{P}^6_{n,0}-\mathbf{P}^5_{n,0})\varepsilon_0$$
$$+(1-\sigma)\sum_{m=1}^{N}\{(\mathbf{P}^6_{n,m}-\mathbf{P}^5_{n,m})\varepsilon_{c,m}+(\mathbf{Q}^6_{n,m}-\mathbf{P}^5_{n,m})\varepsilon_{s,m}\} \quad \text{(C.21)}$$

$$\tau_S \frac{dl_{Ss,n}}{dt'} = (1-\sigma)\sum_{m=1}^{N}\left\{[\mathbf{R}^2_{n,m}+\mathbf{R}^4_{n,m}-\mathbf{R}^1_{n,m}-\mathbf{R}^3_{n,m}]w_{c,m}+[\mathbf{S}^2_{n,m}+\mathbf{S}^4_{n,m}-\mathbf{S}^1_{n,m}-\mathbf{S}^3_{n,m}]w_{s,m}\right\}$$
$$-l_{Ss,n}-n\tau_S\nu l_{Sc,n}+(1-\sigma)\sum_{m=1}^{N}\{(\mathbf{R}^6_{n,m}-\mathbf{R}^5_{n,m})\varepsilon_{c,m}+(\mathbf{S}^6_{n,m}-\mathbf{S}^5_{n,m})\varepsilon_{s,m}\}. \quad \text{(C.22)}$$

The final two equations to complete the system are the linear plenum and throttle dynamics from equations (B.37) and (B.38), which are rewritten below:

$$\frac{dp_P}{dt'} = \frac{\gamma A_C P_a}{V_P}w_0 - \frac{\gamma A_T P_a}{V_P}w_T$$
$$\frac{dw_T}{dt'} = \frac{1}{L_T}p_P - \frac{k_T\bar{W}_0 A_C}{L_T A_T}w_T. \quad \text{(C.23)}$$

The above $6N+5$ linear equations (C.14 to C.23) can now be directly arranged in the state-space matrix form ($d\vec{x}/dt' = \mathbf{A}\vec{x}+\mathbf{B}\vec{u}$) in terms of the $6N+5$ unknown elements of $\vec{x}$.

To complete the state-space representation of the compressor used for active control methods, the output vector ($\vec{y}$) must be written as linear combinations of the compressor state vector ($\vec{x}$) and the input vector ($\vec{u}$) in the form $\vec{y} = \mathbf{C}\vec{x} + \mathbf{D}\vec{u}$, as described in equation (4.3). The method detailed below is for the specific case of using the upstream static pressure harmonics as the output vector, which was the output considered for all active control analyses in this thesis.

The static pressure at the compressor inlet face (station 1 in the compression system, Figure 2-1) can be written as the difference between the total pressure and the dynamic

head, as in

$$P_1' = P_{t1}' - \frac{1}{2}(V_1'^2 + W_1'^2). \tag{C.24}$$

Linearizing this equation yields the following expression for the pressure perturbations:

$$p_2' = p_{t2}' - \bar{V}'_1 v_1' + \bar{W}'_1 w_1'. \tag{C.25}$$

Define $\mathbf{P}, \mathbf{Q}, \mathbf{R}, \mathbf{S}$ matrices to represent the products $\bar{V}_1' v_1'$ and $\bar{W}_1' w_1'$ up to the $N^{\text{th}}$ harmonic:

$$\begin{aligned}
\bar{W}_1' w_1' &\equiv \left\{ \sum_{m=0}^{N} (\mathbf{P}^8_{n,m} w_{c,m} + \mathbf{Q}^8_{n,m} w_{s,m}), \sum_{m=0}^{N} (\mathbf{R}^8_{n,m} w_{c,m} + \mathbf{S}^8_{n,m} w_{s,m}) \right\}_{0,N} \\
\bar{V}_1' v_1' &\equiv \left\{ \sum_{m=0}^{N} (\mathbf{P}^9_{n,m} w_{c,m} + \mathbf{Q}^9_{n,m} w_{s,m}), \sum_{m=0}^{N} (\mathbf{R}^9_{n,m} w_{c,m} + \mathbf{S}^9_{n,m} w_{s,m}) \right\}_{0,N}.
\end{aligned} \tag{C.26}$$

Substitute these expressions, and equation (B.26) for the total pressure perturbation, into equation (C.25) to give

$$\begin{aligned}
p_2' &= -(z_1' - z_0') \frac{dw_0}{dt'} - \left\{ \frac{1}{n} \frac{dw_{c,n}}{dt'}, \frac{1}{n} \frac{dw_{s,n}}{dt'} \right\}_{1,N} - \left\{ \sum_{m=0}^{N} ([\mathbf{P}^8_{n,m} + \mathbf{P}^9_{n,m}] w_{c,m} + [\mathbf{Q}^8_{n,m} + \mathbf{Q}^9_{n,m}] w_{s,m}), \right. \\
&\left. \sum_{m=0}^{N} ([\mathbf{R}^8_{n,m} + \mathbf{R}^9_{n,m}] w_{c,m} + [\mathbf{S}^8_{n,m} + \mathbf{R}^9_{n,m}] w_{s,m}) \right\}_{0,N}.
\end{aligned} \tag{C.27}$$

The time derivative terms $\frac{dw_0}{dt'}$, $\frac{dw_{c,n}}{dt'}$ and $\frac{dw_{s,n}}{dt'}$ can be replaced with their representation in terms of elements of $\vec{x}$ from equation (C.14). Define the first $N$ harmonics of $p_2'$ with the following series notation:

$$p_2' \equiv p_{20} + \{p_{2c,n}, p_{2s,n}\}_{1,N}, \tag{C.28}$$

so that the output vector $\vec{y}$ is given by

$$\vec{y} = [p_{20} \;\; p_{2c,1} \cdots p_{2c,n} \;\; p_{2s,1} \cdots p_{2s,n}]^T. \tag{C.29}$$

The following $2N + 1$ equations, one for each harmonic, can the be found from matching

like harmonics in equation (C.27):

$$
\begin{aligned}
p_{20} \;=\; & -\frac{z_1'-z_0'}{L_C+\mu}\left(\sum_{m=1}^{N}\left\{[\mathbf{P}^2_{0,m}+\mathbf{P}^4_{0,m}-(z_3'-z_2')\mathbf{P}^7_{0,m}]w_{c,m}+[\mathbf{Q}^2_{0,m}+\mathbf{Q}^4_{0,m}-(z_3'-z_2')\mathbf{Q}^7_{0,m}]w_{s,m}\right\}\right. \\
& \left.+[\mathbf{P}^2_{0,0}+\mathbf{P}^4_{0,0}-(z_3'-z_2')\mathbf{P}^7_{0,0}]w_0-l_{R0}-l_{S0}+\mathbf{P}^6_{0,0}\varepsilon_0+\sum_{m=1}^{N}\{\mathbf{P}^6_{0,m}\varepsilon_{c,m}+\mathbf{Q}^6_{0,m}\varepsilon_{s,m}\}\right) \\
& -\sum_{m=1}^{N}\left\{[\mathbf{P}^8_{0,m}+\mathbf{P}^9_{0,m}]w_{c,m}+[\mathbf{Q}^8_{0,m}+\mathbf{Q}^9_{0,m}]w_{s,m}\right\} \qquad \text{(C.30)}
\end{aligned}
$$

$$
\begin{aligned}
p_{2c,n} \;=\; & -\frac{1}{2+n\mu}\left(\sum_{m=1}^{N}\left\{[\mathbf{P}^2_{n,m}+\mathbf{P}^4_{n,m}-\mathbf{P}^7_{n,m}]w_{c,m}+[\mathbf{Q}^2_{n,m}+\mathbf{Q}^4_{n,m}-\mathbf{Q}^7_{n,m}]w_{s,m}\right\}\right. \\
& +[\mathbf{P}^2_{n,0}+\mathbf{P}^4_{n,0}-\mathbf{P}^7_{n,0}]w_0+[\nu-n(\lambda-\nu\mu)]w_{s,n}-l_{Rc,n}-l_{Sc,n}+\mathbf{P}^6_{n,0}\varepsilon_0 \\
& \left.+\sum_{m=1}^{N}\{\mathbf{P}^6_{n,m}\varepsilon_{c,m}+\mathbf{Q}^6_{n,m}\varepsilon_{s,m}\}\right)-\sum_{m=1}^{N}\left\{[\mathbf{P}^8_{n,m}+\mathbf{P}^9_{n,m}]w_{c,m}+[\mathbf{Q}^8_{n,m}+\mathbf{Q}^9_{n,m}]w_{s,m}\right\} \qquad \text{(C.31)}
\end{aligned}
$$

$$
\begin{aligned}
p_{2s,n} \;=\; & -\frac{1}{2+n\mu}\left(\sum_{m=1}^{N}\left\{[\mathbf{R}^2_{n,m}+\mathbf{R}^4_{n,m}-\mathbf{R}^7_{n,m}]w_{c,m}+[\mathbf{S}^2_{n,m}+\mathbf{S}^4_{n,m}-\mathbf{S}^7_{n,m}]w_{s,m}\right\}\right. \\
& \left.-[\nu-n(\lambda-\nu\mu)]w_{c,n}-l_{Rs,n}-l_{Ss,n}+\sum_{m=1}^{N}\{\mathbf{R}^6_{n,m}\varepsilon_{c,m}+\mathbf{S}^6_{n,m}\varepsilon_{s,m}\}\right) \\
& -\sum_{m=1}^{N}\left\{[\mathbf{R}^8_{n,m}+\mathbf{R}^9_{n,m}]w_{c,m}+[\mathbf{S}^8_{n,m}+\mathbf{S}^9_{n,m}]w_{s,m}\right\}. \qquad \text{(C.32)}
\end{aligned}
$$

These equations can now be directly arranged in the matrix form $\vec{y} = \mathbf{C}\vec{x} + \mathbf{D}\vec{u}$ for use in equation (4.3).

# APPENDIX D

# DEVELOPMENT OF TOTAL-TO-STATIC PRESSURE RISE CHARACTERISTICS AND EXIT FLOW ANGLE RELATIONS FOR MIT 3-STAGE AND NASA STAGE-37 COMPRESSORS

The family of axisymmetric pressure rise characteristics and exit flow angle relationships are described here for the MIT 3-stage and NASA Stage-37 compressors. These relationships are developed as explicit functions of the inlet axial velocity, tangential velocity and the tip clearance, as required by the rotating tip clearance asymmetry model.

## D.1 MIT 3-Stage

The axisymmetric exit flow angle and pressure rise characteristics for the MIT 3-stage compressor have been represented by analytical formulas that capture the overall trends typically found in multistage compressors. The formulas have been simplified with approximations specific to the MIT compressor. First, the flow exited the last stator row in the axial direction, so the exit flow angle was assumed to be zero for all operating conditions:

$$\beta_2(W, V, \varepsilon) = 0\,. \tag{D.1}$$

Second, the pressure rise characteristics were assumed to be independent of the upstream tangential velocity since the first blade row was comprised of inlet guide vanes. The actual pressure rise characteristic with losses was written as a cubic polynomial in axial velocity, and the isentropic characteristic was linear in axial velocity:

$$\Psi(V,W,\varepsilon) = A(\delta\varepsilon)\,W^3 + B(\delta\varepsilon)\,W^2 + C(\delta\varepsilon)\,W + D(\delta\varepsilon) \tag{D.2}$$

$$\Psi_i(V,W,\varepsilon) = E(\delta\varepsilon)\,W + G(\delta\varepsilon)\,. \tag{D.3}$$

The polynomial coefficients were functions of $\delta\varepsilon$, defined here to be the difference between the actual and the nominal tip clearance, nondimensionalized by the average rotor chord.

The polynomial coefficients were computed in the manner described by Graf [25]. The nominal characteristic with losses was adjusted to pass through two defined operating points representing the peak, $(\bar{W}_p, \bar{\Psi}_p)$, and a "hinge" point, $(\bar{W}_m, \bar{\Psi}_m)$, shown in Figure D-1. The variation in peak pressure rise with tip clearance was set by the parameter $\frac{d\bar{\Psi}_p}{d\varepsilon}$, chosen to cause a 5% decrease in peak pressure rise with a clearance increase of 1% chord. The flow coefficient at the peak was adjusted by the factor, $k$, so that the peaks of the family of characteristics with varying tip clearance were aligned along a 60° line. The hinge point was modified through a parameter, $m$, so that the family of characteristics did not overlap. The values of these parameters, listed in Table D.1, were chosen to be consistent with the typical compressor data described in Section 1.2.2. The operating points at the peak and hinge points for the family of characteristics in terms of these factors were:

$$\begin{aligned} W_p(\varepsilon) &= \bar{W}_p(1 - k\,\delta\varepsilon) \\ \Psi_p(\varepsilon) &= \bar{\Psi}_p(1 + \frac{d\bar{\Psi}_p}{d\varepsilon}\,\delta\varepsilon) \end{aligned} \tag{D.4}$$

$$\begin{aligned} W_m(\varepsilon) &= \bar{W}_m(1 + m\,\delta\varepsilon) \\ \Psi_m(\varepsilon) &= \bar{\Psi}_m\,. \end{aligned} \tag{D.5}$$

To reduce the number of unknowns, the coefficient $B$ was set to zero. The remaining polynomial coefficients were then calculated as

$$\begin{aligned} A &= \frac{-(\Psi_p - \Psi_m)}{(W_m - W_p)^2(W_m + 2W_p)} \\ C &= -\frac{3}{W_p^2}A \\ D &= \Psi_p - \frac{2}{3}W_pC\,. \end{aligned} \tag{D.6}$$

The isentropic characteristics were assumed to have slopes equal to the actual characteristic slopes at the design point, $(\bar{W}_d, \bar{\Psi}_d)$. The ratio of the isentropic to the actual characteristics at the design point was given by the parameter, $\eta$. Graf used this parameter to represent the efficiency of the compressor, but his definition of efficiency differed from the definition in this thesis in equation (2.20). The parameter $\eta$ was used here simply to construct the representative family of isentropic characteristics. The polynomial coefficients for these characteristics were given as

$$\begin{aligned} E &= 3\bar{W}_d^2 A + C \\ G &= \frac{1}{\eta}\Psi_d - \bar{W}_d E. \end{aligned} \tag{D.7}$$

Graf showed that $\eta$ was affected by tip clearance through the relation

$$\eta = \bar{\eta}\,\frac{\left(1 + \frac{6\,\delta\varepsilon}{AR}\right)}{\left(1 + \frac{2\,\delta\varepsilon}{AR}\right)}, \tag{D.8}$$

where $\bar{\eta}$ is a constant, and $AR$ is the blade aspect ratio. The parameters $\bar{\eta}$ and $AR$ used for the MIT compressor are also listed in Table D.1. The resultant family of actual and isentropic pressure rise characteristics based on these polynomials are shown in Figure 3-1.

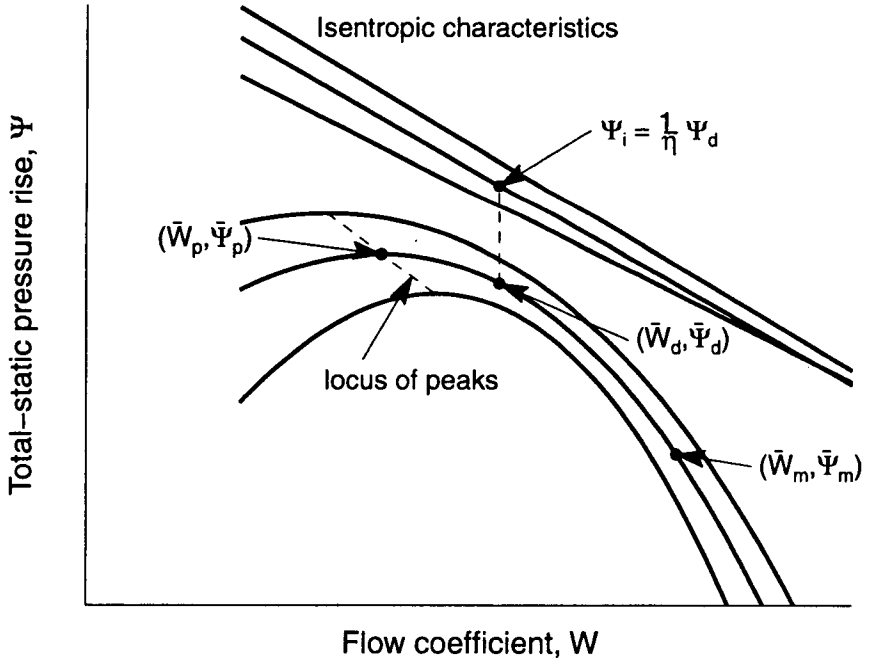


**Figure D-1:** Schematic of actual and isentropic compressor pressure rise characteristics. Adapted from Graf [25].

**Table D.1:** Parameters used to calculate the MIT pressure rise characteristics.

| | | | |
|---|---|---|---|
| $\bar{W}_p$ | 0.5 | $\bar{\Psi}_p$ | 0.8 |
| $\bar{W}_d$ | 0.61 | $\bar{\Psi}_d$ | 0.7407 |
| $\bar{W}_m$ | 0.75 | $\bar{\Psi}_m$ | 0.4 |
| $\frac{d\bar{\Psi}_p}{d\epsilon}$ | -5.0 | $k$ | -4.619 |
| $m$ | -1.5 | $B$ | 0.0 |
| $\bar{\eta}$ | 0.8 | $AR$ | 1.7 |

## D.2 NASA Stage-37

The axisymmetric exit flow angle and pressure rise characteristics for the NASA compressor are based on computed flow fields using the Stage-37 blade geometry for different tip clearance and pressure ratios. Although solutions were only obtained for axial inlet flow, the absence of an inlet guide vane implied that Stage-37 was a swirl-sensitive compressor. To obtain the characteristics' dependencies on inlet tangential velocity, the solutions were fit to a two-dimensional blade model of the stage, where the loss coefficient and deviation for each blade row depended only on the relative inlet flow angle and the tip clearance. The two-dimensional blade row model is discussed first to motivate the method used to process the CFD flow fields. The computed flows are then described, followed by the reduction procedures used to generate the individual blade row loss and deviation curves.

### Two-dimensional Blade Row Model of Stage-37

The two-dimensional cascade model of Stage-37 in Figure D-2 was used to construct relations governing the overall pressure rise and exit flow angle. The rotor inlet corresponded to station (1) of the original compressor model (Figure 2-1) and the stator exit corresponded to station (2). The relative velocity triangles are indicated on Figure D-2, where $\beta$ was defined as the *relative* flow angle at the inlet or exit of each blade row. Unless otherwise noted, the flow variables have been nondimensionalized as in Chapter 2.

All assumptions for the original compressor model in Section 2.1 were applied here. The flow was assumed to be incompressible and axisymmetric, which implied that the axial velocity, $W$, was uniform. The relative exit flow angle and loss coefficient for each blade

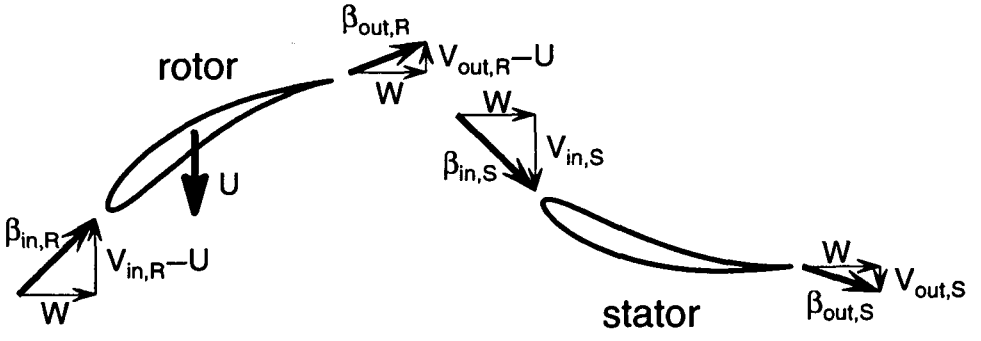


**Figure D-2:** Two-dimensional blade model of Stage-37 used for constructing pressure rise characteristics and exit flow angle relation.

row were then functions only of the local relative inlet flow angle and the tip clearance [36]:

$$\begin{aligned}
\beta_{out,R}(\beta_{in,R},\varepsilon) &= \tan^{-1}\left(\frac{V_{out,R}-U}{W}\right) \\
\beta_{out,S}(\beta_{in,S},\varepsilon) &= \tan^{-1}\left(\frac{V_{out,S}}{W}\right) \\
\xi_R(\beta_{in,R},\varepsilon) &= \frac{L_R}{\frac{1}{2}\left[W^2+(V_{in,R}-U)^2\right]} \\
\xi_S(\beta_{in,S},\varepsilon) &= \frac{L_S}{\frac{1}{2}\left[W^2+V_{in,S}^2\right]}
\end{aligned} \tag{D.9}$$

where $L_R$ and $L_S$ are the relative total pressure losses across the rotor and stator, respectively. Since the relative inlet flow angle to the stator was given by

$$\tan\beta_{in,S} = \tan\beta_{out,R} + \frac{U}{W}, \tag{D.10}$$

all four parameters in equation (D.9) were functions only of the rotor inlet velocity and the tip clearance.

The nondimensional total-to-static pressure rise was the sum of the pressure changes across each region in the stage:

$$\begin{aligned}
\Psi &= (P_{t_{out,R}}-P_{t_{in,R}}) + (P_{t_{in,S}}-P_{t_{out,R}}) - (P_{t_{in,S}}-P_{t_{out,S}}) - (P_{t_{out,S}}-P_{out,S}) \\
&= \text{(rotor work} - \text{loss)} + \text{(gap loss)} - \text{(stator loss)} - \text{(exit dynamic head)}
\end{aligned} \tag{D.11}$$

Assuming no loss in the gap region, the actual and isentropic pressure rise characteristics

could be expressed in terms of the parameters in equation (D.9):

$$\begin{aligned}\Psi &= U(U + W\tan\beta_{out,R} - V_{in,R}) - \frac{1}{2}W^2\sec^2\beta_{out,S} - \frac{1}{2}\xi_R W^2\sec^2\beta_{in,R} - \frac{1}{2}\xi_S W^2\sec^2\beta_{in,S} \\ \Psi_i &= U(U + W\tan\beta_{out,R} - V_{in_R}) - \frac{1}{2}W^2\sec^2\beta_{out,S}\,. \end{aligned} \tag{D.12}$$

Through equations (D.9, D.10), these characteristics were only functions of $V_{in,R}$, $W$, and $\varepsilon$, and so could be used directly in the rotating tip clearance asymmetry model. The exit flow angles and total pressure loss coefficients used in equation (D.12) for Stage-37 are described in the following section.

### Stage-37 Loss Coefficients and Exit Flow Angles

The performance of Stage-37 at 100% design speed was calculated by Hathaway [32] at the NASA Lewis Research Center using Adamczyk's three-dimensional, viscous flow, blade passage code [1]. Calculations were performed for three tip clearances and various pressure ratios between design operation and stall (Table D.2). The three tip clearances were chosen as the minimum, average and maximum tip clearances induced by shaft displacement in the Stage-37 magnetic bearing experiment [72].

**Table D.2:** Scope of CFD calculations performed using Stage-37 geometry [32].

| tip clearance (inches) | static pressure ratio across stage | | | | | | |
|---|---|---|---|---|---|---|---|
| 0.01 | 1.12 | 1.47 | 1.59 | 1.71 | 1.83 | 1.89 | 1.91 |
| 0.02 | 1.12 | 1.47 | 1.59 | 1.71 | 1.83 | 1.88 | 1.89 |
| 0.03 | 1.12 | 1.47 | 1.59 | 1.71 | 1.82 | 1.84 | |

The flow fields were reduced to obtain the average loss coefficient and exit flow angle for each blade row. Compromises were required because the computed flows were three-dimensional and compressible, but the blade row characteristics in equation (D.12) were based on two-dimensional, incompressible flow fields. The most important figure of merit was to accurately capture the total-to-static pressure rise across the stage, since it is known that this has a strong influence on stability prediction. The second figure of merit was to capture the flow local to the blade rows as accurately as possible. Since the background flow nonuniformities and the rotating stall modes were generated at the compressor, the flow

near the blades was felt to be more critical to compressor dynamics than the flow further up or downstream. The third figure of merit was to accurately reproduce the flow near stall at the expense of accuracy near design, if necessary. The assessments of active control in Chapter 4, and effects of tip clearance asymmetry in Chapter 3 are more concerned with operation at stall than at design.

To represent the Stage-37 flow by the incompressible model, a single value of density was required that was valid for the flow throughout the compressor and for all operating conditions. The two-dimensional total pressure rise across the rotor, in *dimensional* form, is given by Euler's equation with losses:

$$\tilde{P}_{t_{out,R}} - \tilde{P}_{t_{in,R}} = \tilde{\rho}\tilde{U}(\tilde{V}_{out,R} - \tilde{V}_{in,R}) - \tilde{L}_R \,. \tag{D.13}$$

To match the overall pressure rise as well as the velocities local to the blade rows, equation (D.13) shows that the value of density in the two-dimensional model should equal the actual density at the rotor exit. This value of density was chosen as the area-averaged density at the rotor exit plane, taken for the nominal clearance calculation just before stall.

The modeled blade row losses and local velocities were reduced from the three-dimensional flow field at each operating condition in the following manner: The modeled axial velocity was taken as the area-averaged velocity at the mid-gap region, which was the best measure of the average flow coefficient through the entire stage. The modeled rotor loss was the difference between the mass averaged relative total pressures at the inlet and exit of the rotor row. The modeled stator loss was calculated similarly across the stator row. The actual tangential velocity at the stator exit plane was area-averaged to give the modeled tangential velocity. The tangential velocity at the rotor exit was chosen as the value that matched the total pressure rise across the rotor through equation D.13. In nondimensional form, this tangential velocity was given as

$$V_{out,R} = \frac{1}{U}\left(P_{t_{out,R}} - P_{t_{in,R}} + L_R\right) . \tag{D.14}$$

The overall pressure rise characteristics compared well when the rotor exit velocity was solved for in this manner, although the values of tangential velocity were approximately 10-20% lower than the actual, area-averaged values.

The relative flow angles for the two-dimensional model were then calculated for each operating condition from the velocity triangles:

$$\begin{aligned}
\tan\beta_{in,R} &= -\frac{U}{W} \\
\tan\beta_{out,R} &= \frac{V_{out,R} - U}{W} \\
\tan\beta_{in,S} &= \tan\beta_{out,R} + \frac{U}{W} \\
\tan\beta_{out,S} &= \frac{V_{out,S}}{W} .
\end{aligned} \tag{D.15}$$

The loss coefficients and exit flow angles for the rotor and stator were correlated against the respective inlet flow angles (Figure D-4). Quadratic polynomials were used to fit the dependencies with tip clearance. The dependencies with $\beta_{in}$ were fit with quadratic polynomials for the exit flow angles, and cubic polynomials were used for the loss coefficients.

The family of modeled total-to-static characteristics compared well to the characteristics of the computed flow fields (Figure D-3). The variation with changing tip clearance was captured, as were the overall pressure levels near stall.

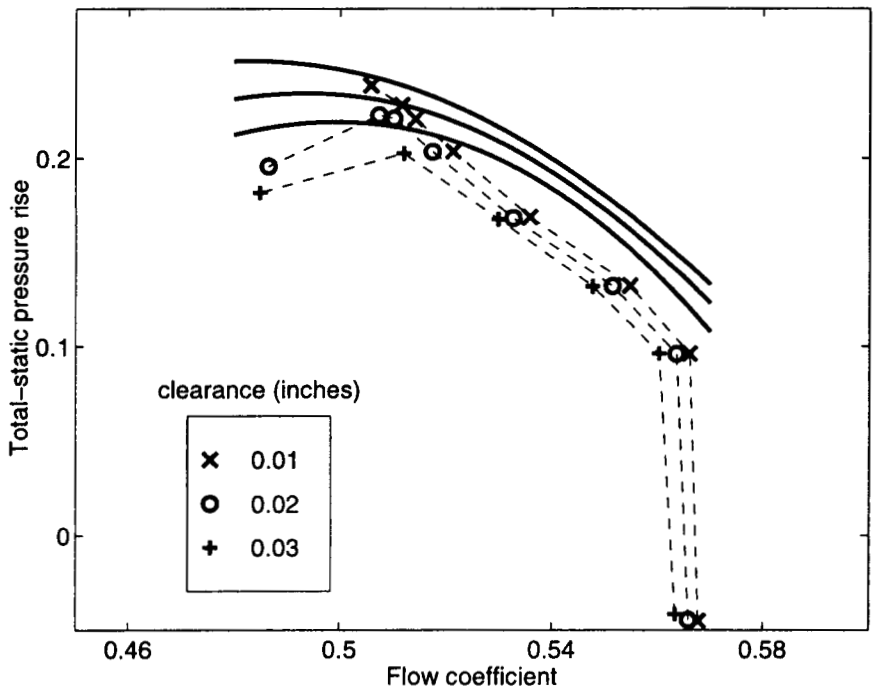


**Figure D-3:** Comparison of Stage-37 total-to-static characteristics between two-dimensional model (lines) and computed three-dimensional flow fields (symbols).

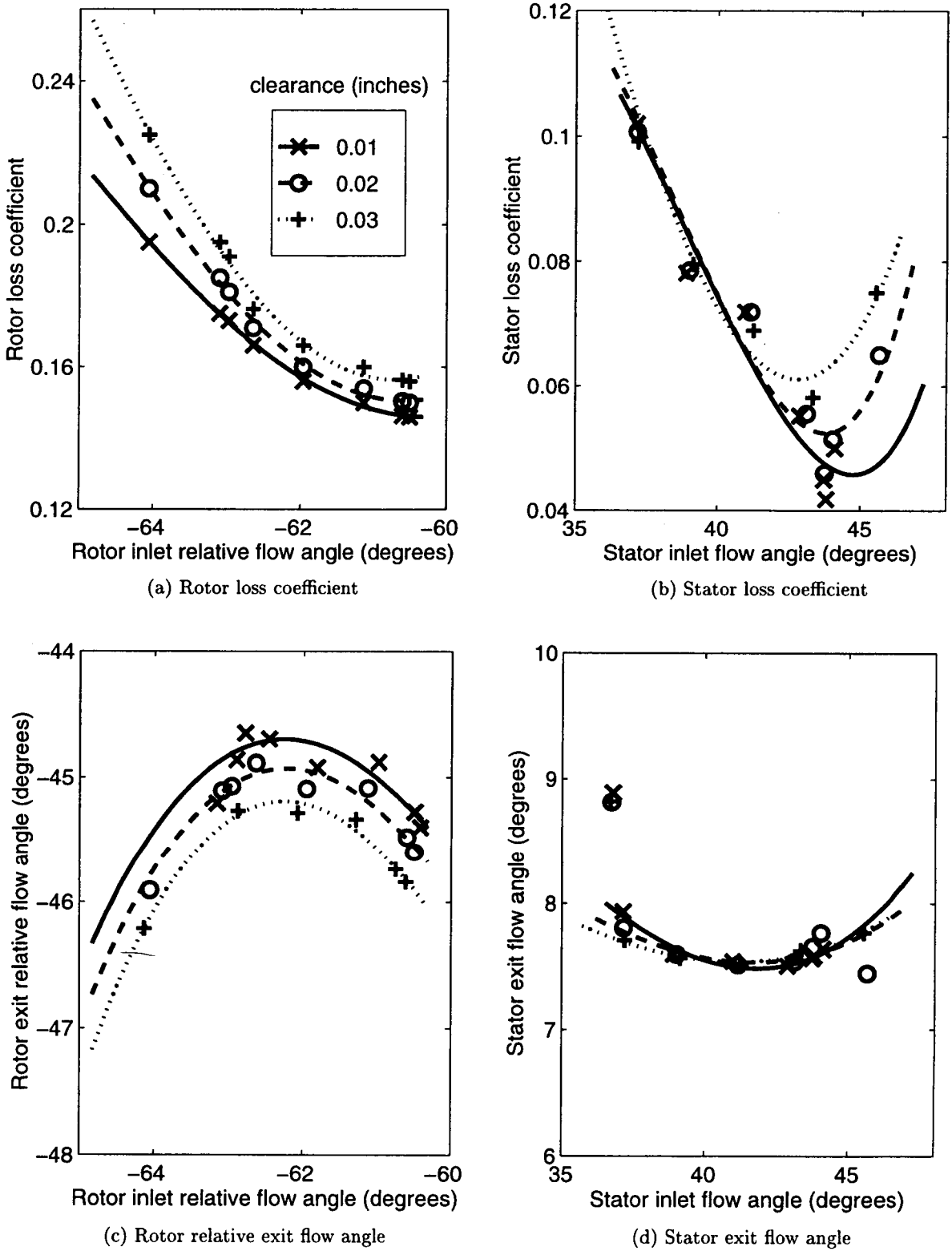


(a) Rotor loss coefficient

(b) Stator loss coefficient

(c) Rotor relative exit flow angle

(d) Stator exit flow angle

**Figure D-4:** Polynomial fits of Stage-37 rotor and stator loss coefficients and relative exit flow angles. Symbols indicate two-dimensional loss coefficients and angles calculated directly from computed three-dimensional flow fields.

# APPENDIX E

# DETAILS OF 3-D ACTUATOR PLANE COMPRESSOR MODEL

This appendix contains details on calculating the three-dimensional rotating stall modes using the rectilinear actuator plane compressor model. This model is used in Chapter 5 to calculate the eigenvalues and mode shapes for the $(n, j)$ modes. Equations are developed to represent the unsteady flow perturbations through the blade-free regions and across the blade rows, subject to the modeling assumptions and geometry definitions in Section 5.1. Analytic solutions for the modes are found for the case of spanwise uniform background flow. A numerical solution procedure is also developed for the case of nonuniform background flow, which was used to calculate the modes in Section 5.4.

## E.1 Linearized Equations in Blade-Free Regions

The flow in the blade-free regions is represented by the three-dimensional, incompressible Euler equations in nondimensional form:

$$\begin{aligned}
\frac{\partial U}{\partial t} + U\frac{\partial U}{\partial r} + V\frac{\partial U}{\partial \theta} + W\frac{\partial U}{\partial z} + \frac{\partial P}{\partial r} &= 0 \quad \text{(spanwise momentum)} \\
\frac{\partial V}{\partial t} + U\frac{\partial V}{\partial r} + V\frac{\partial V}{\partial \theta} + W\frac{\partial V}{\partial z} + \frac{\partial P}{\partial \theta} &= 0 \quad \text{(tangential momentum)} \\
\frac{\partial W}{\partial t} + U\frac{\partial W}{\partial r} + V\frac{\partial W}{\partial \theta} + W\frac{\partial W}{\partial z} + \frac{\partial P}{\partial z} &= 0 \quad \text{(axial momentum)} \\
\frac{\partial U}{\partial r} + \frac{\partial V}{\partial \theta} + \frac{\partial W}{\partial z} &= 0 \quad \text{(continuity)} .
\end{aligned} \tag{E.1}$$

The flow field can be separated into the steady, axisymmetric background flow and the unsteady, three-dimensional perturbations:

$$\begin{aligned} U(r,\theta,z,t) &= \bar{U}(r,z) + u(r,\theta,z,t) \\ V(r,\theta,z,t) &= \bar{V}(r,z) + v(r,\theta,z,t) \\ W(r,\theta,z,t) &= \bar{W}(r,z) + w(r,\theta,z,t) \\ P(r,\theta,z,t) &= \bar{P}(r,z) + p(r,\theta,z,t)\ . \end{aligned} \tag{E.2}$$

These decompositions are substituted into the Euler equations. Collecting the first order terms yields the following linearized equations:

$$\begin{aligned} \frac{\partial u}{\partial t} + \bar{U}\frac{\partial u}{\partial r} + u\frac{\partial \bar{U}}{\partial r} + \bar{V}\frac{\partial u}{\partial \theta} + \bar{W}\frac{\partial u}{\partial z} + w\frac{\partial \bar{U}}{\partial z} + \frac{\partial p}{\partial r} &= 0 \\ \frac{\partial v}{\partial t} + \bar{U}\frac{\partial v}{\partial r} + u\frac{\partial \bar{V}}{\partial r} + \bar{V}\frac{\partial v}{\partial \theta} + \bar{W}\frac{\partial v}{\partial z} + w\frac{\partial \bar{V}}{\partial z} + \frac{\partial p}{\partial \theta} &= 0 \\ \frac{\partial w}{\partial t} + \bar{U}\frac{\partial w}{\partial r} + u\frac{\partial \bar{W}}{\partial r} + \bar{V}\frac{\partial w}{\partial \theta} + \bar{W}\frac{\partial w}{\partial z} + w\frac{\partial \bar{W}}{\partial z} + \frac{\partial p}{\partial z} &= 0 \\ \frac{\partial u}{\partial r} + \frac{\partial v}{\partial \theta} + \frac{\partial w}{\partial z} &= 0\ . \end{aligned} \tag{E.3}$$

Solutions to these equations are found for each linearized mode of the compression system. Since equations (E.3) are first-order and homogeneous, each mode will have exponential temporal behavior. Also, the perturbations must be periodic around the circumference, and so can be written as the sum of their Fourier harmonics. Therefore, the linearized flow variables can be written in the following form:

$$v(r,\theta,z,t) = \mathcal{R}e\left\{\sum_{n=-\infty}^{\infty} v_n(r,z)\mathrm{e}^{in\theta}\mathrm{e}^{i\omega t}\right\}\ . \tag{E.4}$$

Since the background flow is axisymmetric, the circumferential harmonics will not be coupled in each mode. Thus, the circumferential shape of each mode can be written in terms of a single harmonic $n$ of the above series. The linear equations can then be manipulated with complex-valued perturbational flow quantities, returning only to the real values using equation (E.4) after solving for the mode shapes. The linearized equations that govern the

development of a single mode can then be expressed in matrix form as

$$\frac{\partial}{\partial z}\begin{pmatrix} u_n \\ v_n \\ w_n \\ p_n \end{pmatrix} + \begin{bmatrix} \frac{\bar{U}}{\bar{W}} & 0 & 0 & \frac{1}{\bar{W}} \\ 0 & \frac{\bar{U}}{\bar{W}} & 0 & 0 \\ 1 & 0 & 0 & 0 \\ -\bar{W} & 0 & \bar{U} & 0 \end{bmatrix} \frac{\partial}{\partial r}\begin{pmatrix} u_n \\ v_n \\ w_n \\ p_n \end{pmatrix} + \cdots$$

$$\cdots + \begin{bmatrix} \frac{1}{\bar{W}}\left(i\omega + in\bar{V} + \frac{\partial \bar{U}}{\partial r}\right) & 0 & \frac{1}{\bar{W}}\frac{\partial \bar{U}}{\partial z} & 0 \\ \frac{1}{\bar{W}}\frac{\partial \bar{V}}{\partial r} & \frac{i\omega + in\bar{V}}{\bar{W}} & \frac{1}{\bar{W}}\frac{\partial \bar{V}}{\partial z} & \frac{in}{\bar{W}} \\ 0 & in & 0 & 0 \\ \frac{\partial \bar{W}}{\partial r} & -in\bar{W} & i\omega + in\bar{V} + \frac{\partial \bar{W}}{\partial z} & 0 \end{bmatrix} \begin{pmatrix} u_n \\ v_n \\ w_n \\ p_n \end{pmatrix} = 0 \,. \quad \text{(E.5)}$$

### E.1.1 Perturbations in Uniform Background Flow

Analytic solutions can be found for the case of uniform duct geometry with uniform background flow. Assume the duct has a constant hub-to-tip ratio $r_h$, and the uniform background flow is given by $\bar{V}$ and $\bar{W}$ ($\bar{U} = 0$). To solve for the linearized perturbations, first decompose the mode shape into its spanwise ($j$) and axial ($\hat{l}$) wave numbers:

$$\begin{pmatrix} u_n \\ v_n \\ w_n \\ p_n \end{pmatrix} = \sum_{j=0}^{\infty} \begin{pmatrix} \hat{u}_{n,j} \sin(\pi j \frac{r-r_h}{1-r_h}) \\ \hat{v}_{n,j} \cos(\pi j \frac{r-r_h}{1-r_h}) \\ \hat{w}_{n,j} \cos(\pi j \frac{r-r_h}{1-r_h}) \\ \hat{p}_{n,j} \cos(\pi j \frac{r-r_h}{1-r_h}) \end{pmatrix} e^{\hat{l}_{n,j} z} \,. \quad \text{(E.6)}$$

The above decomposition was chosen to enable a complete solution to the linearized Euler equations, and to enforce the boundary condition that the spanwise velocity, $u$, is zero at the casing walls, $r = r_h$ and $r = 1$. Substituting this series decomposition into equation (E.5) returns the following set of equations which must be true for all $n$ and $j$:

$$\begin{bmatrix} \hat{l}_{n,j} + \frac{i\omega + in\bar{V}}{\bar{W}} & 0 & 0 & -\frac{k_j}{\bar{W}} \\ 0 & \hat{l}_{n,j} + \frac{i\omega + in\bar{V}}{\bar{W}} & 0 & \frac{in}{\bar{W}} \\ k_j & in & \hat{l}_{n,j} & 0 \\ -k_j & -in & \frac{i\omega + in\bar{V}}{\bar{W}} & \frac{\hat{l}_{n,j}}{\bar{W}} \end{bmatrix} \begin{pmatrix} \hat{u}_{n,j} \\ \hat{v}_{n,j} \\ \hat{w}_{n,j} \\ \hat{p}_{n,j} \end{pmatrix} = 0 \quad \text{(E.7)}$$

where $k_j \equiv \frac{\pi j}{1-r_h}$.

Nontrivial solutions for the disturbance flow field occur when the determinant of the above matrix is zero, which yields the following fourth-order equation for $\hat{l}_{n,j}$:

$$\left(\hat{l}_{n,j} + \frac{i\omega + in\bar{V}}{\bar{W}}\right)^2 \left(\hat{l}_{n,j}^2 - [n^2 + k_j^2]\right) = 0 \,, \tag{E.8}$$

which implies $\hat{l}_{n,j} = -\frac{i\omega+in\bar{V}}{\bar{W}}$, $\sqrt{n^2+k_j^2}$, $-\sqrt{n^2+k_j^2}$. Define $l_{n,j} \equiv \sqrt{n^2+k_j^2}$ and $\alpha \equiv \frac{\omega+\bar{V}}{\bar{W}}$. Then the complete solution for the flow perturbation with $n^{\text{th}}$ circumferential harmonic and $j^{\text{th}}$ radial mode is given by

$$\begin{pmatrix} u_{n,j} \\ v_{n,j} \\ w_{n,j} \\ p_{n,j} \end{pmatrix} = \left\{ b_{+_{n,j}} \begin{pmatrix} -k_j \\ in \\ l_{n,j} \\ -\bar{W}(l_{n,j} + i\alpha) \end{pmatrix} e^{l_{n,j}z} + b_{-_{n,j}} \begin{pmatrix} -k_j \\ in \\ -l_{n,j} \\ \bar{W}(l_{n,j} - i\alpha) \end{pmatrix} e^{-l_{n,j}z} + \cdots \right.$$
$$\left. \cdots + a_{2_{n,j}} \begin{pmatrix} 0 \\ i\alpha \\ in \\ 0 \end{pmatrix} e^{-i\alpha z} + a_{3_{n,j}} \begin{pmatrix} -i\alpha \\ 0 \\ -k_j \\ 0 \end{pmatrix} e^{-i\alpha z} \right\} \begin{pmatrix} \sin k_j(r - r_h) \\ \cos k_j(r - r_h) \\ \cos k_j(r - r_h) \\ \cos k_j(r - r_h) \end{pmatrix} e^{in\theta} \tag{E.9}$$

for constants $a_{2_{n,j}}$, $a_{3_{n,j}}$, $b_{+_{n,j}}$ and $b_{-_{n,j}}$ to be determined by the boundary conditions.

The four components of the perturbation in equation (E.9) have physical significance. The $b_+$ and $b_-$ terms denote the potential components of the disturbance that exponentially grow and decay, respectively, in the axial direction. The other two terms refer to vortical components of the flow which convect downstream with the background flow field. $a_2$ exists in 2-D analyses, but $a_3$ is unique to 3-D disturbances. The important observation is that only the potential terms are associated with pressure disturbances in uniform background flow, which is not the case for nonuniform background flow.

## E.2 Matching Conditions Across Compressor Disk

To relate the form of the perturbations upstream and downstream of the compressor, four matching conditions for velocity and pressure are required across the actuator disk. The axial and spanwise velocities are assumed to be continuous across the disk. The tangential

velocity is assumed to be given by the flow tangency condition at the last blade row; and the pressure rise is determined by the quasi-steady pressure rise from the isentropic characteristic, plus correction terms to account for axial flow accelerations and unsteady losses.

The general form of these relations is written in equation (5.1). For the harmonic representation of the modes (equation E.4), the matching conditions for the velocity across the disk (from station (1) to (2) in Figure 5-1) can be written for each $n$ as

$$\begin{aligned} u_{n,1} &= u_{n,2} \\ w_{n,1} &= w_{n,2} \\ v_{n,2} &= w_{n,2} \tan\beta_2 \ . \end{aligned} \tag{E.10}$$

Similarly, the pressure matching conditions, including the effects of unsteady losses, are given by

$$\begin{aligned} p_{n,2} - p_{t_{n,1}} &= \frac{d\Psi_i}{dW} w_{n,1} - l_{Rn} - l_{Sn} - in\lambda w_{n,1} - i\omega\mu w_{n,1} \\ (1 + i\omega\tau_R + in\tau_R)\, l_{Rn} &= \sigma(\frac{d\Psi_i}{dW} - \frac{d\Psi}{dW}) w_{n,1} \\ (1 + i\omega\tau_S)\, l_{Sn} &= (1-\sigma)(\frac{d\Psi_i}{dW} - \frac{d\Psi}{dW}) w_{n,1} \end{aligned} \tag{E.11}$$

where the total pressure disturbance is $p_t = p + \bar{U}u + \bar{V}v + \bar{W}w$.

## E.3 Modes of Compression System in Uniform Flow

The natural modes of the compression system are given by the solution to the above equations in the blade row and blade-free regions, subject to homogeneous far-field boundary conditions. The equations here are applicable for uniform background flow fields with either uniform or nonuniform characteristic slope profiles.

Any linear disturbance to the flow in a blade-free region can be expressed through equation (E.9) in terms of a series of four sets of parameters: $\{a_{2_{n,j}}, a_{3_{n,j}}, b_{+_{n,j}}$ and $b_{-_{n,j}}\}$. Therefore for every $n, j$ there are 8 unknown parameters (4 in the upstream duct, and 4 in the downstream duct).

Four of these unknowns for every $n, j$ can be eliminated through boundary conditions. For the purposes of applying the far-field boundary conditions, the upstream and downstream duct lengths are assumed to be infinite. The boundary conditions are:

- Far upstream of the compressor, the flow is assumed to have no disturbances (all disturbances are generated by the compressor). Therefore $a_{2_{n,j}} = a_{3_{n,j}} = b_{-_{n,j}} = 0$.
- Far downstream of the compressor, the pressure perturbations cannot grow exponentially, which implies $b_{+_{n,j}} = 0$.

The perturbations at the inlet to the compressor face ($z = 0^-$) can therefore be written as

$$\begin{pmatrix} u_n \\ v_n \\ w_n \\ p_n \end{pmatrix} = \sum_{j=0}^{\infty} b_{+_{n,j}} \begin{pmatrix} -k_j \\ in \\ l_{n,j} \\ -\bar{W}(l_{n,j} + i\alpha) \end{pmatrix} \begin{pmatrix} \sin k_j(r - r_h) \\ \cos k_j(r - r_h) \\ \cos k_j(r - r_h) \\ \cos k_j(r - r_h) \end{pmatrix} e^{in\theta}, \tag{E.12}$$

and the perturbations at the exit plane of the actuator disk ($z = 0^+$) are

$$\begin{pmatrix} u_n \\ v_n \\ w_n \\ p_n \end{pmatrix} = \sum_{j=0}^{\infty} \left\{ a_{2_{n,j}} \begin{pmatrix} 0 \\ i\alpha \\ in \\ 0 \end{pmatrix} + a_{3_{n,j}} \begin{pmatrix} -i\alpha \\ 0 \\ -k_j \\ 0 \end{pmatrix} + \cdots \right. \tag{E.13}$$

$$\left. \cdots + b_{-_{n,j}} \begin{pmatrix} -k_j \\ in \\ -l_{n,j} \\ \bar{W}(l_{n,j} - i\alpha) \end{pmatrix} \right\} \begin{pmatrix} \sin k_j(r - r_h) \\ \cos k_j(r - r_h) \\ \cos k_j(r - r_h) \\ \cos k_j(r - r_h) \end{pmatrix} e^{in\theta}.$$

The remaining four unknown parameters for every $(n, j)$ can then be related through the four matching conditions. Applying the three velocity matching conditions in equa-

tion (E.10) to the form of the flow disturbance gives

$$\begin{aligned}
\sum_{j=0}^{\infty}\left(-k_j\, b_{+_{n,j}} + i\alpha\, a_{2_{n,j}} + k_j\, b_{-_{n,j}}\right)\sin k_j(r-r_h) &= 0 \\
\sum_{j=0}^{\infty}\left(l_{n,j}\, b_{+_{n,j}} + k_j\, a_{2_{n,j}} - in\, a_{3_{n,j}} + l_{n,j}\, b_{-_{n,j}}\right)\cos k_j(r-r_h) &= 0 \\
\sum_{j=0}^{\infty}\left(-l_{n,j}\tan\beta_2\, b_{+_{n,j}} + i\alpha\, a_{3_{n,j}} + in\, b_{-_{n,j}}\right)\cos k_j(r-r_h) &= 0 \qquad \text{(E.14)}
\end{aligned}$$

The three pressure rise and unsteady loss conditions (equation E.11) can be combined into one equation by defining a harmonic decomposition for the unsteady losses, identical to that for velocity and pressure:

$$l_R(r,\theta,t) = \mathcal{R}e\left\{\sum_{n=-\infty}^{\infty}\sum_{j=0}^{\infty} l_{R_{n,j}}\cos k_j(r-r_h)e^{in\theta}e^{i\omega t}\right\}. \qquad \text{(E.15)}$$

A similar equation applies for $l_S$. The linearized unsteady loss equations can be written as

$$\begin{aligned}
\sum_{j=0}^{\infty}\left\{(1+i\omega\tau_R+in\tau_R)l_{R_{n,j}} - \sigma(\frac{d\Psi_i}{dW}-\frac{d\Psi}{dW})l_{n,j}\, b_{+_{n,j}}\right\}\cos k_j(r-r_h) &= 0 \\
\sum_{j=0}^{\infty}\left\{(1+i\omega\tau_S)l_{S_{n,j}} - (1-\sigma)(\frac{d\Psi_i}{dW}-\frac{d\Psi}{dW})l_{n,j}\, b_{+_{n,j}}\right\}\cos k_j(r-r_h) &= 0\,. \qquad \text{(E.16)}
\end{aligned}$$

Substituting these into the pressure rise equation gives

$$\begin{aligned}
\sum_{j=0}^{\infty}\Bigg\{\Bigg[i\omega(1+\mu l_{n,j}) + in\lambda l_{n,j} + l_{n,j}\left(\frac{d\Psi_i}{dW}-\frac{d\Psi}{dW}\right)\left(\frac{\sigma}{1+i\omega\tau_R+in\tau_R}+\frac{1-\sigma}{1+i\omega\tau_S}\right) - \cdots \\
\cdots - l_{n,j}\frac{d\Psi_i}{dW}\Bigg]\, b_{+_{n,j}} + \bar{W}(l_{n,j}-i\alpha)\, b_{-_{n,j}}\Bigg\}\cos k_j(r-r_h) = 0\,. \qquad \text{(E.17)}
\end{aligned}$$

Equations (E.14) and (E.17) represent the four conditions matching the upstream and downstream perturbation components for each harmonic. To solve for the unknowns $a_{2_{n,j}}, a_{3_{n,j}}, b_{+_{n,j}}$ and $b_{-_{n,j}}$, two cases are considered. For the first case, all compressor parameters are uniform; in the second case, the compressor slope, $d\Psi/dW$, is nonuniform.

### E.3.1 Uniform compressor parameters

For conditions where the compressor parameters $d\Psi/dW$, $d\Psi_i/dW$, $\beta_2$, $\mu$, $\lambda$, $\tau_R$, $\tau_S$ and $\sigma$ are uniform, all coefficients in the matching conditions are constants. Each series in equations (E.14) and (E.17) represents a sum of linearly independent equations in $\sin k_j(r - r_h)$ or $\cos k_j(r - r_h)$. Since each series equals zero, this implies that every coefficient of $\sin k_j(r - r_h)$ or $\cos k_j(r - r_h)$ must also equal zero. Therefore, every $(n, j)$ component to the disturbance is independent of the others, and can be examined separately.

The four matching conditions for each harmonic $(n, j)$, arranged in matrix form, are

$$\begin{bmatrix} -k_j & i\alpha & 0 & k_j \\ l_{n,j} & k_j & -in & l_{n,j} \\ -l_{n,j}\tan\beta_2 & 0 & i\alpha & in \\ \mathbf{X} & 0 & 0 & \bar{W}(l_{n,j} - i\alpha) \end{bmatrix} \begin{pmatrix} b_{+_{n,j}} \\ a_{2_{n,j}} \\ a_{3_{n,j}} \\ b_{-_{n,j}} \end{pmatrix} = 0\,, \tag{E.18}$$

where $\mathbf{X}$ is defined as

$$\mathbf{X} = i\omega(1 + \mu l_{n,j}) + in\lambda l_{n,j} - l_{n,j}\frac{d\Psi_i}{dW} + l_{n,j}\left(\frac{d\Psi_i}{dW} - \frac{d\Psi}{dW}\right)\left(\frac{\sigma}{1 + i\omega\tau_R + in\tau_R} + \frac{1-\sigma}{1 + i\omega\tau_S}\right).$$

Non-zero amplitude rotating stall modes are found only when the determinant of this matrix is zero. This condition yields

$$i\alpha(l_{n,j} - i\alpha)\left[l_{n,j}\mathbf{X} - \bar{W}(inl_{n,j}\tan\beta_2 - k_j^2 - i\alpha l_{n,j})\right] = 0\,. \tag{E.19}$$

Two solutions are given by $\alpha = 0$ and $\alpha = -il_{n,j}$. These solutions however are seen to be non-physical because they violate the exponential behavior in the axial direction assumed for the mode shapes in the solution for equation (E.9). Meaningful rotating stall eigenvalues are found by setting the right-most parenthesis term to zero. This results in a third order equation for $\omega$, which can be solved numerically. Three eigenvalues are found for each $(n, j)$. Two correspond to the unsteady loss dynamics. These have a very large, negative growth rate (typically 3–10 times the rotor frequency) and so can be ignored. The third eigenvalue has the highest growth rate, and corresponds to the physical rotating stall mode.

An analytic expression for the eigenvalue of the rotating stall mode can be obtained

by neglecting unsteady loss modeling. Setting $\tau_R = \tau_S = 0$ results in

$$i\omega(1+\mu l_{n,j}) + in\lambda l_{n,j} - l_{n,j}\frac{d\Psi}{dW} = \bar{W}\left(in\tan\beta_2 - i\alpha - \frac{k_j^2}{l_{n,j}}\right). \tag{E.20}$$

This equation is simplified by expressing $\tan\beta_2$ in terms of the steady tangential velocity in the downstream duct, $\bar{V} = \Omega_2 + \bar{W}\tan\beta_2$. $\Omega_2$ is defined as 0 if the final blade row is a stator, or 1 if the final blade row is a rotor, and $\beta_2$ is taken to be positive if the *relative* flow is in the positive tangential direction. Equation (E.20) then becomes

$$i\omega(2+\mu l_{n,j}) = l_{n,j}\frac{d\Psi}{dW} - \bar{W}\frac{k_j^2}{l_{n,j}} - in(\Omega_2 + \lambda l_{n,j}). \tag{E.21}$$

Finally, the eigenvalue for the $(n,j)$ mode is

$$\omega_{n,j} = -\frac{n(\Omega_2 + \lambda l_{n,j}) + i\left(l_{n,j}\frac{d\Psi}{dW} - \bar{W}\frac{k_j^2}{l_{n,j}}\right)}{2+\mu l_{n,j}}. \tag{E.22}$$

The mode shape for each $(n,j)$ can now be found by substituting the value of $\omega_{n,j}$ in the matrix equation (E.18), and solving for the eigenvectors. These eigenvectors give the relative weighting of $b_{+_{n,j}}$, $a_{2_{n,j}}$, $a_{3_{n,j}}$ and $b_{-_{n,j}}$ in each mode, which can then be substituted back into equation (E.9) for the mode shapes.

### E.3.2 Nonuniform compressor slope

For conditions where the compressor slope varies across the span, the spanwise harmonics are coupled through the pressure rise matching condition. Since this case has only been considered in this thesis for situations where unsteady losses are ignored, the pressure rise condition in equation (E.17) is rewritten below for $\tau = 0$:

$$\sum_{j=0}^{\infty}\left\{\left[i\omega(1+\mu l_{n,j}) + in\lambda l_{n,j} + l_{n,j}\frac{d\Psi}{dW}\right] b_{+_{n,j}} + \bar{W}(l_{n,j} - i\alpha)\, b_{-_{n,j}}\right\}\cos jr^* = 0 \tag{E.23}$$

where $r^*$ is defined as $\pi(r - r_h)/(1 - r_h)$. To express this as a sum of linearly independent equations in $\cos jr^*$, the slope is decomposed into its radial harmonics over $r^*$ as:

$$\frac{d\Psi}{dW} = \sum_{m=0}^{\infty} f_m \cos mr^* . \tag{E.24}$$

The term involving the slope in the pressure rise equation can then be written as

$$\begin{aligned}
\sum_{j=0}^{\infty} l_{n,j} \frac{d\Psi}{dW} b_{+_{n,j}} \cos jr^* &= \sum_{j=0}^{\infty}\sum_{m=0}^{\infty} l_{n,j} b_{+_{n,j}} f_m \cos mr^* \cos jr^* \\
&= \frac{1}{2}\sum_{j=0}^{\infty}\sum_{m=0}^{\infty} l_{n,j} b_{+_{n,j}} f_m \left[\cos(m-j)r^* + \cos(m+j)r^*\right] \\
&= \left\{ l_{n,0} b_{+_{n,0}} f_0 + \frac{1}{2}\sum_{m=1}^{\infty} l_{n,m} b_{+_{n,m}} f_m \right\} \cos 0r^* + \cdots \qquad \text{(E.25)} \\
\cdots + \frac{1}{2}\sum_{j=1}^{\infty} \left\{ \sum_{m=0}^{j} l_{n,m} b_{+_{n,m}} f_{j-m} + \sum_{m=0}^{\infty} \left( l_{n,m} b_{+_{n,m}} f_{j+m} + l_{n,j+m} b_{+_{n,j+m}} f_m \right) \right\} &\cos jr^* .
\end{aligned}$$

Also, the term in equation (E.23) with $b_{-_{n,j}}$ can be written in terms of $b_{+_{n,j}}$. Since the three velocity matching conditions in equation (E.14) do not involve compressor parameters that vary in $r$, they can be combined to show (for all $j$):

$$\bar{W}(l_{n,j} - i\alpha)\, b_{-_{n,j}} = \left( \bar{W}\frac{k_j^2}{l_{n,j}} + i(\omega + n\Omega_2) \right) b_{+_{n,j}} . \tag{E.26}$$

Substitute equations (E.26) and (E.25) into (E.23), and collect like-terms in $\cos jr^*$. Then for $j = 0$

$$\left( i\omega_{n,0}(2 + \mu l_{n,0}) + in(\lambda l_{n,0} + \Omega_2) + \bar{W}\frac{k_0^2}{l_{n,0}} \right) b_{+_{n,0}} + \left( l_{n,0} b_{+_{n,0}} f_0 + \frac{1}{2}\sum_{m=1}^{\infty} l_{n,m} b_{+_{n,m}} f_m \right) = 0 \tag{E.27}$$

and for all $j \geq 1$

$$\begin{aligned}
&\left( i\omega(2 + \mu l_{n,j}) + in(\lambda l_{n,j} + \Omega_2) + \bar{W}\frac{k_j^2}{l_{n,j}} \right) b_{+_{n,j}} + \cdots \qquad \text{(E.28)} \\
&\quad \frac{1}{2}\left\{ \sum_{m=0}^{j} l_{n,m} b_{+_{n,m}} f_{j-m} + \sum_{m=0}^{\infty} \left( l_{n,m} b_{+_{n,m}} f_{j+m} + l_{n,j+m} b_{+_{n,j+m}} f_m \right) \right\} = 0 .
\end{aligned}$$

The only unknowns in equations (E.27) and (E.28) are $\omega$ and the set of $b_{+_{n,j}}$. To solve for these unknowns, truncate the set of equations for $j = [0 \ldots J]$. Then there are $J+1$ equations for the $J+1$ unknown $b_{+_{n,j}}$ and the unknown $\omega$. Since these equations are linear in $\omega$, they can be arranged in the matrix form

$$[\mathbf{A} + i\omega\mathbf{B}] \begin{pmatrix} b_{+_{n,0}} \\ \vdots \\ b_{+_{n,J}} \end{pmatrix} = 0\,, \tag{E.29}$$

for $J+1 \times J+1$ sized arrays $\mathbf{A}$ and $\mathbf{B}$. This is a *generalized* eigenvalue problem, which can be solved with standard techniques in MATLAB [50]. For the results in Section 5.3, $J = 20$ was used to provide adequate solutions for the first 5 spanwise modes.

## E.4 Modes in Nonuniform Background Flow

For cases of nonuniform background flow in Section 5.4, the analytic form for the linearized flow perturbations becomes very complex (see Drazin and Reid [14] for analytic solutions of perturbations in nonuniform flow). It is instead chosen to discretize the flow field in the spanwise and axial directions and numerically solve for the perturbations using CFD-type techniques.

The four linearized equations (E.5) are discretized along orthogonal computational $(\eta, \zeta)$ coordinates in exactly the same manner as described in Section 6.4 for the *Generalized Body Force Model.* Casing wall and far-field boundary conditions are also applied in the same manner. The only two deviations from the numerical procedure in 6.4 are that here, the equations are solved in a rectilinear, rather than annular, domain, and that the matching conditions (E.10) and (E.11) are used to relate the upstream and downstream flow fields, rather than solving for the continuous flow changes through a blade row.

# APPENDIX F

# SPANWISE VARIATION OF CHARACTERISTIC SLOPE

Characteristics are computed for an example compressor in this appendix, and used to provide numerical values for the spanwise variation of the characteristic slope in Section 5.3. The compressor is represented by a lossless inlet guide vane, followed by a rotor cascade (Figure F-1). The geometry and background flow are assumed to be uniform in the spanwise direction, but the rotor total pressure loss coefficient varied according to cascade data obtained from [61] (replotted in Figure F-2).

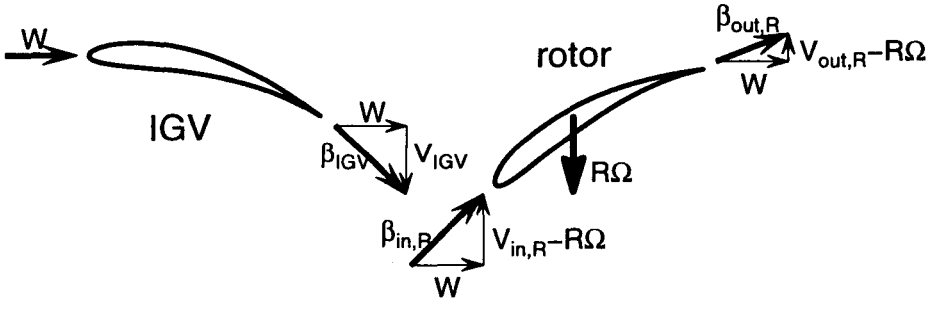


**Figure F-1:** Two-dimensional compressor representation used for constructing pressure rise characteristics. Flow angles are shown in the relative frame of each blade row.

The pressure rise characteristic is computed separately at each spanwise position. Two-dimensional flow is assumed across each spanwise strip, with velocity components defined in Figure F-1. In dimensional form, the total-to-static pressure rise is given by

$$\tilde{P}_{out,R} - \tilde{P}_{t_{in,R}} = \tilde{\rho}\tilde{R}\,\tilde{\Omega}(\tilde{V}_{out,R} - \tilde{V}_{in,R}) - \frac{1}{2}\tilde{\rho}(\tilde{W}^2 + [\tilde{V}_{in,R} - \tilde{R}\,\tilde{\Omega}]^2)\xi - \frac{1}{2}\tilde{\rho}(\tilde{W}^2 + \tilde{V}^2_{out,R})\,. \tag{F.1}$$

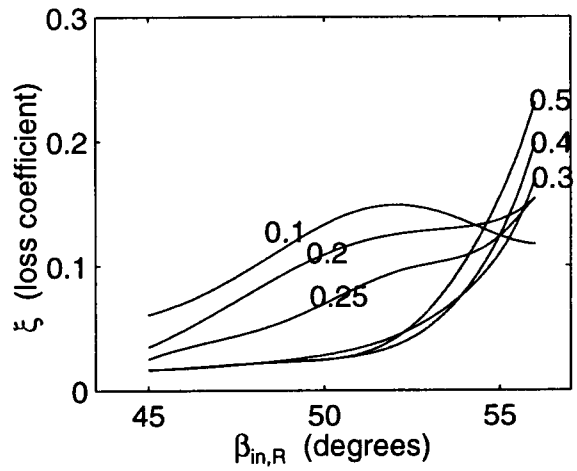


**Figure F-2:** Rotor cascade total pressure loss coefficient as function of relative inlet flow angle, obtained from [61]. Curves provided at six spanwise positions, indicated by fraction immersion across span.

Nondimensionalizing this relation by $\tilde{\rho}$, $\tilde{R}$ and $\tilde{\Omega}$ (as in Chapter 5) yields

$$\Psi = (V_{out,R} - V_{in,R}) - \frac{1}{2}(W^2 + [V_{in,R} - 1]^2)\xi - \frac{1}{2}(W^2 + V_{out,R}^2) \,. \tag{F.2}$$

The absolute velocities at rotor inlet and exit are expressed in terms of the relative flow angles as

$$\begin{aligned} V_{in,R} &= W \tan\beta_{IGV} \\ V_{out,R} &= 1 + W \tan\beta_{out,R} \,. \end{aligned} \tag{F.3}$$

It is assumed that the relative exit flow angles are fixed for all flow coefficients. In particular, $\beta_{IGV} = 35°$, and $\beta_{out,R} = -25°$. The relative flow angle at the rotor inlet is then given by

$$\tan\beta_{in,R} = \tan\beta_{IGV} - \frac{1}{W} \,. \tag{F.4}$$

Substituting these relations into equation (F.2), and taking the derivative of the resulting

equation with respect to $W$ gives

$$\begin{aligned}\frac{d\Psi}{dW} &= (\tan\beta_{out,R} - \tan\beta_{IGV}) - \frac{1}{2}(2W + 2\tan\beta_{IGV})\xi - \cdots \\ &\cdots - \frac{1}{2}(W^2 + [V_{in,R} - 1]^2)\frac{\partial\xi}{\partial W} - \frac{1}{2}(2W + 2[1 + W\tan\beta_{out,R}]\tan\beta_{out,R}) \,.\end{aligned} \tag{F.5}$$

The derivative of loss coefficient, $\xi(\beta_{in,R})$, can be obtained from

$$\begin{aligned}\frac{\partial\xi}{\partial W} &= \frac{d\xi}{d\beta_{in,R}}\frac{\partial\beta_{in,R}}{\partial\tan\beta_{in,R}}\frac{\partial\tan\beta_{in,R}}{\partial W} \\ &= \frac{d\xi}{d\beta_{in,R}}\left(\cos^2\beta_{in,R}\right)\frac{1}{W^2} \\ &= \frac{d\xi}{d\beta_{in,R}}\frac{1}{W^2 + (V_{in,R} - 1)^2} \,.\end{aligned} \tag{F.6}$$

Therefore, the final form of the characteristic slope is

$$\begin{aligned}\frac{d\Psi}{dW} &= (\tan\beta_{out,R} - \tan\beta_{IGV}) - \frac{1}{2}\xi(2W + 2[W\tan\beta_{IGV} - 1]\tan\beta_{IGV}) - \cdots \\ &\cdots - \frac{1}{2}(W^2 + [V_{in,R} - 1]^2)\frac{\partial\xi}{\partial W} - \frac{1}{2}(2W + 2[1 + W\tan\beta_{out,R}]\tan\beta_{out,R}) \\ &= (\xi - 1)\tan\beta_{IGV} - W(\xi\sec^2\beta_{IGV} + \sec^2\beta_{R,out}) - \frac{1}{2}\frac{d\xi}{d\beta_{in,R}} \,.\end{aligned} \tag{F.7}$$

Figure 5-6 shows the values of characteristic slope from equation (F.7) at each spanwise position over a range of axial velocities approaching stall.

# APPENDIX G

# DETAILS OF 3-D ACTUATOR DUCT COMPRESSOR MODELS

The equations for the unsteady flow through the actuator duct compressor representations in Chapter 5 are developed in this appendix. Only uniform rectilinear duct geometries with uniform background flow are considered. Equations for the flow outside the blade row regions are identical to those for the actuator disk model (Appendix E), and will not be re-derived here.

Five different actuator duct models are considered, each generating the pressure rise in a different manner. Section G.1 develops the general form of flow perturbations within the blade regions, which are the same for each model. The matching conditions across the interfaces between blade row and blade-free regions differ between the models, as does the value of a body force to induce losses. The choice of matching conditions and body forces, described in Section G.2, leads to differences in the stability of the modes.

The method for computing the rotating stall modes of the actuator duct model is described in Section G.3 for a single blade row. Actuator duct analyses of multistage compressors (not considered in Chapter 5) can be computed by extending this procedure.

## G.1 Flow Within the Blade Rows

Blade row regions are modeled as high solidity, flat-plate blades with zero thickness (Figure 5-18). To simplify the analysis, it is assumed that the leading edge plane is at $z = 0$,

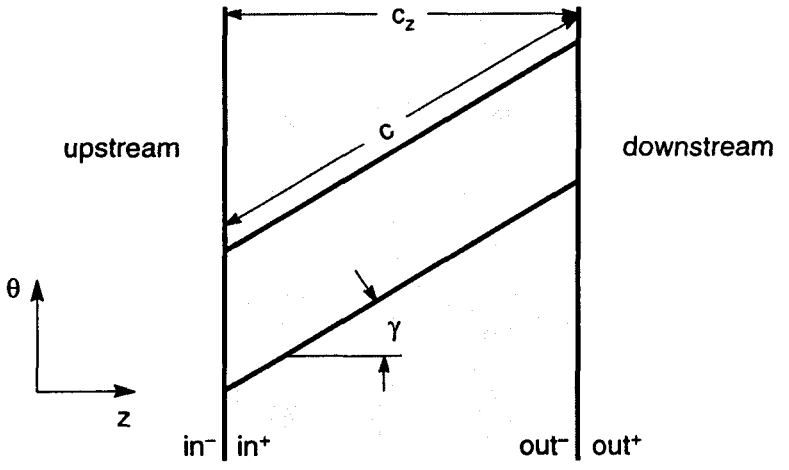


**Figure G-1:** Definition of geometrical variables in actuator duct model (spanwise direction is not shown). Blades of chord length $c$ are inclined at stagger angle $\gamma$.

and the trailing edge plane at $z = c_z$. The flow is represented by the two-dimensional Euler equations, applied in the relative frame of the blade row along the stagger angle, $\gamma$:

$$\begin{aligned}
\frac{\partial U}{\partial r} + \frac{\partial W/\cos\gamma}{\partial z/\cos\gamma} &= 0 \\
\frac{\partial U}{\partial t'} + U\frac{\partial U}{\partial r} + \frac{W}{\cos\gamma}\frac{\partial U}{\partial z/\cos\gamma} + \frac{\partial P}{\partial r} &= 0 \\
\frac{\partial W/\cos\gamma}{\partial t'} + U\frac{\partial W/\cos\gamma}{\partial r} + \frac{W}{\cos\gamma}\frac{\partial W/\cos\gamma}{\partial z/\cos\gamma} + \frac{\partial P}{\partial z/\cos\gamma} &= F(W/cos\gamma)\,. \qquad \text{(G.1)}
\end{aligned}$$

The chord-wise momentum equation includes the effect of a body force, $F$, to cause pressure changes across the blade row. The body force is assumed to be a function of the local chord-wise velocity, which implies it is a function of the local axial velocity $W$. Time derivatives in the relative frame are related to the absolute frame by $\partial/\partial t' = \partial/\partial t + \Omega\,\partial/\partial\theta$, where $\Omega = 1$ or 0 depending on whether the blade row is a rotor or stator (see Section 2.2 for details on transforming equations between rotating frames).

Equations (G.1) can be simplified in the absolute frame as

$$\begin{aligned}
\frac{\partial U}{\partial r} + \frac{\partial W}{\partial z} &= 0 \\
\frac{\partial U}{\partial t} + \frac{\partial U}{\partial \theta} + U\frac{\partial U}{\partial r} + W\frac{\partial U}{\partial z} + \frac{\partial P}{\partial r} &= 0 \\
\frac{\partial W}{\partial t} + \frac{\partial W}{\partial \theta} + U\frac{\partial W}{\partial r} + W\frac{\partial W}{\partial z} + \cos^2\gamma\frac{\partial P}{\partial z} &= F(W)\,. \qquad \text{(G.2)}
\end{aligned}$$

These equations can be linearized about a uniform steady flow, yielding

$$\begin{aligned} \frac{\partial u}{\partial r} + \frac{\partial w}{\partial z} &= 0 \\ \frac{\partial u}{\partial t} + \frac{\partial u}{\partial \theta} + \bar{W}\frac{\partial u}{\partial z} + \frac{\partial p}{\partial r} &= 0 \\ \frac{\partial w}{\partial t} + \frac{\partial u}{\partial \theta} + \bar{W}\frac{\partial w}{\partial z} + \cos^2\gamma\frac{\partial p}{\partial z} &= \frac{dF}{dW}w \,. \end{aligned} \tag{G.3}$$

The solution is simplified by expressing the linearized flow variables by the exponential form in equations (E.4) and (E.6). Wavenumbers in the tangential and spanwise directions are given by $n$ and $j$, and the disturbances vary axially as $\exp(\hat{l}_{n,j}\, z)$ for some, as of yet, unknown $\hat{l}_{n,j}$. Equations (G.3) can then be written in matrix form, valid for all $n$ and $j$:

$$\begin{bmatrix} i\omega + in\Omega + \bar{W}\hat{l}_{n,j} & 0 & -k_j \\ 0 & i\omega + in\Omega + \bar{W}\hat{l}_{n,j} - \frac{dF}{dW} & \hat{l}_{n,j}\cos^2\gamma \\ k_j & \hat{l}_{n,j} & 0 \end{bmatrix} \begin{pmatrix} \hat{u}_{n,j} \\ \hat{w}_{n,j} \\ \hat{p}_{n,j} \end{pmatrix} = 0 \,, \tag{G.4}$$

where $k_j = \frac{\pi j}{1-r_h}$. For non-zero disturbances, the determinant of the matrix above must be zero:

$$(i\omega + in\Omega + \bar{W}\hat{l}_{n,j})(\hat{l}^2_{n,j}\cos^2\gamma - k_j^2) + \frac{dF}{dW}k_j^2 = 0 \,. \tag{G.5}$$

This cubic equation yields three values of $\hat{l}_{n,j}$ for each $(n,j)$ mode. If there is no body force, then the solutions are $\hat{l}_{n,j} = \pm k_j/\cos\gamma$, $-(i\omega + in\Omega)/\bar{W}$. These represent two potential disturbances (one growing, one decaying), and a vortical disturbance. For the case of a non-zero body force, the solution to equation (G.5) is computed numerically. In either case, the three solutions for $\hat{l}_{n,j}$ are defined as $l_{1_{n,j}}$, $l_{2_{n,j}}$ and $l_{3_{n,j}}$. The general form of the linear flow perturbations within the blade region for each $(n,j)$ mode can then be

expressed as

$$\begin{pmatrix} u_{n,j} \\ w_{n,j} \\ p_{n,j} \end{pmatrix} = \left\{ d_{1_{n,j}} \begin{pmatrix} k_j \\ -k_j^2/l_{1_{n,j}} \\ i\omega + in\Omega + \bar{W} l_{1_{n,j}} \end{pmatrix} e^{l_{1_{n,j}} z} + d_{2_{n,j}} \begin{pmatrix} k_j \\ -k_j^2/l_{2_{n,j}} \\ i\omega + in\Omega + \bar{W} l_{2_{n,j}} \end{pmatrix} e^{l_{2_{n,j}} z} + \cdots \right.$$
$$\left. \cdots + d_{3_{n,j}} \begin{pmatrix} k_j \\ -k_j^2/l_{3_{n,j}} \\ i\omega + in\Omega + \bar{W} l_{3_{n,j}} \end{pmatrix} e^{l_{3_{n,j}} z} \right\} \begin{pmatrix} \sin k_j(r - r_h) \\ \cos k_j(r - r_h) \\ \cos k_j(r - r_h) \end{pmatrix} e^{in\theta} \qquad \text{(G.6)}$$

for unknown constants $d_{1_{n,j}}$, $d_{2_{n,j}}$ and $d_{3_{n,j}}$.

The three constants $d_{1_{n,j}}$, $d_{2_{n,j}}$ and $d_{3_{n,j}}$ are determined by matching the above perturbations to those in the blade-free regions adjoining the blade row. Perturbations in pressure, spanwise velocity and axial velocity at the inlet and exit of the blade row can be read directly from equation (G.6) at $z = 0$ and $c_z$. The tangential velocity and total pressure disturbances can then be expressed in terms of $p$ and $w$:

$$\begin{aligned} v_{n,j} &= w_{n,j} \tan\gamma \\ p_{t_{n,j}} &= p_{n,j} + \bar{W} w_{n,j} + (\Omega + \bar{W} \tan\gamma) v_{n,j} \ . \end{aligned} \qquad \text{(G.7)}$$

## G.2 Matching Conditions for Different Blade Models

For a single blade row compressor, there are 7 unknowns determining the structure of each $(n, j)$ mode: the upstream disturbance is written in terms of one variable, $b_{+_{n,j}}$, through equation (E.12); the downstream disturbance is expressed in terms of three variables, $a_{2_{n,j}}$, $a_{3_{n,j}}$ and $b_{-_{n,j}}$, through equation (E.12); and the flow within the blade row depends on $d_{1_{n,j}}$, $d_{2_{n,j}}$ and $d_{3_{n,j}}$ from equation (G.6). Therefore, seven matching conditions are required to complete the system and solve for the eigenmodes. These conditions are:

- continuity of $u$ and $w$ across the leading edge plane,
- continuity of $u$, $v$ and $w$ across the trailing edge plane,
- specified changes in $p$ across the leading and trailing edge planes.

The five actuator disk models in Section 5.5.1 differ in their methods of enforcing the pressure rise characteristic across the blade row. Each model has a unique pair of pressure matching conditions for the leading and trailing edges, as well as different values for the body force derivative $dF/dW$. These conditions are described below using the nomenclature in Figure G-1 (e.g. $p_{t,out-}$ is the total pressure disturbance just inside the trailing edge plane).

**Model (a): All pressure rise at leading edge**

This model does not use a body force. The entire total-to-static pressure rise characteristic is enforced across the leading edge ($P_{in+} - P_{t,in-} = \Psi$), and the pressure is continuous across the trailing edge ($P_{out+} - P_{out-} = 0$). The linearized form of these matching conditions are

$$\begin{aligned} \text{inlet:} \quad & p_{in+} - p_{t,in-} = \frac{d\Psi}{dW} w_{in-} \\ \text{exit:} \quad & p_{out+} - p_{out-} = 0 \,. \end{aligned} \tag{G.8}$$

**Model (b): Pressure rise from turning at leading edge, losses at trailing edge**

This model does not use a body force. The change in tangential velocity at the leading edge of the rotor causes a jump in total pressure, $P_{t,in+} - P_{t,in-} = \Omega(V_{in+} - V_{in-})$. For steady conditions, $\bar{V}$ is zero upstream, and is $\Omega + \bar{W}\tan\gamma$ throughout the blade row. Given the above pressure jump at the leading edge, the pressure must drop at the trailing edge by the following value of loss to satisfy the overall characteristic:

$$L = \Omega(\Omega + \bar{W}\tan\gamma) - \Psi - \frac{1}{2}\bar{W}^2\sec^2\gamma \,. \tag{G.9}$$

The linearized form of the matching conditions at both faces of the blade row are then

$$\begin{aligned} \text{inlet:} \quad & p_{t,in+} - p_{t,in-} = \Omega(w_{in-}\tan\gamma - v_{in-}) \\ \text{exit:} \quad & p_{out+} - p_{out-} = \left(\frac{d\Psi}{dW} + \bar{W}\sec^2\gamma\right) \,. \end{aligned} \tag{G.10}$$

**Model (c): All pressure rise at trailing edge**

This model does not use a body force. The entire total-to-static pressure rise characteristic is enforced across the trailing edge ($P_{out+} - P_{t,out-} = \Psi$), and the pressure is continuous across the leading edge ($P_{in+} - P_{in-} = 0$). The linearized form of these matching conditions are

$$\begin{aligned} \text{inlet:} \quad & p_{in+} - p_{in-} = 0 \\ \text{exit:} \quad & p_{out+} - p_{t,out-} = \frac{d\Psi}{dW} w_{out-} \ . \end{aligned} \tag{G.11}$$

**Model (d): Pressure rise from turning at leading edge, losses from body force**

The turning at the leading edge causes a pressure rise, exactly as in model (b), and the pressure is continuous across the trailing edge, as in (a). The linearized form of these equations can be found above. The loss $L$ from equation (G.9) is distributed evenly along the chord through the body force $F$. In steady-state, the pressure change across the blade from a uniform body force is given by $\Delta\bar{P} = c\bar{F}$, so $\bar{F} = -\bar{L}/c$. The derivative of the body force used in Section G.1 is therefore given by

$$\frac{dF}{dW} = \frac{1}{c}\left(\frac{d\Psi}{dW} + \bar{W}\sec^2\gamma\right) \ . \tag{G.12}$$

**Model (e): All pressure rise from body force**

The pressure is continuous at the leading edge, exactly as in model (c), and across the trailing edge, as in (a). In steady flow, all pressure rise is caused by the body force, $\bar{F} = (\Psi + \bar{W}^2/2)/c$. The derivative of the body force is therefore

$$\frac{dF}{dW} = \frac{1}{c}\left(\frac{d\Psi}{dW} + \bar{W}\right) \ . \tag{G.13}$$

## G.3 Rotating Stall Modes of Actuator Duct Model

One mode for each value of $(n, j)$ can be found by calculating the non-trivial solution for the seven mode shape variables with the seven matching conditions.

The five velocity matching conditions are identical for each model. Equating the ap-

propriate velocity disturbances at the leading edge plane ($z = 0$) and the trailing edge plane ($z = c_z$), provides the following 5 equations, written in matrix form:

$$\begin{bmatrix} k_j & k_j & k_j & k_j & 0 & 0 & 0 \\ l_{n,j} & \frac{k_j}{l_{1_{n,j}}} & \frac{k_j}{l_{2_{n,j}}} & \frac{k_j}{l_{3_{n,j}}} & 0 & 0 & 0 \\ 0 & k_j e^{l_{1_{n,j}} c_z} & k_j e^{l_{2_{n,j}} c_z} & k_j e^{l_{3_{n,j}} c_z} & 0 & i\alpha & k_j \\ 0 & \frac{k_j \tan\gamma}{l_{1_{n,j}}} e^{l_{1_{n,j}} c_z} & \frac{k_j \tan\gamma}{l_{2_{n,j}}} e^{l_{2_{n,j}} c_z} & \frac{k_j \tan\gamma}{l_{3_{n,j}}} e^{l_{3_{n,j}} c_z} & i\alpha & 0 & in \\ 0 & \frac{k_j}{l_{1_{n,j}}} e^{l_{1_{n,j}} c_z} & \frac{k_j}{l_{2_{n,j}}} e^{l_{2_{n,j}} c_z} & \frac{k_j}{l_{3_{n,j}}} e^{l_{3_{n,j}} c_z} & in & -k_j & -l_{n,j} \end{bmatrix} \begin{pmatrix} b_{+_{n,j}} \\ d_{1_{n,j}} \\ d_{2_{n,j}} \\ d_{3_{n,j}} \\ a_{2_{n,j}} \\ a_{3_{n,j}} \\ b_{-_{n,j}} \end{pmatrix} = 0 \,. \quad \text{(G.14)}$$

The remaining two equations to complete the 7×7 matrix come from the appropriate pressure matching conditions, depending on the model type. All parameters within the matrix are known quantities except for the eigenvalue $\omega_{n,j}$ which contributes to the variables $l_{1_{n,j}}$, $l_{2_{n,j}}$, $l_{3_{n,j}}$ and $i\alpha$. A non-trivial solution for the rotating stall mode is found for the value of $\omega_{n,j}$ that sets the determinant of the matrix to zero.

The matrix is not linear in $\omega_{n,j}$ because of exponential terms like $\exp(l_{n,j}\, c_z)$. Therefore, the eigenmodes can not be found using traditional eigenvalue techniques. A computational/graphical method used by Hendricks [35] has been adopted. Determinants of the 7×7 matrix are first calculated over a fine range of values for $\omega_{n,j}$ in the complex plane. Then contours of the imaginary and real parts of the determinants are plotted. The eigenvalue will reside at the crossing of the zero contours for each part. The eigenvector, corresponding to the mode shape, is computed by substituting the eigenvalue back into the $7 \times 7$ matrix and solving for $b_{+_{n,j}}$, $d_{1_{n,j}}$, $d_{2_{n,j}}$, $d_{3_{n,j}}$, $a_{2_{n,j}}$, $a_{3_{n,j}}$ and $b_{-_{n,j}}$.

# APPENDIX H

# DETAILS OF 3-D GENERALIZED BODY FORCE COMPRESSOR MODEL

This appendix contains the details omitted in Chapter 6 about the three-dimensional body force compressor model. The first section describes the stream function calculation to solve for the steady background flow field. The second section describes how the discretized form of the linearized stability model is formed and used to calculate the rotating stall modes.

## H.1 Steady Axisymmetric Flow

The steady, axisymmetric flow field is modeled by the set of Euler equations with body forces (6.4). It is presumed that the inlet flow conditions, and the relations for the body forces in terms local flow variables, $\bar{F}_\theta(\bar{V},\bar{W})$ and $\bar{F}_L(\bar{V},\bar{W})$, are known ($\bar{F}_r$ is assumed to be zero). Given these relations, this section describes how to compute the steady flow field $\bar{U}$, $\bar{V}$, $\bar{W}$ and $\bar{P}$ throughout the compressor.

### H.1.1 Stream Function Representation

The number of unknown variables can be reduced by representing $\bar{U}$ and $\bar{W}$ in terms of a stream function, $\Psi(r,z)$:

$$\bar{W} = \frac{1}{r}\frac{\partial \Psi}{\partial r}, \quad \bar{U} = -\frac{1}{r}\frac{\partial \Psi}{\partial z}\,. \tag{H.1}$$

For steady incompressible, inviscid flow in *Cartesian* coordinates, the total pressure and tangential velocity are simply convected along streamlines. The shape of the streamlines is in turn dependent on variations of $\bar{P}_t$ and $\bar{V}$. These conditions are expressed as

$$\begin{aligned} \bar{P}_t &= \bar{P}_t(\Psi) \\ \bar{V} &= \bar{V}(\Psi) \\ \nabla^2\Psi &= \frac{\partial}{\partial\Psi}\left(\bar{P}_t - \frac{1}{2}\bar{V}^2\right), \end{aligned} \tag{H.2}$$

where $\partial/\partial\Psi = \left(\bar{W}\partial/\partial r - \bar{U}\partial/\partial z\right)/(\bar{U}^2 + \bar{W}^2)$.

An analogous form to these equations can be derived for flow with body forces in *cylindrical* coordinates. From equations (6.4), the change in $\bar{P}_t$ and $r\bar{V}$ along a streamline are linked to the body forces by

$$\begin{aligned} \vec{\bar{V}} \cdot \vec{\nabla}\bar{P}_t &= \bar{U}\frac{\partial \bar{P}_t}{\partial r} + \bar{W}\frac{\partial \bar{P}_t}{\partial z} &&= -(\bar{U}^2 + \bar{W}^2)^{\frac{1}{2}}\bar{F}_L + r\Omega\bar{F}_\theta \\ \vec{\bar{V}} \cdot \vec{\nabla}(r\bar{V}) &= \bar{U}\frac{\partial r\bar{V}}{\partial r} + \bar{W}\frac{\partial r\bar{V}}{\partial z} &&= r\bar{F}_\theta \,. \end{aligned} \tag{H.3}$$

The elliptical governing equation for $\Psi$ is found by expressing the second component of $\vec{\bar{V}} \times \vec{\nabla}\bar{P}_t - \frac{\bar{V}}{r}\vec{\bar{V}} \times \vec{\nabla}(r\bar{V})$ in terms of the body forces through equation (6.4):

$$\bar{W}\frac{\partial \bar{P}_t}{\partial r} - \bar{U}\frac{\partial \bar{P}_t}{\partial z} - \frac{\bar{V}}{r}\left(\bar{W}\frac{\partial r\bar{V}}{\partial r} - \bar{U}\frac{\partial r\bar{V}}{\partial z}\right) = \bar{W}\bar{F}_r - \bar{U}\bar{F}_z + (\bar{U}^2 + \bar{W}^2)\left(\frac{\partial \bar{W}}{\partial r} - \frac{\partial \bar{U}}{\partial z}\right). \tag{H.4}$$

Equations (H.3) and (H.4) can be expressed solely in terms of $\bar{P}_t$, $r\bar{V}$ and $\Psi$. These parameters represent the three working variables for computing the steady flow field in cylindrical coordinates.

$$\frac{\partial\Psi}{\partial r}\left(\frac{\partial \bar{P}_t}{\partial z} - \Omega\frac{\partial r\bar{V}}{\partial z}\right) - \frac{\partial\Psi}{\partial z}\left(\frac{\partial \bar{P}_t}{\partial r} - \Omega\frac{\partial r\bar{V}}{\partial r}\right) + \left(\frac{\partial\Psi}{\partial r}^2 + \frac{\partial\Psi}{\partial z}^2\right)^{\frac{1}{2}}\bar{F}_L = 0 \tag{H.5}$$

$$\frac{\partial\Psi}{\partial r}\frac{\partial r\bar{V}}{\partial z} - \frac{\partial\Psi}{\partial z}\frac{\partial r\bar{V}}{\partial r} - r^2\bar{F}_\theta = 0 \tag{H.6}$$

$$\frac{\partial\Psi}{\partial r}\left(\frac{\partial\bar{P}_t}{\partial r}-\frac{r\bar{V}}{r^2}\frac{\partial r\bar{V}}{\partial r}\right)+\frac{\partial\Psi}{\partial z}\left(\frac{\partial\bar{P}_t}{\partial z}-\frac{r\bar{V}}{r^2}\frac{\partial r\bar{V}}{\partial z}\right)-\left(\frac{\partial\Psi}{\partial r}\frac{\partial\bar{F}_r}{\partial r}+\frac{\partial\Psi}{\partial z}\frac{\partial\bar{F}_z}{\partial z}\right)-\cdots \tag{H.7}$$

$$\cdots-\frac{1}{r^2}\left(\frac{\partial\Psi}{\partial r}^2+\frac{\partial\Psi}{\partial z}^2\right)\left(\frac{\partial^2\Psi}{\partial r^2}+\frac{\partial^2\Psi}{\partial z^2}-\frac{1}{r}\frac{\partial\Psi}{\partial r}\right) = 0\,.$$

### H.1.2 Computational Procedure

Solutions to equations (H.5)-(H.7) are numerically obtained over a regular grid in the $(r,z)$ plane. Figure I-1 shows a sample grid, and depicts the $(\eta,\zeta)$ coordinates used in the computation. There are a total of $M\times N$ nodes, where $M$ and $N$ are the number of nodes across the span and along the axial direction, respectively. At each node, $\bar{P}_t$, $r\bar{V}$ and $\Psi$ are unknown. Therefore, there are a total of $3\times M\times N$ unknowns, requiring as many discretized equations for their solution. The discretized versions of equations (H.5)-(H.7) can be obtained using the transformations given in Appendix I.

The three governing flow equations are applied at all interior nodes. In blade-free regions the body forces are set to zero. Modifications and substitutions to these equations are applied along the grid boundaries as described below.

**Upstream boundary** At the inlet to the compression system the flow conditions are known. The radial profile of $\Psi$ is calculated from $\bar{W}(r)$ using $\Psi=\int_0^r \bar{W}r\,dr$. The values of $\bar{P}_t$, $r\bar{V}$ and $\Psi$ are imposed at each node of the inlet boundary.

**Downstream boundary** Far downstream, the flow is assumed to be in radial equilibrium, i.e. $\bar{U}=0$. For these nodes, the elliptical $\Psi$ equation (H.7) is replaced with $\partial\Psi/\partial z=0$.

**Casing walls** Along the inner and outer casing walls (constant $\eta$), the streamlines must follow the gridlines. To enforce this, equation (H.7) is replaced with $\partial\Psi/\partial\zeta=0$.

Consistent solutions to all $3\times M\times N$ equations are found by iteration. An initial estimate of the flow field is obtained by simply convecting the inlet conditions through the compressor along the $\zeta$-gridlines. Based on this estimate, the body forces (which generally depend on the flow) are calculated. The set of all discretized equations can then be combined in the

matrix form $\mathbf{A}\vec{x} = 0$:

$$\begin{bmatrix} \text{equation 1} \\ \text{equation 2} \\ \vdots \\ \text{equation } 3NM \end{bmatrix} \begin{pmatrix} \vdots \\ \Psi_{\eta,\zeta} \\ \bar{P}_{t\ \eta,\zeta} \\ (r\bar{V})_{\eta,\zeta} \\ \vdots \end{pmatrix} = 0 \ . \tag{H.8}$$

Each row of $\mathbf{A}$ represents one discretized equation, and the vector $\vec{x}$ represents the unknown values of $\bar{P}_t$, $r\bar{V}$ and $\Psi$ at all grid nodes.

The solution to $\mathbf{A}\vec{x} = 0$ is found using a matrix analogy of the Newton-Raphson method. For scalar functions, the Newton-Raphson method converges to roots of the equation $A(x) = 0$ in the following way: A first-order approximation to $A(x)$ is written as $A(x) = A(x_k) + \partial A/\partial x|_k \, (x - x_k)$. From an initial estimate for the root, $x_k$, an improved approximation can then be found as $x_{k+1} = x_k - A(x_k) \, / \, (\partial A/\partial x|_k)$.

For the matrix version of Newton's method, an analogy of $\partial A/\partial x$ must be found. A $3NM \times 3NM$ matrix $\mathbf{B}$ is created from the set of discrete governing equations, such that $\mathbf{B}_{i,j} = \partial(\text{equation}_i)/\partial x_j$. That is, each row in $\mathbf{B}$ contains the derivatives of the corresponding equation in $\mathbf{A}$ with respect to the variables in $\vec{x}$. Where necessary, values of the body force and other flow variables are evaluated using the most recent estimate of $\vec{x}_k$.

Constructing elements of $\mathbf{B}$ from the discretized form of equations (H.5)-(H.7) is straightforward, except for terms containing a body force. Since $\bar{F}_\theta$ and $\bar{F}_L$ depend on the flow, their derivatives with respect to $\vec{x}$ are found from a first-order Taylor series expansion about $\vec{x}_k$:

$$F(V,W) = F(V_k,W_k) + \left.\frac{\partial F}{\partial V}\right|_k \frac{\delta(rV)}{r} + \frac{1}{r}\left.\frac{\partial F}{\partial W}\right|_k \delta\left(\frac{\partial \Psi}{\partial r}\right) \ . \tag{H.9}$$

Therefore, equations in $\mathbf{A}$ with $\bar{F}_\theta$ and $\bar{F}_L$ will create terms containing $\frac{\partial F_\theta}{\partial V}$, $\frac{\partial F_\theta}{\partial W}$, $\frac{\partial F_L}{\partial V}$ and $\frac{\partial F_L}{\partial W}$ at elements in $\mathbf{B}$ corresponding to derivatives with respect to $rV$ and $\Psi$.

To converge to the steady flow solution, $\vec{x}_k$ is improved as $\vec{x}_{k+1} = \vec{x}_k + \delta\vec{x}$ where $\delta\vec{x} = -\mathbf{B}^{-1}\,[\mathbf{A}\vec{x}_k]$. For each step, the values of $\mathbf{A}$ and $\mathbf{B}$ must be updated. This process is continued until residuals in $\|\vec{x}_{k+1} - \vec{x}_k\|$ and $\|\mathbf{A}\vec{x}_k\|$ are sufficiently small. For the calcula-

tions in this thesis, the iterations continued until the solutions could no longer converge.

## H.2 Calculation of Rotating Stall Modes

The linearized stability model has been reduced in Section 6.4 to the matrix equation (6.22): $\mathbf{A}\vec{x} + i\omega\mathbf{B}\vec{x} = 0$. The matrices $\mathbf{A}$ and $\mathbf{B}$ are very large for the grids in this thesis (approximately 10 thousand rows and columns). They also have complex-valued entries and no symmetrical properties, so standard eigenvalue techniques are difficult to implement on computers with modest resources.

The solution method used in this thesis is an *inverse iteration* technique described by Golub and Van Loan [21]. This four-step procedure takes an initial estimate of $\omega$, and converges to the nearest eigenvalue in the complex-plane.

1. Begin with an initial value of $\omega$, and two random vectors $\vec{x}_k$ and $\vec{y}_k$.

2. Solve for $\vec{x}_{k+1}$ and $\vec{y}_{k+1}$ in equation (H.10). Repeat this step for 6–10 iterations, each time updating $\vec{x}_k$ and $\vec{y}_k$.

$$\begin{aligned} [\mathbf{A} + i\omega\mathbf{B}]\,\vec{x}_{k+1} &= \mathbf{B}\vec{x}_k \\ [\mathbf{A} + i\omega\mathbf{B}]^{\mathrm{T}}\,\vec{y}_{k+1} &= \mathbf{B}^{\mathrm{T}}\vec{y}_k\ . \end{aligned} \tag{H.10}$$

   This is best performed by first calculating the LU decomposition of $\mathbf{A} + i\omega\mathbf{B}$. $\vec{x}_k$ and $\vec{y}_k$ are then computed by fore- and back-substitution of the equations $\mathbf{LU}\vec{x}_{k+1} = \mathbf{B}\vec{x}_k$ and $\mathbf{U}^{\mathrm{T}}\mathbf{L}^{\mathrm{T}}\vec{y}_{k+1} = \mathbf{B}^{\mathrm{T}}\vec{y}_k$.

3. Update $\omega$ with the value from

$$-i\omega = \frac{\vec{y}^{\mathrm{T}}\mathbf{A}\,\vec{x}}{\vec{y}^{\mathrm{T}}\mathbf{B}\,\vec{x}}\ . \tag{H.11}$$

4. Repeat steps 2 and 3 twice more to converge on the actual eigenvalue, $\omega$, and eigenvector, $\vec{x}$, of the rotating stall mode.

# APPENDIX I

# TRANSFORMATION OF FLOW EQUATIONS TO COMPUTATIONAL COORDINATES

The eigenmodes of the three-dimensional body force model in Appendix H are solved numerically over a computational grid. The numerics are facilitated by first transforming the physical grid in $(z, r)$ onto a $(\eta, \zeta)$ computational plane (Figure I-1) so that the transformed grid lines are orthogonal and evenly spaced. Node spacing in the $(\eta, \zeta)$ plane is chosen so that $\Delta\eta = \Delta\zeta = 1$. This appendix describes the transformation of partial derivatives from the physical domain, the discretization of these derivatives in the computational domain, and the evaluation of the metrics between coordinate systems.

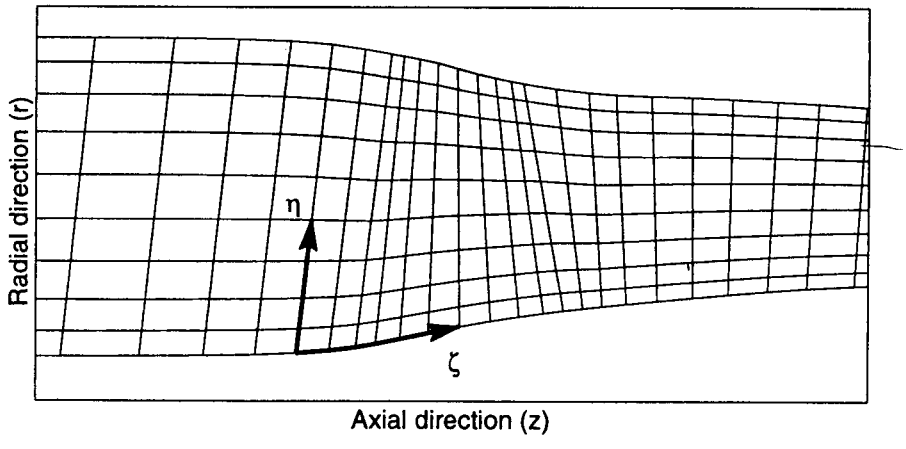


**Figure I-1:** Illustration of physical $(r, z)$ and computational $(\eta, \zeta)$ coordinates for example grid.

### Derivatives in the Computational Plane

The only derivatives of flow properties used by the three-dimensional body force compressor model that require transformation are: $\partial/\partial r$, $\partial/\partial z$, and $\partial^2/\partial r^2 + \partial^2/\partial z^2$. Derivatives with respect to $\theta$ are not considered because they are either zero (for the steady flow model), or accounted for by the tangential wavenumber $n$ (for the linearized flow model).

The relevant derivatives are transformed into the $(\eta, \zeta)$ plane below, arbitrarily using the flow variable $P(r, z)$ for illustration.

$$\begin{aligned}
\frac{\partial P}{\partial r} &= \frac{\partial \eta}{\partial r}\frac{\partial P}{\partial \eta} + \frac{\partial \zeta}{\partial r}\frac{\partial P}{\partial \zeta} \\
\frac{\partial P}{\partial z} &= \frac{\partial \eta}{\partial z}\frac{\partial P}{\partial \eta} + \frac{\partial \zeta}{\partial z}\frac{\partial P}{\partial \zeta} \\
\frac{\partial^2 P}{\partial r^2} + \frac{\partial^2 P}{\partial z^2} &= \left(\frac{\partial \eta}{\partial r}^2 + \frac{\partial \eta}{\partial z}^2\right)\frac{\partial^2 P}{\partial \eta^2} + 2\left(\frac{\partial \zeta}{\partial r}\frac{\partial \eta}{\partial r} + \frac{\partial \zeta}{\partial z}\frac{\partial \eta}{\partial z}\right)\frac{\partial P^2}{\partial \eta \partial \zeta} + \cdots \\
&\quad \cdots + \left(\frac{\partial \zeta}{\partial r}^2 + \frac{\partial \zeta}{\partial z}^2\right)\frac{\partial^2 P}{\partial \zeta^2} + \left(\frac{\partial^2 \eta}{\partial r^2} + \frac{\partial^2 \eta}{\partial z^2}\right)\frac{\partial P}{\partial \eta} + \left(\frac{\partial^2 \zeta}{\partial r^2} + \frac{\partial^2 \zeta}{\partial z^2}\right)\frac{\partial P}{\partial \zeta} .
\end{aligned} \tag{I.1}$$

### Evaluation of Metrics

The metrics in equation (I.1) are evaluated using standard transformation procedures found in CFD textbooks (i.e. [3]). The first order metrics can be written as

$$\begin{aligned}
\frac{\partial \zeta}{\partial z} &= \frac{1}{J}\frac{\partial r}{\partial \eta} \\
\frac{\partial \zeta}{\partial r} &= -\frac{1}{J}\frac{\partial z}{\partial \eta} \\
\frac{\partial \eta}{\partial z} &= -\frac{1}{J}\frac{\partial r}{\partial \zeta} \\
\frac{\partial \eta}{\partial r} &= \frac{1}{J}\frac{\partial z}{\partial \zeta} ,
\end{aligned} \tag{I.2}$$

where the Jacobian, $J$, is

$$J = \frac{\partial z}{\partial \zeta}\frac{\partial r}{\partial \eta} - \frac{\partial r}{\partial \zeta}\frac{\partial z}{\partial \eta} . \tag{I.3}$$

The second order metrics are

$$\begin{aligned}
\frac{\partial^2\zeta}{\partial z^2} &= \frac{1}{J^3}\left(J\frac{\partial r}{\partial\eta}\frac{\partial r^2}{\partial\eta\partial\zeta} - \frac{\partial J}{\partial\zeta}\frac{\partial r}{\partial\eta}^2 - J\frac{\partial r}{\partial\zeta}\frac{\partial^2 r}{\partial\eta^2} + \frac{\partial J}{\partial\eta}\frac{\partial r}{\partial\zeta}\frac{\partial r}{\partial\eta}\right) \\
\frac{\partial^2\zeta}{\partial r^2} &= \frac{1}{J^3}\left(J\frac{\partial z}{\partial\eta}\frac{\partial z^2}{\partial\eta\partial\zeta} - \frac{\partial J}{\partial\zeta}\frac{\partial z}{\partial\eta}^2 - J\frac{\partial z}{\partial\zeta}\frac{\partial^2 z}{\partial\eta^2} + \frac{\partial J}{\partial\eta}\frac{\partial z}{\partial\zeta}\frac{\partial z}{\partial\eta}\right) \\
\frac{\partial^2\eta}{\partial z^2} &= \frac{1}{J^3}\left(J\frac{\partial r}{\partial\zeta}\frac{\partial r^2}{\partial\eta\partial\zeta} - \frac{\partial J}{\partial\eta}\frac{\partial r}{\partial\zeta}^2 - J\frac{\partial r}{\partial\eta}\frac{\partial^2 r}{\partial\zeta^2} + \frac{\partial J}{\partial\zeta}\frac{\partial r}{\partial\eta}\frac{\partial r}{\partial\zeta}\right) \\
\frac{\partial^2\eta}{\partial r^2} &= \frac{1}{J^3}\left(J\frac{\partial z}{\partial\zeta}\frac{\partial z^2}{\partial\eta\partial\zeta} - \frac{\partial J}{\partial\eta}\frac{\partial z}{\partial\zeta}^2 - J\frac{\partial z}{\partial\eta}\frac{\partial^2 z}{\partial\zeta^2} + \frac{\partial J}{\partial\zeta}\frac{\partial z}{\partial\eta}\frac{\partial z}{\partial\zeta}\right),
\end{aligned} \tag{I.4}$$

where the derivatives of the Jacobian are

$$\begin{aligned}
\frac{\partial J}{\partial\zeta} &= \frac{\partial^2 z}{\partial\zeta^2}\frac{\partial r}{\partial\eta} + \frac{\partial z}{\partial\zeta}\frac{\partial r^2}{\partial\eta\partial\zeta} - \frac{\partial^2 r}{\partial\zeta^2}\frac{\partial z}{\partial\eta} - \frac{\partial r}{\partial\zeta}\frac{\partial z^2}{\partial\eta\partial\zeta} \\
\frac{\partial J}{\partial\eta} &= \frac{\partial z^2}{\partial\eta\partial\zeta}\frac{\partial r}{\partial\eta} + \frac{\partial z}{\partial\zeta}\frac{\partial^2 r}{\partial\eta^2} - \frac{\partial r^2}{\partial\eta\partial\zeta}\frac{\partial z}{\partial\eta} - \frac{\partial r}{\partial\zeta}\frac{\partial^2 z}{\partial\eta^2}.
\end{aligned} \tag{I.5}$$

**Discretization in the Computational Plane**

Derivatives of $P$ with $\eta$ and $\zeta$ in equation (I.1), and the above metrics are easily performed on the evenly-spaced, orthogonal $(\eta, \zeta)$ grid. The following second-order differencing scheme is used for nodes away from the edges:

$$\begin{aligned}
\frac{\partial P}{\partial\eta} &= \frac{1}{2}(P_{\eta+1,\zeta} - P_{\eta-1,\zeta}) \\
\frac{\partial P}{\partial\zeta} &= \frac{1}{2}(P_{\eta,\zeta+1} - P_{\eta,\zeta-1}) \\
\frac{\partial^2 P}{\partial\eta^2} &= P_{\eta+1,\zeta} - 2P_{\eta,\zeta} + P_{\eta-1,\zeta} \\
\frac{\partial P^2}{\partial\eta\partial\zeta} &= \frac{1}{4}(P_{\eta+1,\zeta+1} - P_{\eta+1,\zeta-1} - P_{\eta-1,\zeta+1} + P_{\eta-1,\zeta-1}) \\
\frac{\partial^2 P}{\partial\zeta^2} &= P_{\eta,\zeta+1} - 2P_{\eta,\zeta} + P_{\eta,\zeta-1}.
\end{aligned} \tag{I.6}$$

For nodes on grid boundaries, a one-sided approach is used. Equations in the body force model (Section 6.4 and Appendix H.1.2) require only first-order derivatives on grid boundaries. The discretization scheme takes the value at the boundary plus at two inner nodes to preserve the second-order accuracy of the numerical scheme. For example, $\partial P/\partial\zeta$ at the

inlet boundary plane is discretized as

$$\frac{\partial P}{\partial \zeta} = \frac{1}{2}(-P_{\eta,\zeta+2} + 4P_{\eta,\zeta+1} - 3P_{\eta,\zeta}) \ . \tag{I.7}$$

Discretizations with $\zeta$ and $\eta$ at all other grid boundaries are expressed similarly.

# APPENDIX J

# TWO-DIMENSIONAL VERSION OF GENERALIZED BODY FORCE COMPRESSOR MODEL

A two-dimensional version of the three-dimensional body force compressor model in Chapter 6 is developed in this Appendix. The first section describes how parameters for the 2-D model are constructed based on the three-dimensional flow field. The governing equations of motion are derived in the next section, followed by the numerical solution process for steady, axisymmetric flow. In the last section, the two-dimensional linearized stability model is created, with a description of how to solve for the eigenmodes.

## J.1 Converting 3-D to 2-D Flow

The purpose of the two-dimensional model is to calculate the stability of flow fields corresponding to the three-dimensional background flows, but without radial variations. By comparing with 3-D stability model results, the specific effect of radial flow variations on compressor stall can be isolated. Therefore, the two-dimensional model should represent a radially-averaged version of the 3-D model.

Parameters for the 2-D model can be obtained once the steady, axisymmetric 3-D flows have been computed. Inputs to the 2-D model are divided into three parts: those dealing with compressor geometry, inlet flow conditions and blade row performance.

### Geometry:

Geometrical parameters of the 2-D model are chosen along the mean-radius line, $R(z)$ (Figure J-1). The cross-sectional area is $A(z)$, and the axial projection of the mean-radius blade chord is $c_z$. Also required by the model is the relative blade angle, $\beta_d(z)$, as measured along $R(z)$. Nondimensionalization parameters are kept the same as for the 3-D geometry, so that back-to-back stability comparisons will be possible.

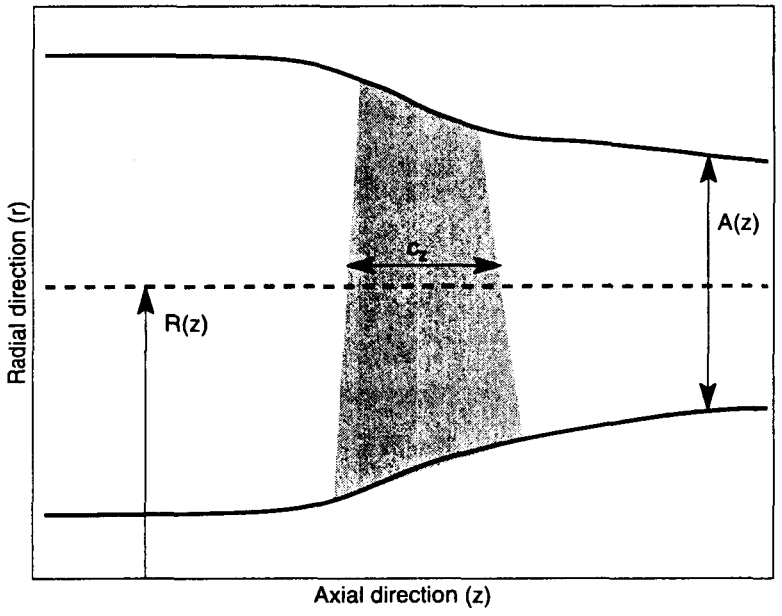


**Figure J-1:** Illustration of 2-D compressor model parameters.

### Inflow conditions:

The steady inflow conditions for the 2-D model are radial averages of the 3-D flows at the inlet plane. An area average is used for the axial velocity, $\bar{W}_0$, so that the value of flow coefficient is consistent. For all computations, the inlet tangential velocity is zero for both 3-D and 2-D models. The inlet pressure, $\bar{P}_0$, is back-calculated from a mass-average of the total pressure.

### Blade performance:

The overall steady loss and turning of each blade row is conserved between the 2-D and 3-D models. The loss is equal to the difference in mass-averaged rotary total pressure

(equation 6.7) across the 3-D blade row. Blade turning was kept the same by taking the 2-D blade row turning coefficient, $k$, as the value along the mean-radius.

Deriving the 2-D model parameters in this way guarantees that the overall pressure-rise characteristic will be the same as that produced by the 3-D calculations.

## J.2 Governing Equations

The governing equations of motion for three-dimensional flow (equations 6.1 and 6.2) can be written for two-dimensional flow along the mean-radius line. Outside of the blade rows, mass conservation and the changes in axial and tangential momentum are given by

$$\begin{aligned} \frac{1}{R}\frac{\partial V}{\partial \theta} + \frac{1}{A}\frac{\partial AW}{\partial z} &= 0 \\ \frac{\partial V}{\partial t} + \frac{V}{R}\frac{\partial V}{\partial \theta} + W\frac{\partial V}{\partial z} + \frac{1}{R}\frac{\partial P}{\partial \theta} &= 0 \\ \frac{\partial W}{\partial t} + \frac{V}{R}\frac{\partial W}{\partial \theta} + W\frac{\partial W}{\partial z} + \frac{\partial P}{\partial z} &= 0\,. \end{aligned} \tag{J.1}$$

Within the blade rows, the expressions are

$$\begin{aligned} \frac{1}{A}\frac{\partial AW}{\partial z} &= 0 \\ \frac{\partial V}{\partial t} + \Omega\frac{\partial V}{\partial \theta} + W\frac{\partial V}{\partial z} &= F_\theta \\ \frac{\partial W}{\partial t} + \Omega\frac{\partial W}{\partial \theta} + W\frac{\partial W}{\partial z} + \frac{\partial P}{\partial z} &= F_z\,, \end{aligned} \tag{J.2}$$

where $\Omega$ is 0 for a stator and 1 for a rotor. The axial body force is expressed in terms of the loss and turning body forces by

$$WF_z + (V - R\Omega)F_\theta + WF_L = 0\,. \tag{J.3}$$

Correlations for the body forces are identical to those developed for the three-dimensional model in equations (6.5) and (6.9):

$$F_\theta = kW\left[W\tan\beta_d - (V - R\Omega)\right] \tag{J.4}$$

$$F_L = \frac{1}{2c_z}\left[W^2 + (V - R\Omega)^2\right]\xi(\beta)\,. \tag{J.5}$$

Similarly to the 3-D analysis, an elliptical equation in pressure is desired for the linearized 2-D model. The governing equations for blade-free regions can be manipulated to obtain

$$\frac{1}{R^2}\frac{\partial^2 P}{\partial \theta^2} + \frac{\partial^2 P}{\partial z^2} + \frac{1}{A}\frac{dA}{dz}\frac{\partial P}{\partial z} + \frac{1}{R^2}\frac{\partial V^2}{\partial \theta} + \frac{\partial W^2}{\partial z} + \frac{2}{R}\frac{\partial W}{\partial \theta}\frac{\partial V}{\partial z} + \cdots$$
$$\cdots + \frac{1}{R^2}\frac{dR}{dz}\left(W\frac{\partial V}{\partial \theta} - V\frac{\partial W}{\partial \theta}\right) - W^2\frac{d}{dz}\left(\frac{1}{A}\frac{dA}{dz}\right) = 0\,. \tag{J.6}$$

The corresponding equation in the blade row regions is given by

$$\frac{\partial^2 P}{\partial z^2} + \frac{1}{A}\frac{dA}{dz}\frac{\partial P}{\partial z} + \frac{\partial W^2}{\partial z} - W^2\frac{d}{dz}\left(\frac{1}{A}\frac{dA}{dz}\right) - \frac{\partial F_z}{\partial z} - \frac{F_z}{A}\frac{dA}{dz} = 0\,. \tag{J.7}$$

## J.3 Steady Flow

The steady, axisymmetric 2-D compressor flow is required as input to the stability model. Rather than radially averaging an entire 3-D flow field, a more consistent solution is obtained by solving for the background flow satisfying the governing equations in the 2-D model.

Identical equations are obtained for steady, axisymmetric flow within the blade-free or blade row regions:

$$\begin{aligned} \frac{1}{A}\frac{dA\bar{W}}{dz} &= 0 \\ \bar{W}\frac{d\bar{V}}{dz} &= \bar{F}_\theta \\ \bar{W}\frac{d\bar{W}}{dz} + \frac{d\bar{P}}{dz} &= \bar{F}_z\,. \end{aligned} \tag{J.8}$$

These equations can be combined, along with the definition of $F_L$, to express changes in total pressure:

$$\frac{d\bar{P}_t}{dz} = R\Omega\frac{d\bar{V}}{dz} - \bar{F}_L\,. \tag{J.9}$$

Numerical solutions of these equations can be found from the inlet conditions by marching from node to node along the mean-radius line. Values at each node are defined by the subscript $j$, beginning with $j = 0$ at the inlet. The steady axial velocity is directly calculated

from mass conservation:

$$\bar{W}_j = \bar{W}_0 A_0 / A_j \ . \tag{J.10}$$

$\bar{V}(z)$ is computed by integrating the tangential body force:

$$\bar{V}_j = \bar{V}_{j-1} + \frac{1}{2}\left(\frac{\bar{F}_{\theta,j}}{\bar{W}_j} + \frac{\bar{F}_{\theta,j-1}}{\bar{W}_{j-1}}\right)(z_j - z_{j-1}) \ . \tag{J.11}$$

However, $\bar{F}_{\theta,j}$ implicitly depends on $\bar{V}_j$ through equation (J.4). Combining these equations leads to the value of $\bar{V}$ at node $j$:

$$\bar{V}_j = \frac{\bar{V}_{j-1} + \frac{1}{2}(z_j - z_{j-1})\left[k(\bar{W}_j \tan\beta_{d,j} + R_j\Omega) + \bar{F}_{\theta,j-1}/\bar{W}_{j-1}\right]}{1 + \frac{k}{2}(z_j - z_{j-1})} \ . \tag{J.12}$$

Once $\bar{W}_j$ and $\bar{V}_j$ are known, then so are $F_{\theta,j}$ and $F_{L,j}$. The total pressure is calculated by integrating the loss body force:

$$\bar{P}_{t,j} = \bar{P}_{t,j-1} + \Omega\frac{(R_j + R_{j-1})}{2}(\bar{V}_j - \bar{V}_{j-1}) - \frac{1}{2}(\bar{F}_{L,j} - \bar{F}_{L,j-1})(z_j - z_{j-1}) \ . \tag{J.13}$$

The final background flows passed to the stability analysis are computed by a two-step process:

1. 2-D flows are first calculated at many operating points using values of $\bar{F}_L$ based on averaged losses in the 3-D compressor flow. The losses are distributed in a fixed manner across the blade chord using the same shape factor, $f$, from the 3-D analysis (equation 6.8).

2. Loss coefficient correlations are found at every node within the blade rows. Each local $\xi(\beta)$ is calculated from equation (J.5) using the fixed $\bar{F}_L$ and computed velocities from the first step. Steady 2-D flow fields are then recalculated using these correlations instead of the fixed losses.

Completing this procedure ensures that a consistent set of body forces, velocities and body force derivatives are sent to the two-dimensional stability analysis. Derivatives of the body forces with respect to local velocity are calculated using equations (6.6) and (6.10).

## J.4 Linear, Unsteady Flow

The stability analysis calculates the behavior of linearized, unsteady two-dimensional perturbations superimposed on the background flow. Just as in the 3-D model, these perturbations can be expressed as a sum of independent modes with circumferential wavenumbers $n$ and temporal eigenvalue $\omega_n$:

$$v(\theta, z, t) = \mathcal{R}e\left\{ \sum_{n=-\infty}^{\infty} v_n(z) \mathrm{e}^{in\theta} \mathrm{e}^{i\omega_n t} \right\} . \tag{J.14}$$

Numerical computation of the mode shape is simplified in the 2-D case since numerical gridding is only required along the axial direction.

The governing equations for conservation of mass, axial and tangential momentum are linearized in both compressor regions. In the blade-free regions, the linearized equations can be combined in the following matrix form:

$$\begin{bmatrix} \bar{W} & 0 & 0 \\ 0 & \bar{W} & 1 \\ 0 & 1 & 0 \end{bmatrix} \frac{d}{dz} \begin{pmatrix} v_n \\ w_n \\ p_n \end{pmatrix} + \begin{bmatrix} i\omega_n + \frac{in\bar{V}}{R} & 0 & \frac{in}{R} \\ 0 & i\omega_n + \frac{in\bar{V}}{R} - \frac{\bar{W}}{A}\frac{dA}{dz} & 0 \\ \frac{in}{R} & \frac{1}{A}\frac{dA}{dz} & 0 \end{bmatrix} \begin{pmatrix} v_n \\ w_n \\ p_n \end{pmatrix} = 0 . \tag{J.15}$$

Within the blade rows the expressions are

$$\begin{bmatrix} \bar{W} & 0 & 0 & 0 & 0 \\ 0 & \bar{W} & 1 & 0 & 0 \\ 0 & 1 & 0 & 0 & 0 \end{bmatrix} \frac{d}{dz} \begin{pmatrix} v_n \\ w_n \\ p_n \\ f_{\theta,n} \\ f_{z,n} \end{pmatrix} + \cdots$$

$$\cdots + \begin{bmatrix} i\omega_n + in\Omega & \frac{\bar{F}_\theta}{\bar{W}} & 0 & -1 & 0 \\ 0 & i\omega_n + in\Omega - \frac{\bar{W}}{A}\frac{dA}{dz} & 0 & 0 & -1 \\ 0 & \frac{1}{A}\frac{dA}{dz} & 0 & 0 & 0 \end{bmatrix} \begin{pmatrix} v_n \\ w_n \\ p_n \\ f_{\theta,n} \\ f_{z,n} \end{pmatrix} = 0 . \tag{J.16}$$

Two more equations are required to completely determine the flow within the blade rows. The body force disturbances, $f_{\theta,n}$ and $f_{L,n}$, are assumed to behave according to the

same first-order lag conditions as in the 3-D model (equations 6.14 and 6.15). $f_{L,n}$ is related to $f_{z,n}$ through the linearized form of equation (J.3):

$$-\bar{W} f_{z,n} = \bar{W} f_{L,n} + (\bar{V} - R\Omega) f_{\theta,n} + \bar{F}_\theta v_n + (\bar{F}_z + \bar{F}_L) w_n \ . \tag{J.17}$$

The final form for the remaining two equations in the blade rows are

$$(1 + i\omega_n \tau_\delta + in\Omega\tau_\delta) f_{\theta,n} \ = \ \frac{\partial F_\theta}{\partial W} w_n + \frac{\partial F_\theta}{\partial V} v_n \tag{J.18}$$

and

$$\left\{ [(i\omega_n + in\Omega)\tau_L + 1] \frac{\bar{F}_\theta}{\bar{W}} + \frac{\partial F_L}{\partial V} \right\} v_n + \left\{ [(i\omega_n + in\Omega)\tau_L + 1] \frac{\bar{F}_z + \bar{F}_L}{\bar{W}} + \frac{\partial F_L}{\partial W} \right\} w_n + \cdots$$
$$\cdots + [(i\omega_n + in\Omega)\tau_L + 1] f_{z,n} + \left( \frac{\bar{V} - r\Omega}{\bar{W}} \right) [(i\omega_n + in\Omega)\tau_L + 1] f_{\theta,n} \ = \ 0 \ . \tag{J.19}$$

Similarly to the 3-D model, pressure perturbations are more accurately computed by elliptical equations in $p$. Linearized forms of equations (J.6) and (J.7) are used in lieu of the continuity equation in the interior nodes of the grid. Outside of the blade rows, the appropriate equation is given by

$$\frac{d^2 p_n}{dz^2} - \frac{n^2 p_n}{R^2} + \frac{1}{A}\frac{dA}{dz}\frac{dp_n}{dz} - 2\frac{\bar{W}}{A}\frac{dA}{dz}\frac{dw_n}{dz} - 2\bar{W}\frac{d}{dz}\left(\frac{1}{A}\frac{dA}{dz}\right) w_n + \frac{in}{R^2}\frac{dR}{dz}(\bar{W} v_n - \bar{V} w_n) = 0 \, , \tag{J.20}$$

and within the blade rows,

$$\frac{d^2 p_n}{dz^2} + \frac{1}{A}\frac{dA}{dz}\frac{dp_n}{dz} - 2\frac{\bar{W}}{A}\frac{dA}{dz}\frac{dw_n}{dz} - 2\bar{W}\frac{d}{dz}\left(\frac{1}{A}\frac{dA}{dz}\right) w_n - \frac{1}{A}\frac{dA}{dz} f_{z,n} - \frac{df_{z,n}}{dz} = 0 \ . \tag{J.21}$$

Boundary conditions are identical to those in the 3-D stability model. Far upstream of the compressor, where the compressor geometry is axially uniform, the pressure perturbations will behave as $\exp(+nz)$. Far downstream, they decay as $\exp(-nz)$. Also, vortical disturbances are assumed to be generated only by the blade rows, and not convect into the

compressor. These conditions are expressed as

$$\begin{aligned} \text{far upstream:} \quad & \frac{dp_n}{dz} = n\, p_n \\ & \frac{dv_n}{dz} - \frac{in}{R} w_n = 0 \\ \text{far downstream:} \quad & \frac{dp_n}{dz} = -n\, p_n \ . \end{aligned} \tag{J.22}$$

Finally, to suppress spurious, numerical sources of mass, the third equation at the inlet plane must be the linearized form of mass continuity. This is required for analyses that use elliptical pressure equations rather than enforcing continuity throughout [57].

Numerical solutions for the eigenvalues and mode shapes are performed identically to the three-dimensional analysis (Section 6.4.1). The system of linearized equations are discretized at every node in the grid, and combined in the same matrix form as equation (6.22). Solutions are found by using packaged direct eigenvalue solvers, such as those provided by MATLAB [50].

# APPENDIX K

# STABILITY CRITERIA BASED ON ENERGY ARGUMENTS

Approximate stability criteria used in Section 7.2.3 for quasi-2D modes in general flows are developed in this appendix. The criteria are based on the conservation of disturbance energy in the annuli surrounding the compressor, with specific approximations for the quasi-2D mode shapes calculated using the body force compressor model in Chapter 7. The *Weighted Integrated Mean Slope* criterion, appropriate for circumferential flow distortions, is shown to be a specific example of the general three-dimensional stability criteria.

## K.1 Exact Stability Criterion

The vector form of the linearized momentum equation within the blade free regions is given by

$$\frac{\partial \vec{v}}{\partial t} + (\vec{v} \cdot \nabla)\vec{V} + (\vec{V} \cdot \nabla)\vec{v} + \nabla p = 0 \,. \tag{K.1}$$

Take the dot product of $\vec{v}$ with this equation. Using continuity, ($\nabla \cdot \vec{v} = \nabla \cdot \vec{V} = 0$), each term can be simplified as:

$$\begin{aligned} \vec{v} \cdot \frac{\partial \vec{v}}{\partial t} &= \frac{\partial}{\partial t}\left(\frac{\|\vec{v}\|^2}{2}\right) \\ \vec{v} \cdot (\vec{V} \cdot \nabla)\vec{v} &= \frac{1}{2}\nabla \cdot (\|\vec{v}\|^2 \vec{V}) \\ \vec{v} \cdot \nabla p &= \nabla \cdot (p\vec{v}) \,. \end{aligned}$$

The equation can then be written as

$$\frac{\partial}{\partial t}\left(\frac{\|\vec{v}\|^2}{2}\right) + \nabla \cdot \left(\frac{\|\vec{v}\|^2}{2}\vec{\vec{V}} + p\vec{v}\right) = -\vec{v} \cdot (\vec{v} \cdot \nabla)\vec{\vec{V}} \; . \tag{K.2}$$

Integrate (K.2) through a volume $\mathcal{V}$, enclosed by the surface $\mathcal{S}$, applying Gauss' Divergence Theorem to the second term:

$$\frac{\partial}{\partial t}\int_{\mathcal{V}} \frac{\|\vec{v}\|^2}{2}\, d\mathcal{V} + \int_{\mathcal{S}} \left[\frac{\|\vec{v}\|^2}{2}\vec{\vec{V}} + p\vec{v}\right] \cdot d\mathcal{S} = -\int_{\mathcal{V}} \vec{v} \cdot (\vec{v} \cdot \nabla)\vec{\vec{V}}\, d\mathcal{V} \; . \tag{K.3}$$

Equation (K.3) is the incompressible form of the "Disturbance-Energy Corollary" derived by Fréchette [18] except for the addition of the right-hand side term. This term is generally non-zero for nonuniform background flows. Although none of the terms in equation (K.3) are actually equal to the disturbance energy in the flow, they do represent useful second-order energy-like quantities related to the amplitude of the flow perturbation. In fact, Myers [55] proved that this equation is a *complete* representation of the conservation law on total fluid energy to second-order (for the case of incompressible, inviscid flow) despite containing only first order perturbation terms. Even for arbitrary disturbances in arbitrary flow fields, second order flow perturbation terms only affect the conservation law on total energy at orders $\delta^3$ and higher.

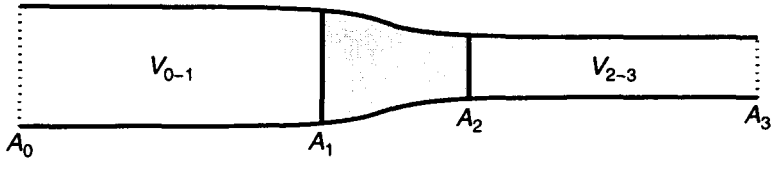


**Figure K-1:** Definitions of annuli volumes and cross-sectional areas.

The usefulness of equation (K.3) is found by summing the integrals upstream and downstream of the compressor, using the notation in Figure K-1. The surface integrals along the inner and outer walls (where $\vec{v} \perp d\mathcal{S}$) are zero. Also, the planes at stations (0) through (3) are taken to be perpendicular to the axial direction. Therefore, $\vec{V} \cdot d\mathcal{S} = W\, d\mathcal{A}$, where $\mathcal{A}$ is the area of the plane. So, applying equation (K.3) in regions 0–1 and 2–3, and summing the results yields:

$$\frac{\partial}{\partial t}(E_{0-1} + E_{2-3}) = (F_1 - F_0) + (F_3 - F_2) - (Q_{0-1} + Q_{2-3}) \, , \tag{K.4}$$

where

$$
\begin{aligned}
E &= \int_{\mathcal{V}} \frac{\|\vec{v}\|^2}{2}\, d\mathcal{V} \\
F &= \int_{\mathcal{A}} \left[ \frac{\|\vec{v}\|^2}{2} \bar{W} + pw \right] d\mathcal{A} \\
Q &= \int_{\mathcal{V}} \vec{v} \cdot (\vec{v} \cdot \nabla) \vec{\bar{V}}\, d\mathcal{V} \, .
\end{aligned}
$$

Therefore the rate of change of the kinetic energy-like term, $E$, in the upstream and downstream ducts is equal to the difference in the fluxes, $F$, across the axial planes bounding the ducts, minus the terms $Q$, caused by the interaction of the nonuniform mean flow and the linearized flow disturbances. A method is shown in Appendix L to evaluate the area integrals of the products of first-order terms (such $pw$) based on their mode shapes.

Simplifications can be made to equation (K.4) by noting that $F_0 = 0$ because all perturbations are identically zero at the far-upstream inlet plane. Similarly, at the exit of the compression system, $F_3$ can be simplified using $p_3 = 0$.

At neutral stability, the magnitude of the disturbance will not change, and so the time derivatives of $E_{0-1}$ and $E_{2-3}$ must be identically zero. Therefore, the following relation represents the general stability criterion for any disturbance mode:

$$
\int_{\mathcal{A}_2} \left[ \frac{\|\vec{v}\|^2}{2} \bar{W} + pw \right] d\mathcal{A}_2 - \int_{\mathcal{A}_1} \left[ \frac{\|\vec{v}\|^2}{2} \bar{W} + pw \right] d\mathcal{A}_1 - \int_{\mathcal{A}_3} \frac{\|\vec{v}\|^2}{2} \bar{W}\, d\mathcal{A}_3 = -(Q_{0-1} + Q_{2-3}) \, . \tag{K.5}
$$

## K.2 Approximations for Quasi-2D Modes

Equation (K.5) can be further simplified for the case of quasi-2D disturbances at neutral stability using three approximations. These approximations are justified based on observations of mode shapes calculated by the body force compressor model in Chapter 7.

1. In the downstream duct, the flux of $\|\vec{v}\|^2$ at neutral stability was approximately equal across planes 2 and 3. Specifically, at neutral stability,

$$
\int_{\mathcal{A}_2} \frac{\|\vec{v}\|^2}{2} \bar{W}\, d\mathcal{A}_2 \approx \int_{\mathcal{A}_3} \frac{\|\vec{v}\|^2}{2} \bar{W}\, d\mathcal{A}_3 \, . \tag{K.6}
$$

Equation (K.6) is exactly true for the $(n, 0)$ modes in uniform background flow where the flow angle at the exit of the compressor is specified. This can be proven by substituting the analytic mode shapes in the downstream duct found in Appendix E.3. For the general case of nonuniform flows, equation (K.6) is still approximately true at neutral stability, as shown by the example in Figure K-2a for parametric study P.

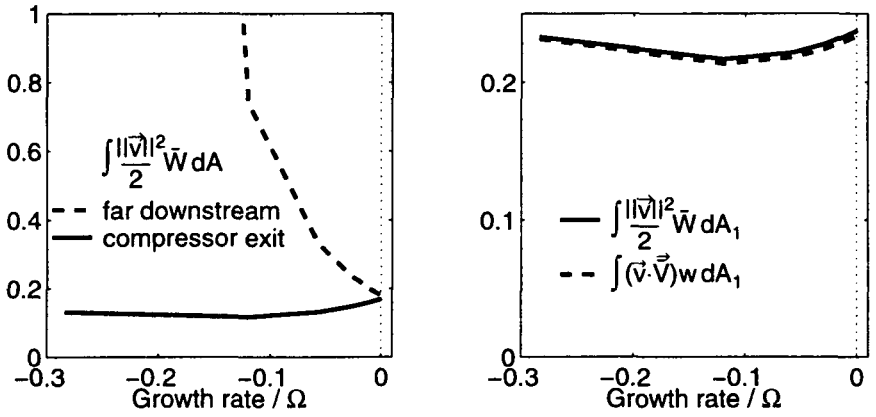


(a) Approximation 1.

(b) Approximation 2.

**Figure K-2:** Assessment of approximations (1) and (2) using results for the mode shape and growth rate of the (1,0) mode in parametric study P.

2. At the inlet to the compressor, station (1), the following approximations are valid:

$$\int_{\mathcal{A}_1} \|\vec{v}\|^2 \bar{W} \, d\mathcal{A}_1 \approx 2 \int_{\mathcal{A}_1} w^2 \bar{W} \, d\mathcal{A}_1 \approx 2 \int_{\mathcal{A}_1} w(\vec{v} \cdot \vec{\bar{V}}) \, d\mathcal{A}_1 \, . \tag{K.7}$$

Again, these are exactly true for two-dimensional analyses, for which, upstream of the compressor, $u = \bar{U} = 0$, $\bar{V} = 0$, and $v = iw$. For the quasi-2D modes in three-dimensional flow, the approximations are good. For the case of study P (Figure K-2b) the difference between approximations is less than 2%.

By making this approximation, $F_1$ can be expressed in terms of the total pressure perturbation at the inlet to the compressor:

$$F_1 = \int_{\mathcal{A}_1} \left[ \frac{\|\vec{v}\|^2}{2} \bar{W} + pw \right] d\mathcal{A}_1 \approx \int_{\mathcal{A}_1} (p + \vec{v} \cdot \vec{\bar{V}}) w \, d\mathcal{A}_1 = \int_{\mathcal{A}_1} p_t w \, d\mathcal{A}_1 \, . \tag{K.8}$$

3. Assume that the terms $Q_{0-1}$ and $Q_{2-3}$ are negligible compared to the differences in fluxes in equation (K.5) at neutral stability. Clearly in uniform background flow this

must be true since $Q_{0-1} = Q_{2-3} = 0$. In nonuniform flow, the approximation will be assessed by assuming it is true, then examining the validity of the resulting relation.

The net effect of these approximations is to reduce the exact equation (K.5) into the following form, valid only at neutral stability:

$$\int_{\mathcal{A}_2} pw \, d\mathcal{A}_2 - \int_{\mathcal{A}_1} p_t w \, d\mathcal{A}_1 = 0 \; . \tag{K.9}$$

Equation (K.9) represents the simplified stability criterion for quasi-2D modes in a nonuniform flow field.

The validity of the above stability criterion is demonstrated for compressor configuration P in Figure K-3. The left-hand-side of equation (K.9) is calculated for operating points approaching stall based on the (1,0) mode shape normalized by the maximum axial velocity at the rotor inlet. This normalization was chosen, because for two-dimensional flow, it would result in the integrand equaling the slope of the overall characteristic (shown below). The value of the integral in (K.9) does nearly pass through 0 as the compressor reaches neutral stability, and this stability criterion is over 6 times closer than using the overall slope.

## K.3 Relation to Compressor Performance

The approximated form of the conservation of total-energy law (K.9) is more useful than the exact equation (K.5) because it only involves differences in the pressure and velocity disturbances across the compressor, which can be related to the compressor performance.

### Comparison to Previous Stability Criteria

For the specific example of purely two-dimensional flow, this relation simplifies to a familiar form. Assume the duct area is constant ($\mathcal{A}_1 = \mathcal{A}_2$), and the axial velocity remains constant through the compressor ($w_1 = w_2$). Then equation (K.9) reduces to:

$$\int_0^{2\pi} (p_2 - p_{t1}) \, w \, d\theta = 0 \; . \tag{K.10}$$

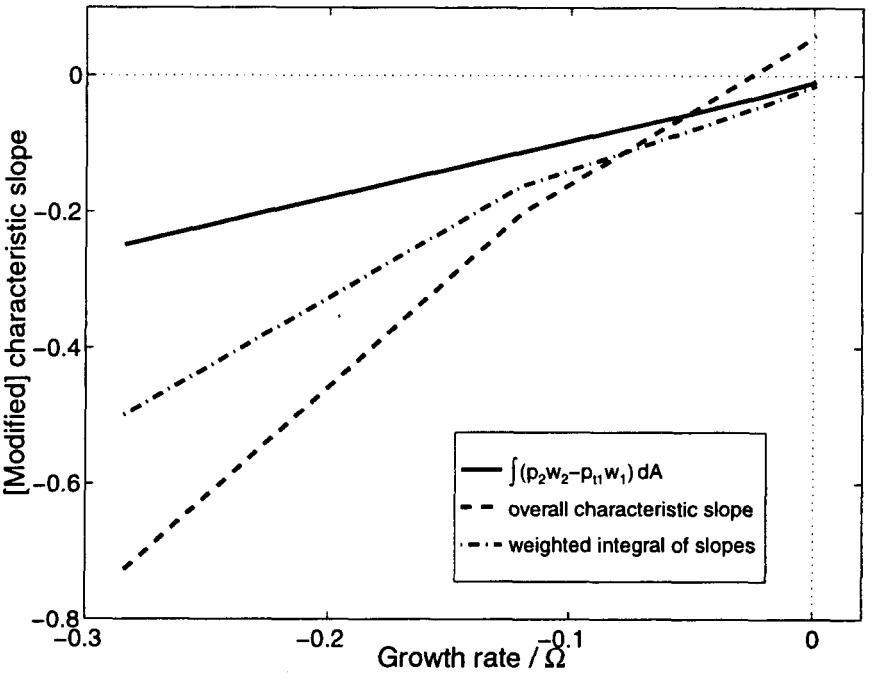


**Figure K-3:** Comparison of values of three stability criteria for (1,0) mode approaching stall for study P. Solid line is for general stability criterion, equation (K.9); dotted line is for sum of weighted slopes across all individual blade rows, equation (K.14)

This is exactly the stability criterion proposed by Gysling [31], but developed here from first principles.

Continue by substituting for the linearized pressure-rise matching condition (without swirl-sensitivity and unsteady losses): $p_2 - p_{t1} = \frac{d\Psi}{dW} w - \lambda \frac{\partial w}{\partial \theta} - \mu \frac{\partial w}{\partial t}$. By Appendix L, terms of $p_2 - p_{t1}$ that are 90° out-of-phase with $w$ will not contribute to the integral in (K.10), which leaves only

$$\int_0^{2\pi} \frac{d\Psi}{dW} w^2 \, d\theta = 0 \, . \tag{K.11}$$

This is exactly the *Weighted Integrated Mean Slope* stability criteria first proposed for circumferentially nonuniform two-dimensional flow fields in Chapter 3. Therefore, the circumferentially weighted slope criteria is simply a two-dimensional case of the general stability criterion (K.9) for three-dimensional flows.

### Relation to slopes of blade row characteristics

The general stability criterion in (K.9) would be more useful if it could be written in terms of the compressor slope, analogously to equation (K.11) for two-dimensional flow. Unfortunately, three-dimensional flow disturbances are not uniform through the blade rows. The axial velocity perturbations from the quasi-2D modes vary in the axial direction, which can be seen in Appendix M by comparing the mode shapes at the compressor inlet and exit planes. However, an approximation can be made by representing the overall pressure rise as a sum of jumps across each blade row, where the change in axial velocity is not as large. To simplify the following expressions, the compressor annulus was assumed to have uniform area.

The total-to-static pressure rise in equation (K.9) can be approximated with the total-static pressure rise across the first blade row, and the static-static pressure rise across subsequent blade rows. The expression is vastly simplified by considering here only uniform area annuli.

$$\int_{\mathcal{A}} (p_2 w_2 - p_{t1} w_1)\, d\mathcal{A} \approx \int_{\mathcal{A}} \Big\{ [(p_{out} - p_{t,in}) w_{in}]_{\text{blade 1}} + [(p_{out} - p_{in}) w_{in}]_{\text{blade 2}} + \cdots \\ \cdots + [(p_{out} - p_{in}) w_{in}]_{\text{blade N}} \Big\}\, d\mathcal{A} \,. \tag{K.12}$$

In the body force model, the pressure rise actually depends on the distribution of $\vec{F}$. However, across each radial strip of a blade row, the pressure rise for quasi-2D modes should be similar to that obtained by 2-D theory, namely:

$$\Delta p \approx \left( -i[\omega + n\Omega]\mu + \frac{\partial \Psi_{SS}}{\partial W} \right) w_{in} + \frac{\partial \Psi_{SS}}{\partial V} v_{in} \,. \tag{K.13}$$

The parameters $\mu$ and $\Omega$ refer to properties of the individual blade row only, and $\frac{\partial \Psi_{SS}}{\partial V}$ and $\frac{\partial \Psi_{SS}}{\partial W}$ are the slopes of the static-to-static pressure rise characteristic of that blade row. The general stability criteria can then be approximated as

$$\int_{\mathcal{A}} \left\{ \left[ \left( \frac{\partial \Psi_{TS}}{\partial W} w_{in} + \frac{\partial \Psi_{TS}}{\partial V} v_{in} \right) w_{in} \right]_{\text{blade 1}} + \sum_{k=2}^{N} \left[ \left( \frac{\partial \Psi_{SS}}{\partial W} w_{in} + \frac{\partial \Psi_{SS}}{\partial V} v_{in} \right) w_{in} \right]_{\text{blade k}} \right\} = 0 \tag{K.14}$$

For the example case of compressor configuration P, this approximated criterion also pro-

vides a relatively accurate depiction of the stall point, as seen by the third line in Figure K-3.

The purpose behind deriving equation (K.14) was simply to demonstrate that the stall point for quasi-2D modes is given by the integral of the blade row characteristic's slopes around the annulus, weighted by the mode shape. This criteria is essentially the same as for flows with circumferential nonuniformities in Chapter 3, but with two main differences:

1. The balance between positive and negative characteristic slope is along the radial rather than circumferential direction.

2. The pressure rise across each blade is individually accounted for because the axial velocity disturbance varies through the compressor.

It should be noted that *none* of these forms of stability criteria for quasi-2D modes can directly be used for stall prediction. Knowledge of the radial and axial variations of the stall mode are still required for weighting the slopes in equation (K.14); and both the exact stability criterion (K.5) and approximate criterion (K.9) are expressed solely in terms of the mode shape. However, they do provide an understanding of the balance that must be met for the compressor to become unstable. Useful implications of these energy-based stability criteria are discussed in Section 7.2.3.

## K.4 Difficulties with Energy Method for Higher-Order 3-D Modes

The energy conservation method used for quasi-2D modes does not yield a simple balance between the disturbances at the inlet and exit of the compressor for higher-order 3-D modes. The difficulty is that the first approximation made to simplify equation (K.5) is invalid: the terms $F_2$ and $F_3$ are not similar, and so do not cancel. Even in uniform background flow, Equation (K.6) can only reduce to

$$\int_{\mathcal{A}} (p_2 w_2 - p_{t1} w_1)\, d\mathcal{A} = \frac{1}{2} \int_{\mathcal{A}} \left( \|\vec{v}_3\|^2 \bar{W}_3 - \|\vec{v}_2\|^2 \bar{W}_2 \right) d\mathcal{A}\,. \tag{K.15}$$

From the analytic form of the $(n, j)$ mode shape at neutral stability, calculated in Appendix E.1.1 for rectilinear ducts, the following relation holds:

$$\frac{\int_{\mathcal{A}_3} \|\vec{v}_3\|^2 \bar{W}_3 \, d\mathcal{A}_3}{\int_{\mathcal{A}_2} \|\vec{v}_2\|^2 \bar{W}_2 \, d\mathcal{A}_2} = \frac{4k_j^2 + n^2}{2k_j^2 + n^2}, \quad \text{where } k_j = \frac{\pi j}{1 - r_h} \,. \tag{K.16}$$

The above ratio of integrals is equal to one for 2-D modes, but is between one and two for higher-order radial modes. Therefore, the right-hand-side of equation (K.15) is zero only for 2-D modes. For 3-D modes at neutral stability, the left-hand-side of equation (K.15) must be positive to balance the right-hand-side, meaning the compressor must be operating at a more positive slope than for 2-D modes. This is the energy-based argument for why 3-D modes are more stable than 2-D modes. More importantly, it demonstrates that there are residual terms to the stability criterion (K.9) which cannot be related to the compressor performance. Although the general conservation of energy law (K.5) is always valid, a method has yet to be found that reduces it into a more useful stability criterion applicable for higher-order three-dimensional modes.

## K.5 Accuracy of IMS Condition Based on WIMS Condition

This section demonstrates that the accuracy of the IMS stability criterion for steady distorted flow [43] is merely a consequence of the more general WIMS condition. This statement was first proposed in Section 3.4.3.

Consider the following example of sinusoidal slope and mode amplitude variations that are induced by an offset, whirling shaft at stall (Figure K-4). In the relative frame of the

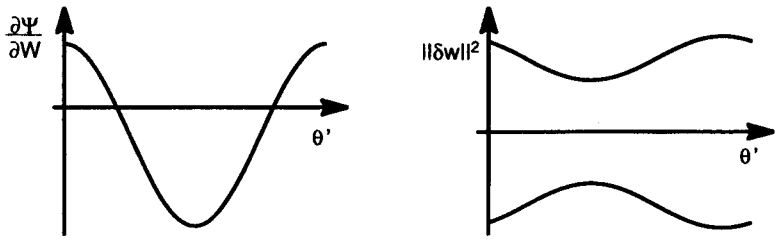


**Figure K-4:** Illustration of slope and mode amplitude variation around the annulus in the relative frame of the rotating clearance asymmetry.

rotating clearance asymmetry, the slope variation is defined as $\frac{d\Psi}{dW} = A + B\cos\theta'$, and the square of the mode amplitude variation is $||w||^2 = C + D\cos(\theta' + \phi)$ for some constants

$A, B, C, D$ and $\phi$. The time-averaged disturbance flow energy production (equation 3.6) is then

$$\begin{aligned}\overline{\delta E} &= \frac{1}{4\pi}\int_0^{2\pi}\frac{d\Psi}{dW}\,||w||^2\,d\theta' \\ &= \frac{1}{4\pi}\int_0^{2\pi}(A+B\cos\theta')(C+D\cos(\theta'+\phi))\;d\theta' \\ &= \frac{AC}{2}+\frac{BD}{4}\cos\phi. \end{aligned} \tag{K.17}$$

According to the WIMS condition, at neutral stability the above quantity must be zero. However, the integrated mean slope is identically $A$. Therefore, the solution for the integrated mean slope at neutral stability is

$$\text{IMS}_{\text{stall}} = -\frac{BD}{2C}\cos\phi\,. \tag{K.18}$$

The integrated mean slope at stall is identically zero when $\phi = \pm 90°$, irregardless of the size of the slope or mode envelope nonuniformities. Conditions when the slope and mode shape variations were 90 degrees out of phase were found for tip clearance asymmetries that were rotating at frequencies away from the rotating stall frequency. Specifically, this condition was approximately satisfied for stationary mean flow nonuniformities (Figure 3-26). Therefore, the IMS=0 stall point condition for steady background flow nonuniformities is merely a simplification of the WIMS=0 criterion for the case when the slope variation is in quadrature with the mode amplitude modulation.

# APPENDIX L

# PRODUCTS OF LINEARIZED FLOW QUANTITIES

Integrals of the products of linearized flow quantities, used in the compressor stability criteria derived in Section 7.2.3, are evaluated in this appendix. All such integrals are of the form:

$$I = \int_{\mathcal{A}} pw \, d\mathcal{A} \tag{L.1}$$

where $w$ and $p$ are linearized, three-dimensional flow perturbations, and $\mathcal{A}$ is the cross-sectional area of the compressor annulus at a fixed axial position. The area integral can be expressed in terms of $r$ and $\theta$:

$$I = \int_{r_h}^{r_t} r \left\{ \int_0^{2\pi} pw \, d\theta \right\} dr \, . \tag{L.2}$$

Recall that the each mode shape for $p$ and $w$ are of the form (from equation 6.11):

$$p(r, \theta, z, t) = \mathcal{R}e \left\{ p_n(r, z) e^{in\theta} e^{i\omega t} \right\} , \tag{L.3}$$

where $p_n$ is a complex valued quantity. To multiply linearized quantities, they must be represented in real form. Therefore, rewrite $w$ and $p$ in the form:

$$p(r, \theta, z, t) = p_r(r, z) \cos(n\theta + \omega t) - p_i(r, z) \sin(n\theta + \omega t) \, , \tag{L.4}$$

where $p_r$ and $p_i$ represent the real and imaginary components, respectively, of $p_n$. Then the inner integral of equation (L.1) is given by:

$$\begin{aligned}\int_0^{2\pi} pw\,d\theta &= \int_0^{2\pi} [p_r\cos(n\theta+\omega t) - p_i\sin(n\theta+\omega t)]\,[w_r\cos(n\theta+\omega t) - w_i\sin(n\theta+\omega t)]\,d\theta \\ &= \int_0^{2\pi} \Big[p_r w_r\cos^2(n\theta+\omega t) + p_i w_i\sin^2(n\theta+\omega t) - \cdots \\ &\qquad \cdots - (p_r w_i + p_i w_r)\cos(n\theta+\omega t)\sin(n\theta+\omega t)\Big]\,d\theta \\ &= \pi(p_r w_r + p_i w_i) \qquad \text{(L.5)}\end{aligned}$$

The physical meaning of this integral can be understood by looking at the phasers of $w_n$ and $p_n$ in the complex plane (Figure L-1). Then equation (L.5) can be written as

$$\begin{aligned}\int_0^{2\pi} pw\,d\theta &= \pi(\|p_n\|\cos\angle p\,\|w_n\|\cos\angle w + \|p_n\|\sin\angle p\,\|w_n\|\sin\angle w) \\ &= \pi\,\|p_n\|\,\|w_n\|\cos(\angle p - \angle w)\ . \qquad \text{(L.6)}\end{aligned}$$

The original integral is then given by:

$$\int_{\mathcal{A}} pw\,d\mathcal{A} = \pi\int_{r_h}^{r_t} \|p_n\|\,\|w_n\|\cos(\angle p - \angle w)\,r\,dr\ . \qquad \text{(L.7)}$$

The integrand is the product of the amplitudes of $p_n$ and $w_n$ times the inner phase angle. An important example is when $p_n$ is out-of-phase with $w_n$, for which $I$ is identically zero.

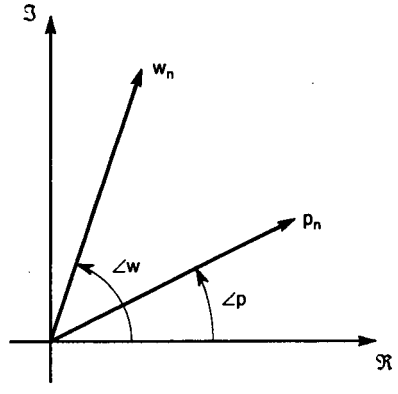


**Figure L-1:** Phasers of $w_n$ and $p_n$ in the complex plane.

# APPENDIX M

# RESULTS FROM PARAMETRIC STUDIES USING 3-D BODY FORCE MODEL

The first section of this appendix contains an exact description of the parameters used to calculate the flow fields for the 18 parametric studies in Chapter 6. The second section provides plots of the results of the steady and unsteady compressor models for each parametric study.

## M.1 Information on Each Configuration

To initiate calculations with the steady body force compressor model (Section 6.2), the following parameters are required:

- Meridional geometry (hub-to-tip ratio, number of blades, gap lengths, etc.)
- Blade geometry for flow turning (inlet and exit blade angles, turning coefficient $k(r)$)
- Blade losses correlated to the mean flow coefficient.

Description of these parameters are provided for each compressor configuration used in the parametric study. For the blade angles and $k(r)$, values at the hub, mid-span and tip are provided (angles are in the frame relative to the blade); all intermediate values are determined by a second-order polynomial fit across the span. Similarly, the values of nondimensional losses are provided at the mid-span location only as a function of the indicated flow coefficient (measured far-upstream). Mid-span losses for other operating conditions

are calculated by a second-order polynomial interpolation. The radial distribution of loss is determined from the mid-span value using a parabolic fit through the provided hub:mid-span:tip ratios. For every blade row the shape factor for the loss body force was given by $f = 2.4s^2 - 4.8s + 2.6$, where $s \in \{0, 1\}$ is the normalized distance across the blade chord in the meridional plane.

## Configuration (A) – Single-Stage Baseline

Compressor geometry: Casing $r_t = 1$, $r_h = 0.7$. Far-field boundaries at $z = -4, 4$. Rotor inlet/exit at $z = 0$, 0.1601, stator inlet/exit at $z = 0.2051$, 0.4397.

Blade row turning:

| | Rotor | | Stator | |
|---|---|---|---|---|
| | $\beta_{in}$ | $\beta_{out}$ | $\beta_{in}$ | $\beta_{out}$ |
| hub | -51° | -25° | 39° | 3.5° |
| mid | -56° | -43° | 36° | 3.0° |
| tip | -62° | -53° | 34.5° | 2.5° |

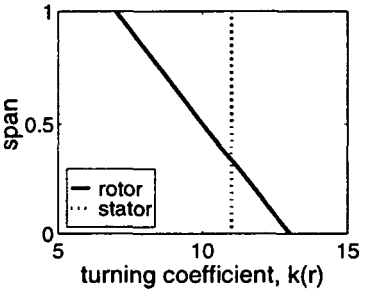


Blade row losses:

| Flow coefficient | 0.375 | 0.450 | 0.600 |
|---|---|---|---|
| Rotor loss (mid-span) | 0.0035 | 0.033 | 0.080 |
| Stator loss (mid-span) | 0.015 | 0.0075 | 0.018 |

| | hub | mid | tip |
|---|---|---|---|
| Rotor loss ratio | 1 | 1.75 | 4 |
| Stator loss ratio | 1 | 1.5 | 2 |

## Configuration (B) – Maximum Rotor Loss Variation

Compressor geometry and blade row turning: same as configuration (A).

Blade row losses:

| Flow coefficient | 0.375 | 0.450 | 0.600 |
|---|---|---|---|
| Rotor loss (mid-span) | 0.0035 | 0.033 | 0.080 |
| Stator loss (mid-span) | 0.015 | 0.0075 | 0.018 |

| | hub | mid | tip |
|---|---|---|---|
| Rotor loss ratio | 1 | 2.75 | 8 |
| Stator loss ratio | 1 | 1.5 | 2 |

## Configuration (C) – Radially Uniform Rotor Loss

Compressor geometry and blade row turning: same as configuration (A).

Blade row losses:

| Flow coefficient | 0.375 | 0.450 | 0.600 |
|---|---|---|---|
| Rotor loss (mid-span) | 0.0035 | 0.033 | 0.080 |
| Stator loss (mid-span) | 0.015 | 0.0075 | 0.018 |

| | hub | mid | tip |
|---|---|---|---|
| Rotor loss ratio | 1 | 1 | 1 |
| Stator loss ratio | 1 | 1.5 | 2 |

## Configuration (D) – Radially Uniform Rotor and Stator Loss

Compressor geometry and blade row turning: same as configuration (A).

Blade row losses:

| Flow coefficient | 0.375 | 0.450 | 0.600 |
|---|---|---|---|
| Rotor loss (mid-span) | 0.0035 | 0.033 | 0.080 |
| Stator loss (mid-span) | 0.015 | 0.0075 | 0.018 |

| | hub | mid | tip |
|---|---|---|---|
| Rotor loss ratio | 1 | 1 | 1 |
| Stator loss ratio | 1 | 1 | 1 |

## Configuration (G) – Maximum Rotor Exit Angle Variation

Compressor geometry and blade row losses: same as configuration (A).

Blade row turning:

| | Rotor | | Stator | |
|---|---|---|---|---|
| | $\beta_{in}$ | $\beta_{out}$ | $\beta_{in}$ | $\beta_{out}$ |
| hub | -51° | -23° | 39° | 3.5° |
| mid | -56° | -43° | 36° | 3.0° |
| tip | -62° | -73° | 34.5° | 2.5° |

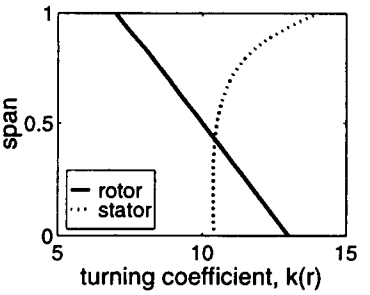


## Configuration (H) – Radially Uniform Rotor Exit Angle

Compressor geometry and blade row losses: same as configuration (A).

Blade row turning:

| | Rotor | | Stator | |
|---|---|---|---|---|
| | $\beta_{in}$ | $\beta_{out}$ | $\beta_{in}$ | $\beta_{out}$ |
| hub | -51° | -43° | 39° | 3.5° |
| mid | -56° | -43° | 36° | 3.0° |
| tip | -62° | -43° | 34.5° | 2.5° |

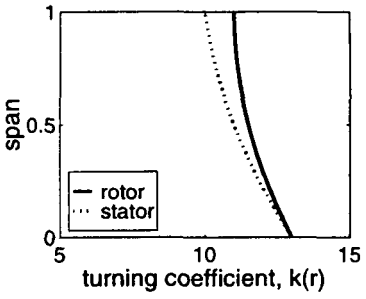


## Configuration (J) – Maximum Stator Exit Angle Variation

Compressor geometry and blade row losses: same as configuration (A).

Blade row turning:

| | Rotor | | Stator | |
|---|---|---|---|---|
| | $\beta_{in}$ | $\beta_{out}$ | $\beta_{in}$ | $\beta_{out}$ |
| hub | -51° | -25° | 39° | -5° |
| mid | -56° | -43° | 36° | 3° |
| tip | -62° | -53° | 34.5° | 15° |

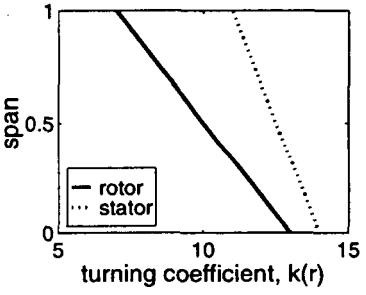


## Configuration (K) – Maximum Hub-to-Tip Ratio

Compressor geometry: Casing $r_t = 1$, $r_h = 0.9$. Far-field boundaries at $z = -4, 4$. Rotor inlet/exit at $z = 0$, 0.1606, stator inlet/exit at $z = 0.2056$, 0.4405.

Blade row turning:

| | Rotor | | Stator | |
|---|---|---|---|---|
| | $\beta_{in}$ | $\beta_{out}$ | $\beta_{in}$ | $\beta_{out}$ |
| hub | -54.2° | -37.9° | 36.8° | 3.2° |
| mid | -56° | -43° | 36° | 3° |
| tip | -57.9° | -47.2° | 35.3° | 2.8° |

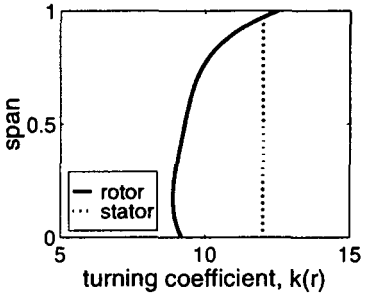


Blade row losses: same function of span as configuration (A).

## Configuration (L) – Minimum Hub-to-Tip Ratio

Compressor geometry: Casing $r_t = 1$, $r_h = 0.35$. Far-field boundaries at $z = -4, 4$. Rotor inlet/exit at $z = 0$, 0.12, stator inlet/exit at $z = 0.1659$, 0.3933.

Blade row turning:

| | Rotor | | Stator | |
|---|---|---|---|---|
| | $\beta_{in}$ | $\beta_{out}$ | $\beta_{in}$ | $\beta_{out}$ |
| hub | -48.3° | -12.9° | 40.3° | 3.8° |
| mid | -57° | -42.9° | 36.2° | 3° |
| tip | -72.2° | -69.2° | 30.0° | 0.1° |

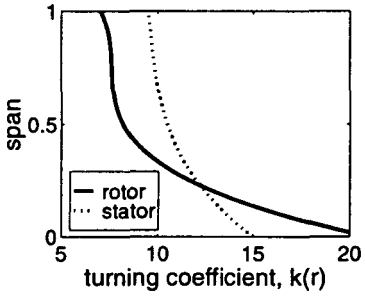


Blade row losses: same function of span as configuration (A).

## Configuration (P) – Minimum Gap Length

Compressor geometry: Same as configuration (A), except gap length decreased. Rotor inlet/exit at $z = 0$, 0.1601, stator inlet/exit at $z = 0.1821$, 0.4167.

Blade row turning and losses: same as configuration (A).

## Configuration (Q) – Maximum Gap Length

Compressor geometry: Same as configuration (A), except gap length increased. Rotor inlet/exit at $z = 0$, 0.1601, stator inlet/exit at $z = 0.3091$, 0.5437.

Blade row turning and losses: same as configuration (A).

## Configuration (R) – Gradual Annulus Area Convergence

Compressor geometry: Cross-section area of annulus given by

$$A = \begin{cases} 1.0681 + 0.5341\, e^{-(z-0.1826)} & \text{for } z \geq 0.1826 \\ 2.1363 - 0.5341\, e^{(z-0.1826)} & \text{for } z < 0.1826 \end{cases}$$

Casing $r_t = 0.85 + A/10.6814$, $r_h = 0.85 - A/10.6814$. Far-field boundaries at $z = -4, 4$. Rotor inlet/exit at $z = 0$, 0.1601, stator inlet/exit at $z = 0.2051$, 0.4397.

Blade row turning: same as configuration (A).

Blade row losses:

| Flow coefficient | 0.2812 | 0.3375 | 0.450 |
|---|---|---|---|
| Rotor loss (mid-span) | 0.0035 | 0.033 | 0.080 |
| Stator loss (mid-span) | 0.015 | 0.0075 | 0.018 |

| | hub | mid | tip |
|---|---|---|---|
| Rotor loss ratio | 1 | 1.75 | 4 |
| Stator loss ratio | 1 | 1.5 | 2 |

## Configuration (S) – Rapid Annulus Area Convergence

Compressor geometry: Cross-section area of annulus given by

$$A = \begin{cases} 1.0681 + 0.5341\, e^{-8(z-0.1826)} & \text{for } z \geq 0.1826 \\ 2.1363 - 0.5341\, e^{8(z-0.1826)} & \text{for } z < 0.1826 \end{cases}$$

Casing $r_t = 0.85 + A/10.6814$, $r_h = 0.85 - A/10.6814$. Far-field boundaries at $z = -4, 4$. Rotor inlet/exit at $z = 0$, 0.1601, stator inlet/exit at $z = 0.2051$, 0.4397.

Blade row turning: same as configuration (A); Blade row losses: same as configuration (R).

## Configuration (T) – Inlet Velocity Distortion (High Tip Velocity)

Compressor geometry and blade row turning: same as configuration (A).

Inlet flow profile:

$$\bar{W}(r) = W_0 \left[1 + 0.2 \cos\left(\pi \frac{r - r_h}{r_t - r_h}\right)\right]$$

Blade row losses: used loss-coefficient correlations $\xi(\beta)$ from flow fields generated by configuration (A).

## Configuration (U) – Inlet Velocity Distortion (Low Tip Velocity)

Compressor geometry and blade row turning: same as configuration (A).

Inlet flow profile:

$$\bar{W}(r) = W_0 \left[1 - 0.2\cos\left(\pi \frac{r - r_h}{r_t - r_h}\right)\right]$$

Blade row losses: used loss-coefficient correlations $\xi(\beta)$ from flow fields generated by configuration (A).

## Configuration (V) – Multistage Baseline

Compressor geometry: Casing $r_t = 1$, $r_h = 0.75$. Far-field boundaries at $z = -4, 4.856$.

| | IGV | Rotor 1 | Stator 1 | Rotor 2 | Stator 2 |
|---|---|---|---|---|---|
| $z$ at inlet | 0 | 0.2003 | 0.3650 | 0.5602 | 0.7248 |
| $z$ at exit | 0.1408 | 0.3005 | 0.4961 | 0.6603 | 0.8559 |

Blade row turning:

| | IGV | | Rotors | | Stators | |
|---|---|---|---|---|---|---|
| | $\beta_{in}$ | $\beta_{out}$ | $\beta_{in}$ | $\beta_{out}$ | $\beta_{in}$ | $\beta_{out}$ |
| hub | 0° | 8° | -54° | -22° | 49° | 8° |
| mid | 0° | 9° | -57.8° | -40.7° | 46° | 9° |
| tip | 0° | 7.5° | -63° | -47° | 55.5° | 7.5° |
| $k$ | 20 | | 25 | | 25 | |

Blade row losses:

| Flow coefficient | 0.429 | 0.454 | 0.665 |
|---|---|---|---|
| IGV loss (mid-span) | 0.0081 | 0.0091 | 0.0195 |
| Rotor loss (mid-span) | 0.0376 | 0.0234 | 0.0357 |
| Stator loss (mid-span) | 0.0220 | 0.0176 | 0.0363 |

| | hub | mid | tip |
|---|---|---|---|
| IGV loss ratio | 1 | 1 | 1 |
| Rotor loss ratio | 1 | 1.5 | 3 |
| Stator loss ratio | 1 | 1.5 | 2 |

## Configuration (W) – Moderate Mismatching

Compressor geometry: same as configuration (V).

Blade row turning: same as configuration (V), except IGV angles adjusted by $-15°$.

Blade row losses: same as configuration (V), except used loss-coefficient correlations $\xi(\beta)$ for Rotor-1 from flow fields generated by configuration (V).

### Configuration (X) – Maximum Mismatching

Compressor geometry: same as configuration (V).

Blade row turning and losses: same as configuration (W), except IGV angles adjusted by $-25°$.

## M.2 Graphs of Steady and Unsteady Flow Field Results

The following pages show the steady flow fields and stall modes computed for each parametric study. Three pages of figures are provided for each study, each described below:

1. Spanwise profiles of loss and relative exit flow angles for the rotor and stator are plotted; also spanwise profiles of the axial velocity and static pressure at the rotor inlet, mid-gap and stator exit planes. Each variable is plotted at three to five operating points approaching stall (denoted by the thickest line). The operating points used are marked by solid circles on the compressor characteristic on the succeeding page.
2. The overall pressure rise characteristic is plotted at the top. Noted on the characteristic are the stall points as predicted by the 3-D and the 2-D models. For 3 cases where the stall mode from 3-D analysis is *not* the (1,0) mode, then the neutral stability point of the (1,0) mode is also marked. The solid circles are the 3–5 operating points corresponding to the steady flow profiles on the preceding page. The second graph shows all eigenvalues for circumferential harmonics of $n = 1$, 2, 3 and 15 computed by the 3-D model at the closest operating point to stall.
3. Spanwise profiles of the amplitude of the axial velocity and static pressure perturbations are plotted, corresponding to both the (1,0) and (1,1) modes at the stall point of the compressor. Each mode is normalized by the amplitude of $\delta w$ at the leading edge of the first rotor at the hub. Spanwise profiles of the slope of three characteristics are also plotted for the same operating point. The "compressor" characteristic is defined as the difference between the static pressure profile at the exit of the last blade row and the inlet total pressure profile at the inlet of the first blade row. "Rotor" and "stator" characteristics are defined analogously about the individual blade rows. The slopes are calculated as the derivative of the characteristic $\Psi(r)$ by the inlet velocity $\bar{W}(r)$ at each value of $r$.

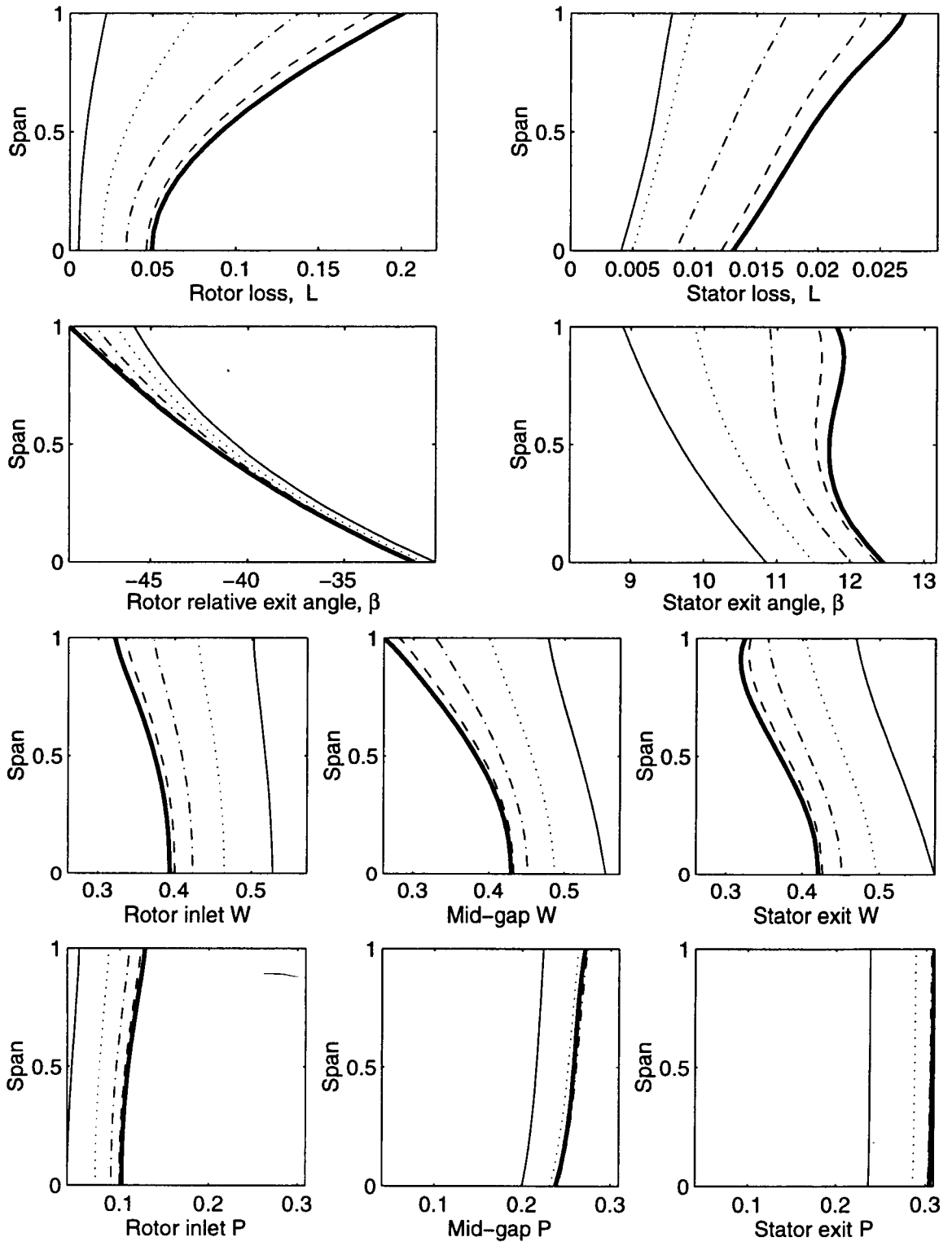


**Figure M-1:** Spanwise profiles of the background flow fields for parametric study A.

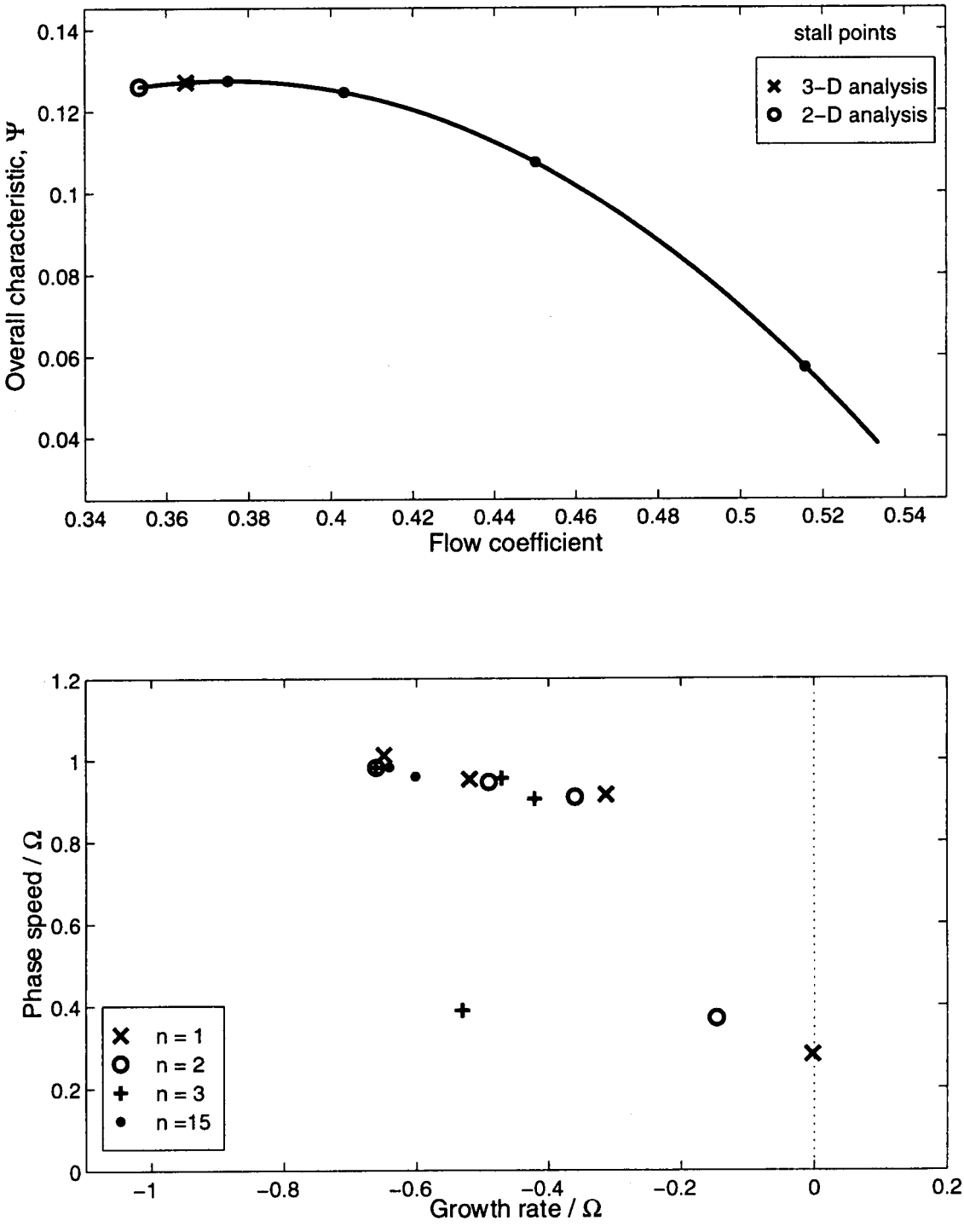


**Figure M-2:** Points of neutral stability on overall characteristic, and eigenvalues at stall for parametric study A.

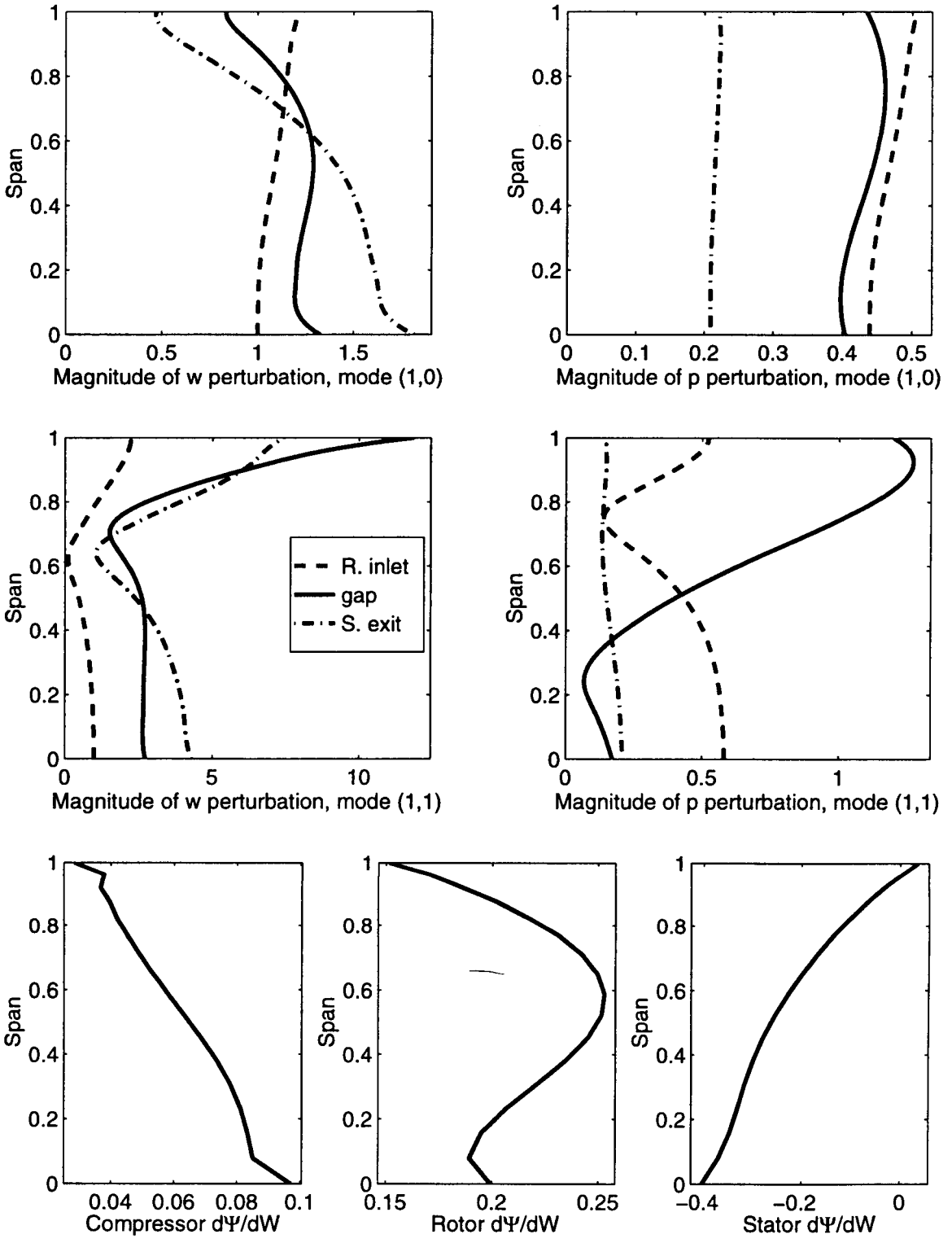


**Figure M-3:** (1,0) and (1,1) mode shapes, and slope variations for parametric study A.

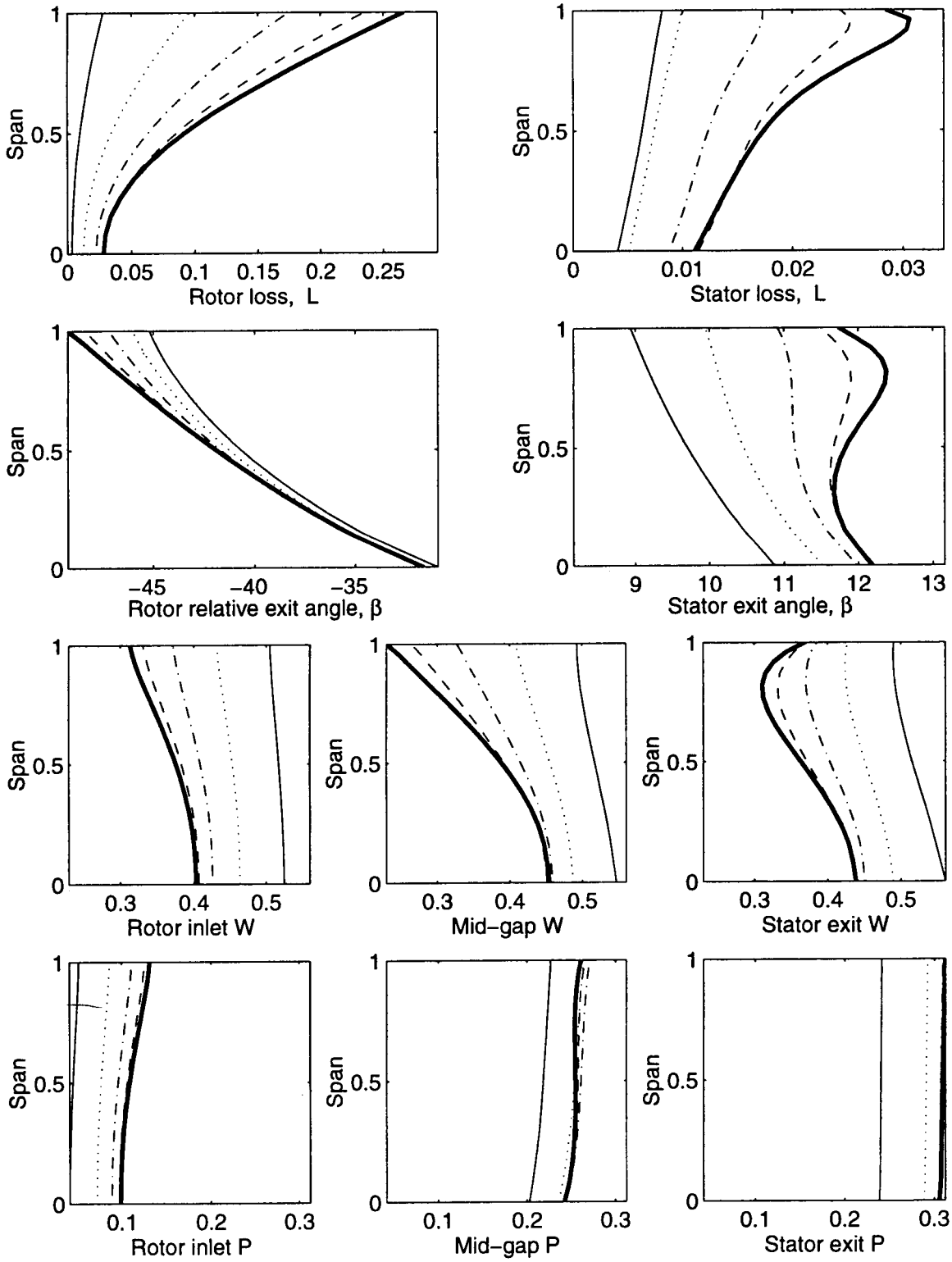


**Figure M-4:** Spanwise profiles of the background flow fields for parametric study B.

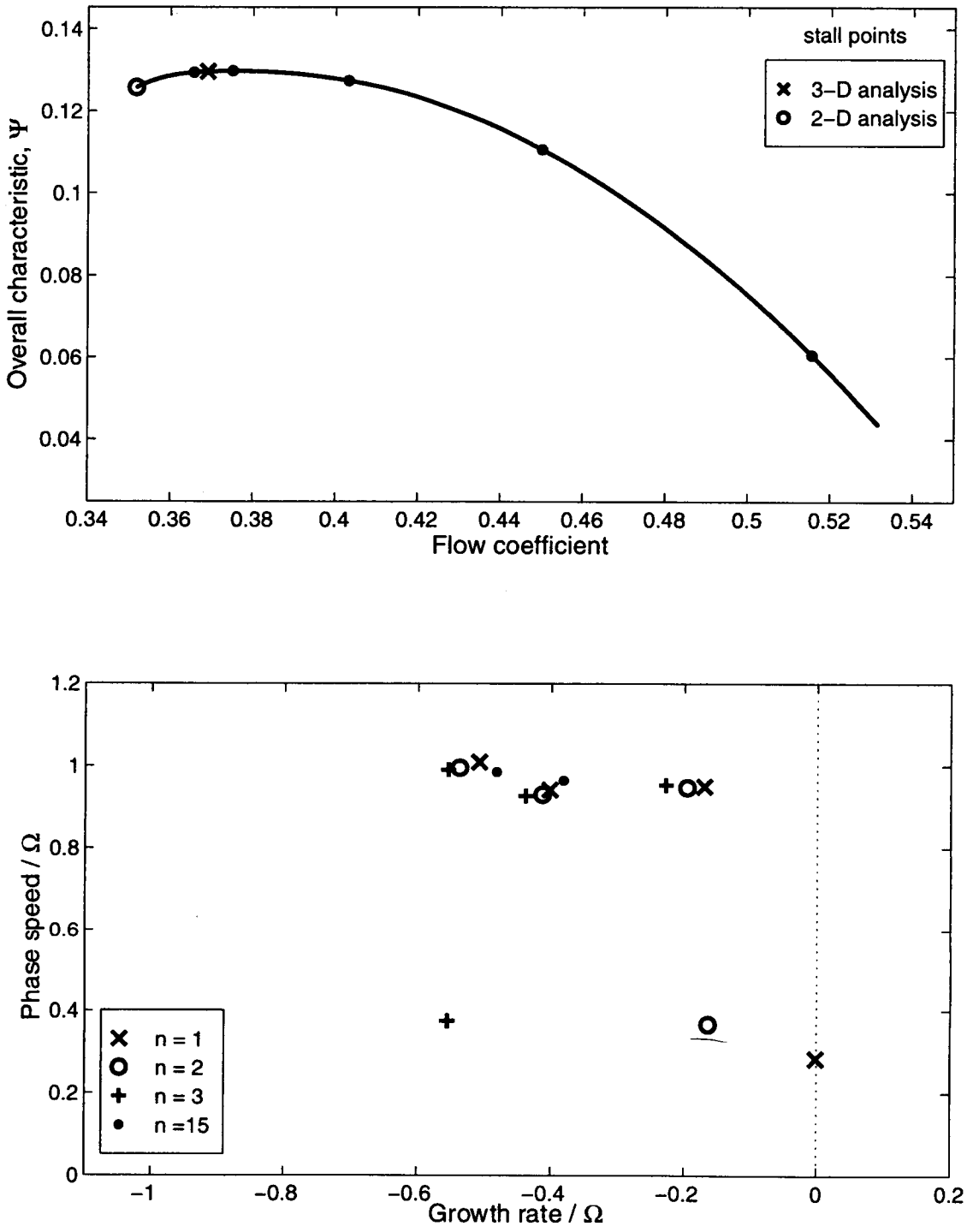


**Figure M-5:** Points of neutral stability on overall characteristic, and eigenvalues at stall for parametric study B.

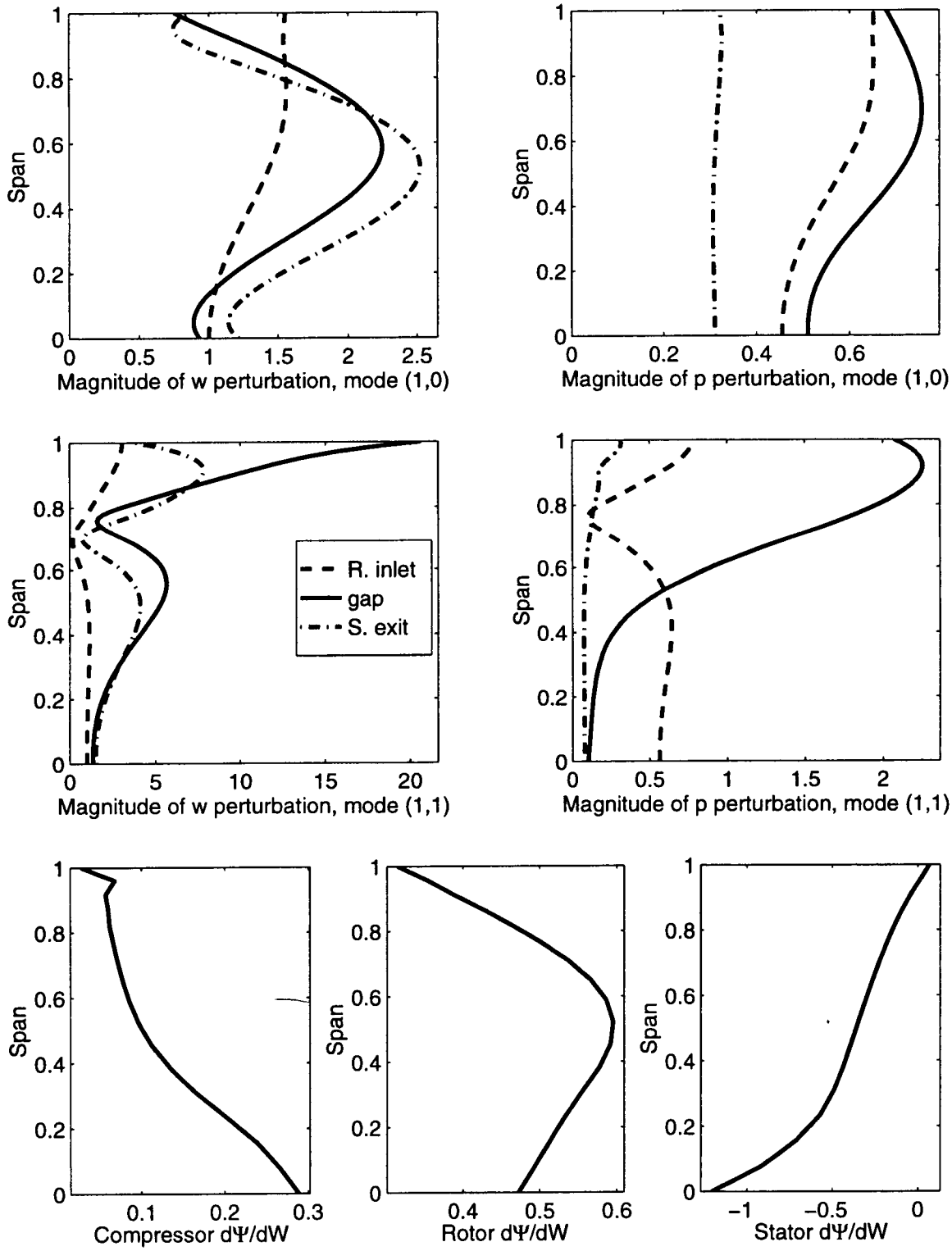


**Figure M-6:** (1,0) and (1,1) mode shapes, and slope variations for parametric study B.

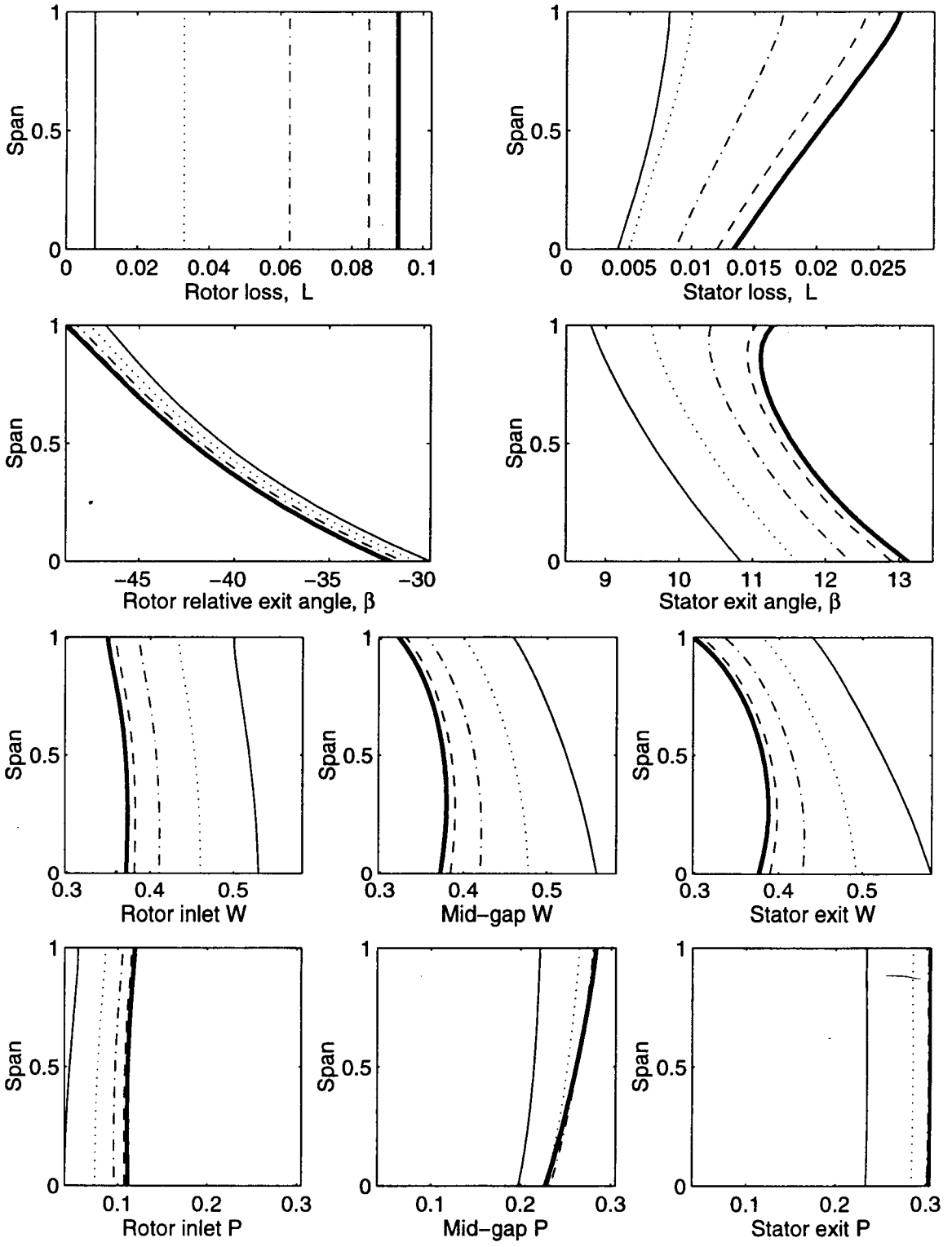


**Figure M-7:** Spanwise profiles of the background flow fields for parametric study C.

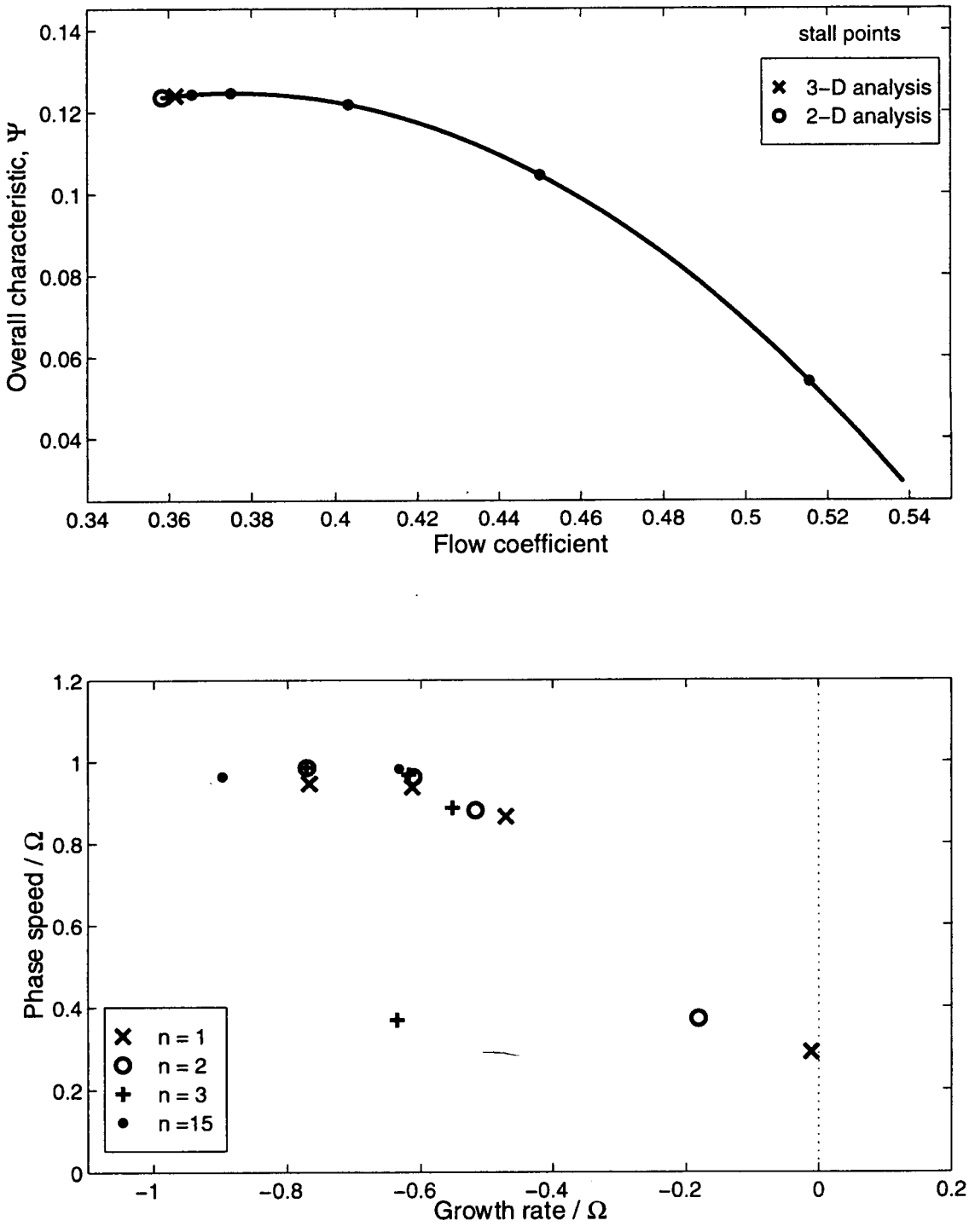


**Figure M-8:** Points of neutral stability on overall characteristic, and eigenvalues at stall for parametric study C.

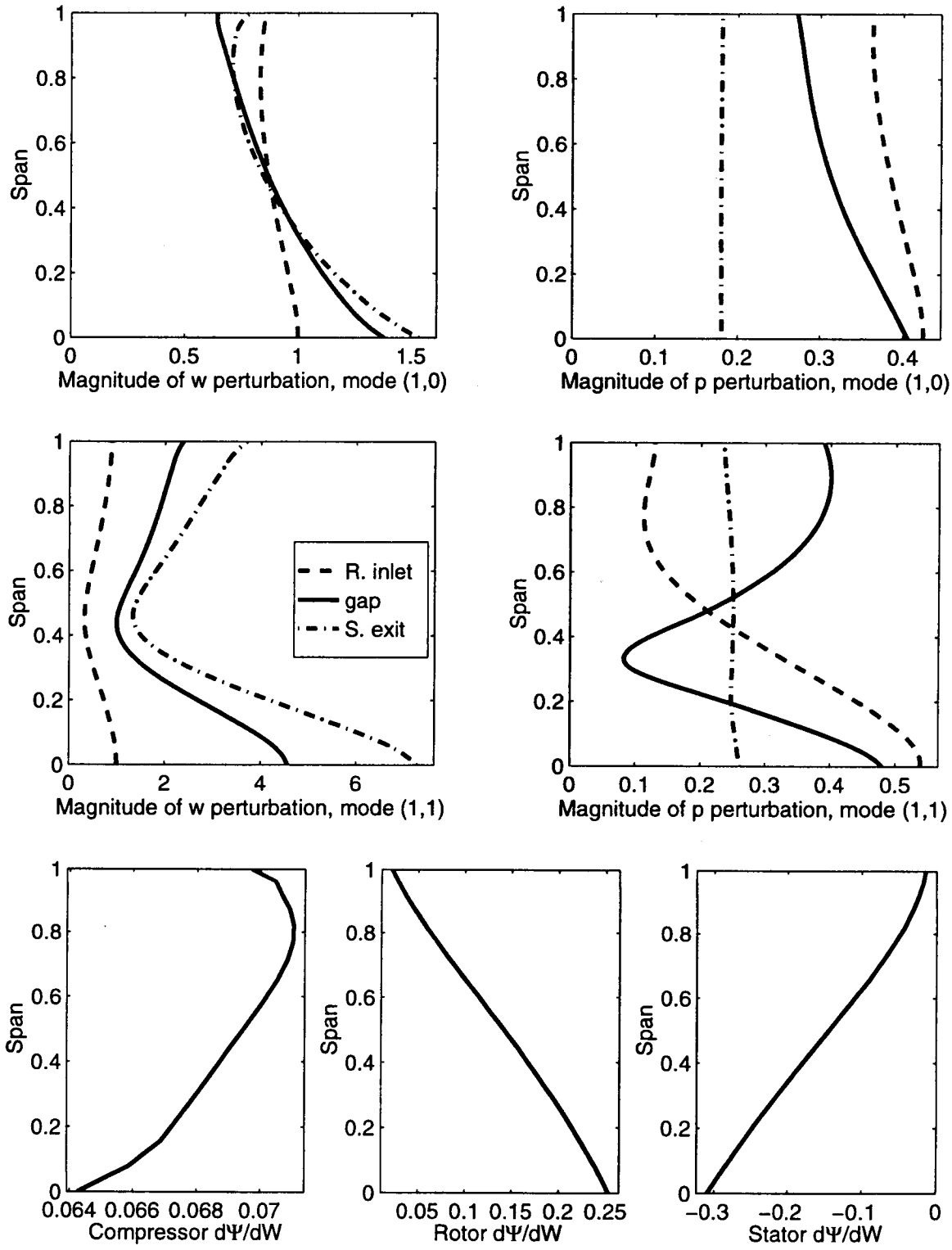


**Figure M-9:** (1,0) and (1,1) mode shapes, and slope variations for parametric study C.

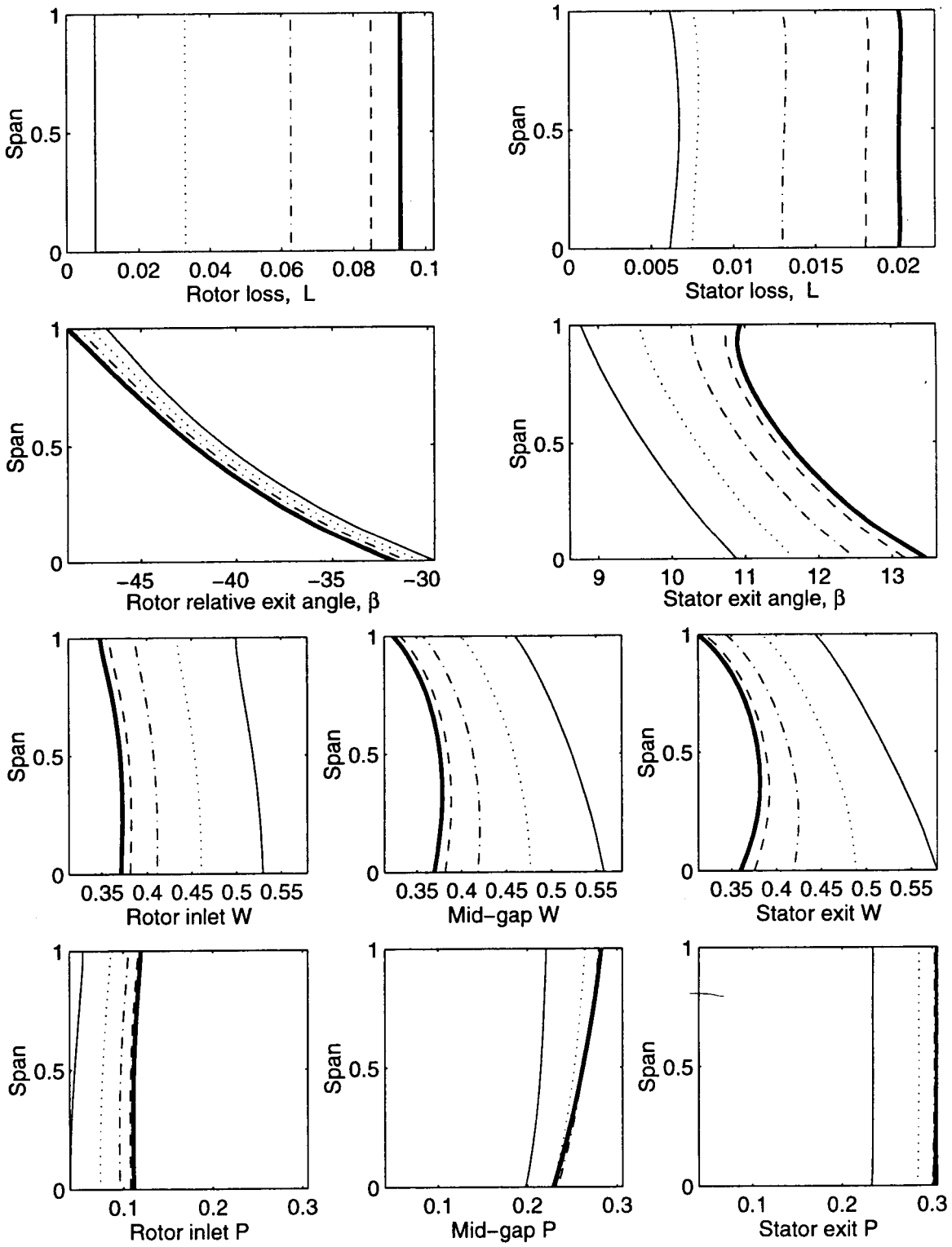


**Figure M-10:** Spanwise profiles of the background flow fields for parametric study D.

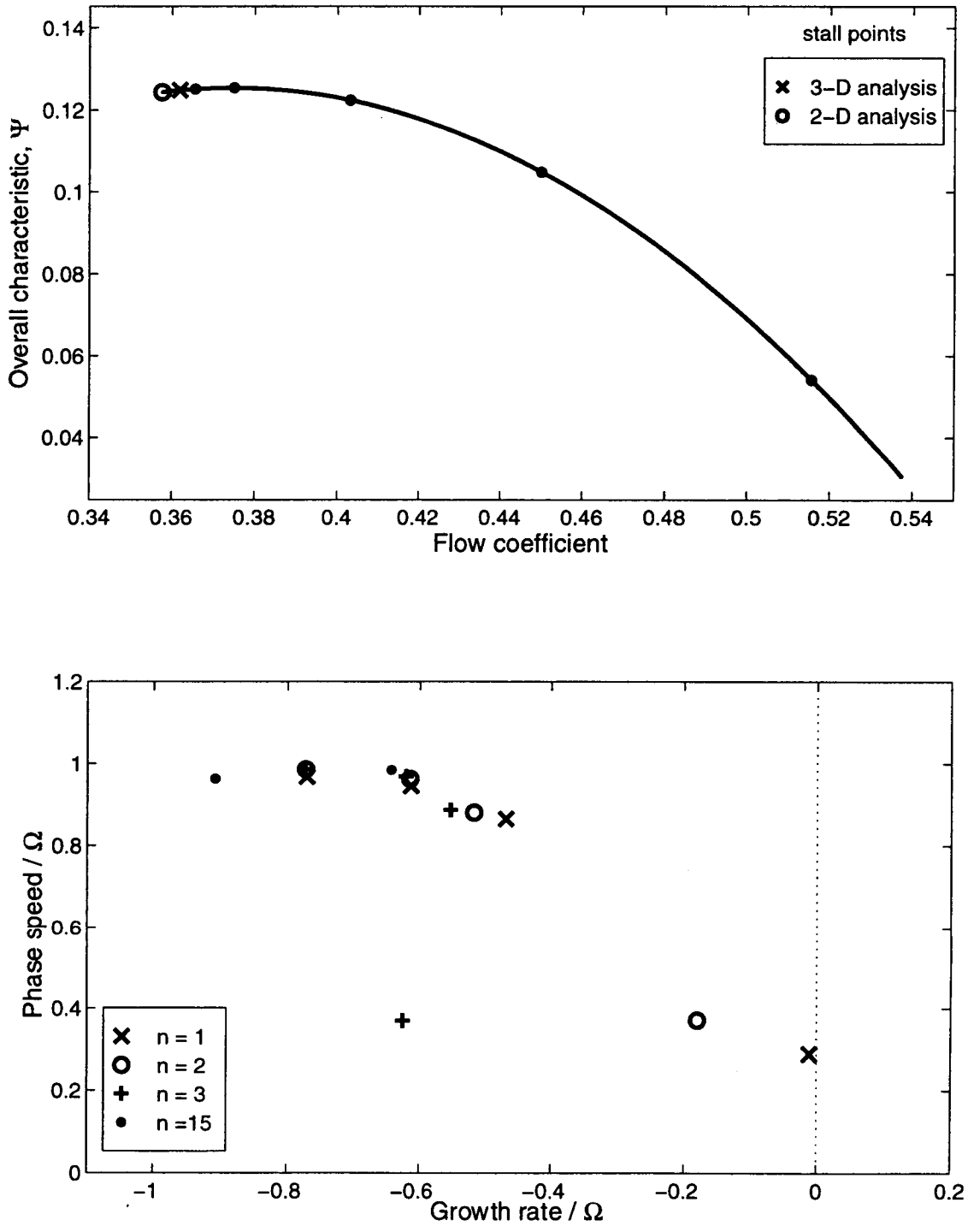


**Figure M-11:** Points of neutral stability on overall characteristic, and eigenvalues at stall for parametric study D.

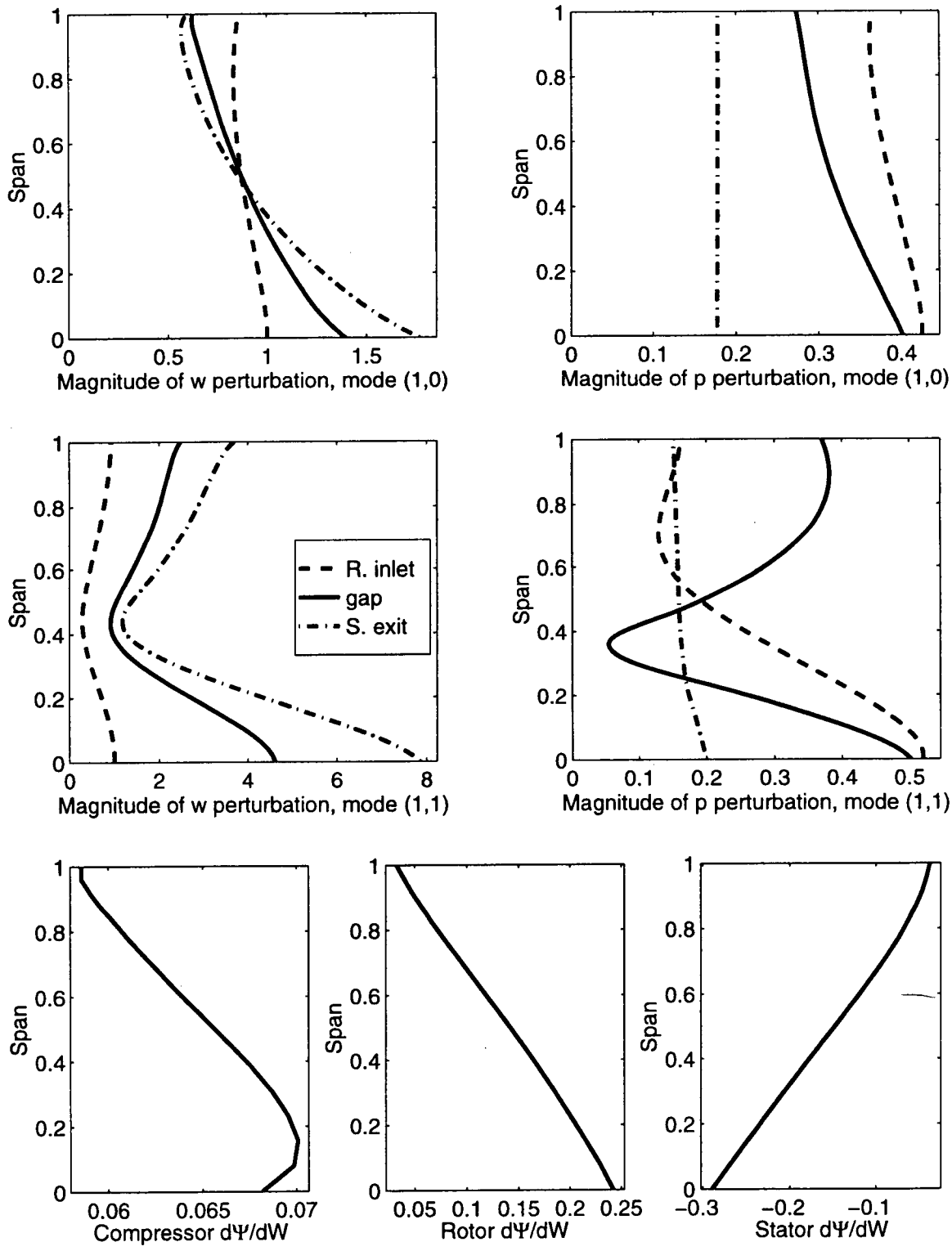


**Figure M-12:** (1,0) and (1,1) mode shapes, and slope variations for parametric study D.

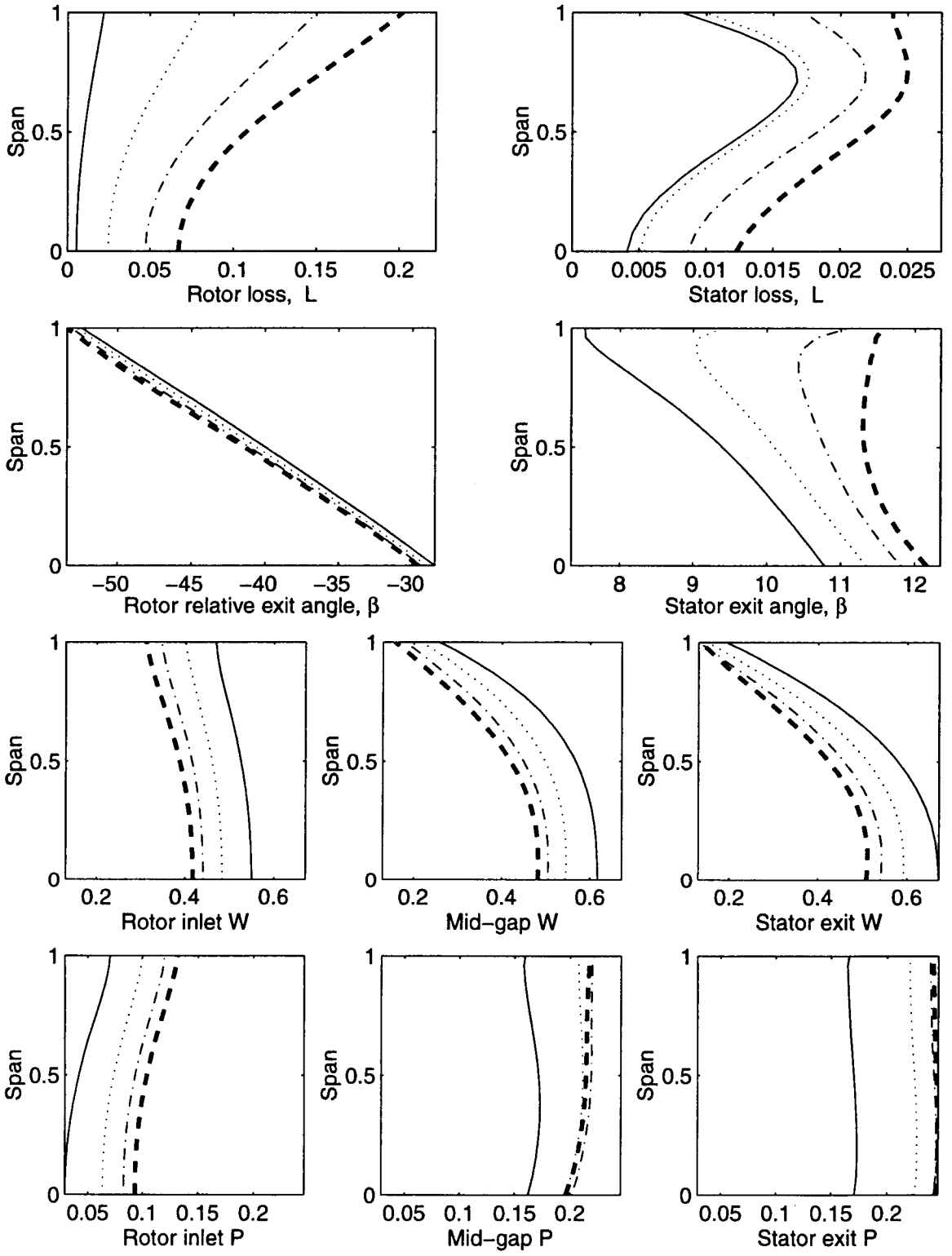


**Figure M-13:** Spanwise profiles of the background flow fields for parametric study G.

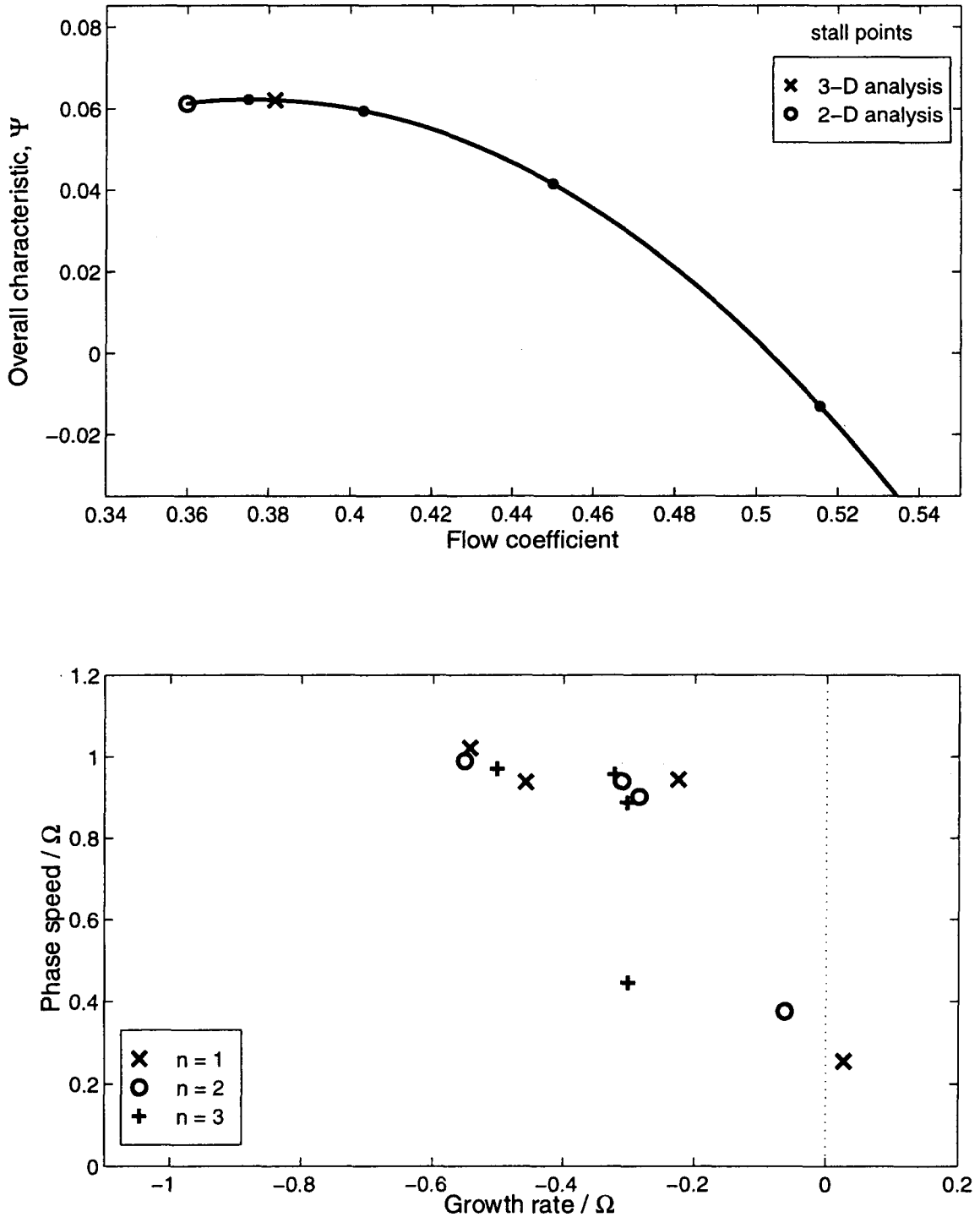


**Figure M-14:** Points of neutral stability on overall characteristic, and eigenvalues at stall for parametric study G.

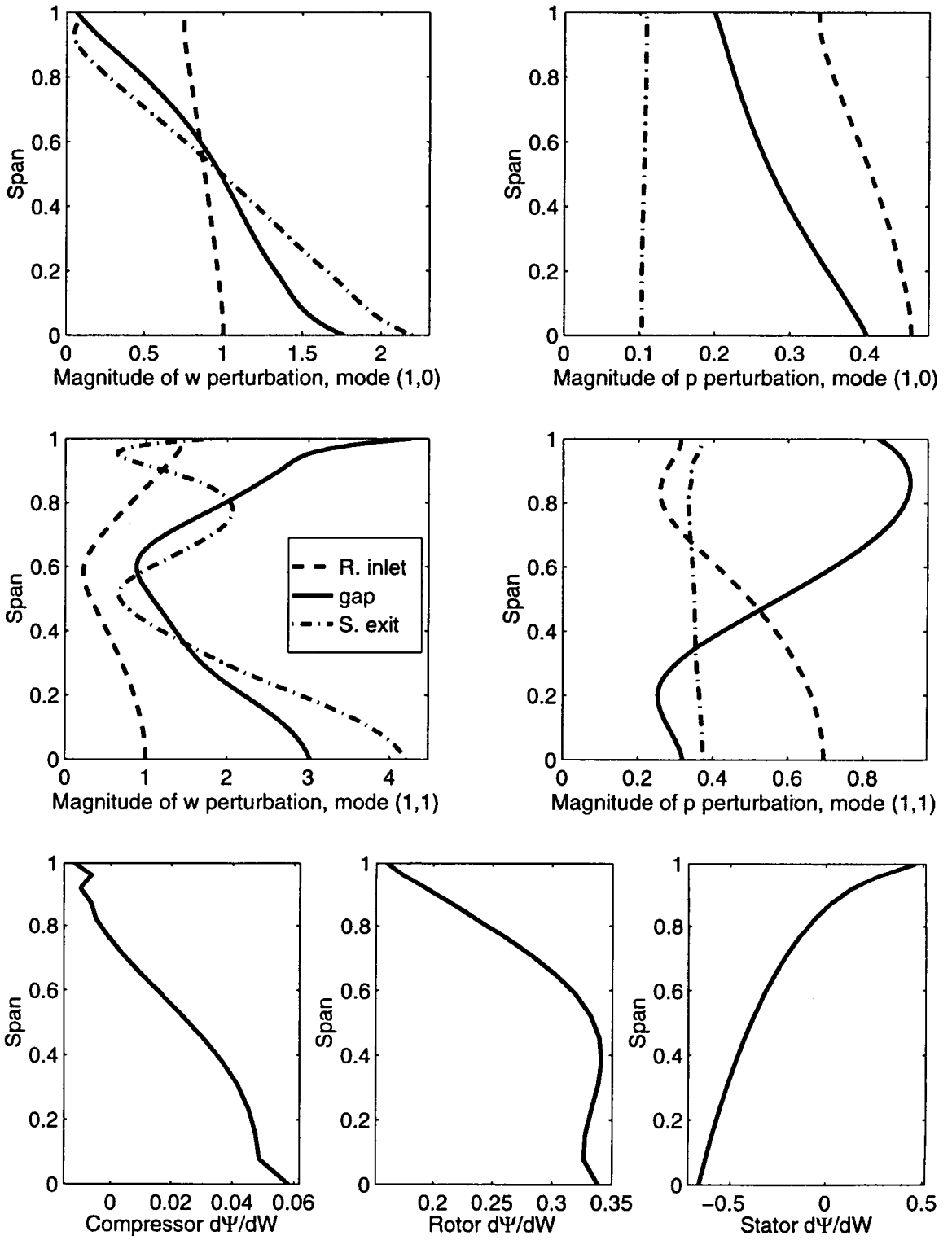


**Figure M-15:** (1,0) and (1,1) mode shapes, and slope variations for parametric study G.

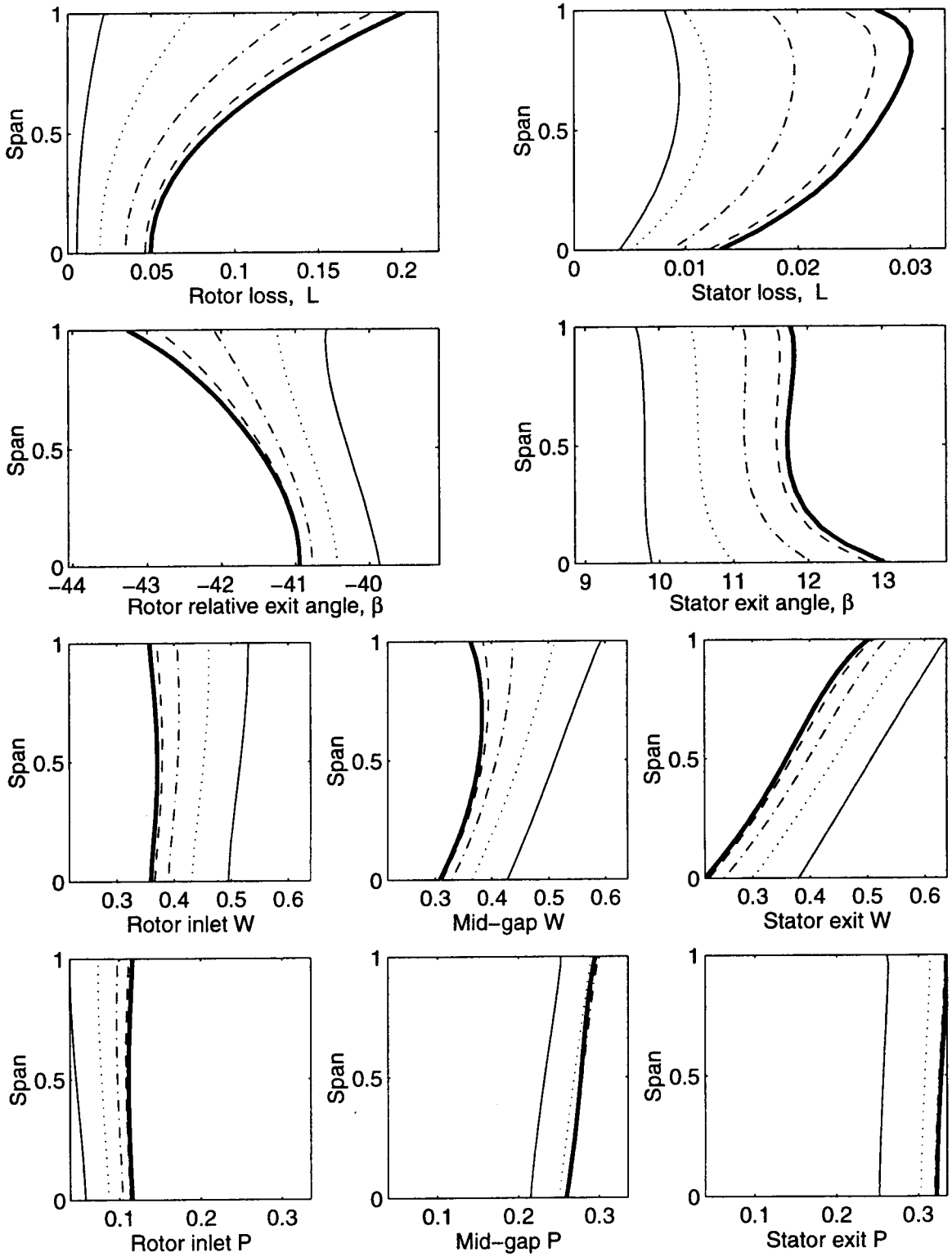


**Figure M-16:** Spanwise profiles of the background flow fields for parametric study H.

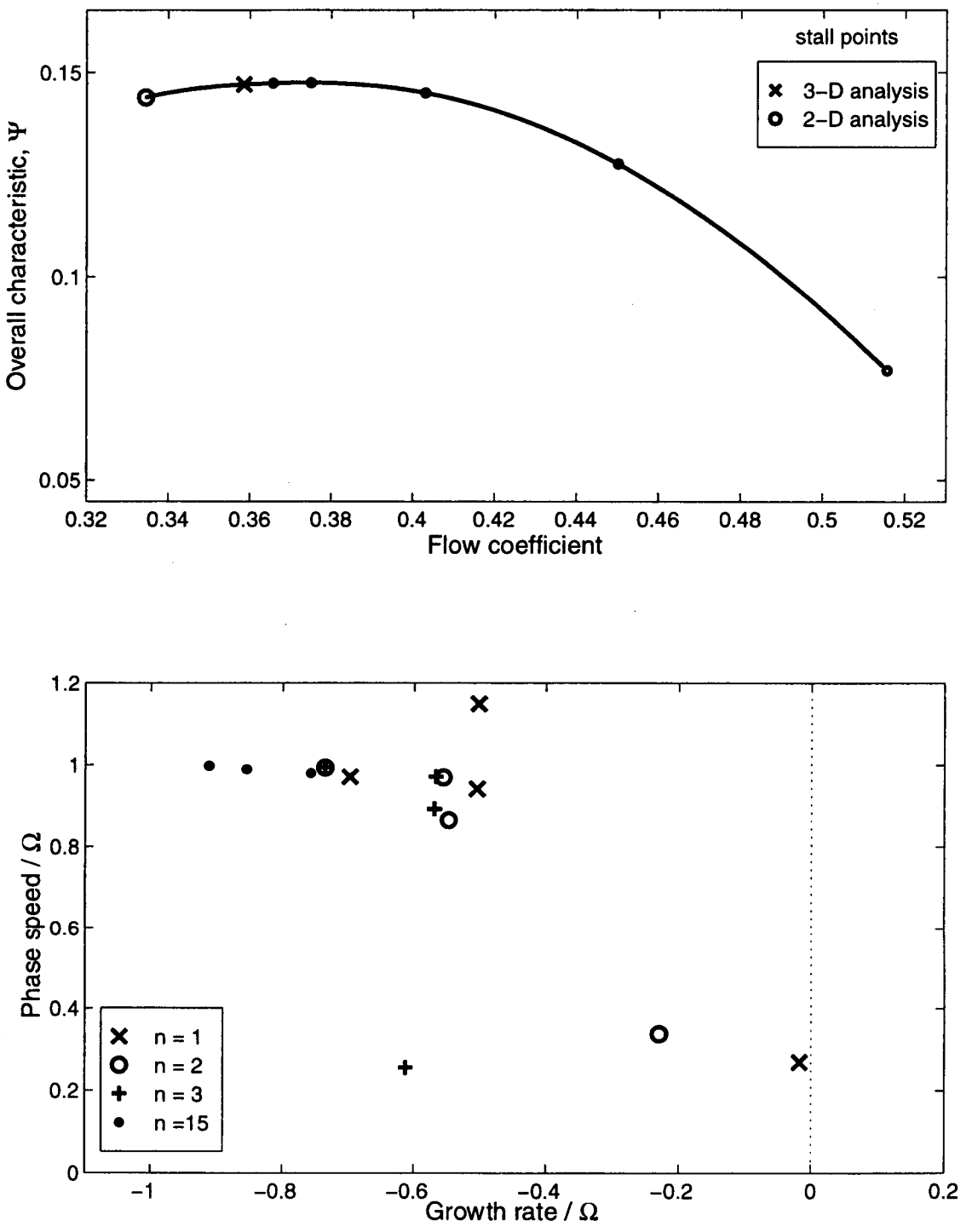


**Figure M-17:** Points of neutral stability on overall characteristic, and eigenvalues at stall for parametric study H.

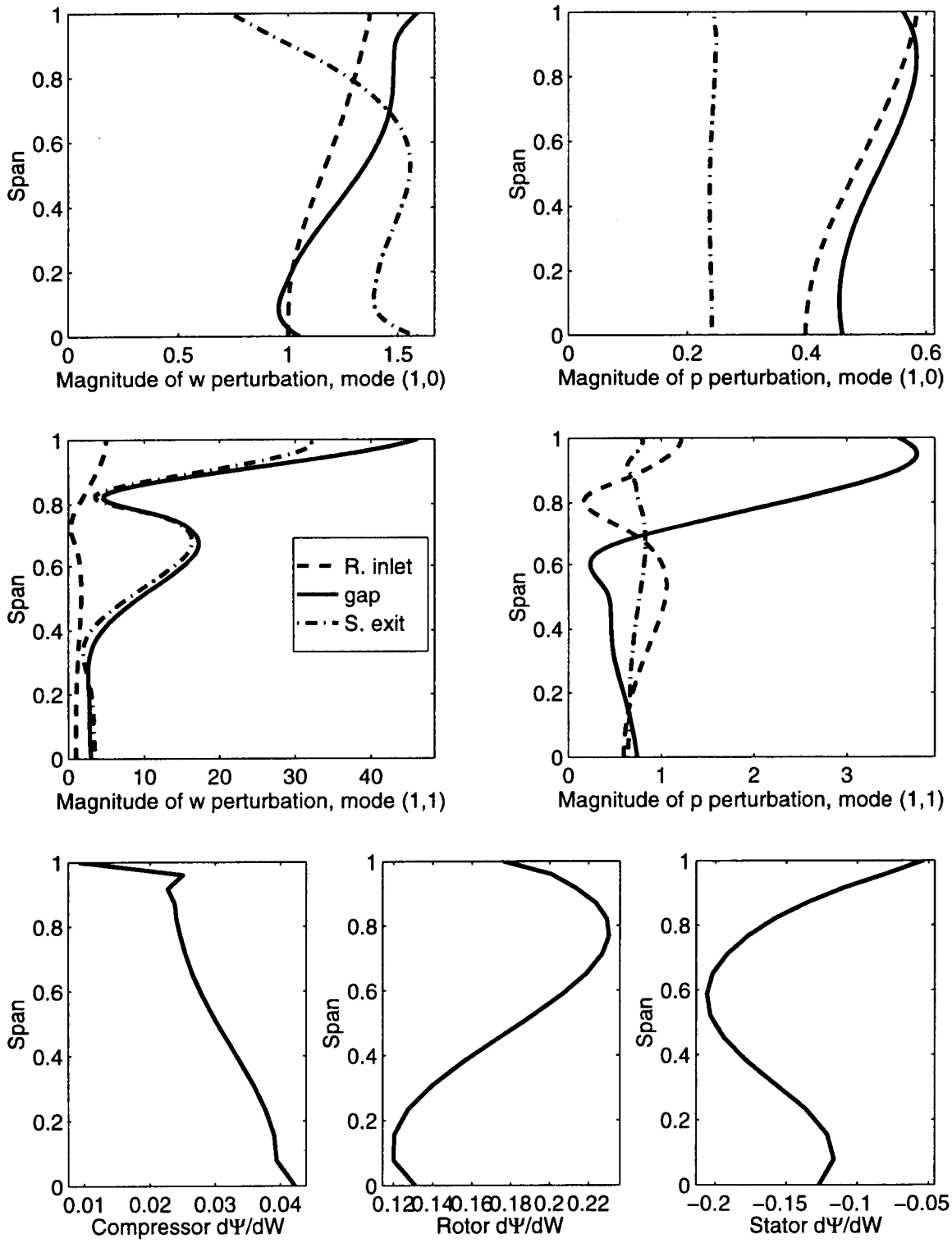


**Figure M-18:** (1,0) and (1,1) mode shapes, and slope variations for parametric study H.

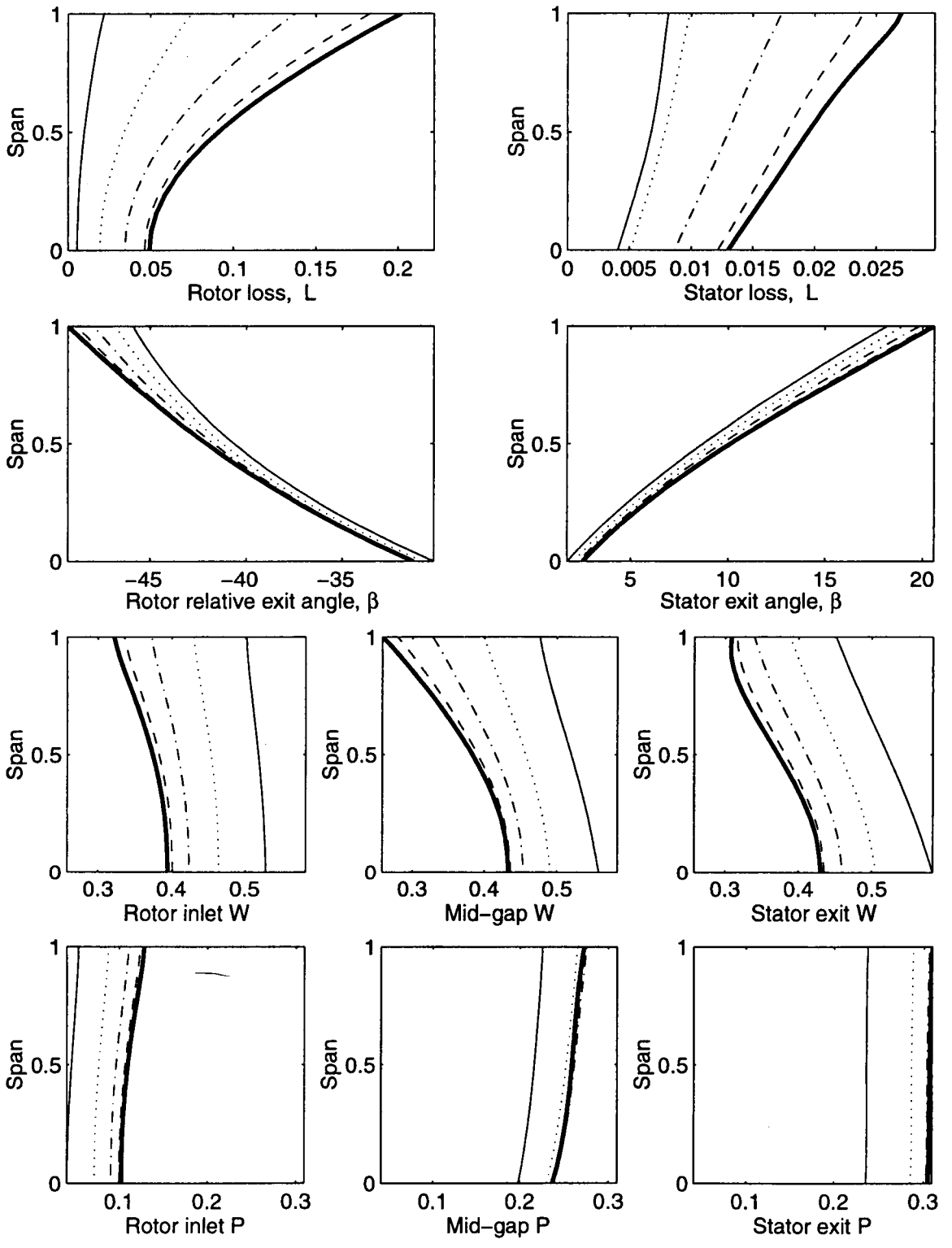


**Figure M-19:** Spanwise profiles of the background flow fields for parametric study J.

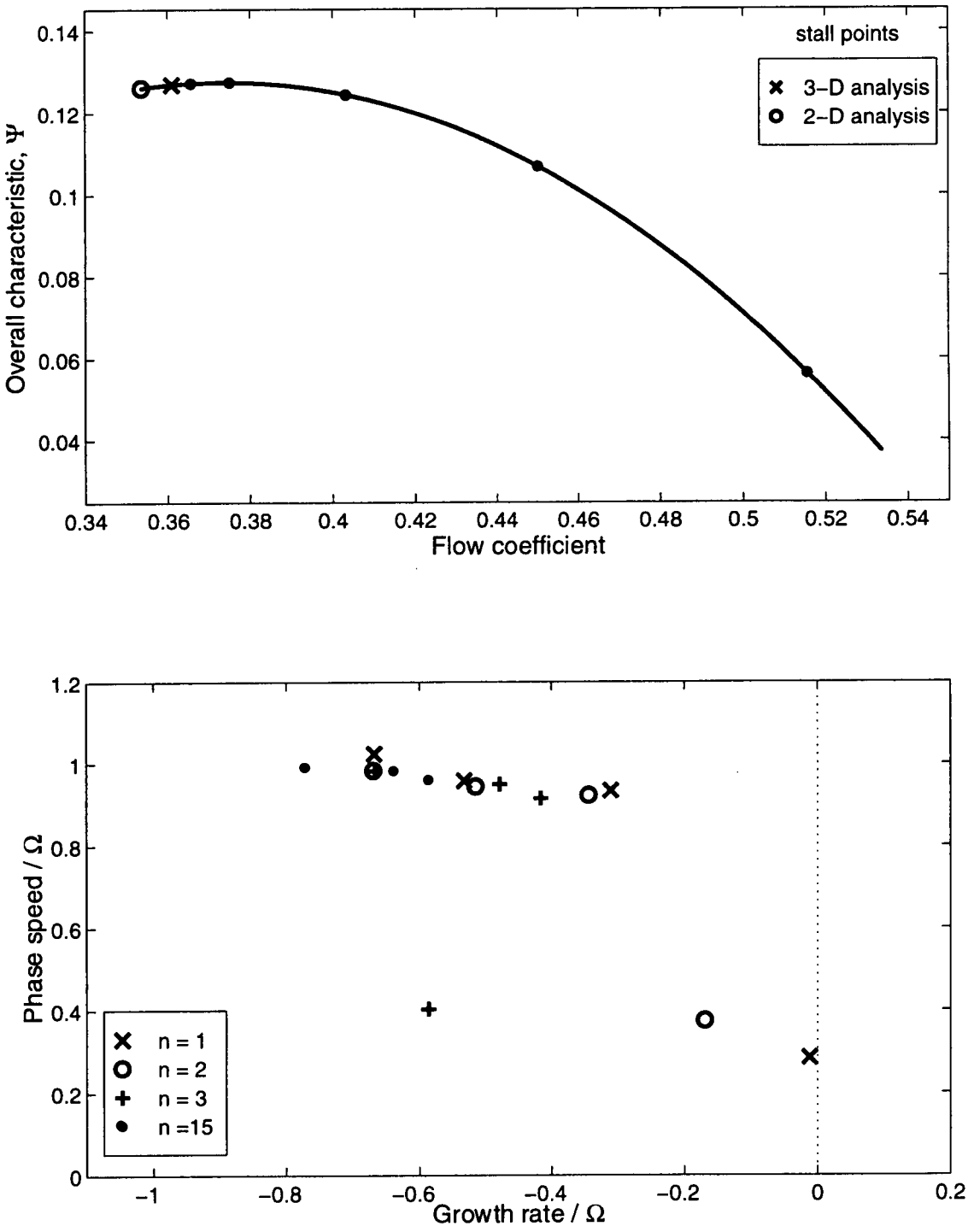


**Figure M-20:** Points of neutral stability on overall characteristic, and eigenvalues at stall for parametric study J.

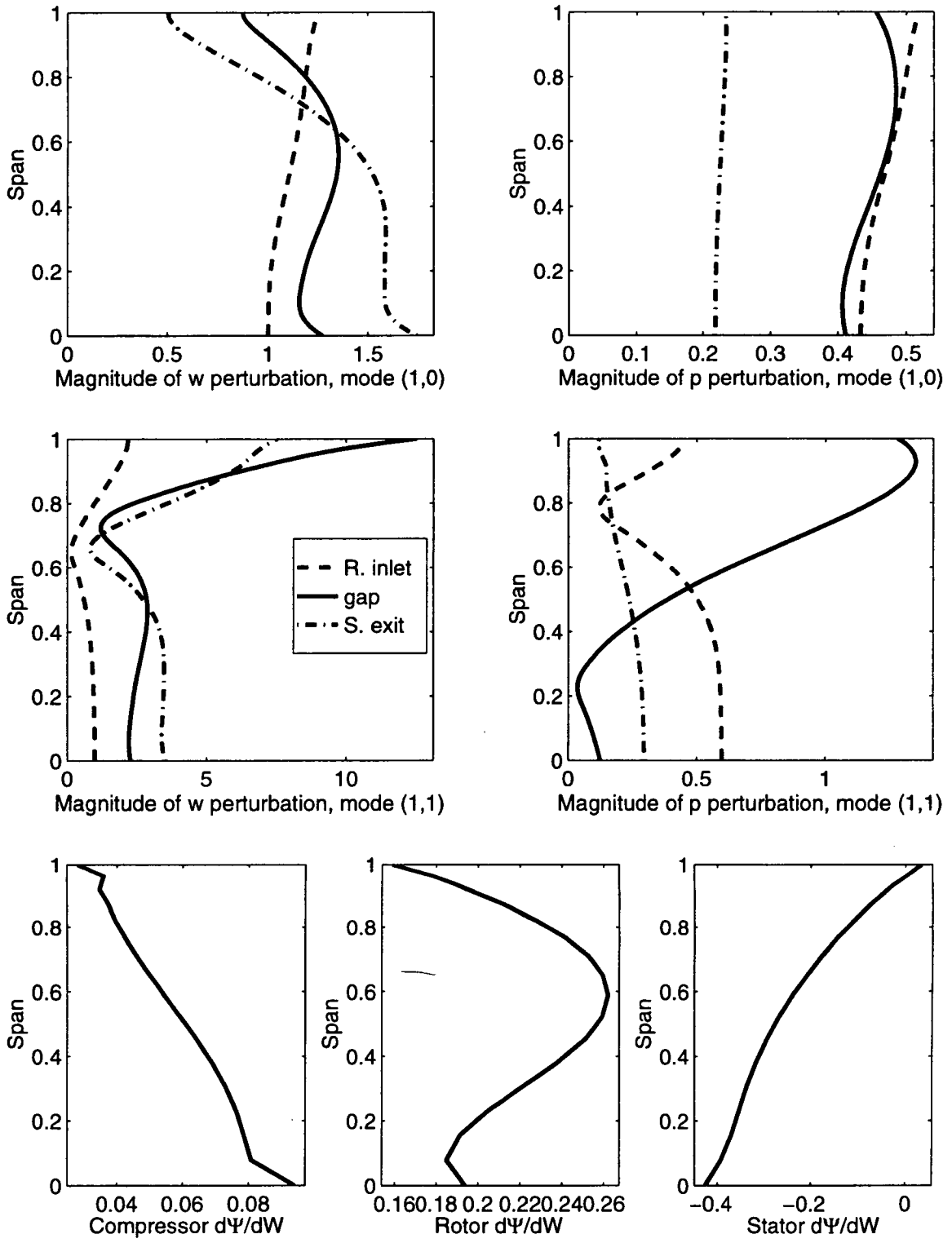


**Figure M-21:** (1,0) and (1,1) mode shapes, and slope variations for parametric study J.

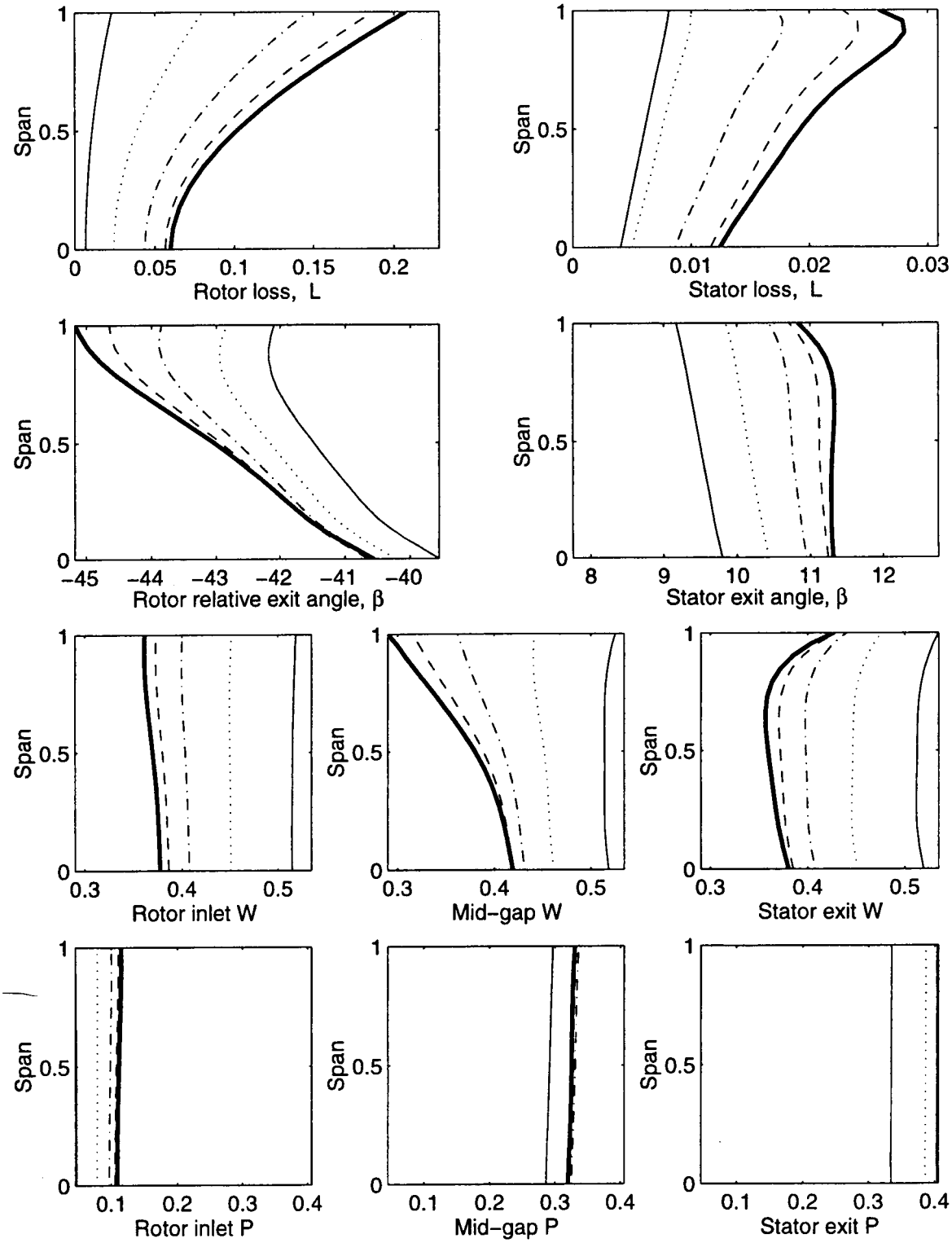


**Figure M-22:** Spanwise profiles of the background flow fields for parametric study K.

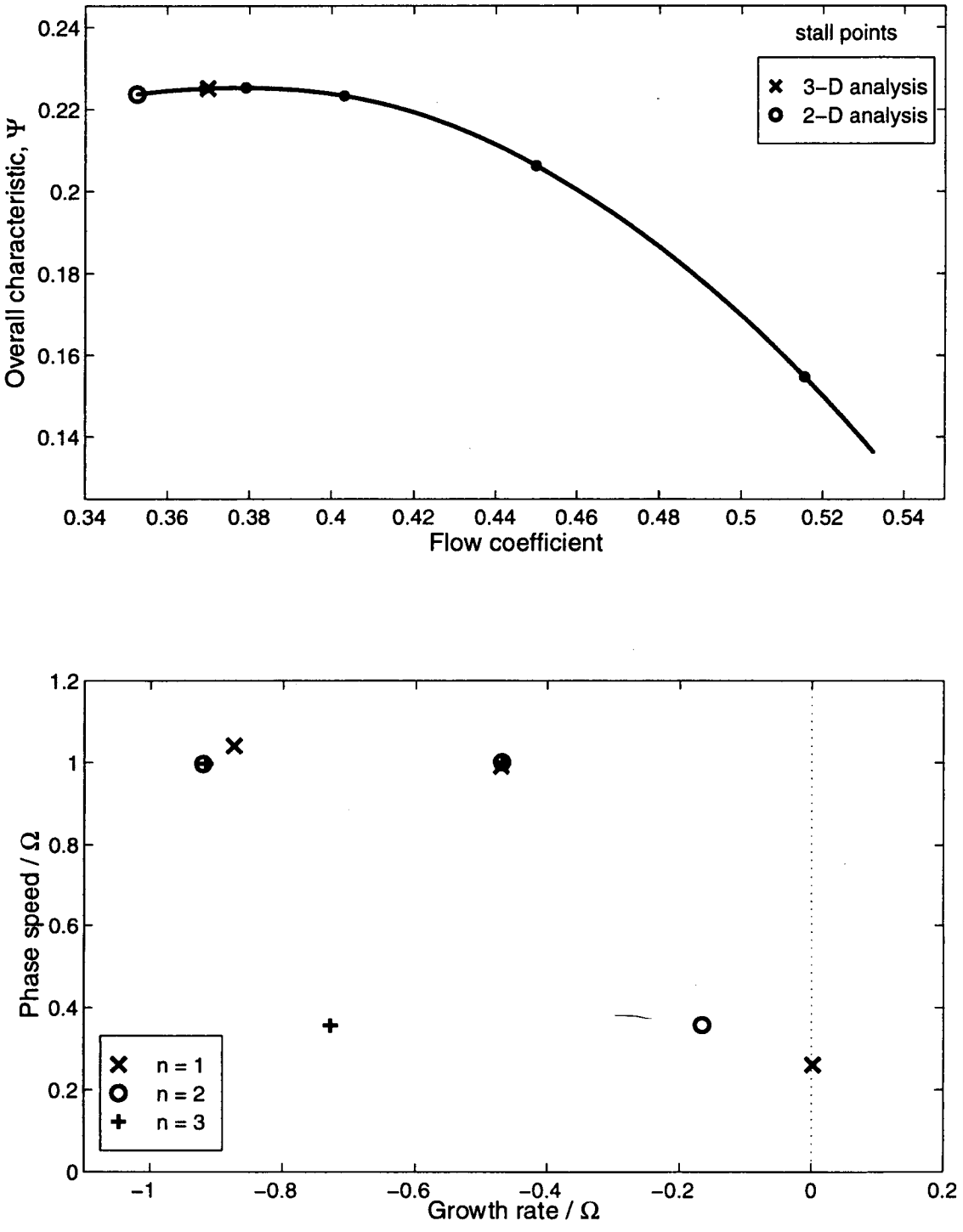


**Figure M-23:** Points of neutral stability on overall characteristic, and eigenvalues at stall for parametric study K.

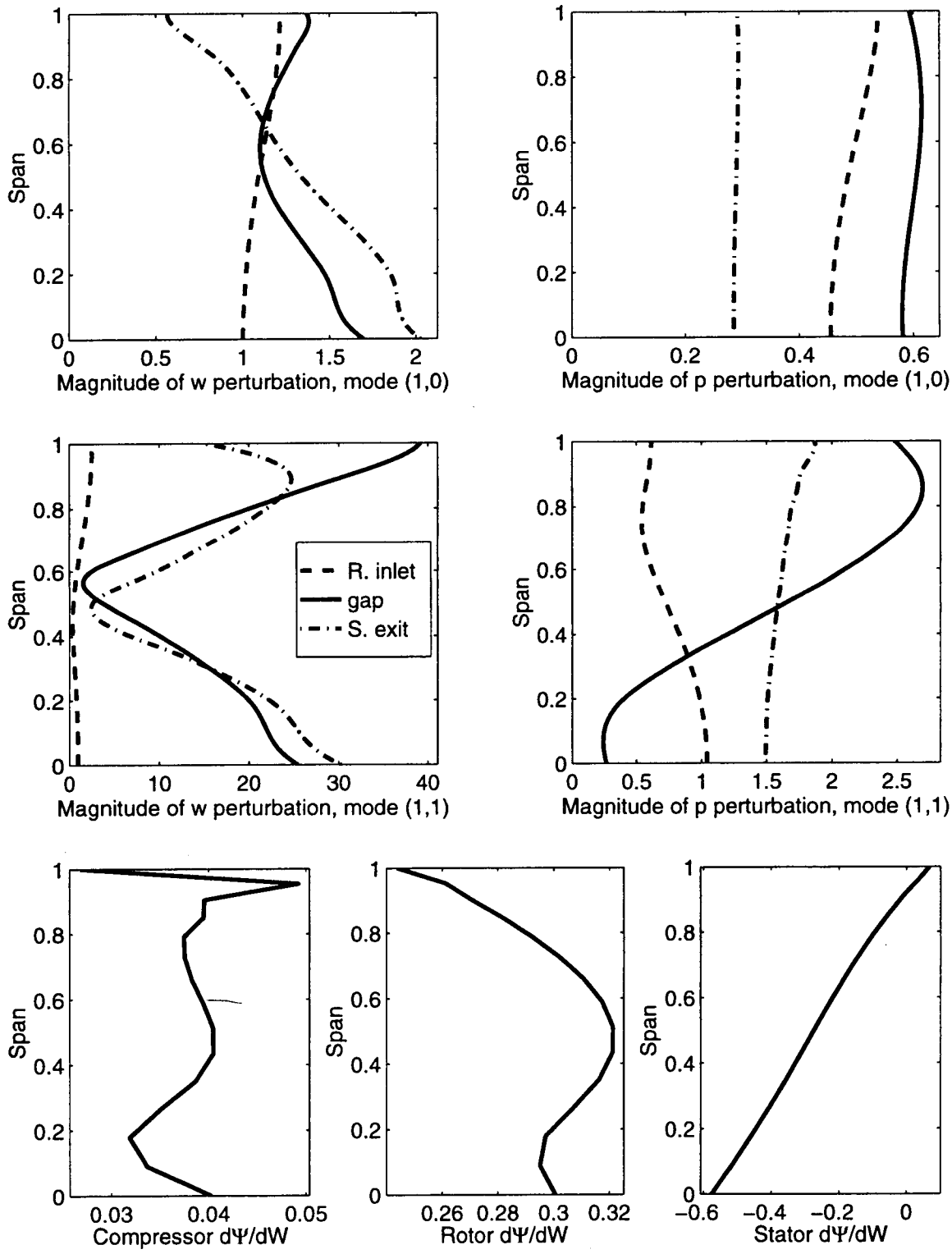


**Figure M-24:** (1,0) and (1,1) mode shapes, and slope variations for parametric study K.

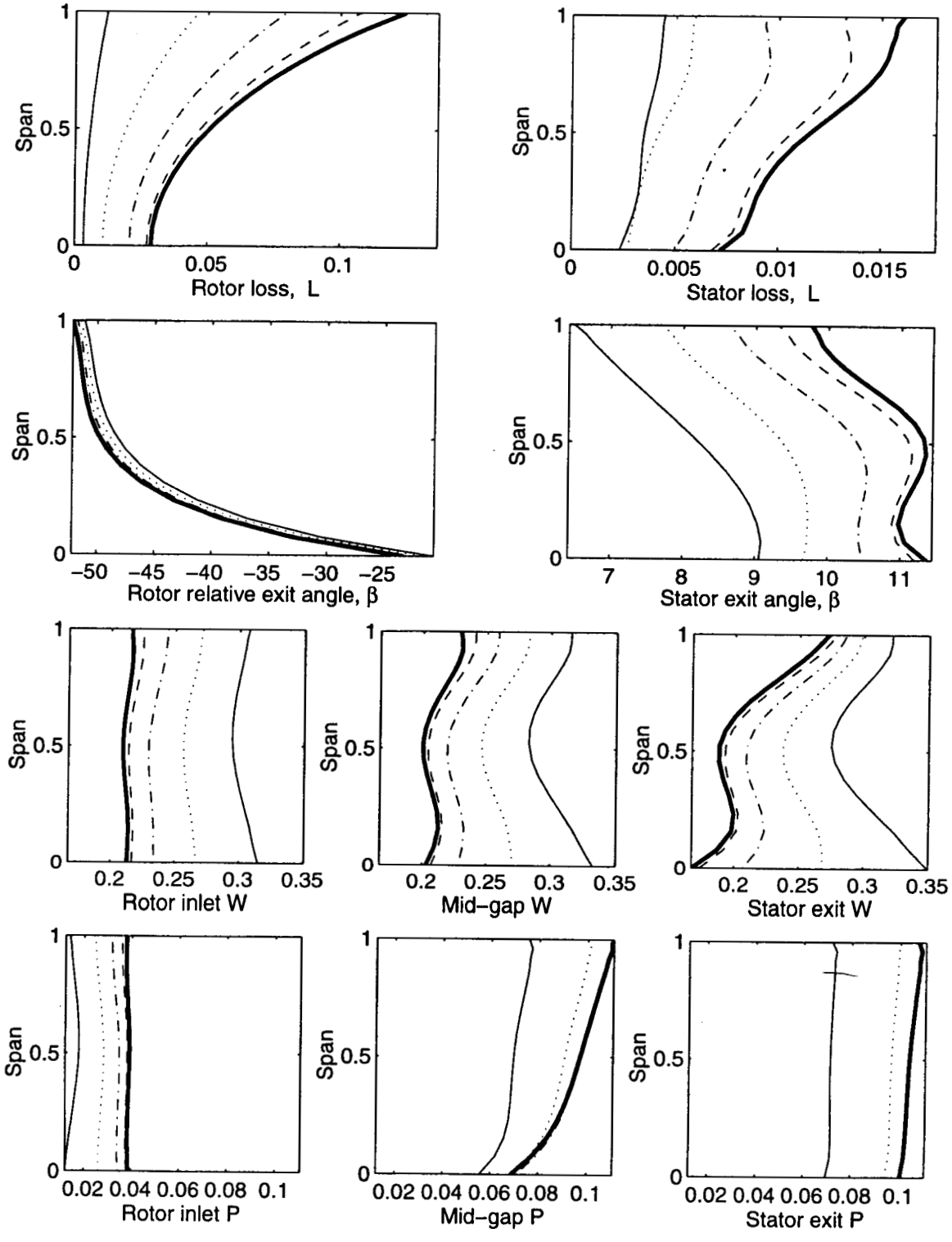


**Figure M-25:** Spanwise profiles of the background flow fields for parametric study L.

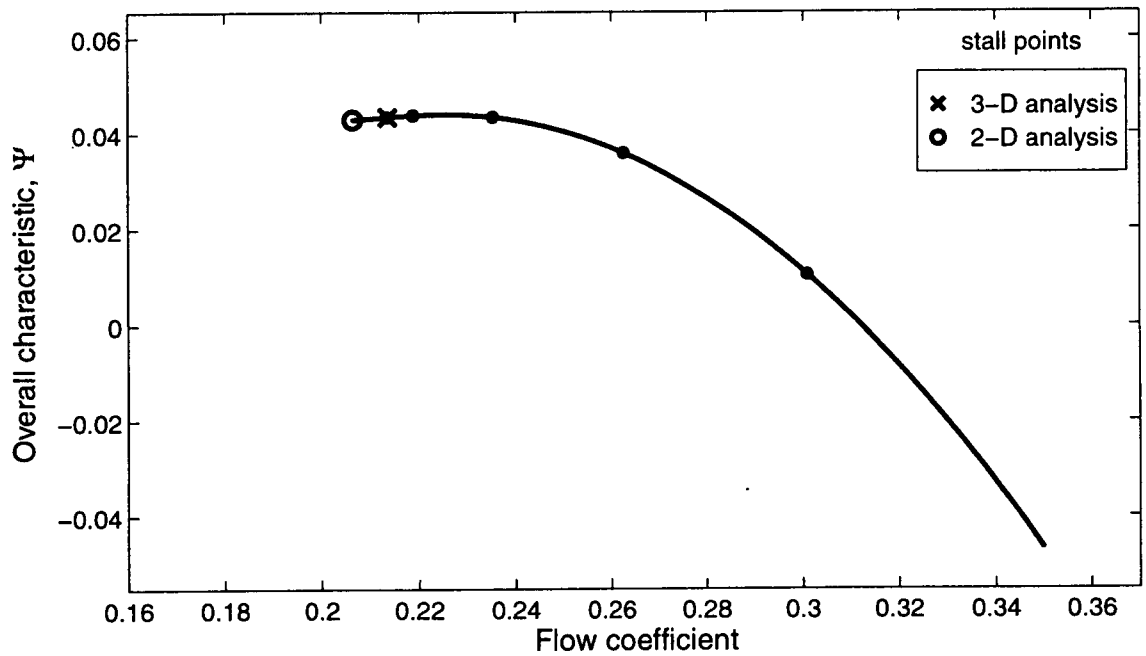


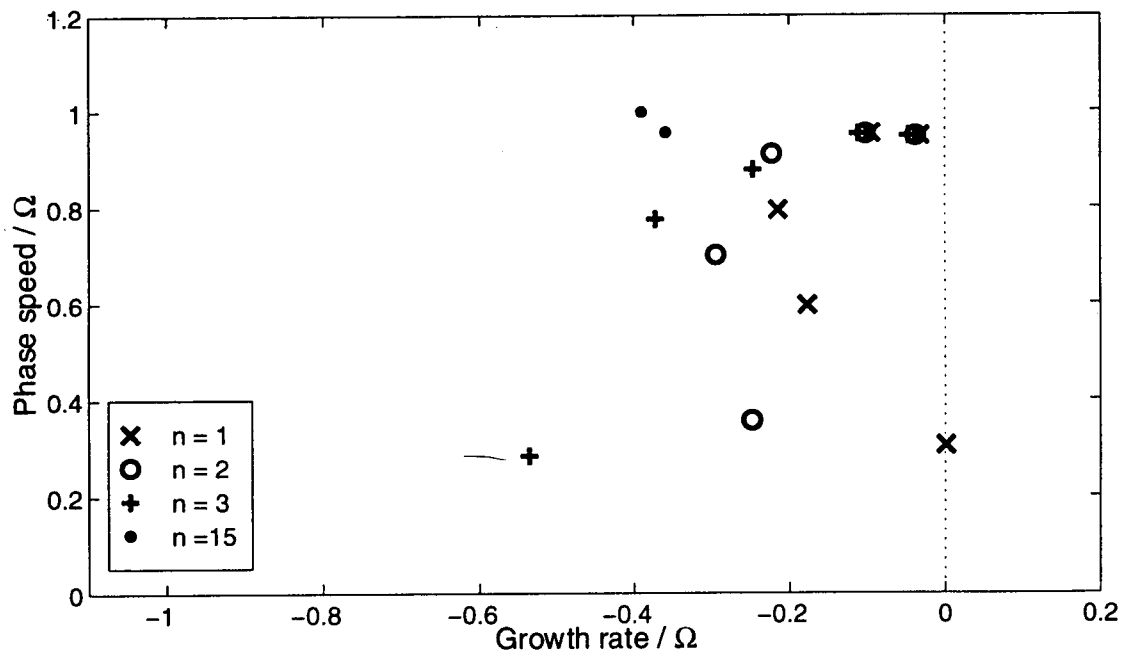


**Figure M-26:** Points of neutral stability on overall characteristic, and eigenvalues at stall for parametric study L.

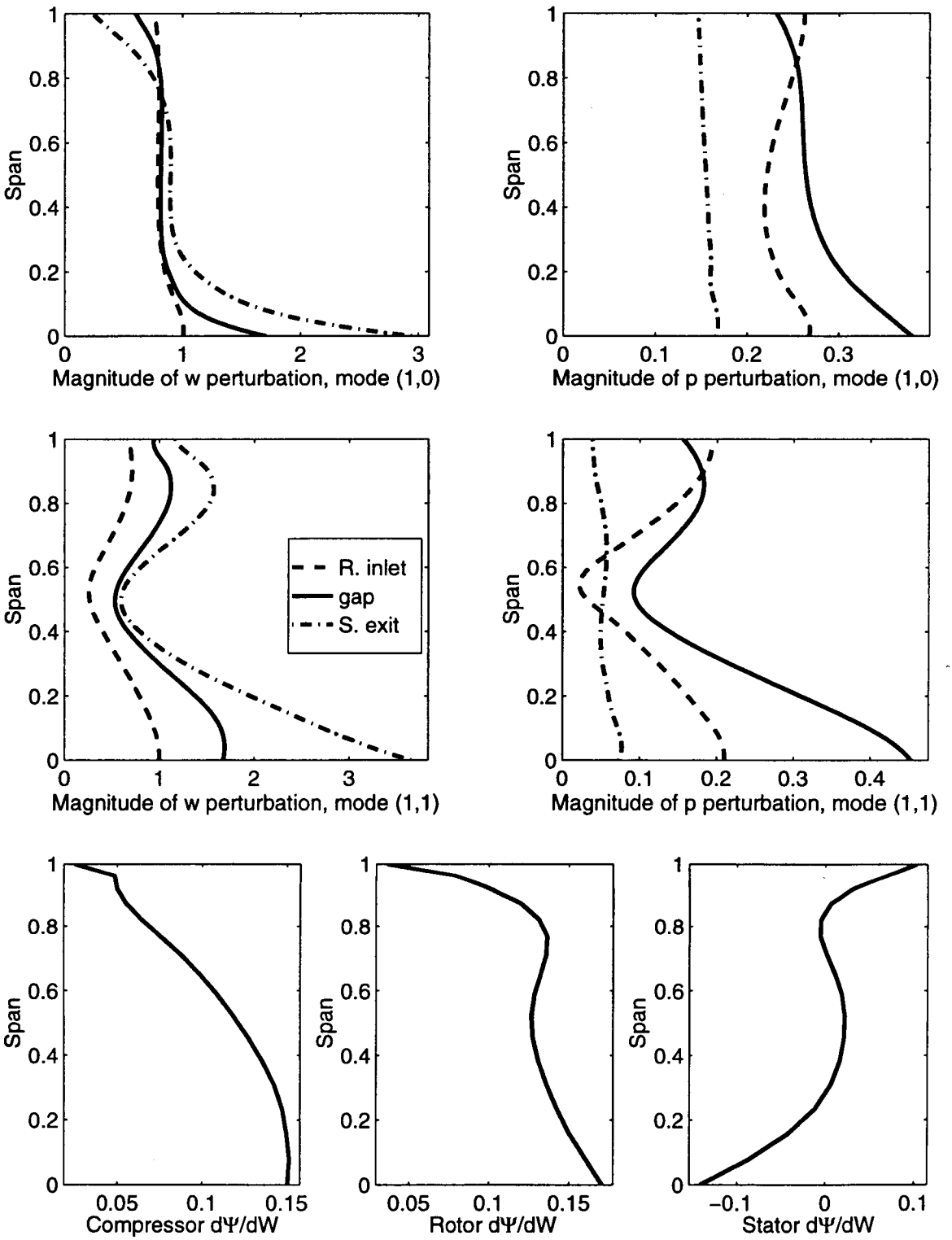


**Figure M-27:** (1,0) and (1,1) mode shapes, and slope variations for parametric study L.

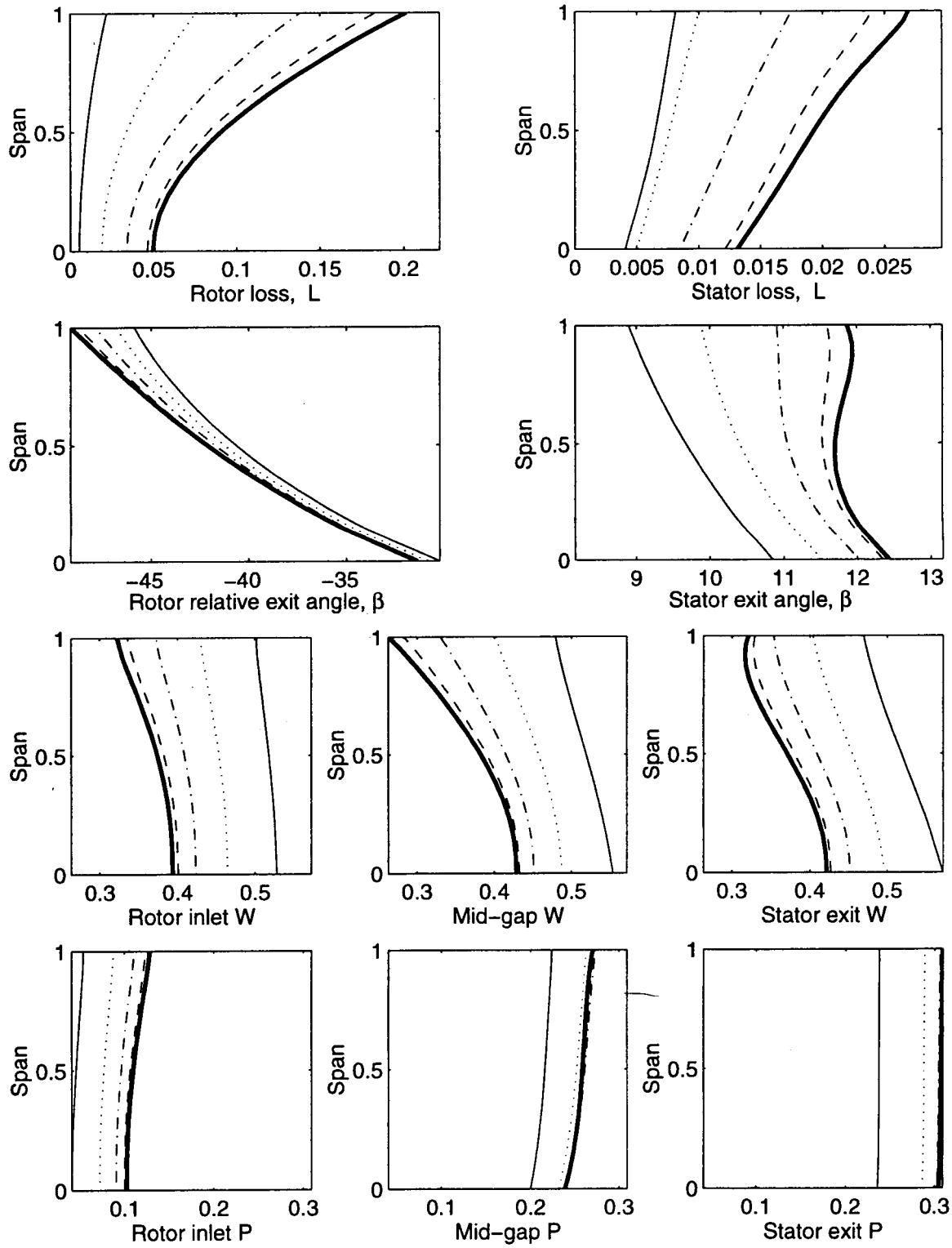


**Figure M-28:** Spanwise profiles of the background flow fields for parametric study P.

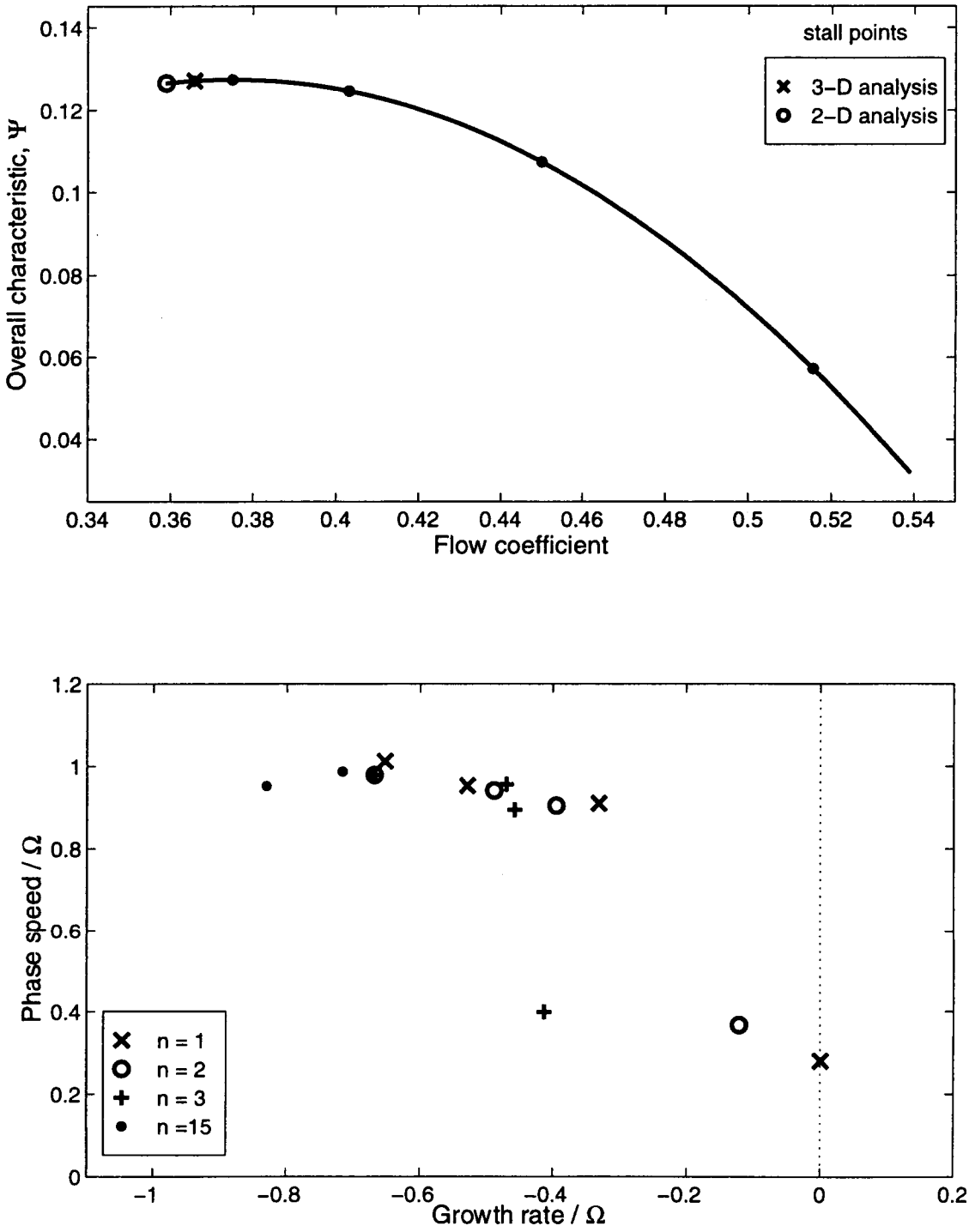


**Figure M-29:** Points of neutral stability on overall characteristic, and eigenvalues at stall for parametric study P.

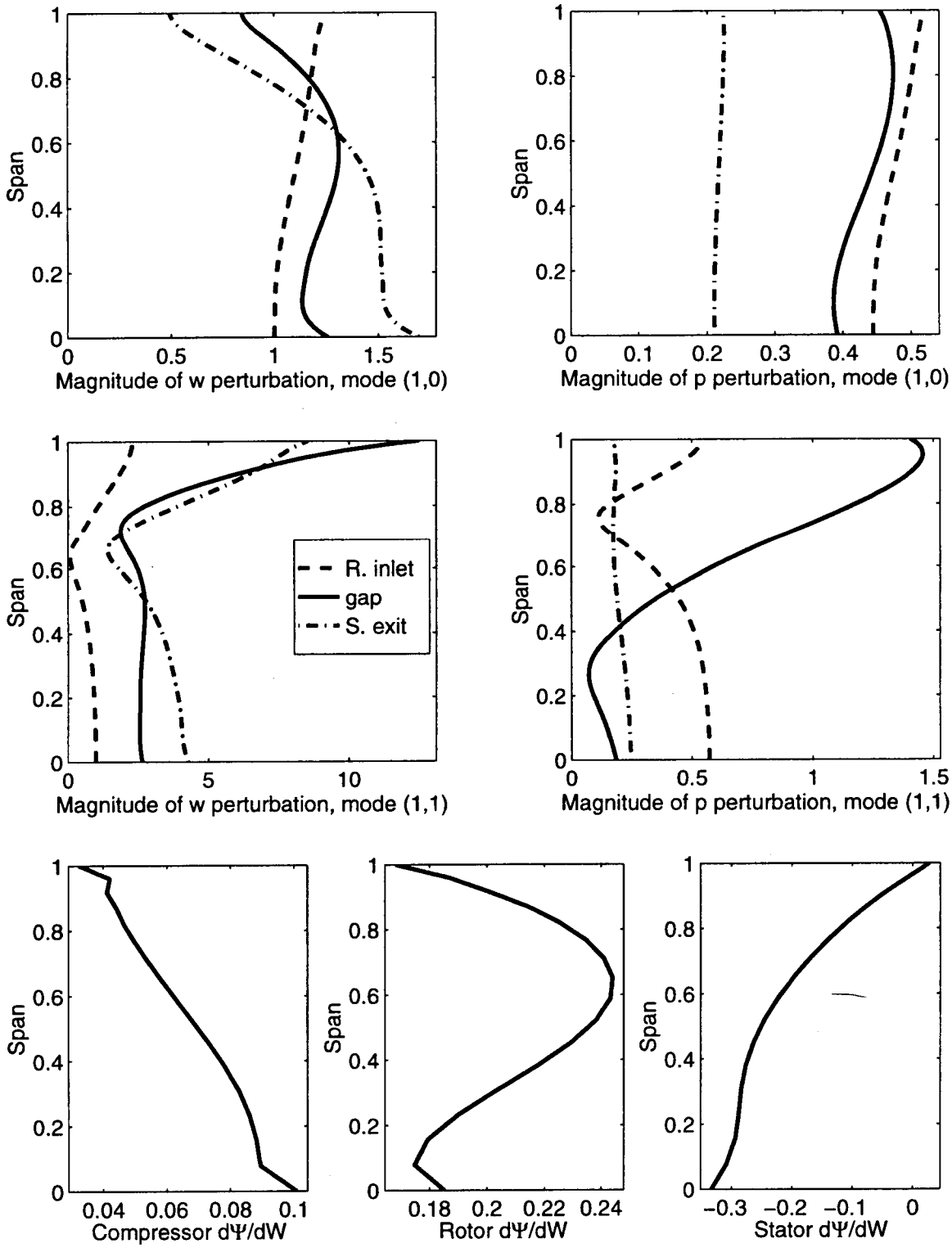


**Figure M-30:** (1,0) and (1,1) mode shapes, and slope variations for parametric study P.

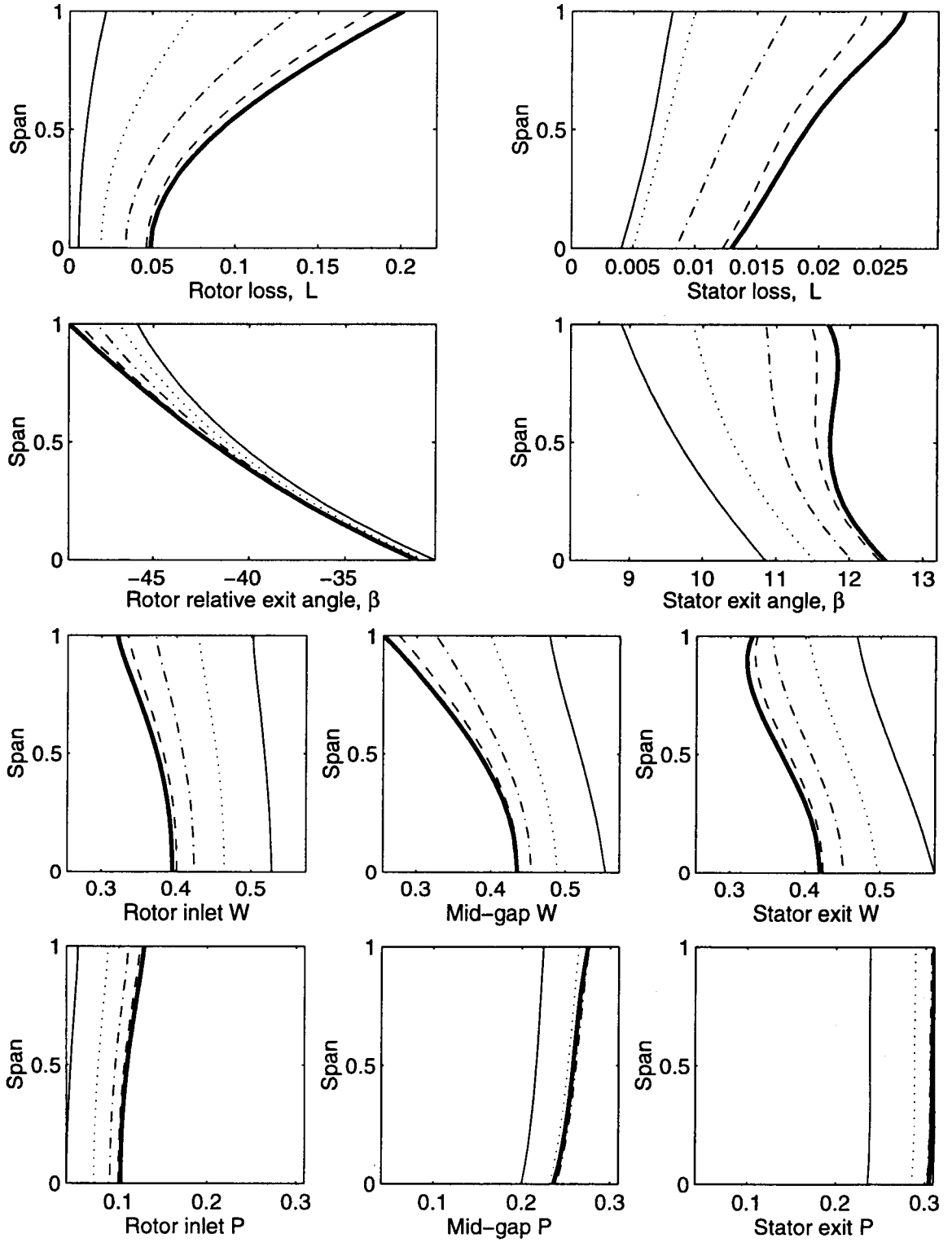


**Figure M-31:** Spanwise profiles of the background flow fields for parametric study Q.

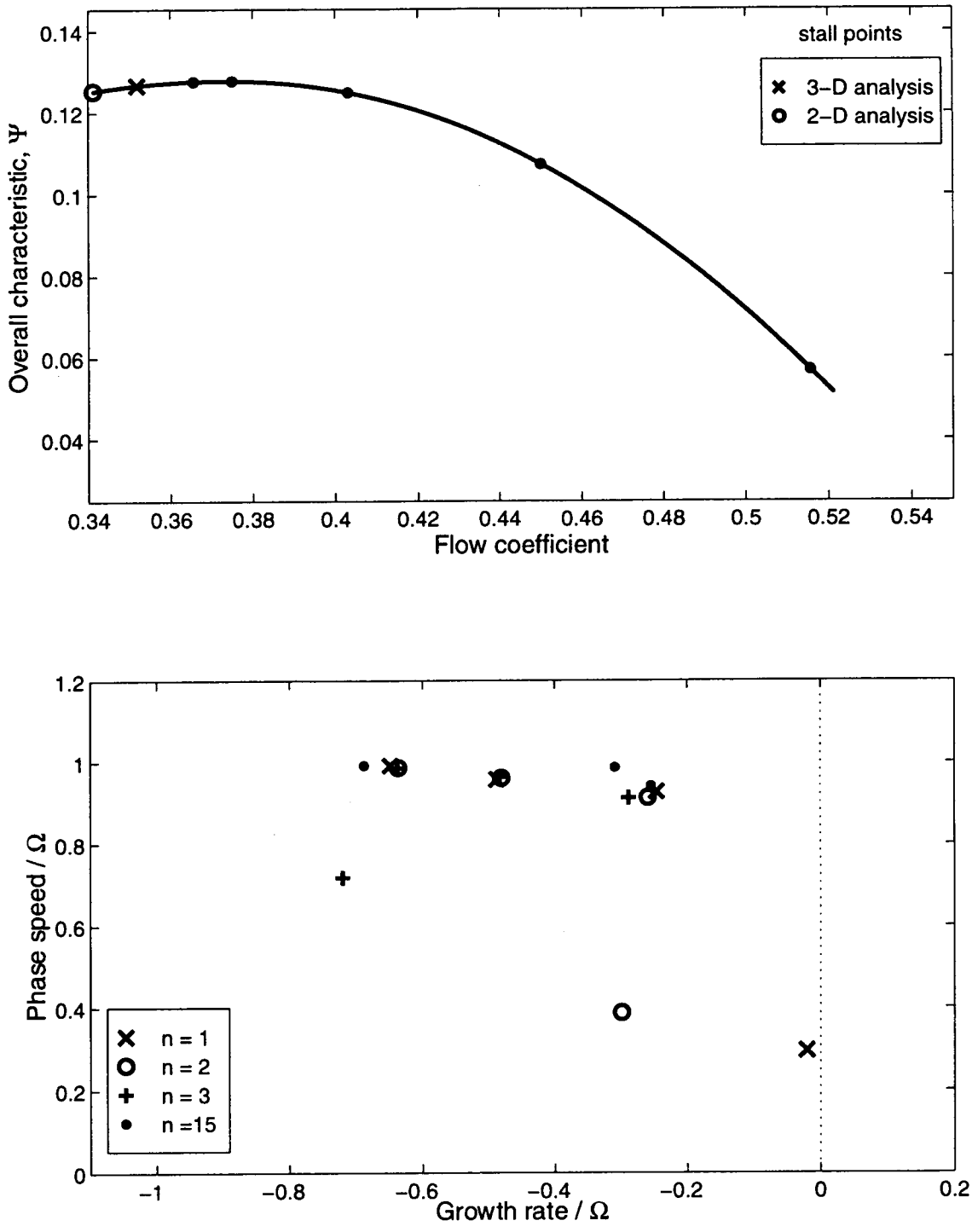


**Figure M-32:** Points of neutral stability on overall characteristic, and eigenvalues at stall for parametric study Q.

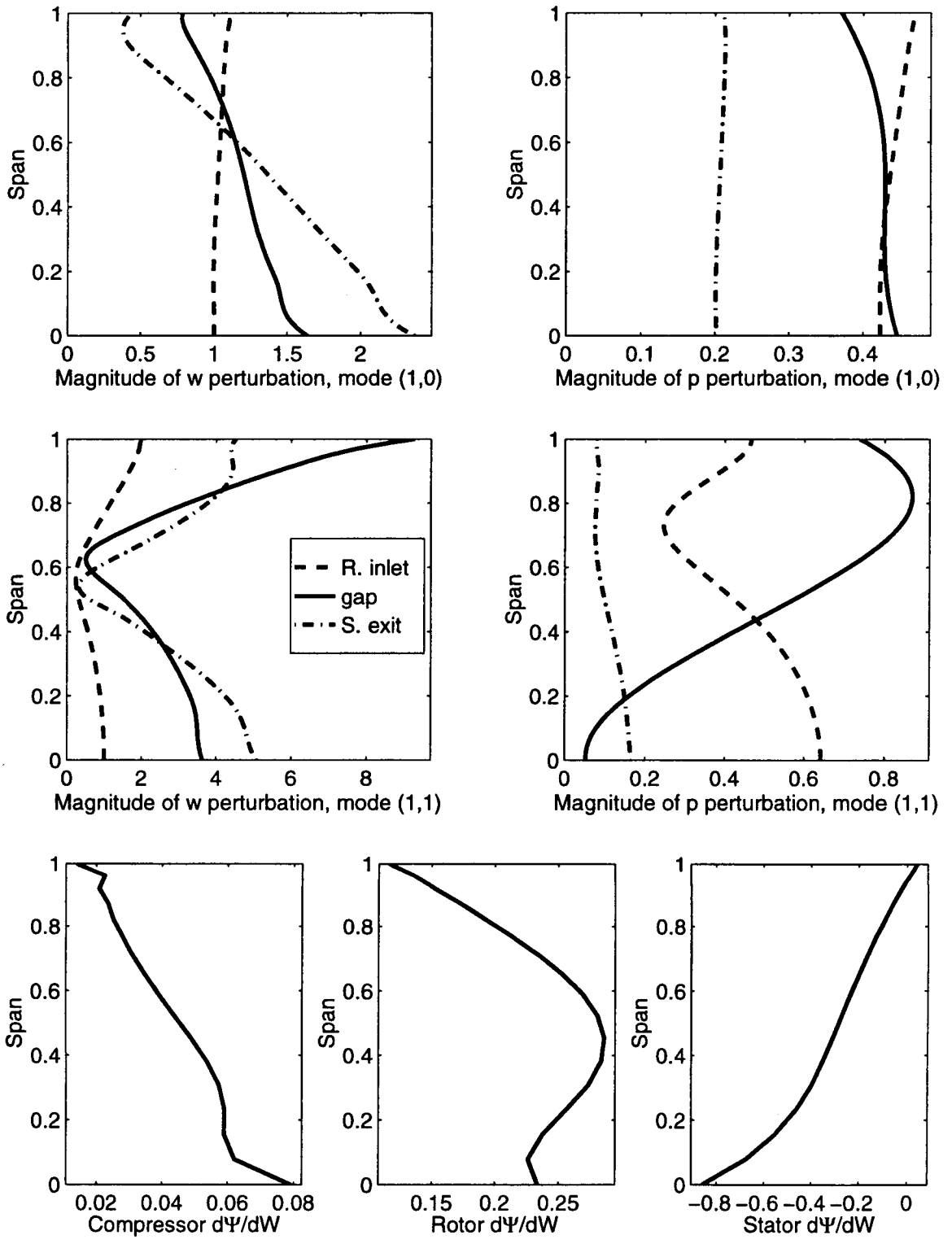


**Figure M-33:** (1,0) and (1,1) mode shapes, and slope variations for parametric study Q.

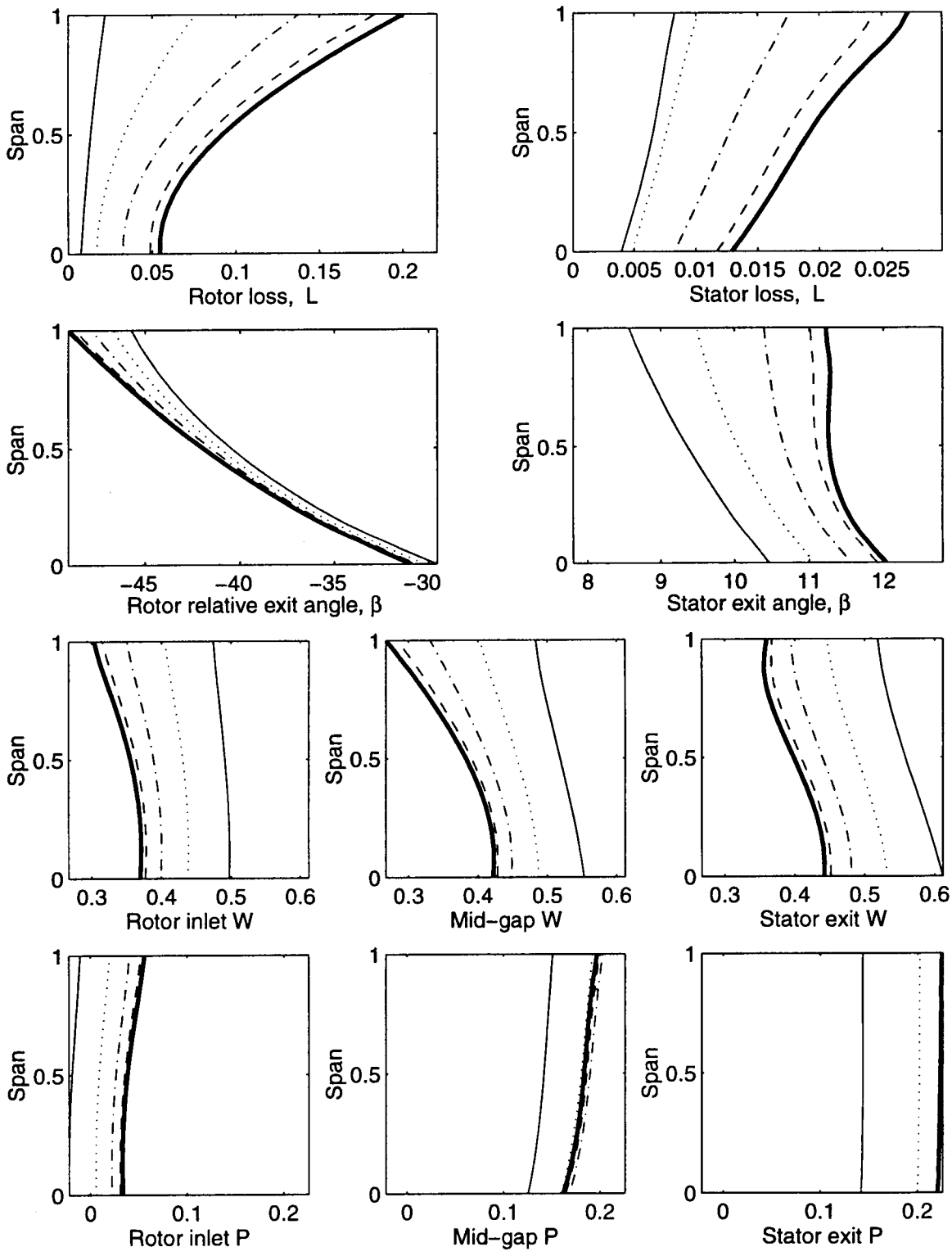


**Figure M-34:** Spanwise profiles of the background flow fields for parametric study R.

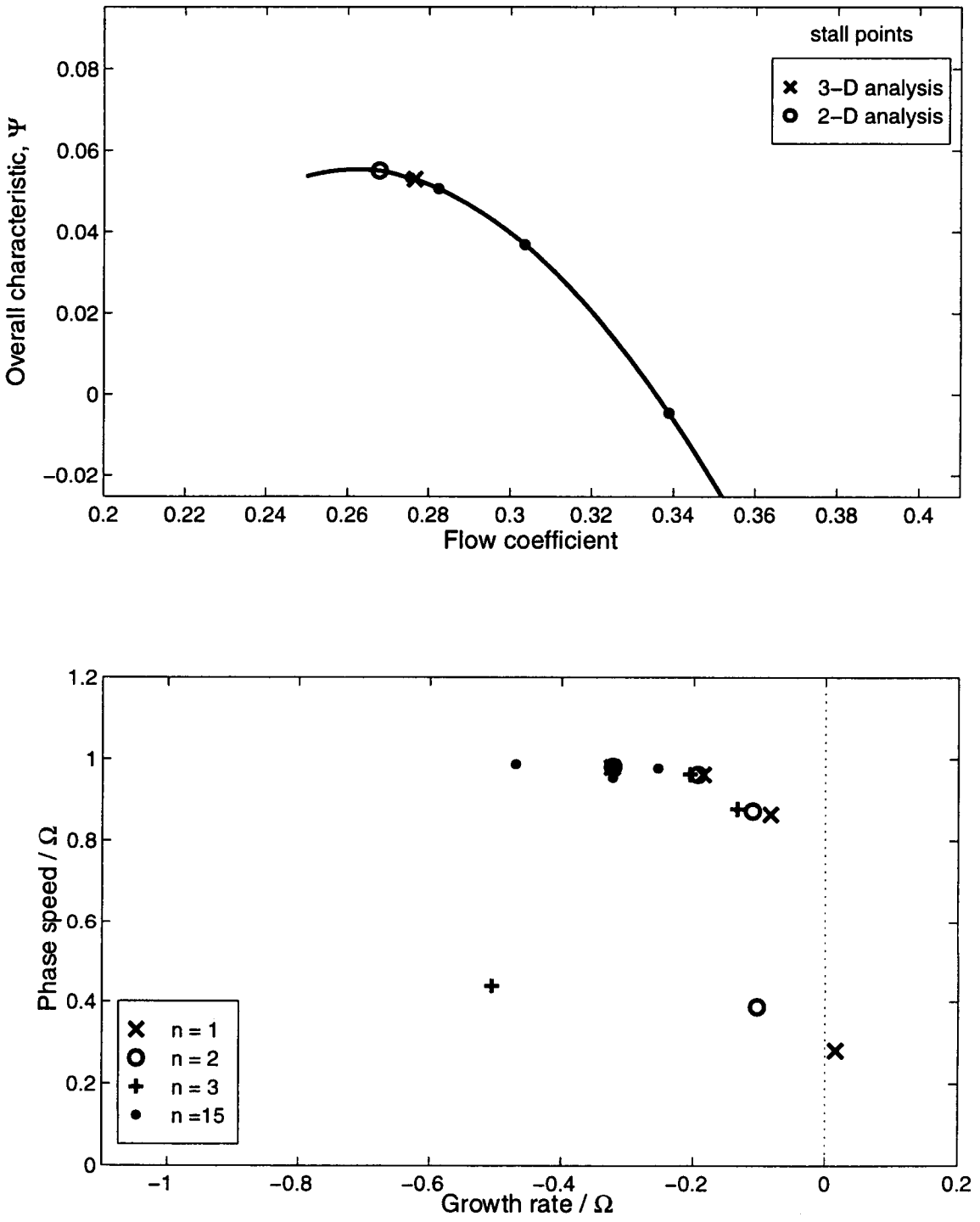


**Figure M-35:** Points of neutral stability on overall characteristic, and eigenvalues at stall for parametric study R.

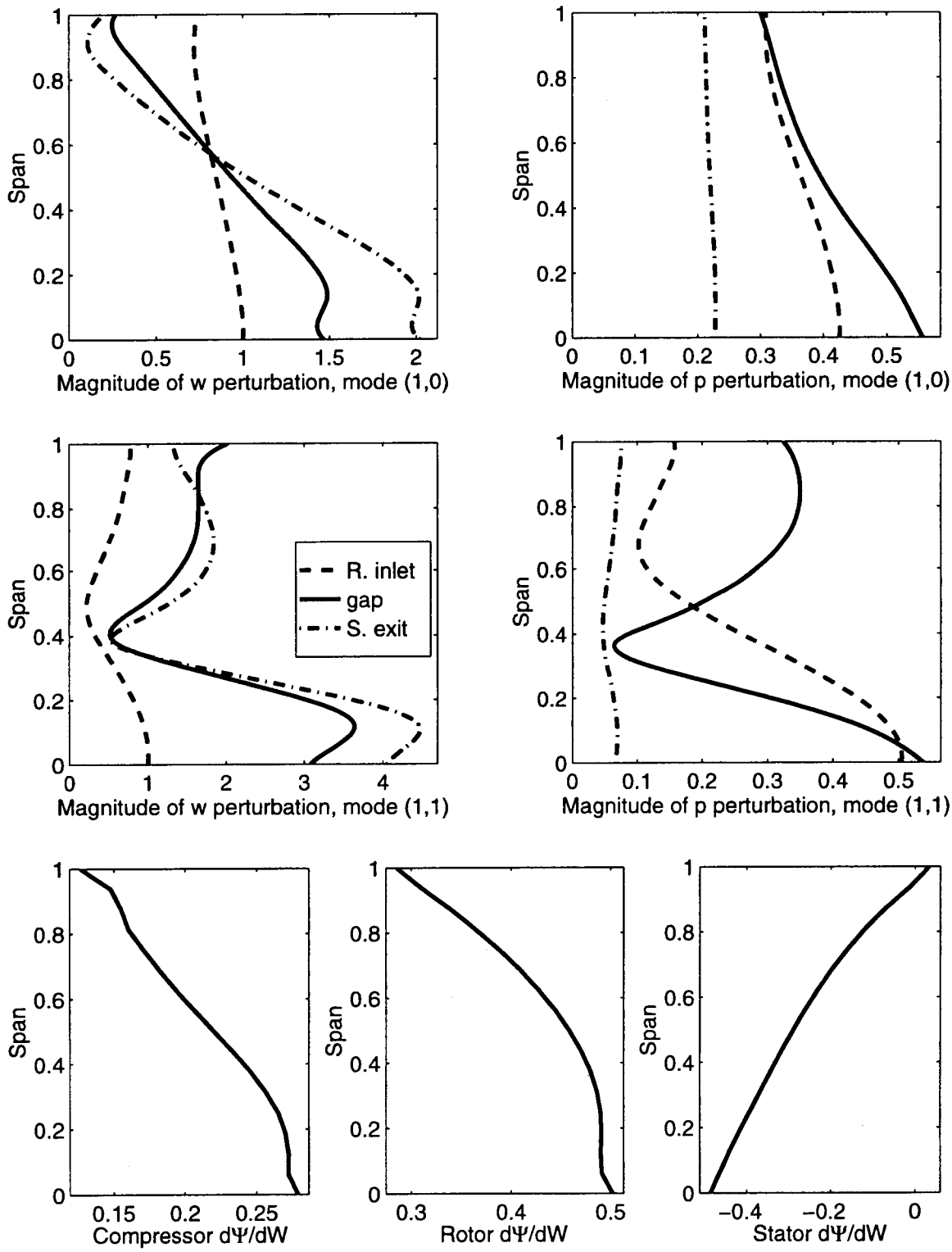


**Figure M-36:** (1,0) and (1,1) mode shapes, and slope variations for parametric study R.

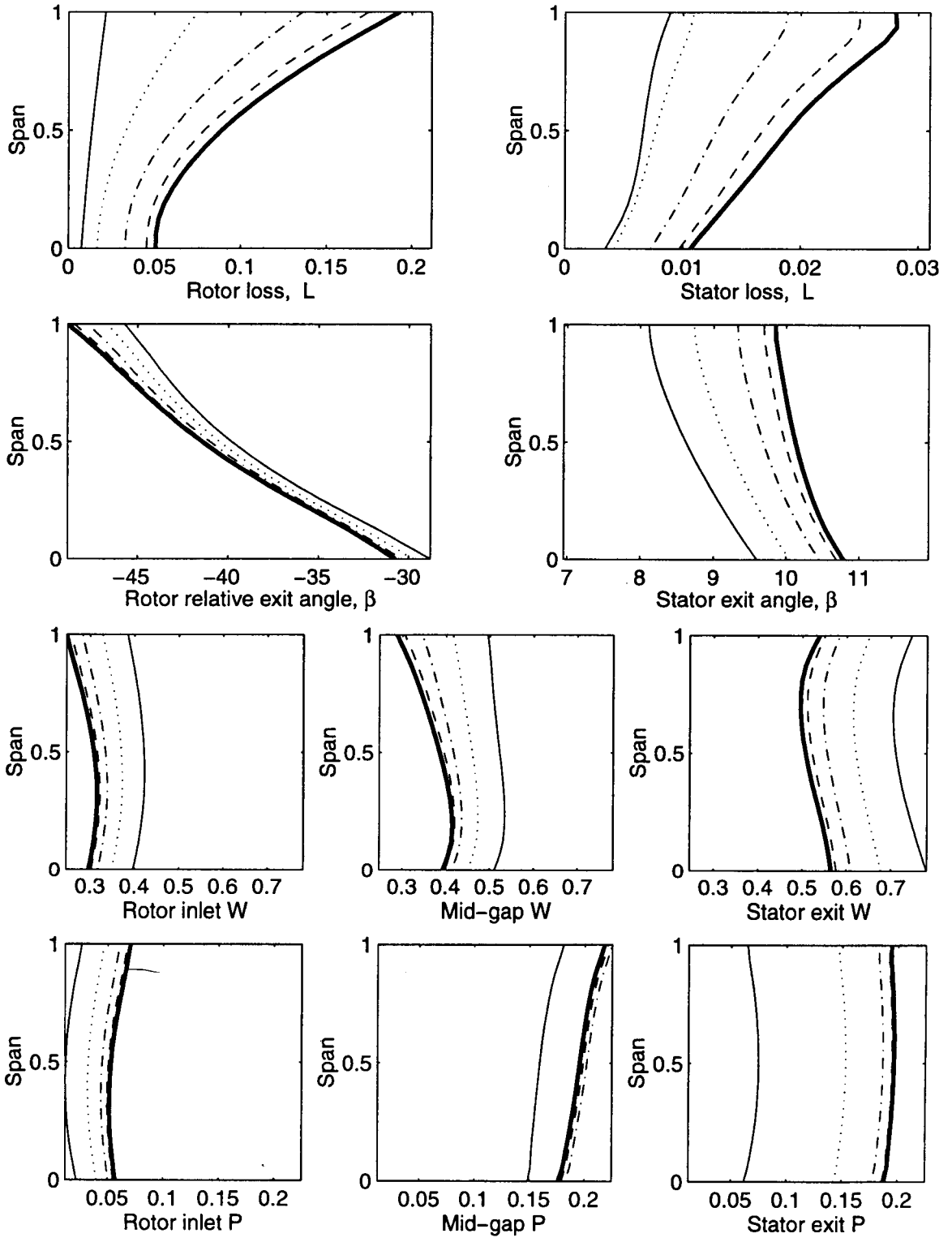


**Figure M-37:** Spanwise profiles of the background flow fields for parametric study S.

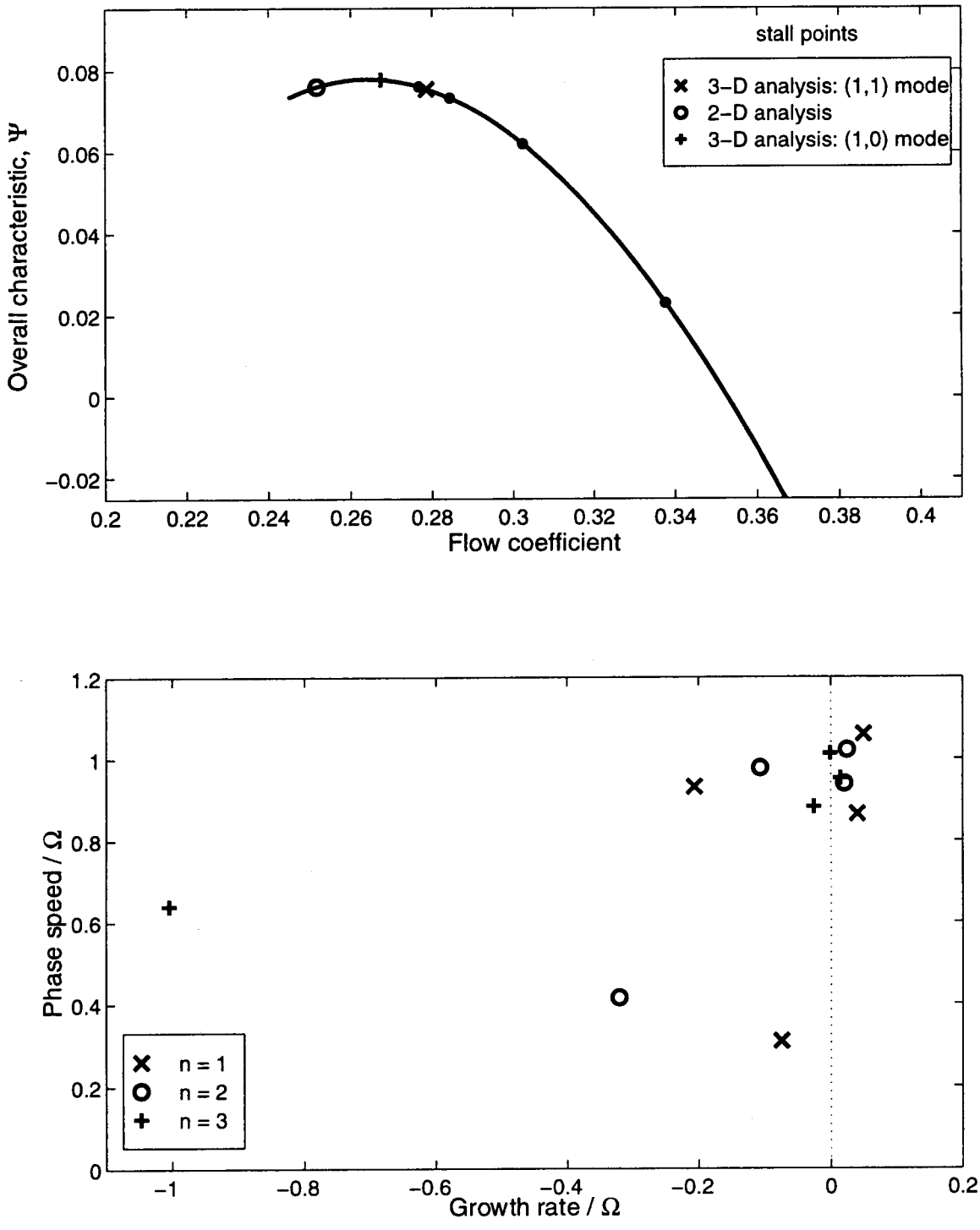


**Figure M-38:** Points of neutral stability on overall characteristic, and eigenvalues at stall for parametric study S.

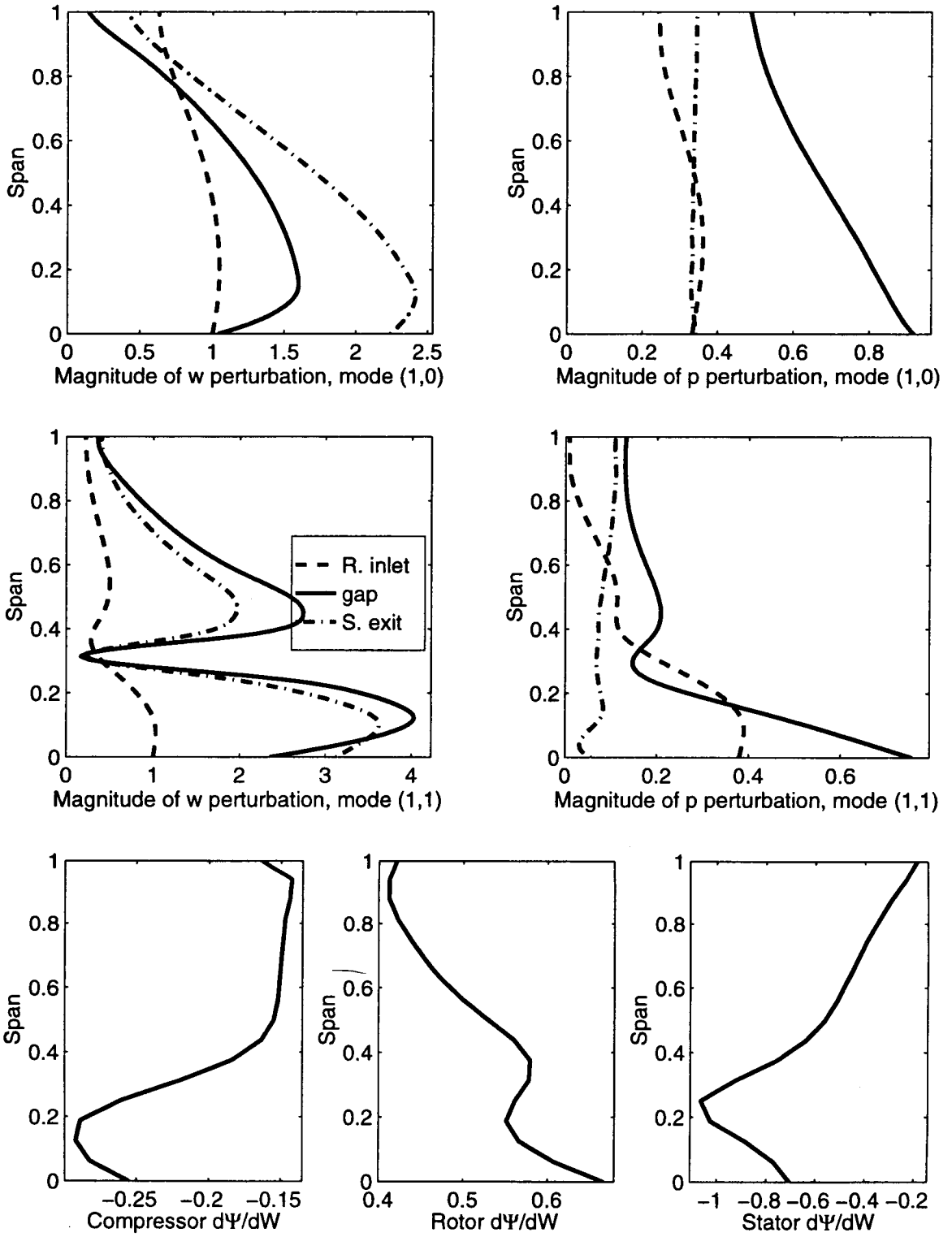


**Figure M-39:** (1,0) and (1,1) mode shapes, and slope variations for parametric study S.

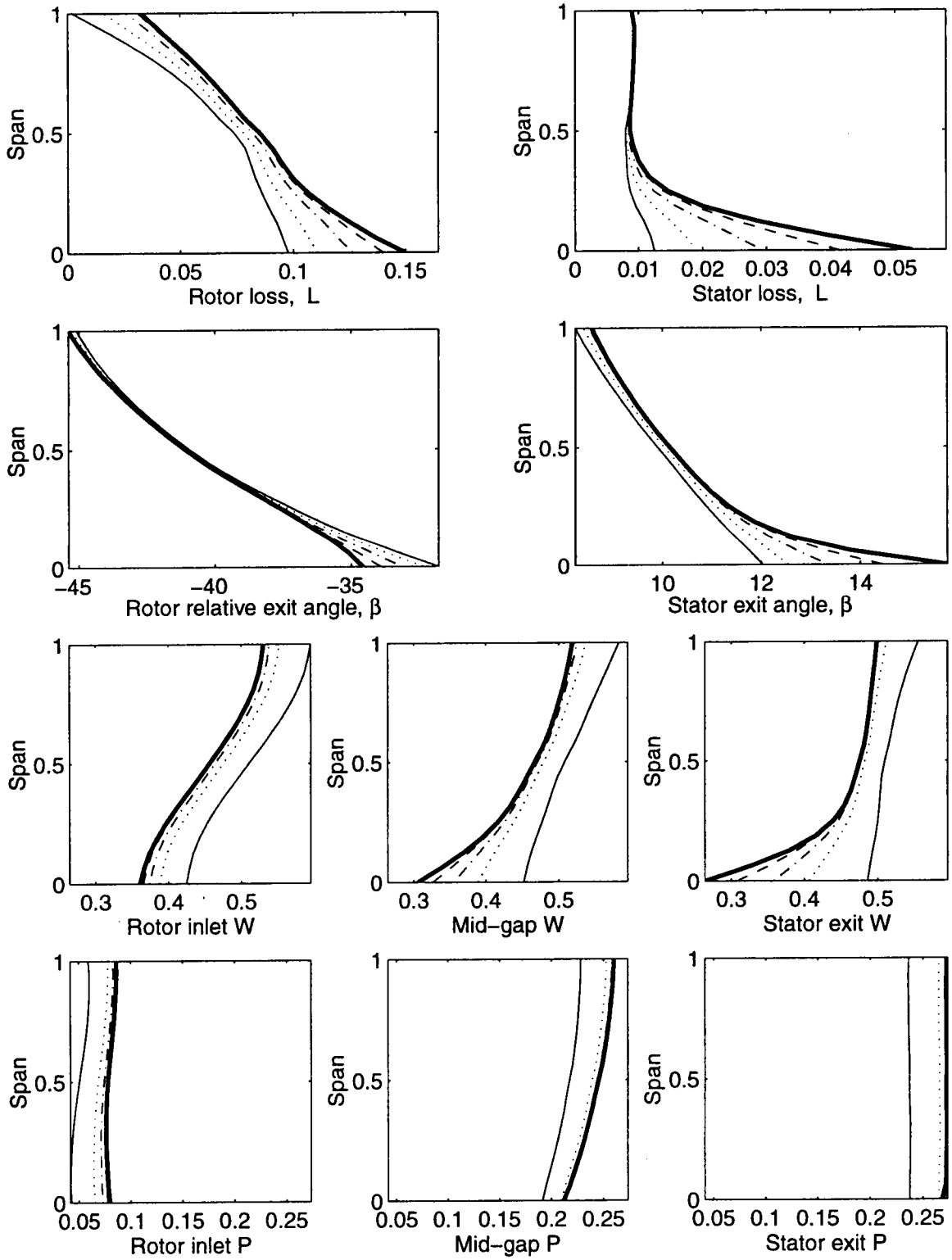


**Figure M-40:** Spanwise profiles of the background flow fields for parametric study T.

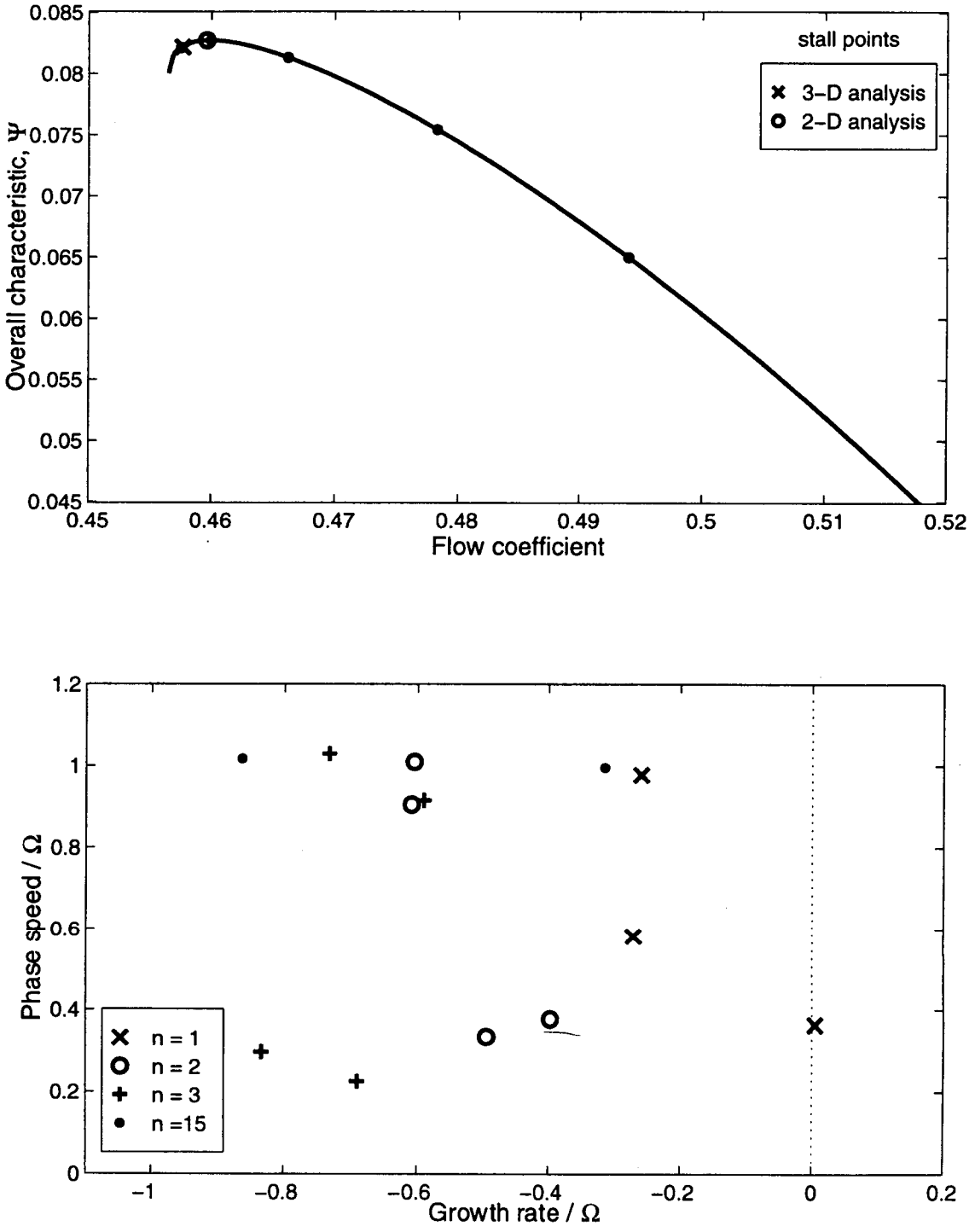


**Figure M-41:** Points of neutral stability on overall characteristic, and eigenvalues at stall for parametric study T.

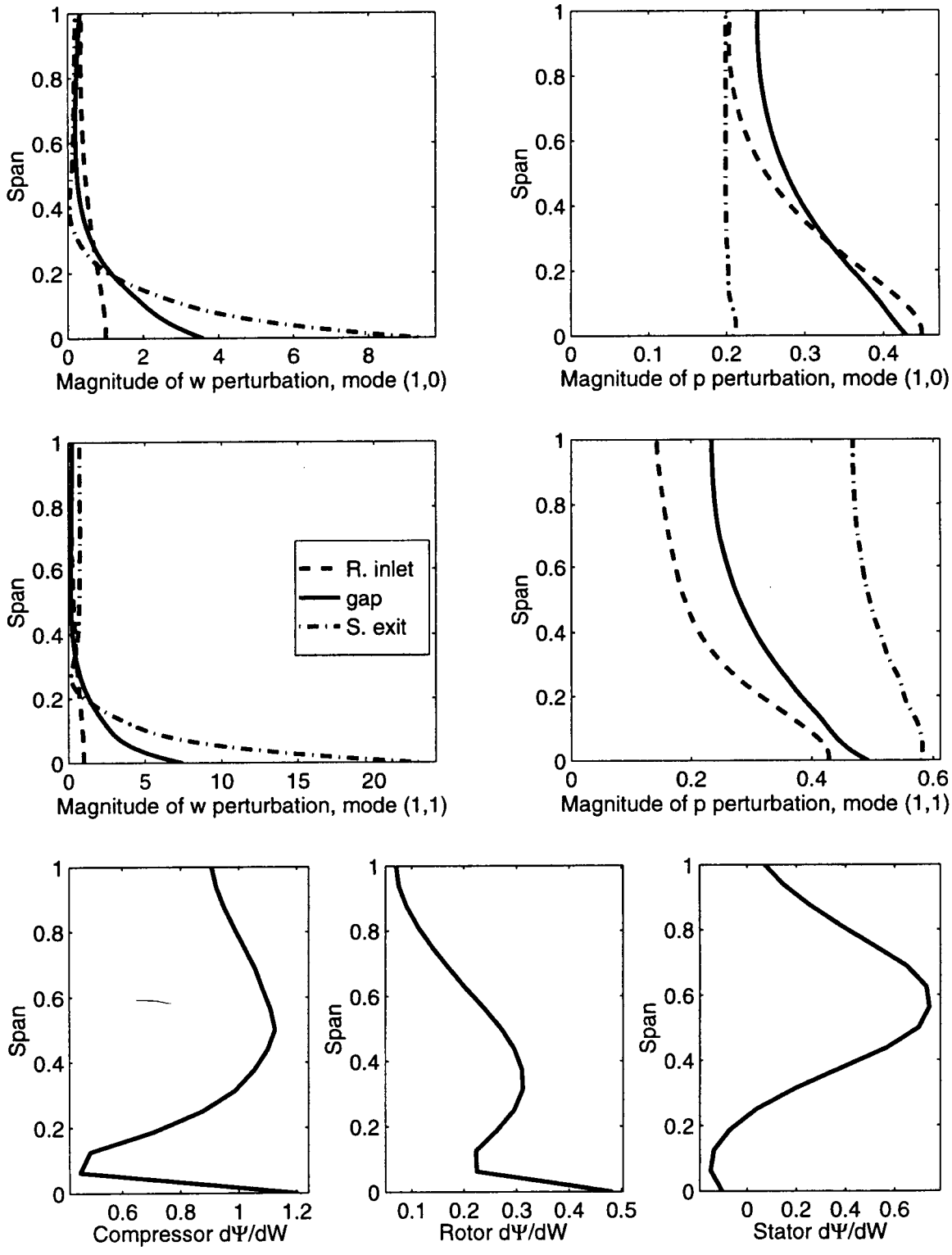


**Figure M-42:** (1,0) and (1,1) mode shapes, and slope variations for parametric study T.

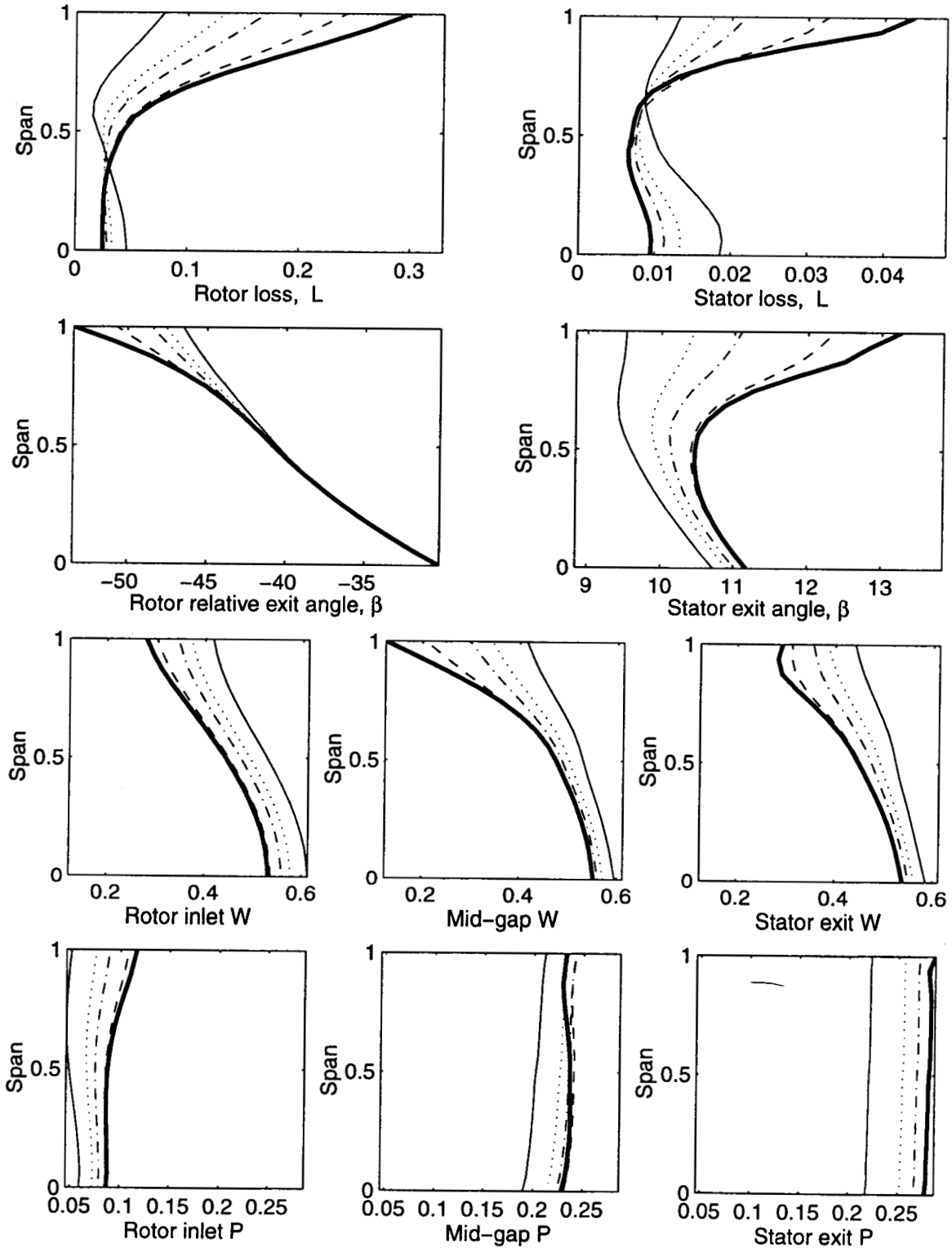


**Figure M-43:** Spanwise profiles of the background flow fields for parametric study U.

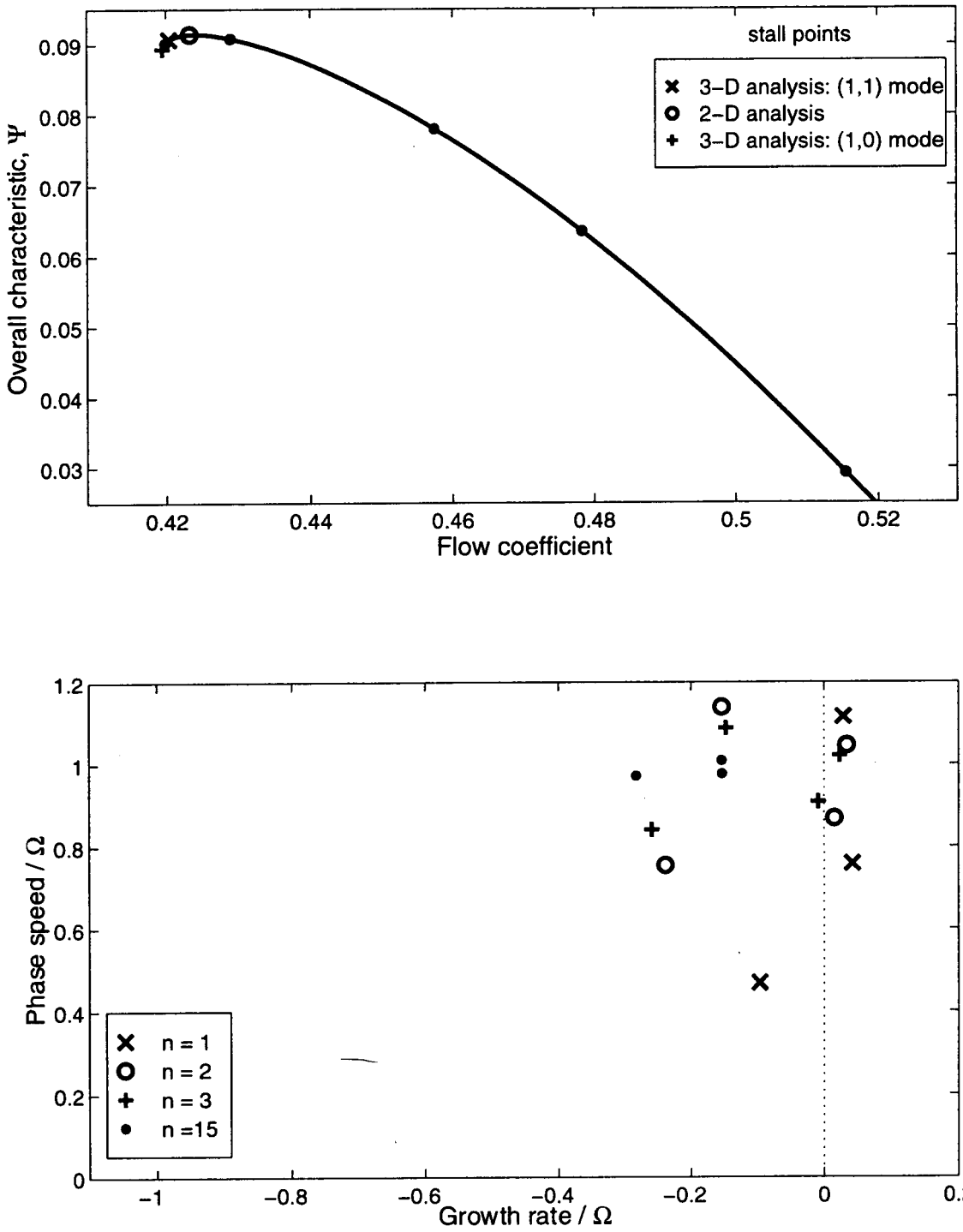


**Figure M-44:** Points of neutral stability on overall characteristic, and eigenvalues at stall for parametric study U.

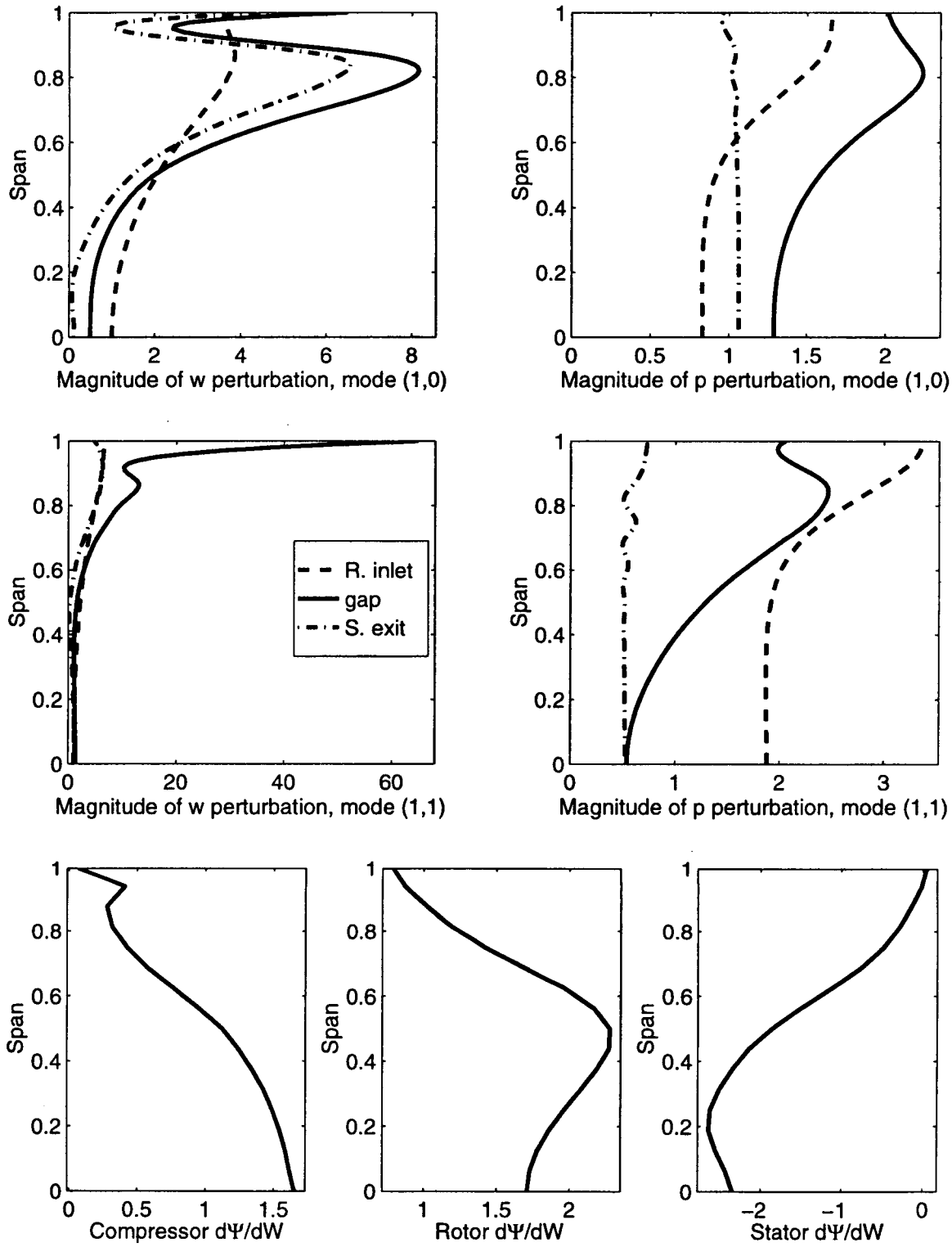


**Figure M-45:** (1,0) and (1,1) mode shapes, and slope variations for parametric study U.

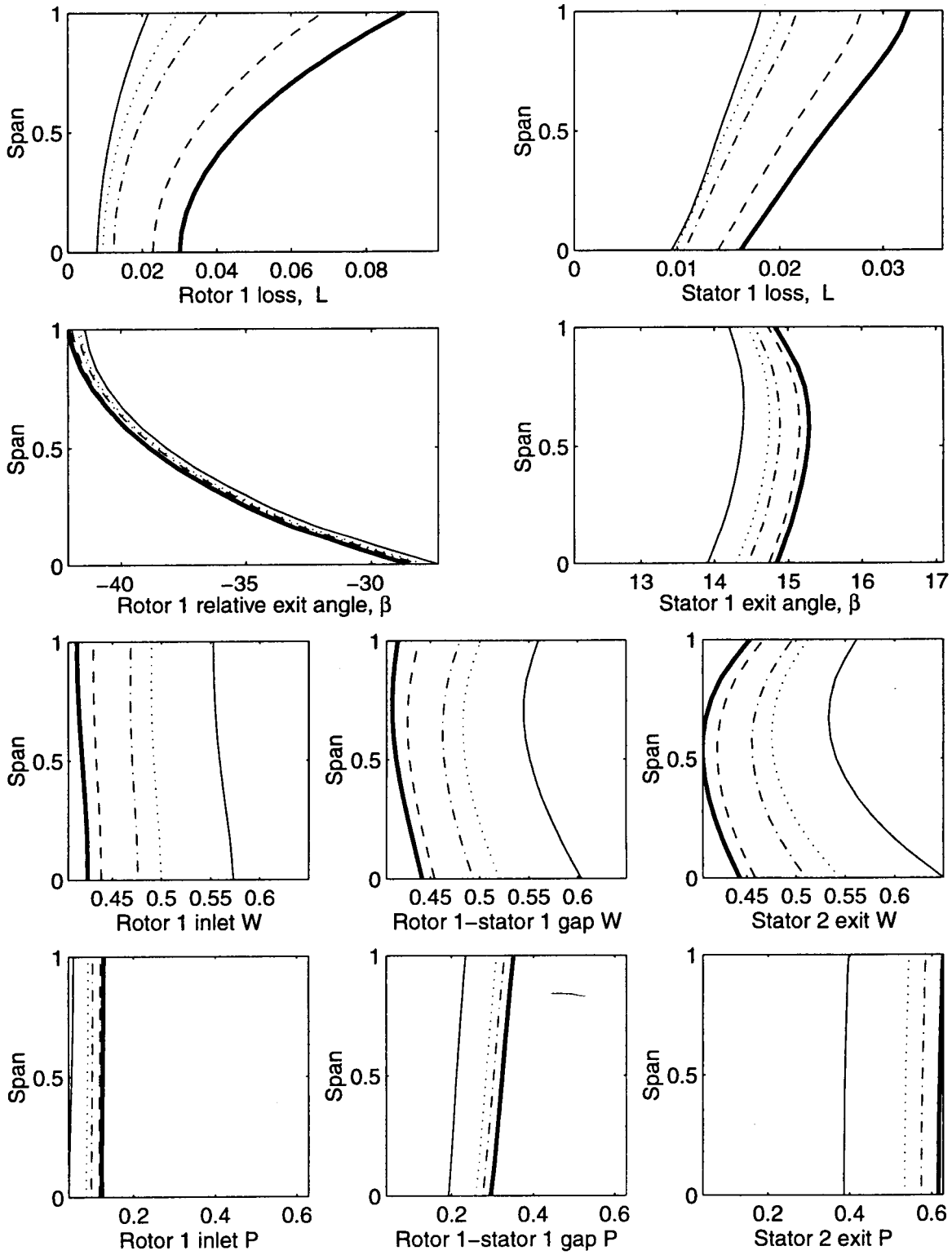


**Figure M-46:** Spanwise profiles of the background flow fields for parametric study V.

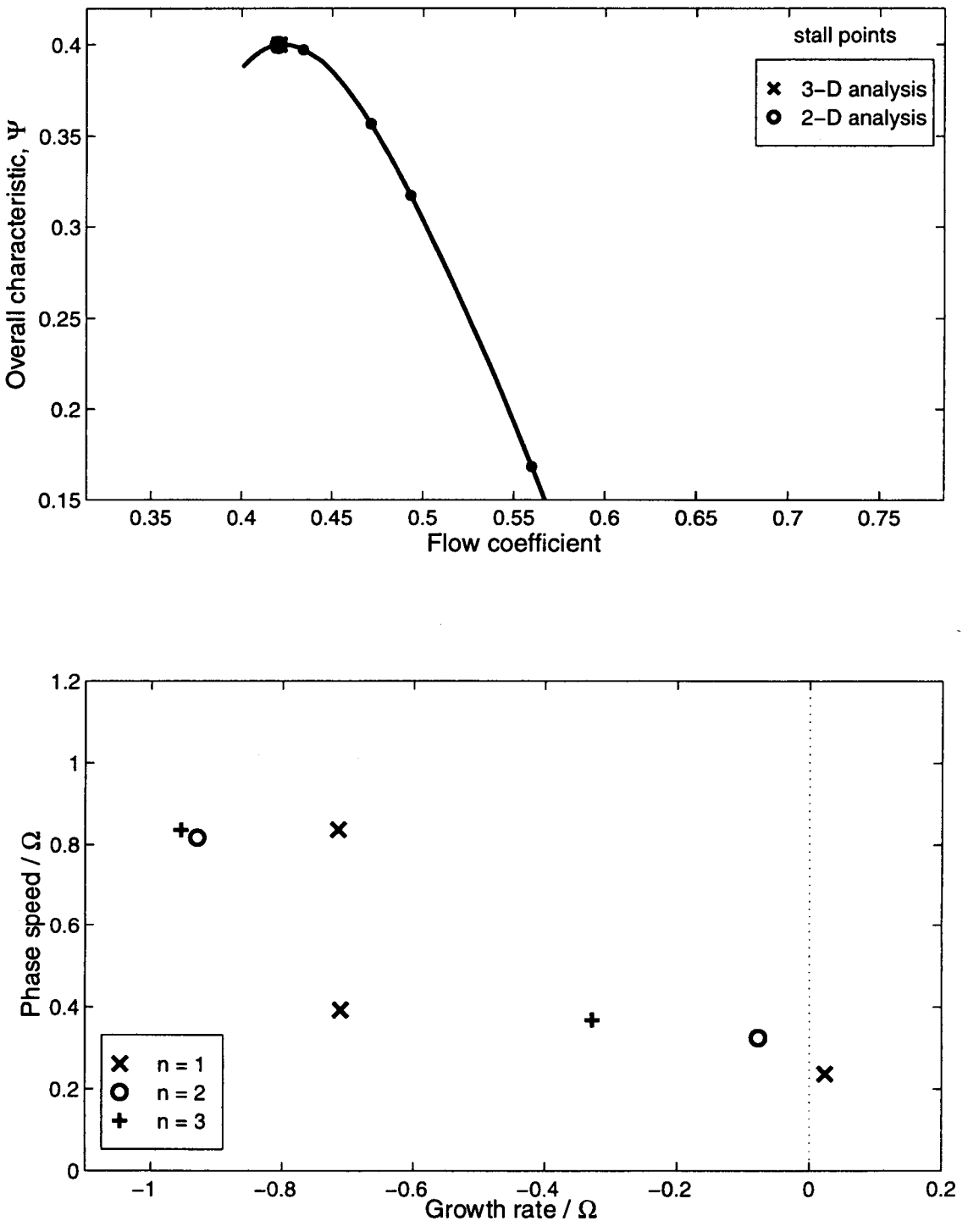


**Figure M-47:** Points of neutral stability on overall characteristic, and eigenvalues at stall for parametric study V.

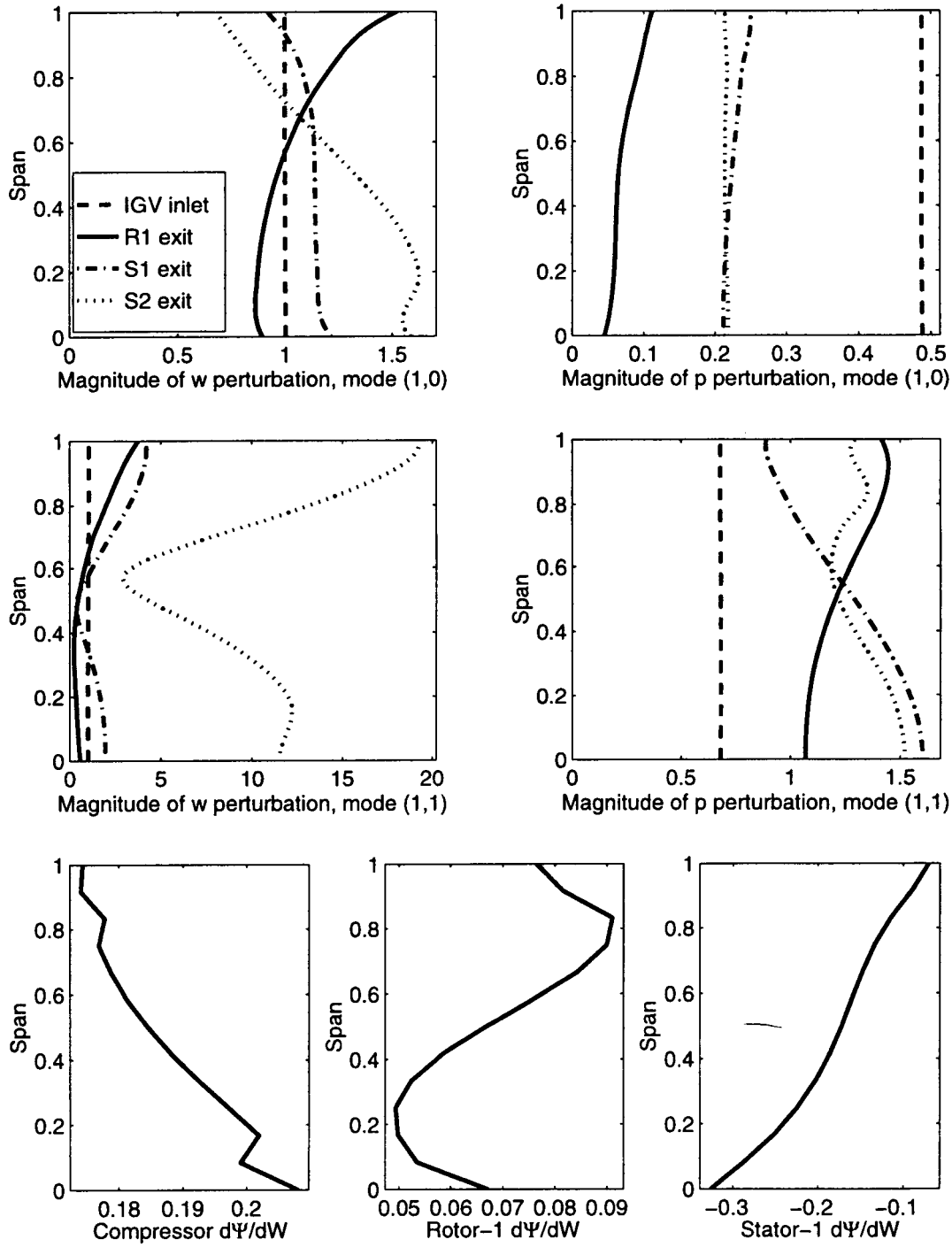


**Figure M-48:** (1,0) and (1,1) mode shapes, and slope variations for parametric study V.

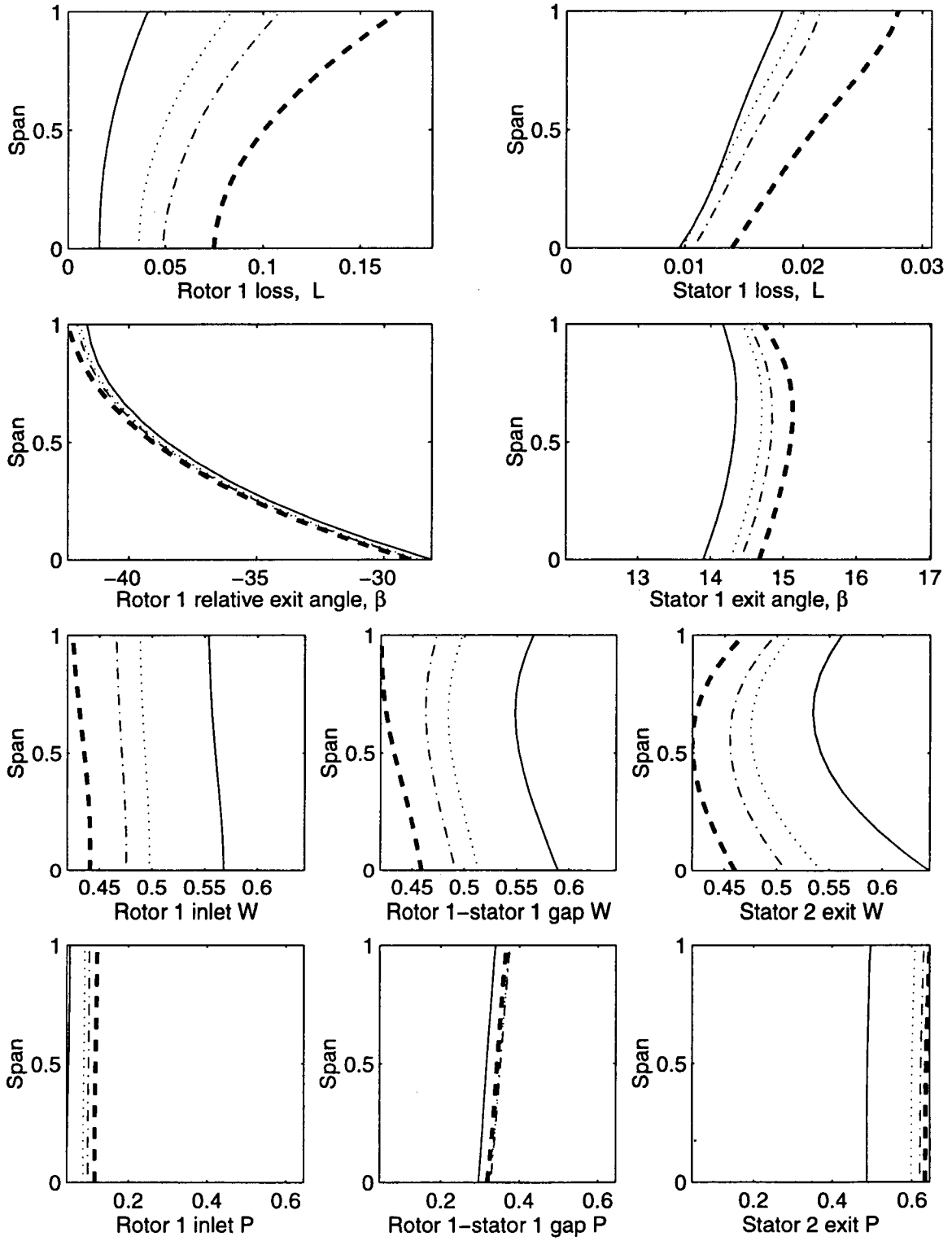


**Figure M-49:** Spanwise profiles of the background flow fields for parametric study W.

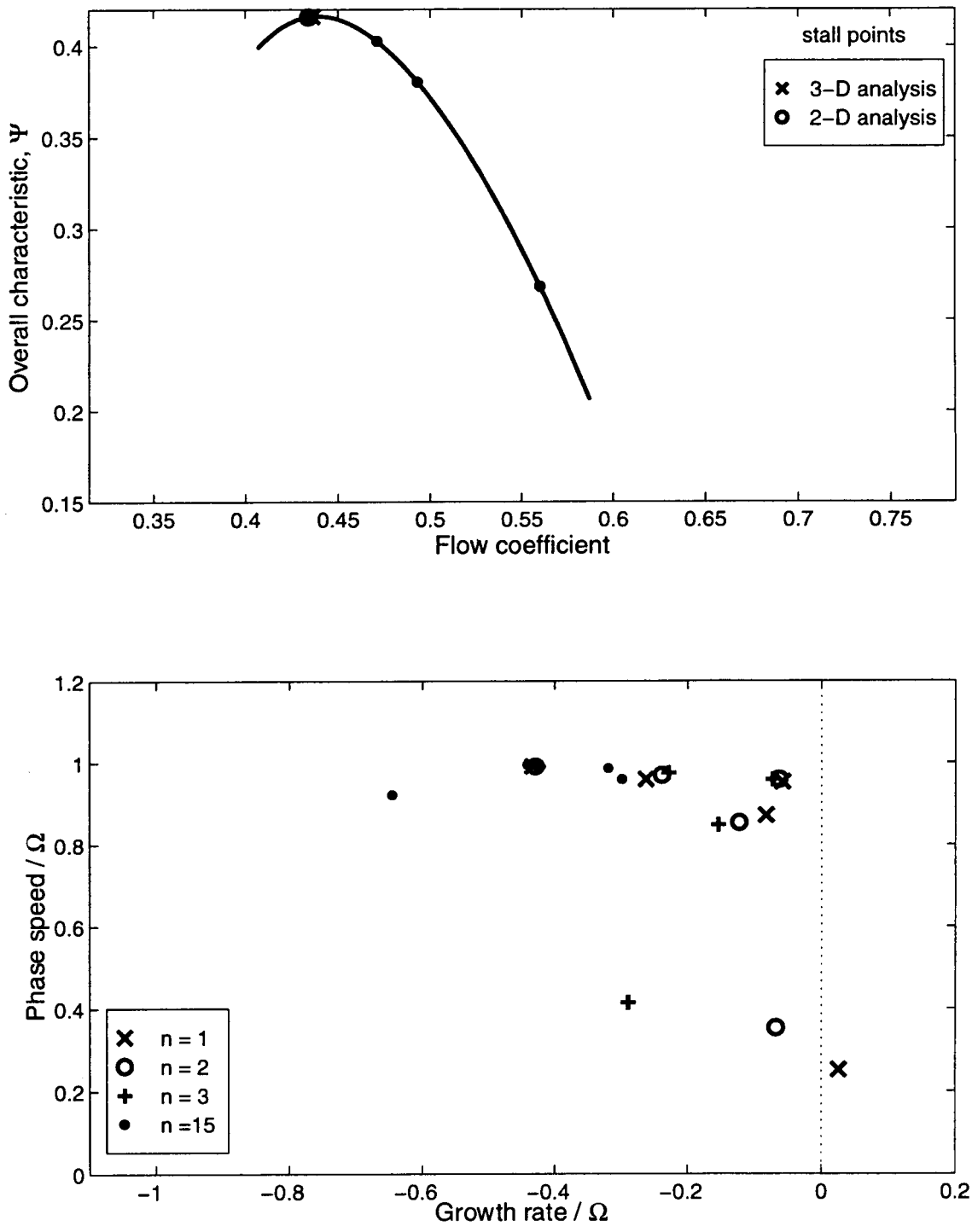


**Figure M-50:** Points of neutral stability on overall characteristic, and eigenvalues at stall for parametric study W.

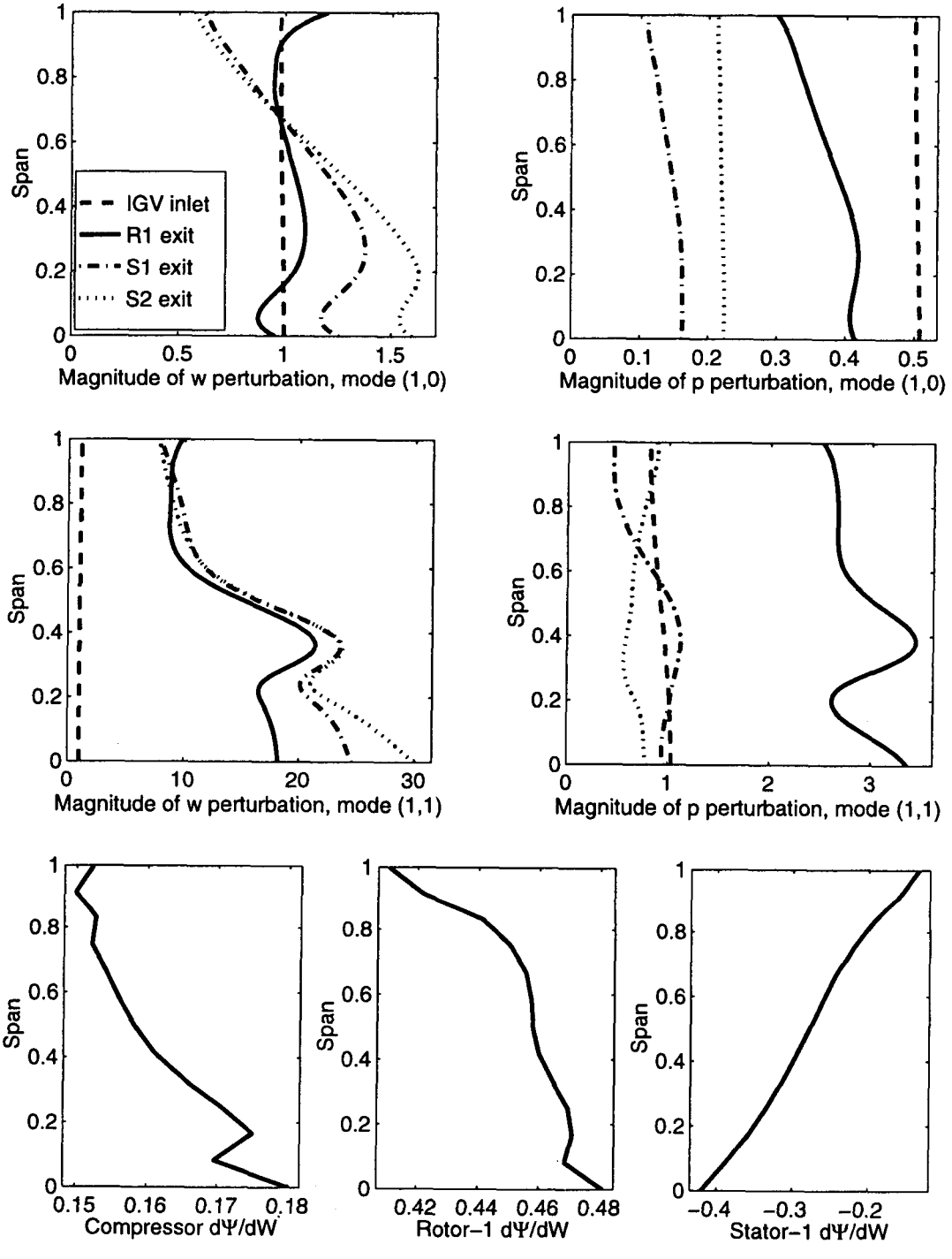


**Figure M-51:** (1,0) and (1,1) mode shapes, and slope variations for parametric study W.

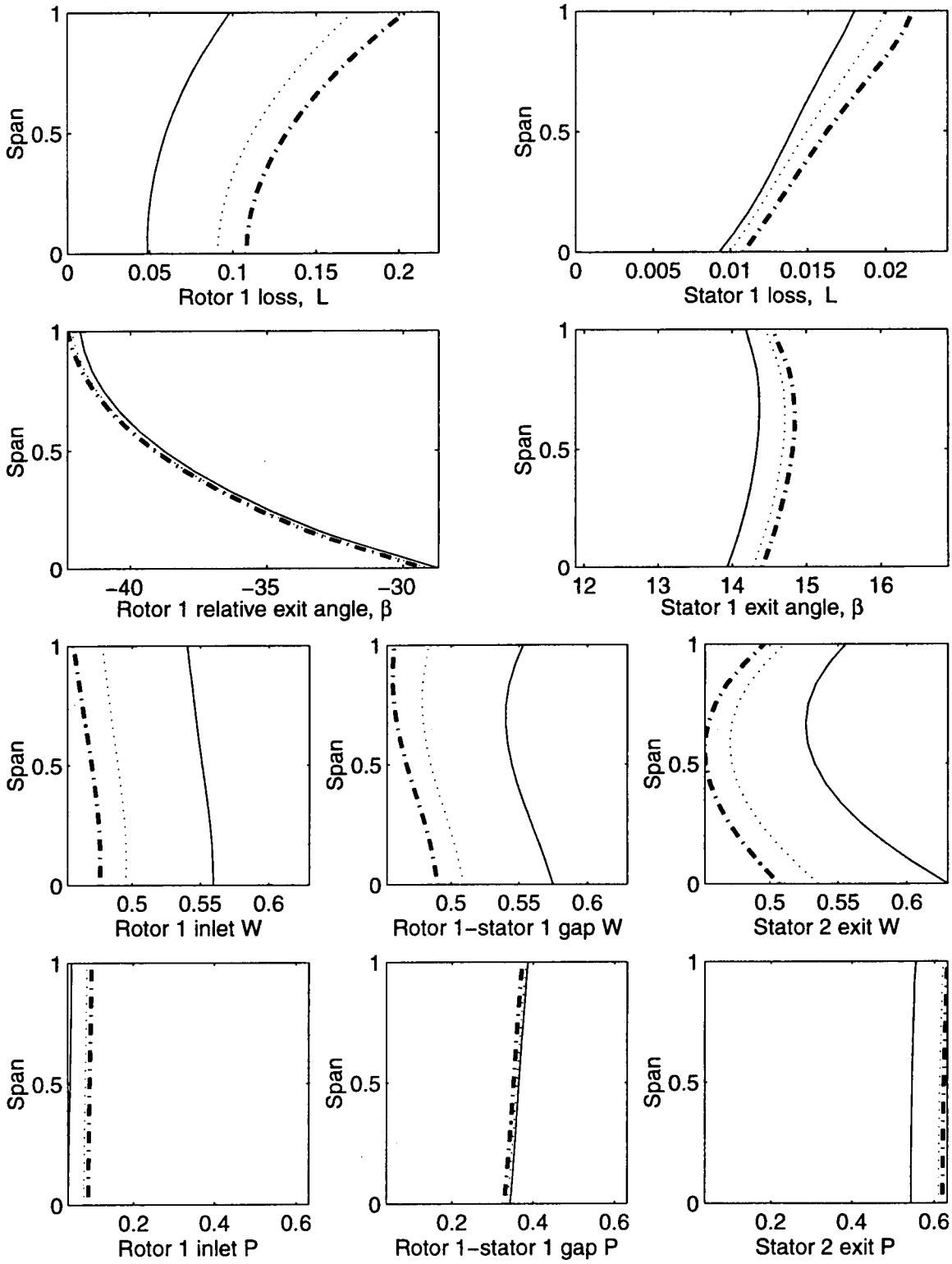


**Figure M-52:** Spanwise profiles of the background flow fields for parametric study X.

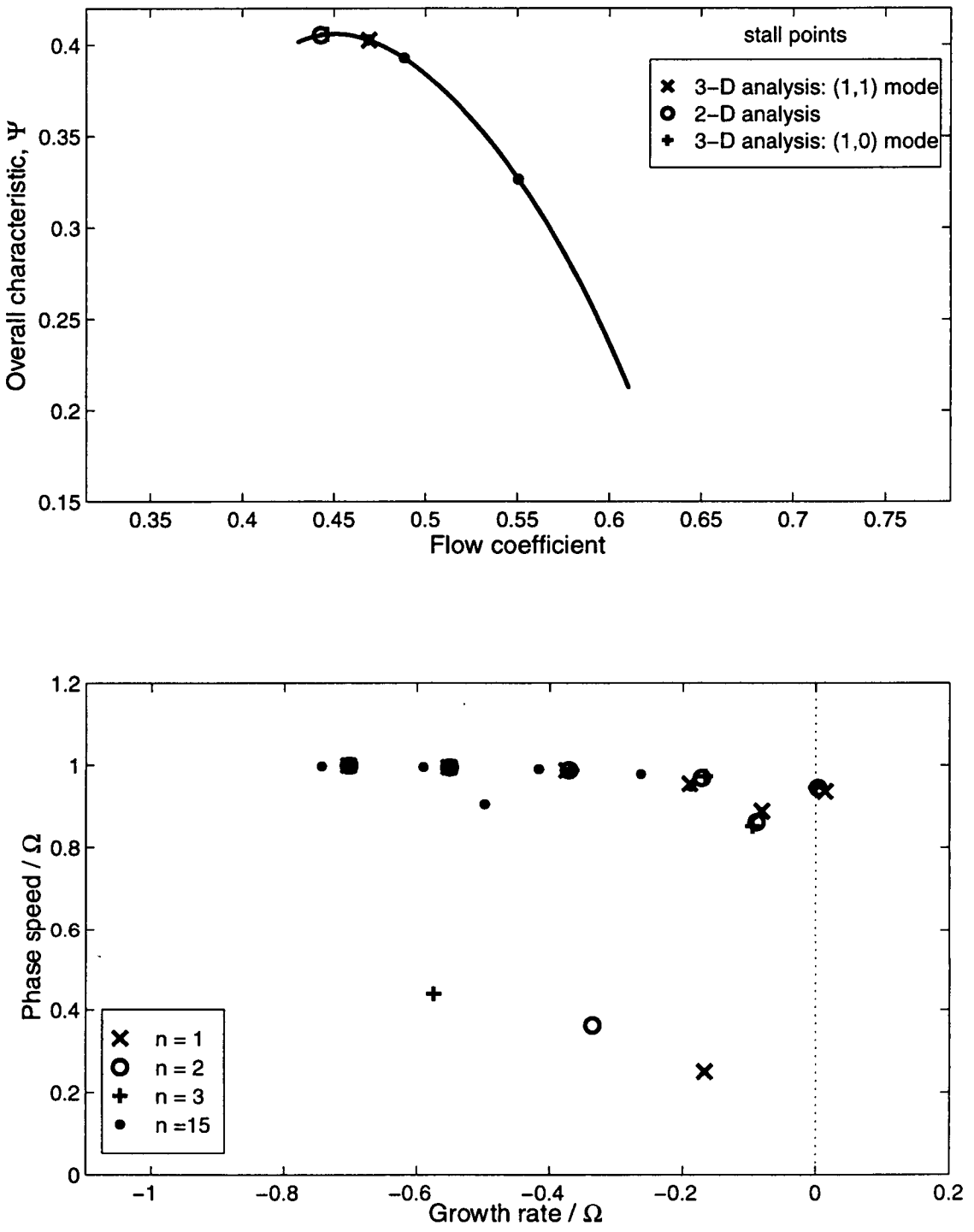


**Figure M-53:** Points of neutral stability on overall characteristic, and eigenvalues at stall for parametric study X.

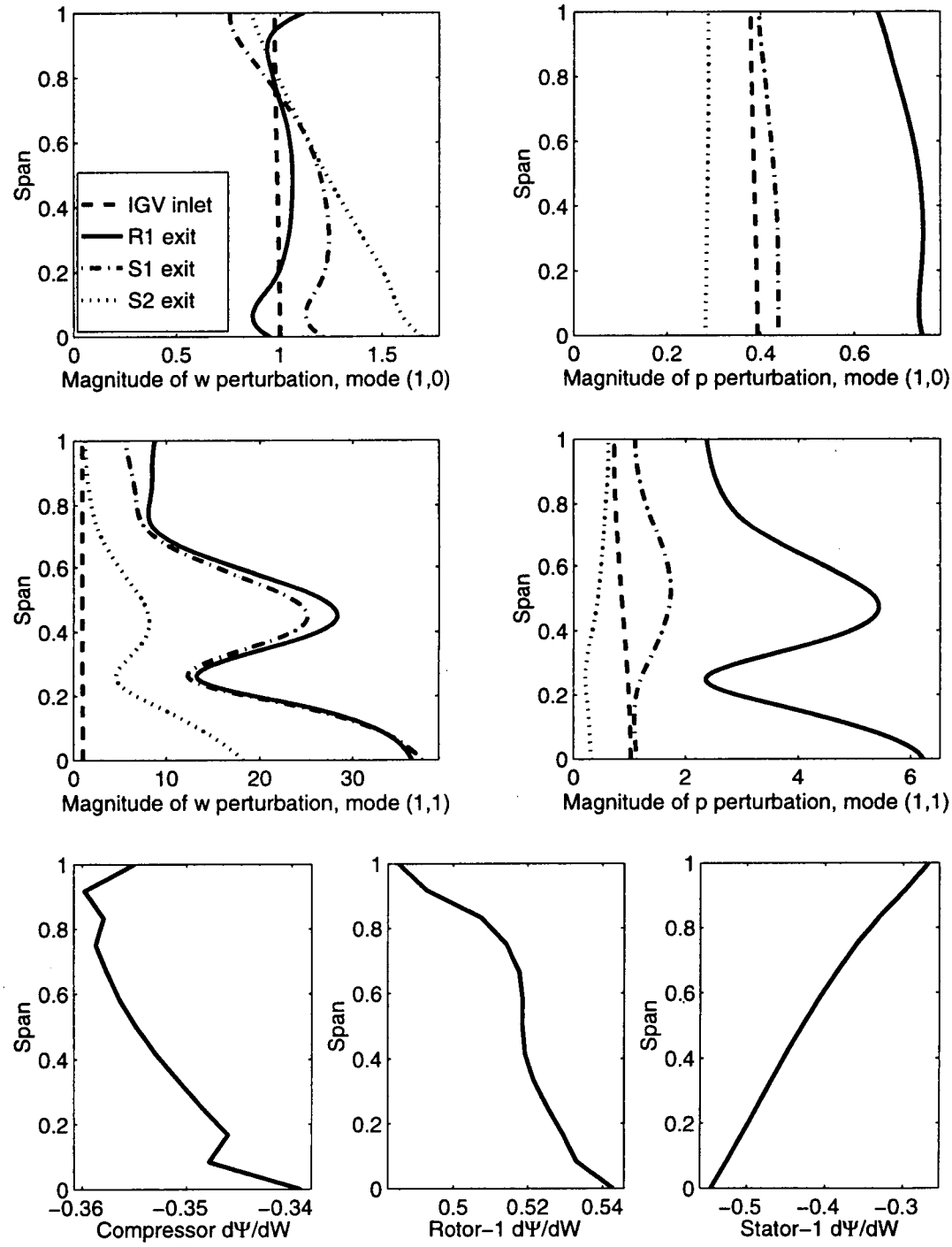


**Figure M-54:** (1,0) and (1,1) mode shapes, and slope variations for parametric study X.

# BIBLIOGRAPHY


[1] ADAMCZYK, J., CELESTINA, M., BEACH, T., AND BARNETT, M. "Simulation of Three-Dimensional Viscous Flow Within a Multistage Turbine". *ASME Journal of Turbomachinery, Vol. 112* (July 1990), pp. 370–376.

[2] AL-NAHWI, A., 1998. Massachusetts Institute of Technology, Personal Communication.

[3] ANDERSON, D., TANNEHILL, J., AND PLETCHER, R. *Computational Fluid Mechanics and Heat Transfer.* Hemisphere Publishing Corp., New York, 1984.

[4] CAMP, T., AND I.J., D. "A Study of Spike and Modal Stall Phenomena in a Low Speed Axial Compressor". *ASME Journal of Turbomachinery, Vol. 120* (July 1998), pp. 393–401.

[5] CAO, R.-J., AND ZHOU, S. "A 3D Rotating Stall Stability Model for Axial Flow Compressor". ASME paper 97-GT-209 (1997).

[6] CHUE, R., HYNES, T., GREITZER, E., TAN, C., AND LONGLEY, J. "Calculations of Inlet Distortion Induced Compressor Flow Field Instability". *International Journal of Heat and Fluid Flow, Vol. 10*, No. 3 (Sept. 1989), pp. 211–223.

[7] CUMPSTY, N. *Compressor Aerodynamics.* Longman Scientific and Technical, Essex, England, 1989.

[8] CUMPSTY, N., AND GREITZER, E. "A Simple Model for Compressor Stall Cell Propagation". *ASME Engineering for Power, Vol. 104* (Jan. 1982), pp. 170–176.

[9] DAY, I. "Stall and Surge in Axial Flow Compressors". In *Axial Flow Compressors.* von Karman Institute for Fluid Dynamics, Lecture Series 1992-02, 1992.

[10] DAY, I. "Review of Stall, Surge and Active Control in Axial Compressors". Eleventh International Symposium of Air Breathing Engines, ISABE 93-7011 (1993), pp. 97–105.

[11] DAY, I. "Stall Inception in Axial Flow Compressors". *ASME Journal of Turbomachinery, Vol. 115* (Jan. 1993), pp. 1–9.

[12] DAY, I., BREUER, T., ESCURET, J., CHERRETT, M., AND WILSON, A. "Stall Inception and the Prospects for Active Control in Four High Speed Compressors". ASME paper 97-GT-281 (1997).

[13] DAY, I., AND FREEMAN, C. "The Unstable Behavior of Low and High Speed Compressors". ASME paper 93-GT-26 (1993).

[14] DRAZIN, P., AND REID, W. *Hydrodynamic Stability.* Cambridge University Press, Cambridge, 1981.

[15] EHRICH, F. *Handbook of Rotordynamics.* McGraw-Hill Inc., New York, 1992.

[16] EPSTEIN, A., FFOWCS WILLIAMS, J., AND GREITZER, E. "Active Suppression of Aerodynamic Instabilities in Turbomachines". *AIAA Journal of Propulsion and Power, Vol. 5* (1989), pp. 204–211.

[17] ESCURET, J., AND GARNIER, V. "Numerical Simulations of Surge and Rotating Stall in Multi-Stage Axial-Flow Compressors". AIAA paper 94-3202 (1993).

[18] FRÉCHETTE, L. "Implications of Stability Modeling for High-Speed Axial Compressor Design". Master's thesis, Massachusetts Institute of Technology, 1997.

[19] GHIA, K., HANKEY, W., AND HODGE, J. "Use of Primitive Variables in the Solution of Incompressible Navier-Stokes Equations". *AIAA Journal, Vol. 17* (1979), pp. 298–301.

[20] GOLDSTEIN, M. "Scattering and Distortion of the Unsteady Motion on Transversely Sheared Mean Flows". *Journal of Fluid Mechanics, Vol. 91* (1979), pp. 601–632.

[21] GOLUB, G., AND VAN LOAN, C. *Matrix Computations.* Johns Hopkins University Press, Baltimore, 1983.

[22] GONG, Y., 1997. Massachusetts Institute of Technology, Personal Communication.

[23] GONG, Y., TAN, C.; GORDON, K., AND GREITZER, E. "A Computational Model for Short Wavelength Stall Inception and Development in Multi-Stage Compressors". ASME paper 98-GT-476 (1998).

[24] GORRELL, S., AND RUSSLER, P. "Stall Inception in a High-Speed Low Aspect Ratio Fan Including the Effects of Casing Treatments". ASME paper 94-GT-322 (1994).

[25] GRAF, M. "Effects of Asymmetric Tip Clearance on Compressor Stability". Master's thesis, Massachusetts Institute of Technology, 1996.

[26] GRAF, M., WONG, T., GREITZER, E., MARBLE, F., TAN, C., SHIN, H.-W., AND WISLER, D. "Effects of Non-axisymmetric Tip Clearance on Axial Compressor Performance and Stability". ASME paper 97-GT-406 (1997).

[27] GREITZER, E. "Surge and Rotating Stall in Axial Flow Compressors, Part I: Theoretical Compression System Model". *ASME Engineering for Power, Vol. 98*, No. 2 (Apr. 1976), pp. 190–198.

[28] GREITZER, E. "Surge and Rotating Stall in Axial Flow Compressors, Part II: Experimental Results and Comparison With Theory". *ASME Engineering for Power, Vol. 98*, No. 2 (Apr. 1976), pp. 199–217.

[29] GREITZER, E. "Coupled Compressor-Diffuser Flow Instability". *J. Aircraft, Vol. 14* (Mar. 1977), pp. 233–238.

[30] GREITZER, E. "Review — Axial Compressor Stall Phenomena". *ASME Journal of Fluids Engineering, Vol. 102* (June 1980), pp. 134–151.

[31] GYSLING, D. *Dynamic Control of Rotating Stall in Axial Flow Compressors Using Aeromechanical Feedback.* PhD thesis, Massachusetts Institute of Technology, 1993.

[32] HATHAWAY, M., 1998. NASA Lewis Research Center, Personal Communication.

[33] HAYNES, J. *Active Control of Rotating Stall in a Three-Stage Axial Compressor.* PhD thesis, Massachusetts Institute of Technology, 1993.

[34] HAYNES, J., HENDRICKS, G., AND EPSTEIN, A. "Active Stabilization of Rotating Stall in a Three-Stage Axial Compressor". *ASME Journal of Turbomachinery, Vol. 116* (Apr. 1994), pp. 226–239.

[35] HENDRICKS, G., BONNAURE, L., LONGLEY, J., GREITZER, E., AND EPSTEIN, A. "Analysis of Rotating Stall Onset in High Speed Axial Flow Compressors". AIAA paper 93-2233 (1993).

[36] HILL, P., AND PETERSON, C. *Mechanics and Thermodynamics of Propulsion.* Addison-Wesley Publishing Co., Reading, MA, 1992.

[37] HORLOCK, J. *Axial Flow Compressors.* Robert E. Krieger, New York, 1973.

[38] HORLOCK, J., AND GREITZER, E. "Non-uniform flows in axial compressors due to tip clearance variation". *IMechE, Proc. Instn. Mech. Engrs., Vol. 197C* (1983), pp. 173–178.

[39] HORLOCK, J., AND MARSH, H. "Flow Models for Turbomachines". *Journal Mechanical Engineering Science, Vol. 13*, No. 5 (1971), pp. 358–368.

[40] HOYING, D., 1995. Massachusetts Institute of Technology, Personal Communication.

[41] HOYING, D. *Blade Passage Flow Structure Effects on Axial Compressor Rotating Stall Inception.* PhD thesis, Massachusetts Institute of Technology, 1996.

[42] HOYING, D., TAN, C., VO, H., AND GREITZER, E. "Role of Blade Passage Flow Structures in Axial Compressor Rotating Stall Inception". ASME paper 98-GT-588 (1998).

[43] HYNES, T., AND GREITZER, E. "A Method for Assessing Effects of Circumferential Flow Distortion on Compressor Stability". *ASME Journal of Turbomachinery, Vol. 109* (July 1987), pp. 371–379.

[44] JACKSON, A. "Stall Cell Development in an Axial Compressor". ASME paper 86-GT-249 (1986).

[45] JANSEN, W., AND MOFFATT, W. "The Off-Design Analysis of Axial-Flow Compressors". *ASME Journal of Engineering for Power* (Oct. 1967), pp. 453–462.

[46] KOCH, C. "Stalling Pressure Rise Capability of Axial Flow Compressor Stages". *ASME Journal of Engineering for Power, Vol. 103*, No. 4 (1981), pp. 645–656.

[47] LONGLEY, J. "A Review of Non-Steady Flow Models for Compressor Stability". ASME paper 93-GT-17 (1993).

[48] LONGLEY, J., SHIN, H.-W., PLUMLEY, R., SILKOWSKI, P., DAY, I., GREITZER, E., TAN, C., AND WISLER, D. "Effects of Rotating Inlet Distortion on Multistage Compressor Stability". *ASME Journal of Turbomachinery, Vol. 118* (Apr. 1996), pp. 181–188.

[49] MATHIOUDAKIS, K. "Prediction of Small Rotating Stall in Axial Compressors Using Actuator Disk Theory". ASME Paper 85-GT-224 (1985).

[50] MATLAB, 1994. 4.2c for UNIX Workstations, The MathWorks Inc.

[51] MAZZAWY, R. "Multiple Segment Parallel Compressor Model for Circumferential Flow Distortion". *ASME Journal of Engineering for Power, Vol. 99* (1977), pp. 228–246.

[52] MCDOUGALL, N., CUMPSTY, N., AND HYNES, T. "Stall Inception in Axial Compressors". *ASME Journal of Turbomachinery, Vol. 112* (Jan. 1990), pp. 116–125.

[53] MOORE, F. "A Theory of Rotating Stall of Multistage Axial Compressors: Part I — Small Disturbances". *ASME Journal of Engineering for Gas Turbines and Power, Vol. 106* (1984), pp. 313–320.

[54] MOORE, R., AND REID, L. "Performance of Single-Stage Axial-Flow Transonic Compressor With Rotor and Stator Aspect Ratios of 1.19 and 1.26, Respectively, and With Design Pressure Ratio of 2.05". NASA TP 1659 (Apr. 1980).

[55] MYERS, M. "Transport of Energy by Disturbances in Arbitrary Steady Flows". *Journal of Fluid Mechanics, Vol. 226* (1991), pp. 383–400.

[56] NAGANO, S., MACHIDA, Y., AND TAKATA, H. "Dynamic Performance of Stalled Blade Rows". JSME Paper 11 (1971).

[57] ORSZAG, S., ISRAELI, M., AND DEVILLE, M. "Boundary Conditions for Incompressible Flows". *J. Sci. Comput., Vol. 1*, No. 1 (1986), pp. 48–56.

[58] REID, C. "The Response of Axial Flow Compressors to Intake Flow Distortion". ASME paper 69-GT-29 (1969).

[59] REID, L., AND MOORE, R. "Performance of Single-Stage Axial-Flow Transonic Compressor With Rotor and Stator Aspect Ratios of 1.19 nd 1.26, Respectively, and With Design Pressure Ratio of 1.82". NASA TP 1338 (1978).

[60] ROBINSON, C. "Endwall Flows and Blading Design for Axial Compressors". In *Axial Flow Compressors.* von Karman Institute for Fluid Dynamics, Lecture Series 1992-02, 1992.

[61] SASAKI, I., AND TAKATA, H. "Rotating Stall in Blade Rows Operating in Shear Flow (2nd Report: The Case of Shear Flow with Piecewise Linear Velocity Profile)". *Bulletin of the JSME, Vol. 27*, No. 225 (Mar. 1984), pp. 411–418.

[62] SEKIDO, T., SASAKI, I., AND TAKATA, H. "Rotating Stall in Blade Rows Operating in Shear Flow (1st Report: The Case of Shear Flow With Linear Velocity Profile)". *Bulletin of the JSME, Vol. 24*, No. 198 (Dec. 1981), pp. 2074–2081.

[63] SILKOWSKI, P. "Measurements of Rotor Stalling in a Mismatched Multistage Compressor". Tech. Rep. 221, Massachusetts Institute of Technology, Gas Turbine Lab Report, Apr. 1995.

[64] SMITH, L. "The Effect of Tip Clearance on the Peak Pressure Rise of Axial-flow Fans and Compressors". *ASME Symposium on Stall* (1958), pp. 149–152.

[65] SMITH, L. "Casing Boundary Layers in Multistage Axial-Flow Compressors". *Proceedings of the Symposium on Flow Research on Blading* (1969), pp. 275–304.

[66] SOUNDRANAYAGAM, M. *Rotating Stall Inception in Fans of Low Hub-Tip Ratio.* PhD thesis, Cranfield Institute of Technology, 1991.

[67] SOUNDRANAYAGAM, M., AND ELDER, R. "A Study of Stall in a Low Hub/Tip Ratio Fan". *ASME Journal of Turbomachinery, Vol. 115* (Jan. 1993), pp. 10–18.

[68] SPAKOVSZKY, Z., 1998. Massachusetts Institute of Technology, Gas Turbine Lab, Personal Communication.

[69] SPAKOVSZKY, Z., VAN SCHALKWYK, C., WEIGL, H., PADUANO, J., SUDER, K., AND BRIGHT, M. "Rotating Stall Control in a High-Speed Stage with Inlet Distortion, Part II — Circumferential Distortion". ASME paper 98-GT-265 (1998).

[70] SPAKOVSZKY, Z., WEIGL, H., PADUANO, J., VAN SCHALKWYK, C., SUDER, K., AND BRIGHT, M. "Rotating Stall Control in a High-Speed Stage with Inlet Distortion, Part I — Radial Distortion". ASME paper 98-GT-264 (1998).

[71] STRANG, E. "Influence of Unsteady Losses and Deviation on Compression System Stability with Inlet Distortion". Master's thesis, Massachusetts Institute of Technology, 1991.

[72] STRAZISAR, A., 1997. NASA Lewis Research Center, Personal Communication.

[73] STRAZISAR, A., WOOD, J., HATHAWAY, M., AND SUDER, K. "Laser Anemometer Measurements in a Transonic Axial-Flow Fan Rotor". NASA TP 2879 (1989).

[74] SUN, X.-F. "Three-Dimensional Compressible Flow Stability Theory of Rotating Stall". Tech. Rep. BH-B4765, Department of Jet Propulsion, Beijing University of Aeronautics and Astronautics, May 1996.

[75] TRYFONIDIS, H., ETCHEVERS, O., PADUANO, J., EPSTEIN, A., AND HENDRICKS, G. "Prestall Behavior of Several High-Speed Compressors". *ASME Journal of Turbomachinery, Vol. 117* (1995), pp. 62–80.

[76] VAN SCHALKWYK, C. *Active Control of Rotating Stall With Inlet Distortion.* PhD thesis, Massachusetts Institute of Technology, 1996.

[77] VAN SCHALKWYK, C., PADUANO, J., GREITZER, E., AND EPSTEIN, A. "Active Stabilization of Axial Compressors with Circumferential Inlet Distortion". ASME Paper 97-GT-279 (1997).

[78] WEIGL, H. *Active Stabilization of Rotating Stall and Surge in a Transonic Single Stage Axial Compressor.* PhD thesis, Massachusetts Institute of Technology, 1997.

[79] WEIGL, H., PADUANO, J., FRÉCHETTE, L., EPSTEIN, A., GREITZER, E., BRIGHT, M., AND STRAZISAR, A. "Active Stabilization of Rotating Stall and Surge in a Transonic Single Stage Axial Compressor". ASME Paper 97-GT-411 (1997).

[80] WISLER, D. "Advanced Compressor and Fan Systems". Tech. rep., General Electric Aircraft Engine Business Group Publication, Cincinnati, Ohio, 1985.

[81] WISLER, D. "Aerodynamic Effects of Tip Clearance, Shrouds, Leakage Flow, Casing Treatment and Trenching in Compressor Design". In *Tip Clearance Effects in Axial Turbomachines.* von Karman Institute for Fluid Dynamics, Lecture Series 1985-05, 1985.

[82] WISLER, D. "Loss Reduction in Axial-Flow Compressors Through Low-Speed Model Testing". *ASME Journal of Engineering for Gas Turbines and Power, Vol. 107* (1985), pp. 354–363.

[83] YEH, H. "An Actuator Disc Analysis of Inlet Distortion and Rotating Stall in Axial Flow Turbomachines". *Journal of the Aero/Space Sciences, Vol. 22*, No. 3 (Nov. 1959), pp. 739–753.

## TASK III: Development of an Effective Computational Methodology for Body Force Representation of High-speed Rotor 37

### Summary

A framework for an effective computational methodology for characterizing the stability and the impact of distortion in high-speed multi-stage compressor is being developed. The methodology consists of using a few isolated-blade row Navier-Stokes solutions for each blade row to construct a body force database. The purpose of the body force database is to replace each blade row in a multi-stage compressor by a body force distribution to produce same pressure rise and flow turning. To do this, each body force database is generated in such a way that it can respond to the changes in local flow conditions. Once the database is generated, no further Navier-Stokes computations are necessary. The process is repeated for every blade row in the multi-stage compressor. The body forces are then embedded as source terms in an Euler solver. The method is developed to have the capability to compute the performance in a flow that has radial as well as circumferential non-uniformity with a length scale larger than a blade pitch; thus it can potentially be used to characterize the stability of a compressor under design. It is these two latter features as well as the accompanying procedure to obtain the body force representation that distinguish the present methodology from the streamline curvature method.

The overall computational procedures have been developed. A dimensional analysis was carried out to determine the local flow conditions for parameterizing the magnitudes of the local body force representation of blade rows. An Euler solver was modified to embed the body forces as source terms.

The results from the dimensional analysis show that the body forces can be parameterized in terms of the two relative flow angles, the relative Mach number, and the Reynolds number. For flow in a high-speed transonic blade row, they can be parameterized in terms of the local relative Mach number alone. It is deduced that the performance and the flow distribution of a single blade row subjected to radial inlet distortions can be predicted

using the body force database created from the Navier-Stokes solutions with uniform inlet conditions. Likewise, the performance at an operating point, other than those from which the database for the body forces were extracted, can be computed as well.

## 1. Introduction

Gong [1], as described in Task I above, had developed a model for simulating axial compressor stall inception associated with both long- and short-wavelength disturbances. Individual blade rows were represented by a body force distribution formulated in terms of the blade's pressure rise and flow turning characteristics. The computational model uses a body force distribution that responds to local flow conditions. To achieve this, knowledge about the compressor performance and geometry must be known prior to modeling. The implication of Gong's work is that current thinking on stability modeling by viewing a compressor blade row as a body force distribution appears adequate for situations that have been examined. Such a representation was also determined to be adequate in a separate collaborative research involving NASA GRC, Boeing Commercial Airplane Company, Pratt & Whitney and MIT to incorporate Gong's formulation into WIND code for simulating the aerodynamic coupling between inlet flow and high speed fan stage in high bypass engine for advanced subsonic transport. This was implemented successfully and the work has been published (Hsiao, et al [2001]). Despite the success, there is a need to develop a rational and rigorous procedure for generating body force representation of compressor blade from CFD solutions. Task III essentially constitutes a step taken towards developing such a methodology.

In the past, the body force representation was based on correlation and meanline analysis as was implemented in streamline curvature and throughflow methods in implicit terms. However, the present proposed methodology, to be described later, explicitly obtains the body force representation of each blade row in a multi-stage compressor from the "best" available three-dimensional Navier-Stokes solver on a physically consistent basis.

Whereas a streamline curvature method or throughflow analysis is only capable of computing turbomachinery performance in a flow with radial flow variations, the technical framework under which the present proposed methodology is implemented in such that it can compute the performance in a flow that has radial as well as circumferential variations (with length-scales larger than the blade pitch). As such, it can

be used to characterize the stability of a compressor under design. It is these two latter aspects, namely how body force representation of a blade row is constructed and the ability to deal with a flow with circumferential non-uniformities, that distinguish the present method from the others.

Thus the overall goal is to first develop the methodology for extracting body force representation of blade row from computed flow field based on the best available Navier-Stokes solver. This is then to be followed by applying the methodology to the following practical situations:

(1) Effect of inlet distortion on high-speed axial compressor performance and stability margin

(2) Response of high-speed axial compressor to various distribution of jet actuation in the tip region

(3) Inlet-engine interactions in propulsion system representative of JSF types

This report is organized as follows. The main ideas associated with the body force formulation are first illustrated by the presentation of the physical concepts and the development of a basic computational model. New capabilities added to the existing model are assessed and validated. Specifically, the applicability of the model is first assessed by an extraction of the appropriate body force representation of an isolated blade row and subsequently by a successful replication of the flow field by applying the new representation. Having accomplished the first step, a dimensional analysis is carried out to identify a set of local flow parameters that set the magnitudes of the forces. The use of this set of the local flow parameters for correlating the response of the body forces with respect to the changes in local flow conditions is illustrated for a blade row subjected to a non-uniform inlet flow.

Finally, key results from the development and application of the computational methodology are presented and suggestions for future work are delineated.

## 2. Development Of Computational Methodology

### 2.1 Body Force Formulation

As was alluded to in the introduction, the first part of the computational methodology consists body force formulation. A simple graphical representation is shown in Figure 2.1. Figure 2.1(a) represents a conventional CFD approach, e.g. three-dimensional Navier-Stokes analysis, to compute the flow in a blade row. Figure 2.1(b) shows the axi-symmetric Euler approach with the basic body force representation to produce the identical flow turning and total-pressure rise: the effects of the blade geometries are replaced by equivalent local body forces. Figure 2.2 illustrates the body force methodology in a three-dimensional view. At each point within the blade row, the body forces can conveniently be described in terms of their three components: $F_x$, $F_\theta$, $F_r$, i.e. the axial, tangential, and radial forces, respectively, or a component normal to the flow and a component parallel to the flow.

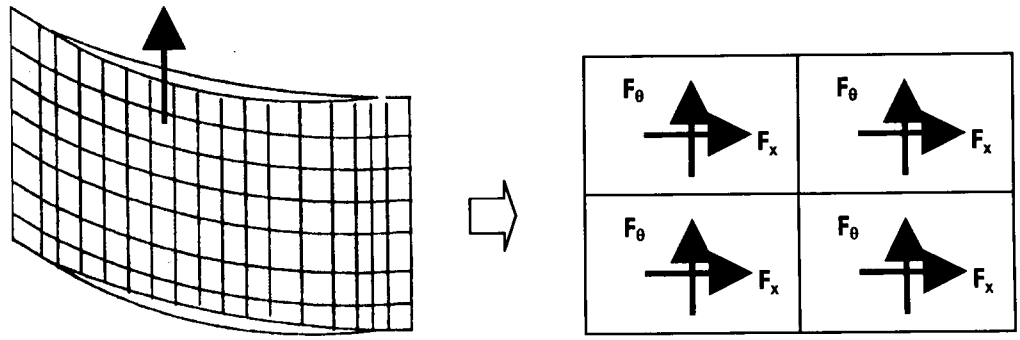


(a) (b)

Figure 2.1: Computational methodology: (a) conventional CFD approach and (b) axi-symmetric Euler with body force approach

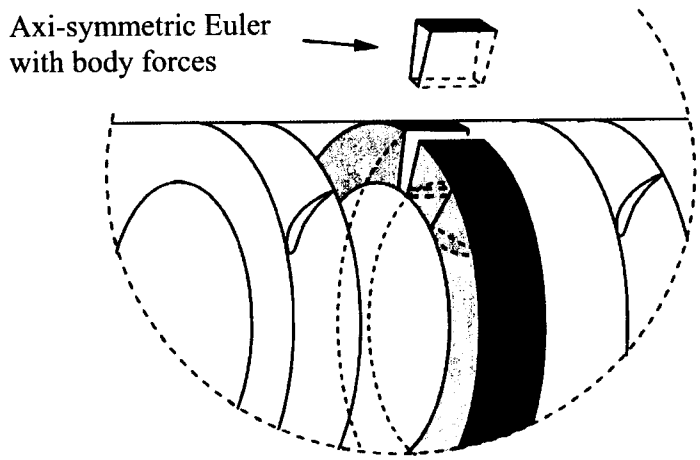


Figure 2.2: Three-dimensional illustration of the model using the body force distributions [8]

## 2.2 Overall Computational Procedure

The overall computational procedures can be summarized in two flow charts: one for validating the basic body force concept (Figure 2.3) and the other for calculating the compressor performance using the appropriate body force database (Figure 2.4).

### 2.2.1 Procedure for Concept Validation

A Navier-Stokes solver is used to obtain detailed three-dimensional flow solutions at a mass flow for a given isolated blade row. From the solutions, body forces are extracted by solving the integral form of the momentum equations around the control volumes. The extracted body forces are then substituted as source terms in an Euler flow solver. For the validation step, an Euler computation is performed with the inflow and outflow boundary conditions used to obtain the Navier-Stokes solutions from which the body forces were extracted. The Euler solutions provide one- and two-dimensional mass- and area-averaged profiles of flow variables at various cross sections along the axial direction, as well as the compressor pressure rise to compare against the Navier-Stokes solutions.

### 2.2.2 Procedure for Flow Analysis with a Body Force Database

The procedure for practical applications involves two steps. The first step consists of generating a body force database for a given blade row (or a set of blade rows). This step is illustrated graphically in Figure 2.4. A Navier-Stokes solver is first used to compute detailed flow fields at various mass flows on a constant speed-line. From the Navier-Stokes solutions, a body force database is constructed. Once the database is available, no further Navier-Stokes computations are required. This step is performed for each blade-row in a multi-stage compressor. Using the body force database, the response of the compressor under different inflow boundary conditions are carried out using the axi-symmetric Euler solver. Having specified the inflow and outflow boundary conditions of interest, the solver computes the appropriate local flow conditions. The local flow conditions are fed into the database to update the local body forces and the associated flow

field. This step is repeated until the solution reaches an equilibrium state( Figure 2.5).

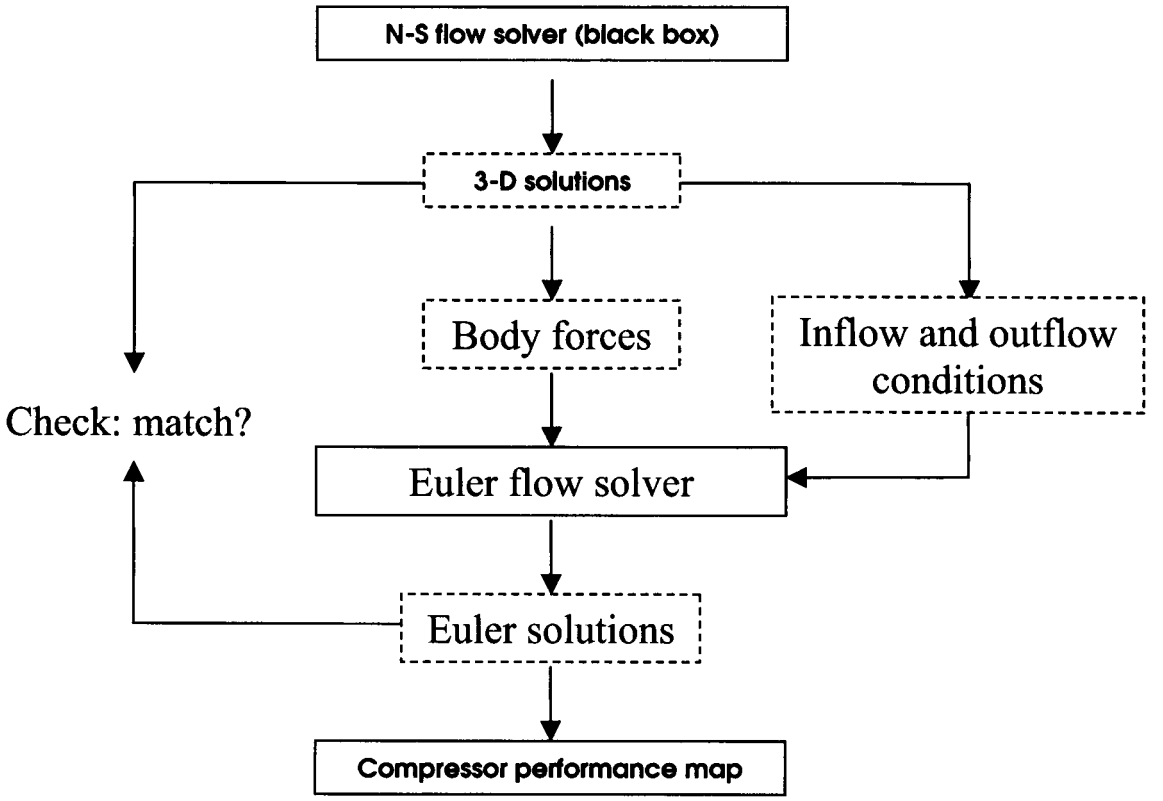


Figure 2.3: Computational methodology for the concept validation

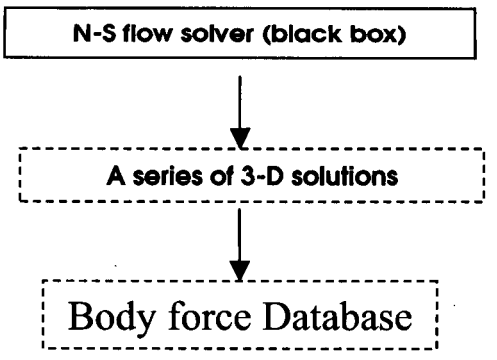


Figure 2.4: Generation of a body force database

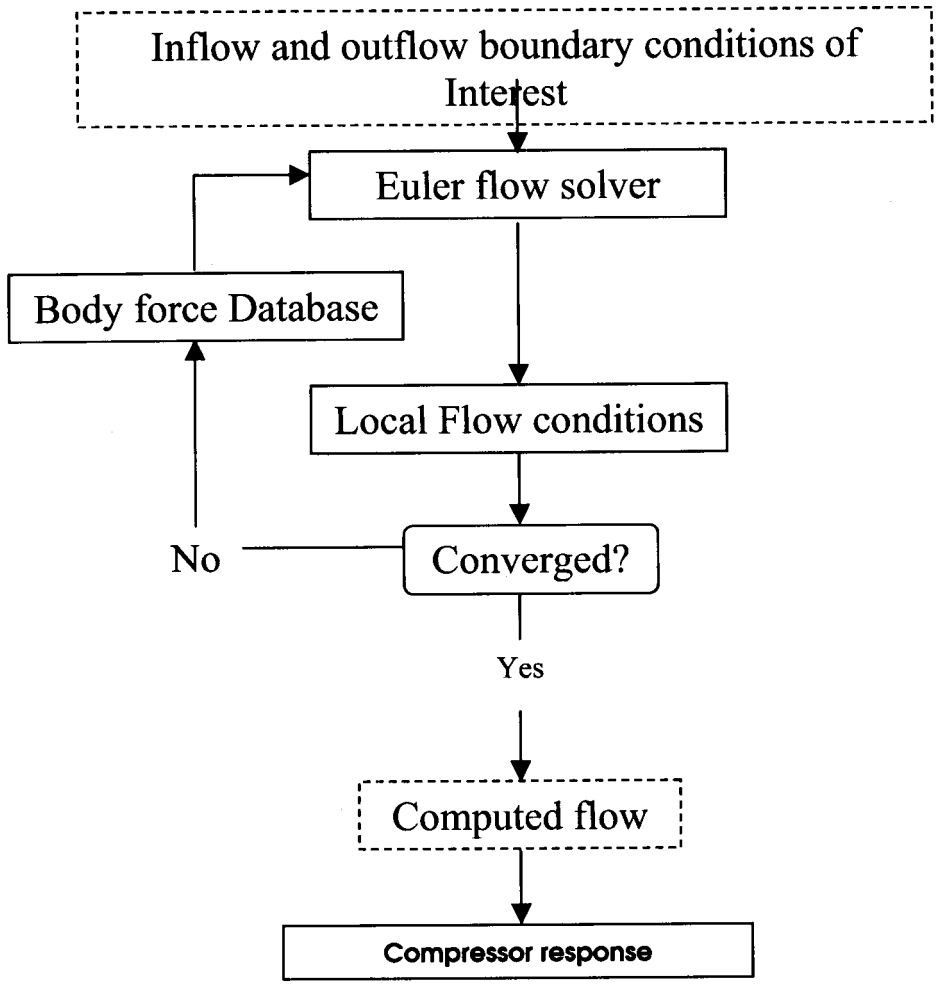


Figure 2.5: Computational procedure for compressor map generation

## 2.3 Generation of Body-Force Database

The generation of the body force database and its subsequent use to compute compressor response to varying flow conditions underpin the practical applicability of the methodology. In this section we describe the steps to accomplish this. These consist of (1) generating the body force data base, and (2) identifying the local flow conditions which can be employed to parameterize the forces.

### 2.3.1 Parametric Representation of Body Forces

Computing compressor performance for a new operating point is achievable if the body forces are capable of responding to the changes in the inflow and outflow boundary as well as the operating conditions. The changes in the inflow and outflow boundary conditions include that in radial total pressure, total temperature, axial, and/or tangential velocity profiles in the upstream region, and/or exit static pressure profile in the downstream region of the blade row.

Since those changes usually dictate the changes in the local flow conditions in the blade row, one of the main goal of the parameterization is to enable the body-forces to respond to the changes in the local flow conditions rather than the boundary or operating conditions. To determine what those local flow conditions are, a dimensional analysis using the Π-Theorem has been implemented implemented.

#### 2.3.1.1 Dimensional Analysis

The first part of the dimensional analysis consists of identifying all the possible independent variables in the governing equations of interest. In this case, the governing equations of interest are the Navier-Stokes equations. Assuming the body forces can be written in terms of some unknown functions of the independent variables of the Navier-

Stokes equations in cylindrical coordinates in the relative frame, the following three equations can be obtained:

$$\begin{aligned} F_x &= f_z(\rho,[V_x]_R,[V_r]_R,[V_\theta]_R,p,\mu,r) \\ F_\theta &= f_\theta(\rho,[V_x]_R,[V_r]_R,[V_\theta]_R,p,\mu,r) \\ F_r &= f_r(\rho,[V_x]_R,[V_r]_R,[V_\theta]_R,p,\mu,r) \end{aligned} \tag{1}$$

where in the left hand side, $F_x$, $F_\theta$, and $F_r$ denote the axial, tangential, and radial forces per unit mass, respectively. The physical quantities in the right hand side are the independent variables in the governing equations. Namely, they are density, three velocity components, static pressure, dynamic viscosity, and the radius (or any other appropriate characteristic length of the blade), respectively. The subscript R in Equations 1 denotes the relative frame of reference.

Since Equation 1 share the common variables, they can be written in terms of a vector form by first defining the body-force vector as follows:

$$\vec{F} = [F_x \quad F_\theta \quad F_r]^T \tag{2}.$$

Using Equation 2, Equations 1 can be rewritten as

$$\vec{F} = \vec{f}(\rho, V_x, V_r, V_\theta, p, \mu, r) \tag{3}$$

Applying the Π-Theorem to Equation 3 produces the following functional relationship:

$$\frac{r\vec{F}}{U_R^2} = \vec{f}(\alpha_r, \alpha_\theta, M_R, Re_R) \tag{4}$$

where $U_R$ is the magnitude of the local relative velocity. Equation 4 implies that the non-dimensional form of the body forces is a function of the following dimensionless

variables: relative radial and tangential flow angle, relative Mach number, and the Reynolds number.

#### 2.3.1.2 Subsonic Flows

In general, the relative flow angles in Equation 4 should always be considered for the subsonic flow regime: conceptually, the body forces are proportional to the relative flow angles. This statement is also supported by Gong's work [1]. If the compressibility effect is significant, the relative Mach number should also be included to reflect the effect, in addition to the relative flow angles. In other words, the functional form now becomes

$$\frac{r\vec{F}}{U_R^2} = \vec{f}(\alpha_r, \alpha_\theta, M_R) \qquad (5).$$

If the Reynolds number is considerably low, then the Reynolds number must be included as well, i.e.

$$\frac{r\vec{F}}{U_R^2} = \vec{f}(\alpha_r, \alpha_\theta, M_R, Re_R) \qquad (6)$$

#### 2.3.1.3 Supersonic Flows

For supersonic flows, however, it was found that the relative flow angles could be neglected: the shock waves within the blade passage determine and fix the downstream flow angles. Given the inflow and metal angles, the downstream flow angles can be analytically estimated by using the shock theory. The computed local flow angles from the Navier-Stokes solutions in this flow regime show that their magnitudes do not change at all, although the body forces change noticeably. Therefore, it is concluded that for the supersonic flows, the non-dimensional form of the body forces can be parameterized as:

$$\frac{r\vec{F}}{U_R^2} = \vec{f}(M_R) \qquad (7)$$

For the high Reynolds number flow considered here, the Reynolds number dependence can be neglected. That is, the only local flow condition required to parameterize the body forces is the local relative Mach number. In high-speed (transonic) blade rows, Equation 7 is used for the parameterization.

### 2.3.2 Generation Procedure

### 2.3.3

Having identified the local relative Mach number as the sole local flow quantity by which the magnitudes of the body forces at each point in the blade row region can be estimated in the supersonic flow regime, a general procedure adapted to generate a consistent body-force database will be demonstrated here.

To generate the database, several Navier-Stokes solutions of a blade row for various mass flows on a constant speed-line are required in order to estimate the governing relationships between the relative Mach number and the body forces. The solutions from an adequate number of mass flows are necessary to generate the database. To estimate the body force components between any two points along the speed-line, an interpolation scheme was employed.

## 3. Results and Discussions

Computed results from three examples based on NASA Rotor 37 are presented in this section to validate the computational methodology and to demonstrate its applications. The NASA Rotor 37 is a high-speed research compressor with a high-pressure ratio. It was developed and tested by the NASA in late 1970s as a part of their research program on evaluating the overall performance characteristics of four single stages, i.e. Rotors 35, 36, 37, and 38, that are representative of inlet, middle, and rear stages of an eight-stage 20:1 pressure ratio core compressor.

The rotor has an aspect ratio of 1.19, with an inlet hub-tip ratio of 0.7. It was designed for a total pressure ratio of 2.106 at a mass flow of 20.20 kilograms per second, with the inlet rotor-tip speed of 455 meters per second. In experimental test at design speed, however, the total pressure ratio across the rotor was determined to be 2.056, with an efficiency of 0.876, and actual mass flow rate of 20.74 kilograms per second.

The original configuration of the experimental hardware testing performed by the NASA was a single-stage compressor consisting of a rotor blade row followed by a stator blade row. However, in the current work, the stator blade row was not computationally modeled.

These three examples would serve to demonstrate the capability of the computational methodology (1) to replicate a flow field from which the body forces are extracted, (2) to respond to non-uniform radial inlet distortions using a body force representation that responds to local flow conditions, and (3) to predict the compressor performance at a completely new operating point, of which mass flow is located within the range of the body force database.

### 3.1 Validation of Procedural Steps of Methodology

In the first example, the body forces were extracted from the Navier-Stokes solutions at one operating point at the design speed and directly substituted in the blade row region in an Euler computation to reproduce the same flow field by matching the mass flow.

The main goal of the test case was simply to illustrate that the body forces can be substituted for the effects of the blade row. The redistribution capability of the body forces was examined in the remaining two examples.

To construct the body forces in the blade row, steady state Navier-Stokes solutions that correspond to 98% design mass flow of the compressor and its grid domain were obtained. The Navier-Stokes solutions were post-processed first to determine the operating and boundary conditions and to understand the overall flow characteristics of the compressor.

The boundary conditions obtained were then used for the Euler computations performed later in the process. These same pre-processing steps were taken for all the examples presented here.

### 3.1.1 Computational Results

Computed results based on Euler Solver with body force representation of rotor 37 were post-processed to obtain the axial variation of the pressure, the temperature rise (both total and static), and the velocity components. These are assessed and compared against those from the Navier-Stokes solutions, and they are shown in Figure 3.1.

The axial velocity and static pressure at each axial location were obtained by using area-averaging technique to conserve mass flow and axial force, respectively. The mass-averaging technique was used for all other variables. The static pressure in the region near the trailing edge of the blade was over-predicted by approximately 5.5 % of the static pressure computed from the Navier-Stokes solutions. Also, it was under-predicted in the upstream region by 5 % of that from the Navier-Stokes solutions. This caused a higher axial velocity in the region also by about 5 % of the axial velocity computed from the Navier-Stokes solutions. However, the two important flow quantities, total-pressure rise and tangential velocity representing the flow turning show excellent agreements. In general, the profiles demonstrate good agreements between the Navier-Stokes and Euler solutions.

Two-dimensional radial profiles at three different axial locations were also generated from both the Euler and Navier-Stokes solutions for comparisons and assessments. As shown in Figure 3.2, the three locations correspond to cross sections at two grid points prior to the leading edge, mid-chord, and two grid points after the trailing edge. The two-dimensional profiles at two grid points prior to the leading edge shown in Figure 3.3 are in good agreement. Matching the upstream conditions ensures that the body forces in the blade region would encounter similar flow conditions as given by the Navier-Stokes solutions. The profiles at the mid chord section in Figure 3.4 indicate that the flow quantities appear to evolve in a manner to yield the same amount of blade work being

added into the flow, as should be. Likewise, the comparisons of the profiles at the cross section after the trailing edge shown in Figure 3.5 show a similar trend.

The radial profiles near the end-walls in Figures 3.3, 3.4, and 3.6 show minor inconsistencies between the Euler and Navier-Stokes solutions. There are two main reasons for these. The first is that the shear forces near the end-walls in the upstream region were not modeled, causing a mismatch of the profiles near the end-walls prior to the leading edge. Since the flow conditions near the end-walls at this section are not identical, all subsequent downstream profiles near the end-walls would not be matched. This discrepancy can be corrected through the use of an appropriate shear force distribution on the hub and shroud. The second could be due to the fact that an Euler solver using different wall boundary conditions was employed to obtain the solutions. The differences had altered the profiles near and on the wall boundaries. The comparison of the pressure rise characteristics at the given operating point in Figure 3.7 also shows excellent agreement. The present results show that the use of an Euler solver with an embedded body force representation of a blade row yields a flow and blade-row performance in accord with that given by the Navier-Stokes solutions.

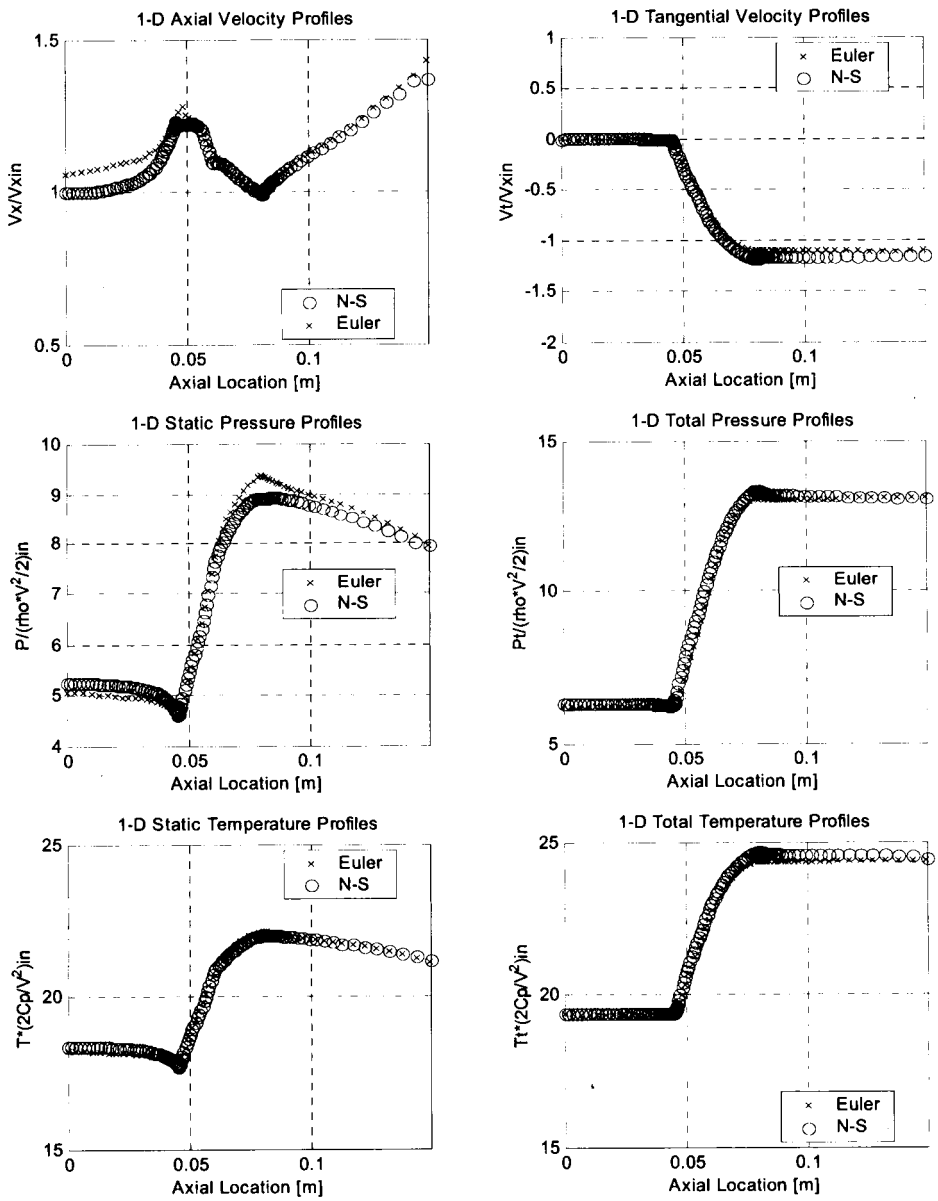


Figure 3.1: Comparisons of one-dimensional profiles of averaged flow solutions. All quantities are mass averaged except axial velocity and static pressure for which area-averaging technique was used.

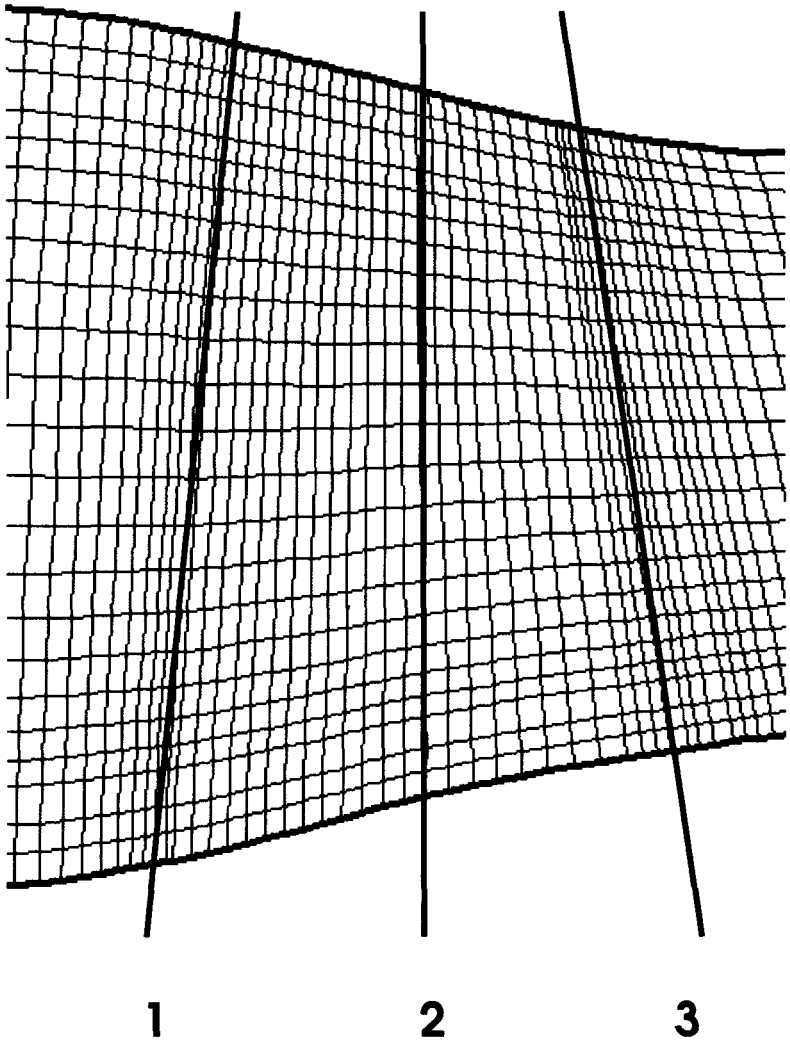


Figure 3.2: Illustration of cross sections chosen for comparisons of two-dimensional radial profiles: (1) two grid points prior to the leading edge, (2) mid-chord, and (3) two grid points after the trailing edge

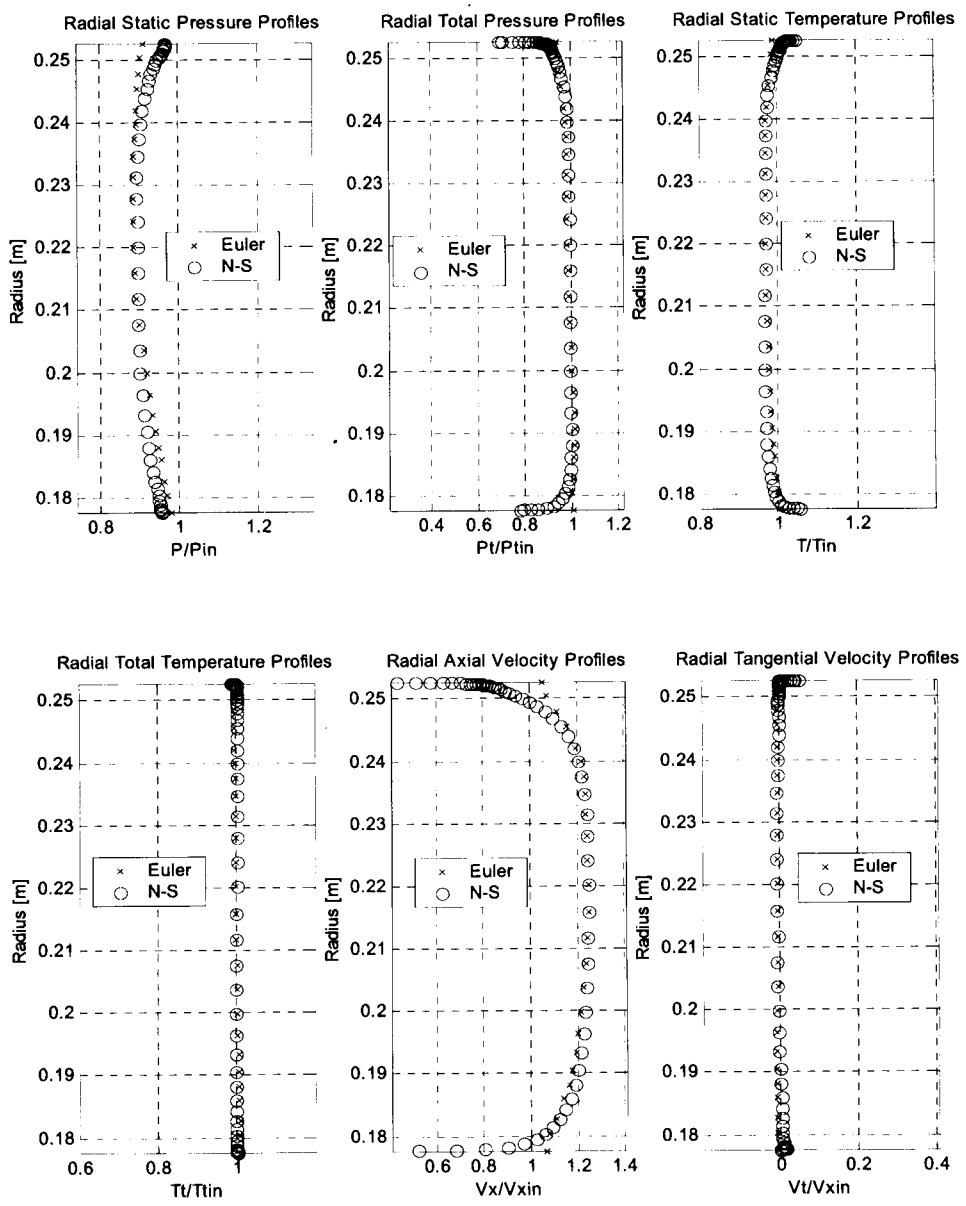


Figure 3.3: Comparisons of radial profiles prior to the leading edge from the first test case

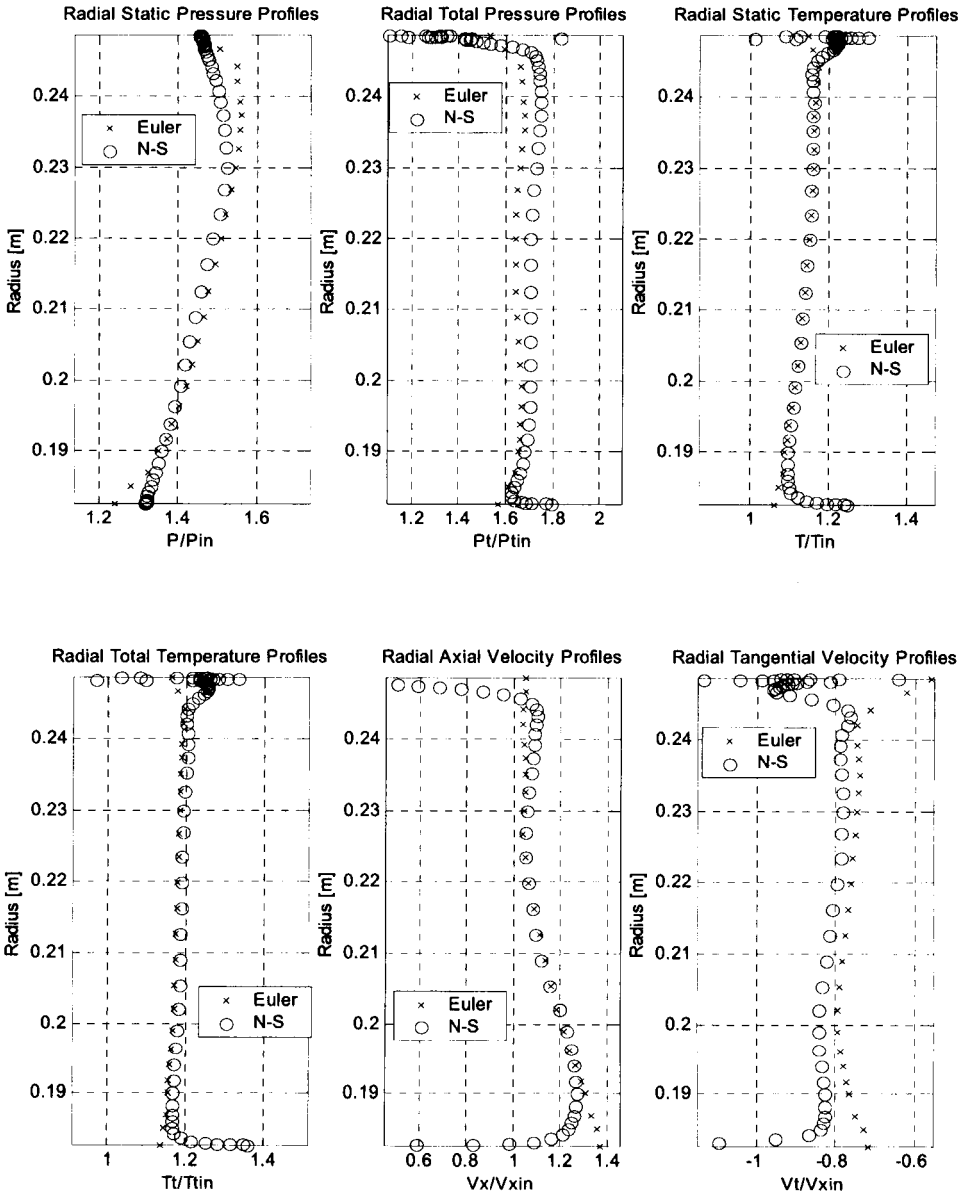


Figure 3.4: Comparisons of radial profiles at the mid-chord from the first test case

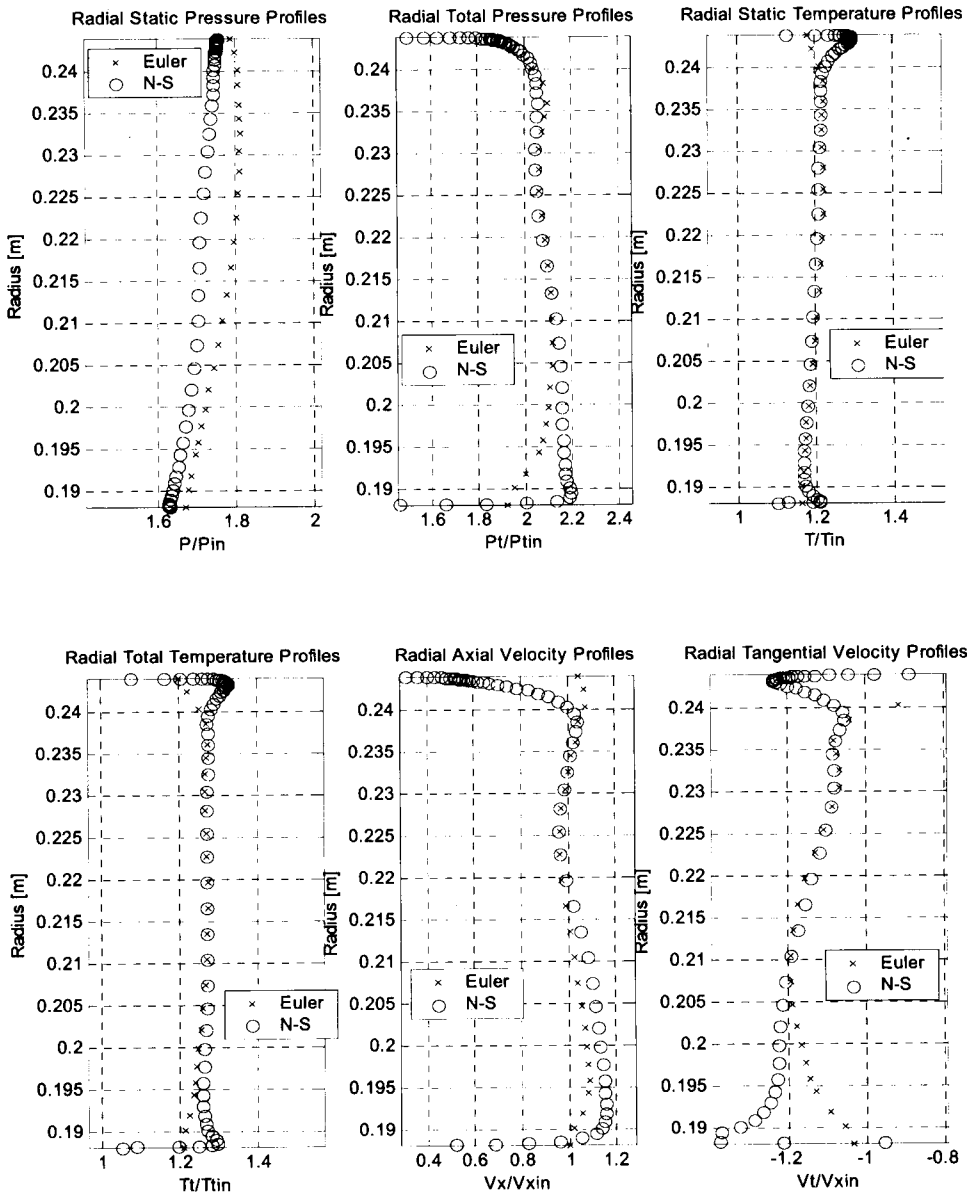


Figure 3.5: Comparisons of radial profiles after the trailing edge from the first test case

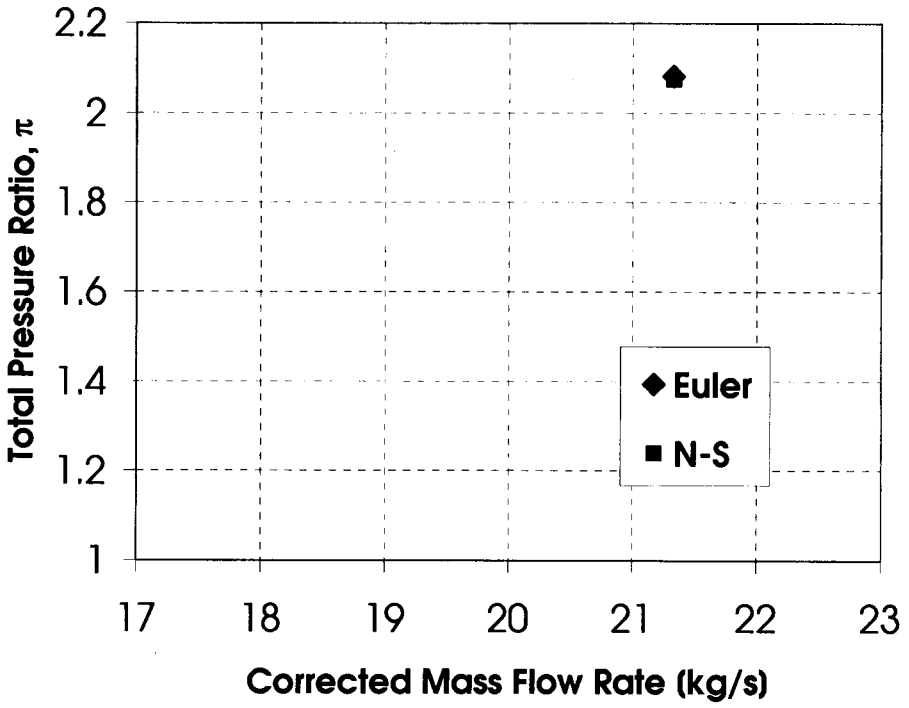


Figure 3.6: Comparisons of pressure-rise characteristics from the first test case

### 3.2 Redistribution of Body forces

In the second example, a body force database was generated by adapting the procedures described in the above. The local relative Mach numbers in the blade row region were used as the controlling parameter to determine the magnitudes of the body forces. The resulting database contains three relative Mach numbers and their corresponding body force components for each computational cell in the body force grid system.

Using the body force database generated, the replication of operating point 4, shown in Figure 3.7, was first selected for further validating the applicability of the approach. Inflow and outflow boundary conditions constructed from the Navier-Stokes solutions at this operating point were used to compute the flow field. One- and two-dimensional profiles obtained from the computed flow field are presented in Figures 3.8, 3.9, 3.10, and 3.11.

The averaged one-dimensional profiles in Figure 3.8 show good agreements. All the flow quantities obtained from the Euler solutions except the axial velocity profile exhibit no major deviations from that of the original Navier-Stokes solutions. Nevertheless, the axial velocity profiles for this test case are considerably well matched compared to the first test case.

From the comparisons of the two-dimensional profiles, it is deduced that the relative Mach number is indeed adequate to redistribute the body forces in the supersonic flow regime. This deduction is based on the excellent agreements shown in Figures 3.9, 3.10, and 3.11. However, mismatches in the tangential velocity profiles at the mid chord and after the trailing edge indicate that the amount of work added to the flow near the end-wall boundaries may not be quite accurate. This discrepancy was also observed in the first example. The suggestion put forward should resolve this discrepancy observed in the end walls.

Two additional Euler computations were carried out to simulate the pressure-rise characteristics of the rotor at operating points 3 and 5 using the computed flow at point 4 as initial conditions. These operating points are denoted in Figure 3.7. Detailed one- and two-dimensional profiles obtained from the computed flow at the two additional operating points are not shown here as there are no noticeable differences.

Instead, pressure-rise characteristics computed from the Euler solutions are compared against that from the Navier-Stokes solutions for all three operating points; these are presented in Figure 3.12. The figure shows that the pressure-rise characteristics were well predicted with a maximum discrepancy of approximately 2.3 % of the peak pressure rise. From this comparison, it can be concluded that the computational methodology developed in the current work is capable of redistributing the body forces on a consistent basis.

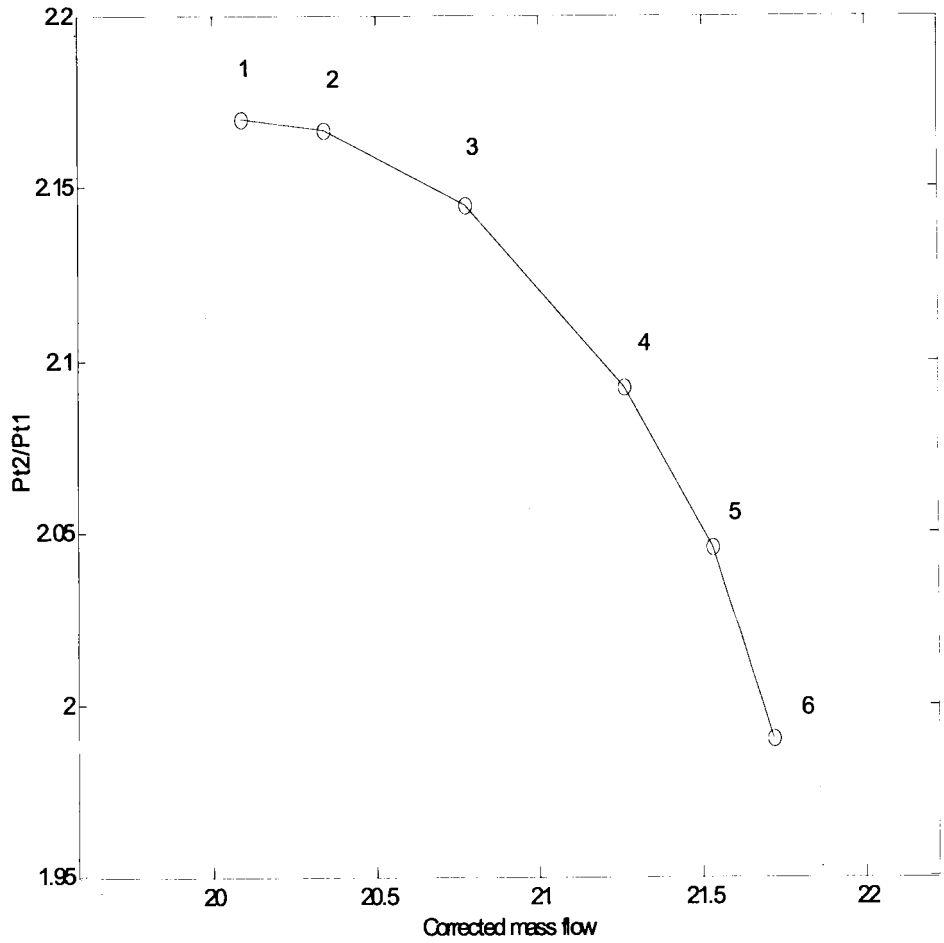


Figure 3.7: Computed Pressure-rise characteristic curve of NASA Rotor 37 on its design speed-line

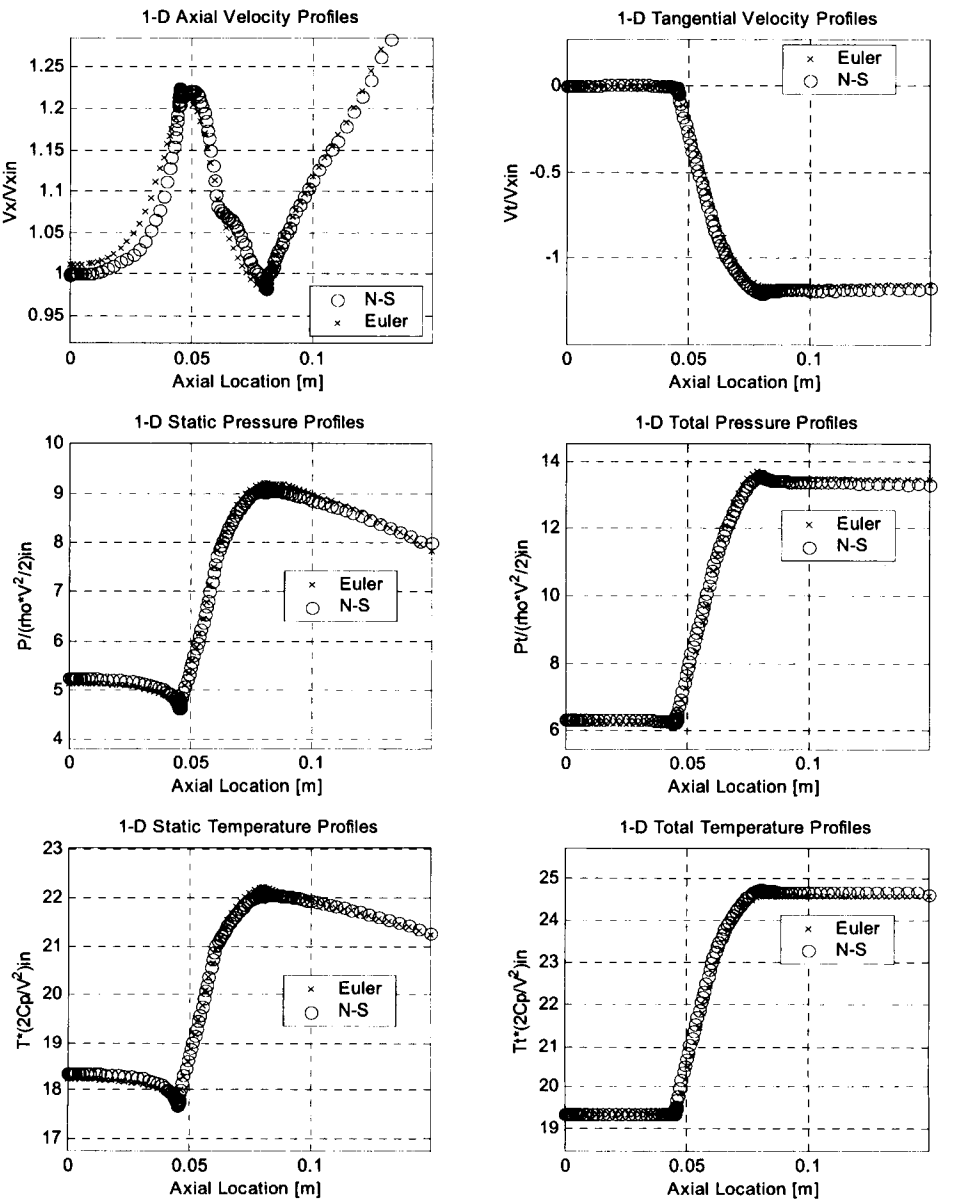


Figure 3.8: Comparisons of one-dimensional profiles of averaged flow solutions from the operating point number 4. All quantities are mass averaged except axial velocity and static pressure for which area-averaging technique was used.

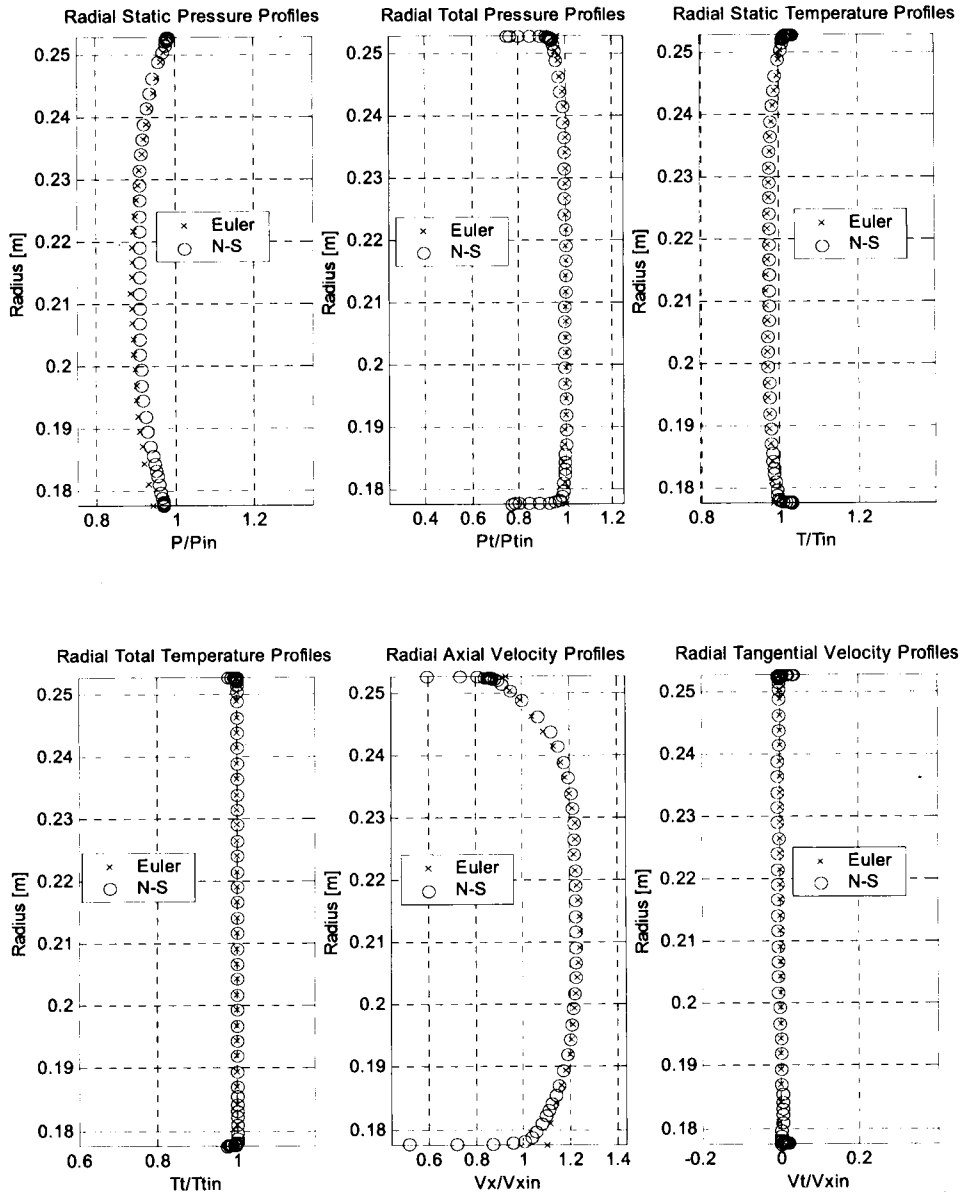


Figure 3.9: Comparisons of radial profiles prior to the leading edge from operating point 4

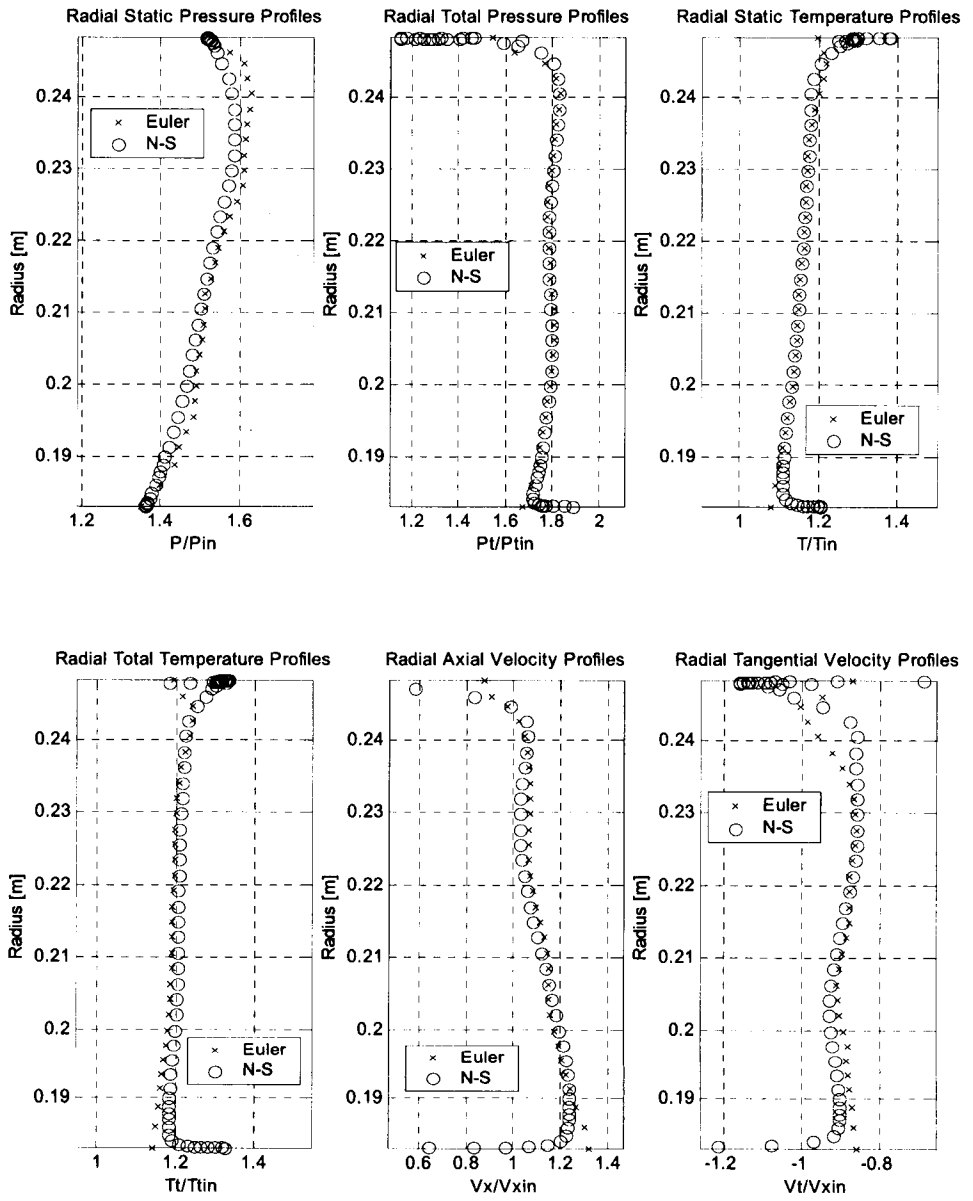


Figure 3.10: Comparisons of radial profiles at the mid-chord from operating point 4

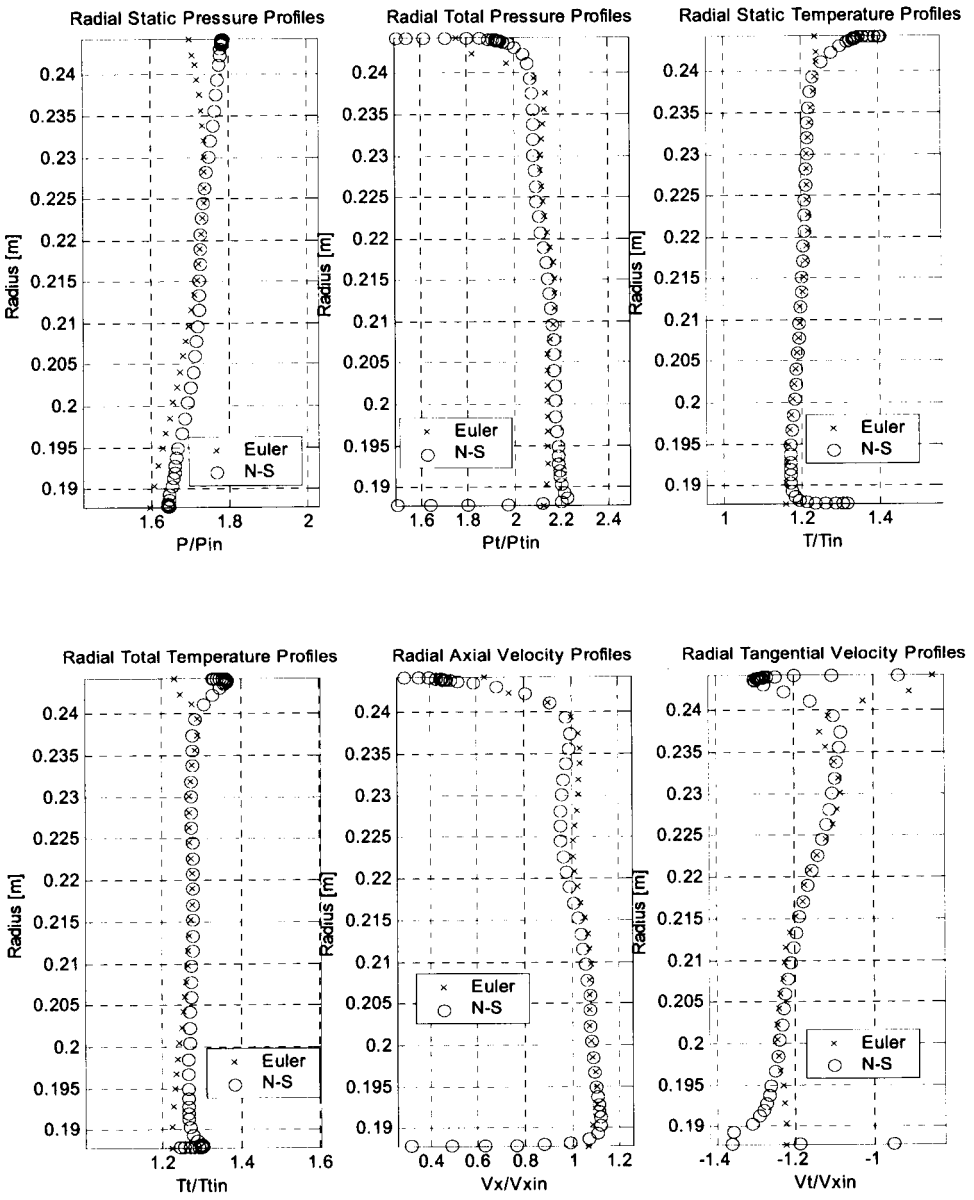


Figure 3.11: Comparisons of radial profiles after the trailing edge from operating point 4

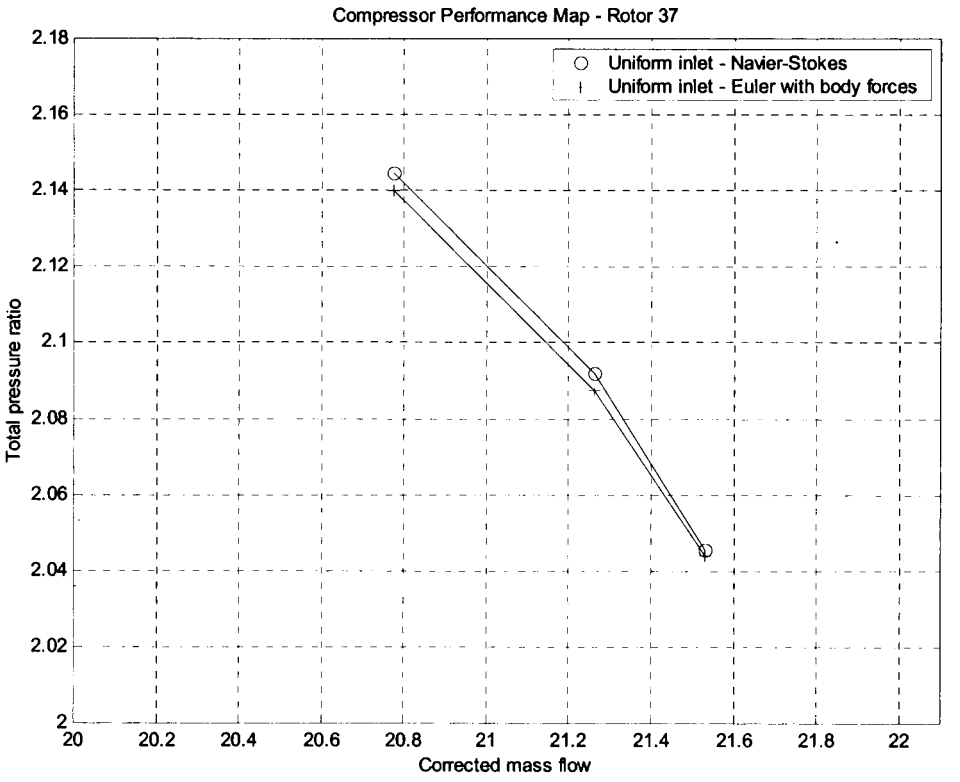


Figure 3.12: Comparisons of pressure-rise characteristics for three operating points from which the body-force database was generated

### 3.3 Radial Inlet Distortions

The steady state Euler solutions were obtained by applying the inflow and outflow boundary conditions constructed from the Navier-Stokes solutions with the radial inlet distortions. The converged solutions from operating point 4, shown in Figure 3.7, were selected as the initial conditions for this computation.

One-dimensional profiles that delineate the axial variations of the flow variables across the blade row are shown in Figure 3.13. It can be seen that the tangential velocity after the trailing edge was under-predicted by approximately 5 % of that from the Navier-Stokes

solutions. This also caused the total-pressure rise and the total-temperature rise to be approximately 1.0 % and 1.2 % less when compared to the total-pressure rise and the total-temperature rise computed from the Navier-Stokes solutions, respectively. Although the actual magnitudes of the static pressure and temperature near the inflow and outflow boundaries were differed from the Navier-Stokes solutions by a maximum of approximately 6 % of the static pressure at the exit, the pressure and temperature rises across the blade row were well predicted. In general, two-dimensional profiles in figure 3.14 to figure 3.16 also show good agreements, except near the end-wall boundaries.

The comparison of the pressure-rise characteristics subjected to the radial inlet distortions presented in Figure 3.17 indicates that the Euler computation with the body force formulation well captured the overall change of the rotor performance. The pressure-rise predicted by the body force formulation was found to be also less than that from the corresponding Navier-Stokes solutions by 1.2 % of the pressure-rise, exhibiting the same trend as in the uniform inlet cases.

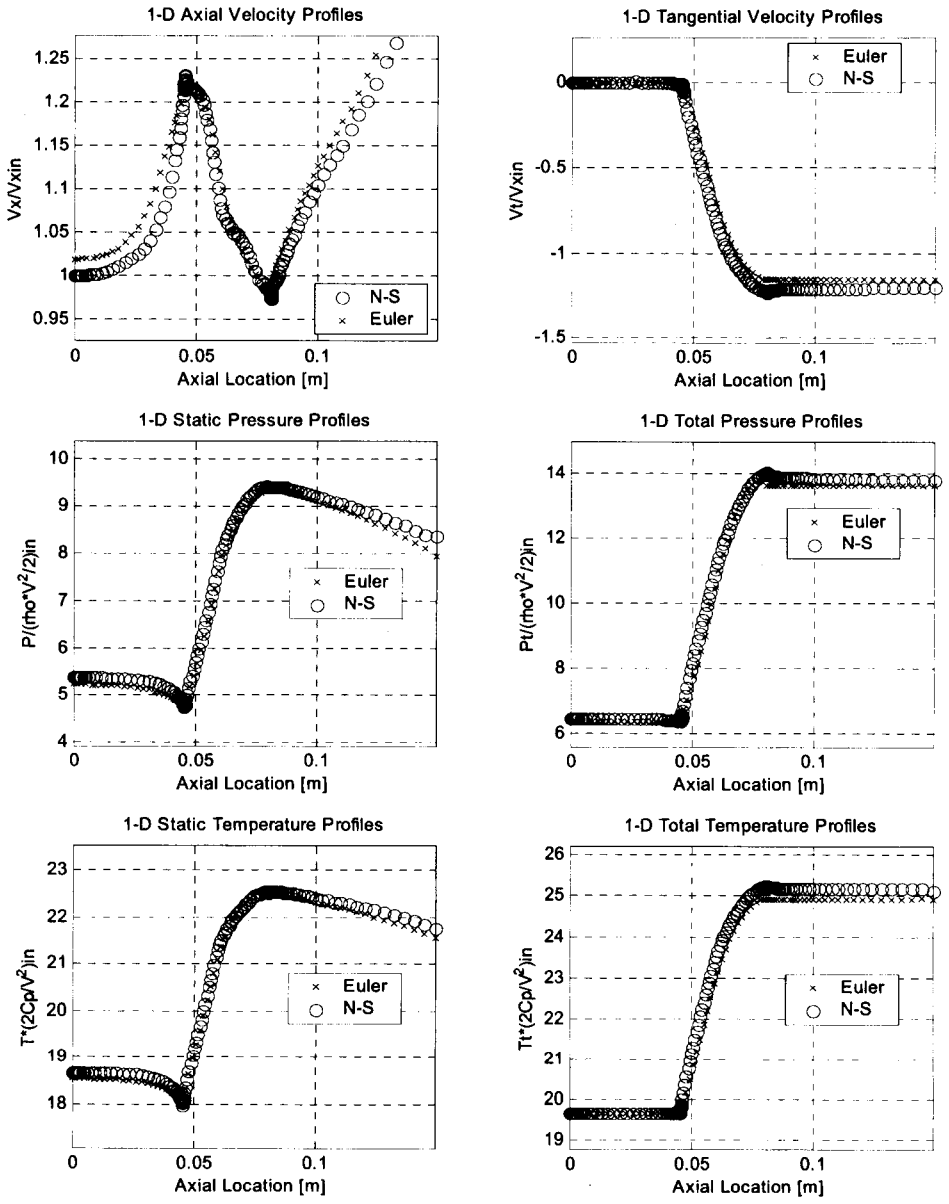


Figure 3.13: Comparisons of one-dimensional profiles of averaged flow solutions from the radial inlet distortion case. All quantities are mass averaged except axial velocity and static pressure for which area-averaging technique was used.

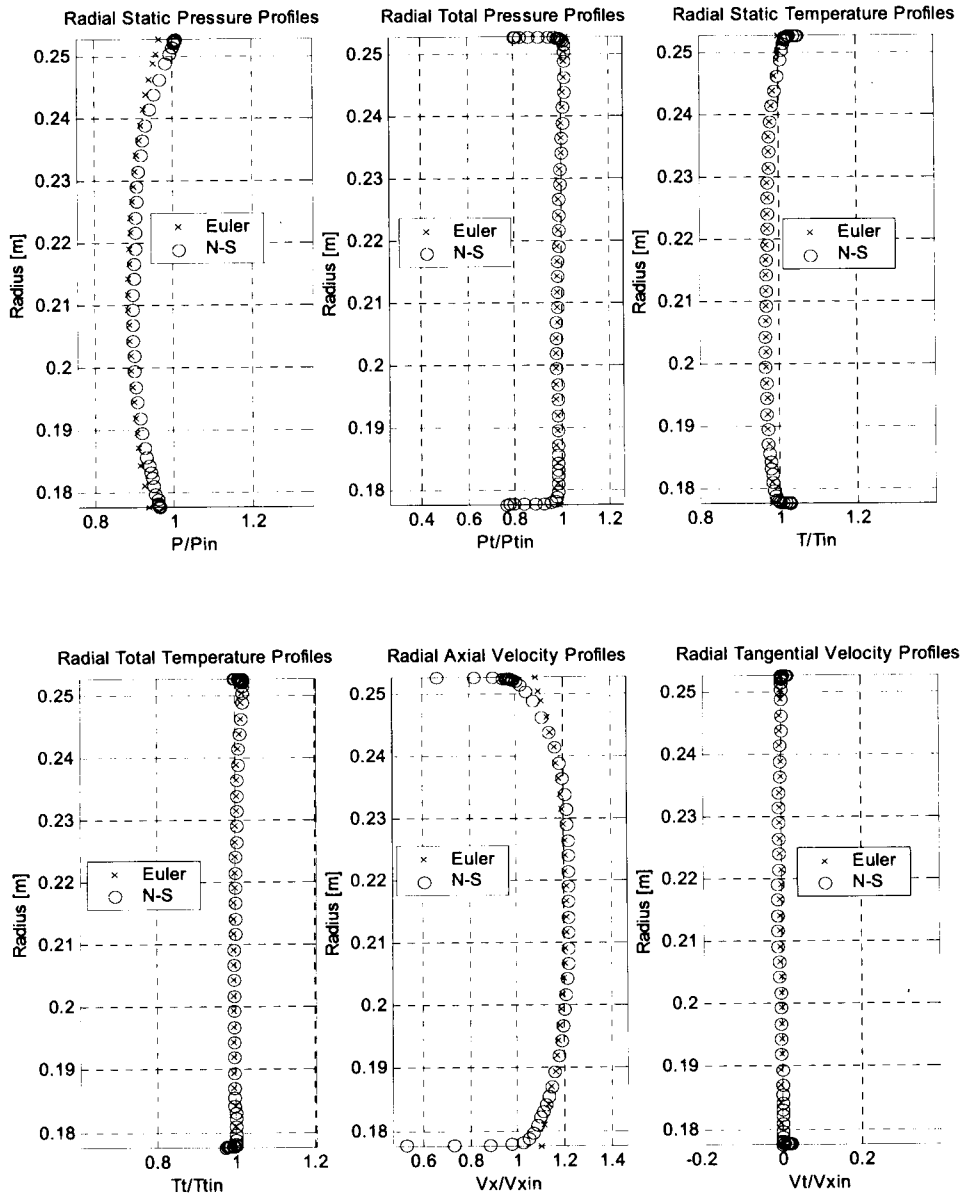


Figure 3.14: Comparisons of radial profiles prior to the leading edge from the radial inlet distortion case

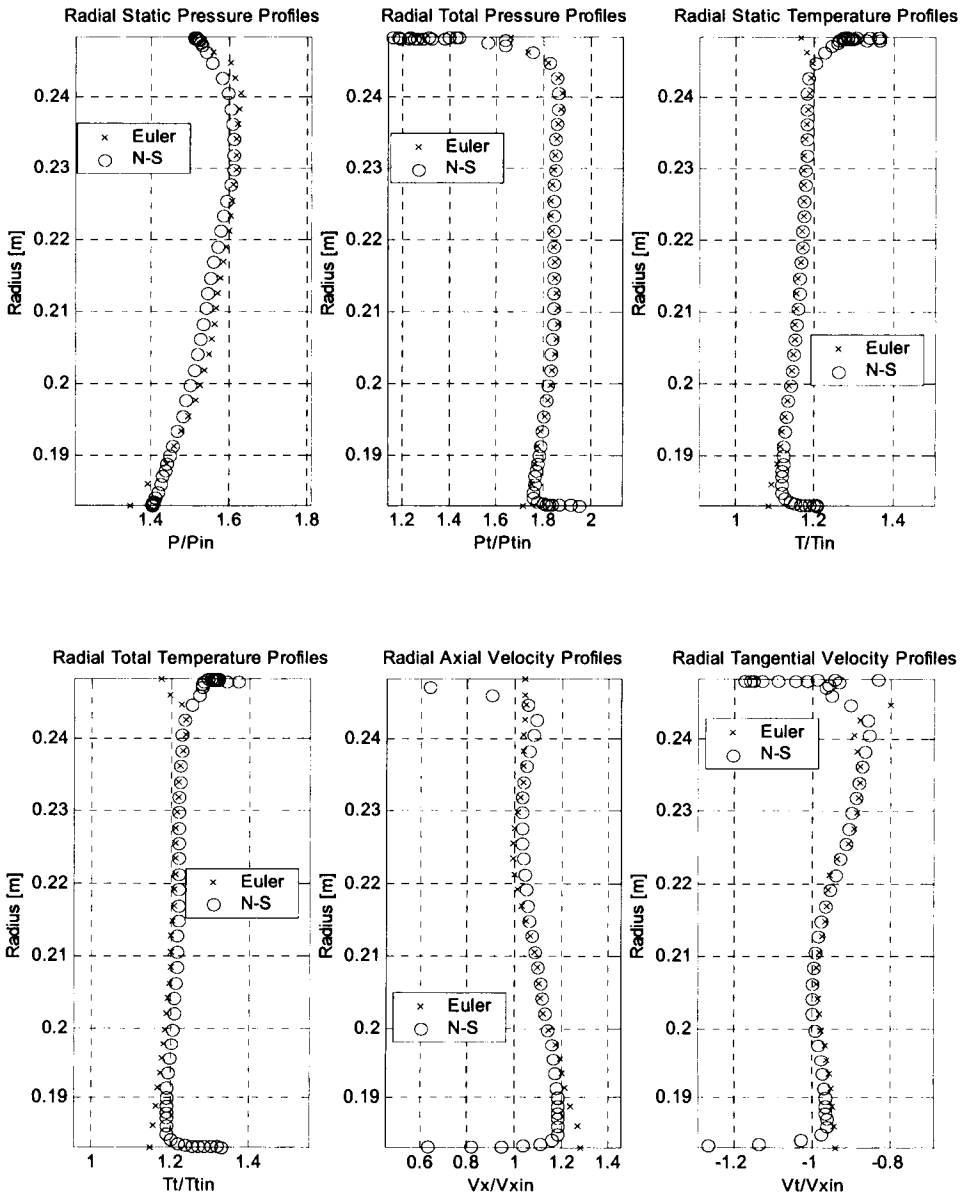


Figure 3.15: Comparisons of radial profiles at the mid-chord from the radial inlet distortion case

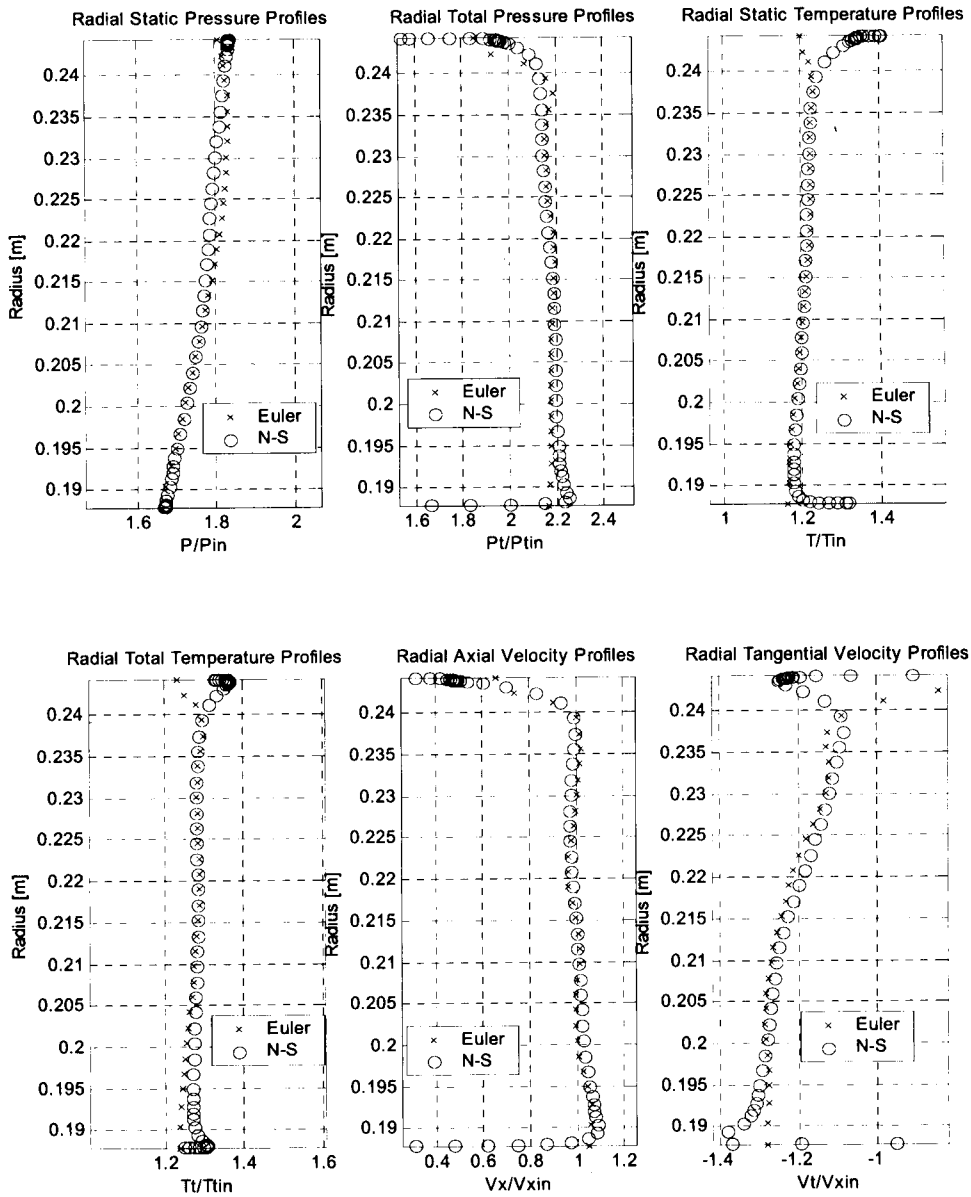


Figure 3.16: Comparisons of radial profiles after the trailing edge from the radial inlet distortion case

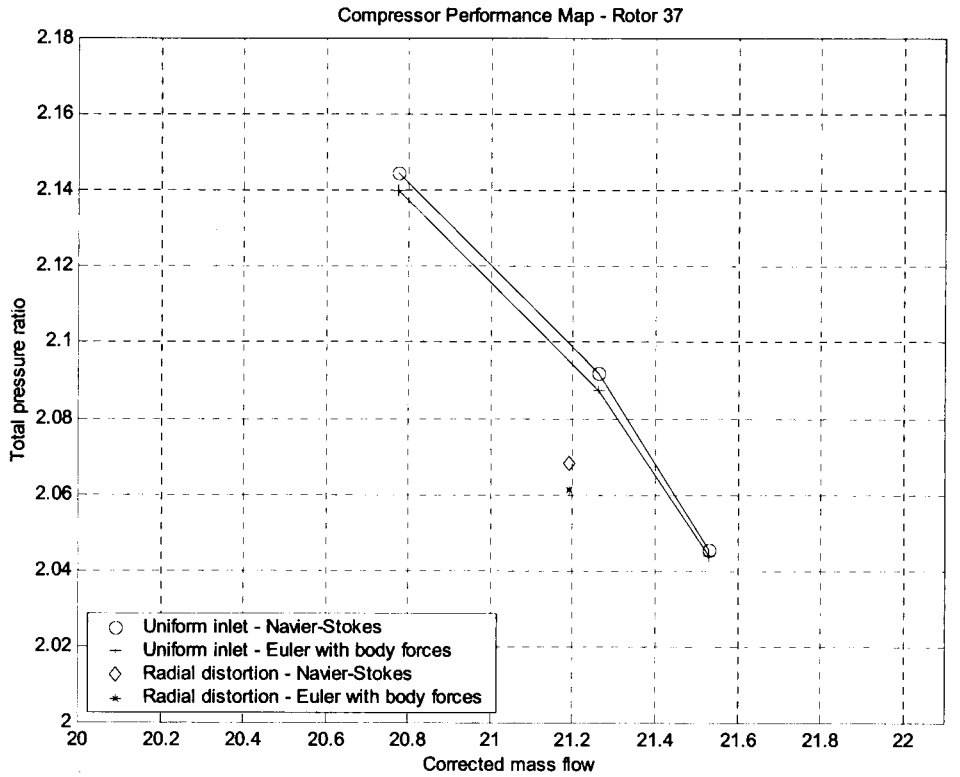


Figure 3.17: Comparisons of pressure-rise characteristics between the uniform inlet and radial inlet distortion cases

## 4. Summary and Concluding Remarks

### 4.1 Summary

The development of the computational methodology consists of using a few isolated-blade row Navier-Stokes solutions for each blade row to construct a body force database. The purpose of the body force database is to replace each blade row in a multi-stage compressor by a body force distribution to produce same pressure rise and flow turning. To do this, each body force database is generated in such a way that it can respond to the changes in local flow conditions and redistributes itself instantaneously. Once the database is generated, no further Navier-Stokes computations are necessary. The process is repeated for every blade row in the multi-stage compressor. Numerical predictions under a new set of inflow and outflow boundary and operating conditions can be carried out by using an Euler code with the body force databases.

The overall computational procedures for the concept validation as well as for the flow analysis with a body force database were developed. The corresponding body forces were embedded as source terms in the Euler equations.

A dimensional analysis was implemented to determine the local flow conditions that parameterize the magnitudes of the body forces. Three examples based on the use of the NASA Rotor 37 were presented to assess the physical consistency of the methodology. All the corresponding computational results from the test cases and their comparisons against the Navier-Stokes solutions are given in Section 3. Conclusions deduced from the computational results are provided in the next sub-section.

### 4.2 Concluding Remarks

In general, the body forces can be parameterized in terms of the two relative flow angles, the relative Mach number and the Reynolds number when the flow relative to the blade is subsonic. For high-speed transonic flows, they can be parameterized in terms of local relative Mach number alone.

The physical consistency of the methodology developed here was demonstrated by the excellent agreements of both the one-dimensional variations and two-dimensional profiles of the flow quantities as well as the compressor performance obtained from the first example. The performance of a compressor blade row at a new operating point can be accurately predicted by using the body force database, which is created from the Navier-Stokes solutions with uniform inlet conditions. This capability was shown in the second example. The third example showed that the flow field subjected to radial inlet distortions could be predicted using the same body force database. The conclusions deduced from these three examples demonstrated the utility of the methodology for predicting the performance and the flow distribution in a multi-stage compressor.

## 4.3 Future Work

While the results presented in this thesis are for a high-speed transonic blade row where the body forces can be parameterized in terms of the local relative Mach number, the application of the methodology to subsonic blade row will be demonstrated next. Here, the body forces will have to be parameterized in terms of the local relative Mach number, and the two local relative flow angles as well.

The radial profiles near the end-walls of a blade row can be improved by modeling the body forces created by the viscous effects, as shown in Figure 4.1, in the upstream region of the blade row. The implementation is relative simple and will be incorporated into the Euler code.

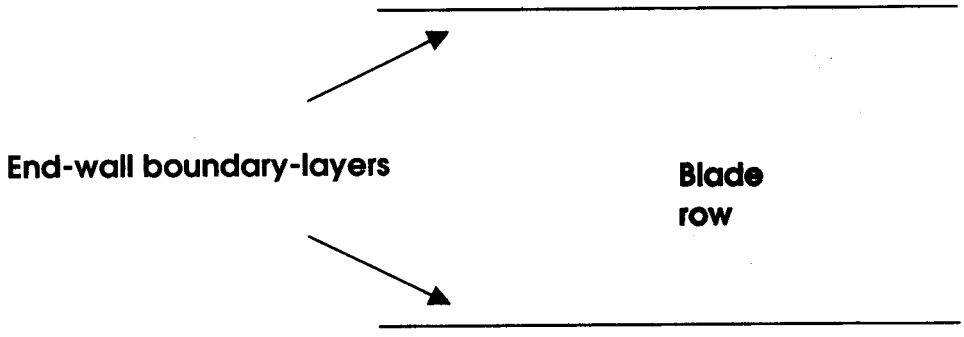


**Figure 4.1: End-wall boundary layer model**

## 5. REFERENCES


[1] Gong, Y., Tan, C. S., Gordon, K. A., Greitzer, E. M., "A Computational Model for Short-wavelength Stall Inception and Development in Multistage Compressors," ASME JOURNAL OF TURBOMACHINERY, Vol. 121, 1999, pp. 726-734. Also Gong's doctoral thesis on "A Computational Model for Rotating Stall and Inlet Distortions in Multistage Compressors", 1999, Department of Aero. & Astro., MIT.

[2] E. Hsiao, M. Naimi, J. P. Lewis, K. Dalbey, Y. Gong, C. Tan, "Actuator Duct Model of Turbomachinery Components for Powered-Nacelle Navier-Stokes Calculations," AIAA JOURNAL OF PROPULSION AND POWER, Vol. 17 No. 4 2001, pp. 919-927.

[3] K. Suder, 1999, Private Communication.

## TASK IV: Development of Circumferential Inlet Distortion through a Representative Eleven Stage High-speed Axial Compressor


### Summary

The concepts and the procedure developed in Task I and Task III were used to determine the response of an eleven-stage high-speed compressor to an inlet distortion of $180^0$ circumferential extent for contrasting against its performance under uniform inlet flow. Using the computed results at the inlet to and outlet of the compressor, the computed total pressure ratio and efficiency for the clean condition are determined to be 14.22 and 76.9% respectively. As for the distorted case, these are determined to be 10.35 and 71.8% respectively, showing deterioration in both the computed total pressure ratio (14.22 vs 10.35) and the efficiency (76.9% vs 71.8%).

The physical consistency of the computed flow field was assessed as a means of demonstrating the applicability and utility of the body force representation for inlet distortion computations. Specifically the computed evolution of the distorted pattern in static pressure and total pressure from compressor inlet to exit is examined.

For the eleven-stage compressor examined here, the deterioration in performance has been found to be particularly severe in the last 2 stages. This suggests that the last two stages could be redesigned to alleviate the observed deterioration thus making the compressor performance insensitive to circumferential inlet distortion. This can potentially be accomplished by first determining what should the body force distribution of the last two stages should be to achieve minimal or no deterioration in performance in the last two stages. One can then in principle proceed to determine the blade design to yield such a body force distribution.

## 1.0 Introduction

Results from computing the response of an eleven stage high-speed compressor (representative of current design) to a circumferential inlet distortion are described in Task IV here. Section 2.0 briefly described the procedure used and key results are presented in Section 3.

## 2.0 Technical Approach And Methodology

This section presents the framework for the use of body forces to represent blade row effects. This is followed by a presentation of the implementation of the methodology for computing the axisymmetric flow field and the response of an 11-stage compressor to circumferential inlet distortion.

### 2.1 Governing Equations

Within a blade row, by integrating the unsteady, three-dimensional, compressible Navier-Stokes equations in the circumferential direction, a system of unsteady axisymmetric equations in the *x-r* plane is obtained. These equations contain terms representing "body forces". The resulting equations incorporating body forces are given by

$$\frac{\partial\left(b\overline{U}\right)}{\partial t}+\frac{\partial\left(b\overline{F}_{inv}\right)}{\partial x}+\frac{\partial\left(b\overline{H}_{inv}\right)}{\partial r}=b\overline{S}+\overline{F} \tag{2.1}$$

where the overbar represents a circumferentially averaged property, and

$$\overline{U}=\begin{vmatrix} r\overline{\rho} \\ r\overline{\rho}\overline{V}_x \\ r\overline{\rho}\overline{V}_\theta \\ r\overline{\rho}\overline{V}_r \\ r\overline{\rho}\overline{e}_t \end{vmatrix},\ \overline{F}_{inv}=\begin{vmatrix} r\overline{\rho}\overline{V}_x \\ r\left(\overline{\rho}\overline{V}_x^{\,2}+\overline{p}\right) \\ r\overline{\rho}\overline{V}_x\overline{V}_\theta \\ r\overline{\rho}\overline{V}_x\overline{V}_r \\ r\overline{V}_x\left(\overline{\rho}\overline{e}_t+\overline{p}\right) \end{vmatrix},\ \overline{H}_{inv}=\begin{vmatrix} r\overline{\rho}\overline{V}_r \\ r\overline{\rho}\overline{V}_x\overline{V}_r \\ r\overline{\rho}\overline{V}_\theta\overline{V}_r \\ r\left(\overline{\rho}\overline{V}_r^{\,2}+\overline{p}\right) \\ r\overline{V}_r\left(\overline{\rho}\overline{e}_t+\overline{p}\right) \end{vmatrix},\ \overline{S}=\begin{vmatrix} 0 \\ 0 \\ -\overline{\rho}\overline{V}_\theta\overline{V}_r \\ \overline{\rho}\overline{V}_\theta^{\,2}+\overline{p} \\ 0 \end{vmatrix},\ \overline{F}=\begin{vmatrix} 0 \\ r\overline{\rho}f_x \\ r\overline{\rho}f_\theta \\ r\overline{\rho}f_r \\ r\overline{\rho}\left(\vec{f}\cdot\vec{V}\right) \end{vmatrix}$$

$\vec{f}$ is the body force per unit mass with components $f_x$, $f_\theta$ and $f_r$; and $b$ is a blockage factor defined as the ratio of the angular pitch at a general point $(x,r)$ to that at the leading edge. Its value corresponds to 1 for blades with zero thickness and to some value less than 1 when blades of finite thickness are present.

Eq. (2.1) shows that the action of a blade-row on the flow may be represented by an axisymmetric flow field in pitchwise-averaged flow properties and an appropriately derived distributed body force $\vec{f}(x,r)$. Physically, this is equivalent to using an infinite number of blades, with the flow being axisymmetric in each infinitesimal blade passage. As described in Task 1 to Task 3, such a representation is adequate for assessing the response of a blade row or compressor to circumferential flow non-uniformity with length scale larger than a blade pitch.

In the work described in this Task, Eq. (2.1) is solved numerically using the CFD code used for Task 1 and Task 3. The equations are discretized spatially and, using zero flow and zero compressor speed conditions as the initial condition, are marched in time using the five-step Runge-Kutta time-marching scheme. The imposed boundary conditions are total pressure, total temperature and flow angles at the upstream boundary, as well as throttle setting.

### 2.2 Description of the 11-stage Axial Compressor

The 11-stage axial compressor, representative of current design, comprises an IGV followed by 11 stages, leading to 23 blade rows in total. The configuration is shown in Fig. 2.1. The procedure for implementation of the body force representation is presented in Sections 2.3. A representative grid with a resolution of 342x80x12 is shown in Fig. 2.2.

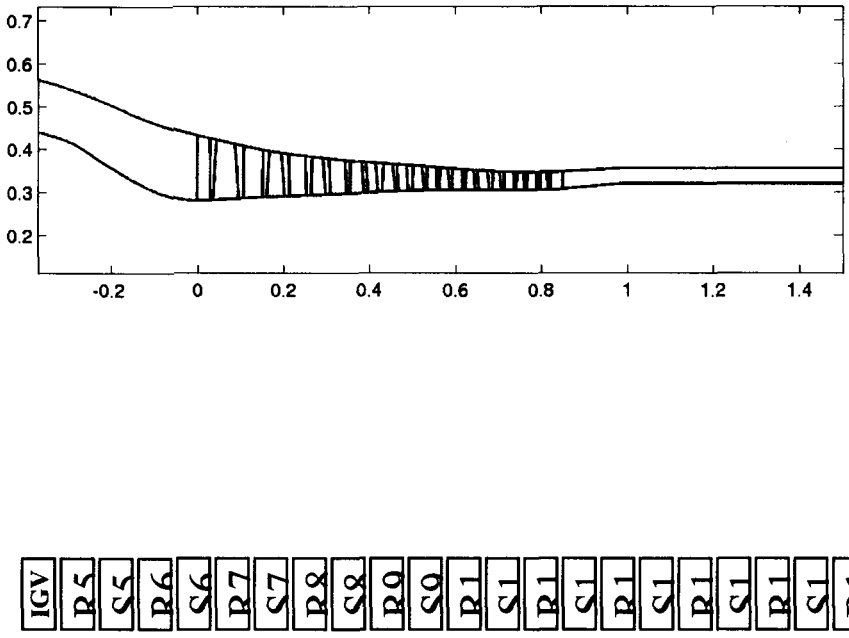


Fig. 2.1 Configuration of 11-stage Axial Compressor

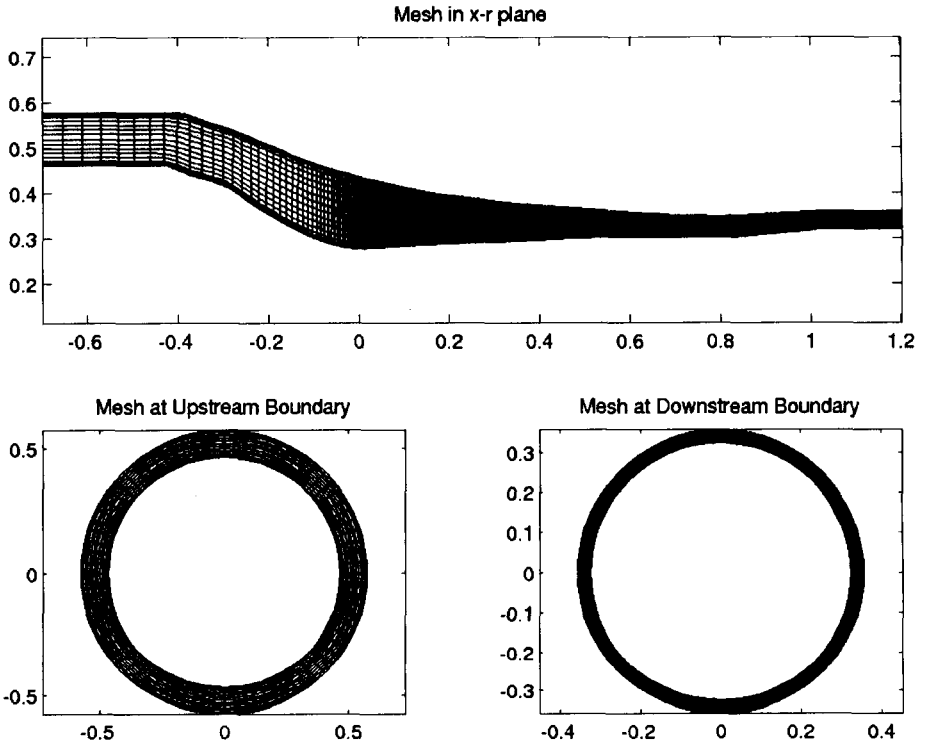


Fig. 2.2 Mesh for the 11-stage Compressor (342x80x12)

## 2.3 Implementation of Methodology for Computing Compressor Response to Inlet Distortion

For the case of inlet distortion, a total pressure distortion is imposed at the upstream boundary. The low and high total pressure regions each occupy a circumferential extent of $180^0$ and the distortion is defined by $\frac{P_{t,high} - P_{t,low}}{\frac{1}{2}\rho U^2} = 0.49$. The flow field and total pressure ratios are computed at a corrected mass flow of 53.94 kg/s. To determine the effects of inlet distortion on the performance of the compressor, the total pressure ratio for an axisymmetric flow at the same corrected mass flow is computed. For both axisymmetric flow and inlet distortion, the transient phase of the computations requires the body forces to vary transiently in response to a time-varying flow field.

The local blade force comprises of 2 components, $\vec{F}_n$ which is normal to the blade and $\vec{F}_p$ which is parallel to the blade. $\vec{F}_n$ is considered to be due to the pressure loading and $\vec{F}_p$ the viscous shear. It can be shown that these force components depend on local flow properties. The relationship can be expressed as

$$\vec{F}_n = -K_n(\Delta\beta, M, \mathrm{Re})\frac{(\vec{V}_{rel}\cdot\hat{\eta})(\vec{V}_{rel}\cdot\hat{\xi})}{h}\hat{n} \tag{2.2}$$

$$\vec{F}_p = -K_p(\Delta\beta, M, \mathrm{Re})\frac{\vec{V}_{rel}\cdot\vec{V}_{rel}}{h}\hat{p} \tag{2.3}$$

$K_n$ and $K_p$ are coefficients, which, in general, depend on local deviation angle $\Delta\beta$, Mach number $M$ and Reynolds number Re. $\vec{V}_{rel}$ is the relative velocity vector. $\hat{\eta}$ and $\hat{\xi}$ are unit vectors parallel and normal to the blade surface respectively. $\hat{n}$ and $\hat{p}$ are unit vectors normal and parallel to $\vec{V}_{rel}$ respectively.

In this work, $K_n$ and $K_p$ are assumed constant and are determined from

$$K_n = 4.2 - 2\alpha \tag{2.4}$$

$$K_p = 0.04 \tag{2.5}$$

The use of Eqns. (2.4) and (2.5) is motivated by their simplicity and ability to reproduce loss and deviation trends in cascades. The results and discussion of the compressor response to inlet distortion based on the formulation described by Eqns. (2.2) to (2.5) are presented in Section 3.

## 3.0 Results And Discussion For Inlet Distortion Computations

In this section, results for the calculation of the 11-stage compressor under circumferential inlet distortion are presented. The procedure has been presented in Section 2.0. The flow field is analyzed for self consistency as a means for assessing the applicability of the body force representation to determine multi-stage high-speed axial compressor response to inlet distortion and to determine which specific stage is less tolerant to circumferential distorted flow.

The analysis begins with the observation of deterioration, as compared to axisymmetric flow, in overall total pressure ratio and efficiency under distorted inlet flow (Section 3.1.1). Closer examination of the total pressure ratio and efficiency of the individual stages shows that this deterioration is due largely to the last 2 stages (Section 3.1.2). The particularly severe deterioration in total pressure ratio in these stages is associated with the manner in which the distortion travels from the far upstream boundary to the IGV inlet (Section 3.3) and then through the 11 stages (Section 3.4). These points will be elaborated upon in the following sections.

### 3.1 Compressor Performance

#### 3.1.1 Overall Performance

For the same corrected mass flow, the total pressure ratio and adiabatic efficiency of the whole compressor for each inlet condition is tabulated in Table 3.1.

| Inlet Condition | Corrected Mass Flow (kg/s) | Total Pressure Ratio | Adiabatic Efficiency (%) |
|---|---|---|---|
| Axisymmetric | 53.94 | 14.22 | 76.9 |
| Distorted | 53.94 | 10.35 | 71.8 |

Table 3.1 Compressor Performance for Axisymmetric and Distorted Inlet Flow

The compressor experiences deterioration in total pressure ratio and efficiency as a result of inlet distortion. It will be shown in subsequent sections that the deterioration is

associated with the behavior of a static pressure distortion which is eliminated over the last 2 stages.

The efficiency data in Table 3.1 is computed using total pressure and total temperature ratios. To assess the consistency of the computed efficiencies, these are calculated by using another approach that involves the losses generated by the body force representation and the increase in entropy across gaps between blade rows.

As loss can be quantified by increase in entropy, it is useful to relate the efficiency of a compressor to the increase in entropy according to the following equation

$$\eta = \frac{\pi^{\gamma-1/\gamma} - 1}{\left(\pi e^{\Delta s/R}\right)^{\gamma-1/\gamma} - 1} \tag{3.1}$$

where $\pi$ is the total pressure ratio of the compressor.

In the body force representation, losses are generated in blade rows through the dissipative work term $\vec{F}_p \cdot \vec{V}_{rel}$, where $\vec{F}_p$ is the force component in the direction of the relative velocity $\vec{V}_{rel}$. This can be used to calculate the entropy increase due to the 23 blade rows. The rate of entropy generation for each blade row is calculated by a summation over the finite volume cells and is given by

$$\dot{S}_b = \sum_{cells} \frac{\vec{F}_p \cdot \vec{V}_{rel}}{T} \tag{3.2}$$

The change in entropy per unit mass across the blade row, $\Delta s_b$, is determined from the difference in entropy flux across the blade row.

$$\Delta s_b = \frac{\dot{S}_b}{\dot{m}} \tag{3.3}$$

The total change in entropy of the 23 blade rows is given by

$$\Delta s_{bt} = \sum_{\substack{blade \\ rows}} \Delta s_b \tag{3.4}$$

For gaps between blade rows, the entropy increase across each gap is determined from

$$\Delta s_g = c_p \ln \tau_g - R \ln \pi_g \tag{3.5}$$

where $\tau_g$ and $\pi_g$ are static temperature and static pressure ratios across the gap respectively. The total change in entropy of the 22 gaps is given by

$$\Delta s_{gt} = \sum_{gaps} \Delta s_g \tag{3.6}$$

To separate the effects of blade rows and gaps on efficiency, the efficiency is first calculated from Eq. (3.1) using $\Delta s = \Delta s_{bt}$ (blade rows only) and then using $\Delta s = \Delta s_{bt} + \Delta s_{gt}$ (blade rows and gaps). The results for each inlet condition are tabulated in Table 3.2.

| Inlet Condition | η (Blade Rows Only) | η (Blade Rows and Gaps) | Δη Due to Gaps |
|---|---|---|---|
| Clean | 78.2% | 76.6% | 1.6% |
| Distorted | 73.7% | 71.4% | 2.3% |

Table 3.2 Adiabatic Efficiency Calculated from Losses in Blade Rows and Gaps

The data of Table 3.2 demonstrates that the effects of gaps can be significant in a compressor with a large number of gaps (22 in the case of the 11-stage compressor) in which numerical dissipations occur. The larger decrement in calculated efficiency of 2.3% for distorted flow (as shown in the far right column of Table 3.2) as compared to 1.6% for clean flow could be due to numerical dissipation in the circumferential direction. The contribution from numerical dissipation in principle can be quantified through implementation of additional calculations with varying degrees of grid resolution and through extrapolation of the computed results. However, this has not been done here.

The computed distribution of entropy rise across the stages for clean and distorted inlet flow conditions is shown in Figs. 3.1(a) and (b) respectively. Entropy rise is defined non-dimensionally as $\frac{T_{ref}\Delta s}{U_{ref}^2}$. It is observed that for rotors, losses are highest for the first and

last stages. For stators, losses are highest for the first stage. The entropy rise across gaps is highest at the last stage.

### 3.1.2 Stage Performance

For distorted flow, the deterioration in total pressure ratio over the clean flow condition is calculated in each of the 11 stages and presented in Fig. 3.2. This deterioration is defined by the ratio $\frac{\pi_{clean} - \pi_{distorted}}{\pi_{ave} - 1}$, where $\pi_{clean}$ and $\pi_{distorted}$ are stage total pressure ratios for the clean and distorted inlet conditions respectively. $\pi_{ave}$ is the average stage total pressure ratio for the 11 stages. The deterioration can be seen to be particularly severe in the last 2 stages.

The percentage decrease in efficiency, defined as $\left(\frac{\eta_{clean} - \eta_{distorted}}{\eta_{clean}}\right) \times 100\%$, for each stage is shown in Fig. 3.3. The deterioration in efficiency is found to be most severe in the last 2 stages.

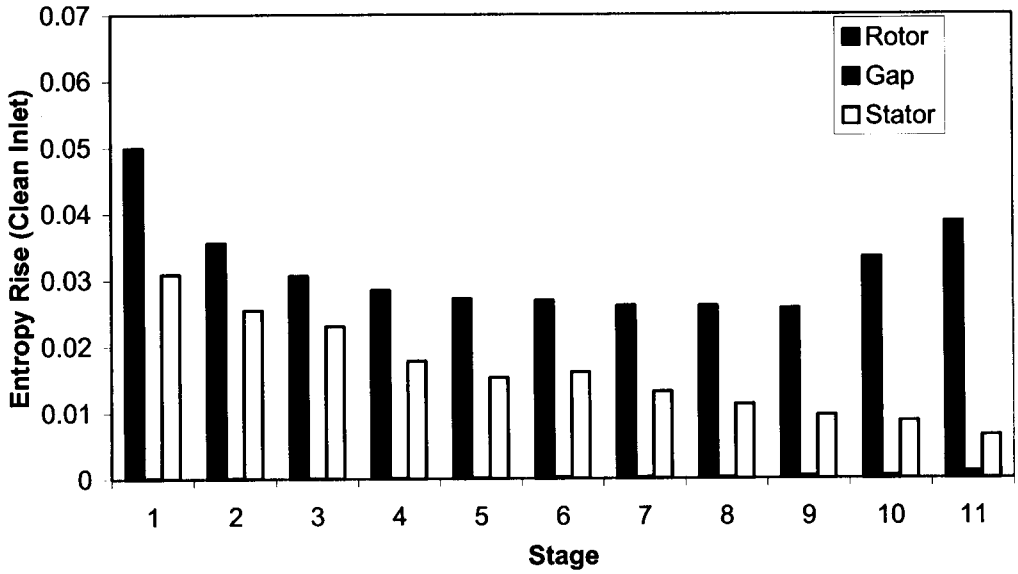


(a)

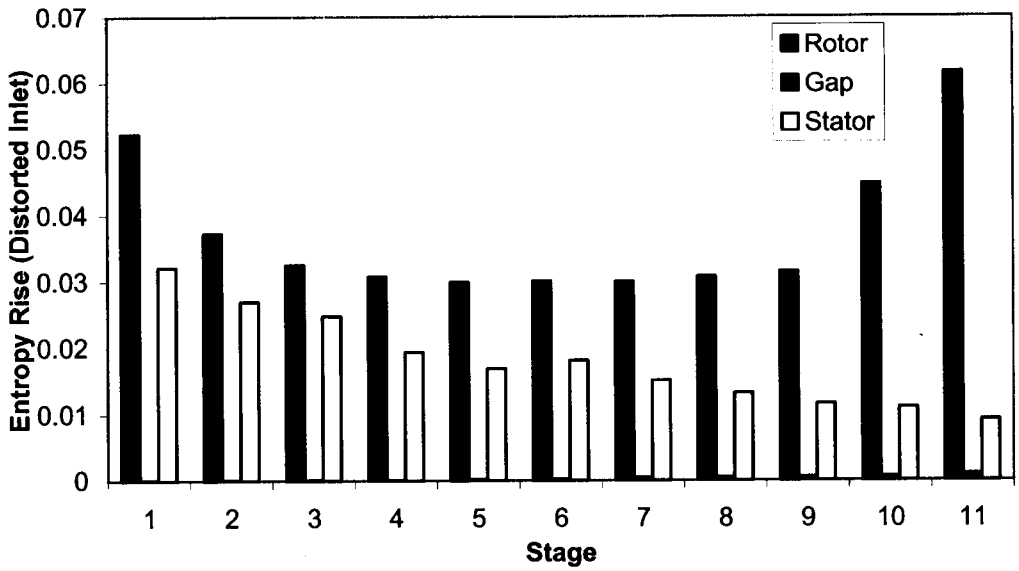


(b)

Fig. 3.1 Distribution of Entropy Rise Across the Stages for (a) Clean Inlet Flow (b) Distorted Inlet Flow

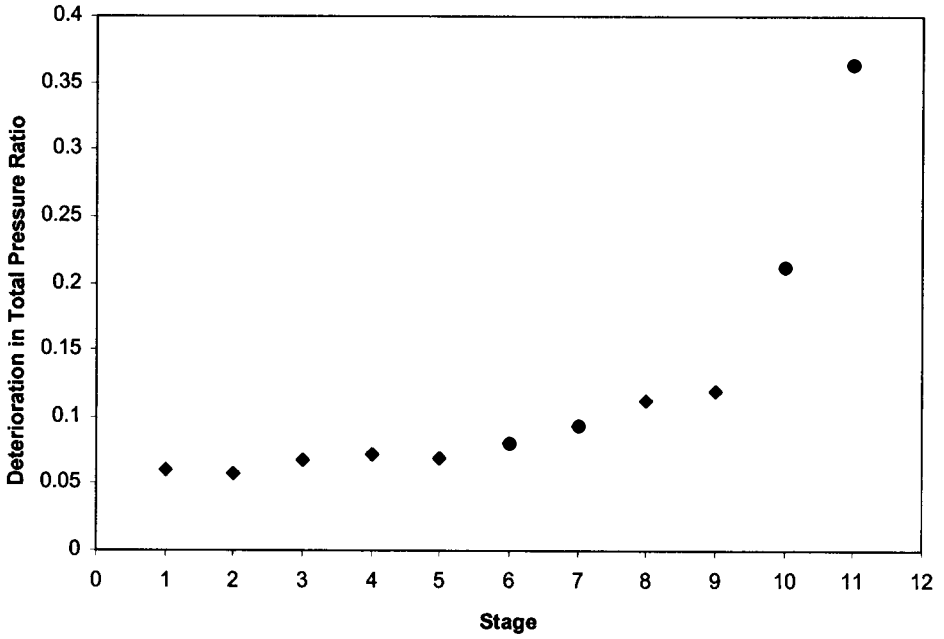


Fig. 3.2 Deterioration in Stage Total Pressure Ratio

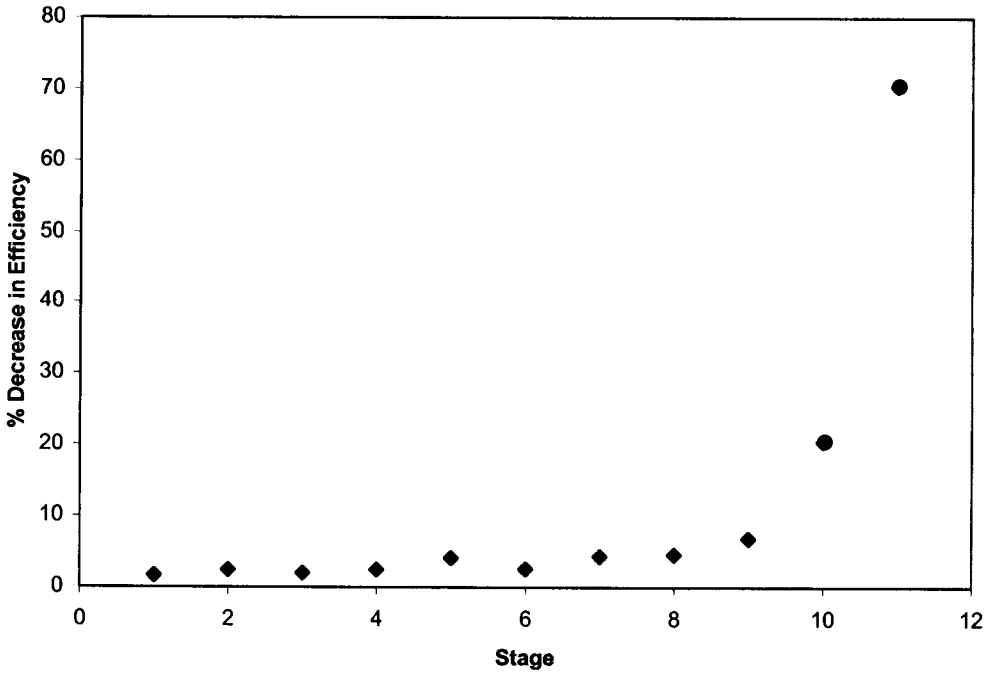


Fig. 3.3 Deterioration in Efficiency

It can be seen from the data of Figs. 3.2 and 3.3 that, although the same computational model (Eqns. (2.2) to (2.5)) is used in all the stages to compute the body forces from local flow conditions, inlet distortion produces varying degrees of performance deterioration among the stages. Certain stages are found to be insensitive to inlet distortion as compared to other stages (for example, from Figs. 3.2 and 3.3, the first 3 stages are insensitive to inlet distortion as compared to the last 2 stages). This suggests, hypothetically, that it may be possible to design a compressor that is insensitive to inlet distortion by modifying Eqns. (2.2) to (2.5) appropriately. The resulting body force representation can then be used to determine the blade geometry of a compressor whose performance does not deteriorate significantly with inlet distortion.

The particularly severe deterioration in performance in the last two stages is associated with the formation of a static pressure distortion at the IGV inlet (Section 3.3), its amplification through the first 9 stages (Section 3.4.1) and its abrupt elimination through the final 2 stages (Section 3.4.2). These will be described in the following sections as part of an analysis of the computed flow field. The physical consistency of the computed flow field will also be assessed as a means of demonstrating the utility of the body force representation for inlet distortion computations.

### 3.2 Static Pressure at Compressor Outlet

The static pressure at the compressor outlet appears to have an important effect on the manner in which the inlet distortion propagates from the upstream boundary and through the compressor.

The computed mid-radius static pressure (defined as $P/P_{ref}$ where $P_{ref}$ is reference pressure, selected to be the total pressure at the upstream boundary. Plots of static pressure will use this definition hereon) at the compressor exit is shown in Fig. 3.4 and is examined for consistency with the condition of circumferential uniformity before beginning an analysis of the propagation of the distortion. This can be seen to be uniform circumferentially as expected.

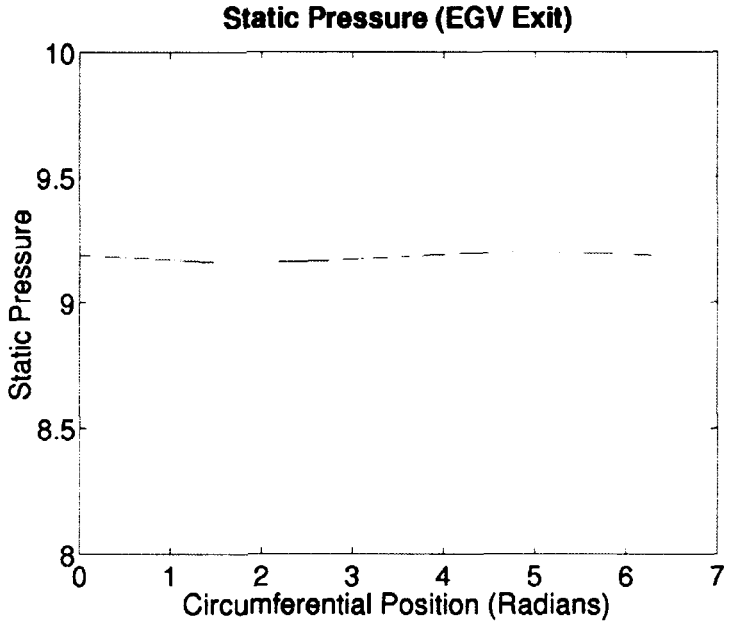


Fig. 3.4 Computed Mid-radius Static Pressure at Compressor Exit

### 3.3 Distortion Behavior from Upstream Boundary to IGV Inlet

Two essential phenomena will be analyzed for consistency in this section. The first phenomenon is the formation of a static pressure distortion at the IGV inlet. This gives rise to changes in the velocity distortion and the circumferential extent of the low total pressure section of the distortion, as well as an induced swirl. The second one is the asymmetric character of the velocity distortion at the IGV inlet.

#### 3.3.2 Formation of Static Pressure Distortion at IGV Inlet

The change in circumferential extent of the low total pressure section can be explained by first considering the result presented previously in Section 3.1, that static pressure is uniform at the compressor exit. Also, in compressors, the variation of static pressure rise $\psi$ (defined as $\frac{\Delta P_s}{\frac{1}{2}\rho U^2}$) with flow coefficient $\phi$ follows a decreasing trend as shown in Fig. 3.5.

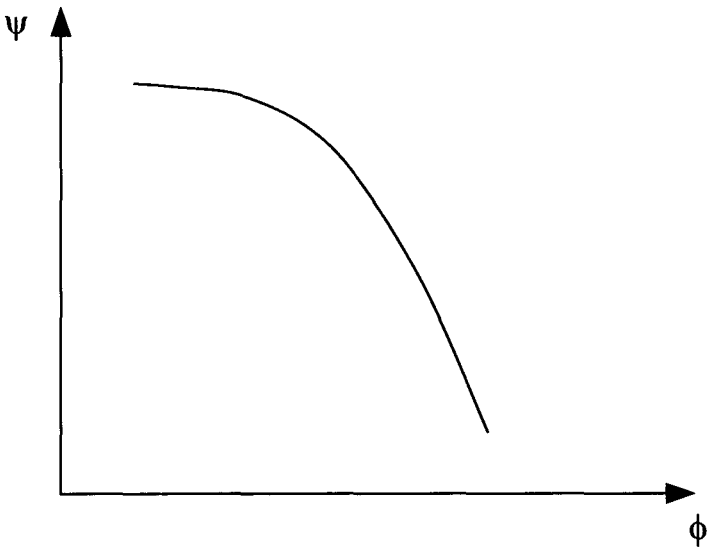


Fig. 3.5 Variation of Pressure Rise with Flow Coefficient

The region of lower flow in the distorted sector corresponds to higher loading, and hence static pressure there is reduced as the inlet distortion travels from the upstream boundary (where static pressure is circumferentially uniform) to the IGV inlet, leading to a static pressure distortion at the IGV inlet. The reduction in static pressure also leads to an increase in velocity (conversely, the static pressure and velocity in the high total pressure region are increased and decreased respectively), leading to an attenuation of the velocity distortion at the IGV inlet. By continuity and knowing that total pressure is convected with streamlines, the circumferential extent of the low total pressure region is expected to be reduced as it travels towards the IGV inlet, giving rise to an induced swirl.

The computed flow field is examined for consistency with the expected flow features. The computed mid-span static pressure at the IGV inlet as shown in Fig. 3.6 indicates that a static pressure distortion does indeed form at the IGV inlet. The computations also reveal the associated attenuation in the velocity distortion as shown in Fig. 3.7 which are plots of the mid-span flow coefficient at the upstream boundary (Fig. 3.7(a)) and IGV inlet (Fig.3.7(b)). The computed mid-span total pressures (defined as $P_t/P_{ref}$ where $P_{ref}$ is reference pressure, selected to be the total pressure at the upstream boundary) at the upstream boundary and the IGV inlet show consistency with the expected reduction in

circumferential extent of the low total pressure region, as indicated in Fig. 3.8. Finally, the existence of an induced swirl can be seen from the plot of mid-span flow angles at the IGV inlet, as shown in Fig. 3.9.

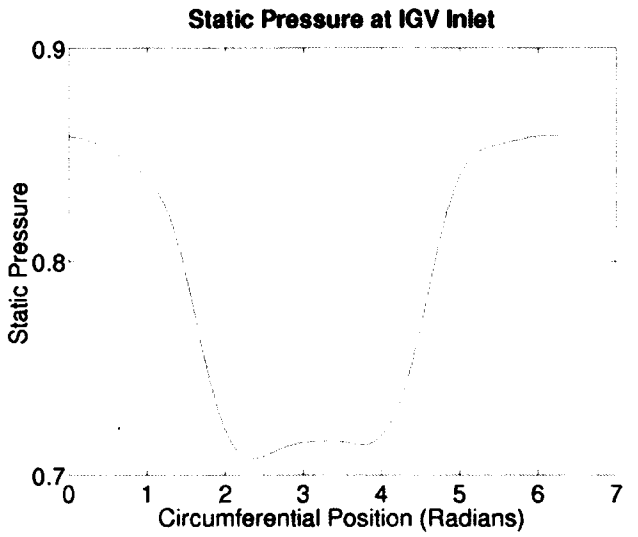


Fig. 3.6 Static Pressure Distortion at the Mid-span of the IGV Inlet

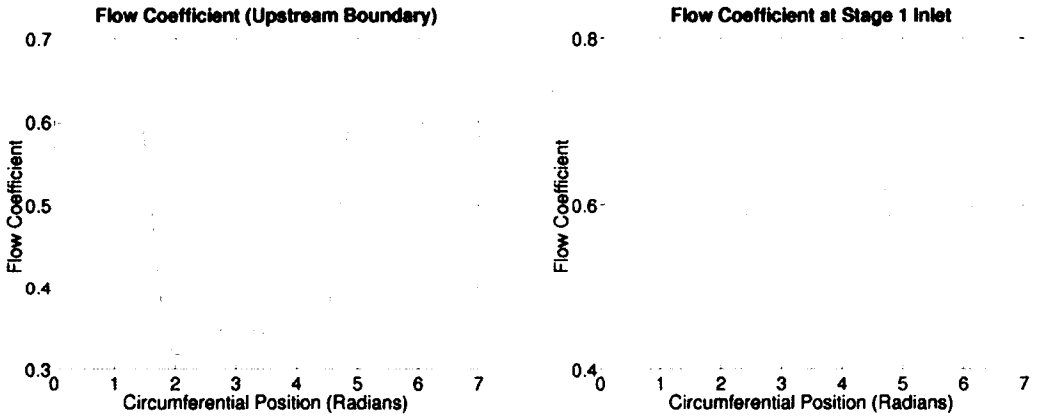


(a) (b)

Fig. 3.7 Mid-span Velocity Distributions at (a) Upstream Boundary and (b) IGV Inlet, Showing Attenuation of the Velocity Distortion at the IGV Inlet

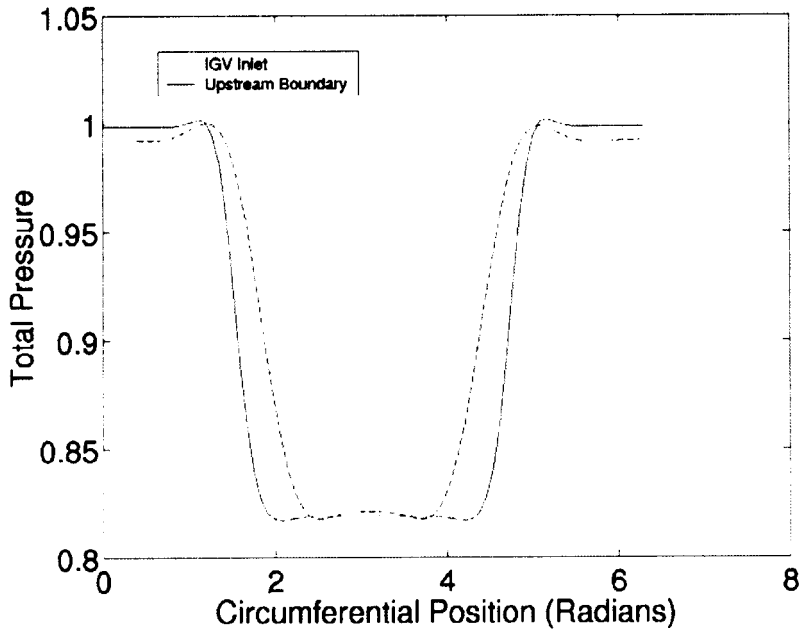


Fig. 3.8 Total Pressure at Mid-span of the IGV Inlet, Showing Reduction of Circumferential Extent of Low Total Pressure Region from Upstream Boundary to IGV Inlet.

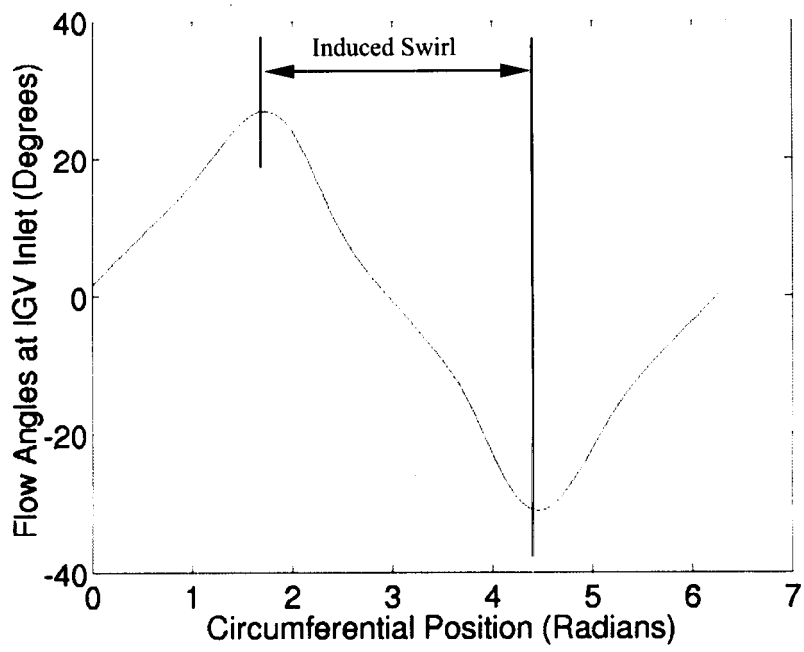


Fig. 3.9 Flow Angles at IGV Inlet, Showing Induced Swirl.

### 3.4 Distortion Propagation Through Compressor Stages

Having established the occurrence of a static pressure distortion at the IGV inlet, this section examines its propagation through the compressor stages. The manner in which the propagation occurs will lead to an understanding as to why deterioration in total pressure ratio is particularly significant in the last 2 stages as compared to the other stages (Fig. 3.1).

The key features of the propagation of the static pressure distortion are

- Amplification through the first 9 stages
- Strong attenuation within the last 2 stages, resulting in no circumferential variation at the compressor exit. It will be shown that this takes place in a manner, which leads to severe deterioration in total pressure ratio.

These features are illustrated in Fig. 3.10 which shows the mid-span static pressure range at the inlet of each stage and will be further described in Sections 3.4.1 and 3.4.2. Static pressure range is defined as $\frac{P_{max} - P_{min}}{\frac{1}{2}\rho U^2}$ at the mid-span and is used here as a measure of the severity of distortion.

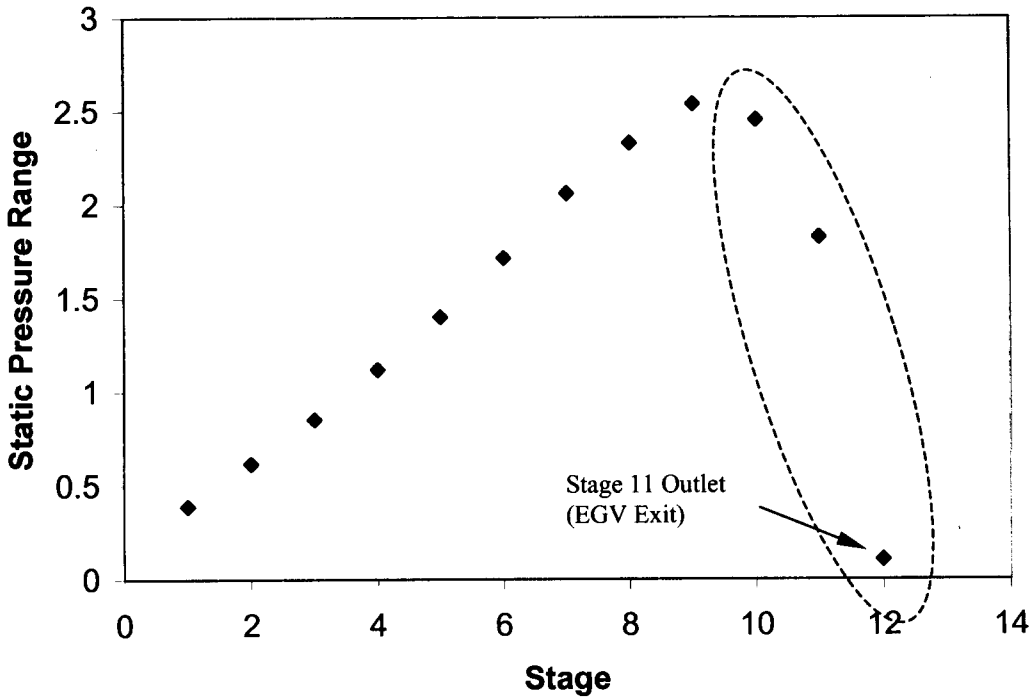


Fig. 3.10 Range of Static Pressure for Each Stage, with the Circled Region Showing Strong Attenuation in Static Pressure Distortion Across the Last 2 Stages

### 3.4.1 Amplification of Static Pressure Distortion Through First 9 Stages

The amplification effect of the static pressure distortion is observed, from inspection of data at various axial locations as shown in Fig. 3.11, to occur through the first 9 stages.

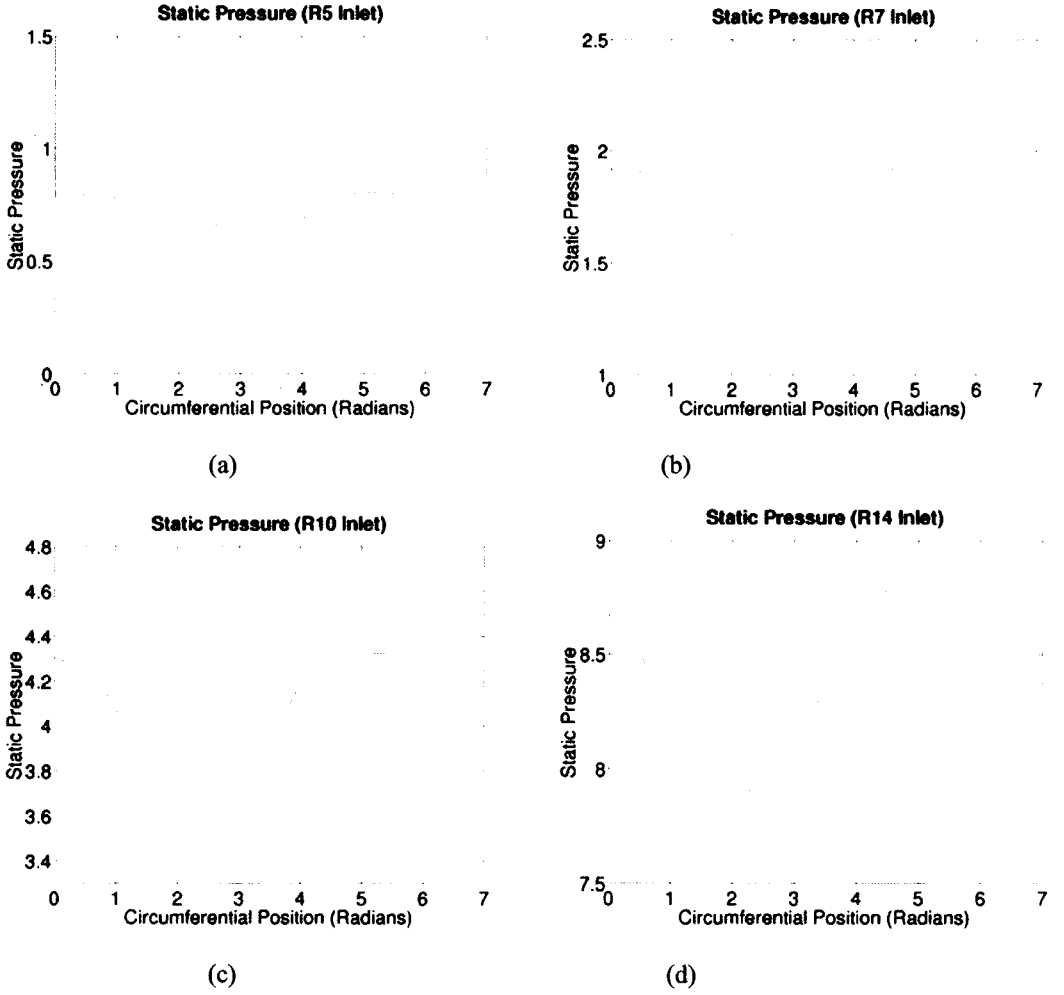


Fig. 3.11 Amplification of Static Pressure Distortion, as Shown by Mid-span Static Pressure at (a)Stage 1 Inlet, (b)Stage 3 Inlet, (c) Stage 5 Outlet and (d)Stage 9 Outlet

### 3.4.2 Attenuation of Static Pressure Distortion Through Last 2 Stages

The static pressure distortion cannot be amplified throughout the compressor, but must be attenuated at some stage since the condition of uniform static pressure at the compressor exit must be satisfied. The attenuation is achieved in the last 2 stages, most noticeably in the last stage (stage 11), as shown in Fig. 3.12 which shows the pressure distortion at mid-span being abruptly eliminated, resulting in a uniform distribution at the compressor exit (stage 11 outlet).

Closer examination of Fig. 3.12 shows that the elimination of the distortion involves static pressure reduction in certain areas. The total pressure also falls in these areas, as shown in Fig. 3.13 which plots $P_t/P_{ref}$. Upon examining the mass-averaged total pressure rise across each of the 11 stages as shown in Fig. 3.14, it is found that the mass-averaged total pressure actually falls across stage 11, resulting in the severe deterioration in total pressure ratio over the clean inlet condition, as observed previously in Fig. 3.1. It is uncertain as to how the number of stages over which amplification or attenuation takes place could be determined. Future work in this area is recommended.

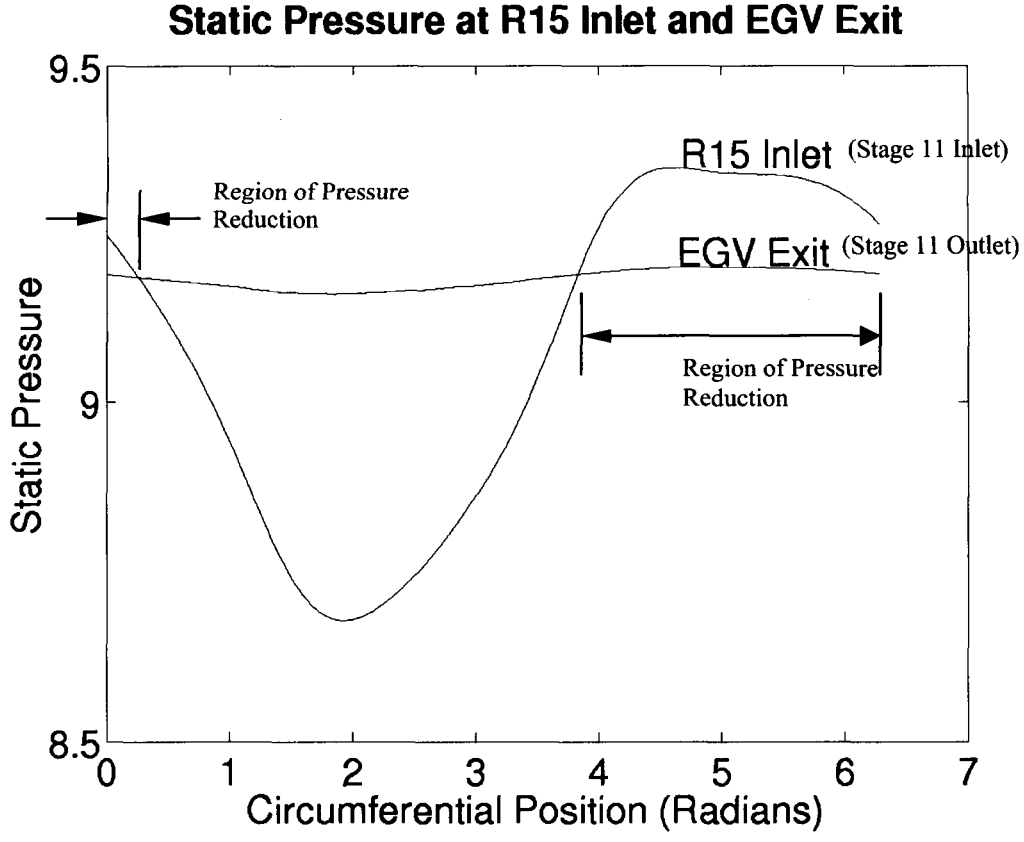


Fig. 3.12 Elimination of Static Pressure Distortion Across Stage 11, Showing Regions in which Pressure is Reduced

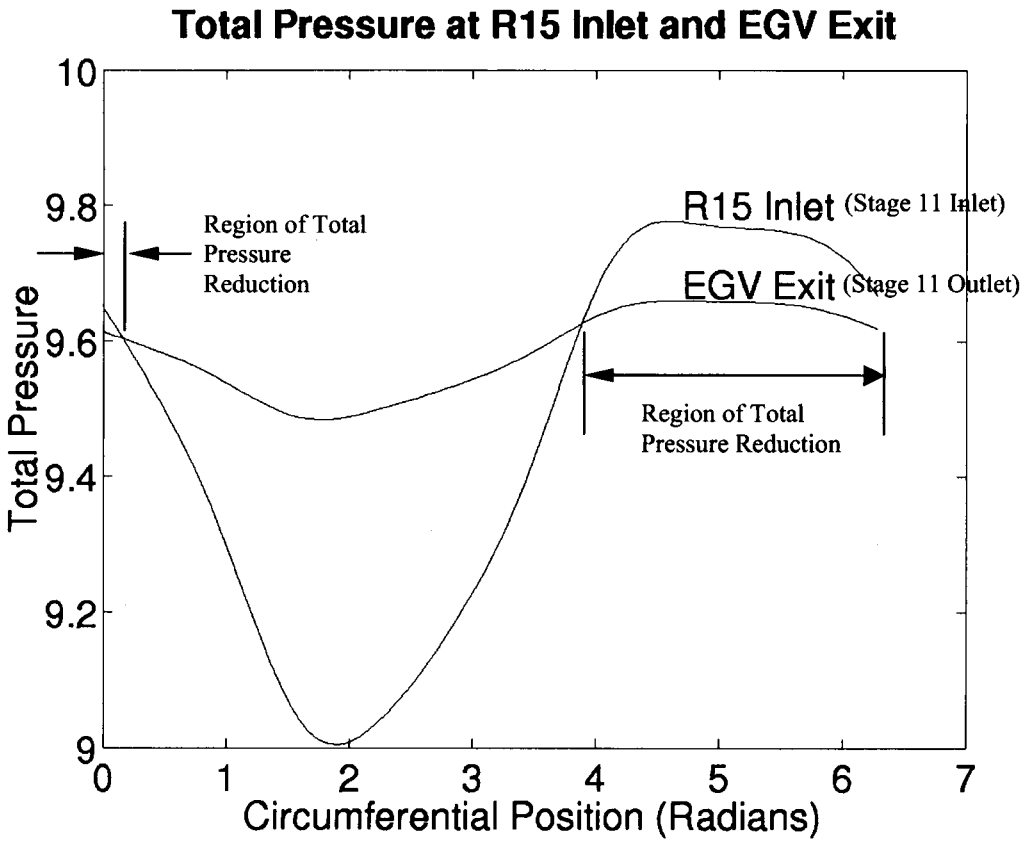


Fig. 3.13 Total Pressure at R15 Inlet and EGV Exit (Stage 11 Inlet and Outlet Respectively), Showing Regions in which Total Pressure is Reduced

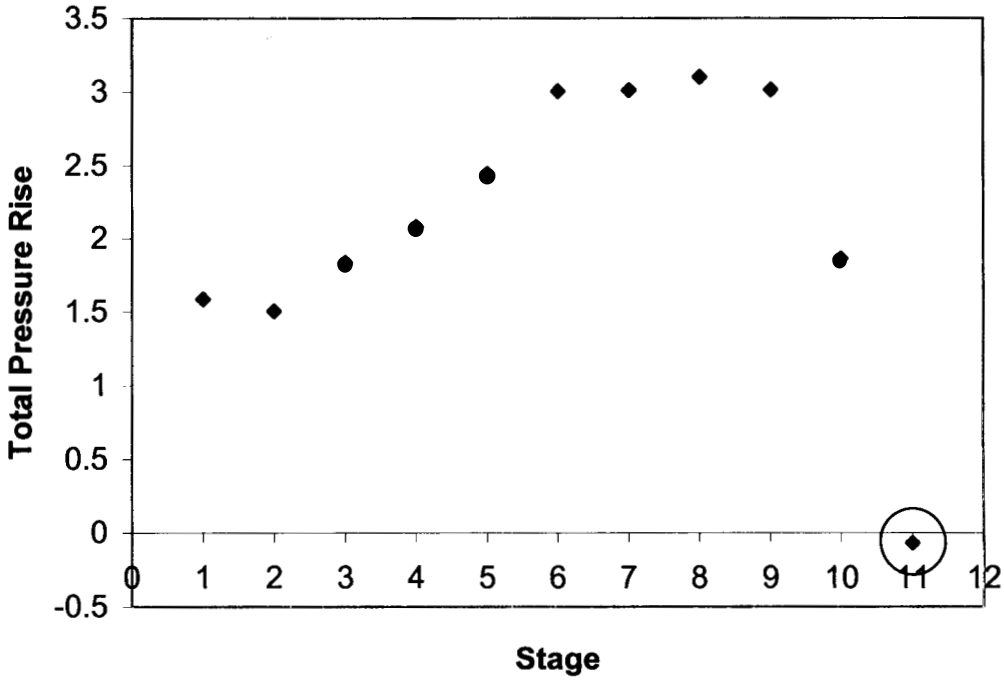


Fig. 3.14 Total Pressure Rise Across Each Stage, Showing that Total Pressure Actually Falls Across Stage 11 (Circled). Total Pressure Rise for a Stage is

Defined as $\frac{P_{t,outlet} - P_{t,inlet}}{\frac{1}{2}\rho U^2}$

### 3.5 Summary and recommendations for future work.

The concepts and the procedure developed in Task I and Task III have been used to determine the response of an eleven-stage high-speed compressor to an inlet distortion of $180^0$ circumferential extent for contrasting against its performance under uniform inlet flow. Using the computed results at the inlet to and outlet of the compressor, the computed total pressure ratio and efficiency for the clean condition are 14.22 and 76.9% respectively. Similarly, for the distorted case, these are 10.35 and 71.8% respectively, showing a deterioration in efficiency of 5%. For the eleven stage compressor examined here, the deterioration in performance has been found to be particularly severe in the last 2 stages. This suggests that the last two stages could be redesigned to alleviate the observed

deterioration thus making the compressor performance insensitive to circumferential inlet distortion.

Task IV has only addressed the performance of the eleven stage high-speed compressor in response to a circumferential inlet distortion in terms of resulting change in pressure ratio and efficiency. The next step would be the application of such a framework to address the operability issues of compressor due to inlet distortion of various types.

## *OVERALL SUMMARY*

Four separate tasks are reported. The first task is on "A Computational Model for Short Wavelength Stall Inception and Development In Multi-Stage Compressors"; the second task is on "Three-dimensional Rotating Stall Inception and Effects of Rotating Tip Clearance Asymmetry in Axial Compressors"; the third task is on "Development of an Effective Computational Methodology for Body Force Representation of High-speed Rotor 37"; and the fourth task is on "Development of Circumferential Inlet Distortion through a Representative Eleven Stage High-speed axial compressor". The common theme that threaded throughout these four tasks is the conceptual framework that consists of quantifying flow processes at the fan/compressor blade passage level to define the compressor performance characteristics needed for addressing physical phenomena such compressor aerodynamic instability and compressor response to flow distoriton with length scales larger than compressor blade-to-blade spacing at the system level. The results from these two levels can be synthesized to: (1) simulate compressor aerodynamic instability inception local to a blade rotor tip and its development from a local flow event into the nonlinear limit cycle instability that involves the entire compressor as was demonstrated in the first task; (2) determine the conditions under which compressor stability assessment based on two-dimensional model may not be adequate and the effects of self-induced flow distortion on compressor stability limit as in the second task; (3) elucidate its potential applicability for compressor map generation under uniform as well as non-uniform inlet flow given three-dimensional Navier-Stokes solution for each individual blade row as was demonstrated in the third task; and (4) quantify multistage compressor response to inlet distortion in stagnation pressure as illustrated in the fourth task;

The physical principles involved are as follows. The action of a blade row in the flow field which gives rise to pressure changes, flow turning, and energy exchanges can be achieved by replacing the blade row with an "equivalent" body force. The body force representation itself can be arrived at by averaging the flow equations across a blade passage. The key to suitable representation is the ability to characterize the body force in terms of the blade row flow dynamics. The requirements are: (i) the physical laws (mass, momentum and energy conservation) must be satisfied on a blade average basis (i.e. the effects of the pertinent blade-passage flow features must be reflected in the representation on a blade-passage average basis); (ii) there must be correct dependencies on geometry for its application in design environment; (iii) for steady-state axisymmetric flow, the blade-row must reproduce the overall pressure rise and turning angle; (iv) the body forces must be able to respond to unsteady three-dimensional flow variations; and (v) the model must be able to capture the correct time and length scales of the relevant flow events.

The concept of body force representation of blade-row is not new. However modern CFD tools now provide the means to establish such body force representation of blade-row/compressor on a rigorous basis. An implication from the results of this research program is the potential of the use of row-by-row body force representation in a multistage compressor for characterizing the operability and performance on a first principle basis.